



University  
of Glasgow

<https://theses.gla.ac.uk/30720/>

Theses digitisation:

<https://www.gla.ac.uk/myglasgow/research/enlighten/theses/digitisation/>

This is a digitised version of the original print thesis.

Copyright and moral rights for this work are retained by the author

A copy can be downloaded for personal non-commercial research or study,  
without prior permission or charge

This work cannot be reproduced or quoted extensively from without first  
obtaining permission in writing from the author

The content must not be changed in any way or sold commercially in any  
format or medium without the formal permission of the author

When referring to this work, full bibliographic details including the author,  
title, awarding institution and date of the thesis must be given

Enlighten: Theses

<https://theses.gla.ac.uk/>  
[research-enlighten@glasgow.ac.uk](mailto:research-enlighten@glasgow.ac.uk)

HARD X-RAY EMISSION  
AND  
MASS MOTION  
IN SOLAR FLARES

by

Alexander N. McClymont

Thesis  
submitted to the  
University of Glasgow  
for the Degree of  
Ph.D.

Department of Astronomy  
University of Glasgow  
Glasgow, G12 8QW

January 1976

ProQuest Number: 10760467

All rights reserved

INFORMATION TO ALL USERS

The quality of this reproduction is dependent upon the quality of the copy submitted.

In the unlikely event that the author did not send a complete manuscript and there are missing pages, these will be noted. Also, if material had to be removed, a note will indicate the deletion.



ProQuest 10760467

Published by ProQuest LLC (2018). Copyright of the Dissertation is held by the Author.

All rights reserved.

This work is protected against unauthorized copying under Title 17, United States Code  
Microform Edition © ProQuest LLC.

ProQuest LLC.  
789 East Eisenhower Parkway  
P.O. Box 1346  
Ann Arbor, MI 48106 – 1346

Thesis  
4342  
Copy 1.



*to my parents*

## SUMMARY

Solar flares are perhaps the most remarkable transient events within the solar system. A century of observation has done little to elucidate their true nature. Their secrets are hidden even from the sophisticated satellite experiments which have kept up an intensive surveillance for the last decade. These experiments have, however, produced an indigestible mass of data. From these we must try to synthesis an overall picture of the flare and identify the physical processes responsible.

In this thesis two aspects of the flare problem are considered. The first concerns hard X-ray emission during the impulsive phase of the flare. The electron trap model of the hard X-ray source is analysed in detail and the predicted directivity and polarisation of its emission found to be compatible with hard X-ray observational data. Secondly, a self-consistent model of the soft X-ray flare is developed. Mass motion, which has previously been ignored in such models, is shown to be of vital importance.

In Chapter I, the observational evidence concerning all types of flare emission is summarised. The coherency of a picture of the flare in which energetic electrons play a central part is pointed out and the significance of hard X-ray emission as an indicator of the properties of these electrons noted. Current hard X-ray source models are described in Chapter II and their predictions for the flare X-radiation outlined. Other topics of importance to the hard X-ray problem - bremsstrahlung radiation, the albedo effect and modulation of the X-ray flux - are also discussed here. Finally, the predictions of the source models are compared with observation and important areas of experimental and theoretical research suggested.

The electron trap hard X-ray source model is analysed in Chapter III. This model, whose properties have only been guessed at until now, postulates that high energy electrons are trapped in a coronal magnetic arch where they emit bremsstrahlung radiation while decaying

collisionally on the time scale of the hard X-ray burst decay. Directivity and polarisation of the emission are predicted for a variety of trapped electron distributions over energy and pitch angle. Predicted properties of the hard X-ray emission are presented in Chapters IV and V. Chapter IV is concerned with the total X-ray flux from the trap while Chapter V deals with some aspects of the spatially resolved emission, in particular the predicted "behind-the-limb" X-ray flux. In both chapters, results are compared with the observational data available and observations which could help to discriminate between this and other source models suggested.

In Chapter VI a model of the soft X-ray flare is developed. The model consists of a high density coronal filament into the centre of which energy is injected during the impulsive phase of the flare. First, the potential importance of mass motion in this situation is demonstrated by dimensional analysis. Then a numerical treatment of the fluid dynamic equations is developed. Computational results describing the evolution of the filament, under a variety of conditions, are presented in Chapter VII. Conclusions drawn from the dimensional analysis are vindicated and deeper insight into the energy transport processes operating in the filament obtained. The soft X-ray differential emission measure is examined and it is suggested that the form is compatible with that inferred from observation.

## PREFACE

This thesis is concerned with two aspects of the solar flare problem. Production of hard X-rays during the impulsive phase of a flare is the first topic. The electron trap model of the hard X-ray source, whose properties have until now only been guessed at, is analysed in detail. Directivity and polarisation of the emission are predicted for a variety of trapped electron distributions and found to be compatible with hard X-ray observational data. Secondly, a model of a filamentary soft X-ray source is constructed. The importance of mass motion, a feature previously ignored in analyses of this type, is established.

In Chapter I a general account of solar flares is given. A more specialised discussion of hard X-ray observation and theory is presented in Chapter II. The electron trap model is analysed in Chapter III and the predicted properties of hard X-ray emission are described in Chapters IV and V. In Chapter VI the filament model of the soft X-ray source is developed. The importance of mass motion is demonstrated first by dimensional analysis, then by numerical solution of the fluid dynamic equations. Computational results are presented in Chapter VII.

The original research in this thesis is contained in Chapters III - VII. The work described in Chapters VI and VII was undertaken in cooperation with Ian Craig, to whom I am grateful for many valuable and stimulating discussions.

The work of this thesis was carried out while I was a research student in the Department of Astronomy, University of Glasgow, from 1972 - 1975. I am deeply grateful to my supervisor, Dr. John C. Brown for his guidance, constant encouragement and friendship during the period of this work. I thank also Professor P.A. Sweet for his encouragement and helpful advice, and Matthew Robertson for useful discussions. I am indebted to Mrs. L. Williamson for her magical

transformation of a patchwork of illegible scribbles into the finished manuscript, and to Pat Moran of the Computing Service for much advice and assistance concerning computing facilities.

Session 1973 - 1974 was spent on leave at the Astronomy Centre, University of Sussex, and I am grateful to Professors R.J. Tayler and L. Mestel and all members of that department for their hospitality.

Lastly, I thank my parents and friends for their encouragement and moral support, and the Science Research Council for financial support.

## CONTENTS

	Page
<u>CHAPTER I</u> SOLAR FLARES	
1      Introduction	1
2      Radio Emission	3
3      Infra-Red	3
4      Optical Observations	4
5      EUV Emission	5
6      Soft X-ray Observations	6
7      Hard X-rays	7
8 $\gamma$ -ray Observations	8
9      Interplanetary Particles	9
10      Implications of Observations - Flare Theory	10
11      Bibliography	14
<u>CHAPTER II</u> HARD X-RAY SOURCE MODELS	
1      Introduction	21
2      Bremsstrahlung Radiation	22
3      The Albedo Effect	34
4      Modulation of Hard X-rays	39
5      The Thick Target Model	44
6      The Thin Target Model	47
7      The Electron Trap Model	49
8      The Thermal Model	52
9      The Reacceleration Model	53
10      Hard X-rays - Theory and Practice	53
<u>CHAPTER III</u> THE ELECTRON TRAP MODEL - ANALYSIS	
1      Introduction	61
2      Discussion of Previous Work	68
3      The Trapping Magnetic Field	84
4      The Dipole Field	92
5      The Linecharges Field	94
6      The Monopoles Field	98
7      The Trapped Electron Distribution Function	105

		Page
8	X-ray Emission from an Assembly of Trapped Electrons	109
9	Polarisation of X-ray Emission from the Trap	118
10	The Model Atmosphere	130
11	Summary of Analysis and Computational Procedure	133
<u>CHAPTER IV</u>	THE ELECTRON TRAP MODEL - DIRECTIVITY AND POLARISATION OF X-RAY EMISSION	
1	Introduction	143
2	Preliminary Investigations	144
3	Electron Distribution (i)	156
4	Electron Distribution (ii)	174
5	Electron Distribution (iii)	187
6	Electron Distribution (iv)	191
7	Summary and Conclusions	208
8	Comparison of Results with Observation	210
<u>CHAPTER V</u>	THE ELECTRON TRAP MODEL - SPATIAL DISTRIBUTION OF X-RAY FLUX AND POLARISATION	
1	Introduction	215
2	Electron Distribution (ii)	219
3	Electron Distribution (iii)	224
4	Electron Distribution (iv)	228
5	Summary and Comparison with Observation	231
<u>CHAPTER VI</u>	MASS MOTION IN A HEATED FILAMENT - ANALYSIS AND COMPUTATIONAL PROCEDURE	
1	Introduction	235
2	Discussion of Previous Work	236
3	The Importance of Mass Motion	238
4	Definition of the Problem	241
5	The Equations	249
6	Numerical Method for Solution of the Equations	256
7	Formulation of the Finite Difference Equations	264
8	Solution of the Finite Difference Equations	270

	Page
<u>CHAPTER VII</u> MASS MOTION IN A HEATED FILAMENT - COMPUTATIONAL RESULTS	
1 Introduction	275
2 Preliminary Investigations	276
3 Model I	282
4 Model II	292
5 Model III	299
6 Model IV	303
7 Energy Transport in the Filament	307
8 The Soft X-ray Differential Emission Measure	320
9 Electron Heating	331
10 Summary, Discussion and Comparison with Observation	335
<u>REFERENCES</u>	346

CHAPTER ISOLAR FLARES1. INTRODUCTION

Introducing a paper on the structure of the sun in 1895, E.J. Wilczynski wrote "almost every student of solar physics has his own theory, and usually he himself is the only one that believes in it". Our knowledge of the internal structure of the sun has vastly improved since the turn of the century and despite recent controversy over the solar neutrino flux, most astronomers accept that the basic physics of stellar structure is well understood.

But the above quoted statement exactly describes the state of the study of surface phenomena on the sun today. In particular, solar flares. Although the existence of solar flares has been recognised since their first detection by Hodgson (1859) and Carrington (1859), a century of observation and theoretical study has done little to elucidate the nature of the mechanism which gives rise to these violent events.

The rate of collection of data on solar flares lurched upwards with the dawning of the age of Technology. Observations outside the optical window became possible when radio-astronomy got under way in the 1920's, and the recent innovation of satellite platforms gave experimenters their first opportunity to study emission from flares in the EUV, soft X-ray, hard X-ray and  $\gamma$ -ray bands.

In addition to this extension of the observable range of electromagnetic radiation from 4 decades to 10 decades, the ability to place instruments outside the Earth's atmosphere has also enabled particle emission from the sun to be studied directly for the first time.

Solar flares are notable for their diversity. A flare which covers a great area of the photosphere or is brighter in  $H\alpha$  light than another may not produce a greater X-ray flux nor eject a larger

plasma cloud into inter-planetary space. The areal extent and brightness of a flare in  $H\alpha$  emission is still used to classify flares because  $H\alpha$  was the best available means of observing flares until comparatively recently. However observations of the flare in other energy bands now show that this historically important means of classification is only a rough guide to the character of the individual flare.

The total energy release during a large flare can be as high as  $3 \times 10^{32}$  ergs. Approximately half of this energy is released in the impulsive phase of the flare, which lasts for a few minutes and the rest is released slowly over a period of hours in the decay phase. The minimum energy observed appears to be limited only by the detection capabilities of instrumentation. It would perhaps give some clue to the mechanism responsible for the triggering of flares if a minimum energy cut-off were found, but even very small point brightenings, which occur very frequently, exhibit flare-like properties. Large flares are perhaps easier to study theoretically than small flares since, although they occur infrequently, there is greater uniformity in their characteristics.

In the following sections a brief description of the observational techniques and results in each regime of the electromagnetic spectrum is given, in order of increasing quantum energy. A summary of the observations of particle emission follows. Then all the observations are drawn together to synthesise an overall picture of the flare. The relevance of the work described in this thesis to the flare problem is noted. In the following sections I have tried to present the information in a readable form by giving few references in the text. The final section of this chapter is a bibliography giving a selection of references to work in each area. These are listed in chronological order within each subdivision. These references are not listed in the bibliography at the end of the thesis unless they are referred to elsewhere.

## 2. RADIO EMISSION

Although the amount of energy emitted by a flare at wavelengths longer than 1 mm is only  $\sim 10^{25}$  erg - of order  $10^{-7}$  of the flare energy - these emissions are a sensitive indicator of the presence of energetic particles in the flare.

The most important type of radio emission for this purpose is the microwave burst which is often observed in the impulsive phase of a flare. This form of emission is thought to be gyro-synchrotron radiation from electrons of energy  $\sim 100$  keV - 1000 keV spiralling in a coronal magnetic field. We are particularly interested in the microwave burst since it is highly correlated with the hard X-ray emission, which a major part of this thesis is concerned with. This correlation is discussed further in § 10 and in Chapter III.

Type III bursts are also indicative of particle acceleration in the flare, as it is generally accepted that this type of emission is due to the excitation of plasma oscillations in the corona by streams of fast ( $\sim 100$  keV) electrons.

## 3. INFRA-RED

Although no observations of infra-red flare emission have been reported, Ohki and Hudson (1975) have studied possible sources of infra-red emission, and conclude that the detection of radiation in this waveband is a strong possibility. They show that if the energy spectrum of the electrons which produce synchrotron microwave emission extends to high enough energy ( $\sim 10$  MeV) detectable emission should be produced at the long wavelength end of the terrestrial atmosphere window (350 $\mu$ ). Another possible impulsive source of infra-red emission is the long wavelength tail of the white light optical continuum, which may be more easily detectable than in the optical region. Considering the gradual component of the flare,

they suggest that emission from hot coronal X-ray sources and from the  $H\alpha$  flare may be detectable in the infra-red waveband.

#### 4. OPTICAL OBSERVATIONS

White light continuum emission from a flare in 1859 made possible its detection by Carrington and Hodgson. But such flares are unusual. Two theories have been proposed to account for these events. Stein & Nay (1963) suggested that the white light was synchrotron radiation from very high energy electrons, but it is now believed to be more likely that overheating of the photosphere to produce enhanced emission, possibly by a beam of high energy electrons, is responsible. Both of these processes require that a considerable fraction of the flare energy is carried by very high energy electrons, which may be the reason for the rarity of white light events.

The energy in optical flare emission is estimated to be  $\approx 10^{31}$  ergs in a large flare, which is  $\lesssim 10\%$  of the total energy in a flare of this size.

Historically, the most important wavelength for flare observations is the  $H\alpha$  line. Narrowband optical observations in this region of the spectrum reveal a wealth of detail of the spatial structure in the flare region, but the information is difficult to interpret in an objective manner.

Two important results have been obtained by optical observation. Firstly, the Balmer lines are found to be greatly broadened in a flare. Stark broadening caused by enhanced electron density is generally accepted as being the cause of this phenomena. The degree of broadening implies an electron density of at least  $10^{13} \text{ cm}^{-3}$  in the flare region, and together with data on line intensities indicates that the electron temperature is slightly less than  $10^4 \text{ K}$  in disk flares, where the deeper layers of the flare are seen. The temperature

is higher for limb flares, in which the lower regions of the flare are obscured due to the greater optical thickness. These data also imply that the emitting layer is very thin. Thus the optical flare is probably highly filamented.

A second important aspect of  $H\alpha$  observations arises because the optical waveband is at present the only region in the electromagnetic spectrum where high angular resolution is obtainable.  $H\alpha$  filter-grams of limb flares reveal motions in the flaring chromosphere and corona. Thus at least some of the flare energy appears in dynamical form. The most spectacular form of mass motion in an energetic sense is the ejection into interplanetary space, at a velocity of up to  $1000 \text{ km sec}^{-1}$ , of a plasma blob whose mass can be of order  $10^{16} \text{ gm}$  in a large flare. This can carry off half the total flare energy. Research on mass motion appears to be largely phenomenological, typical observations being described in the Proceedings of the Ninth Nobel Symposium (1968).

Perhaps the most important use of optical observations is in the measurement of chromospheric magnetic field strengths, which can be determined by measuring the Zeeman splitting of optical lines. These potentially important observations are unfortunately somewhat restricted in usefulness as only the longitudinal component of the magnetic field can be confidently inferred. Furthermore, fine structure in the magnetic field pattern is seen in high resolution magneto-grams. Lower resolution observations can be misleading as they show only a smeared out average field strength, which may be considerably lower than the true field strength at a point if the magnetic flux is concentrated in narrow regions.

## 5. EUV EMISSION

Radiation in the far ultra-violet ( $100 \text{ \AA} \lesssim \lambda \lesssim 1000 \text{ \AA}$ ) during flares has been observed extensively by rocket and satellite experiments during the last decade, in particular by the much publicised Skylab

mission. Sudden frequency deviations in terrestrial radio signals caused by ionisation in the Earth's upper atmosphere have also been used to infer EUV fluxes by Donnelly (1967). SFD measurements are obviously less expensive to perform than satellite experiments, but have two disadvantages - only relative EUV fluxes can be inferred accurately and spatial resolution is unobtainable.

EUV emission is modulated rapidly, being closely correlated with the time variation of the hard X-ray flux. Therefore the mechanisms which energise the two events must be closely coupled. It is possible that the EUV reion is heated by X-ray emitting non-thermal electrons. Kane and Donnelly (1971) show that the EUV emission is recombination radiation, which must arise in a region of density greater than  $10^{11} \text{ cm}^{-3}$  in order that the modulation be as rapid as that observed. Estimates of the total energy in EUV are comparable with that of the optical flare.

## 6. SOFT X-RAY OBSERVATIONS

Soft X-ray emission from flares in the waveband 2-30 Å has been observed extensively in both line and continuum during the last decade. Recently, spatially resolved pictures have been obtained using pinhole cameras, collimating systems and grazing incidence telescopes. The continuum soft X-ray emission is thermal bremsstrahlung while line emission originates from highly ionised heavy ions. Observation indicates that the emission arises in a multi-thermal plasma at temperatures around  $10^7$  K. Source densities are thought to lie in the range  $10^{10} - 10^{12} \text{ cm}^{-3}$ , although values as high as  $10^{13} \text{ cm}^{-3}$  have been proposed. The source volume is estimated to be  $10^{25} - 10^{29} \text{ cm}^3$ , which is certainly compatible with typical flare volumes of  $10^{29} \text{ cm}^3$ .

The soft X-ray flux follows the same pattern of development as the optical flare. The energy inferred to reside in the hot plasma is found to correlate with the time-integrated microwave and hard X-ray flux. This suggests that the optical and soft X-ray

flares are heated by the same mechanism which gives rise to the hard X-ray and microwave burst. If the hard X-ray emission is assumed to be due to bremsstrahlung of non-thermal electrons, the energy carried by these is found to be sufficient to heat the soft X-ray and optical flares, providing a low energy cut off in the non-thermal electron energy spectrum of around 10 KeV is assumed. It is still not clear from observation where this low energy cut-off occurs, but Kahler & Kreplin (1971) claim that the non-thermal spectrum extends down to less than 5 KeV in some cases.

## 7. HARD X-RAYS

Since a large part of this thesis is concerned with the development of the electron trap hard X-ray source model, hard X-ray flare observations are discussed in more detail in Chapter II. Only a brief summary is given here.

Photons in the energy band 10-500 KeV have been observed by balloon, rocket and satellite experiments since 1959. Measurements, using scintillation counters, are broad-band ( $\sim 50\%$  spectral resolution) and have a time resolution of  $\gtrsim 1$  second. An exciting possibility which has now become technically feasible is the direct spatial resolution of hard X-rays. This development should add considerably to our knowledge of the X-ray source structure. The only evidence available at present concerning the size of the X-ray source is the observation by Takakura et al (1971) that the emission is localised in a region of  $\lesssim 5 \times 10^9$  cm in one horizontal dimension.

The hard X-ray burst is one aspect of the impulsive phase of the flare. Photon flux falls steeply with increasing energy, the spectrum approximating to a power law. Many observations show a steepening of the spectrum by several powers at some point in the spectrum, usually around 70-100 KeV. Modulation of the X-ray flux with a period of  $\sim 30$  seconds has been found in major events. Hoyng et al (1975) have obtained the dynamic spectrum of the photon flux in the large flare of 4 August 1972, which shows periodicities

of 30, 60 and 120 seconds. These oscillations, which are all present near the start of the burst, die out in order of decreasing frequency.

First measurements of the polarisation of hard X-ray emission obtained by Tindo et al (1970). The large degree of polarisation found ( $\sim 10 - 40\%$ ) serves to confirm the non-thermal nature of the hard X-ray generation mechanism. The few results available are suggestive but not conclusive and confirmation of these observations is urgently required.

## 8. $\gamma$ -RAY OBSERVATIONS

Measurements of continuum emission up to 7 MeV have now been obtained. Gruber (1973) found that the photon spectrum of a large flare could be described by a power law of spectral index  $\sim 3.2$  from 25 KeV to 600 KeV, at which point the spectrum hardened, the spectral index falling to  $\sim 1.2$ . Similar results were obtained by Suri et al (1975), who observed the large flare of 4 August 1972. They found that the power law spectrum in the hard X-ray regime extended unbroken up to 700 KeV. Above this energy the spectrum flattened before falling off again around 3 MeV.

Chupp et al (1973) detected line emission at 0.51 MeV and 2.2 MeV, which they attributed to electron-positron annihilation and to deuteron formation respectively. Unidentified statistically significant peaks were also found at 1.6, 4.4 and 6.1 MeV.

The measured line strength at 0.51 MeV and 2.2 MeV, and an upper limit to the possible contribution of unresolved lines in the "bump" in the spectrum obtained by Suri et al indicate that the energy carried by high-energy protons is small compared to the flare energy.

## 9. INTERPLANETARY PARTICLES

The ejection of particles into interplanetary space during a flare occurs in two forms. Firstly, individual particles of high energy have been detected by satellite borne instruments. The amount of energy carried by these particles is thought to be  $\sim 10^{30}$  ergs in a large flare, that is,  $\sim 1\%$  of the total flare energy. However, such observations are important as they give direct confirmation of the existence of non-thermal processes in flares. When the transit time of the particles is allowed for, it is found that they must have been accelerated close to the flash phase of the flare.

Electrons with energies  $\sim 100$  KeV appear to have a power law spectrum similar to that required to explain the hard X-ray burst in terms of electron-proton bremsstrahlung. Lin & Datlowe (1973) have examined the relationship between the spectra of interplanetary electrons and the corresponding X-ray burst. They conclude that the thin target X-ray source model (see Chapter II) best fits these observations. However, it must be noted that the number of interplanetary electrons is much smaller than the number required to produce the hard X-ray burst, which suggests that electrons which do escape are atypical of those in the flare region.

The second type of particle emission from flares takes the form of a blob of plasma which is ejected at a velocity of  $\sim 10^3$  km  $\text{sec}^{-1}$ . The interaction of this plasma with the Earth's magnetosphere produces the well-known flare associated terrestrial magnetic storms. Although individual particle energies in the plasma cloud are  $\sim 1$  KeV, the large mass, estimated to be  $\sim 5 \times 10^{16}$  gm, and large macroscopic velocity of the cloud gives it a kinetic energy comparable to the total flare energy.

## 10. IMPLICATIONS OF OBSERVATIONS - FLARE THEORY

The major implications of the observations described in the previous sections may be summarised as follows.

- (a) Microwave emission implies the presence of non-thermal electrons with energies of  $\sim 100$  KeV.
- (b) Optical observations show details of chromospheric structure and indicate that the emission arises in a region of density  $\sim 10^{13}$   $\text{cm}^{-3}$  at temperature  $\sim 10^4$  K. They also allow the inference of photospheric magnetic fields.
- (c) EUV emission is closely correlated with the hard X-ray burst and arises in a region of density  $\sim 10^{11}$   $\text{cm}^{-3}$  and temperature  $\sim 10^5$  K.
- (d) Soft X-ray observations indicate the existence of a multi-thermal plasma at temperatures  $\sim 10^7$  K. The source density is probably  $10^{10} - 10^{12}$   $\text{cm}^{-3}$ .
- (e) Hard X-ray emission is thought to be bremsstrahlung radiation from electrons in the energy range 10-200 KeV. A very large number of electrons ( $> 10^{39}$  in a large burst) is required to explain the observed X-ray flux. These electrons probably carry enough energy to heat the soft X-ray and optical flares.
- (f)  $\gamma$ -ray continuum emission suggests that the energy spectrum of hard X-ray producing electrons extends up to  $\sim 1$  MeV. Line emission indicates that nuclear interactions take place in flares.
- (g) Interplanetary electrons have a similar spectrum to those thought to produce hard X-ray emission, but their numbers are much smaller. The ejection of a large blob of plasma from a flare can carry off half the total flare energy.

The evolution of various type of flare emission are shown schematically in Figure 10.1. Microwave, EUV, hard X-ray and  $\gamma$ -ray emission have a spiky, "impulsive" time profile. Although these profiles usually appear to be very similar, details such as the exact time of occurrence, or the amplitude, of each spike do not always match precisely.

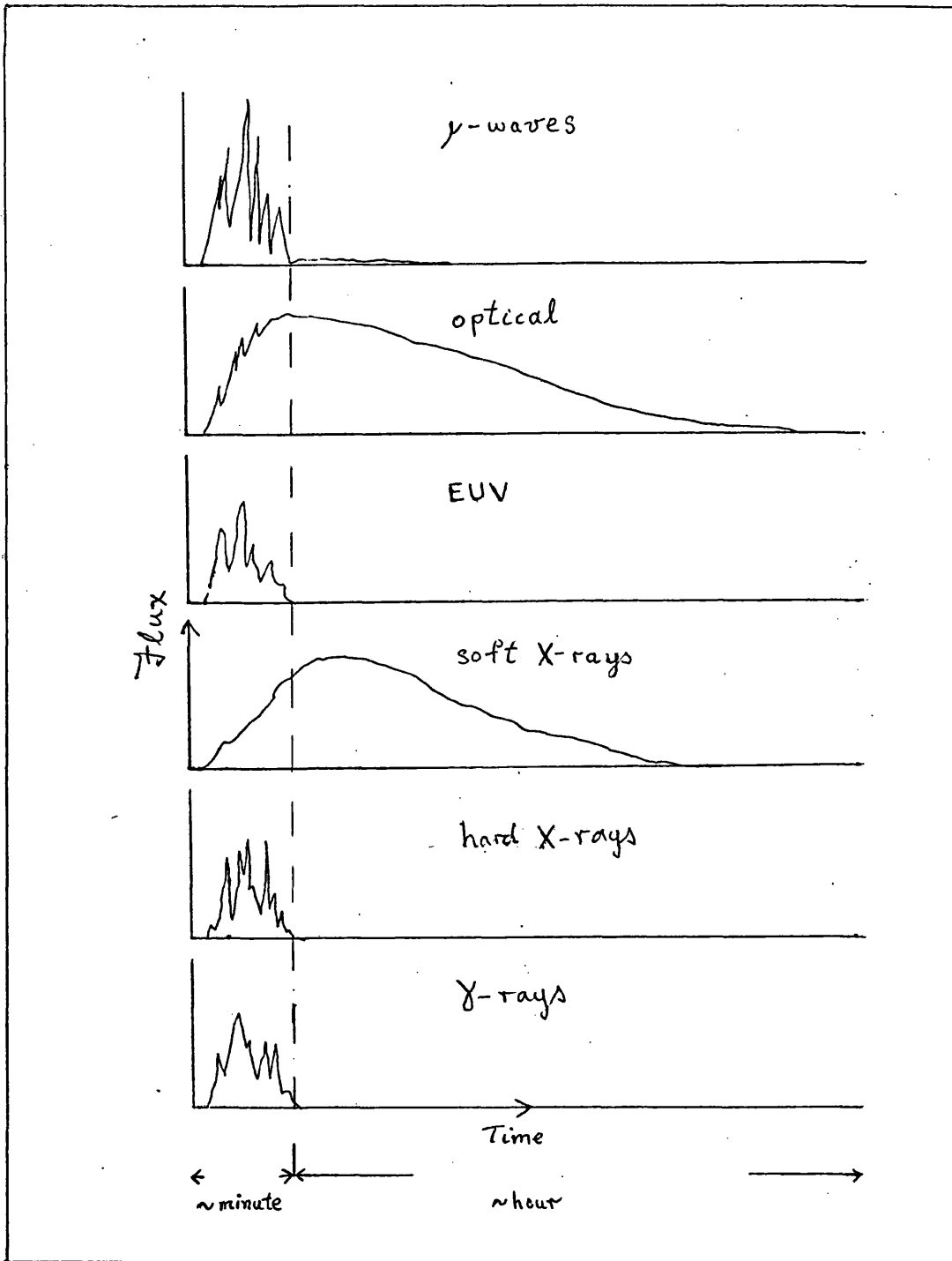


Figure 10.1 Schematic illustration of the evolution of electro-magnetic radiation from a flare, as a function of photon energy. The impulsive phase, lasting a few minutes, is followed by a long decay phase.

The similarity of these profiles suggests that the emissions have a common origin. The microwave burst implies the presence of non-thermal electrons, which also give a feasible explanation of the hard X-ray burst. Only  $\sim 10^{-5}$  of the energy carried by non-thermal electrons can be emitted as hard X-radiation because electron-electron collisions absorb the bulk of it, thereby heating the flare plasma. Since the non-thermal energy inferred from hard X-ray data is usually comparable with the total flare energy, it is reasonable to suppose that the thermal flare emissions - EUV, soft X-rays and optical - are all a direct consequence of heating of the flare by non-thermal electrons.

This hypothesis implies the acceleration of a very large number of electrons to high energy. Acceleration of particles in a region of reconnecting magnetic field is usually invoked. It is generally accepted that the energy expended in a large flare can be stored in a small deviation of the pre-flare magnetic field from a potential configuration, but little is known of the process which converts magnetic energy to particle kinetic energy. Flare-associated high energy protons ( $\sim$ GeV) are detected in interplanetary space, but observations of the flare  $\gamma$ -ray flux suggest that the total non-thermal proton energy is much smaller than the inferred electron energy. Therefore a requirement of the acceleration mechanism is that it should accelerate many electrons to intermediate energies and a small number of protons to high energy.

Energy can only be released in a region of magnetic field reconnection if the surrounding atmosphere is ionised so that currents may flow. Therefore the corona is regarded as the most suitable site for particle acceleration. Paradoxically, the corona is the part of the solar atmosphere least able to supply the vast number of electrons needed on the "non-thermal electron" hypothesis outlined above. An upward streaming of electrons from the chromosphere to replace those accelerated must be invoked. It is not yet clear whether such electron streams can exist in the solar atmosphere, nor, for that matter, whether acceleration at a neutral sheet can produce fast electrons at a high enough rate.

Most aspects of the flare fall neatly into place in the picture given above, but doubts have been expressed because of the large number of non-thermal electrons required and the unproven ability of magnetic field annihilation to release energy fast enough. Alternative flare theories have been proposed in which the photospheric acoustic flux, which is suppressed in sunspots, provides the flare energy. The accumulation of only one percent of the "missing" flux would be sufficient to supply a hundred small flares or one large flare per day.

Flares usually develop in regions where the gradient of the photospheric magnetic field is large, and in particular are associated with the "neutral line" separating regions of opposite magnetic polarity in complex sunspot groups. This fact, together with the observation that the topology of the post-flare magnetic field is frequently simpler than that existing prior to the flare, provides support for the schematic description given above, in which fast electrons play a leading part. The study of characteristics of the non-thermal electrons is clearly of key importance to the establishment of this theory.

This thesis is concerned with two manifestations of non-thermal electrons. Hard X-ray emission, produced by electron-proton bremsstrahlung, gives the most direct information concerning these. Gyro-synchrotron microwave radiation from fast electrons is sensitive to the poorly known magnetic field structure of the source, while interplanetary electrons probably have their spectrum modified during escape from the flare region and passage through the corona. But hard X-ray emission should provide an indication of the true properties of the non-thermal electrons in the flare itself. In Chapter II, current models of the hard X-ray source are discussed and their predictions compared with observation. One of these models, the electron trap, which has not previously been treated theoretically, is analysed in detail in Chapters III - V. In Chapters VI and VII a model of the soft X-ray flare heated by fast electrons is constructed. Implications for the role of non-thermal electrons in this context are

less direct, but the initial evolution of the soft X-ray flare predicted by the model is shown to be compatible with observation.

## 11. BIBLIOGRAPHY

### The state of solar physics

Wilczynski, E.J. 1895: *Astrophys. J.* 1, 112

### Radio

#### Reviews:-

Wild, J.P., Smerd, S.F. & Weiss, A.A. 1963: *Ann.Rev. Astron. Astrophys.* 1, 291.

Takakura, T. 1967: *Solar Phys.* 1, 304.

Takakura, T. 1969: in de Jager & Svestka (eds) Solar Flares & Space Research p 165.

Labrum, N.R. 1972: in McIntosh & Dryer (eds) Solar Activity Observation and Reduction, p 93.

#### Observations:-

Wild, J.P. 1969: *Solar Phys.* 9, 260.

Wild, J.P. 1970: *Proc.Astron.Soc.Australia* 1, 365.

Pick M., Martes, M.J., Axion F & Mercier, C. 1975: *Solar Phys.* 42, 461.

Rosenberg, H. 1975: *Solar Phys.* 42, 247.

### Infra-Red

Okhi, K. & Hudson, H.S., 1975: *Solar Phys.* 43, 405.

### Optical

#### White light continuum emission:-

Carrington, R.C., 1859: *MNRAS* 20, 13.

Hodgson, R., 1859: *MNRAS* 20, 15.

Stein, W.A. & Nay, E.P. 1963: *J. Geophys. Res.* 68, 65.

Svestka, Z. 1966: *Space Sci. Rev.* 5, 388.

de Mastus H. & Stover, R.R. 1967: *Publ. Astron. Soc. Pacific* 79, 615.

- Najita, K. & Orrall, F.Q. 1970, Solar Phys. 15, 176.
- McIntosh, P.S. & Donnelly, R.F. 1972: Solar Phys. 23, 444.
- Hudson, H. 1972: Solar Phys. 24, 414.
- Mackado, M.E. & Rust, D.M. 1974: Solar Phys. 38, 499.

Classification of Flares:-

- Smith, H.J. & Smith, E.P. 1963: Solar Flares, McMillan.
- Svestka, Z. 1969: in de Jager & Svestka (eds). Solar Flares and Space Research, p.16.

Energy in the Optical Flare:-

- Ellison, M.A. 1963: Planet. Space Sci., 11, 597.
- Bruzek, A. 1967: in Xanthakis (ed) Solar Physics, Interscience p.301.
- Dizer, M. 1969: Solar Phys. 10, 416.

Inference of density and dimensions of the optical flare:-

- Suemoto Z. & Hiei E. 1959: Publ. Astron. Soc. Japan, 11, 185.
- de Feiter, L.D. 1966: Analysis of the Balmer Spectrum of Solar Flares, Reidel.
- Svestka, Z. 1969: op cit.
- Svestka, Z. 1972: Ann.Rev. Astron. & Astrophys. 10, 1.

Mass motion in flares:-

- Zirin, H. 1966: The Solar Atmosphere, Blaisdell, Waltham, Mass.
- Tandberg-Haussen, E. 1967: Solar Activity, Blaisdell, Waltham, Mass.
- Ohman (ed) 1968: Mass Motion in Solar Flares and Related Phenomena, 9th Nobel Symposium, Wiley.

Inference of Chromospheric magnetic fields:-

- Babcock, H.W. 1953: Astrophys. J. 118, 387.
- Severny, A.B. 1969: in de Jager & Svestka (eds) Solar Flares and Space Research, p38.
- McIntosh & Dryer (eds). 1972: Solar Activity Observation and Prediction.

EUV Emission

## Reviews:-

- Friedman, H. 1963: Ann. Rev. Astron. & Astrophys. 1, 59.  
 Goldberg, L. 1967: Ann. Rev. Astron. & Astrophys. 5, 279.  
 Neupert, W.M. 1969: Ann. Rev. Astron. & Astrophys. 7, 121.

## Rocket &amp; Satellite Observations:-

- Hinteregger, H.E. & Hall, L.A. 1968: Solar Phys. 6, 175.  
 Hall, L.A. & Hinteregger, H.E. 1969: in de Jager & Svestka  
 (eds) Solar Flares and Space Research., p81,  
 Hall, L.A. 1972: Solar Phys. 21, 167.  
 Tousey, R, Bartoe, J.D.F., Bohlin, J.D., Brueckner, G.E.,  
 Purcell, J.D., Scherrer, V.E., Sheeley, N.R., Schmacker, R.J.,  
 & Vanhoosier, M.E. 1973: Solar Phys. 33, 265.

## Inference from SFD's:-

- Donnelly, R.F. 1967: ESSA Tech.Rep.IER 19-ITSA 19.  
 Donnelly, R.F. 1969: Astrophys. J. 158, L165.  
 Kane, S.R. & Donnelly, R.F. 1971: Astrophys. J. 164, 151.  
 Donnelly, R.F. 1972: Solar Phys. 20, 188.  
 McIntosh & Donnelly R.F. 1972: op cit.

Soft X-Ray Observations

## Reviews:-

- Friedman, H. 1963: Ann.Rev. Astron. & Astrophys. 1, 59.  
 Goldberg, L. 1967: Ann.Rev. Astron. & Astrophys. 5, 279.  
 Neupert, W.M. 1969: Ann.Rev. Astron. & Astrophys. 7, 121.  
 Culhane, J.L. & Acton, L.W. 1974: Ann. Rev. Astron. &  
 Astrophys. 12, 359.

## Observations:-

- Chubb, T.A., Friedman, H., Kreplin, R.W. & Kupperian, J.E.  
 1957: Nature, 179, 861.  
 Chubb, T.A. Kreplin, R.W. & Friedman, H., 1966: J. Geophys.  
 Res. 71, 3611.

- van Speybrock, L.P., Krieger, A.S. & Vaiana G.S., 1970:  
Nature, 227, 818.
- Culhane, J.L. & Phillips, K.J.H., 1970: Solar Phys. 11, 117.
- Kahler, S.W. & Kreplin, R.W. 1970: Solar Phys. 14, 372.
- Culhane, J.L., Vesecky, J.F. & Phillips, K.J.H. 1971:  
Solar Phys. 15, 394.
- Drake, J.F. 1971: Solar Phys. 16, 157.
- Parkinson, J.H. & Pounds, K.A. 1971, Solar Phys. 17, 416.
- Brinkman, A.C. & Shaw, M.L., 1972: Solar Phys. 23, 120.
- Herring, J.R.H. & Craig, I.J.D., 1973: Solar Phys. 28, 167.
- Neupert, W.M., Thomas, R.J., & Chapman, R.D., 1974: Solar  
Phys. 34, 349.

Observational Techniques:-

- Evans, K. & Pounds, K.A. 1968: Astrophys. J. 152, 319.
- Vaiana, G.S., Reidy, W.P. Zehnpfennig, T., van Speybrock, L.P.,  
& Giacconi, R. 1968: Science 161, 584.
- Dijkstra, J.H., de Graff, W. & Lantwaard, Z.J., 1971: in  
Labrum & Lüst (eds) New Techniques In Space Astronomy,  
I.A.U. Symp. 41, p 207.

Hard X-Rays

Reviews:-

- Friedman, H. 1963: Ann.Rev. Astron. & Astrophys. 1, 159.
- Kane, S.R. 1973 in Ramaty & Stone (eds) High Energy Phenomena  
on the Sun, NASA SP -342, p 55.
- Brown, J.C. 1975: in Kane (ed.) Solar Gamma-X, and EUV Radiation  
IAU Symp. 68, p 245.

Observations (except polarisation):-

- Peterson, L.E. & Winckler, J.R. 1958: Phys. Rev. Letters 1, 205.
- Cline, T.L., Holt, S.S. & Hones, E.W. 1969: J. Geophys.  
Res. 73, 434.
- Kane, S.R. 1969: Astroph. J. 157, L.139.
- Frost, K.J., 1969: Astroph. J. 158, L.159.
- Kane, S.R. & Anderson, K.A. 1970: Astroph. J. 162, 1003.

- Frost, K.J. & Dennis, B.R., 1971: *Astroph. J.* 165, 655.
- Kahler, S.W. & Kreplin, R.W. 1971: *Astroph. J.*, 168, 531.
- Takakura, T., Ohki, K., Shibuya, N., Fujii, M., Matsuoka, M., Miyamoto, S., Nishimura, J., Oda, M., Ogawara, Y. & Ota, S., 1971: *Solar Phys.* 16, 454.
- van Beek, H.F., de Feiter, L.D. & de Jager, C. 1974: in *Proc. Eslab. Symp. (Saulgau, 1973)*.
- Datlowe, D.W., 1975: in Kane (ed). Solar Gamma-, X-, and EUV Radiation, IAU Symp., 68, p.191.
- Hoyng, P., Brown, J.C., Stevens, G.A. & van Beek, H.F., 1975: in Kane (ed) Solar Gamma-, X- and EUV Radiation, IAU Symp. 68, p 233.

Polarisation:-

- Tindo, I.P., Ivanov, V.D., Mandel'shtam, S.L. & Shuryghin, A.I., 1970: *Solar Phys.* 14, 204.
- Tindo, I.P., Ivanov, V.D., Mandel'shtam, S.L. & Shuryghin, A.I., 1972: *Solar Phys.* 24, 429.
- Tindo, I.P., Ivanov, V.D., Valnicek, B. & Livshits, M.A., 1972: *Solar Phys.* 27, 426.
- Tindo, I.P., Mandel'shtam, S.L. & Shuryghin, A.I. 1973: *Solar Phys.* 32, 469.
- Nakada, M.P., Neupert, W.M. & Thomas, R.J., 1974: *Solar Phys.* 37, 429.

$\gamma$ -Rays

Review:-

- Chupp, E.L., Forrest, D.J. & Suri, A.N., 1975: in Kane (ed) Solar  $\gamma$ -, X- and EUV Radiation, I.A.U. Symp. 68, p 341.

Continuum observations:-

- Cline, T.L., Holt, S.S. & Hones, E.W., 1968: *J. Geophys. Res.* 73, 434.
- Gruber, D.E., Peterson, L.E. & Vette, J.I., 1973: in Ramaty & Stone (eds) High Energy Phenomena on the Sun, NASA SP-342, p 147.
- Suri, A.N., Chupp, E.L., Forrest, D.J. & Reppin, C., 1975: *Solar Phys.* 43, 415.

## Line observations:-

Chupp, E.L., Forrest, D.J., Higbie, P.R., Suri, A.N.,  
Tsai, C. & Dunphy, P.P., 1973: Nature, 241, 333.

## Inference of proton numbers:-

Hudson, H.S., 1973, in Ramaty & Stone, (eds) High Energy  
Phenomena on the Sun, NASA SP-342, p 207.

Interplanetary Particles

## Review:-

Lin, R.P., 1974: in Newkirk (ed) Coronal Disturbances  
I.A.U. Symp. 57, p 201.

## Cosmic rays:-

Fichtel, C.E., & McDonald, F.B., 1967: Ann.Rev.Astron. &  
Astrophys. 5, 351.  
Lin, R.P. & Anderson, K.A., 1967: Solar Phys. 1, 446.  
Cline, T.L., & McDonald, F.B., 1968: Solar Phys. 5, 507.  
Svestka, Z. 1969: in de Jager & Svestka (eds) Solar Flares  
and Space Research p.16  
Lin, R.P. 1970: Solar Phys. 12, 266.  
Lin, R.P. & Hudson, H.S., 1971: Solar Phys. 17, 412.  
Datlowe, D.W. & Lin, R.P., 1973: Solar Phys. 32, 459.

## Plasma ejecta:-

Parker, E.N., 1963: Interplanetary Dynamical Processes, Wiley.  
de Jager, C. & Svestka, Z. 1967 (eds) Solar Flares and Space  
Research.  
Stickland, A.C. 1969 (ed) Annals of the IQSY (vols.3 & 4)  
MIT Press.

Flare Theory

Sweet, P.A., 1958: Nuovo Cimento Suppl. 8, Ser. X, 188.

Elliot, H., 1964: Planet. Space Sci. 12, 657.

Petschek, H.E., 1964: in H ess: (ed) AAS-NASA Symp.

Physics of Solar Flares, p 425.

Alfven, H., & Carlquist, P., 1967: Solar Phys. 1, 220.

Pneuman, G.W., 1968: Solar Phys. 8, 142.

Hyder, C.L., 1968: in  hman (ed) Mass Motion in Solar Flares, p57.

Sturrock, P.A., 1972: in McIntosh & Dryer (eds)

Solar Activity Observation and Prediction, p 163.

Parker, E.N., 1973: J. Plasma Phys. 9, 49.

Piddington. J.H., 1973: Solar Phys. 31, 229.

Priest, E.R., 1973: Astrophys. J. 181, 227.

Priest, E.R. & Mayvaerts, J., 1974: Solar Phys. 36, 433.

Sturrock, P.A., 1974: in Newkirk (ed) Coronal Disturbances

I.A.U. Symp. 57, p 437.

Priest, E.R. & Raadu, M.A., 1975: Solar Phys. 43, 177.

CHAPTER IIHARD X-RAY SOURCE MODELS1. INTRODUCTION

Evaluation of the characteristics of hard X-ray emission from the electron trap, described in Chapters III, IV and V, forms a major part of the work of this thesis. In this chapter we examine the properties of hard X-ray source models in general.

—Currently, five hard X-ray source models are generally accepted as having some viability. The main features of each model are outlined in §5-9 of this chapter. In §10, observational evidence concerning flare hard X-ray emission itself, together with other aspects of the flare which are influenced by the choice of X-ray source model, are summarised. The overall flare picture is far from clear since it would be naive to imagine that the highly idealised assumptions made in deducing the characteristics of each model represent an adequate description of the situation in a real flare. Taken in isolation, each model contradicts at least one observation. However, "side effects" are easily invoked in most cases to explain the discrepancies. Finally, the compatibility of each source model with observation is examined in an attempt to identify the most useful areas of experimental and theoretical research.

Before describing the hard X-ray source models, there are three topics of basic importance which warrant detailed discussion. Although Brown (1975) has drawn attention to the possible relevance of the inverse Compton effect studied by Korchak (1971), all current hard X-ray source models invoke collisional bremsstrahlung of high energy electrons (10 - 300 keV) as the X-ray generation mechanism. Therefore in §2 the bremsstrahlung cross-section is discussed. A brief classical derivation is given and the relativistic forms used for the computations in this thesis defined.

Tomblin (1971) pointed out that soft X-ray photons entering the photosphere are not lost, but after Compton scattering may emerge to be detected along with the primary X-ray flux. From the soft X-ray point of view, the most important result of Tomblin's work is the predicted shift of spectrum lines at  $\lambda < 2 \text{ \AA}$ , equivalent to a Doppler shift of  $> 10^3 \text{ km sec}^{-1}$ . At hard X-ray energies, the contribution of "albedo" photons is larger since photo-electric absorption, which dominates the Compton cross-section in the soft X-ray region, is negligible above 20 keV. The hard X-ray albedo effect is discussed in §3.

Observations of the time variation in hard X-ray flux are summarised in §10 of Chapter I and in §10 of this chapter. In §4 the modulation is discussed from a theoretical viewpoint. Since continuous injection models invoke an undefined mechanism in the acceleration region to modulate the spectrum, this discussion centres on the electron trap model, where MHD oscillations of the trap itself allow the possibility of direct modulation of the trapped electron spectrum. Note that in the analysis of the trap model performed in Chapter III, we assume that the trap is static and the electron distribution stationary on the time-scale for traversal of the trap by an electron ( $\sim 1$  second).

## 2. BREMSSTRAHLUNG RADIATION

Here we derive some of the directional and polarisational properties of bremsstrahlung emission in order to gain some insight into the physics of the relativistic cross-sections used in this thesis.

Classically, an electron undergoing acceleration emits bremsstrahlung radiation polarised in the plane containing the direction of acceleration, with an intensity proportional to the square of the acceleration and to the square of the sine of the angle between the direction of emission and that of acceleration (e.g. Lorrain & Corson, 1970).

Thus

$$I \propto (\ddot{\underline{z}}/r)^2 (1 - (\hat{\underline{z}} \cdot \hat{\underline{r}})^2) \quad (2.1)$$

and

$$\hat{\underline{p}} = \frac{\hat{\underline{z}} - (\hat{\underline{z}} \cdot \hat{\underline{r}}) \hat{\underline{r}}}{[1 - (\hat{\underline{z}} \cdot \hat{\underline{r}})^2]^{1/2}} \quad (2.2)$$

where  $I$  is the intensity at a distance  $r$  due to an electron subjected to an acceleration  $\ddot{\underline{z}}$  in the  $\hat{\underline{z}}$  direction. The electric vector is in the direction  $\hat{\underline{p}}$ . This geometry is illustrated in Figure 2.1a, where

$$\cos \theta = \hat{\underline{z}} \cdot \hat{\underline{r}} \quad (2.3)$$

We now consider an electron moving in a hyperbolic orbit about a proton. (Electron-electron bremsstrahlung is negligible except at very high energy). We approximate the force on the electron by an impulse at one point in the orbit, as shown in Figure 2.1b. The significance of the angle  $\psi$  in Figure 2.1 is not precisely defined in this formulation, but it is clear that the angle of deflection is related to the energy of bremsstrahlung photons produced during the encounter. Only low energy photons can be emitted in distant encounters ( $\psi \approx \pi/2$ ), whereas close encounters ( $\psi \approx \pi$ ) deflect the electron strongly and so can produce photons with energy up to the short wavelength limit (cf. (2.17)). A photon at the short wavelength limit carries off all the energy of the electron and therefore has frequency given by  $h\nu = E$ .

Classically, the Fourier components of acceleration of a suddenly deflected electron would extend to infinite frequency and there would be no short wavelength limit. Thus the short wavelength limit is a quantum mechanical phenomena. Combining the geometries of Figure 2.1a and b, we obtain Figure 2.1c. Here  $\theta$  is the angle between the initial velocity of the electron and the direction of emission. The azimuthal angle  $\phi$  defines the direction of deflection of the electron while  $\Phi$  gives the direction of polarisation of the radiation.

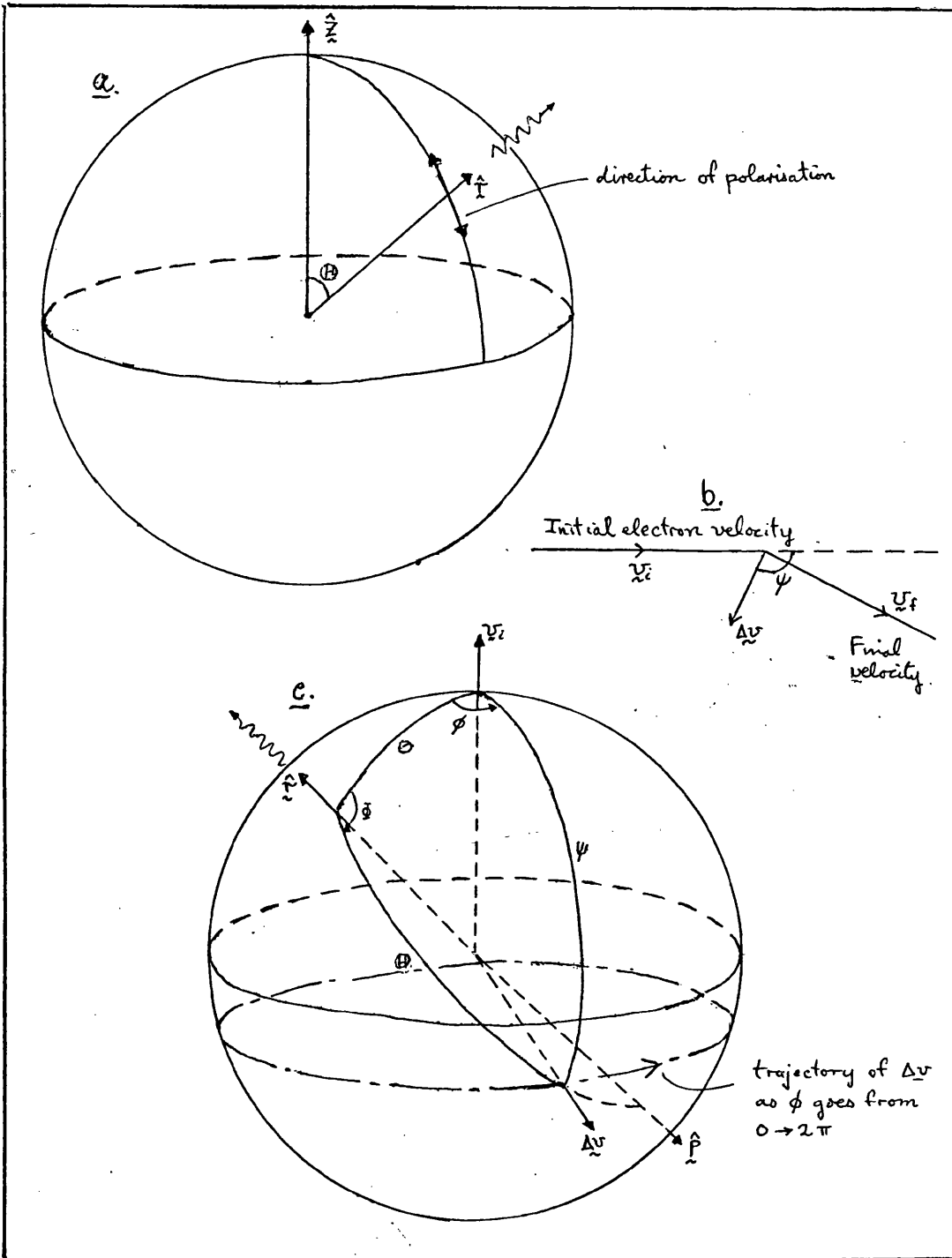


Figure 2.1 Geometry of bremsstrahlung emission.

From (2.1) and (2.2) we obtain

$$I \propto \sin^2 \theta \quad (2.4)$$

so that, if  $n(\phi) d\phi$  electrons with initial velocity  $\underline{v}_i$  are deflected by an amount  $\Delta y$  into azimuthal range  $\phi \rightarrow \phi + d\phi$ ,

$$I(\phi) d\phi \propto \sin^2 \theta n(\phi) d\phi \quad (2.5)$$

where  $I(\phi) d\phi$  is the intensity of radiation whose polarisation vector lies in the direction defined by  $\phi \rightarrow \phi + d\phi$ .

In a beam of electrons impinging on target protons the azimuthal distribution of scattered electrons is uniform, so (2.5) can be written

$$I(\phi) \propto \sin^2 \theta \frac{d\phi}{d\phi} \quad (2.6)$$

We now resolve the electromagnetic wave into components parallel and perpendicular to the initial electron velocity  $\underline{v}_i$ . It is clear from Figure 2.1c, that

$$\left. \begin{aligned} dI_{\parallel} &= I(\phi) d\phi \cos^2 \phi \propto \sin^2 \theta \cos^2 \phi d\phi \\ \text{and} \\ dI_{\perp} &= I(\phi) d\phi \sin^2 \phi \propto \sin^2 \theta \sin^2 \phi d\phi \end{aligned} \right\} \quad (2.7)$$

Integrating (2.7) over azimuth, we obtain the total intensities in the two components, due to all electrons scattered through angle (note that this is a continuous distribution - we should really consider electrons in  $\psi \rightarrow \psi + d\psi$ )

$$\frac{I_{\parallel}}{I} \propto \sigma_{\parallel} \propto \frac{1}{\pi} \int_0^{2\pi} \sin^2 \theta \cos^2 \phi d\phi \quad (2.8)$$

and

$$I_{\perp} \propto \sigma_{\perp} \propto \frac{1}{\pi} \int_0^{2\pi} \sin^2 \theta \sin^2 \phi \, d\phi \quad (2.9)$$

Here  $\sigma_{\parallel}$  and  $\sigma_{\perp}$  denote the cross sections for the two components of emission. The total intensity is given by the integral of (2.6) over all directions of polarisation. The corresponding cross-section is clearly

$$\sigma_{\text{tot}} = \sigma_{\parallel} + \sigma_{\perp} \propto \frac{1}{\pi} \int_0^{2\pi} \sin^2 \theta \, d\phi \quad (2.10)$$

Applying the cosine formula to triangle  $\underline{r}$ ,  $\underline{v}_1$ ,  $\Delta \underline{v}$  in Figure 2.1c, we obtain

$$\cos \theta = \cos \psi \cos \theta + \sin \psi \sin \theta \cos \phi \quad (2.11)$$

Thus

$$\sigma_{\text{tot}} \propto \frac{1}{\pi} \int_0^{2\pi} [1 - (\cos \psi \cos \theta + \sin \psi \sin \theta \cos \phi)^2] d\phi$$

that is

$$\sigma_{\text{tot}} \propto 2 \sin^2 \psi + (3 \cos^2 \psi - 1) \sin^2 \theta \quad (2.12)$$

Application of the sine formula to the same triangle gives

$$\sin \theta \sin \phi = \sin \psi \sin \phi \quad (2.13)$$

Substituting (2.13) in (2.9) gives

$$\sigma_{\perp} \propto \frac{1}{\pi} \sin^2 \psi \int_0^{2\pi} \sin^2 \phi \, d\phi = \sin^2 \psi \quad (2.14)$$

Thus from (2.12) and (2.14), we have

$$\sigma_{\parallel} + \sigma_{\perp} \propto 2 \sin^2 \psi + (3 \cos^2 \psi - 1) \sin^2 \theta \quad (2.15)$$

and

$$\sigma_{\parallel} - \sigma_{\perp} \propto (3 \cos^2 \psi - 1) \sin^2 \theta \quad (2.16)$$

The form of these cross-sections, illustrated in Figure 2.2, changes at a critical scattering angle  $\psi_c$ , given by

$$\psi_c = \cos^{-1} (-1/\sqrt{3}) = 125^\circ \quad (2.17)$$

Thus collisions where  $\psi < \psi_c$  may be classed as distant encounters, while those in which  $\psi > \psi_c$  may be called close encounters. Note also that the cross sections are symmetric about  $\theta = \pi/2$ . This symmetry is lost in the relativistic case due to forward beaming of the photons.

Finally, before presenting the relativistic cross-sections used in Chapters III - V, we note that the electron-proton bremsstrahlung cross-section is much smaller than the electron-electron collision cross-section. Therefore the bulk of the energy carried by a stream of non-thermal electrons is dissipated in heating the ambient plasma, only a small fraction ( $\sim 10^{-5}$ ) being emitted as hard X-radiation.

The relativistic bremsstrahlung cross-sections, differential in photon energy and direction, used in this thesis were calculated in the relativistic Born approximation by Sauter (1934) and corrected by the Coulomb factor (Elwert, 1939). Since unpolarised electrons cannot emit circularly polarised radiation (Gluckstern *et al.*, 1951) the X-ray emission is composed of two orthogonally polarised components.  $\sigma_{\parallel}$  and  $\sigma_{\perp}$  denote the cross sections for bremsstrahlung emission polarised parallel to and perpendicular to the original direction of motion of the bremsstrahlung-producing electrons.

The total cross section is given by

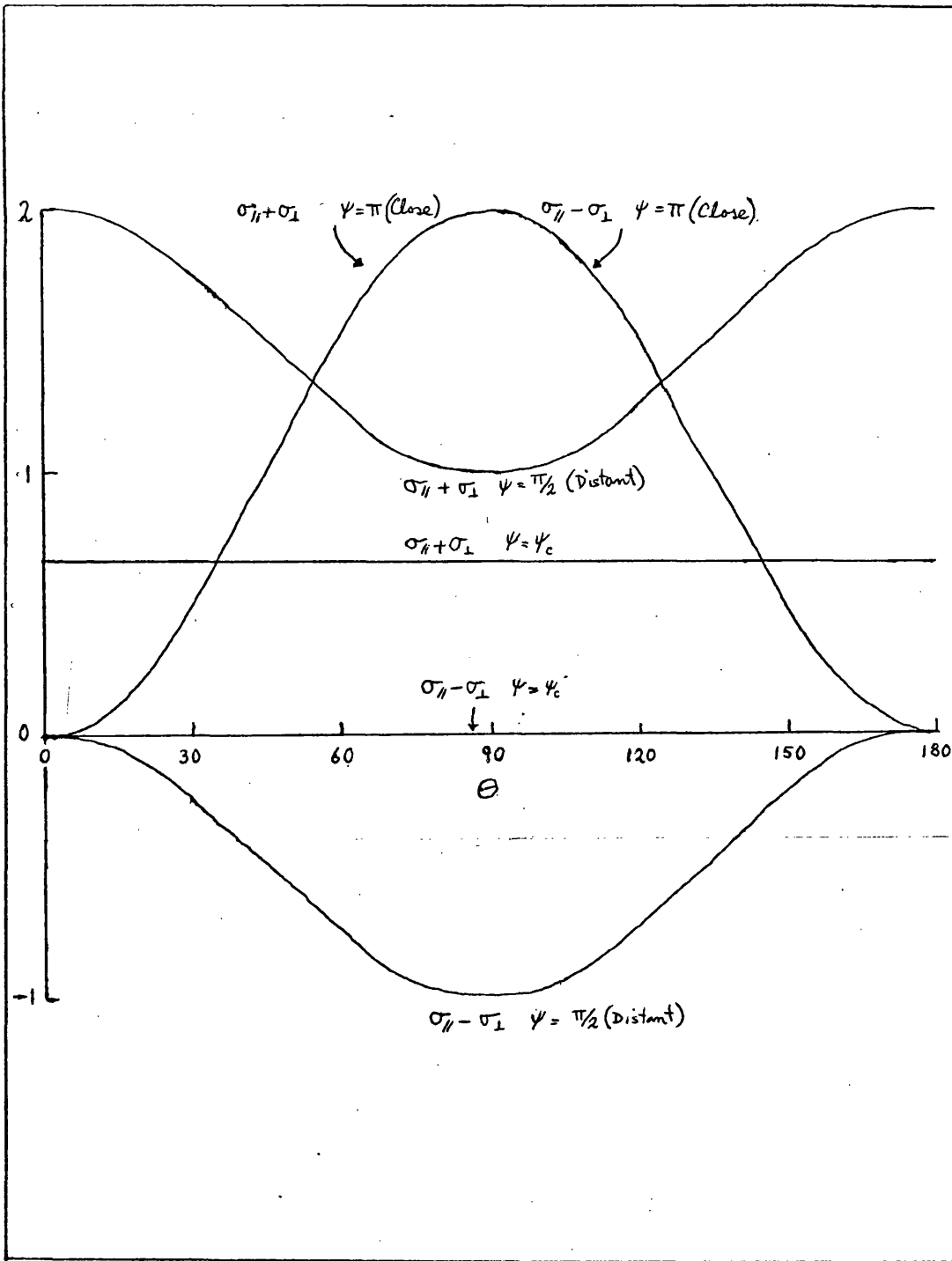


Figure 2.2 Total and polarisation cross-sections (arbitrary units) predicted by a classical analysis.

$$\begin{aligned}
Q_{\pi}(h\nu, \cos\theta, E) &= \frac{d^2 \sigma_{\parallel}}{d(h\nu)d\Omega} + \frac{d^2 \sigma_{\perp}}{d(h\nu)d\Omega} \\
&= \frac{r_0^2}{\pi} \frac{\alpha Z^2}{h\nu} \frac{\epsilon'}{\epsilon} \frac{1 - e^{-2\pi\alpha Z\epsilon/p}}{1 - e^{-2\pi\alpha Z\epsilon'/p'}} \times \\
&\left\{ \frac{2\epsilon^2+1}{p^2 u^4} \sin^2\theta - \frac{1}{p^2 u^2} (\epsilon^2 + 1 + \frac{1}{2} p \cos\theta) - \frac{p(p-k \cos\theta)}{2 u^2 p^2} \right. \\
&- \frac{\ln(\epsilon' + p')}{u p'} + \frac{1}{p' P} \ln \left( \frac{P + p'}{P - p'} \right) \left[ \frac{1}{2u^2} - \frac{k}{u} + \frac{k^2}{2 u P^2} (k - p \cos\theta) \right] \\
&+ \frac{1}{pp'} \ln \left( \frac{\epsilon\epsilon' + pp' - 1}{k} \right) \left[ \frac{\epsilon(3k - \epsilon' p^2)}{p^2 u^4} \sin^2 \theta \right. \\
&\left. \left. + \frac{\epsilon^2 + \epsilon'^2 - \frac{1}{2}}{u^2} - \frac{k}{u p^2} (2\epsilon + \frac{1}{2} \epsilon') + \frac{k}{2u} \left( \frac{\epsilon\epsilon'}{p^2} + 1 \right) \right] \right\} \quad (2.18)
\end{aligned}$$

while the polarisation cross-section is (note  $\sigma_{\parallel} - \sigma_{\perp}$  not  $\sigma_{\perp} - \sigma_{\parallel}$ )

$$\begin{aligned}
Q_p(h\nu, \cos\theta, E) &= \frac{d^2 \sigma_{\parallel}}{d(h\nu)d\Omega} - \frac{d^2 \sigma_{\perp}}{d(h\nu)d\Omega} \\
&= \frac{r_0^2}{\pi} \frac{\alpha Z^2}{h\nu} \frac{\epsilon'}{\epsilon} \frac{1 - e^{-2\pi\alpha Z\epsilon/p}}{1 - e^{-2\pi\alpha Z\epsilon'/p'}} \times \\
&\left\{ \frac{2\epsilon^2+1}{p^2 u^4} \sin^2 \theta - \frac{1 - \epsilon u}{2 p^2 u^2} - \frac{\ln(\epsilon' + p')}{u p'} \right. \\
&+ \frac{1}{p' P} \ln \left( \frac{P + p'}{P - p'} \right) \left[ \frac{1}{2u^2} - \frac{k}{u} \right] \\
&+ \frac{1}{pp'} \ln \left( \frac{\epsilon\epsilon' + pp' - 1}{k} \right) \left[ \frac{\epsilon(3k - \epsilon' p^2)}{p^2 u^4} \sin^2 \theta \right. \\
&\left. - \frac{1}{2u^2} - \frac{k \cos \theta}{2 u^2 p} \right] - \frac{1}{\sin^2\theta} \left[ \frac{u - \epsilon'}{p^2} - \frac{\ln(\epsilon' + p')}{p'} \right]
\end{aligned}$$

$$\begin{aligned}
& + \frac{1}{p'P} \ln \left( \frac{P+p'}{P-p'} \right) \frac{p^2}{p^2} + \frac{1}{pp'} \ln \left( \frac{\epsilon\epsilon' + pp' - 1}{k} \right) \times \\
& \left[ \begin{array}{ccc} \frac{k}{u} & \frac{1 - \epsilon u}{p^2} & -1 \end{array} \right] \left[ \right] \left. \right\} \quad (2.19)
\end{aligned}$$

In these formulae  $h\nu$  is the photon energy and  $E$  is the electron kinetic energy while  $r_0$  is the classical radius of the electron

$$r_0 = \frac{e^2}{mc^2} \quad (2.20)$$

and  $\alpha$  is the fine structure constant

$$\alpha = \frac{e^2 \hbar}{c} \quad (3.21)$$

$Z$  is the atomic number of the scattering centre, and has been taken to be unity. This corresponds to a pure hydrogen plasma and so the fluxes computed in Chapters IV and V are low by a factor of  $\sim 1.8$  due to neglect of heavy ions in the solar corona (Haug, 1972).

$\epsilon$  and  $\epsilon'$  are the initial and final electron energies in units of  $mc^2$  while  $p$  and  $p'$  are the corresponding momenta.  $k$  is the photon energy in units of  $mc^2$  and  $u$  and  $P$  are defined by

$$u = \epsilon - p \cos \theta \quad (2.22)$$

$$p^2 = p'^2 + k^2 - 2pk \cos \theta \quad (2.23)$$

where  $\theta$  is the angle between the direction of emission of the photon and the initial electron velocity.  $\epsilon$ ,  $k$ ,  $\epsilon'$ ,  $p$  and  $p'$  are evaluated using the following relations:-

$$\epsilon = 1 + E/mc^2 \quad (2.24)$$

$$k = h\nu/mc^2 \quad (2.25)$$

$$\epsilon' = \epsilon - k \quad (2.26)$$

$$p^2 = \epsilon^2 - 1 \quad (2.27)$$

$$p'^2 = \epsilon'^2 - 1 \quad (2.28)$$

At the short wavelength limit, as  $k \rightarrow \epsilon$ , (and  $\epsilon'$ ,  $p' \rightarrow 0$ ) the following asymptotic relations are valid

$$e^{-2\pi\alpha Z\epsilon'/p'} \rightarrow 0 \quad (2.29)$$

$$\frac{1}{p'} \ln \left( \frac{P + p'}{P - p'} \right) \rightarrow \frac{2}{P} \quad (2.30)$$

$$\frac{\ln(\epsilon' + p')}{p'} \rightarrow 1 \quad (2.31)$$

$$\frac{1}{pp'} \ln \left( \frac{\epsilon\epsilon' + pp' - 1}{k} \right) \rightarrow \frac{1}{k} \quad (2.32)$$

It must be noted that the polarisation cross-section has been defined with the opposite sign to that used by Elwert and Haug (1970), Haug (1972) and Brown (1972b) who take the polarisation to be negative when the maximum intensity is parallel to the electron velocity.

The total and polarisation cross-sections defined by (2.18) and (2.19) are illustrated in Figures 2.3 and 2.4 for electron energies of 10, 50 and 100 keV. On the contour labelled x in these figures, the bremsstrahlung cross-section is  $10^{-x}$  barn  $\text{keV}^{-1}$   $\text{sterad}^{-1}$  (1 barn =  $10^{-24}$   $\text{cm}^2$ ), except in the hatched region of Figure 2.4, where the cross-section is of the same magnitude but negative. Comparing the 10 keV polarisation cross-section in Figure 2.4 with the results of our classical analysis (Figure 2.2), it is immediately clear that we are justified in identifying the angle  $\psi$  with photon energy. The angle  $\psi_c$  corresponds to a photon energy given by  $\epsilon/E \approx 0.12$ , polarisation being negative at lower photon energies ( $\psi > \psi_c$  - distant encounters) and positive at higher energies ( $\psi < \psi_c$  - close encounters). The

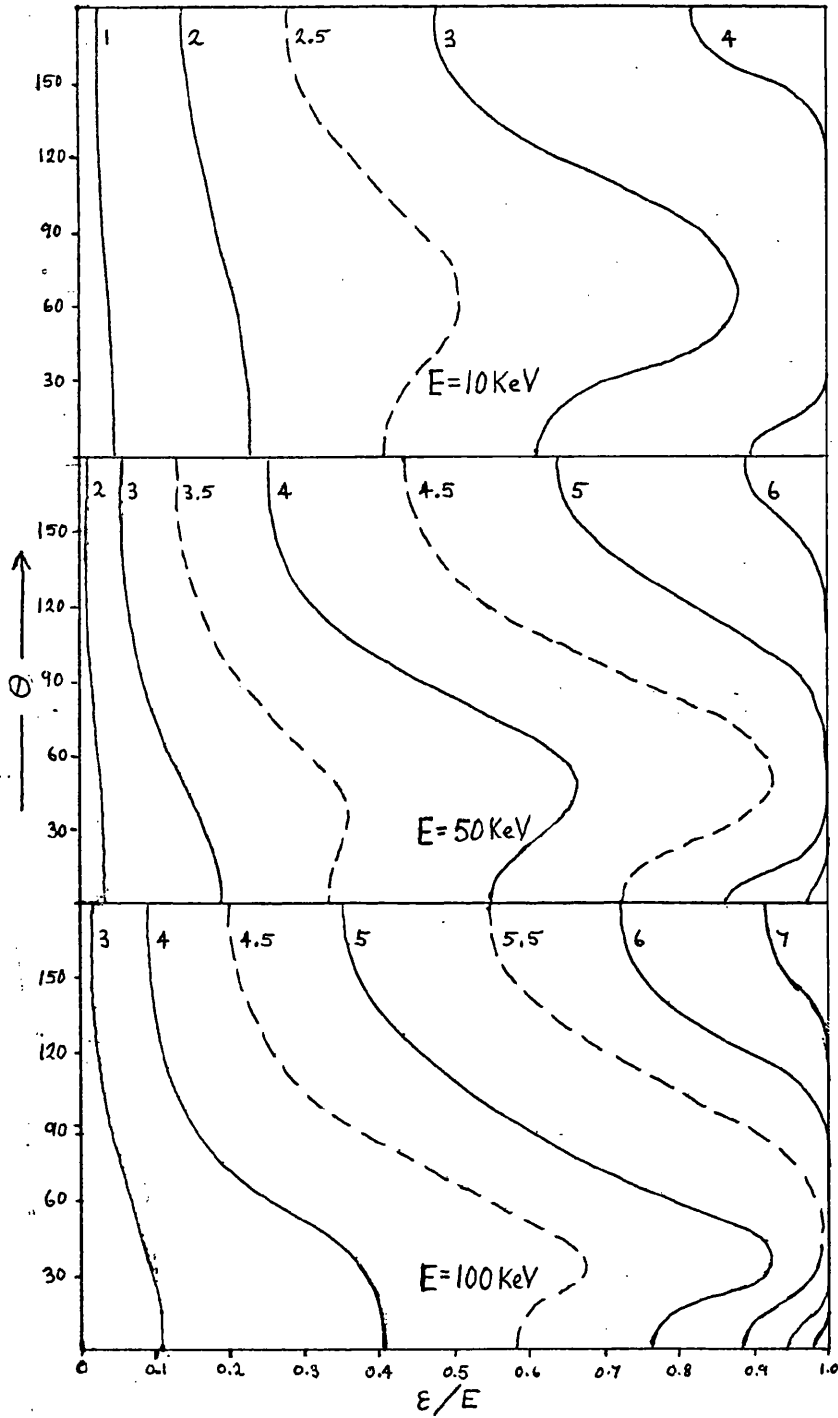


**Figure 2.3** Relativistic total bremsstrahlung cross-sections. On the contour labelled  $x$  the cross-section has a value  $10^{-x} \text{ barn} \cdot \text{keV}^{-1} \text{ sterad}^{-1}$ .

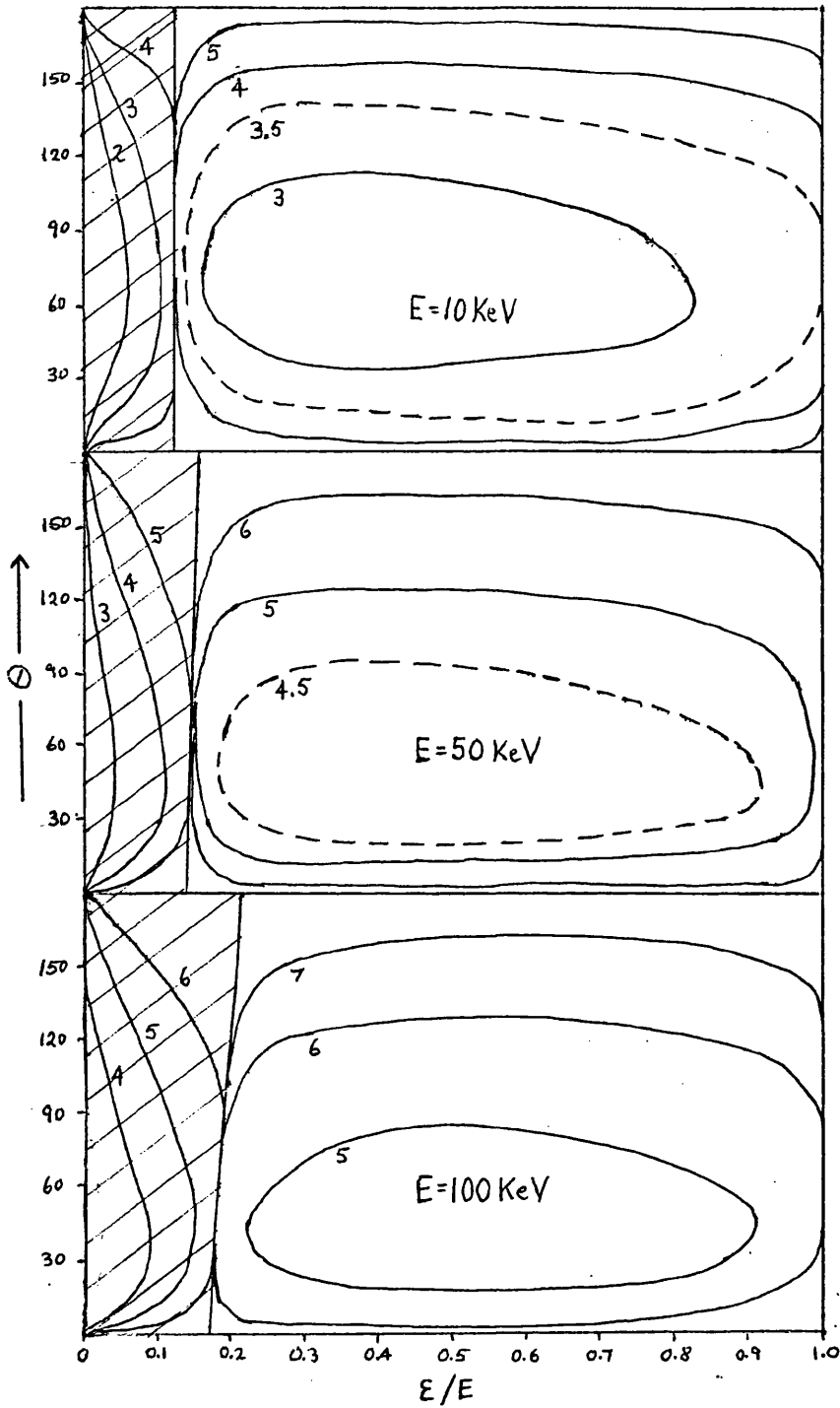


Figure 2.4 Relativistic polarisation bremsstrahlung cross-sections. On the contour labelled  $x$  the cross-section has a value  $10^{-x}$  barn  $\text{keV}^{-1}$  sterad $^{-1}$ , except in the hatched area where the cross-section is of the same magnitude but negative.

sequence of plots in Figure 2.4 illustrates the effect of relativity. With increasing electron energy the position of peak polarisation shifts to smaller  $\theta$  and the photon energy at which the polarisation changes sign becomes  $\theta$ -dependent.

Having established a relationship between the angle  $\psi$  and photon energy  $\epsilon$ , we return to the total cross-section, shown in Figure 2.3. At high photon energy ( $\epsilon/E \gtrsim 0.5$ ) the cross-section peaks at  $\theta \approx \pi/2$ , while at low photon energy the cross-section is maximal at  $\theta=0$ , falling monotonically as  $\theta$  increases. The first result is in agreement with the classical analysis (Figure 2.2) for  $\psi > \psi_c$  (close encounters) but at low energy the behaviour of the cross-section anticipated for distant encounters ( $\psi < \psi_c$  in Figure 2.2) is not found. This is due to the relativistic forward beaming of photons. It is apparent from Figure 2.3 that even for an electron energy as low as 10 keV this effect shifts the peak in the cross-section away from  $\theta = \pi/2$  at high photon energy.

### 3. THE ALBEDO EFFECT

Tomblin's (1972) calculations, mentioned in §1, were extended to the hard X-ray regime by Santangelo *et al* (1973). They took a point source of X-rays 7000 km above the photosphere and, using a Monte Carlo technique, calculated the spectrum of scattered photons emerging from the photosphere. Results obtained for an isotropic point source emitting a power law X-ray spectrum of spectral index 3 are shown in Figure 3.1. Maximum "reflectivity" occurs around 30 keV. Below 20 keV many photons are absorbed photo-electrically, while above  $\sim 50$  keV the energy loss to a photon undergoing Compton scattering becomes considerable. The effect of the albedo contribution is to steepen the observed photon spectrum slightly above 25 keV and to enhance the flux at  $\sim 25$  keV by  $\sim 50\%$ . Neglect of the albedo contribution in the case of an isotropic source could lead to an overestimation of electron numbers by a factor of two. For the thick target model, in which most photons are emitted towards the photosphere, this effect would obviously be more severe.

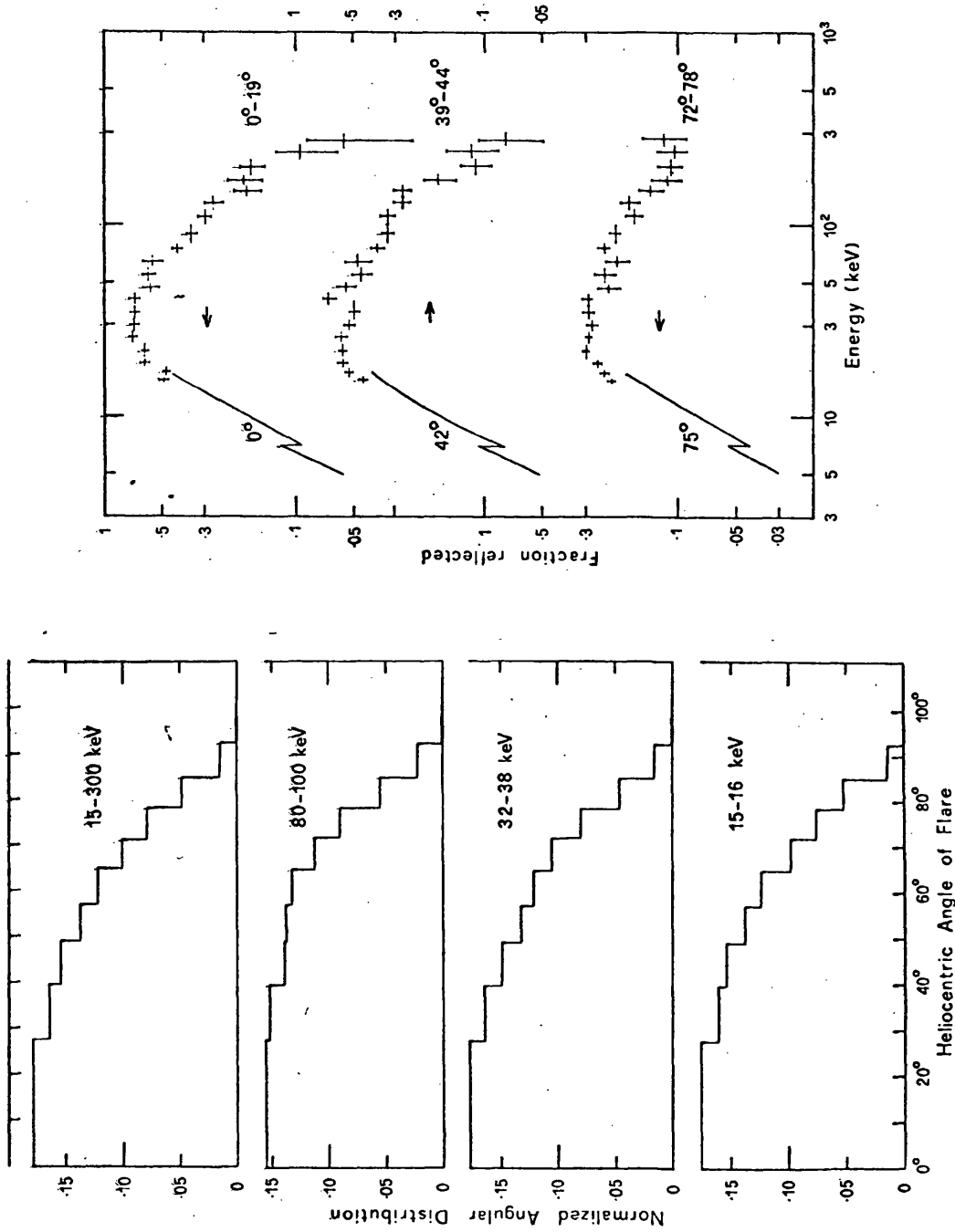


Figure 3.1 Albedo calculations of Santangelo et al (1973).

Upper:-

Percent reflection of energy expressed as a fraction of the flux which arrives directly at the Earth, taking the ratio Fe/H as  $10^{-5}$ . The solid lines are from Tomblin (1972) for an iron ratio of  $1.4 \times 10^{-5}$ . Graphs are shown for three different heliocentric positions of the flare.

Lower:-

Ratio of reflected flux to direct flux as a function of heliocentric angle from the center of the disk to the flare site, for different energy intervals.

The polarisation of albedo X-rays was considered by Brown et al (1974), who argued that a large polarisation, not present in the primary X-ray emission, could be induced in the observed flux by the albedo contribution. This contention was not borne out ( except for unreasonably large source heights ( $\lambda R_{\odot}$ ) ) by the detailed calculations of Beigman (1974), who found that the net polarisation of the albedo contribution is only a few percent.

Detailed calculations of the albedo X-ray flux and polarisation for a non-isotropic primary source have been performed by Henoux (1975), who took the primary source to be a thin target point source in which the electrons stream downwards, at a height of  $10^4$  km. This source model is rather unrealistic since a downward directed electron beam would be expected to produce thick target emission, in which scattering of the electrons considerably modifies the directivity (Brown, 1972b), at a height of  $\sim 10^3$  km (Brown & McClymont, 1975). It seems probable that Henoux's results, some of which are shown in Figure 3.2, would not be greatly changed by the adoption of a thick target source, but this would be worth checking. Henoux finds that the high directivity of the primary source ( $\sim 6$  limb-brightening at 50 keV) is reduced in the total emission to within the observational limit of  $\pm 50\%$  variation set by Datlowe et al (1974). The polarisation is not modified so dramatically, the maximum effect being an enhancement of  $\sim 20\%$  for X-ray bursts midway between disc centre and the solar limb. Unfortunately, Henoux does not give any indication of the ratio of albedo flux to primary source flux at the Earth. As mentioned previously, this could be of importance to the inference of electron fluxes.

It should be noted, however, that the "equivalent thick target parameters" used by Hoyng et al (1975) (see also Brown & Hoyng, 1975) assume an isotropic bremsstrahlung cross-section. Therefore the electron fluxes inferred using this data reduction technique would be reduced by a factor of  $\sim 2$  if the albedo contribution were taken into account, not by the much larger factor implied by the directivity characteristic of the thick target model itself.

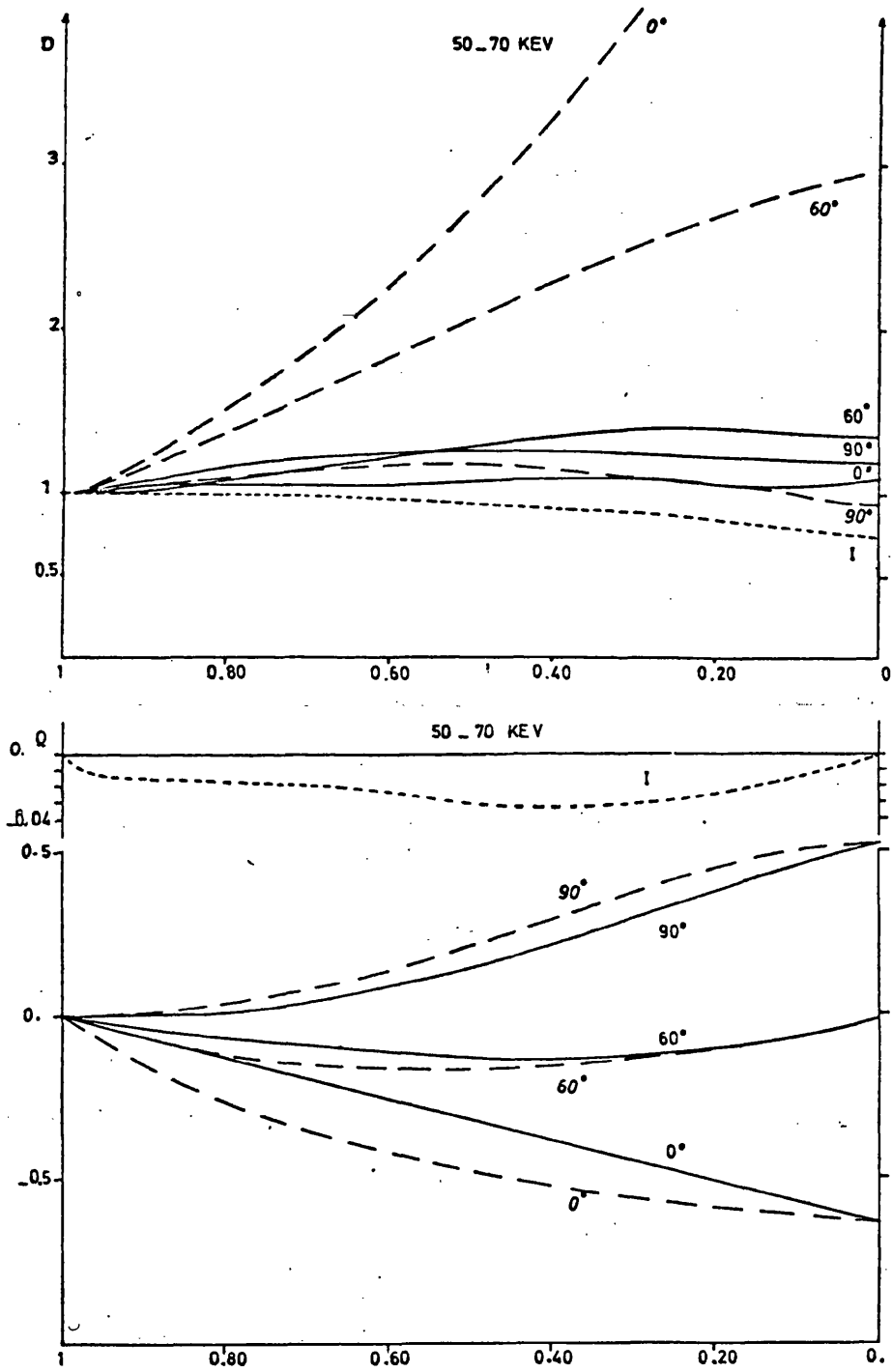


Figure 3.2 Albedo calculations of Henoux (1975).

Upper:— Directivity of the X-rays as a function of  $\cos \theta$ .  $\theta$  is the angle between the magnetic field  $H$  and the line of sight. --- Initial directivity  $D_i(\cos \theta)$  for three different values of the pitch angle  $\alpha$  of the electrons;  $\alpha = 0^\circ, 60^\circ, 90^\circ$ . ——— Resulting directivity  $D_r(\cos \theta)$  for the three sources precendently defined. - - - - - Resulting directivity  $D_r(\cos \theta)$  for an isotropic source with an  $E^{-3.5}$  photon spectrum. The photons are collected in three energy bands: 15-20 keV, 50-70 keV, 120-150 keV.

Lower:— Polarization of the flare X-rays as a function of  $\cos \theta$  --- Initial polarization. The three sources defined in the upper figure are considered. ——— Resulting polarization of the sources described above. - - - - - Resulting polarization for an isotropic source with an  $E^{-3.5}$  photon spectrum.

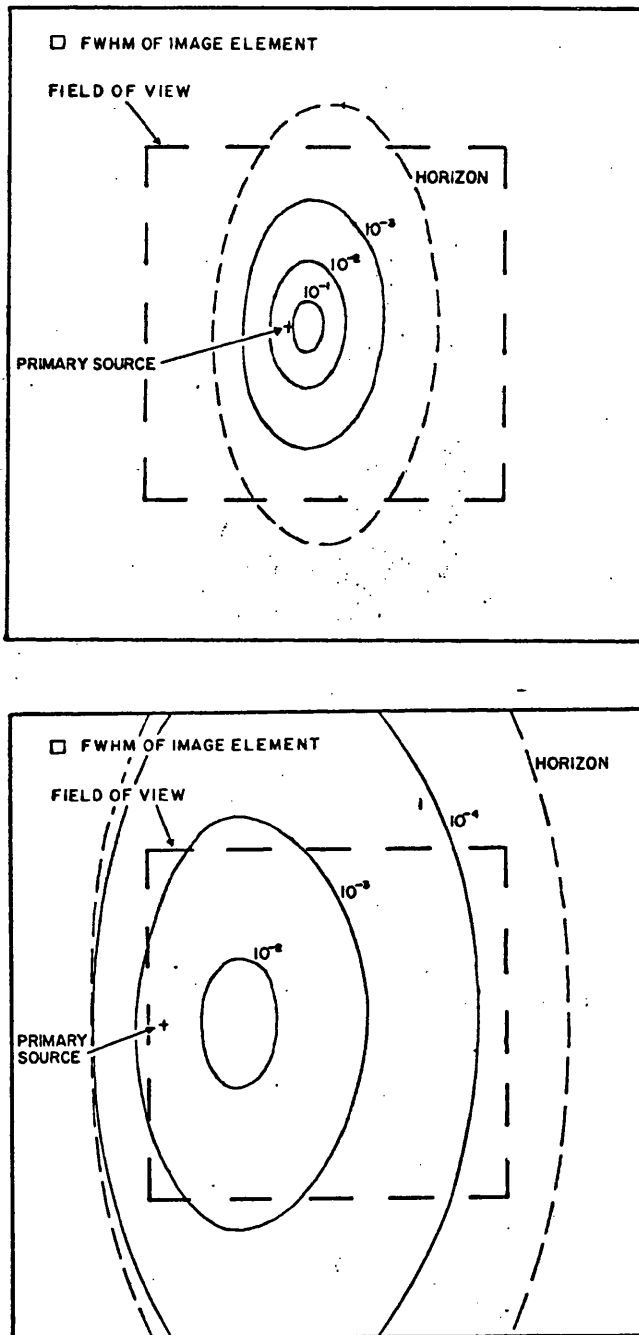


Figure 3.3 Albedo calculations of Brown et al (1975).

Upper:- Albedo count distribution computed for a primary source at height  $h=10^4$  km and  $60'$  from disk center, using the anisotropic Compton cross-section. The results are in the form of isobrightness contours, brightness as a fraction of the primary source flux per image element ( $8'' \times 8''$ ). The size of one image element and of the total field of view of the Utrecht heliograph are indicated

Lower:- As above for  $h=10^4$  km.

Brown et al (1975) have discussed the spatial distribution over the photosphere of emergent albedo X-rays and have demonstrated that the measurement of this distribution by a hard X-ray imaging device provides a feasible method of determining the height of hard X-ray sources. Typical distributions of albedo flux are shown in Figure 3.3.

In summary, the albedo effect enhances the hard X-ray flux by almost a factor of two in the case of an isotropic source, and by a greater amount for a thick target source. Source directivity is drastically reduced, but the polarisation is relatively unaffected.

#### 4. MODULATION OF HARD X-RAYS

Hard X-ray flare emission is observed to be modulated rapidly, on a timescale down to a few seconds. In large bursts the modulation appears to be quasi-periodic. Statistics are too poor in small events to determine whether periodicities exist in the spiky profile. In the thick target and thin target models modulation of the injected electron flux must be invoked to explain the observed time variation. Various authors (for example, Priest & Raadu, 1975) have suggested that instabilities or MHD waves in the neutral sheet assumed to accelerate the fast particles are likely to cause the particle flux to vary rapidly, but no quantitative calculations have been performed.

In the electron trap model, however, MHD oscillations of the trap itself provide a natural explanation of the temporal variation of X-ray emission. A consideration of the number density of fast particles in the trap in a large event reveals that strong interaction of the non-thermal particles, ambient plasma and magnetic field must be anticipated. In a large event, more than  $10^{39}$  electrons of mean energy  $\sim 50$  keV must be injected into a trap whose volume can hardly be greater than  $3 \times 10^{29}$  cm<sup>3</sup>. Therefore the number density of fast particles is  $\sim 3 \times 10^9$  cm<sup>-3</sup> and the resulting pressure  $\sim 150$  dyne cm<sup>-2</sup>. The ambient plasma density in the trap is likely to be  $\sim 10^{10}$  cm<sup>-3</sup>, while the magnetic pressure varies from  $\sim 10^4$  dyne cm<sup>-2</sup> in the limbs of the trap ( $B \approx 500$  G) to  $\sim 100$  dyne cm<sup>-2</sup> at the top ( $B \approx 50$  G). Thus the fast

particle density is not negligible compared to the ambient density and, furthermore, the pressure due to fast particles is comparable to the magnetic pressure and appreciably greater than the ambient gas pressure.

The high density of non-thermal electrons required in the trap poses a problem. Electrostatic considerations require as many protons as electrons to be injected into the trap, on the same time scale. Acceleration of both species on a one-for-one basis implies a non-thermal proton energy  $\approx m_p/m_e \approx 2 \times 10^3$  times higher than the non-thermal electron energy, but according to Hudson (1973), the total proton energy is in fact  $\lesssim 10^{-2}$  of the electron energy. Therefore charge neutralisation must be brought about by the relatively slow redistribution of protons from the dense photosphere.

Kane and Anderson (1970) found that in small hard X-ray burst the spectrum softens during the decay. They pointed out that this is inconsistent with a trapping model at constant density since collisional decay of the electrons (assumed to account for the burst decay and hence implying an ambient density of  $\sim 10^9 \text{ cm}^{-3}$ ) would cause the spectrum to harden. Brown (1972a) showed that if electrons of higher energy have smaller pitch angles they penetrate further down the limbs of the trap and so encounter a higher average density. (c.f. §6 of Chapter IV). For this mechanism to operate successfully over the energy range 10-100 keV, a factor of 200 variation in density is required, which implies that the density scale height in the trap must be  $\lesssim 10^3$  km. While this is feasible, it means that the density distribution in the trap must be very different from that of the quiet corona.

Pitch angle scattering of trapped electrons was studied by Benz & Gold (1971) who concluded that precipitation of the trapped electrons into the chromosphere could be more important than collisional decay in controlling the evolution of the electron distribution. They also show that, under some circumstances, pitch angle scattering may increase the electron mirror heights. Their analysis was performed for high energy ( $\sim 1$  MeV) electrons and it is not clear whether these results are

applicable to the deka-keV electrons assumed to be responsible for hard X-ray emission. While a steady precipitation of electrons into the chromosphere could modify the evolution of the hard X-ray burst, (see Melrose & Brown, 1975), it is unlikely that the enhanced emission due to a bunch of electrons suddenly precipitated into the chromosphere could account for spikes in burst time profile. Since the chromosphere is a thick target, the spikes would have a harder spectrum than the rest of the burst, whereas in fact it is usually softer (see Hoyng, 1975).

Brown (1973b) pointed out that a period of  $\sim 15$  seconds in the modulation of hard X-ray flux is consistent with the transit time of an Alfvén wave moving along a trap of length  $\sim 10^5$  km. Brown & Hoyng (1975) have explained the observed correlation between hard X-ray flux and spectral index in the large event of 4 August, 1972, in terms of a trap model in which oscillations of the trap modulate the electron spectrum via betatron acceleration. Since this affects only the component of electron energy perpendicular to the magnetic field, the assumption of a decreasing pitch angle with increasing electron energy (c.f. §6 of Chapter IV) means that betatron acceleration acts more effectively on the low energy end of the electron spectrum. Therefore the electron energy spectrum steepens as the magnetic field strength increases. Due to the steepness of the electron spectrum, only a small increase in magnetic field strength is necessary to give a large increase in the number of electrons above a certain energy. Thus small ( $\sim 20\%$ ) perturbations on the trapping field can produce the observed spectrally softer peaks in the X-ray burst. The observed trajectory of the 4 August 1972 event in the  $(\mathcal{F}, \gamma)$  plane as shown in Figure 4.1, while Figure 4.2 illustrates the correlation predicted by the betatron model compared with observation. The parameter  $E^*$  is as defined in Chapter IV, §6. (See also Figure 10.2 which illustrates the evolution of  $\mathcal{F}$  and  $\gamma$ ). This model is an exciting breakthrough as it represents the first attempt to explain quantitatively the time-variation of X-ray emission. An extension of the model to include the first order effects of time variation of the trap geometry as well as the modulation of field strength (Brown & McClymont, 1976) allows the possibility of reaching any point in the

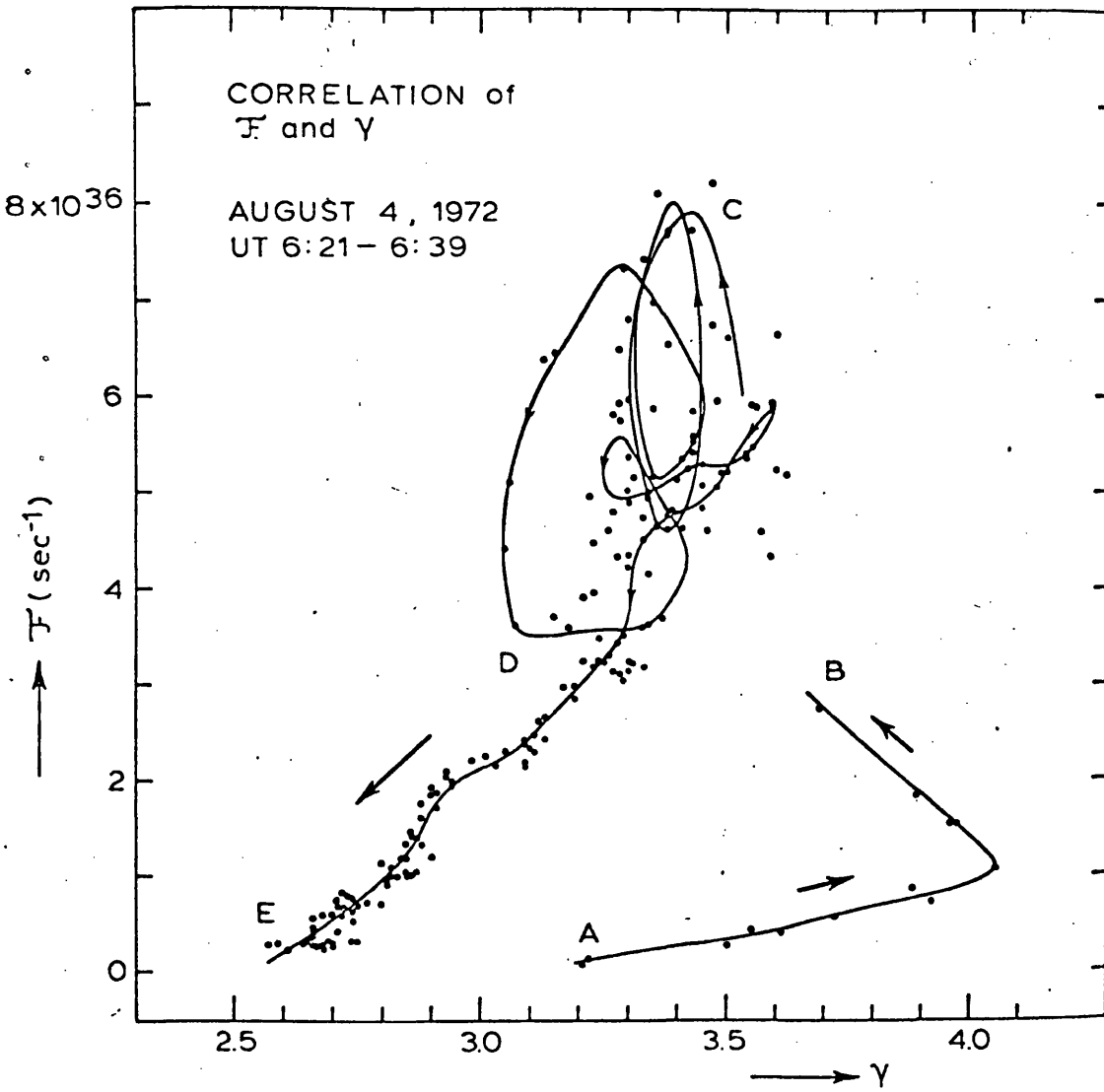


Figure 4.1 Correlation between  $\mathcal{F}$  and  $\gamma$ , from Brown & Hoyng (1975).  
Every 5th data point is shown.

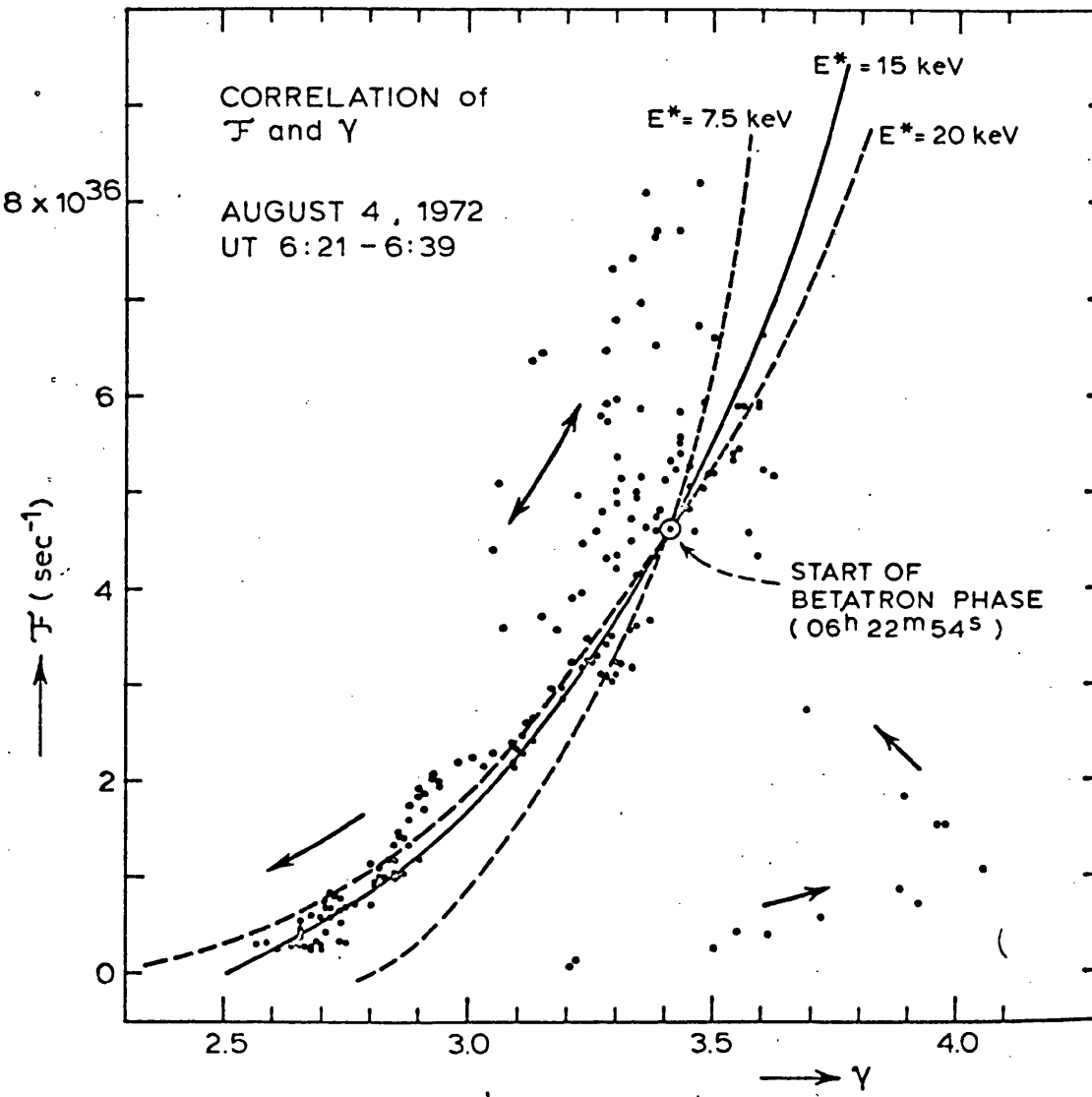


Figure 4.2 Correlation predicted by the betatron model.  
From Brown & Hoynig (1975).

( $\mathcal{J}, \gamma$ ) plane (Figure 4.1) and so reproducing the loops in addition to the "average" correlation. Hopefully further investigations will provide more information concerning both the trap and electron energy/pitch angle relationship. In particular, an analysis of the possible MHD eigenmodes of a vibrating trap is called for.

## 5. THE THICK TARGET MODEL

This model involves continuous injection of non-thermal electrons, assumed to be accelerated in the low corona. The electrons emit bremsstrahlung radiation while undergoing collisional degradation in the chromosphere. Calculations have been performed neglecting scattering of the electrons by Petrosian (1973) and, more realistically, including the effects of scattering, by Brown (1972b). Brown's results for the directivity, polarisation and spectral index are shown in Figure 5.1. The model predicts significant limb-brightening at high photon energy (when the albedo effect is not taken into account), a radial polarisation (assuming a vertical electron beam) rising to 30 - 40% at the limb and a hardening of the spectrum by  $\sim \frac{1}{2}$  a power on going from centre to limb. Collisional hardening of the electron spectrum in the source region leads to the result that the photon spectrum is  $\sim 1$  power harder than the electron spectrum at injection.

The height distribution of thick target emission has been calculated by Brown & McClymont (1975). An electron acceleration site high in the corona is assumed. Results obtained assuming a quiet atmosphere density structure and neglecting directional effects are illustrated in Figure 5.2. Enhanced density in an active region and expansion of the chromosphere under the heating influence of the non-thermal electrons could enhance the coronal emission considerable. As the predicted behind-the-limb fluxes are rather low, it is probably necessary to invoke this effect. Since only the coronal (thin target) emission is seen in a behind the limb event, the X-ray spectrum is predicted to be 2 powers softer than the same event seen on the disc.

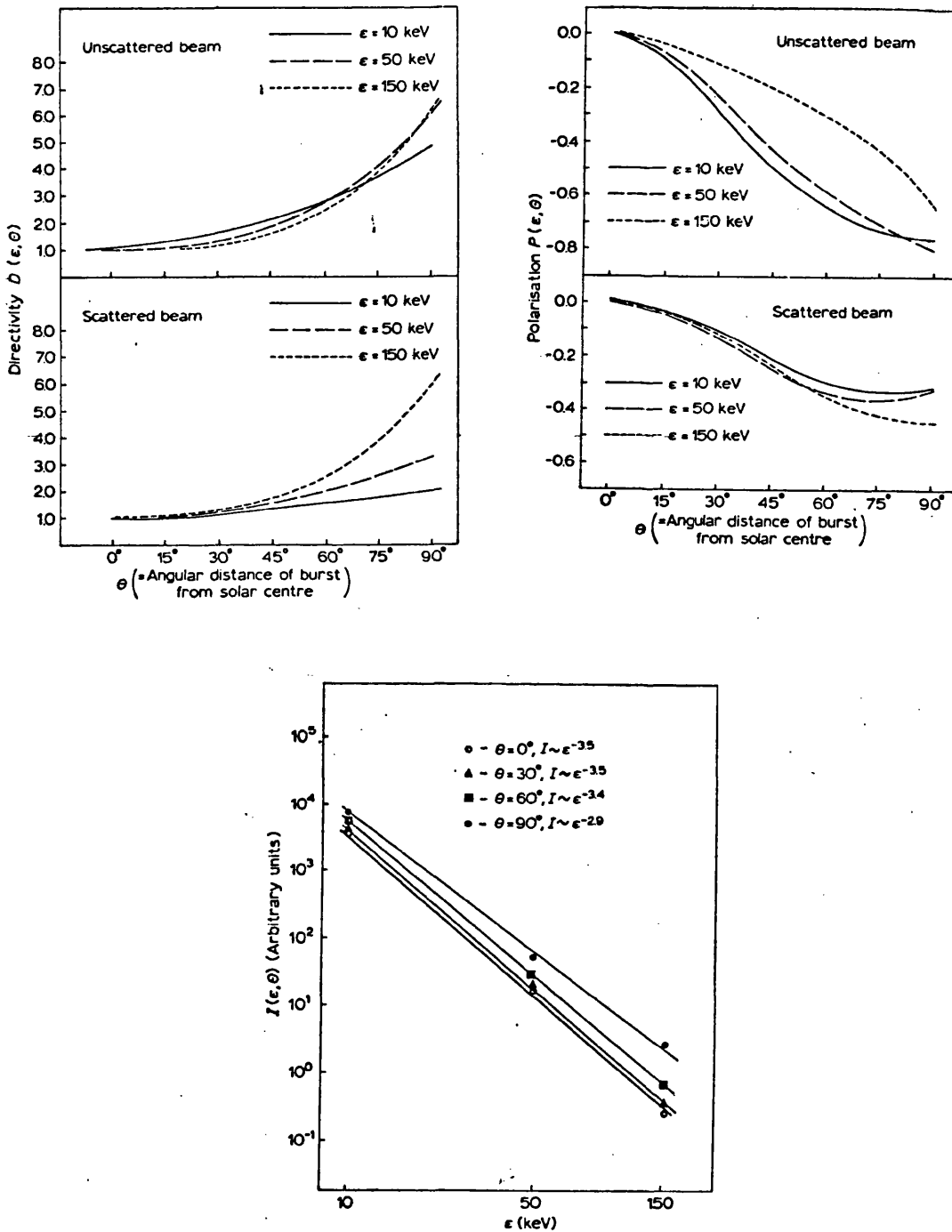


**Figure 5.1** Properties of the thick target model. From Brown (1972b).  
 Upper left:-  
 Directivity of emission from continuous injection model, with and without scattering, as a function of photon energy  $\epsilon$  and of angular heliocentric distance  $\theta$  of source.  
 Upper right:-  
 Polarisation of emission from continuous injection model, with and without scattering, as a function of photon energy  $\epsilon$  and of angular heliocentric distance  $\theta$  of source.  
 Lower:-  
 Dependence of the X-ray spectrum on the direction of observation. Best power law fit is shown for each direction.

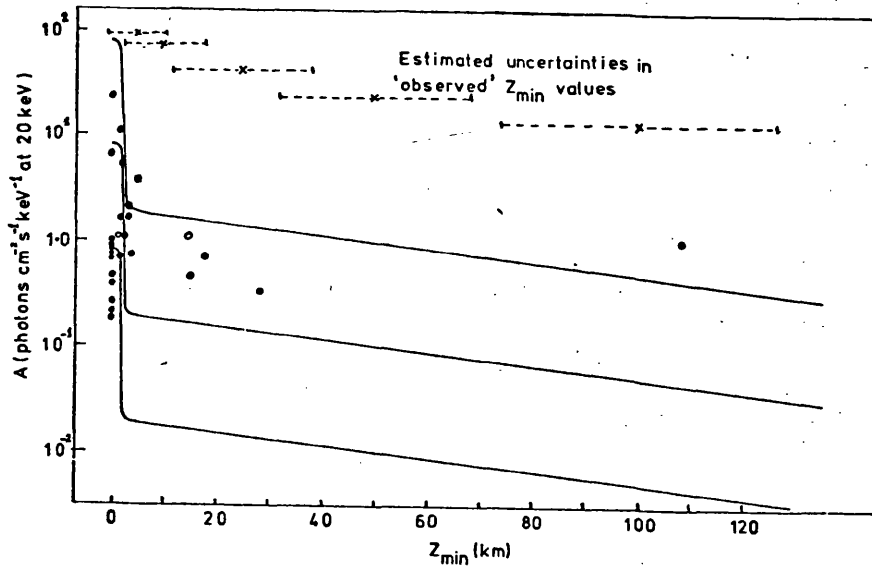
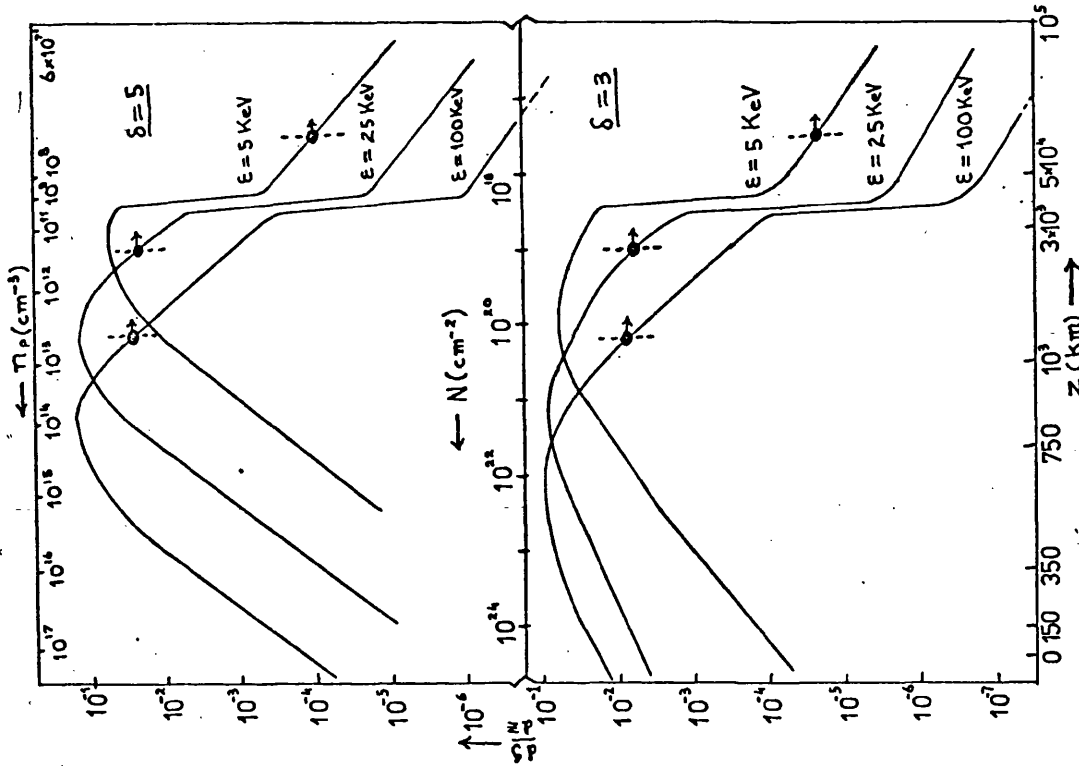


Figure 5.2 From Brown & McClymont (1975).

Upper:-

Emission  $dJ/dZ$  from a vertical electron stream per 100 km of the atmosphere at  $\epsilon=5, 25$  and 100 keV expressed as a fraction of the total thick target emission at the same  $\epsilon$ , plotted against the log of the column density  $N$  ( $\text{cm}^{-2}$ ). Plasma densities  $n_p$  and geometric heights  $Z$  corresponding to each  $N$  also shown on the figure. Arrowed dots indicate the levels above which the overlying atmosphere may be considered a thin target.

Lower:- Predicted thick target flux compared with observations from Roy & Datlowe (1975).

## 6. THE THIN TARGET MODEL

Motivated by the observation of behind-the-limb bursts and of a relationship between hard X-ray and interplanetary electron spectral indices, Datlowe & Lin (1973) proposed a model in which bremsstrahlung-producing electrons stream upward through the corona. This model explains the fact that interplanetary electrons ejected during a flare have a spectrum approximately one power harder than the corresponding hard X-ray burst spectrum. The thin target model was proposed partly because it was believed that the thick target was incompatible with behind-the-limb observations. However, Brown & McClymont (1975) have now shown that it cannot be ruled out on these grounds, provided the acceleration region is sufficiently high in the corona. Brown & McClymont also point out that since the flux of interplanetary electrons is much lower than the electron flux inferred from X-ray measurements, the electron escape probability is likely to be energy dependent. (see also Smith, 1974). Datlowe and Lin (1973) present details of the observations only in the case of one small flare. The interplanetary electron spectrum extends unbroken up to 150 keV, but the hard X-ray spectrum exhibits a break in the region 40 - 60 keV, where the spectral index increases by at least a power. This suggests that the two electron distributions are distinct.

Explicit calculations of the thin target directivity and polarisation have not been made, but Brown (1975) pointed out that Haug's (1972) calculations, shown in Figure 6.1, are applicable to this model. These results could be radically modified if collective scattering and energy losses are important in the corona. Since the majority of photons are beamed upwards, the albedo effect is negligible in the thin target model. Finally, the inefficiency of the thin target model has been commented on by Brown & McClymont (1975). Since electron energy losses in the X-ray source region are required to be small, the already severe problem of electron numbers and total energy

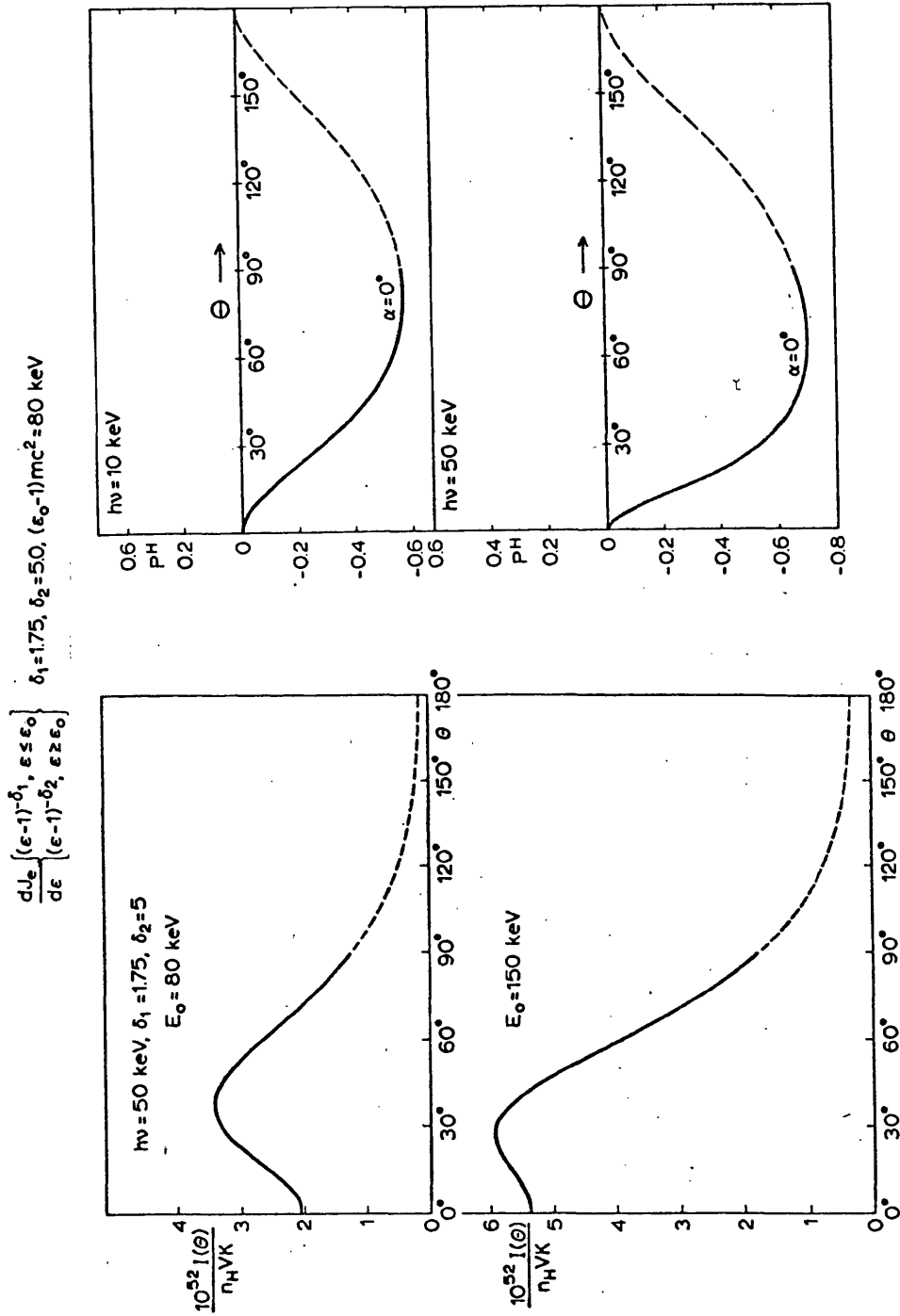


**Figure 6.1** Properties of the thin target model. From Brown (1975).  
 Upper:- Upper limit to the polarisation expected from the thin target model of Datlowe and Lin (1973) at 10 and 50 keV as a function of flare location, based on Haug (1972).  $\theta$  is the distance from the solar centre, so dotted portions are for flares behind the limb.  
 Lower:- Upper limit to relative variation of total burst intensities at 50 keV across the disc in the thin-target model, (based on Elwert and Haug, 1971).  $E_0$  is the electron spectrum 'knee-energy'

is worsened considerably. Because this vast number of electrons is not observed in interplanetary space, they would have to be trapped high in the corona in a low density region where their bremsstrahlung and gyro-synchrotron emission rates are small. One cubic solar radius is a conservative estimate of the trapping volume.

## 7. THE ELECTRON TRAP MODEL

Detailed results for this model are given in Chapters IV and V. Here the main results are summarised in a similar way to the other models discussed above. Figures 7.1 and 7.2, reproductions of Figures 4.3 and 4.4 of Chapter IV, illustrate the centre to limb variation of photon flux, spectral index and polarisation. The electrons have discrete pitch angles and a power law energy spectrum of spectral index 3. Results are shown for a range of pitch angles. In the case illustrated the trap lies on the equator and is orientated in the East-West direction. These results show the main features of the trap model, but it should be remembered that the observed X-ray flux and polarisation depend on trap orientation.

The directivity of X-ray emission from the trap is small ( $\lesssim 30\%$  variation). If the trap contains electrons of small pitch angle the spectrum hardens slightly ( $\sim \frac{1}{4}$  power) at the limb, while for large pitch angles it softens by up to  $\frac{1}{2}$  a power. The degree of polarisation is  $\lesssim 20\%$  in most cases and tends to decrease from centre to limb. It also tends to decrease with increasing photon energy. The direction of polarisation is a complex function of trap orientation and the electron pitch angle distribution. Emission from electron distributions in which small pitch angles predominate is usually polarised parallel to the trap while large pitch angle electrons generally produce X-rays polarised perpendicular to the axis of the trap.

Hard X-ray emission from a trap partly obscured behind the solar limb is discussed in Chapter V. It is found that the X-ray intensity drops off slowly as the trap is occulted, falling by a factor of 2 or 3

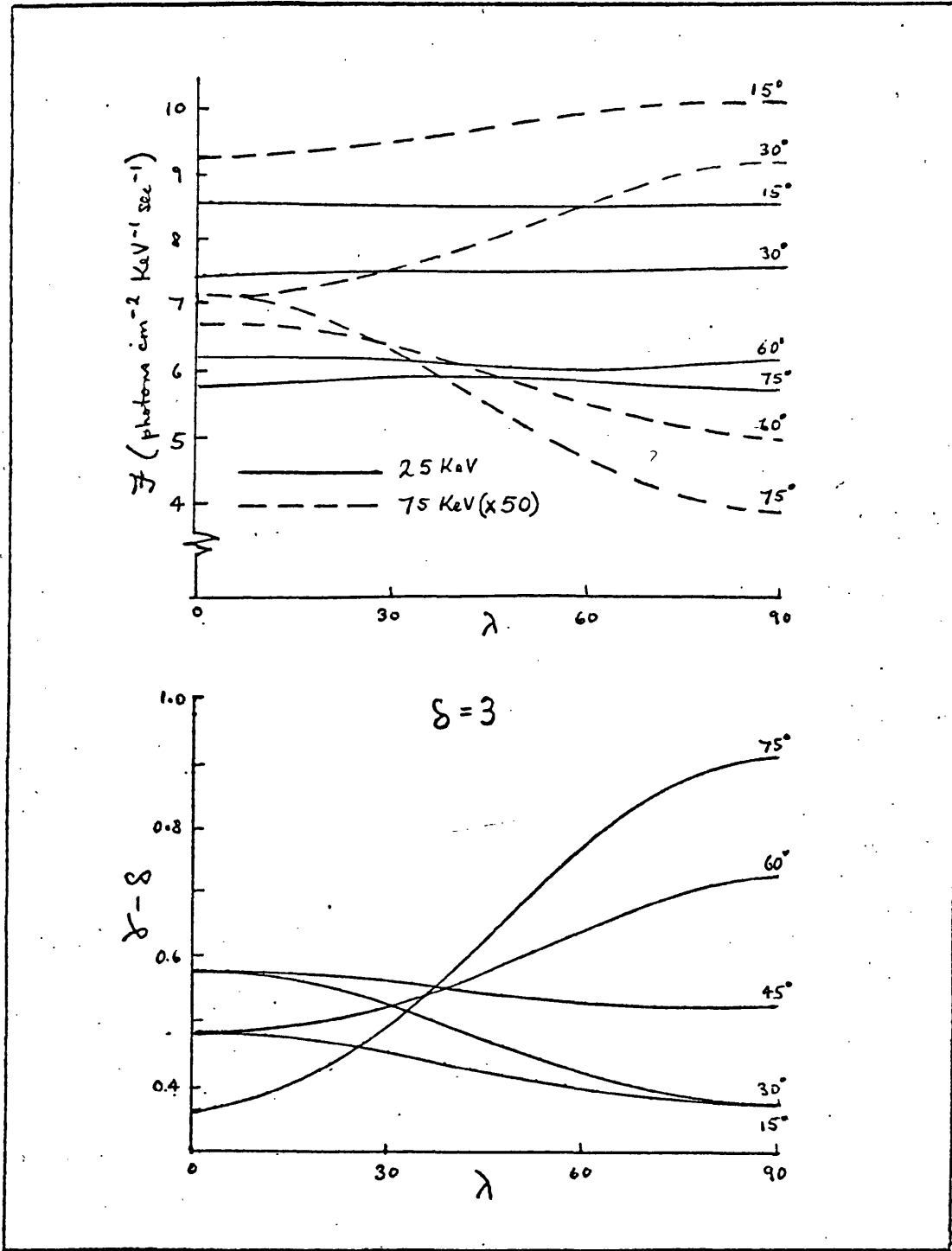


**Figure 7.1** Electron distribution (ii). Directivity (upper figure) and spectral index (lower figure) of X-ray emission from a trap on the equator for a range of initial pitch angles. Fluxes at 75 KeV (broken lines) are scaled up by x 50. The electron spectral index,  $\delta$ , is 3.

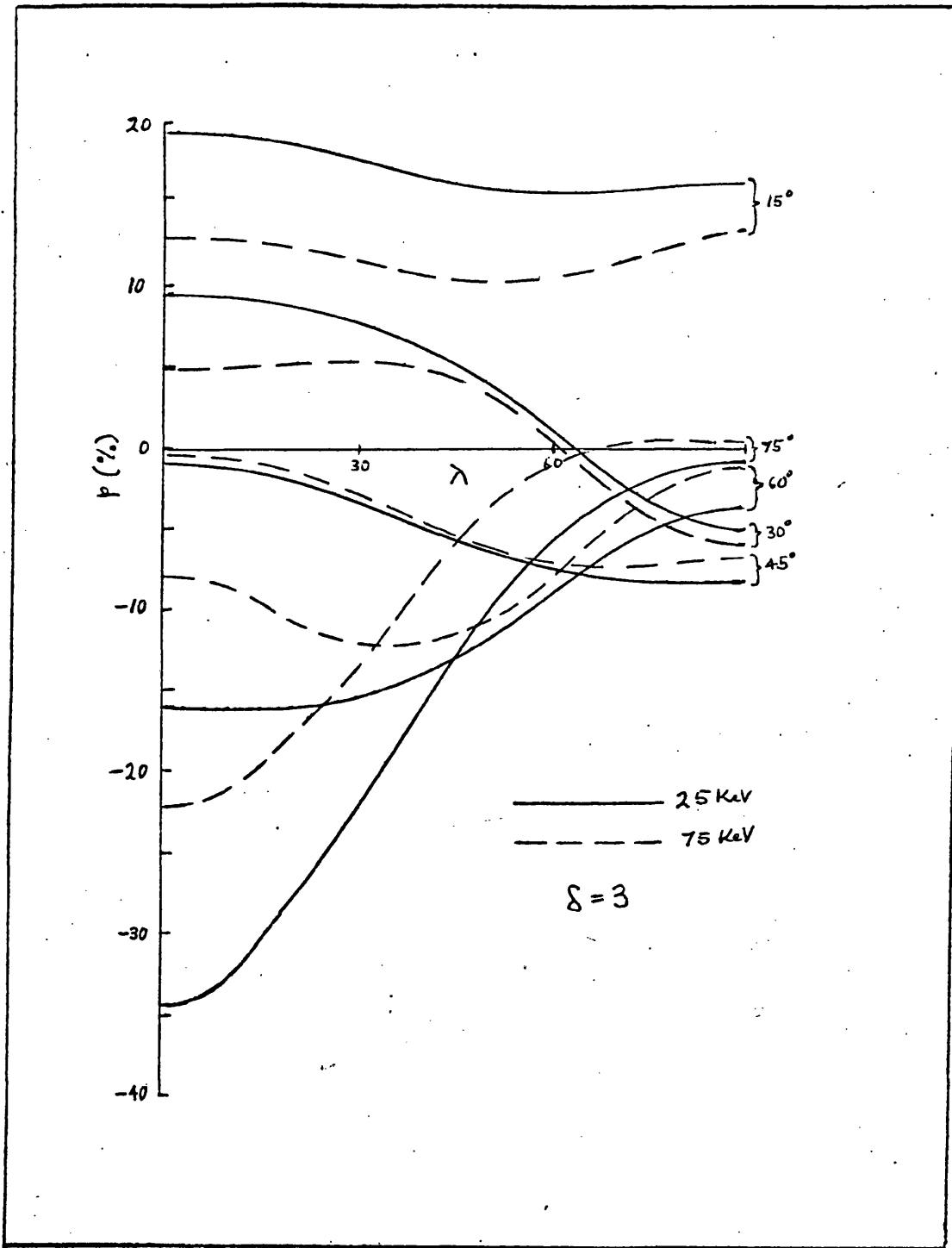


Figure 7.2 Electron distribution (ii). Polarisation at 25 KeV and 75 KeV as a function of longitude for a trap on the equator, for a range of initial pitch angles.

over most of the range of visibility. The final drop to zero flux occurs just as the top of the trap disappears.

## 8. THE THERMAL MODEL

The problem of electron numbers in the source models discussed above makes the search for any alternative explanation of the hard X-ray burst of major importance. In a large event  $4 \times 10^{39}$  electrons of energy greater than 25 keV (Hoyng, 1975), carrying a total energy of  $\sim 2 \times 10^{32}$  ergs, must be accelerated on a timescale of a few minutes. If the electron spectrum is extrapolated down to 10 keV, electron numbers and energy are increased by an order of magnitude. The corona is generally regarded as the most appropriate site for particle acceleration (e.g. Sweet, 1969). In order to supply a large flare the equivalent of all the electrons in the corona over an area of  $2 \times 10^{21}$  cm<sup>2</sup> (for quiet coronal densities), that is  $\sim 100$  times the area of a large flare, must be accelerated. In reality, electrons must be drawn up from the chromosphere to maintain a steady state (see Brown and Melrose, 1975).

The severe requirements on the acceleration mechanism can be reduced by postulating that hard X-ray emission is thermal in origin. This point of view was first expressed by Chubb et al. (1966). Brown (1974b) obtained an expression for the emission measure distribution over temperature required to reproduce any observed photon spectrum, thus showing that thermal and non-thermal sources cannot be distinguished by observation of the X-ray spectrum alone. Most of the controversy over this model has centred on the timescale for cooling since, at the high temperatures required ( $\sim 800 \times 10^6$  K), mean free paths of particles are very large and thermal conduction highly effective (e.g. Brown, 1974b; Kahler, 1971). A review of arguments for and against the thermal interpretation is given by Kahler (1975). The polarisation results of Tindo (1972) suggest that the model is in fact untenable, since a thermal source can only produce unpolarised emission (except for a very small albedo polarisation).

## 9. THE REACCELERATION MODEL

This model represents another attempt to circumvent the electron numbers problem encountered in the continuous injection and trap models. Instead of electrons being accelerated in one region and injected into a trap or thick target in another region, here the two regions are postulated to be identical. If the density in the source is  $\sim 10^{12} \text{ cm}^{-3}$  only  $\sim 10^{35}$  electrons need be involved in X-ray production at any instant. If these same electrons can be continuously reaccelerated while simultaneously producing bremsstrahlung radiation only  $10^{35}$  electrons in the total are needed. Since the X-ray burst can last for  $\sim 10^9$  times the electron collisional decay time, a highly efficient containment mechanism is required.

Hoyng (1975) suggests that Langmuir waves generated in a neutral sheet are responsible for the electron acceleration. Since a very thin sheet, too small to contain the requisite number of electrons, is required, Hoyng suggests that electrons in the surrounding region are energised by Langmuir waves propagating outwards from the sheet. Brown & Melrose (1975), re-examining Hoyng's analysis, confirm the acceptability of most of Hoyng's proposals, but point out that annihilation of magnetic field at a neutral sheet requires the plasma on each side to be swept through the sheet as annihilation proceeds. They show that the electrons cannot therefore be contained and reaccelerated, but that the total number of electrons accelerated is similar to that in the continuous injection model.

This hard X-ray source model is of particular interest as the acceleration mechanism is an intrinsic part of the model. Most conclusions concerning it must be regarded as tentative at this stage, so its progress will be followed with interest.

## 10. HARD X-RAYS - THEORY AND PRACTICE

Time profiles of photon flux and spectral index in typical small and large X-ray bursts (Hoyng (1975)) are illustrated in Figures 10.1

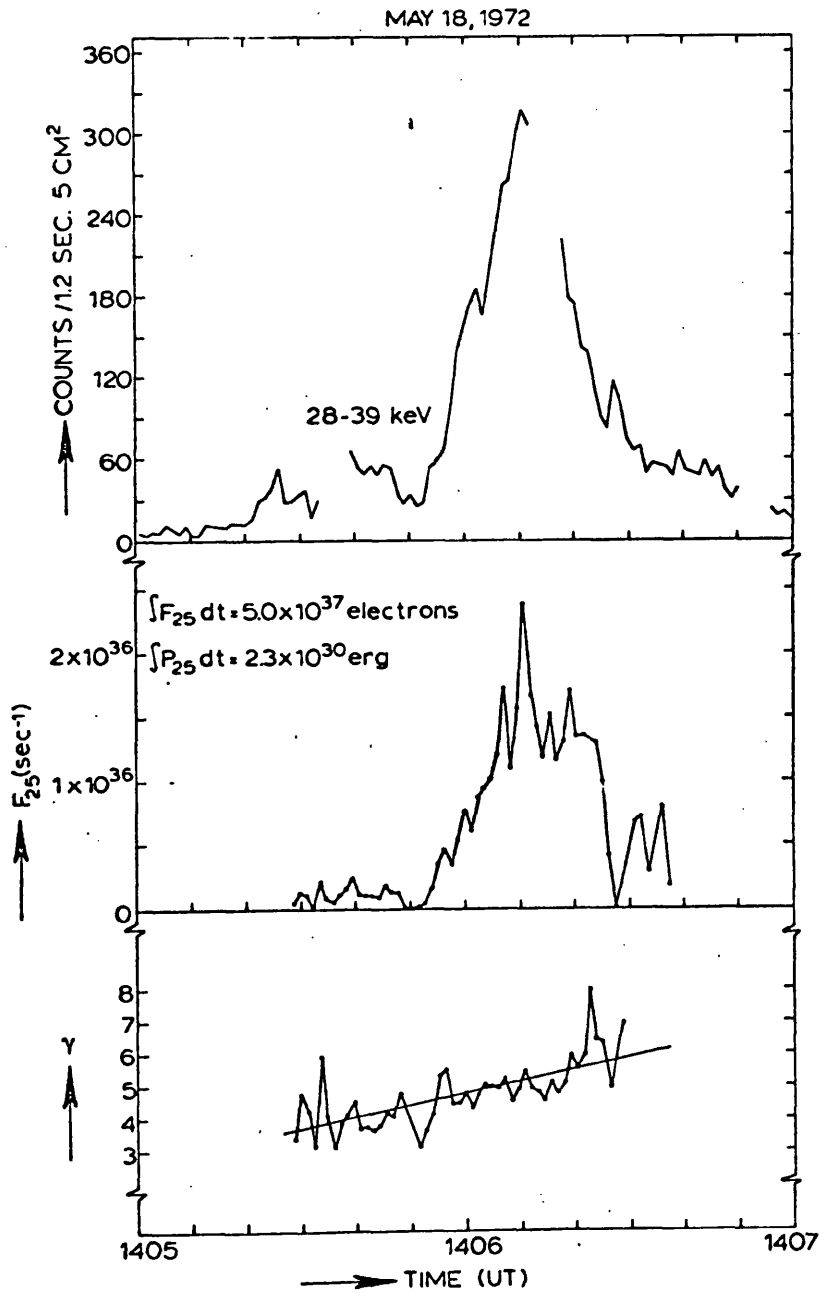
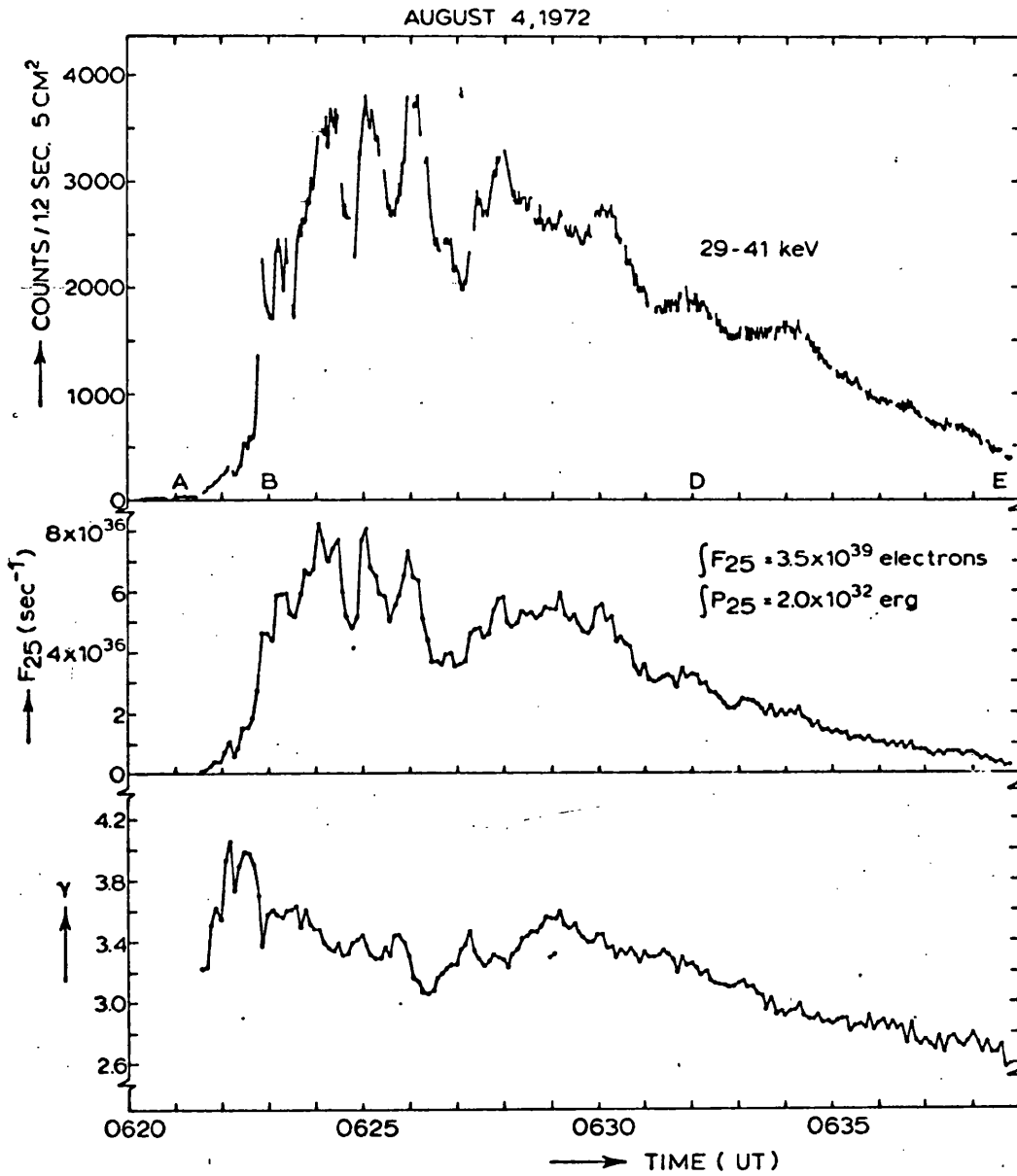


Figure 10.1 Time profile of a small X-ray burst. From Hoyng (1975).

Thick target parameters of the May 18, 1972 event. Fluctuations in  $\gamma$  are minimal at maximal count rate in channel 1.  $\gamma$  increases linearly with time throughout the event; analogous behaviour of  $\gamma$  is seen in all IXBs.



**Figure 10.2** Time profile of a large X-ray burst. From Hoyng (1975).  
 Thick target parameters of the August 4, 1972 event. The accuracy in  $F_{25}$  and  $\gamma$  has increased to a few percent in this case.  $F_{25}$  and  $\gamma$  show a remarkable correlation (fig. 27); at the same time,  $\gamma$  and the count rate in channel 1 anticorrelate in the region A-D (section 2.6.). The letters A-E refer to those in fig. 27.  
 Only every fifth datapoint  $F_{25}$  and  $\gamma$  is shown.

and 10.2. Below are summarised the main observational results which a successful hard X-ray source model should be compatible with. Some of these results are well established, most are best regarded as tentative. On some topics contradictory results have been published by different authors, hence the choice of material here is to a certain extent subjective. It should also be clear that in order to condense hundreds of man-years of research into  $\sim 250$  words, vast generalisations have been made.

- (i) Directivity is low. In statistical studies, Kane (1974) and Datlowe (1975) find less than  $\pm 50\%$  variation from centre to limb.
- (ii) Spectral index increases by  $\sim 1$  power from centre to limb and is the same for behind-the-limb events as for events at the limb. (Datlowe 1975). Kane (1974) finds no significant variation.
- (iii) Heights of hard X-ray emission up to  $10^5$  km in the corona are indicated by behind-the-limb observations (Datlowe et al., 1974; Roy & Datlowe, 1975; McKenzie, 1975).
- (iv) Degree of polarisation is  $\sim 10 - 20\%$  (Tindo et al., 1972; Nakada et al., 1974). Only three measurements have been made. These results are in urgent need of confirmation.
- (v) Direction of polarisation is radial, according to Tindo et al (1972). This conclusion must be regarded as tentative at present (see Nakada et al., (1974)).
- (vi) Modulation of the photon spectrum occurs on a timescale of  $\sim 10-30$  seconds. It is periodic in large bursts (Hoyng et al., 1975).
- (vii) Spectral index in small events increases throughout the burst (IXB's - Hoyng et al, 1975).
- (viii) Spectral index in large events tends to decrease towards the end of the event (Frost & Dennis, 1971; EB's - Hoyng et al, 1975). In the large events of 4 and 7 August 1972, Hoyng et al find a correlation between photon flux and spectral index.

- (ix) Source size of hard X-ray emission is  $\lesssim 5 \times 10^9$  cm in one of its dimensions (Takakura et al., 1971).
- (x) Impulsive microwave emission has a time structure closely correlated with that of the hard X-ray burst (Peterson & Winckler, 1959; Kundu, 1961; and many others).
- (xi) EUV emission, like the microwave burst, is closely correlated with the hard X-ray burst (Donnelly, 1969; Kane & Donnelly, 1971).
- (xii) Soft X-ray emission indicates that the energy in the soft X-ray flare follows roughly the time integral of the energy loss rate of hard X-ray emitting electrons (e.g. Neupert, 1968).
- (xiii) Optical (H $\alpha$ ) emission follows the same pattern as the soft X-ray flare (e.g. Falcianni et al., 1968), but
- (xiv) Optical flashes,  $\sim 5$  seconds duration, coinciding with peaks in the hard X-ray burst, have been reported by Zirin & Tanaka (1973).
- (xv) Interplanetary electrons with energies in the 10 - 100 keV range are accelerated during the impulsive phase of a flare. Their number is much smaller than that inferred to be in the hard X-ray source region. The spectral index of their (power law) energy distribution is  $\sim 1$  power harder than the hard X-ray spectrum. (Lin & Anderson, 1967; Lin, 1970, 1971; Lin & Hudson, 1971; Lin, 1974; Datlowe and Lin, 1973).

These observations are compared with the predictions of the hard X-ray source models in Table 10.1.

The thick target model fulfils most of the requirements of observation. Its main shortcoming is the prediction of a hardening of the X-ray spectrum near the limb. Note, however, that a large number of observational features which it appears to be compatible with rely on hypothesised properties of the acceleration mechanism.

The thin target model, for which observation offers less support, again depends on assumed characteristics of the acceleration mechanism for most of its properties.

Table 10.1 Speculative Properties of Hard X-ray Source Models

Observation	Hard X-ray Source Model					Notes
	Thick Target	Thin Target	Trap	Thermal	Re-Accln	
(i) Directivity	✓	×	✓	✓	✓	a Reduced by albedo in all but thin target.
(ii) $\gamma$ (centre $\rightarrow$ limb)	×	✓	✓	×	?	a Large pitch angles only. b Albedo probably causes hardening.
(iii) Height (behind-the-limb)	✓	✓	✓	?	?	a Flux possibly too low. b Flux possibly too high.
(iv) Degree of Polarisation	✓	×	✓	×	?	a Probably too high.
(v) Direction of Polarisation	✓	✓	?	×	?	a Assumed radial. Nakada et al(1974) suggest not so in all cases.
(vi) Modulation	✓	✓	✓	?	✓	a Vibration of trap. b Depends on conductive timescale.
(vii) $\gamma$ (IXB) Evolution	✓	✓	✓	✓	✓	a If Brown's(1972a) hypothesis correct. b Expected from conductive redistribution.
(viii) $\gamma$ (EB) Evolution	✓	✓	✓	×	✓	a Vibration of trap plus collisional decay.
(ix) Source Size	✓	?	✓	?	✓	
(x) Correlation with microwaves	✓	?	?	×	✓	a Some upward acceleration required. Feasible. b Too many electrons. Overcome with difficulty.
(xi) Correlation with EUV	✓	×	✓	✓	✓	a Some downward acceleration required. b Precipitation required.
(xii-xiv) Correlation with optical & soft X-	✓	×	?	✓	✓	a Precipitation required. Ho flashes require $\gamma$ ( $\nu$ trap vibration) $>$ $\gamma$ ( $\nu$ thick target).
(xv) I.P. Electrons	✓	?	✓	?	✓	a Some upward acceleration required. Feasible. b Too many electrons although spectrum O.K.
Electron energy and numbers	?	×	?	✓	✓	a Inefficient. Places severe requirements on acceleration mechanism.

\* Hypothetical property of acceleration mechanism determines this.

The electron trap is the only model which does not lean heavily on hypothesised characteristics of the acceleration mechanism. It assumes only that  $10^{39}$  electrons can be injected into the trap on a timescale of a few seconds, in itself a severe requirement. (If the "dog-leg" initial phase of  $(\mathcal{F}, \gamma)$  evolution in the 4 August 1972 burst (Figure 4.1) is taken to correspond to the injection phase, then  $\sim 4 \times 10^{39}$  electrons are injected in  $\sim 80$  seconds.)

The thermal model, although avoiding the problem of electron numbers, still requires the fast release of a large amount of energy. Observations of a large degree of polarisation seems to rule out this model. The re-acceleration model appears to satisfy most observational requirements, although detailed predictions have still to be worked out. The difficulty in doing so is clearly comparable with the difficulty in deducing properties of the acceleration region postulated for the continuous injection models.

The following observations are suggested as being of primary importance to the solution of the hard X-ray flare problem:-

- (i) The variation of spectral index with heliocentric distance appears to be a promising technique for discrimination between source models. More work is required to improve Datlowe et al's (1974) statistics.
- (ii) More behind the limb observations are called for. It appears certain that X-ray emission does occur high in the corona, but two quantifying facts are required:- (a) how much intrinsically larger are behind-the-limb bursts than disc events of the same photon flux, and (b) how does the burst intensity vary with distance behind the limb.
- (iii) As anticipated by Korchak (1967) and Elwert (1968), polarisation measurements are clearly a very important diagnostic tool. More observations, in particular of the direction of polarisation, are urgently required. These should be made at higher photon energy than the 15 keV used until now, in order to be certain that unpolarised thermal emission from the soft X-ray flare does not reduce the measured polarisation below its true value.

- (iv) Hard X-ray imaging detectors in the next generation of instruments (NASA Solar Maximum Mission) should provide information not only on the source size, but its structure. These results are eagerly anticipated.

The following are a selection of areas of theoretical work which appear to be of major importance:-

- (i) The thick target model is attractive (Table 10.1) but its predictions contradict the observed position dependence of the spectral index (item (ii)). An independent check on Henoux's (1975) albedo results, using Brown's (1973) prediction of thick target directivities instead of the thin target model taken by Henoux, would be worthwhile. Note that the model does agree with observation in over-the-limb events, although predicted fluxes are rather low, since the thin target coronal emission is 2 powers steeper than the thick target emission seen in disc flares.
- (ii) The spectral index inferred on the thin target model for electrons in the X-ray source region is in excellent agreement with the observed interplanetary electron spectrum. But the extent to which the electron spectrum is changed by propagation effects in the corona is uncertain. More theoretical work on wave-particle interactions in the corona is required.
- (iii) All models except the electron trap depend on the unproven ability of the acceleration mechanism to modulate the electron spectrum in a quasi-periodic manner. This ability should be questioned more closely.
- (iv) The trap model invokes vibration of the trap in order to explain the X-ray modulation. An analysis of the possible eigenmodes of a vibrating trap would be of interest.

CHAPTER IIITHE ELECTRON TRAP MODEL OF HARD X-RAY BURSTS - ANALYSIS  
OF DIRECTIONAL AND POLARISATION PROPERTIES1. INTRODUCTION

The electron trap model, based on the configuration suggested by Takakura & Kai (1966) as a model for solar microwave bursts, seeks to explain hard X-ray emission in terms of bremsstrahlung emission of non-thermal electrons magnetically trapped in the low corona. Although detailed calculations of the directivity and polarisation for the thick target model have been made (Brown, 1972; Petrosian, 1973), the trapping model analyses which have been performed to date (Pinter, 1969; Elwert & Haug, 1970, 1971; Haug, 1972) have neglected the curvature of the trapping field, considering electrons either moving in a horizontal magnetic field or circling horizontally in the vertical limbs of the trap.

Because of the complex geometry of the trap, it is impossible to predict properties of the X-ray emission from such simple idealised models. For example, under some circumstances radiation from the limbs of the trap is polarised in the opposite direction to radiation from the upper part of trap, so that the degree of polarisation observed depends critically on partial cancellation of the two components.

The necessity for a complete treatment of the trap curvature is demonstrated by the following example. We estimate the relative times an electron spends in the limbs and upper part of the trap. From the first adiabatic invariant (Spitzer, 1962) we have

$$\frac{\sin^2 \alpha}{\sin^2 \alpha_0} = \frac{B}{B_0} \quad (1.1)$$

and

$$\sin^2 \alpha_0 = B_0 / B_m \quad (1.2)$$

where  $\alpha$  is the pitch angle of a trapped electron at a point where the magnetic field strength is  $B$  and  $\alpha_0, B_0$  are the corresponding values at the centre of the trap (where the magnetic field is weakest).  $B_m$  is the magnetic field strength at the mirror point of the electron trajectory (where  $\alpha = \pi/2$ ).

Now

$$\frac{ds}{dt} = v_{//} = v \cos \alpha \quad (1.3)$$

where  $s$  is the distance of the electron from the centre of the trap measured along the field line on which the electron is trapped. The total electron velocity is denoted by  $v$  and the component along the magnetic field by  $v_{//}$ . If  $y$  is some function which varies cyclically as the electron traverses back and forth along the trap then the mean value of  $y$  is given by

$$\bar{y} = \frac{\int y dt}{\int dt} \quad (1.4)$$

If we assume that the function  $y$  depends only on the position of the electron, then using (1.3), (1.4) can be written

$$\bar{y} = \frac{\int y(s) \frac{ds}{v \cos \alpha}}{\int \frac{ds}{v \cos \alpha}} \quad (1.5)$$

Substituting from (1.1) and (1.2) this becomes

$$\bar{y} = \frac{\int y(s) (1 - B(s)/B_m)^{-1/2} ds}{\int (1 - B(s)/B_m)^{-1/2} ds} \quad (1.6)$$

As a simple but feasible representation of the trapping field we take

$$B(s) = B_0 (1 + a s^2) \quad (1.7)$$

where  $a$  is a constant defining the scale length of field variation. If the function  $y(s)$  is symmetric about the origin then after substitution from (1.7), (1.6) can be written

$$\bar{y} = \frac{\int_0^{s_m} y(s) (s_m^2 - s^2)^{-1/2} ds}{\int_0^{s_m} (s_m^2 - s^2)^{-1/2} ds} \quad (1.8)$$

where  $s_m$  is the distance of the mirror point from the centre of the trap. Changing the variable to  $x = (s/s_m)^2$  and noting that the denominator is a beta function  $B(\frac{1}{2}, \frac{1}{2}) = \pi$ , this becomes

$$\bar{y} = \frac{1}{\pi} \int_0^1 y(s_m x^{\frac{1}{2}}) x^{-\frac{1}{2}} (1-x)^{-\frac{1}{2}} dy \quad (1.9)$$

We evaluate the mean distance of the electron from the centre of the trap by taking

$$y(s) = |s| \quad (1.10)$$

which, on evaluating (1.9), yields

$$\bar{s} = \frac{2}{\pi} s_m \quad (1.11)$$

This result suggests that the electron spends roughly half of each cycle in the upper part of the trap near the centre and half in the limbs near the mirror points.

A similar result is obtained if we seek the value of  $s = s^*$  for which the electron spends equal times in the regions  $s < s^*$  and  $s > s^*$ . To find  $s^*$  we set  $y = 1$  and  $\bar{y} = \frac{1}{2}$  in (1.9) and replace the upper limit of the integral by  $x^* = (s^*/s_m)^2$ . Then (1.9) can be written

$$B_{(s^*/s_m)^2}(\frac{1}{2}, \frac{1}{2}) = \frac{1}{2} B(\frac{1}{2}, \frac{1}{2}) \quad (1.12)$$

where  $B_x(a, b)$  is the incomplete beta function. From symmetry it is clear that the solution is

$$s^* = \frac{1}{2} s_m \quad (1.13)$$

which confirms the view that radiation from both the limbs and upper part of the trap are important.

Therefore in order to obtain quantitative predictions a complete field model must be defined and analysed in detail.

We are interested in calculating the directivity, polarisation and spatial distribution of hard X-ray emission from the trapping model. We also examine the effect of occultation of the lower part of the trap in a behind-the-limb event. The importance of these characteristics of hard X-ray emission in testing source models against observation, the observational data which has been collected to date, proposed methods of making such observations in the future and the predictions of other hard X-ray source models with regard to these characteristics have been discussed in Chapter II.

The necessary idealisations in our analysis mean that the derived results are best compared with observational data on large events as these usually have a simpler structure than small flares (for example, see Švestka (1969)) and, as discussed in Chapter I, show characteristics which are more repeatable from event to event. In our analysis we are concerned only with the X-ray emission from the trap itself, omitting to take account of the albedo contribution which arises from back scattering of photons from the photosphere (Tomblin, 1972; Santangelo *et al.* 1973; Henoux, 1975) or the thick target emission which may arise if electrons are scattered out of the trap into the dense chromosphere at a sufficiently high rate (Hudson 1972; Melrose and Brown, 1975).

As the bounce period of a trapped electron is only  $\sim 1$  second whereas the collisional decay time scale for a non-thermal electron in the corona is  $\sim 10$ -100 seconds and the transit time of Alfvén type waves propagating along the trap is  $\geq 10$  seconds, (Brown, 1973a) we may take the trap to be static during one electron bounce period and the electron distribution in the trap to be quasi-stationary. Therefore we do not discuss acceleration mechanisms or decay mechanisms here, we merely ask - given an instantaneous electron energy and pitch angle spectrum, what are the characteristics of the resultant hard X-ray emission?

We have studied the hard X-ray emission from four types of electron distribution, namely

- (i) A delta function distribution in both electron energy and pitch angle,
- (ii) A power law electron energy distribution with a singular pitch angle distribution,
- (iii) A power law energy distribution with pitch angle distributions of the form  $\sin^n \alpha$  and  $\cos^n \alpha$ , and
- (iv) A power law energy distribution where pitch angle is a function of electron energy.

Distribution (i) is not considered to be a realistic representation, as it is generally accepted that an electron energy spectrum close to a power law is required to reproduce observed X-ray spectra. It is used in preliminary studies of the sensitivity of directivity and polarisation of hard X-ray emission to magnetic field geometry and atmospheric structure. Using this distribution, investigations into the variation of directivity and polarisation with position and orientation of the trap on the solar disc have been carried out in more detail than is convenient for the other distributions, which require much more computer time.

Distribution (ii) is more acceptable on physical grounds than (i) and is regarded as an intermediate step between distributions (i) and (iii), (iv). Although it is difficult to conceive of a mechanism capable of accelerating electrons in such a manner that the ratio of velocity acquired perpendicular to the field lines to the parallel component is independent of energy, it must be remembered that the factors which determine the form of electron distribution in the trap are completely unknown. This distribution enables us to study the energy dependence of directivity and polarisation for different electron pitch angles.

Distribution (iii) is possibly more realistic than (ii), although

there are no physical grounds for believing this to be the case other than the observation that in nature singular distributions are uncommon. Distribution (ii) can, of course, be regarded as an approximation to a non-singular pitch angle distribution which peaks at the value used in (ii). It is possible that (ii) may approximate the behaviour of high energy electrons while (iii) describes the electrons at the low energy end of the spectrum where random thermal velocities and the enhanced effect of collisions may be expected to produce a more isotropic distribution. By comparing the X-ray emission from distributions (ii) and (iii) we hope to estimate the degree of smudging caused by the presence of electrons with a range of pitch angles. It is also of interest to compare the spatially resolved emission from (ii) and (iii). As all the electrons in distribution (ii) mirror at the same height the spatially resolved X-ray flux (flux per unit length along the trap) becomes infinite at the mirror points, which is not the case in (iii), where the distribution of mirror point heights results in a continuous variation of the flux. Thus spatially resolved observations of the X-ray flux from a coronal trap could permit deductions to be made about the pitch angle distribution of the electrons.

Distribution (iv), which has been invoked by Brown & Hoyng (1975) in order to explain quasi-periodic modulation of the X-ray flux in large flares (see Chapter VI), is the only one considered for which we have a direct physical interpretation. If it is supposed that the electron acceleration is caused by a large scale electric field then the velocity component of an electron parallel to the magnetic field is increased while the component perpendicular to the field remains unchanged (if collisions are ignored). Neglecting the initial thermal velocity of a particle compared to its final velocity and taking all particles to have the same thermal velocity component perpendicular to the field we have

$$\sin \alpha_0 = v_{\perp} / v \quad (1.14)$$

where  $\alpha_0$  is the electron pitch angle at injection,  $v_{\perp}$  is the

perpendicular thermal velocity and  $v$  the final velocity of an electron. Treated non-relativistically, this equation can be written

$$\sin \alpha_0 = (E^*/E)^{\frac{1}{2}} \quad (1.15)$$

where  $E$  is the electron kinetic energy and  $E^*$  a parameter to be identified roughly with the thermal energy of the electrons before run-away occurred. This formula represents a gross simplification as we have ignored details of the actual injection process, but it is reasonable to suppose that the major effect of transferring an electron into the trap would be to change the perpendicular component of its energy, which would only alter the interpretation of  $E^*$ . It is worth noting that a possible explanation of the frequently observed steepening of hard X-ray spectra above  $\sim 70$ -100 keV, as discussed in Chapter II, is provided by this model. Estimating the initial thermal energy,  $E^*$ , to be  $\sim 2$ -5 keV and taking  $E$  to be 70-100 keV in (1.15), we find that  $\alpha_0 \approx 10^\circ$ - $15^\circ$ . From Figures 3.2 - 3.4 we see that this is exactly the range of pitch angle in which we would expect a transition from trapping to escape into the chromosphere.

As the magnetic field structure over an active region is not well known, we take a potential field originating from a bipolar pair of sunspots as a representation of the trapping field. Use of a simple field model has the advantage of allowing upper limits to be set on the directivity and polarisation, as a more complex field structure would tend to reduce anisotropy. The sensitivity of X-ray emission characteristics to the magnetic field geometry has been investigated by comparing results obtained using three different field models.

In showing that the contributions to X-ray flux from both the upper part of the trap and from the limbs are important (Equation (1.13)), we did not take into account the variation in ambient proton density. As the density scale height in the corona is large this does not affect the rough estimates (1.11) and (1.13), but if the characteristics

of the emission from these two regions oppose each other this factor could appreciably influence the results. Therefore we have also examined the sensitivity of the model to atmospheric structure by performing the computations for a range of trap heights.

## 2. DISCUSSION OF PREVIOUS WORK

Although Takakura & Kai (1966) did not explicitly take account of trap geometry, their results are of interest as they found that the predicted decay characteristics of microwave emission from an assembly of trapped electrons with a power law energy spectrum with spectral index 3 to 5 gave good agreement with observation. As this spectrum is similar to that deduced from hard X-ray observations, it supports the hypothesis, suggested by the close time correlation of microwave and hard X-ray emission, that hard X-ray emission may originate from a coronal trap, the electrons responsible for the microwave radiation also emitting X-rays.

Whereas the electron spectrum deduced from the decay of microwave bursts encourages the view that trapped electrons may be responsible for the hard X-ray emission, the observed microwave flux does not. As the intensity of microwave emission is highly sensitive to magnetic field strength, it appears at first sight that the number of electrons in the trap could be deduced from hard X-ray observations and then the magnetic field strength chosen to give the correct microwave flux. However the observed microwave spectrum gives an indication of the strength of the magnetic field in which the radiating electrons are moving so that the electron numbers are in fact independently determined by the microwave data.

Peterson and Winckler (1959), who first pointed out that  $\sim 10^3$ - $10^4$  times as many electrons are needed to account for an observed hard X-ray burst than are required for the coincident microwave burst, suggested that the difference can be reconciled if the field strength in the source is non-uniform and the electrons spend most of their

time in regions of weak magnetic field. An electron would then emit X-rays continuously, but only contribute appreciably to the microwave flux when in a region of strong magnetic field. A ratio of peak emission rate to mean emission rate as large as  $10^4$  requires that trapped electrons be reflected at the mirror points by a sudden increase in magnetic field over a short distance.

To illustrate the severity of this requirement we first use (1.9) to evaluate the mean square magnetic field encountered by an electron moving in the magnetic field given by (1.7). We obtain

$$\bar{B}^2 = B_m^2 \left( \sin^2 \alpha_0 + \frac{3}{8} \cos^4 \alpha_0 \right) \quad (2.1)$$

where  $B_m$  is the mirror point magnetic field and  $\alpha_0$  the pitch angle of the electron at  $s = 0$ . Hence the maximum ratio of peak emission rate to mean emission rate, which occurs in the limit of small pitch angle, is

$$\left( \frac{P_{\text{peak}}}{P_{\text{mean}}} \right)_{\text{max}} = \left( \frac{B_m^2}{\bar{B}^2} \right)_{\text{max}} = 8/3 \quad (2.2)$$

which is nothing like the ratio of  $10^3 - 10^4$  required.

Secondly, we calculate the maximum field allowable in the weak field part of the trap and the maximum length of the strong field region. In the following analysis, subscripts W and S denote the weak and strong field regions respectively. If an electron spends a fraction  $\tau$  of each bounce period in the strong field region, then in order that microwave emission from the weak field region should not contribute appreciably, we require

$$B_w^2 \ll \tau B_s^2 \quad (2.3)$$

Typical field strengths derived from microwave spectra are  $\sim 500$  gauss, which with  $\tau \approx 10^{-4}$  implies

$$B_w \lesssim 5 \text{ gauss} \quad (2.4)$$

This restriction can be removed if it is assumed that the density in the trap is such that

$$\nu_w < \nu_p < \nu_s \quad (2.5)$$

where  $\nu_w$ ,  $\nu_s$  are the frequencies of peak gyro-synchrotron emission in the weak and strong field regions respectively and  $\nu_p$  is the plasma frequency, since radiation from the weak field region is then prevented from propagating. The plasma frequency is given by

$$\nu_p \approx 9 \times 10^3 n_e^{1/2} \text{ Hz} \quad (2.6)$$

where  $n_e$  is in  $\text{cm}^{-3}$  and maximum microwave emission occurs at a frequency given approximately by

$$\nu \approx 8.5 \times 10^6 B \text{ Hz} \quad (2.7)$$

where  $B$  is in gauss. Thus (2.4) can be replaced by the condition

$$B_w^2 \ll 1.1 \times 10^{-6} n_e \ll B_s^2 \quad (2.8)$$

Because the microwave spectrum does not peak sharply the inequalities in (2.5) have been strengthened in (2.8). If  $B_s \sim 500$  gauss, giving peak microwave radiation at 4200 MHz, then suitable values of  $n_e$  and  $B_w$  would be  $n_e \approx 5 \times 10^{10} \text{ cm}^{-3}$  ( $\nu_p \approx 2000$  MHz) and  $B_w \approx 100$  gauss ( $\nu_w \approx 850$  MHz). If a lower density is required to obtain a longer decay time then  $B_w$  must be decreased to satisfy (2.8). If an electron is to pass through the region of field strength  $B_s$ , we must have

$$B_m \geq B_s \quad (2.9)$$

and so

$$\sin^2 \alpha_0 \leq \frac{B_w}{B_s} < \tau^2 \quad (2.10)$$

Thus

$$\alpha_0 \leq \tau^{1/2} \approx 5^\circ \quad (2.11)$$

As  $\alpha$  is small in the weak field region, the time taken to traverse it is

$$t_w \approx L_w/v \quad (2.12)$$

while the time spent in the strong field region at each reflection cannot be less than

$$t_s > 2 L_s/v \quad (2.13)$$

Since

$$\tau \approx t_s/t_w \quad (2.14)$$

we have

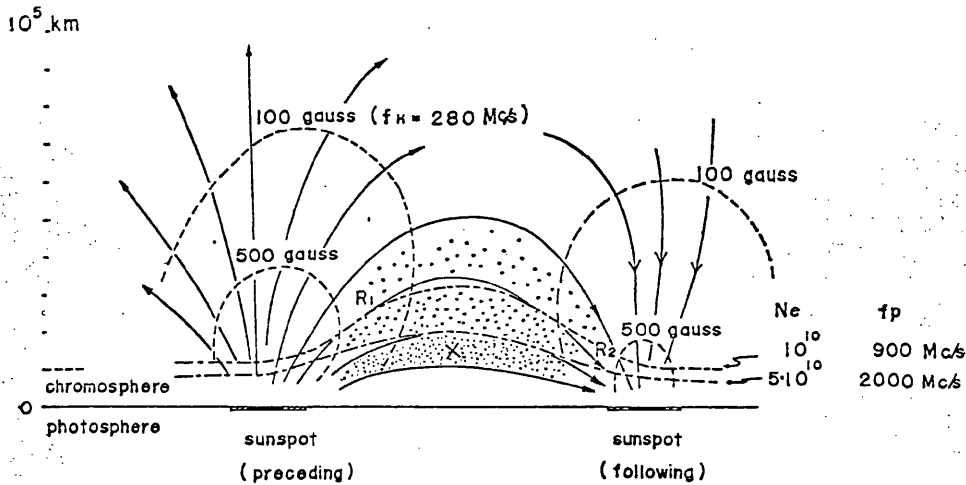
$$L_s/L_w \leq \tau/2 \quad (2.15)$$

Taking  $L_w = 10^{10}$  cm, we have

$$L_s \sim 5 \times 10^5 - 5 \times 10^6 \text{ cm} \quad (2.16)$$

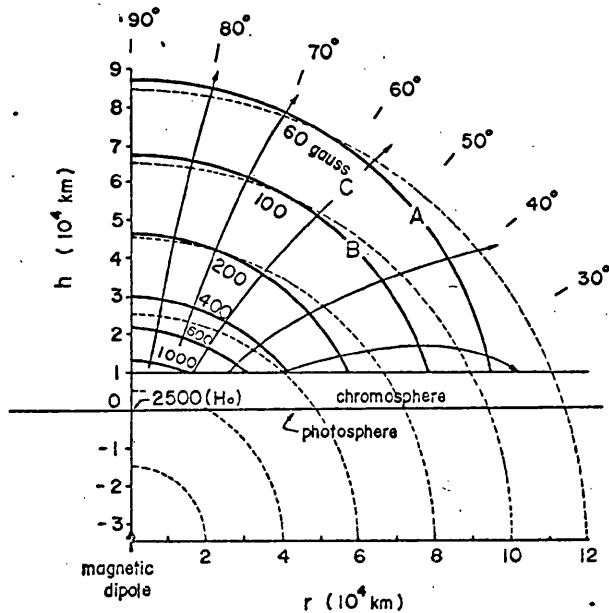
Therefore the magnetic field must increase from 5 gauss (or, if (2.8) is satisfied,  $\leq 100$  gauss) to 500 gauss in a distance of 10 km.

To overcome the problem of discrepancy in electron numbers, Takakura & Kai (1966) proposed a model, shown in Figure 2.1, in which most of the electrons are trapped in a region where the density, and therefore plasma frequency, is sufficiently high that gyro-synchrotron radiation cannot escape. Only a small fraction of the electrons trapped in an outer region of lower density contribute to the microwave burst, the bulk of the microwave emission emanating from



A schematic illustration of a compound model of radio and X-ray bursts.  
 X : Source for hard X-ray burst.  
 $R_1, R_2$ : Sources for microwave impulsive burst.  $R_2$  may not appear as the source if the magnetic field of the following spot is weaker.

Figure 2.1 The electron trap model of Takakura & Kai (1966).



Model of magnetic field in the radio source showing a cross section in the ecliptic plane. A vertical magnetic dipole is situated  $3.5 \times 10^4 \text{ km}$  ( $\approx 0.05$  solar radii) below the photosphere. Equi-strength surfaces of the magnetic field which are axially symmetric about the dipole axis are shown by solid curves. Curves with an arrow indicate lines of magnetic force.

Figure 2.2 The magnetic field model of Takakura & Scalise (1970).

the regions of stronger field near the mirror points, as shown in Figure 2.1. This model is consistent with the discovery (Takakura, 1967) that the microwave emission decays more gradually than the X-ray emission, indicating that although the electrons responsible for these two types of radiation are closely connected, possibly having a common origin and influenced by the same modulation mechanisms, they are not identical.

A model of the trapping field based on the suggestion of Takakura & Kai (1966) was introduced by Takakura & Scalise (1970) who evaluated the centre to limb variation of microwave emission under the assumption of an isotropic pitch angle distribution for the trapped electrons. As the gyro-synchrotron emission originates in the regions of strong magnetic field in the limbs of the trap they represented the trapping field by two independent magnetic fields due to a vertical dipole situated in the photosphere beneath each sunspot as illustrated in Figure 2.2. Although adequate for the calculations performed by Takakura and Scalise, this field is of no use in the calculation of X-ray emission as the field lines are discontinuous at the mid point of the trap and, as was pointed out in §1, we expect the emission from this region to be of importance.

Pintér (1969) examined the distribution of numbers of X-ray bursts in three energy bands against solar longitude and concluded that the distribution peaks at a certain longitude which increases from  $0^\circ$  to  $\sim 40^\circ$  as the photon energy increases from 1 keV to  $\sim 20$  keV. (A more detailed discussion of such observations is given in Chapter II). He then took the simplest possible approximation to a trapping model by considering the electrons to be moving parallel to a horizontal magnetic field orientated in an East-West direction and using a simple approximation to the energy-dependent X-ray bremsstrahlung differential cross-section due to Sommerfeld (1951).

Identifying photon energy with electron energy, and probability of observing a burst with relative intensity of the burst due to directional effects, he showed that the predicted distribution of

bursts, shown in Figure 2.3, agreed closely with the observed distribution. Pintér's analysis is faulty as he only considers electrons moving in one direction along the magnetic field although it is clear that in a trap the net electron flux must be zero. The corrected distribution is shown in Figure 2.4. Here we see that the peak in intensity does not begin to move away from the centre of the solar disc until the electron energy has increased to 40 keV, rather than at 5 keV as found by Pintér. At 60 keV, the directivity is reduced from 2.9 to 1.3. The corrected distribution does not agree with Pintér's observational data.

Elwert & Haug (1970) calculated the directivity and polarisation of X-ray emission from electrons moving along a straight magnetic field line. They considered the case where all electrons have the same pitch angle and also the case of distributed pitch angle where the distribution is of the form  $\sin^n \alpha$ . As they were concerned with the wavelength region 2-10 Å, Elwert & Haug used a non-relativistic bremsstrahlung cross-section so there is no beaming effect and their results apply equally well to the thin target model (see Chapter II) in which electrons move in one direction along the field line, or to the trap model where electrons are moving in both directions.

In this non-relativistic limit the polarisation can be calculated analytically. For example, for a pitch angle distribution

$$f(\alpha) \sim \sin^2 \alpha \quad (2.17)$$

the polarisation is given by

$$P^H(\theta) = \frac{\sin^2 \theta}{10Q + 3 + \cos^2 \theta} \quad (2.18)$$

where  $\theta$  is the angle between the direction of emission and the magnetic field. The direction of polarisation is either parallel to ( $P^H < 0$ ) or perpendicular to ( $P^H > 0$ ) the magnetic field.  $Q$  is a function of photon energy and depends on the electron energy distribution. In the case of a power law energy spectrum, Elwert & Haug show that

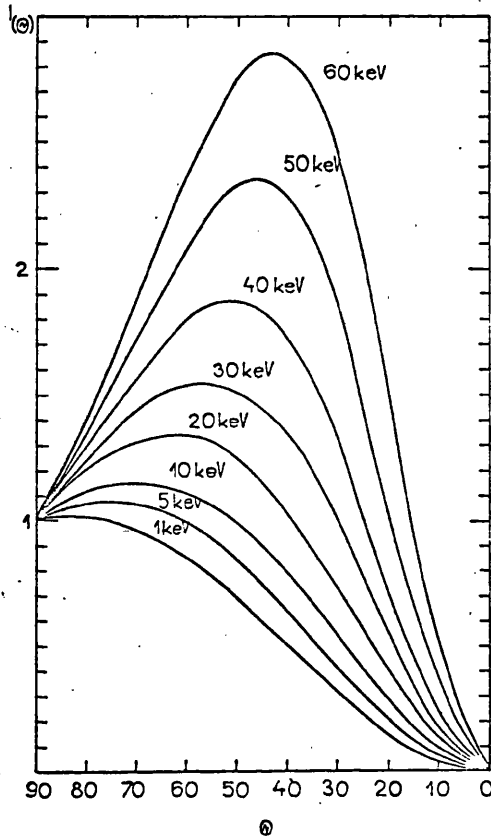


Figure 2.3 Distribution of X-ray burst intensity according to Pinter (1969).  $\theta$  is  $90^\circ$  at disc centre and  $0^\circ$  at the limb.

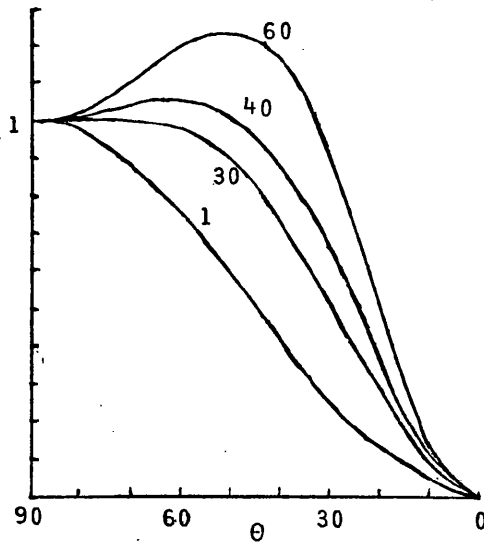


Figure 2.4 Corrected intensity distribution. Figures on curves are photon energies, as in Figure 2.3.

if the Coulomb correction (Elwert, 1939) to the bremsstrahlung cross-section is neglected then  $Q$  is independent of photon energy, being given by

$$Q = \frac{1}{2(\delta-1)} \quad (2.19)$$

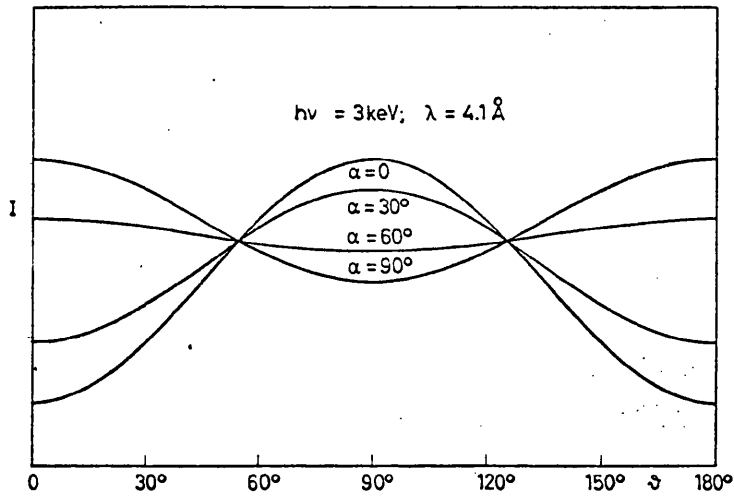
where  $\delta$  is the spectral index.

Results obtained by Elwert & Haug for the directivity and polarisation are reproduced in Figures 2.5 and 2.6. Taken as a non-relativistic, "horizontal magnetic field" approximation to the trap model, these results predict (assuming an equatorial field direction)

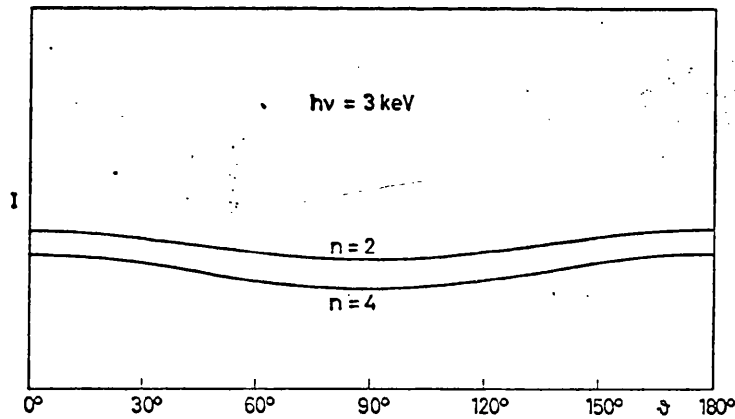
- (a) for a single pitch angle electron distribution with  $\alpha < 55^\circ$ :-
  - (i) limb darkening (minimum  $I_L/I_C \sim 0.2$  for  $\alpha = 0^\circ$ );
  - (ii) East-West polarisation decreasing to zero at the limb (maximum polarisation  $\sim 0.75$  for  $\alpha = 0^\circ$ ),
- (b) for a single pitch angle distribution with  $\alpha > 55^\circ$ :-
  - (i) limb brightening (maximum  $I_L/I_C \sim 1.9$  for  $\alpha = 90^\circ$ );
  - (ii) North-South polarisation decreasing to zero at the limb (maximum polarisation  $\sim 0.7$  for  $\alpha = 90^\circ$ ),
- (c) for a  $\sin^n \alpha$  pitch angle distribution
  - (i) slight limb brightening ( $I_L/I_C \sim 1.25$ )
  - (ii) North-South polarisation ( $\sim 0.2$  for  $n = 2$ ,  $\sim 0.3$  for  $n = 4$ )

If, on the other hand, it is supposed that emission from the (vertical) limbs of the trap, where the electrons have pitch angles of  $\sim 90^\circ$ , predominates, these results predict a limb darkening of a factor of 2 and a North-South polarisation increasing from zero at the centre of the solar disc to  $\sim 0.7$  at the limb.

In 1971 Elwert & Haug extended their directivity calculations to the hard X-ray regime ( $\epsilon > 10$  keV) in the Born approximation (Sauter, 1934). They calculated the directivity of bremsstrahlung radiation from an assembly of electrons with zero pitch angle and an energy spectrum consisting of two power laws so that the spectrum

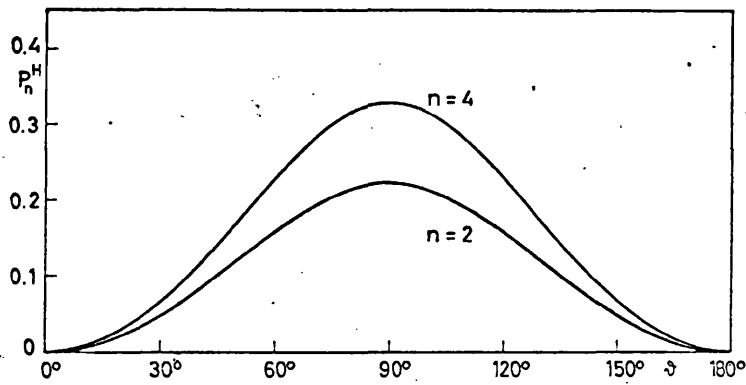
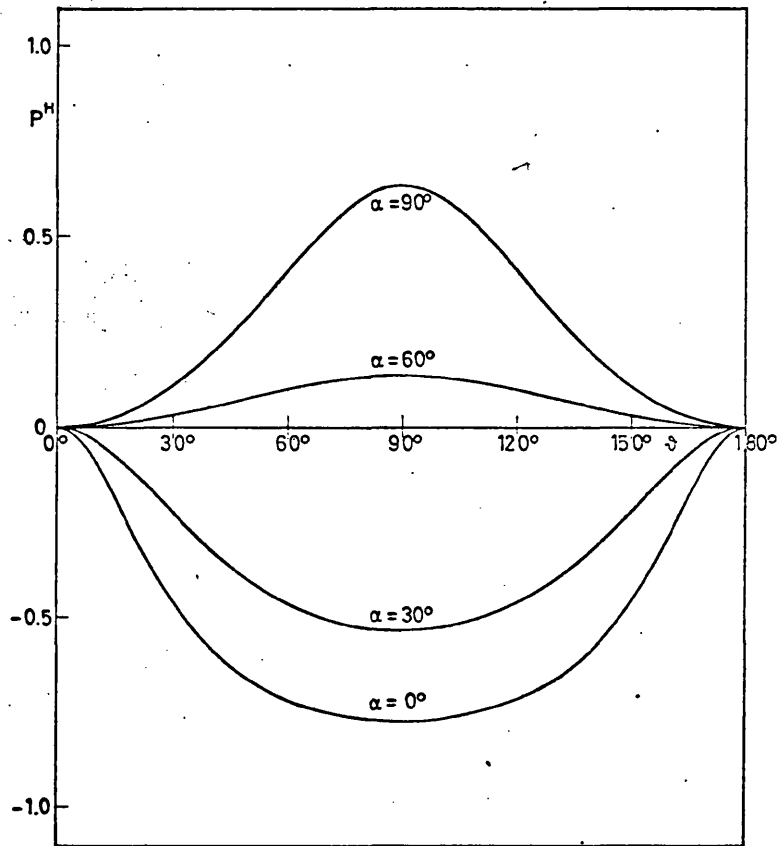


Intensity distribution of the X-radiation (in arbitrary units) for discrete pitch angles  $\alpha$  and  $Q = 0.15$ .



Intensity of the X-radiation (in arbitrary units) for an angular distribution  $F_n(\alpha) = \sin^n \alpha$  and  $Q = 0.15$ .

**Figure 2.5** Directivity of X-ray emission from electrons spiralling along a magnetic field line. From Elwert & Haug (1970).



Polarization curves for an angular distribution  $F_n(\alpha) = \sin^n \alpha$  and  $Q = 0.15$ .

**Figure 2.6** X-ray polarisation predicted by Elwert & Haug (1970) for various electron pitch angle distributions.

steepens above some energy  $E_0$  (Figure 2.7) and from electrons with a power law spectrum modified by an exponential cutoff for pitch angles of  $0^\circ$ ,  $30^\circ$ ,  $60^\circ$  and  $90^\circ$  (Figure 2.8). These results, which illustrate the effect of relativistic beaming, are not directly applicable to a "uniform horizontal magnetic field" approximation to the trapping model as, like Pintér (1969), they consider only electrons moving in one direction along the field line. The intensity distribution predicted by this approximation to the trapping model is obtained by summing over the two electron beams,

$$I_{\text{TRAP}}(\theta) = I(\theta) + I(\pi - \theta) \quad (2.20)$$

Mentally performing this summation on the results illustrated, we see from Figure (2.7) that at the low photon energy of 10 keV we have limb darkening as in the non-relativistic approximation (a) (i) above. However at a photon energy of 50 keV the relativistic forward beaming of photons has inverted the previous results, giving limb brightening for small pitch angles and limb darkening for large pitch angles (Figure 2.8).

Haug (1972), using the same electron energy distributions as Elwert & Haug (1971), extended the polarisation calculations of Elwert & Haug (1970) to hard X-ray energies. Figure 2.9 and 2.10 show some of his results, which are, apart from the asymmetry caused by relativistic beaming, similar to Elwert & Haug's (1970) results. The peak polarisation for a given electron pitch angle does not depend strongly on photon energy but the functional form of dependence of the polarisation on direction becomes more complex as photon energy increases. Approximate predictions of polarisation cannot be obtained directly from these results by using (2.20) since the X-ray fluxes from the two electron beams are different because of relativistic beaming.

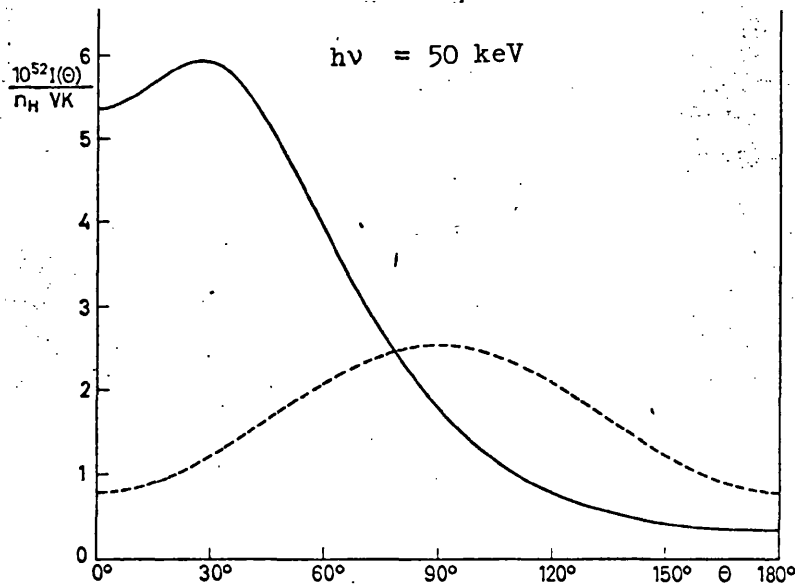
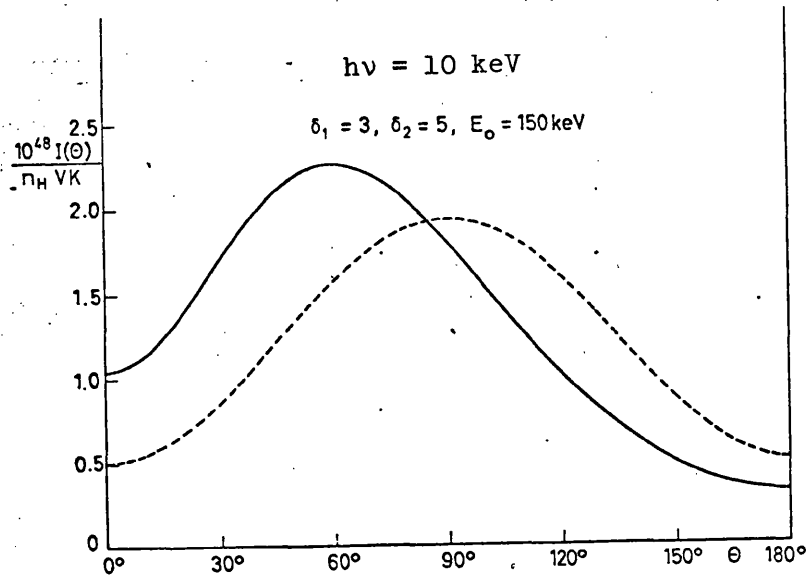


**Figure 2.7** Angular distribution of bremsstrahlung from electrons with a power law energy distribution and zero pitch angle, calculated by Elwert & Haug (1971). There is a break in the spectrum at 150 keV.

$\theta$  is the angle between the magnetic field line and the direction of the observer. The dotted curves show the results obtained from a non-relativistic treatment.

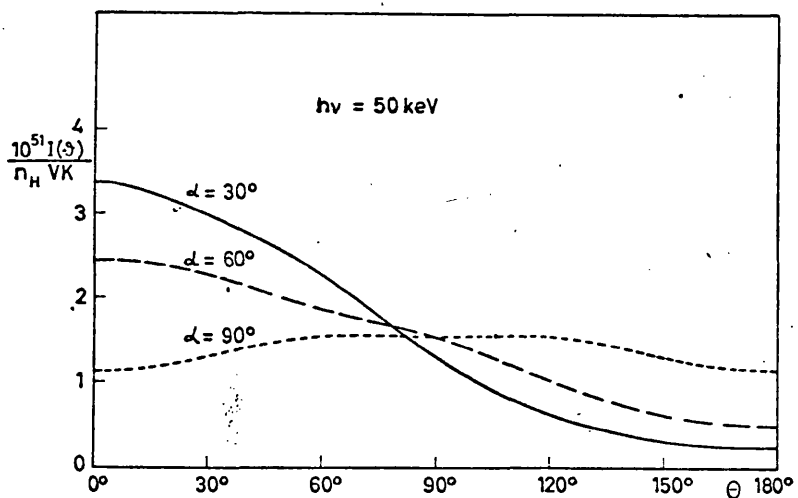
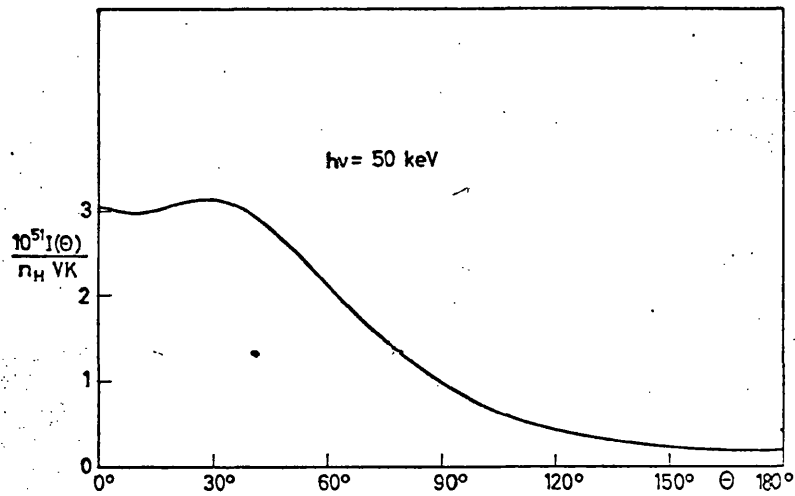


**Figure 2.8** Angular distribution<sub>3</sub> of bremsstrahlung emission from electrons with an  $E^3$  energy distribution having an exponential cutoff at 800 keV. The electrons have pitch angles of  $0^\circ$  (upper figure) and  $30^\circ$ ,  $60^\circ$  and  $90^\circ$  (lower figure).  $\theta$  is the angle between the observer and the magnetic field direction. From Elwert & Haug (1971).

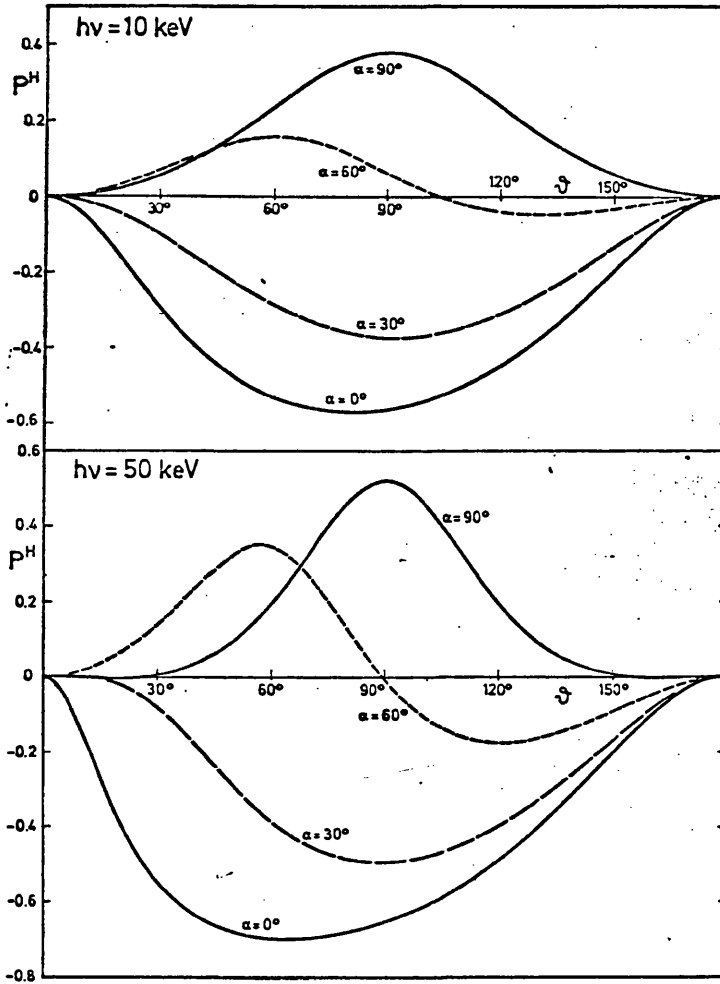
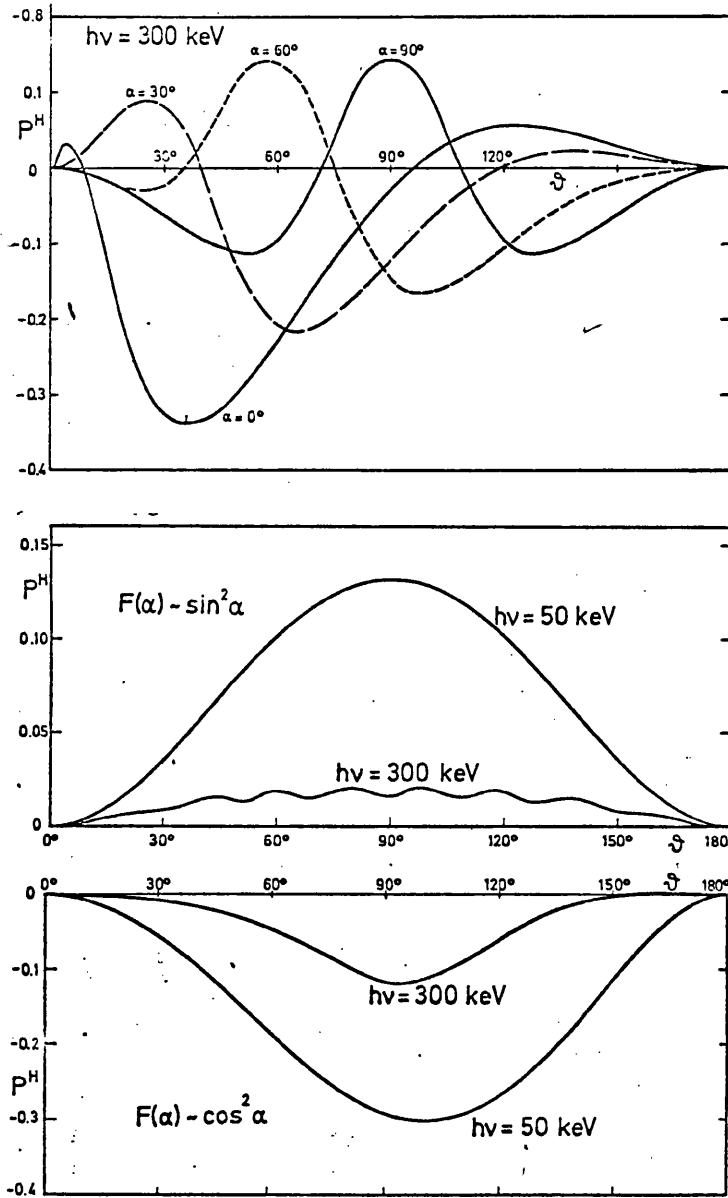


Figure 2.9 Relativistic polarisation, calculated by Haug (1972) for electrons with an  $E^{-1.75}$  energy distribution steepening to  $E^{-5}$  above 80 keV.  $\theta$  is the angle between the magnetic field direction and the line of sight.



**Figure 2.10** Relativistic polarisation of X-ray emission from an  $E^{-3}$  energy distribution of electrons with an exponential cutoff at 800 keV. The polarisation curves for a photon energy of 50 keV (not shown) in the discrete pitch angle case are almost identical to those of Figure 2.9. From Haug(1972).

### 3. THE TRAPPING MAGNETIC FIELD

As the energy density of the coronal magnetic field over an active region is considerably greater than the thermal energy of the ambient plasma the magnetic field must be force-free, although, if the magnetic field is required to store the flare energy prior to release, it must depart from a potential configuration initially. However this deviation need not be large, as the total energy released in a large flare is  $\lesssim 10\%$  of the potential energy in an active region magnetic field. In a large flare where a high density of trapped non-thermal particles is required to explain the observed hard X-ray flux, interaction of the field with the injected fast particles will produce perturbations on the field.

In order to obtain a definitive model of the trapping field we have taken a potential configuration. Three potential field models were examined, the field of a single horizontal dipole, the field of two linecharges and the field of two monopoles. The flux tube in which the fast particles are trapped is taken to lie in the vertical plane passing through a bipolar pair of sunspots and is represented by a single field line, its finite diameter being neglected. This idealisation does not influence the interpretation of results provided the diameter of the flux tube is small in comparison to its length.

Support for this hypothesis is given by  $H\alpha$  and soft X-ray photographs of flaring regions, which show filamentary loop structures with thickness to length ratios of  $\lesssim 1/10$ , although the structures are frequently more complex than those characteristic of a potential field. However, as discussed in §1, we are interested in applying our results to large events in which the magnetic field structure is generally simpler.

The trapping field is specified by 3 parameters as shown in Figure 3.1;  $D$ , the separation of the sources;  $d$ , the depth of the sources below the photosphere, and  $Z_0$ , the height of the top

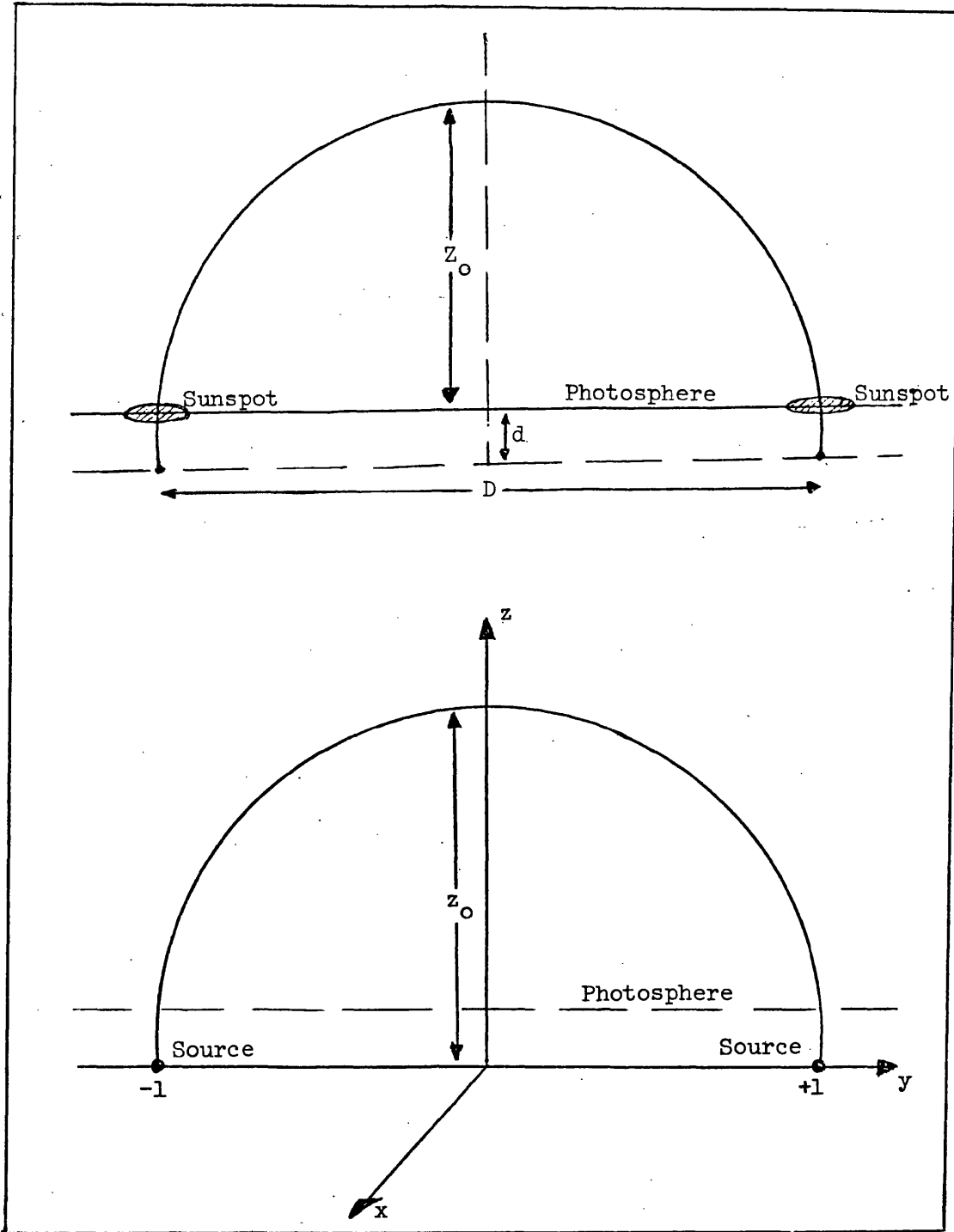


Figure 3.1 Top-Definition of the trap in terms of physical dimensions. Bottom - Mathematical definition used in analysis. The transformation between the two systems is defined by equation (3.3).

of the arch above the photosphere. The positions of the field lines emerging from the photosphere are identified with the positions of the bipolar pair of sunspots. The geometry of the magnetic field and positions of the electron mirror points for a range of pitch angles for each of the three field models is shown in Figures 3.2 - 3.4.

The dipole field, which has been used to represent a coronal trap by Chui (1970) and Pneuman (1972), has the attraction of having a simple mathematical representation. However, as only one source is responsible for the production of the magnetic field the parameter  $d$  cannot be chosen freely, being fixed by the specification of  $Z_0$  and  $D$ . To obtain a realistic value of  $D$ , a large value of  $d$  must be chosen thus placing the dipole far below the photosphere with the result that there is little variation in magnetic field strength in the corona. For example, to obtain a height of  $5 \times 10^4$  km for the top of the arch assuming a sunspot separation of  $10^5$  km, the dipole must be placed at a depth of  $8 \times 10^4$  km. If the magnetic field strength at the photosphere is taken to be 2000 gauss, a rather large field of 700 gauss is found at the top of the trap. As the ratio of field strengths is only  $\sim 3$ , any electron with initial pitch angle  $< 35^\circ$  at the top of the trap will reach the photosphere. The simplicity of the mathematical representation of the dipole is of little advantage in this study as the computation of X-ray emission from the trap must be performed numerically.

The equations describing the linecharges magnetic field model are intermediate in complexity between those of the dipole and monopole fields. Results obtained using this field model are similar to those obtained for the monopoles field which is considered to be the most realistic model. The principal difference between these models lies in the magnetic field gradient in the limbs of the trap. The field strength near the photosphere is

$$B \sim 1/(Z+d) \quad (3.1)$$

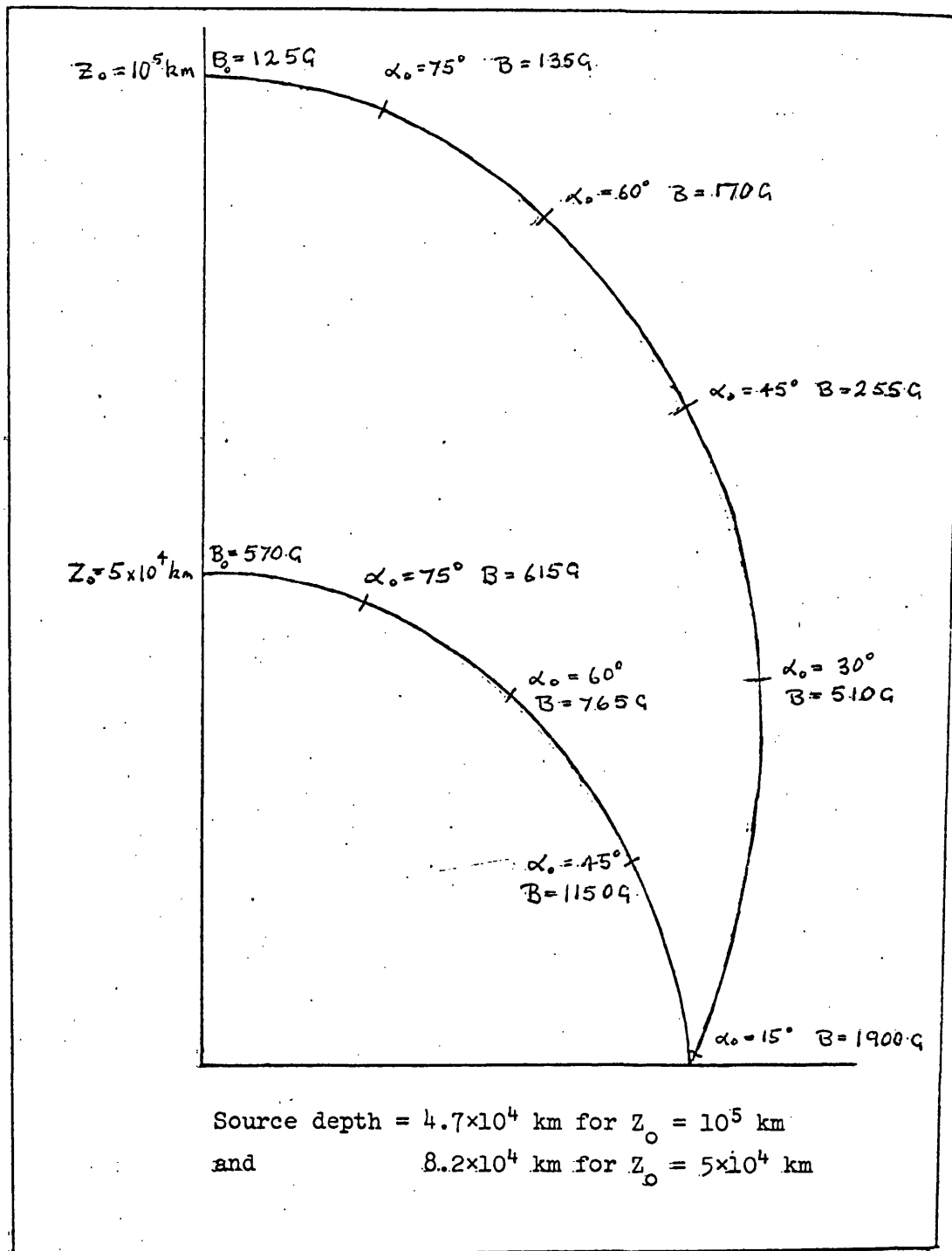


**Figure 3.2** The Dipole magnetic field model. Mirror point heights for electrons of various initial pitch angles are shown, and field strengths at these points for an assumed field of 2000 gauss at the sunspots.

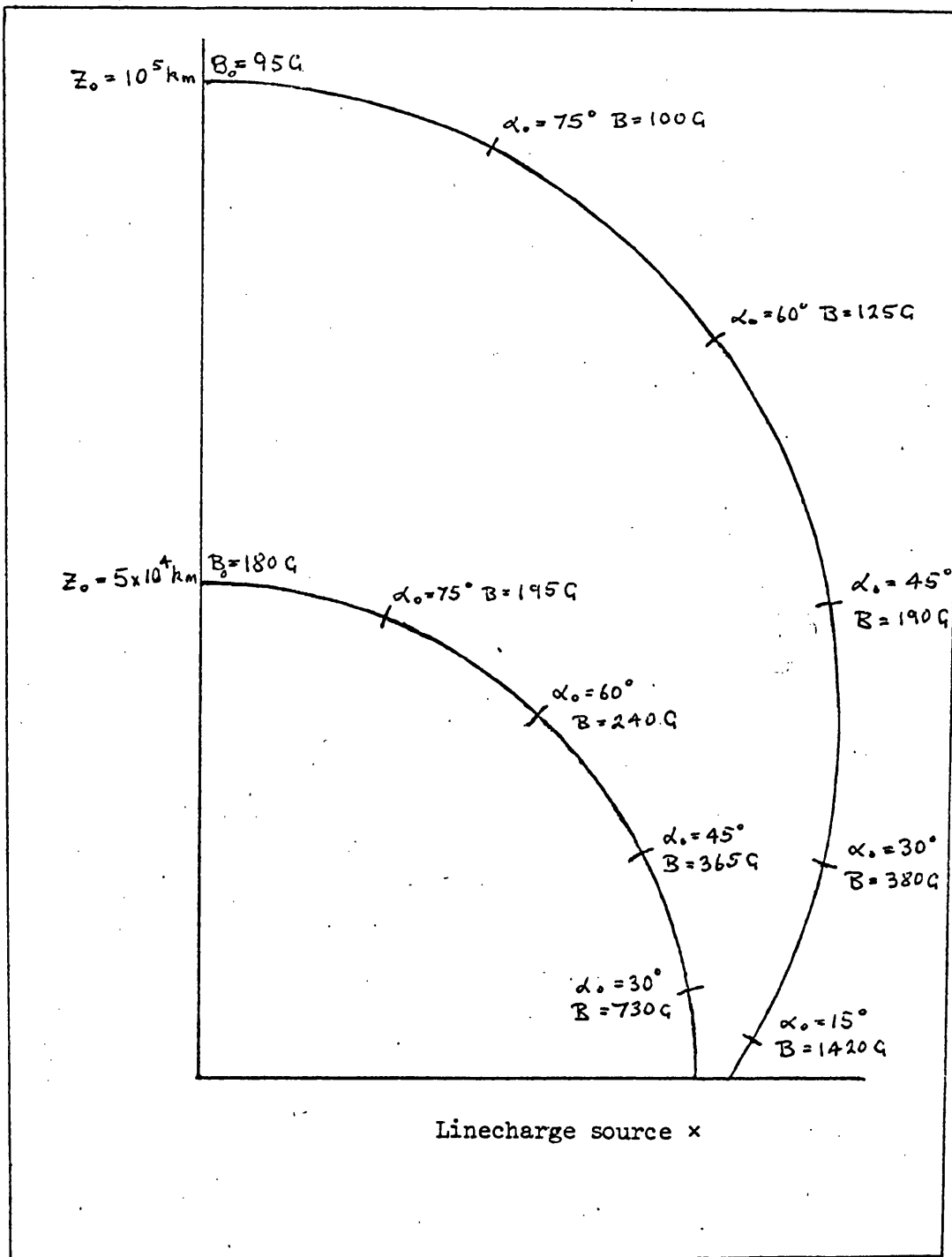


Figure 3.3 The Linecharges magnetic field model.

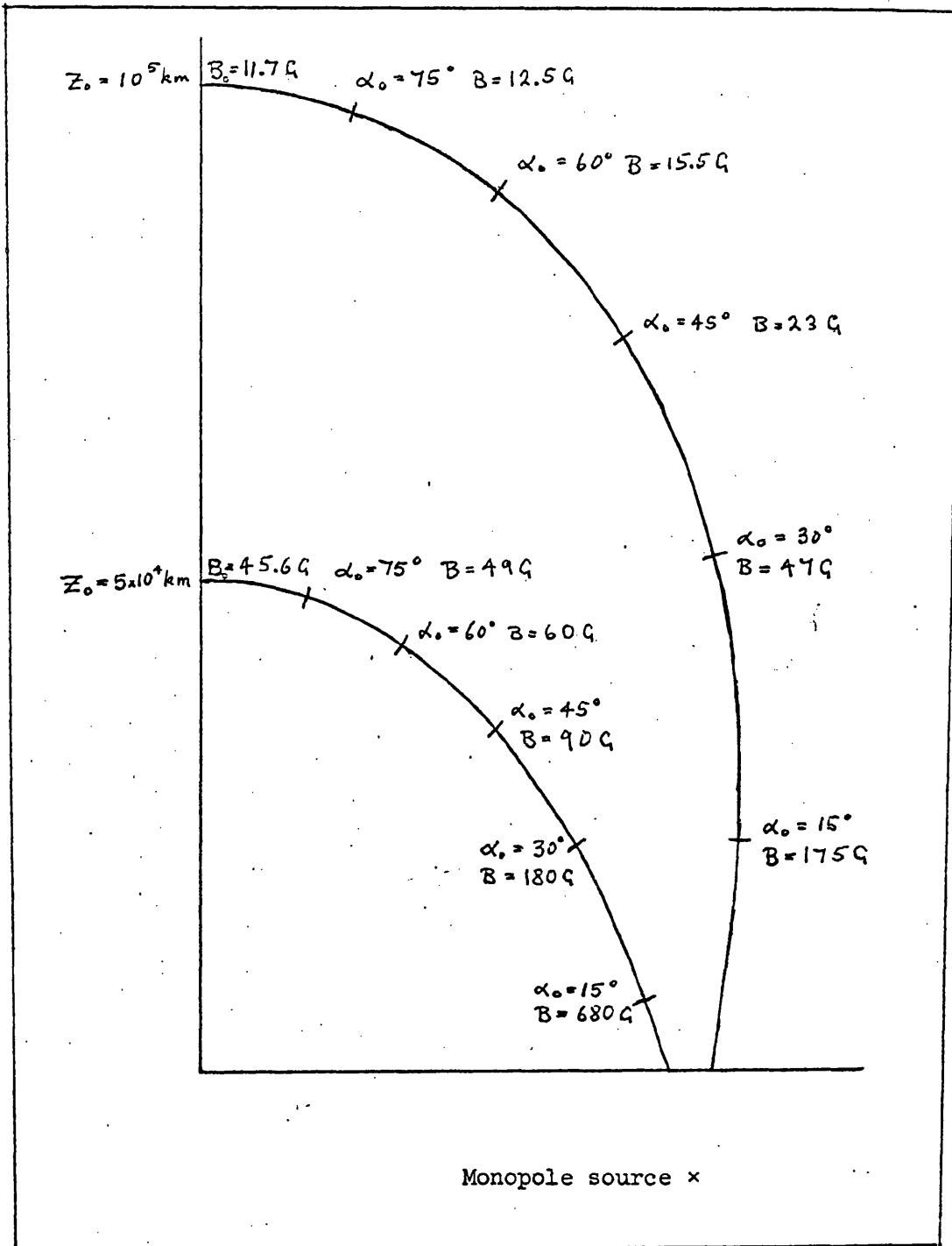


Figure 3.4 The Monopoles magnetic field model.

for the linecharges field and

$$B \sim 1/(Z + d)^2 \quad (3.2)$$

for the monopoles field. The distribution of mirror point heights, which is determined by the rate of convergence of field lines, is shown in Figures 3.3 and 3.4. The monopoles field is closest in appearance to typical coronal structures such as filaments and coronal loops and, in addition, the point sources in this model are good approximations to sunspots whereas the extended line sources of the linecharges field have little physical significance.

The depth beneath the photosphere at which the sources have been set in each of these models has been chosen to be roughly equal to the diameter of a large sunspot and adjusted to give a realistic value of magnetic field strength at the top of the arch. (The effect of this procedure on the characteristics of the X-ray emission is small as it only shifts the particle trajectories slightly with respect to the density structure of the atmosphere). The linecharges sources were set at a depth of  $5 \times 10^3$  km and the monopoles sources at a depth of  $10^4$  km. Setting  $D$  equal to  $10^5$  km and assuming a magnetic field strength of 2000 gauss at the sunspots, the field strength at the top of the arch in the linecharges model is 180 gauss at a height of  $5 \times 10^4$  km and 95 gauss at a height of  $10^5$  km. Corresponding values for the monopoles field are 45 gauss and 12 gauss respectively.

Because the characteristics of the hard X-ray emission from the trap are determined only by its geometry the actual size of the trap can be chosen freely. We define the scale of the trap by taking the distance  $D$  between the sunspots to be  $10^5$  km, a value representative of a large flare, so that if we also assume physically reasonable values for other parameters (for example, total number of trapped electrons) the calculated photon fluxes are representative of what would actually be detected according to the predictions of the model. However, for

the purposes of computation a coordinate system, shown in Figure 3.1, is set up in which the sunspots are at unit distance on either side of the central axis of the trap. The magnetic sources are located at the points  $(0,1,0)$  and  $(0,-1,0)$  and the top of the arch is at  $(0,0,z_0)$ , where  $z_0$  is defined by

$$z_0 = \frac{z_0 + d}{D/2} \quad (3.3)$$

The unit of distance in this coordinate system will be referred to as a "scaled unit".

The trapping field is described, for computational purposes, by a set of functions which depend on position on the field line chosen to represent the flux tube in which the non-thermal electrons are trapped. Position on the field line is defined by an independent variable  $\xi$  which increases monotonically from a value  $\xi_0$  at the top of the arch to a value  $\xi_1$  at the source on the positive y-axis. The functions dependent on  $\xi$  are defined only on the right half ( $y > 0$ ) of the field line. Corresponding values on the left hand side are obtained from symmetry considerations.

Of fundamental importance to the dynamics of trapped particles is the magnetic field strength as a function of position on the field line. This is described by the function  $B(\xi)$ . As the actual value of field strength is irrelevant (providing it is sufficiently large that the Larmor radius is small compared to the scale length for change in the magnetic field),  $B(\xi)$  is measured in arbitrary units. The geometry of the trap is defined by the functions  $z(\xi)$  and  $y(\xi)$ , which are, respectively, height above the sources in scaled units ( $0 < z(\xi) < z_0$ ) and horizontal distance from the central axis of the trap, again in scaled units. Other functions which are used in the equations describing X-ray emission from the trap as formulated in §7 are:-

- (i)  $\frac{dB}{d\xi}$ , the rate of change of magnetic field strength with respect to  $\xi$  ;

- (ii)  $\frac{dl}{d\xi}$  , the rate of change of distance, measured along the field line from the top of the arch in scaled units, with respect to  $\xi$ ;
- (iii)  $\frac{dz}{dl}$  , the rate of change of height with distance along the field line (this is always negative because of the definition of  $l$  ) ;
- (iv)  $\frac{dy}{dl}$  , the rate of change of horizontal distance with distance along the field line.

#### 4. THE DIPOLE FIELD

The field of the dipole (with B in arbitrary units) is given by

$$B = \frac{(1 + 3 \cos^2 \theta)^{\frac{1}{2}}}{r^3} \quad (4.1)$$

where  $r = z_0 \sin^2 \theta$  (4.2)

The variables  $r$  and  $\theta$  are defined in Figure (4.1).

We have

$$z = r \sin \theta \quad (4.3)$$

and  $y = r \cos \theta$  (4.4)

hence  $z = z_0 \sin^3 \theta$  (4.5)

and  $y = z_0 \sin^2 \theta \cos \theta$  (4.6)

Defining the independent variable by

$$\xi = \cos \theta \quad (4.7)$$

we have

$$\xi_0 = 0 \quad (4.8)$$

and  $\xi_1 = 1$  (4.9)

Dropping the constant  $z_0$  from (4.2) since  $B$  is in arbitrary units and substituting in (4.1) this becomes

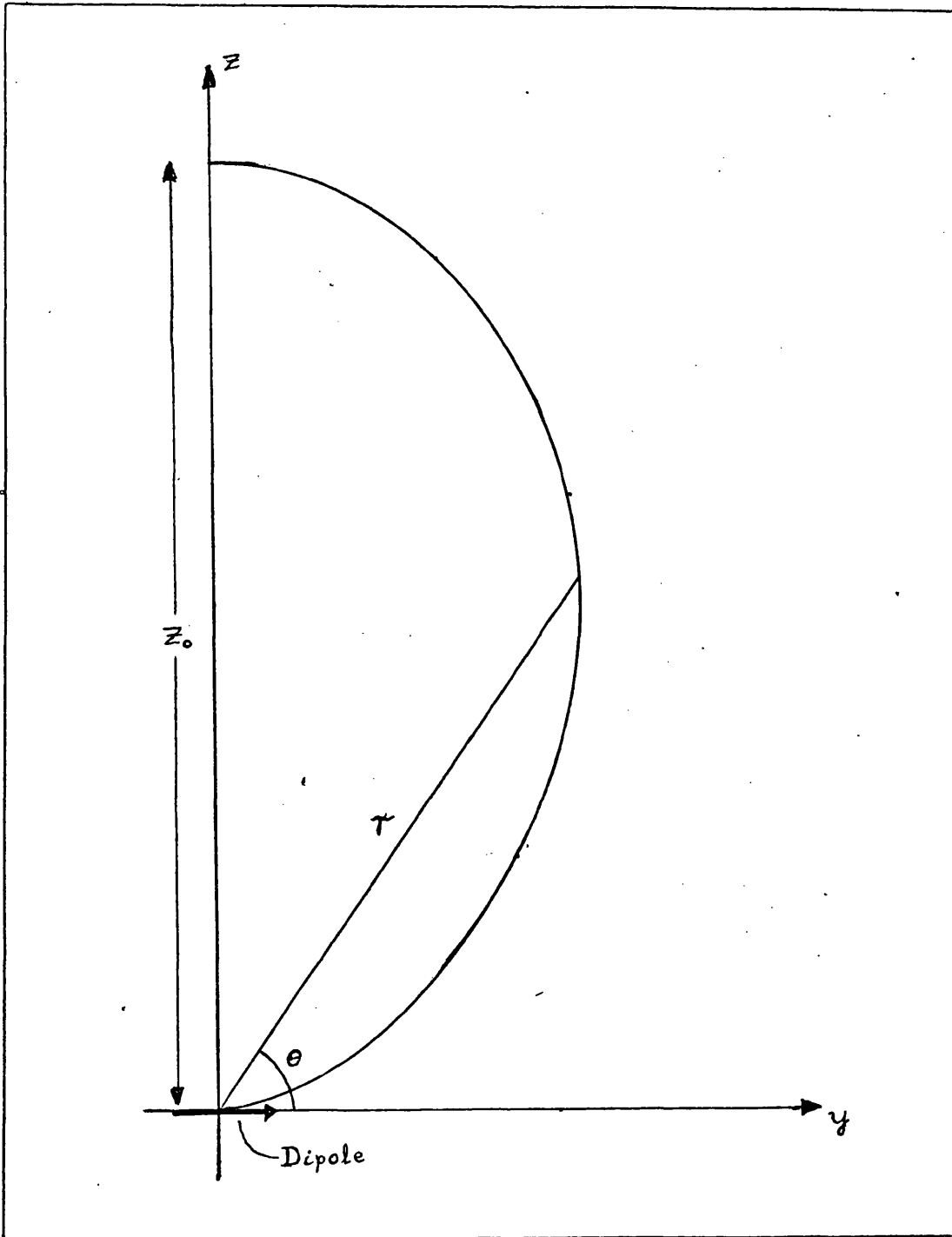


Figure 4.1 Definition of the variables  $r$  and  $\theta$  used in the analysis of the dipole field.

$$B = \frac{(1 + \xi^2)^{\frac{1}{2}}}{(1 - \xi^2)^3} \quad (4.10)$$

From (4.5), (4.6) and (4.7) we obtain

$$z = z_0 (1 - \xi^2)^{\frac{3}{2}} \quad (4.11)$$

and

$$y = z_0 \xi(1 - \xi^2) \quad (4.12)$$

Differentiating (4.10) we have

$$\frac{dB}{d\xi} = \frac{3\xi(3 + 5\xi^2)}{(1 + 3\xi^2)^{\frac{1}{2}}(1 - \xi^2)^4} \quad (4.13)$$

while differentiating (4.11) and (4.12), squaring and adding gives

$$\frac{d\ell}{d\xi} = z_0 (1 + 3\xi^2)^{\frac{1}{2}} \quad (4.14)$$

Differentiating (4.11) and (4.12) and dividing each by (4.14) gives, respectively

$$\frac{dz}{d\ell} = -3\xi \left( \frac{1 - \xi^2}{1 + 3\xi^2} \right)^{\frac{1}{2}} \quad (4.15)$$

and

$$\frac{dy}{d\ell} = \frac{1 - 3\xi^2}{(1 + 3\xi^2)^{\frac{1}{2}}} \quad (4.16)$$

## 5. THE LINECHARGES FIELD

This configuration is produced by two linecharges of opposite sign, located at  $y = +1$  and  $y = -1$ . The sources extend indefinitely in the  $x$  direction. The  $y$ -component of the magnetic field strength (in arbitrary units) is given by

$$B_y = \frac{y-1}{r_2^2} - \frac{y+1}{r_1^2} \quad (5.1)$$

(see Figure 5.1), while the z-component is given by

$$B_z = \frac{z}{r_2^2} - \frac{z}{r_1^2} \quad (5.2)$$

where

$$r_1^2 = (y + 1)^2 + z^2 \quad (5.3)$$

and

$$r_2^2 = (y - 1)^2 + z^2 \quad (5.4)$$

The direction of the field line is defined by

$$\frac{dz}{dy} = \frac{B_z}{B_y} = \frac{z(r_1^2 - r_2^2)}{y(r_1^2 - r_2^2) - (r_1^2 + r_2^2)} \quad (5.5)$$

which reduces to

$$\frac{dz}{dy} = \frac{2yz}{y^2 - z^2 - 1} \quad (5.6)$$

Writing this as

$$2yz \, dy - (y^2 - z^2 - 1) \, dz = 0 \quad (5.7)$$

and multiplying by the integrating factor  $z^{-2}$  we find that on integration

$$y^2/z + z - 1/z = \text{constant} \quad (5.8)$$

which can be expressed as

$$y^2 + (z - \eta)^2 = (1 + \eta^2) \quad (5.9)$$

where  $\eta$  is a constant. This is the equation of a circle centred on  $y = 0$ ,  $z = \eta$ , of radius  $(1 + \eta^2)^{\frac{1}{2}}$ .

We define the independent variable  $\xi$ , and also  $R$ , as in Figure 5.2.

Setting  $z = z_0$  and  $y = 0$  in (5.9) we find that

$$\eta = \frac{z_0^2 - 1}{2z_0} \quad (5.10)$$

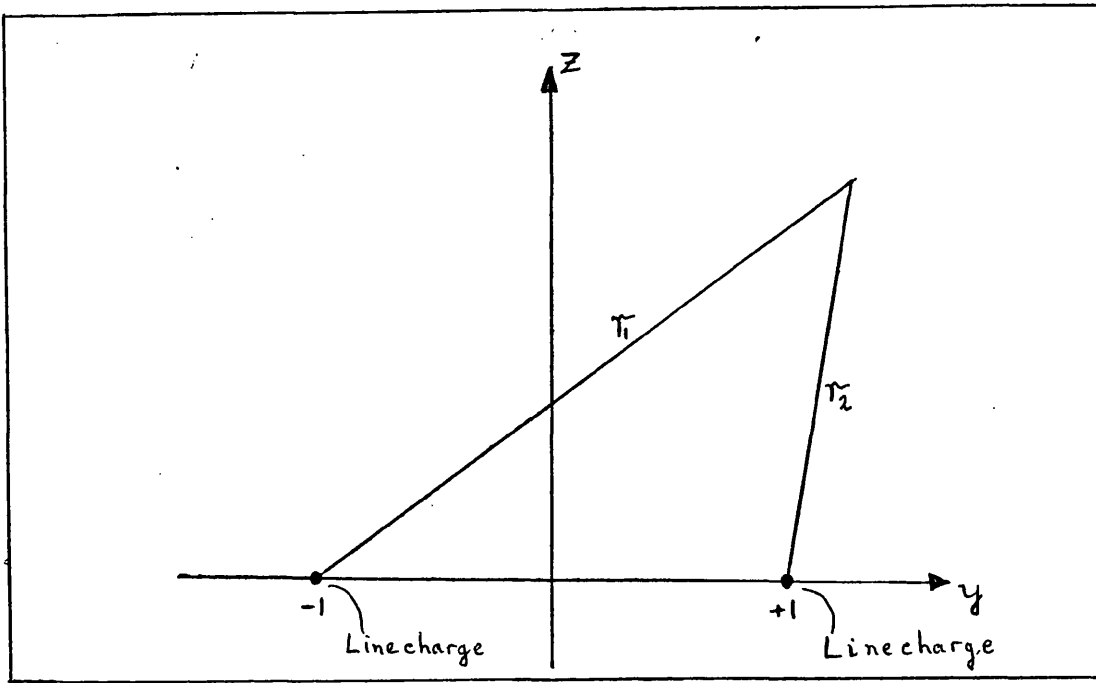


Figure 5.1 Definition of  $r_1$  and  $r_2$  in linecharges model analysis.

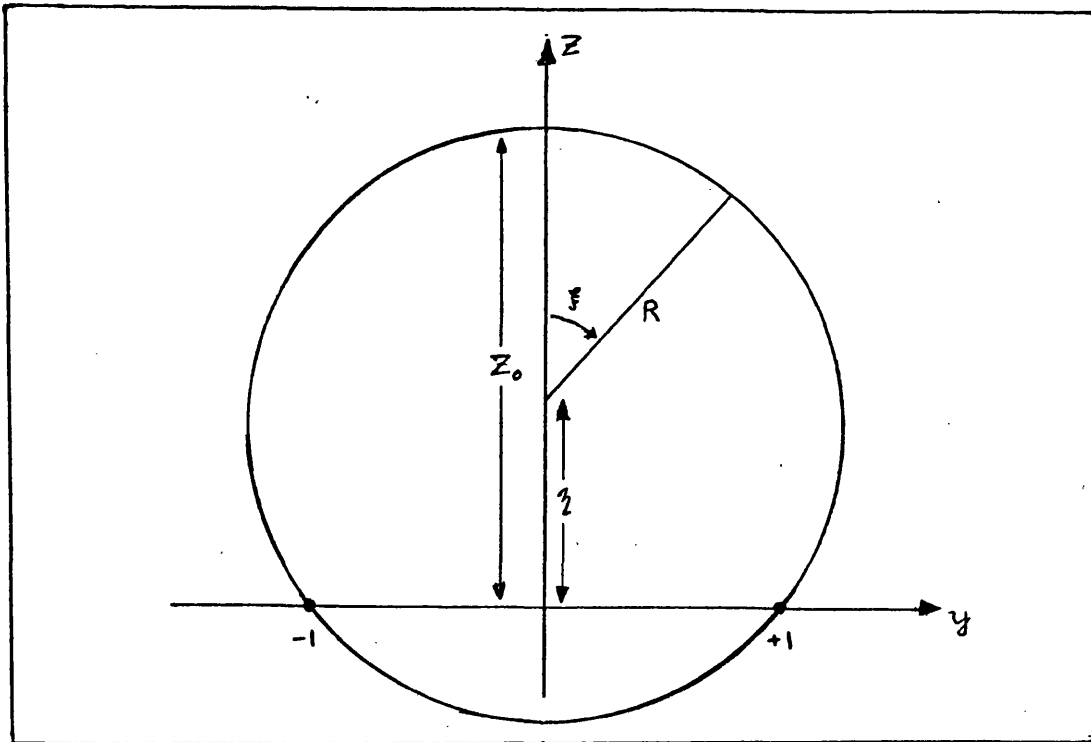


Figure 5.2 Definition of the variables  $\xi$ ,  $\eta$  and  $R$  used in the analysis of the linecharges field model.

and

$$R = \frac{z_0^2 + 1}{2z_0} \quad (5.11)$$

The magnetic field strength is given by

$$B = (B_y^2 + B_z^2)^{\frac{1}{2}} \quad (5.12)$$

Substituting in (5.12) from (5.1) - (5.4) and simplifying leads to the result

$$B = \frac{1}{Rz} \quad (5.13)$$

We have, from Figure 5.2,

$$\xi_0 = 0 \quad (5.14)$$

and

$$\xi_1 = \cos^{-1} (-\eta/R)$$

that is,

$$\xi_1 = \cos^{-1} \left( \frac{1 - z_0^2}{1 + z_0^2} \right) \quad (5.15)$$

and

$$\begin{aligned} z &= \eta + R \cos \xi \\ &= R (\cos \xi + \eta/R) \end{aligned}$$

or

$$z = R (\cos \xi - \cos \xi_1) \quad (5.16)$$

while

$$y = R \sin \xi \quad (5.17)$$

Using (5.13) and (5.16) we can express B in arbitrary units as

$$B = (\cos \xi - \cos \xi_1)^{-1} \quad (5.18)$$

Differentiating (5.18) gives

$$\frac{dB}{d\xi} = \sin \xi (\cos \xi - \cos \xi_1)^{-2} \quad (5.19)$$

From Figure 5.2 we see that

$$\frac{dl}{d\xi} = R \quad (5.20)$$

Using (5.16), (5.17) and (5.20) we obtain

$$\frac{dz}{dl} = -\sin \xi \quad (5.21)$$

and

$$\frac{dy}{dl} = \cos \xi \quad (5.21)$$

The angle  $\xi$ , rather than the apparently more convenient variable  $\cos \xi$ , which would avoid the presence of trigonometrical functions, is used here as the function  $dl/d\xi$  has a singularity at the top of the arch if the cosine of the angle is used as independent variable.

## 6. THE MONOPOLES FIELD

This field geometry is produced by 2 magnetic monopoles of opposite sign located at  $y = -1$  and  $y = +1$ . If  $r_1$  and  $r_2$  are defined as shown in Figure 6.1 the  $y$  and  $z$  components of the magnetic field are given (in arbitrary units) by

$$B_y = \frac{y-1}{r_2^3} - \frac{y+1}{r_1^3} \quad (6.1)$$

$$B_z = \frac{z}{r_2^3} - \frac{z}{r_1^3} \quad (6.2)$$

where  $r_1^2 = (y+1)^2 + z^2 \quad (6.3)$

$$r_2^2 = (y-1)^2 + z^2 \quad (6.4)$$

From (6.1) and (6.2) we have

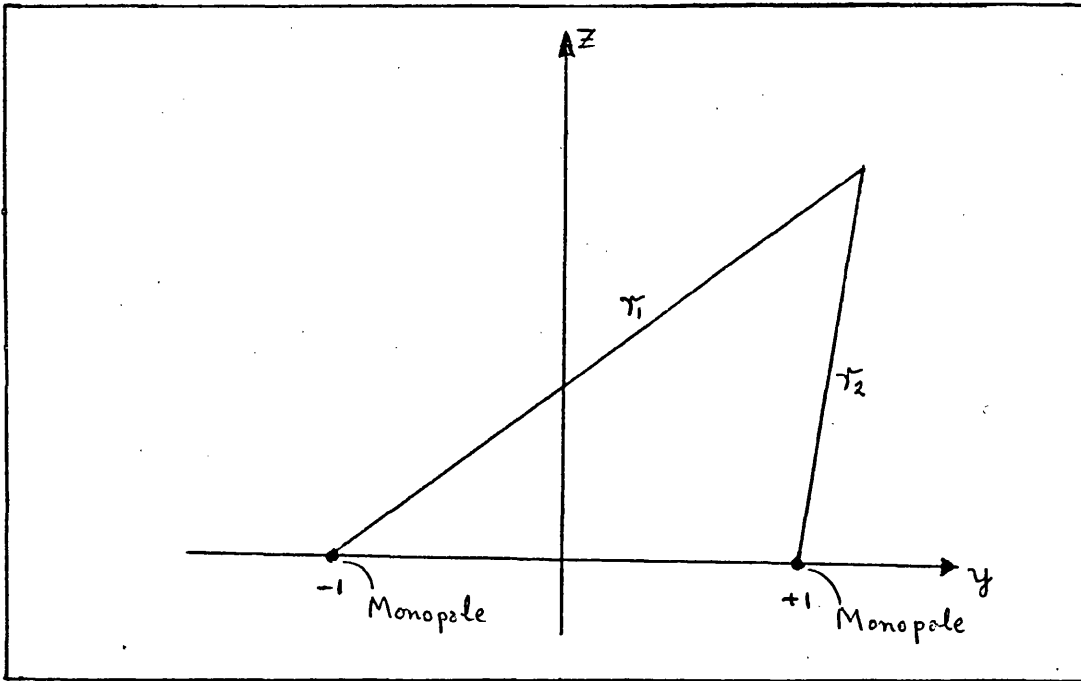


Figure 6.1 Definition of  $r_1$  and  $r_2$  used in analysis of monopoles field model.

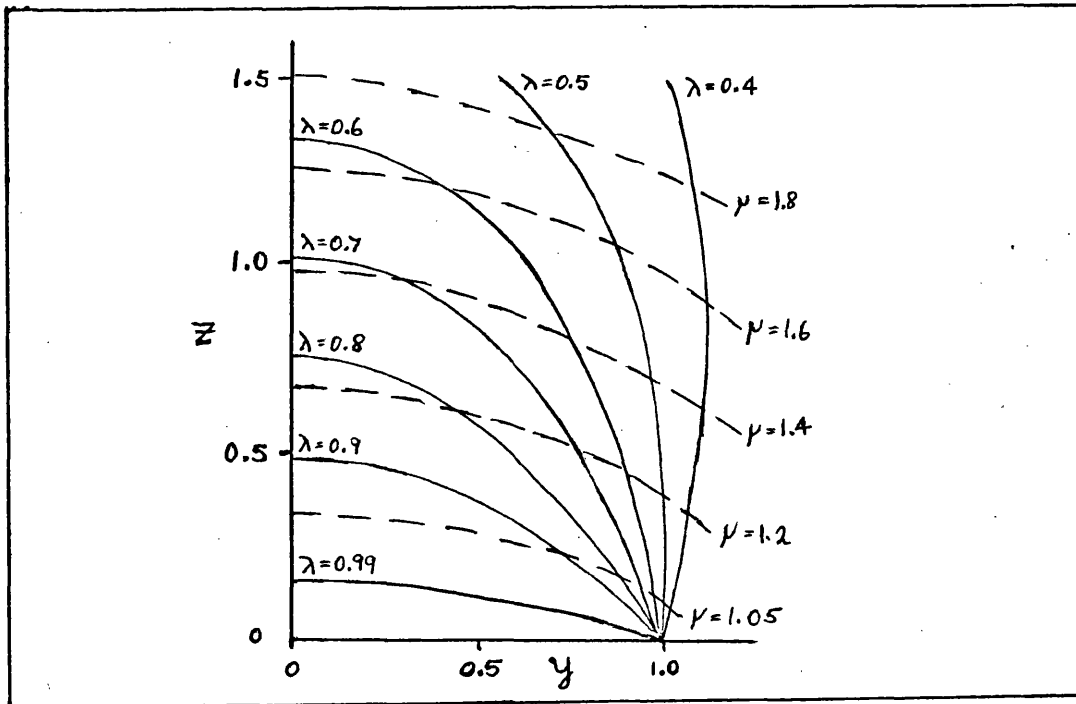


Figure 6.2 Relationship of the  $(\lambda, \mu)$  coordinate system used in the monopoles analysis to the  $(y, z)$  system.

$$\frac{dz}{dy} = \frac{B_z}{B_y} = \frac{z/r_2^3 - z/r_1^3}{(y-1)/r_2^3 - (y+1)/r_1^3} \quad (6.5)$$

which on multiplying by  $z$  can be written

$$\left( \frac{y-1}{r_2^3} - \frac{y+1}{r_1^3} \right) z \frac{dz}{dy} = \frac{z^2}{r_2^3} - \frac{z^2}{r_1^3} \quad (6.6)$$

i.e.

$$\frac{1}{r_2^3} \left[ z^2 - (y-1)z \frac{dz}{dy} \right] = \frac{1}{r_1^3} \left[ z^2 - (y+1)z \frac{dz}{dy} \right] \quad (6.7)$$

Substituting for  $z$  from (6.3) and (6.4)

$$\frac{1}{r_2} - \frac{(y-1) \left[ (y-1) + z \frac{dz}{dy} \right]}{r_2^3} = \frac{1}{r_1} - \frac{(y+1) \left[ (y+1) + z \frac{dz}{dy} \right]}{r_1^3} \quad (6.8)$$

which can be written

$$\frac{1}{r_2} - \frac{(y-1)^{\frac{1}{2}} \frac{d}{dy} (r_2^2)}{r_2^3} = \frac{1}{r_1} - \frac{(y+1)^{\frac{1}{2}} \frac{d}{dy} (r_1^2)}{r_1^3} \quad (6.9)$$

which is just

$$\frac{d}{dy} \left( \frac{y-1}{r_2} \right) = \frac{d}{dy} \left( \frac{y+1}{r_1} \right) \quad (6.10)$$

Integrating, we obtain

$$\frac{y-1}{r_2} - \frac{y+1}{r_1} = \text{constant} \quad (6.11)$$

We write

$$\frac{y+1}{r_1} - \frac{y-1}{r_2} = 2\lambda \quad (6.12)$$

$$\text{and} \quad r_1 + r_2 = 2\mu \quad (6.13)$$

Here  $\lambda$  defines the field line while  $\mu$  defines position on the field line.

From (6.3) and (6.4) we obtain

$$r_1^2 - r_2^2 = 4y \quad (6.14)$$

and

$$r_1^2 + r_2^2 = 2(1+y^2 + z^2) \quad (6.15)$$

Dividing (6.14) by (6.13) we obtain

$$r_1 - r_2 = \frac{2}{\mu} y \quad (6.16)$$

Squaring (6.13) and (6.16) and subtracting

$$r_1 r_2 = \mu^2 - \frac{y^2}{\mu^2} \quad (6.17)$$

Writing (6.12) in the form

$$y(r_2 - r_1) + (r_2 + r_1) = 2\lambda r_1 r_2 \quad (6.18)$$

and substituting from (6.13), (6.16) and (6.17) we obtain

$$-\frac{2}{\mu} y^2 + 2\mu = 2\lambda \left( \mu^2 - \frac{y^2}{\mu^2} \right) \quad (6.19)$$

that is

$$y^2 = \frac{\mu^3(1-\lambda\mu)}{\mu - \lambda} \quad (6.20)$$

Squaring (6.16) and substituting from (6.15) and (6.17) gives

$$2(1+y^2 + z^2) - 2\left(\mu^2 - \frac{y^2}{\mu^2}\right) = \left(\frac{2}{\mu} y\right)^2 \quad (6.21)$$

which reduces to

$$z^2 = (\mu^2 - 1) \left(1 - \frac{y^2}{\mu^2}\right) \quad (6.22)$$

On substituting for  $y$  from (6.20) this can be written

$$z^2 = \frac{\lambda(\mu^2 - 1)^2}{\mu - \lambda} \quad (6.23)$$

Setting  $y = 0$  in (6.20) we find the limiting value of the independent variable

$$\mu_0 = \frac{1}{\lambda} \quad (6.24)$$

and setting  $z = 0$  in (6.23) we find

$$\mu_1 = 1 \quad (6.25)$$

Putting  $\mu = \mu_0$  in (6.23) so that  $z = z_0$ , and solving for  $\lambda$ ,

$$\lambda = (1 + z_0^2)^{-\frac{1}{2}} \quad (6.26)$$

Hence  $\lambda \leq 1$  and  $1 \leq \mu \leq 1/\lambda$ .

The relationship between the  $(y, z)$  and  $(\lambda, \mu)$  coordinate systems is illustrated in Figure 6.2. Note that since  $\mu$  decreases with movement along the field line from top of arch to source, it is not suitable for use as the independent variable. Furthermore, as will be seen later, the functions  $dy/d\mu$  and  $d^2/d\mu^2$  have a singularity at the top of the arch.

From (6.1) and (6.2) we find

$$B = \left[ \left( \frac{y-1}{r_2^3} - \frac{y+1}{r_1^3} \right)^2 + \left( \frac{z}{r_2^3} - \frac{z}{r_1^3} \right)^2 \right]^{\frac{1}{2}} \quad (6.27)$$

which can be written as

$$B = \left( \frac{1}{r_1^4} + \frac{1}{r_2^4} - 2 \frac{y^2 + z^2 - 1}{r_1^3 r_2^3} \right)^{\frac{1}{2}} \quad (6.28)$$

Differentiating (6.20) we obtain

$$2y \frac{dy}{d\mu} = \left( \frac{\mu}{\mu-1} \right)^2 \left[ 3(1-\lambda\mu)(\mu-1) - \mu\lambda(\mu-1) - \mu(1-\lambda\mu) \right] \quad (6.29)$$

Substituting for  $y$  from (6.20) leads to

$$\frac{dy}{d\mu} = \frac{1}{2} \left( \frac{\mu}{(\mu-1)^3(1-\lambda\mu)} \right)^{\frac{1}{2}} \left[ 3(1-\lambda\mu)(\mu-1) - \mu\lambda(\mu-1) - \mu(1-\lambda\mu) \right] \quad (6.30)$$

Treating (6.23) similarly, we obtain

$$\frac{dz}{d\mu} = \frac{1}{2} \left( \frac{\lambda}{(\mu-1)^3} \right)^{\frac{1}{2}} \left[ 3\mu^2 - 4\lambda\mu + 1 \right] \quad (6.31)$$

Squaring and adding (6.30) and (6.31) gives

$$\frac{d\ell}{d\mu} = \frac{-1}{2(\mu-\lambda)^{3/2}} \left\{ \frac{\mu}{1-\lambda\mu} \left[ 3(1-\lambda\mu)(\mu-\lambda) - \lambda\mu(\mu-\lambda) - \mu(1-\lambda\mu) \right]^2 + \lambda \left[ 3\mu^2 - 4\lambda\mu + 1 \right]^2 \right\}^{1/2} \quad (6.32)$$

The negative square root is taken here as  $\mu$  decreases on moving away from the top of the arch. As mentioned previously, (6.30) and (6.32) are singular at the top of the arch.

Therefore we make a change of variable, defining

$$\xi = (1 - \lambda\mu)^{1/2} \quad (6.33)$$

Then  $\xi_0 = 0$  (6.34)

and  $\xi_1 = (1 - \lambda)^{1/2}$  (6.35)

Thus  $\mu = \frac{1}{\lambda} (1 - \xi^2)$  (6.36)

and  $\frac{d\mu}{d\xi} = -\frac{2\xi}{\lambda} = -\frac{2}{\lambda} (1 - \lambda\mu)^{1/2}$  (6.37)

so 
$$\frac{d\ell}{d\xi} = \frac{1}{\lambda(\mu-\lambda)^{3/2}} \left\{ \mu \left[ 3(1-\lambda\mu)(\mu-\lambda) - \lambda\mu(\mu-\lambda) - \mu(1-\lambda\mu) \right]^2 + \lambda(1-\lambda\mu) \left[ 3\mu^2 - 4\lambda\mu + 1 \right]^2 \right\}^{1/2} \quad (6.38)$$

To evaluate  $\frac{dB}{d\xi}$  we use

$$\frac{dB}{d\xi} = \left[ \frac{\partial B}{\partial y} \frac{dy}{d\mu} + \frac{\partial B}{\partial z} \frac{dz}{d\mu} \right] \frac{d\mu}{d\xi} \quad (6.39)$$

Differentiating (6.28) with respect to  $y$  and  $z$ , we obtain

$$\begin{aligned} \frac{\partial B}{\partial y} = & -B^{-1} \left[ (r_2^2)^{-3} \frac{\partial}{\partial y} (r_2^2) + (r_1^2)^{-3} \frac{\partial}{\partial y} (r_1^2) \right. \\ & \left. + \frac{2y}{r_1^3 r_2^3} - \frac{3}{2} (y^2 + z^2 - 1)(r_1^2 r_2^2)^{-5/2} \times \right. \\ & \left. \left( r_1^2 \frac{\partial}{\partial y} (r_2^2) + r_2^2 \frac{\partial}{\partial y} (r_1^2) \right) \right] \quad (6.40) \end{aligned}$$

and

$$\frac{\partial B}{\partial z} = -B^{-1} \left[ (r_2^2)^{-3} \frac{\partial}{\partial z} (r_2^2) + (r_1^2)^{-3} \frac{\partial}{\partial z} (r_1^2) + \frac{2z}{r_1 r_2} - \frac{3}{2} (y^2 + z^2 - 1)(r_1^2 r_2^2)^{-5/2} \times \left( r_1^2 \frac{\partial}{\partial z} (r_2^2) + r_2^2 \frac{\partial}{\partial z} (r_1^2) \right) \right] \quad (6.41)$$

Differentiating (6.3) and (6.4) we find

$$\left. \begin{aligned} \frac{\partial}{\partial y} (r_1^2) &= 2(y+1) \\ \frac{\partial}{\partial y} (r_2^2) &= 2(y-1) \\ \frac{\partial}{\partial z} (r_1^2) &= \frac{\partial}{\partial z} (r_2^2) = 2z \end{aligned} \right\} \quad (6.42)$$

Substituting from (6.42) into (6.40) and (6.41) and using (6.30), (6.31), (6.37) and (6.39) the rate of change of magnetic field with respect to the independent variable can be expressed as

$$\frac{dB}{d\xi} = \frac{2}{B\lambda (\mu-\lambda)^{3/2} r_1^3 r_2^3} \left\{ (\alpha y + \beta) \mu^{1/2} \times \left[ 2\mu (1 + 2\lambda^2) - 3\lambda (1 + \mu^2) \right] + \alpha z \lambda^{1/2} (1-\lambda\mu)^{1/2} \left[ 3\mu^2 - 4\lambda\mu + 1 \right] \right\} \quad (6.43)$$

Where  $\alpha = 1 + a + b$   
 $\beta = a - b$

and 
$$\left. \begin{aligned} a &= \left( \frac{r_2}{r_1} \right)^3 - \frac{3}{2} \frac{y^2 + z^2 - 1}{r_1^2} \\ b &= \left( \frac{r_1}{r_2} \right)^3 - \frac{3}{2} \frac{y^2 + z^2 - 1}{r_2^2} \end{aligned} \right\} \quad (6.44)$$

and B is obtained from (6.28).

Using (6.31) and (6.37) we obtain

$$\frac{dz}{d\xi} = - \left( \frac{1-\lambda\mu}{\lambda(\mu-\lambda)^3} \right)^{\frac{1}{2}} (3\mu^2 - 4\lambda\mu + 1) \quad (6.45)$$

while (6.30) and (6.37) give

$$\frac{dy}{d\xi} = - \left( \frac{\mu}{\lambda^2(\mu-\lambda)^3} \right)^{\frac{1}{2}} \left[ 3(1-\lambda\mu)(\mu-\lambda) - \lambda\mu(\mu-\lambda) - \mu(1-\lambda\mu) \right] \quad (6.46)$$

## 7. THE TRAPPED ELECTRON DISTRIBUTION FUNCTION

In this section we derive the equations describing the steady-state distribution of electrons in the trap. Since the pitch angle of an electron changes continuously as the electron moves along the trap, we introduce the term "initial pitch angle" in order to describe the pitch angle distribution. The initial pitch angle of an electron is the pitch angle it has on passing through the mid-point of the trap and is the minimum pitch angle the electron can have since the magnetic field strength increases monotonically away from the top of the arch.

The distribution of electron energy and pitch angle is defined by the function  $g(E, \alpha_0)$ , the number of electrons with energy in the range  $E$  to  $E + dE$  and initial pitch angle  $\alpha_0$  to  $\alpha_0 + d\alpha_0$  being given by  $g(E, \alpha_0) dE d\alpha_0$ . Since changes in the electron distribution and magnetic field structure during one bounce period are neglected, the pitch angle of an electron at any point in the trap (defined by the positional parameter  $\xi$ ) can be found from the first adiabatic invariant

$$\frac{\sin^2 \alpha(\xi)}{\sin^2 \alpha_0} = \frac{B(\xi)}{B(\xi_0)} \quad (7.1)$$

where  $B(\xi)$  is the magnetic field strength at position  $\xi$ .

We define the position-dependent fast particle density,  $N(\xi, E, \alpha)$  such that the number of non-thermal electrons in a volume  $d\tau$  at position  $\xi$  in the trap, with energy  $E$  to  $E + dE$  and pitch angle  $\alpha$  to  $\alpha + d\alpha$ , is given by

$$\delta N = N(\xi, E, \alpha) d\tau dE d\alpha \quad (7.2)$$

Making use of the symmetry of the trap, we take  $\alpha$  to lie in the interval  $(0, \pi/2)$  and define  $N(\xi, E, \alpha)$  to include electrons of pitch angle  $\alpha$  moving in both directions along the field line.

We now wish to relate the position dependent electron distribution function  $N(\xi, E, \alpha)$  to the defining function  $g(E, \alpha_0)$ . Writing (7.2) as a function of  $\alpha_0$  and integrating along the field line, we obtain

$$g(E, \alpha_0) dE d\alpha_0 = 2 \int_{\xi_0}^{\xi_m(\alpha_0)} N(\xi, E, \alpha(\alpha_0, \xi)) S(\xi) \frac{d\xi}{d\alpha_0} \frac{d\alpha(\alpha_0, \xi)}{d\alpha_0} dE d\alpha_0 d\xi \quad (7.3)$$

$S(\xi)$  is the cross-sectional area of the flux tube, while  $\xi_0$  and  $\xi_m$  are the values of  $\xi$  at the top of the arch and at the mirror point respectively. The integral is multiplied by 2 because the integration extends over only one half of the trap. The pitch angle  $\alpha$  is obtained as a function of  $\alpha_0$  and  $\xi$  from (7.1).

Since electron energy loss and scattering are neglected, conservation of electron flux in the steady state leads to the relation

$$N(\xi_0, E, \alpha_0) S(\xi_0) v_{\parallel}(E, \alpha_0) dE d\alpha_0 = N(\xi, E, \alpha) S(\xi) v_{\parallel}(E, \alpha) dE \frac{d\alpha}{d\alpha_0} d\alpha_0 \quad (\xi \leq \xi_m(\alpha_0)) \quad (7.4)$$

where  $v_{\parallel}(E, \alpha)$  is the electron velocity parallel to the magnetic field, given by

$$v_{\parallel}(E, \alpha) = v(E) \cos \alpha \quad (7.5)$$

$v$  being the velocity of an electron of kinetic energy  $E$ .

The cross sectional area of the flux tube is related to the magnetic field strength by conservation of magnetic flux, so that

$$S(\xi) B(\xi) = S(\xi_0) B(\xi_0) \quad (7.6)$$

since we take the flux tube to be of infinitesimal diameter. From (7.4), (7.5) and (7.6) we obtain

$$N(\xi, E, \alpha) = N(\xi_0, E, \alpha_0) \frac{B(\xi)}{B(\xi_0)} \frac{\cos \alpha_0}{\cos \alpha} \frac{d\alpha_0}{d\alpha} \quad (\xi < \xi_m(\alpha_0)) \quad (7.7)$$

and differentiating (7.1) we find that

$$\frac{d\alpha_0}{d\alpha} = \frac{\tan \alpha_0}{\tan \alpha} \quad (7.8)$$

Thus, from (7.7), (7.8) and (7.1)

$$\frac{N(\xi, E, \alpha)}{B(\xi)^{\frac{1}{2}}} = \frac{N(\xi_0, E, \alpha_0)}{B(\xi_0)^{\frac{1}{2}}} \quad (\xi < \xi_m(\alpha_0)) \quad (7.9)$$

Eliminating  $\cos \alpha$  from (7.7) by use of (7.1), substituting this expression into (7.3) and using (7.6) we obtain

$$g(E, \alpha_0) = 2 \int_{\xi_0}^{\xi_m(\alpha_0)} N(\xi_0, E, \alpha_0) \frac{\cos \alpha_0}{\left[1 - \sin^2 \alpha_0 \frac{B(\xi)}{B(\xi_0)}\right]^{\frac{1}{2}}} S(\xi_0) \frac{d\xi}{d\xi} d\xi \quad (7.10)$$

Thus

$$N(\xi_0, E, \alpha_0) = \frac{g(E, \alpha_0)}{2 S(\xi_0) \cos \alpha_0 \int_{\xi_0}^{\xi_m(\alpha_0)} \left[1 - \sin^2 \alpha_0 \frac{B(\xi)}{B(\xi_0)}\right]^{-\frac{1}{2}} \frac{d\xi}{d\xi} d\xi} \quad (7.11)$$

We note that the integral in the denominator of (7.11) can be written, using (7.1), as

$$I = \int_0^{\xi_m(\alpha_0)} \sec \alpha(\xi) d\xi \quad (7.12)$$

where  $l_m$  is the distance along the field line of the mirror point of the electron trajectory from the centre of the trap.

Using (7.5) to express the integrand as  $v/v_w$  and noting that the velocity is constant, (7.12) can be written

$$I = L(\alpha_0)/2 \quad (7.13)$$

where  $L(\alpha_0)$  is the distance along the field line between the electron mirror points. Thus

$$N(\xi_0, E, \alpha_0) = \frac{g(E, \alpha_0)}{L(\alpha_0) S(\xi_0) \cos \alpha_0} \quad (7.14)$$

where

$$L(\alpha_0) = 2 \int_{\xi_0}^{\xi_m(\alpha_0)} \left[ 1 - \sin^2 \alpha_0 \frac{B(\xi)}{B(\xi_0)} \right]^{-\frac{1}{2}} \frac{d\xi}{d\xi} \quad (7.15)$$

From (7.9) and (7.14) we obtain

$$N(\xi, E, \alpha) = \frac{g(E, \alpha_0)}{L(\alpha_0) S(\xi_0) \cos \alpha_0} \left( \frac{B(\xi)}{B(\xi_0)} \right)^{\frac{1}{2}} (\xi < \xi_m(\alpha_0)) \quad (7.16)$$

Defining  $N^*(\xi, E, \alpha)$  to be the number of trapped electrons per unit distance along the flux tube, so that

$$N^*(\xi, E, \alpha) d\xi = N(\xi, E, \alpha) S(\xi) d\xi \quad (7.17)$$

we obtain, by (7.6) and (7.16)

$$N^*(\xi, E, \alpha) = \frac{g(E, \alpha_0)}{L(\alpha_0) \cos \alpha_0} \left( \frac{B(\xi_0)}{B(\xi)} \right)^{\frac{1}{2}} (\xi < \xi_m(\alpha_0)) \quad (7.18)$$

Multiplying (7.18) by  $d\alpha/d\alpha_0$  (7.8) and using (7.1) we obtain the distribution function in terms of the initial pitch angle distribution

$$N_0^*(\xi, E, \alpha_0) = \frac{g(E, \alpha_0)}{L(\alpha_0) \cos \alpha} \left( \xi > \xi_m(\alpha_0) \right) \quad (7.19)$$

This function together with the X-ray bremsstrahlung crosssections

and the equations describing the trap geometry defines completely the characteristics of X-ray emission from the trapping model.

## 8. BREMSSTRAHLUNG EMISSION FROM AN ASSEMBLY OF TRAPPED ELECTRONS

As we have discussed the X-ray bremsstrahlung cross-sections in detail in Chapter II, here we consider only the incorporation of the cross-sections in the equations describing the distribution of electrons in the trap and the geometry of the trapping field. We also restrict our attention to the derivation of expressions for the X-ray intensity; polarisation of the radiation will be considered in §9.

If  $Q_T(\epsilon, \cos\theta, E)$  is the cross-section for electron-proton bremsstrahlung differential in photon energy and solid angle, then the number of photons of energy  $\epsilon$  to  $\epsilon+d\epsilon$  emitted into solid angle  $d\Omega$  about a direction  $\underline{k}$  due to a number density  $n_e$  of electrons of energy  $E$ , having velocity  $\underline{v}$ , from a volume  $d\tau$  in which the proton density is  $n_p$ , is given by

$$\delta I_1 = n_p d\tau n_e v Q(\epsilon, \cos\theta, E) d\epsilon d\Omega \quad (8.1)$$

where  $\theta$  is the angle between  $\underline{v}$ , the electron velocity vector and  $\underline{k}$ , the direction of the observer.

At any point in the electron trap there is a distribution in electron velocity both in magnitude and direction, therefore (8.1) must be written in a form differential in electron energy and velocity direction. We must also define the angle  $\theta$  in terms of the electron pitch angle  $\alpha$  and an auxiliary angle  $\phi$  defining the azimuthal position of an electron in its helical path.

By application of the cosine formula to the spherical triangle  $\underline{Bky}$  in Figure 8.1,  $\theta$  can be expressed as

$$\cos\theta = \cos\Theta \cos\alpha + \sin\Theta \sin\alpha \cos\phi \quad (8.2)$$

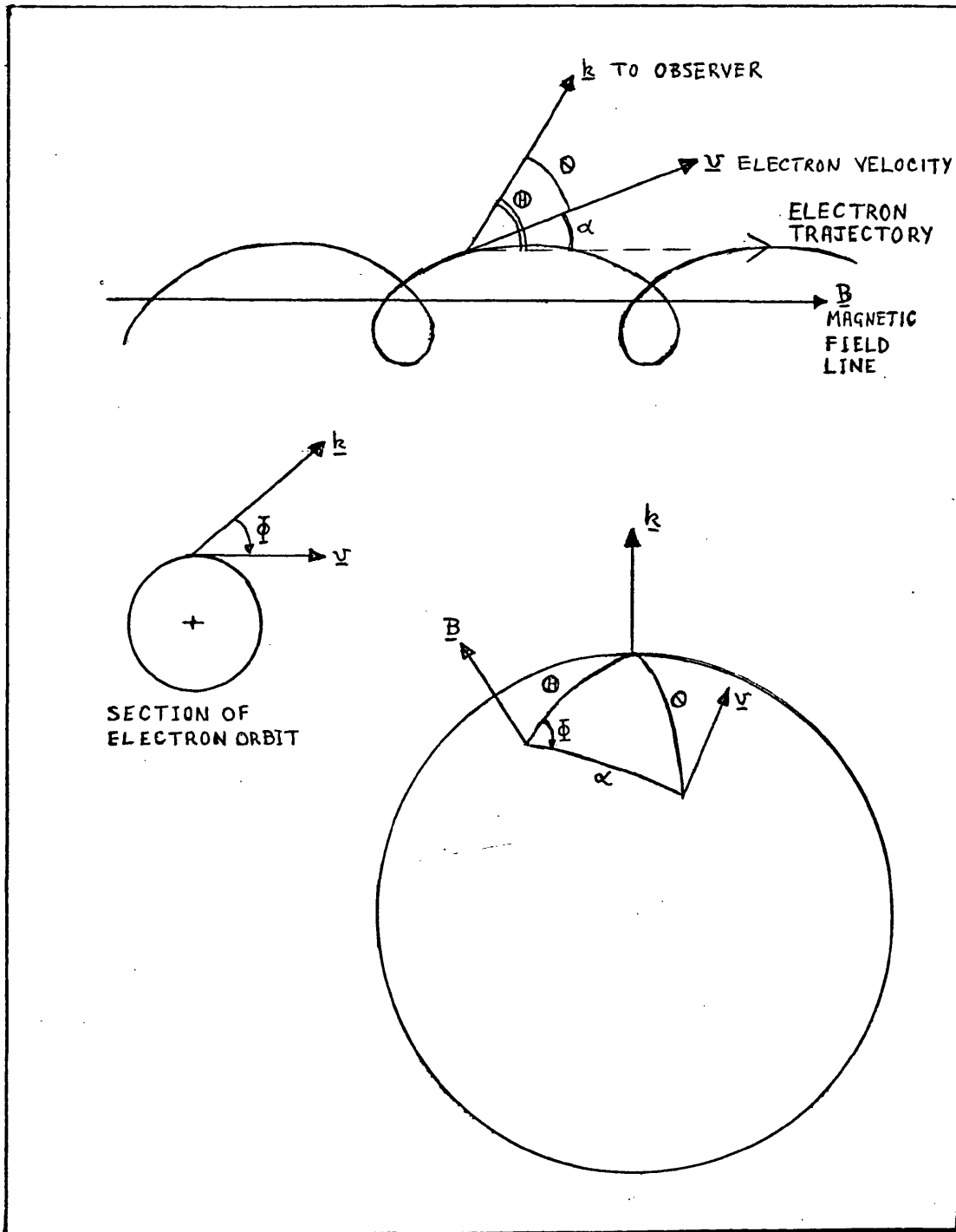


Figure 8.1 Geometry of X-ray emission from an electron spiralling about a magnetic field line.

where  $\theta$  is the angle between the field line  $B$  and the direction of the observer  $k$ .

For the electron trap,

$$n_p d\tau = n_p(\mu) S(\mu) d\ell \quad (8.3)$$

where  $d\ell$  is a distance along the field line and  $S(\mu)$  is the cross-sectional area of the fluxtube,  $\mu$  being the positional parameter (see §7). Allowing for electrons travelling in one direction only along the field line, we can write

$$n_e = \frac{1}{2} N^*(\mu, E, \alpha) dE d\alpha \frac{d\phi}{2\pi} \quad (8.4)$$

thus taking account of the distribution of electron flux over energy and direction. We recall that  $N^*(\xi, E, \alpha)$  was defined in (7.18) as the number of electrons per unit length along the trap, with energy in unit range about  $E$  and pitch angle in unit range about  $\alpha$ .

We also write

$$v(E) = c \beta(E) \quad (8.5)$$

where  $c$  is the speed of light and  $\beta = v/c$ . Thus (8.1) becomes

$$\delta I_2 = \frac{c}{4\pi} n_p(\xi) N^*(\xi, E, \alpha) \beta(E) Q_T(\epsilon, \cos \theta, E) dE d\alpha d\phi d\ell d\epsilon d\Omega \quad (8.6)$$

The contribution to the X-ray flux from electrons travelling in the opposite direction on the field line to that considered in (8.4) is obtained by reversing the velocity vector  $\underline{v}$  depicted in Figure 8.1. Thus, corresponding to the term  $Q_T(\epsilon, \cos \theta(\theta, \alpha, \phi), E) d\phi$  in (8.6) we have

$$Q_T(\epsilon, \cos \theta(\theta, \pi - \alpha, \phi'), E) d\phi' \quad (8.7)$$

Although the azimuthal angle  $\phi$  was defined with respect to the direction  $\underline{k}$  (Figure 8.1),  $\phi$  and  $\phi'$  can in fact incorporate an arbitrary phase angle since an integration over azimuth is performed. The choice of a phase difference of  $\pi$  between these angles leads a particularly simple configuration, illustrated in Figure 8.2, from which it is clear that

$$\left. \begin{aligned} \phi' &= \phi + \pi \\ \alpha' &= \pi - \alpha \\ \theta' &= \pi - \theta \end{aligned} \right\} \quad (8.8)$$

Thus

$$\cos \theta(\theta, \alpha', \phi') = -\cos \theta(\theta, \alpha, \phi) \quad (8.9)$$

and so an azimuth-integrated bremsstrahlung cross-section taking account of all electrons with energy in unit range about  $E$  and pitch angle in unit range about  $\alpha$  can be defined as

$$Q_{ST}(\epsilon, E, \theta, \alpha) = \oint \left[ Q_T(\epsilon, \cos \theta(\theta, \alpha, \phi), E) + Q_T(\epsilon, -\cos \theta(\theta, \alpha, \phi), E) \right] d\phi \quad (8.10)$$

The contribution to the X-ray flux differential in photon energy and solid angle from all electrons with energy  $E$  to  $E + dE$  and pitch angle  $\alpha$  to  $\alpha + d\alpha$  in a length  $d\ell$  of the trap is then given by

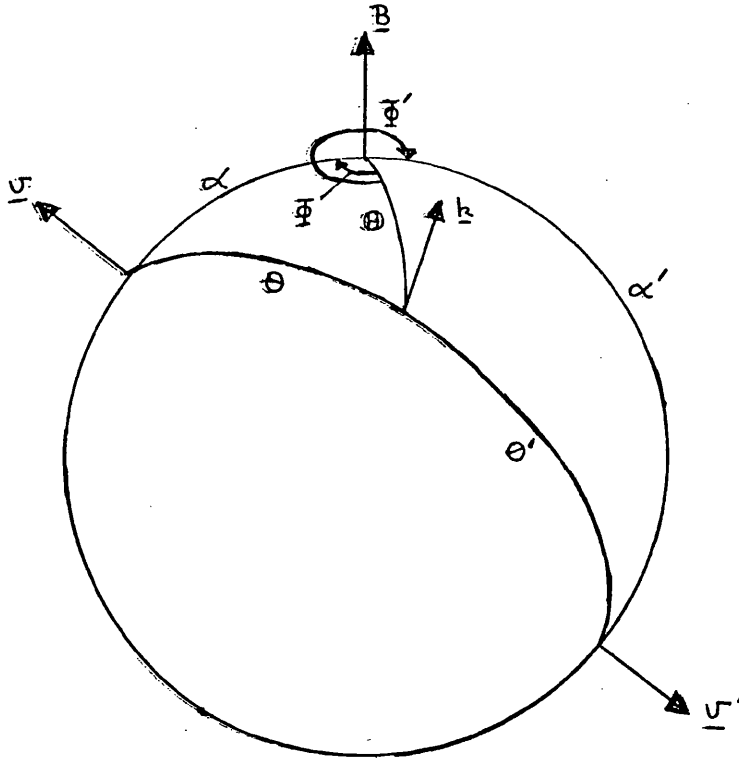


Figure 8.2 Geometry of emission from two electrons moving in opposite directions along the field line  $\underline{B}$  with a phase difference of  $\pi$  between their azimuthal angles  $\phi$  and  $\phi'$ .

$$\delta I_3 = \frac{c}{4\pi} n_p(\xi) N^*(\xi, E, \alpha) \beta(E) Q_{ST}(\epsilon, E, \theta, \alpha) dE d\alpha d\ell d\epsilon d\Omega \quad (8.11)$$

Using (7.19), (8.11) can be written in terms of the initial pitch angle distribution,

$$\delta I_3 = \frac{c}{4\pi} n_p(\xi) \frac{g(E, \alpha_0)}{L(\alpha_0)} \beta(E) Q_{ST}(\epsilon, E, \theta, \alpha) \sec \alpha dE d\alpha_0 d\ell d\epsilon d\Omega \quad (8.12)$$

which, integrated over  $E$  and  $\alpha_0$  gives the differential photon flux from unit length of the trap at position  $\xi$ ,

$$I(\epsilon, \theta, \xi) = \frac{c}{4\pi} n_p(\xi) \int_{\alpha_{\min}}^{\alpha_{\max}(\xi)} \int_{\epsilon}^{\infty} \beta(E) \frac{g(E, \alpha_0)}{L(\alpha_0) \cos \alpha} Q_{ST}(\epsilon, E, \theta, \alpha) dE d\alpha_0 \quad (8.13)$$

The integration over initial pitch angle only extends up to  $\alpha_0 = \alpha_{\max}(\xi)$  as electrons of a larger initial pitch angle are reflected before reaching the point defined by  $\xi$ . We choose the lower limit of integration  $\alpha_{\min}$  so that electrons with this initial pitch angle mirror just above the transition region. We assume that electrons of smaller pitch angle decay rapidly in the dense chromosphere and do not participate in the production of coronal trap X-ray emission.

From (7.1), which gives the dependence of pitch angle on position,

$$\sin^2 \alpha_{\max} = \frac{B(\xi_0)}{B(\xi)} \quad (8.14)$$

To obtain an expression for the total emission (8.13) must be integrated along the field line defining the trap. Note that, in accordance with the definitions made in describing the magnetic field configuration of the trap in §3, (8.13) can only be applied directly in the right hand half of the trap ( $y > 0$ ). To integrate (8.13),  $\theta$ , the angle between the magnetic field and the direction of the observer must be defined as a function of position on the trap. This is done by introducing the angles  $\psi$ ,  $A$  and  $B$  shown in Figure 8.3.  $A$  and  $B$  are polar coordinates defining the orientation of the trap relative to the observer while  $\psi$  is the angle between the magnetic field

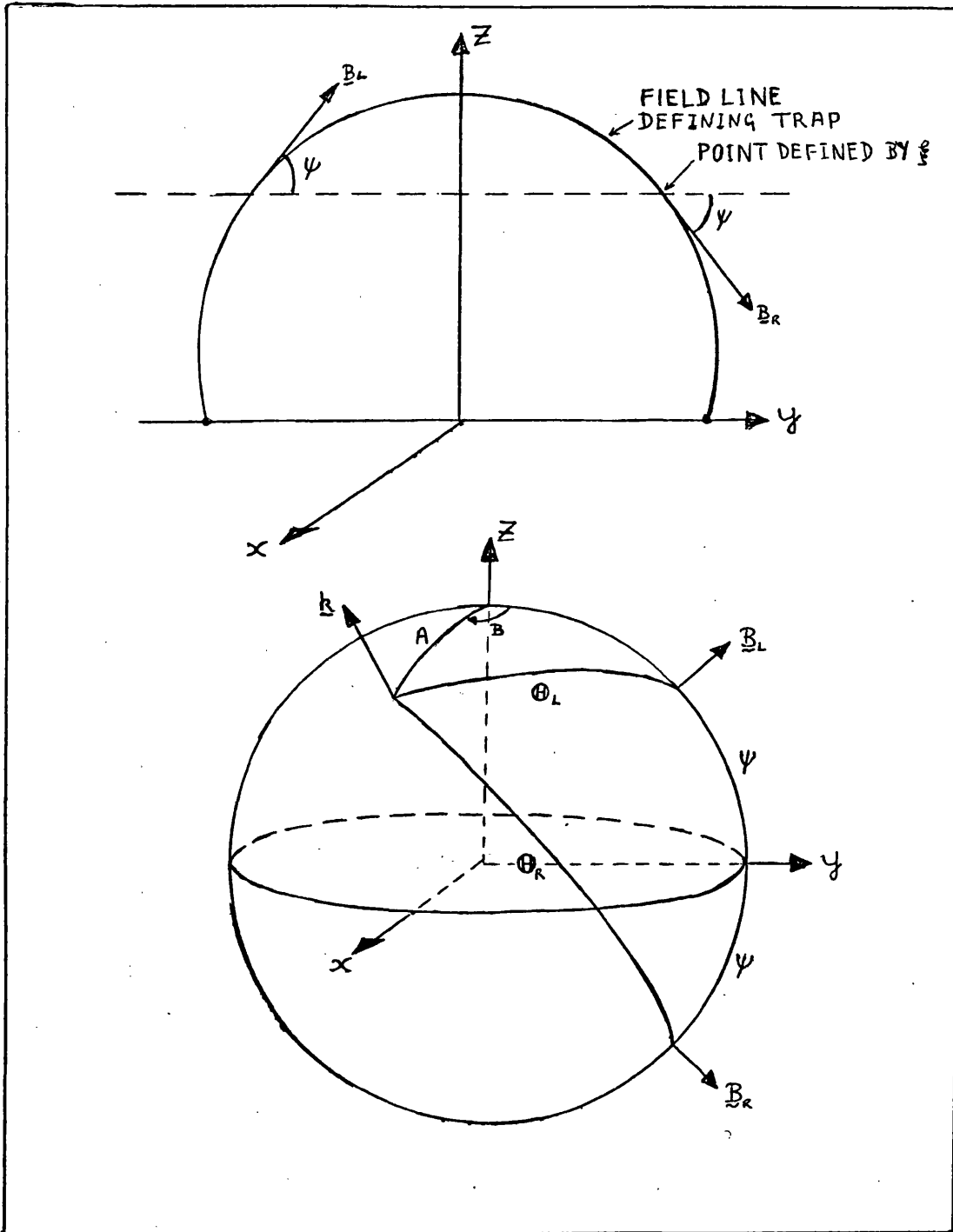


Figure 8.3

Definition of the angles  $\theta_L$  and  $\theta_R$  between the line of sight  $\underline{k}$  and the magnetic field directions  $\underline{B}_L$  and  $\underline{B}_R$  in the left and right halves of the trap. These angles are defined as functions of the angles  $A$  and  $B$ , defining the direction of the observer, and  $\psi$ , which gives the field direction.

direction and the photosphere. Applying the cosine formula to the triangle  $zkB_R$  in Figure 8.3, we obtain

$$\cos \theta_R = -\cos A \sin \psi + \sin A \cos \psi \cos B \quad (8.15)$$

while the angle  $\psi$  is related to the geometry of the magnetic field by

$$\sin \psi = -\frac{dz}{d\ell} \quad ; \quad \cos \psi = \frac{dy}{d\ell} \quad (8.16)$$

Thus the number of photons in unit energy range about  $\epsilon$  emitted per unit time, into unit solid angle about  $\underline{k}$ , from the right hand half of the flux tube, is

$$I_R(\epsilon, A, B) = \int_{\epsilon_0}^{\epsilon_1} I(\epsilon, \theta_R, \xi) \frac{d\ell}{d\xi} d\xi \quad (8.17)$$

where  $I(\epsilon, \theta, \xi)$  is given by (8.13) and  $\theta_R$  is obtained from (8.15) and (8.16).

Referring to Figure 8.3 it is clear that the emission from the left hand half of the flux tube is also given by (8.17) if  $\theta_R$  is replaced by  $\theta_L$ , where  $\theta_L$  is given by (8.15) with  $\psi$  negated. Therefore the total number of photons emitted, per unit time in unit energy range about  $\epsilon$ , into unit solid angle about  $\underline{k}$  is

$$I_T(\epsilon, A, B) = \int_{\epsilon_0}^{\epsilon_1} I(\epsilon, \theta_R, \xi) + I(\epsilon, \theta_L, \xi) \frac{d\ell}{d\xi} d\xi \quad (8.18)$$

where

$$\cos \theta_R = \frac{dz}{d\ell} \cos A + \frac{dy}{d\ell} \sin A \cos B \quad (8.19)$$

$$\text{and } \cos \theta_L = -\frac{dz}{d\ell} \cos A + \frac{dy}{d\ell} \sin A \cos B \quad (8.20)$$

and  $\frac{dz}{d\ell}$ ,  $\frac{dy}{d\ell}$  and  $\frac{d\ell}{d\xi}$  are as defined in §3.

Note that since  $0 < \theta_R, \theta_L < \pi$ , the sines of these angles occurring in (8.2) are correctly given by

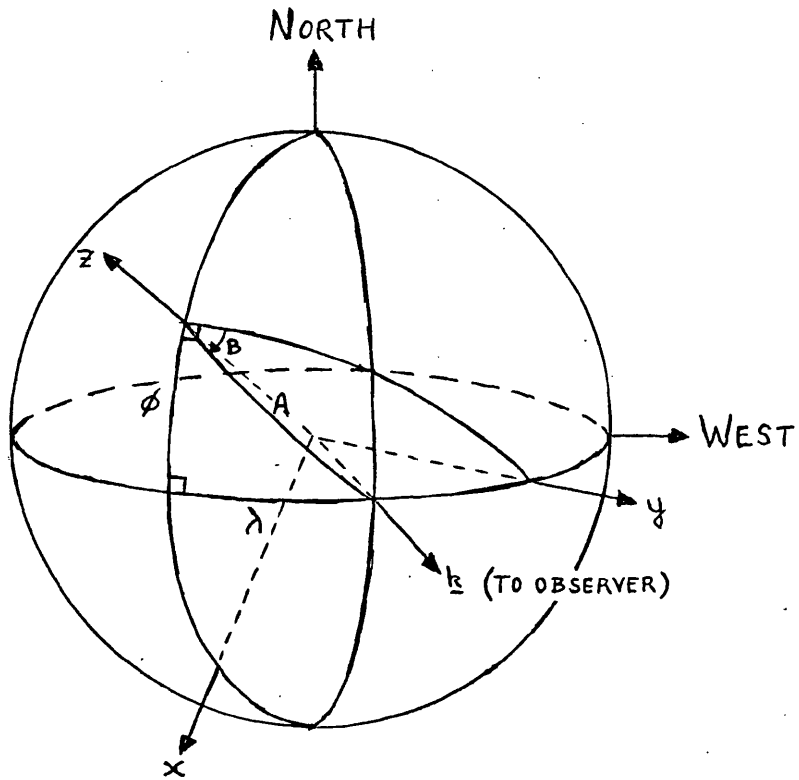


Figure 8.4 The relationship between the polar coordinates A and B which define the orientation of the trap relative to the observer, and the solar longitude  $\lambda$  and latitude  $\phi$  of the trap.

$$\sin \theta_R = \sqrt{1 - \cos^2 \theta_R}, \sin \theta_L = \sqrt{1 - \cos^2 \theta_L} \quad (8.21)$$

To provide an easily assimilated description of the trap orientation we take the pair of bipolar sunspots to lie on a parallel of solar latitude. As the trap may be placed anywhere on the solar surface the constraint of an equatorial magnetic field direction does not exclude any possible orientation of the trap relative to the observer. By placing the trap on the invisible hemisphere of the sun we can observe the directivity and polarisation of X-rays emitted towards the photosphere which are of interest in connection with the albedo effect discussed in Chapter II.

The relationship between the solar longitude  $\lambda$ , which we define to be measured Eastwards from the central meridian, and latitude  $\phi$  and the angles A and B used in (8.19) and (8.20) is illustrated in Figure 8.4. From the triangle with sides  $\lambda, \phi$  and A we obtain by the cosine formula

$$\cos A = \cos \phi \cos \lambda \quad (8.22)$$

and by the sine formula

$$\cos B = \sin \lambda / \sin A \quad (8.23)$$

Since A lies in the range  $[0, \pi]$  and only the cosine of B is required in (8.19) and (8.20), these equations suffice to determine the X-ray emission from the trap for all values of  $\lambda$  and  $\phi$ . However, results are presented only for the left half of the upper hemisphere of the sun ( $0 \leq \lambda \leq \pi$ ,  $0 \leq \phi \leq \pi/2$ ) as characteristics of the X-ray emission from sources in other positions may be easily obtained from these by consideration of symmetry.

## 9. POLARISATION OF X-RAYS EMITTED BY THE TRAPPED ELECTRONS

In this section we evaluate the polarisation of X-ray emission from the trap by combining the bremsstrahlung equations of Chapter II

with those describing the geometry of the trapping field (§3-6) and electron distribution (§7).

First of all we discuss the formulation of our description of polarisation. In Chapter II we showed that bremsstrahlung radiation emitted by a single accelerated electron is completely polarised in the plane containing the direction of acceleration, while the radiation from a beam of electrons which are scattered in random directions is partially polarised, the plane of polarisation lying either in the plane of emission, which is the plane defined by the initial direction of the electron beam and the direction of the observer, or perpendicular to it. Denoting the cross-section for emission of radiation polarised in the plane of emission by  $\sigma_{\parallel}$  and that for radiation polarised perpendicular to it by  $\sigma_{\perp}$ , the degree of polarisation is given by

$$p = \frac{\sigma_{\parallel} - \sigma_{\perp}}{\sigma_{\parallel} + \sigma_{\perp}} \quad (9.1)$$

where the radiation is polarised parallel to the emission plane if  $p$  is positive and perpendicular to it if  $p$  is negative. The convention we have established here is the opposite to that used by Elwert & Haug (1970), Haug (1972) and Brown (1972), who take the polarisation to be negative when the maximum intensity is parallel to the emission plane.

Turning now to the polarisation of radiation emitted by an assembly of trapped electrons, we consider first the emission of radiation from a specified point on the trap due to electrons moving in one direction along the field line. Since the electron velocities are distributed in direction there is no unique plane of emission, but because of the uniform azimuthal distribution of electrons spiralling about the magnetic field line, the plane of polarisation lies parallel or perpendicular to it.

The truth of this statement can be established by a method similar to that used in Chapter II to show that the plane of polarisation of radiation from a beam of electrons is parallel or perpendicular to the beam. It is well known that the intensity observed through a polariser orientated at angle  $\phi$  to some reference direction, from a source of total intensity  $I_0$  with degree of polarisation  $p$ , the plane of polarisation lying at an angle  $\phi$  to the reference direction, is

$$I(\phi) = I_0 \left[ \frac{1+p}{2} \cos^2(\phi - \phi) + \frac{1-p}{2} \sin^2(\phi - \phi) \right] \quad (9.2)$$

which can alternatively be expressed as

$$I(\phi) = I_1 \cos^2(\phi - \phi) + I_2 \sin^2(\phi - \phi) \quad (9.3)$$

if the source is regarded as being composed of two orthogonally polarised components of intensity

$$I_1 = I_0 \frac{1+p}{2} \quad \text{and} \quad I_2 = I_0 \frac{1-p}{2} \quad (9.4)$$

polarised in the directions  $\phi$  and  $\phi + \pi/2$  respectively.

Figure 9.1 shows the angles and directions involved in this discussion and illustrates the orientation of the planes of polarisation of radiation polarised parallel and perpendicular to the plane of emission. The pitch angle  $\alpha$ , azimuthal angle  $\phi$ ,  $\theta$  the angle between the direction of the observer and the magnetic field and  $\theta$  the angle on which the bremsstrahlung cross-sections depend, were discussed in §8. We have introduced the angle  $\chi$ , which defines the plane of polarisation of the component polarised parallel to the plane of emission relative to the magnetic field, and  $\phi$ , the angle at which the observer's polariser is set, again relative to the magnetic field direction.

As the electron distribution does not depend on the azimuthal angle  $\phi$  we can write for the observed intensity, using (9.3)

$$I(\phi) \propto \int \left[ \sigma_{\parallel} \cos^2(\chi - \phi) + \sigma_{\perp} \sin^2(\chi - \phi) \right] d\phi \quad (9.5)$$

For clarity we have not explicitly indicated the angular dependence of the cross-sections nor their dependence on electron and photon energy. After some trigonometric manipulation, (9.5) can be expressed in the form

$$I(\phi) \propto \int \left( \sigma_{\parallel} \cos^2 \chi + \sigma_{\perp} \sin^2 \chi \right) d\phi \cos^2 \phi + \int \left( \sigma_{\parallel} \sin^2 \chi + \sigma_{\perp} \cos^2 \chi \right) d\phi \sin^2 \phi + \int \left( \sigma_{\parallel} - \sigma_{\perp} \right) \sin 2\chi d\phi \cos \phi \sin \phi \quad (9.6)$$

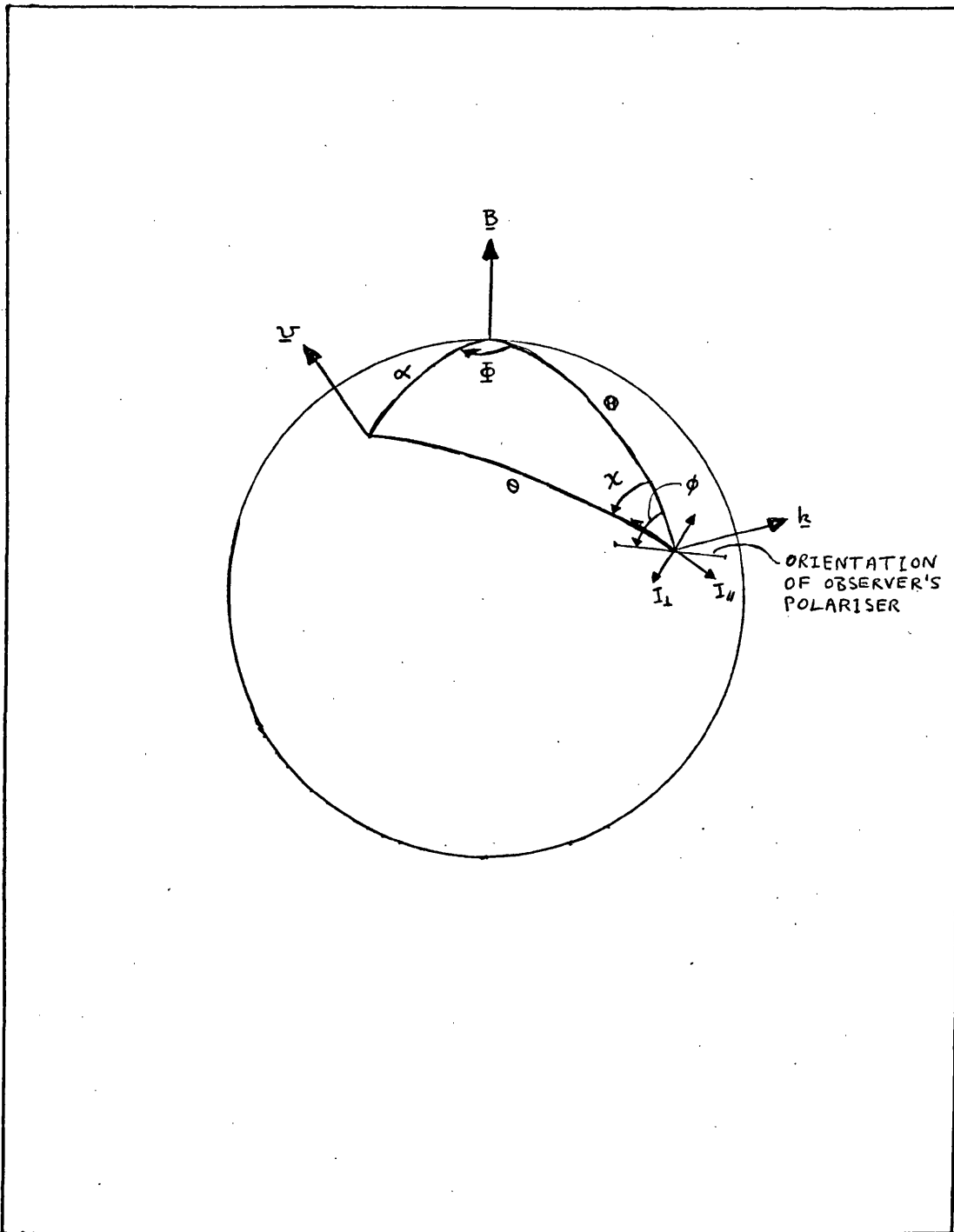


Figure 9.1 Definition of the angles  $\chi$  and  $\phi$  which are used in defining the polarisation of X-ray emission from an electron spiralling about a magnetic field line.

Remembering that the bremsstrahlung cross-sections depend not on  $\theta$  but its cosine, and considering the symmetries about the field direction apparent in Figure 9.1, we see that the last term in (9.6) is identically zero. Therefore we can define the azimuthally integrated cross-sections

$$\sigma_{//}^* = \int (\sigma_{//} \cos^2 \chi + \sigma_{\perp} \sin^2 \chi) d\phi \quad (9.7)$$

and

$$\sigma_{\perp}^* = \int (\sigma_{//} \sin^2 \chi + \sigma_{\perp} \cos^2 \chi) d\phi \quad (9.8)$$

and write (9.6) as

$$I(\phi) \propto \sigma_{//}^* \cos^2 \phi + \sigma_{\perp}^* \sin^2 \phi \quad (9.9)$$

which shows that  $\sigma_{//}^*$  is the cross-section for emission of radiation polarised parallel to the magnetic field and  $\sigma_{\perp}^*$  is the cross-section for emission polarised perpendicular to it.

As the bremsstrahlung cross-sections given in Chapter II are defined as the total cross-section

$$Q_{\text{T}} = \sigma_{//} + \sigma_{\perp} \quad (9.10)$$

and the polarisation cross-section

$$Q_{\text{P}} = \sigma_{//} - \sigma_{\perp} \quad (9.11)$$

we re-express (9.7) and (9.8) in the form

$$\sigma_{//}^* = \int \frac{1}{2} (Q_{\text{T}} + \cos 2\chi Q_{\text{P}}) d\phi \quad (9.12)$$

and

$$\sigma_{\perp}^* = \int \frac{1}{2} (Q_{\text{T}} - \cos 2\chi Q_{\text{P}}) d\phi \quad (9.13)$$

where

$$\cos 2\chi = 2 \cos^2 \chi - 1 \quad (9.14)$$

To carry out the azimuthal integration we must obtain  $\chi$  as a function of  $\phi$ , which we do by applying the cosine formula to the

triangle  $yBk$  in Figure 9.1, obtaining

$$\cos \chi = \frac{\cos \alpha - \cos \theta \cos \theta}{\sin \theta \sin \theta} \quad (9.15)$$

(We already have  $\theta$  as a function of  $\phi$  from (8.2)).

We now consider the contribution to the X-ray emission from electrons travelling in the opposite direction along the field line to those considered above. As in §8 we find it convenient to insert a phase difference of  $\pi$  between the azimuthal angles of the two electron distributions when performing the azimuthal integration. The configuration of the two electron velocity vectors is the same as in Figure 8.2 but in this case the angles  $\chi$  and  $\chi'$  are also defined.

As in §8 we have

$$\left. \begin{aligned} \phi' &= \phi + \pi \\ \alpha' &= \pi - \alpha \\ \theta' &= \pi - \theta \\ \chi' &= \pi + \chi \end{aligned} \right\} \quad (9.16)$$

and, in addition

$$\chi' = \pi + \chi$$

As we have already calculated the azimuth-integrated total cross-section (8.10) we need only evaluate the polarisation cross-section here. We define this as

$$Q_{SP} = (\sigma_{\parallel 1}^* + \sigma_{\perp 2}^*) - (\sigma_{\perp 1}^* + \sigma_{\parallel 2}^*) \quad (9.17)$$

where the subscripts 1 and 2 correspond to the two electron beams moving in opposite directions along the field line. Substituting in (9.17) from (9.12) and (9.13) we obtain

$$Q_{SP}(\epsilon, E, \theta, \alpha) = \int_0^{\phi} \cos 2\chi \left[ Q_P(\epsilon, \cos \theta, E) + \cos 2\chi' Q_P(\epsilon, \cos \theta', E) \right] d\phi \quad (9.18)$$

which becomes, using (9.16)

$$Q_{SP}(\epsilon, E, \theta, \alpha) = \int \cos 2\chi(\theta, \alpha, \phi) \times \left[ Q_P(\epsilon, \cos\theta(\theta, \alpha, \phi), E) + Q_P(\epsilon, -\cos\theta(\theta, \alpha, \phi), E) \right] d\phi \quad (9.19)$$

In order to evaluate the polarisation of X-ray emission from a specified point of the trap we integrate the polarisation cross-section (9.19) over the electron distribution. As this cross-section differs from the total cross-section (8.10) only in that it represents the difference rather than sum of the orthogonally polarised components, we see that substituting  $Q_{SP}$  for  $Q_{ST}$  in (8.13) immediately gives the required result. Thus the intensity difference per unit length of the trap between the parallel and perpendicular components is

$$P(\epsilon, \theta, \xi) = \frac{c}{4\pi} n_p(\xi) \int_{\alpha_{\min}}^{\alpha_{\max}(\xi)} \int_{\epsilon}^{\infty} \beta(E) \frac{g(E, \alpha_0)}{L(\alpha_0) \cos \alpha} \times Q_{SP}(\epsilon, E, \theta, \alpha) dE d\alpha_0 \quad (9.20)$$

The degree of polarisation of X-ray emission at the point on the trap defined by  $\xi$  is

$$p = P(\epsilon, \theta, \xi) / I(\epsilon, \theta, \xi) \quad (9.21)$$

where  $I(\epsilon, \theta, \xi)$  is given by (8.13) and positive  $p$  corresponds to the polarisation vector being directed along the magnetic field. As was the case with (8.13), (9.17) applies only in the right hand half of the trap ( $y > 0$ ).

To obtain the overall polarisation of X-ray emission from the trap we must integrate (9.20) along the field line defining the trap. This integration is more difficult to perform than the corresponding integration of the total cross-section (8.18) as the direction of polarisation, as well as its magnitude, is a function of position on the trap. In order to proceed we must define a reference direction

from which to measure the position of the plane of polarisation and the orientation of the magnetic field line seen in projection by the observer. We take the East-West direction to be the reference direction and measure angles from the West point as shown in Figure 9.2, where the angle  $\Psi$  gives the orientation of the magnetic field line and  $\phi$  defines the plane of polarisation. The lower part of Figure 9.2 represents a polar plot of intensity observed through a polariser at angle  $\phi$  to the reference direction, the intensity being given from (9.3) by

$$I_D(\phi) = I_{//} \cos^2(\phi - \Psi) + I_{\perp} \sin^2(\phi - \Psi) \quad (9.22)$$

where  $I_{//}$  and  $I_{\perp}$  are the intensity of the components of radiation polarised parallel and perpendicular to the field line. These are given by

$$I_{//} = \frac{1}{2} \left[ I(\epsilon, \theta, \mu) + P(\epsilon, \theta, \mu) \right] \quad (9.23)$$

and

$$I_{\perp} = \frac{1}{2} \left[ I(\epsilon, \theta, \mu) - P(\epsilon, \theta, \mu) \right] \quad (9.24)$$

where  $I(\epsilon, \theta, \mu)$  and  $P(\epsilon, \theta, \mu)$  are defined in (8.13) and (9.20) respectively.

Substituting from (9.23) and (9.24) and performing some trigonometric manipulation we can write (9.22) in the form

$$I_D(\phi) = \frac{1}{2} \left[ I + P \cos 2\Psi \cos 2\phi + P \sin 2\Psi \sin 2\phi \right] \quad (9.25)$$

In considering the directivity of X-ray emission we found that (Figure 8.3, Equation (8.18)) the emission from the corresponding point on the left half of the trap ( $y < 0$ ) could be found by substituting  $\theta_L$ , the angle between the direction of the observer and the magnetic field line on the left side of the trap, for  $\theta_R$  in (8.17). In dealing with the polarisation we must also take account of the fact that the angle between the observer's polariser and the direction of the magnetic field he sees in projection,  $\psi_L$ , is different from the corresponding angle  $\psi_R$  in the right half of the trap. Thus the sum of the contributions

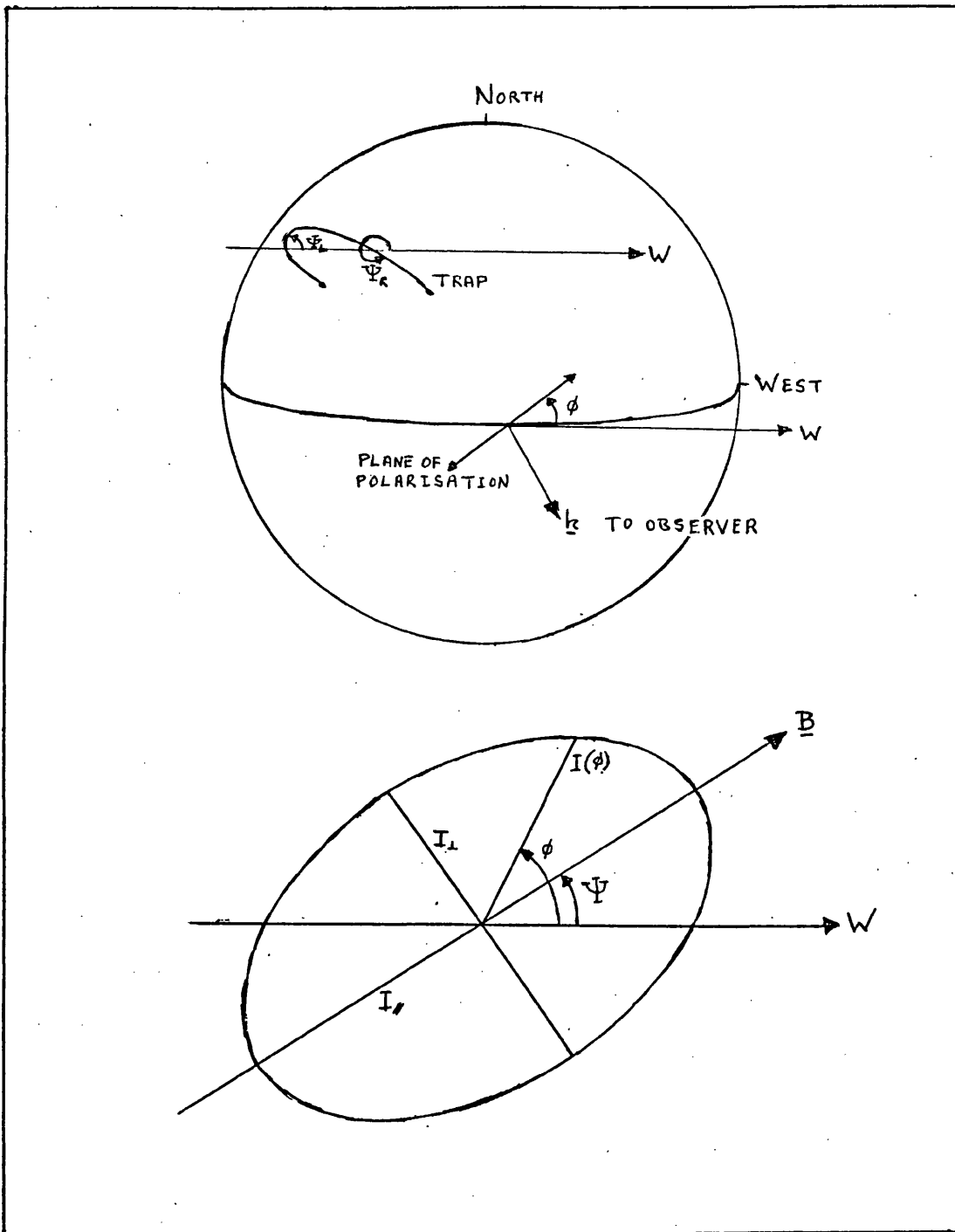


Figure 9.2 Definition of the angles  $\Psi$  and  $\phi$ , which give the magnetic field direction and plane of polarisation respectively, as seen by the observer. The West point is taken as the reference direction.

(9.25) from each half of the trap is

$$\begin{aligned}
 I_D(\phi) = \frac{1}{2} & \left[ (I(\epsilon, \theta_R, \xi) + I(\epsilon, \theta_L, \xi)) \right. \\
 & + (P(\epsilon, \theta_R, \xi) \cos 2\psi_R + P(\epsilon, \theta_L, \xi) \cos 2\psi_L) \cos 2\phi \\
 & \left. + (P(\epsilon, \theta_R, \xi) \sin 2\psi_R + P(\epsilon, \theta_L, \xi) \sin 2\psi_L) \sin 2\phi \right] \quad (9.26)
 \end{aligned}$$

Therefore we define

$$F_0(\epsilon) = \int_{\xi_0}^{\xi_1} [I(\epsilon, \theta_R, \xi) + I(\epsilon, \theta_L, \xi)] \frac{d\xi}{d\xi} d\xi, \quad (9.27)$$

$$F_1(\epsilon) = \int_{\xi_0}^{\xi_1} [P(\epsilon, \theta_R, \xi) \cos 2\psi_R + P(\epsilon, \theta_L, \xi) \cos 2\psi_L] \frac{d\xi}{d\xi} d\xi \quad (9.28)$$

and

$$F_2(\epsilon) = \int_{\xi_0}^{\xi_1} [P(\epsilon, \theta_R, \xi) \sin 2\psi_R + P(\epsilon, \theta_L, \xi) \sin 2\psi_L] \frac{d\xi}{d\xi} d\xi \quad (9.29)$$

so that

$$I_D(\phi) = \frac{1}{2} (F_0 + F_1 \cos 2\phi + F_2 \sin 2\phi) \quad (9.30)$$

Note that in (9.27) and (9.29)  $\theta_R$ ,  $\theta_L$ ,  $\psi_R$  and  $\psi_L$  are functions of position on the trap. It should also be borne in mind that  $I_D(\phi)$  given by (9.30) is a function of photon energy and also depends on the position of the trap on the solar disc. We also note that  $F_0$  given by (9.27) is identical to the total intensity  $I_T(\epsilon, A, B)$  defined in (8.18). It is clear from (9.30) that this is the case since the total intensity is equal to  $I_D(\phi) + I_D(\phi + \pi/2)$ , which is just  $F_0$ .

To find the orientation of the plane of polarisation we differentiate (9.30) with respect to  $\phi$  and set the result equal to zero, which gives

$$\tan 2\phi_0 = F_2/F_1 \quad (9.31)$$

The direction defined by  $\phi_0$  ( $-\pi/4 < \phi_0 < \pi/4$ ) may be a maximum or minimum

of intensity. Substituting from (9.31) into (9.30) we obtain

$$I_D(\phi) = \frac{1}{2} \left[ F_0 + \frac{F_1}{\cos 2\phi_0} \cos 2(\phi - \phi_0) \right] \quad (9.32)$$

Since

$$|\cos \phi| = (1 + \tan^2 \phi)^{-\frac{1}{2}} \quad (9.33)$$

and  $\cos 2\phi_0 \geq 0$  since  $-\pi/4 < \phi_0 \leq \pi/4$  we have, from (9.31)

$$\cos 2\phi_0 = (1 + (F_2/F_1)^2)^{-\frac{1}{2}} \quad (9.34)$$

which, substituted in (9.32) gives

$$I_D(\phi) = \frac{1}{2} \left[ F_0 + \text{sign}(F_1) (F_1^2 + F_2^2)^{\frac{1}{2}} \cos 2(\phi - \phi_0) \right] \quad (9.35)$$

From this equation we see that the orientation of the plane of polarisation is defined by  $\phi_0$  if  $F_1 > 0$  and by  $\phi_0 + \pi/2$  if  $F_1 < 0$ .

If we define  $\phi_0$  by

$$\left. \begin{aligned} \sin 2\phi_0 &= F_2 / (F_1^2 + F_2^2)^{\frac{1}{2}} \\ \cos 2\phi_0 &= F_1 / (F_1^2 + F_2^2)^{\frac{1}{2}} \end{aligned} \right\} \quad (9.36)$$

instead of (9.31),  $\phi_0$  always gives the direction of maximum intensity.

Then (9.35) can be written

$$I_D(\phi) = \frac{1}{2} \left[ F_0 + (F_1^2 + F_2^2)^{\frac{1}{2}} \cos 2(\phi - \phi_0) \right] \quad (9.37)$$

Evaluating (9.37) for  $\phi = \phi_0$  and  $\phi = \phi_0 + \pi/2$ , we obtain the degree of polarisation,

$$p = \frac{(F_1^2 + F_2^2)^{\frac{1}{2}}}{F_0} \quad (9.38)$$

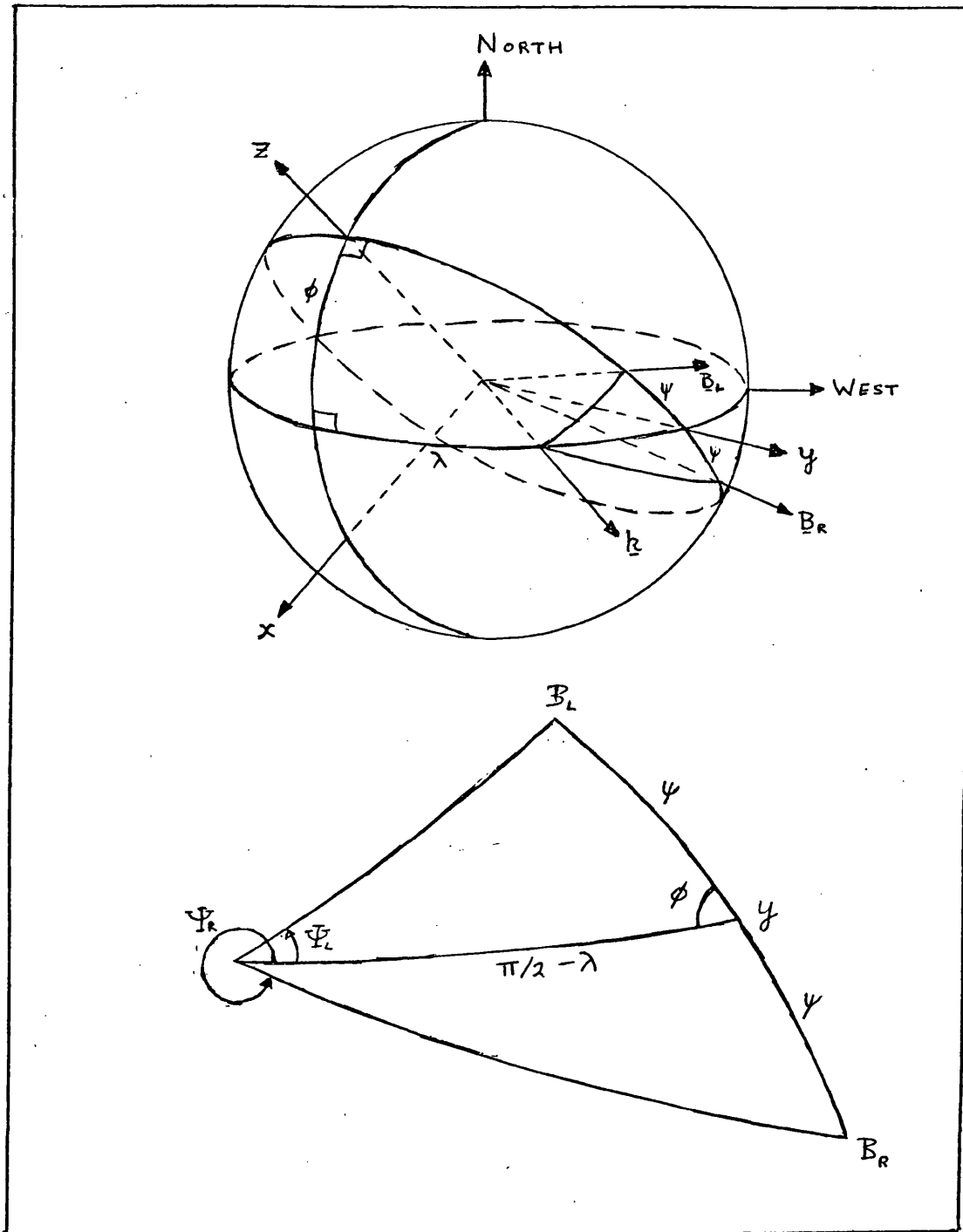


Figure 9.3 Relationship of the angles  $\psi_L$  and  $\psi_R$  to the position of the trap on the solar surface, defined by  $(\lambda, \phi)$  and the field direction, given by  $\psi$ , at the point  $\xi$  on the trap.

The remaining task to be performed in this analysis is the evaluation of the angles  $\Psi_R$  and  $\Psi_L$ . The geometry defined in Figure 9.2 is shown in more detail and related to the angles  $\lambda$ ,  $\phi$  and  $\psi$  in Figure 9.3. Applying the 4 parts formula to the spherical triangles  $k B_R y$  and  $k B_L y$  in Figure 9.3, we obtain

$$\tan \Psi_R = \frac{\sin \phi \sin \psi}{-\cos \lambda \cos \psi - \sin \lambda \sin \psi \cos \phi} \quad (9.39)$$

and

$$\tan \Psi_L = \frac{\sin \phi \sin \psi}{\cos \lambda \cos \psi - \sin \lambda \sin \psi \cos \phi} \quad (9.40)$$

The fact that  $\Psi_R$  and  $\Psi_L$  can take all values in  $[0, 2\pi]$ , but are only defined to a factor of  $\pi$  by (9.39) and (9.40), is not important. We use only  $2\Psi_R$  and  $2\Psi_L$  in (9.28) and (9.29) and these are completely defined.

## 10. THE MODEL ATMOSPHERE

So far we have not discussed the form of the atmospheric density structure. As little is known about coronal densities in flaring regions, we have adopted the quiet atmosphere model of Reimers (1972), illustrated in Figure 10.1. It is believed that the major difference between a flaring and non-flaring atmosphere is that the density is a few times higher during a flare. Provided that the density is not so high as to drastically reduce the lifetime of high energy electrons, its value is not too important as it serves only to determine the magnitude of the X-ray flux from the trap. We are more concerned with the density scale height which, as discussed in §1, influences the relative strengths of emission from the top of the trap and from near the mirror points, and so can change the overall directivity and polarisation of X-ray emission from the trap.

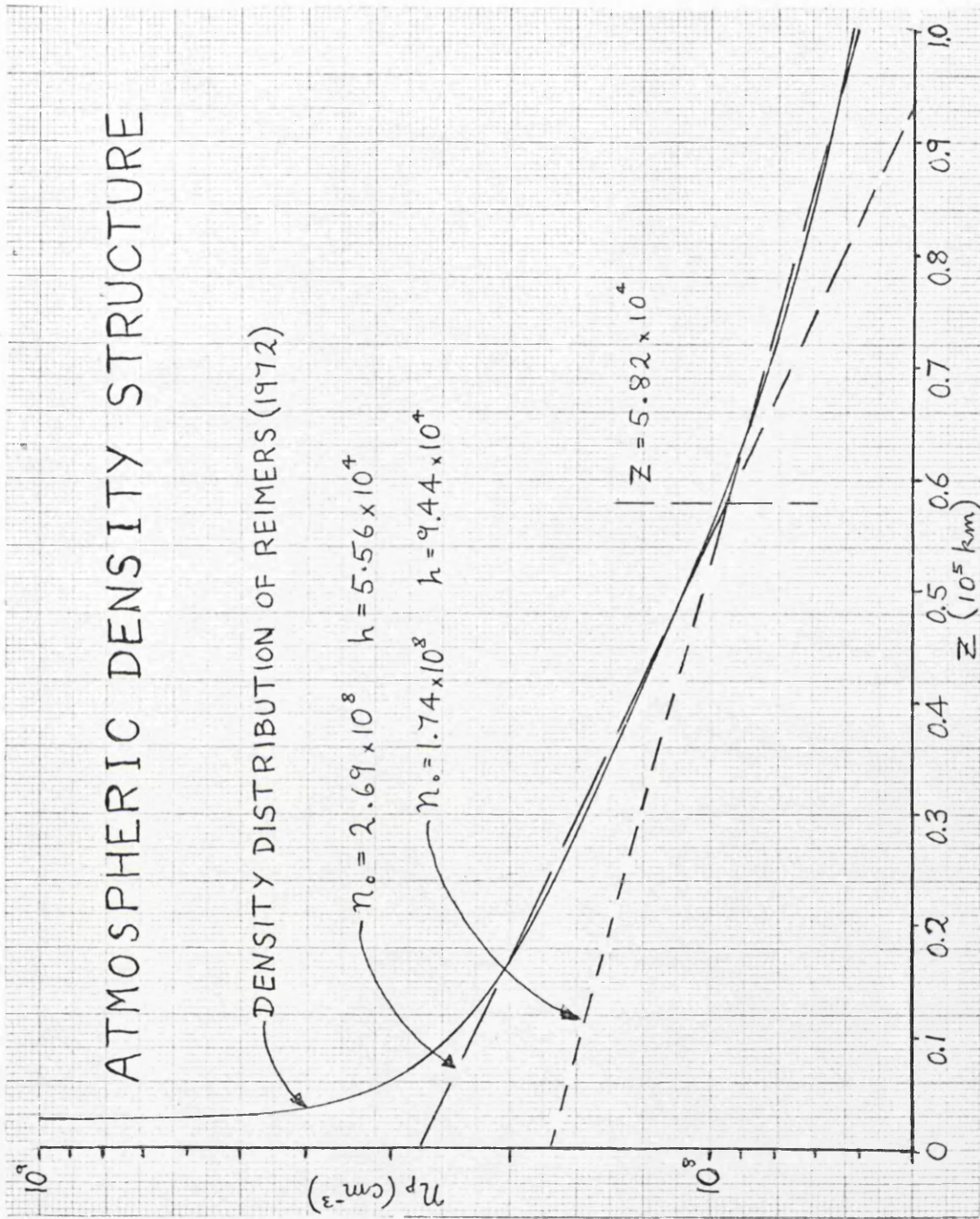


Figure 10.1

The quiet atmosphere density structure derived by Reimers (1972) and the two isothermal atmosphere approximations to it which we use in our computations.

Although data on the flaring corona is scarce, a few analyses of active region atmospheres have been carried out. Christiansen *et al.* (1960) found the density to be enhanced by a factor of 3 over normal coronal densities while the scale height remained the same as in the quiet atmosphere. Similar results have been obtained by Boardman & Billings (1969) and Stewart (1973). Therefore we have some grounds for assuming that the density scale height in a flaring region will not be too different from that of the quiet corona.

For computational purposes we have represented the quiet atmosphere model of Reimers (1972) by

$$n_p(z) = n_o e^{-z/h} \quad (10.1)$$

where

$$n_o = 2.69 \times 10^8 \text{ cm}^{-3}; \quad h = 5.56 \times 10^4 \text{ km for } z < 5.82 \times 10^4 \text{ km} \quad (10.2)$$

and

$$n_o = 1.74 \times 10^8 \text{ cm}^{-3}; \quad h = 9.44 \times 10^4 \text{ km for } z > 5.82 \times 10^4 \text{ km} \quad (10.3)$$

This representation, shown in Figure 10.1, is accurate to a few percent in the range  $10^4 \text{ km} < z < 10^5 \text{ km}$ .

Even if the ambient density structure in the trap is similar to that of the quiet corona, the injection of a large number of fast particles into the trap may alter this situation considerably. In Chapter II we pointed out that in a large flare the number density of high energy electrons in the trap must be comparable with the ambient density, and that their pressure may be considerably greater than the ambient pressure. In that situation it makes no sense to consider the particle distribution in the trap to consist of two components, ambient and injected. The ambient particles will be strongly affected by injected component and the pre-flare density structure will lose its significance. For the present, however, we assume that this does not happen.

## 11. SUMMARY OF ANALYSIS AND COMPUTATIONAL PROCEDURE

In this section we give the final formulation of the equations describing the characteristics of X-ray emission from the trap. First of all we define a set of parameters which are more convenient to use than the set  $I$ ,  $P$ ,  $F_0$ ,  $F_1$ , and  $F_2$  derived in §8 and §9 which are in a mixed system of units, due to the fact that the bremsstrahlung cross-sections (Chapter II) are in millibarns/keV and the functions  $L(\alpha_0)$  (57) and  $dI/d\mu$  (§3) in scaled units. We then derive relationships between the new set of parameters  $I_0$ ,  $P_0$ ,  $f_0$ ,  $f_1$  and  $f_2$  and the quantities used in presenting the results. In the case of X-ray emission from a specified point on the trap, differential with respect to trap length, we give the photon flux at the Earth from a length of the trap corresponding to 1 arc second at the Earth, that is  $\sim 725$  km. Predicted photon fluxes at the Earth are given when the X-ray emission from the whole trap is considered. Finally we consider each of the electron distribution functions introduced in §1 and describe some of the methods and techniques required to evaluate the integrals numerically.

In place of the functions  $I$  and  $P$  given by (8.13) and (9.20) we define

$$\left. \begin{array}{l} I_0 \\ P_0 \end{array} \right\} (\epsilon, \xi, \lambda, \phi) = n_8(\mu) \int_{\alpha_{\min}}^{\alpha_{\max}(\xi)} \int_{\epsilon}^{\infty} \beta(E) \frac{g_{39}(E, \alpha_0)}{L(\alpha_0) \cos \alpha} \times$$

$$\left. \begin{array}{l} \{Q_{ST}\} \\ \{Q_{SP}\} \end{array} \right\} (\epsilon, E, \theta, \alpha) dE d\alpha_0 \quad \left\{ \begin{array}{l} (11.1) \\ (11.2) \end{array} \right.$$

where  $n_8(\mu)$  is the proton density in units of  $10^8 \text{ cm}^{-3}$ ;  $\beta(E)$  is the velocity of an electron of kinetic energy  $E$  divided by the speed of light and is given by

$$\beta(E) = \frac{(E^2 + 2 m_e c^2 E)^{1/2}}{E + m_e c^2} \quad (11.3)$$

where  $m_e$  is the electron rest mass;

$g_{39}(E, \alpha_0)$  is the electron distribution function and is equal to the number of electrons in units of  $10^{39}$  injected into the trap with energy (in keV) in unit range about  $E$  and initial pitch angle in unit range about  $\alpha_0$ ;  $L(\alpha_0)$ , given by (7.15), is the distance in scaled units covered by an electron of initial pitch angle  $\alpha_0$  in travelling from one mirror point to the other;  $\cos \alpha$  is obtained from

$$\cos \alpha = (1 - \sin^2 \alpha)^{\frac{1}{2}} \quad (11.4)$$

where  $\sin \alpha(\xi, \alpha_0)$  is given by (7.1);

the cross-sections  $Q_{ST}$  and  $Q_{SP}$  are defined in (8.10) and (9.19) respectively and their dependence on position on the trap is given by (9.15), (8.2), (8.19), (8.22 and (8.23);  $\alpha_{\max}(\xi)$  is the largest initial pitch angle an electron can have without being reflected before reaching the point specified by  $\xi$  and  $\alpha_{\min}$  is the smallest initial pitch an electron can have without penetrating to the dense chromosphere and decaying rapidly there.

The X-ray flux at the Earth from an arc second length of the trap is given by

$$\mathcal{F}_0 = \frac{c}{4\pi} \times \frac{10^8 \times 10^{39} \times 10^{-27}}{D/2} \frac{1}{4\pi R^2} \frac{R}{206265} I_0 \quad (11.5)$$

where  $c$  is the speed of light =  $3 \times 10^{10} \text{ cm sec}^{-1}$ , the factors of  $10^8$  and  $10^{39}$  are respectively the normalisation factors for proton density and fast electron numbers,  $10^{-27}$  is the conversion factor  $\text{cm}^2/\text{millibarn}$ ,  $D/2 = 5 \times 10^9 \text{ cm}$  is the unit of scaled length,  $R = 1.4996 \times 10^{13} \text{ cm}$  is the astronomical unit and 206265 is the number of arc seconds in one radian. On evaluating (11.5), we find

$$\mathcal{F}_0(\epsilon, \xi, \lambda, \phi) = 1.23 I_0 \text{ photon cm}^{-2} \text{ sec}^{-1} \text{ keV}^{-1} \text{ arcsec}^{-1} \quad (11.6)$$

Note that this is the flux per arc second length of the trap and not the flux which would be observed by an instrument with a one arc second

field of view seeing the trap in projection. The polarisation is given by an expression of the same form as (9.21)

$$p = P_o/I_o \quad (11.7)$$

the polarisation vector lying parallel to the magnetic field if  $p$  is positive and perpendicular to it if  $p$  is negative.

The characteristics of X-ray emission from the trap as a whole are defined by expressions involving  $I_o$  and  $P_o$  analogous to (9.27), (9.28) and (9.29). We write

$$f_o = \int_{\xi_0}^{\xi_1} \left[ I_o(\epsilon, \theta_R, \xi) + I_o(\epsilon, \theta_L, \xi) \right] \frac{d\ell}{d\xi} d\xi \quad (11.8)$$

$$\left. \begin{array}{l} f_1 \\ f_2 \end{array} \right\} = \int_{\xi_0}^{\xi_1} \left[ P_o(\epsilon, \theta_R, \xi) \begin{Bmatrix} \cos \\ \sin \end{Bmatrix} 2 \Psi_R + P_o(\epsilon, \theta_L, \xi) \begin{Bmatrix} \cos \\ \sin \end{Bmatrix} 2 \Psi_L \right] \frac{d\ell}{d\xi} d\xi \quad \begin{array}{l} (11.9) \\ (11.10) \end{array}$$

In addition to the subsidiary equations giving the directional dependence of the cross-sections mentioned above we require also (8.20) which defines  $\theta_L$  as a function of position and (9.36), (9.40) which give  $\Psi_R$  and  $\Psi_L$ .

In this case the X-ray flux at the Earth is given

$$\mathcal{F}_1 = \frac{c}{4\pi} \times 10^8 \times 10^{39} \times 10^{-27} \frac{1}{4\pi R} f_o \quad (11.11)$$

The factor  $D/2$  which appeared in (11.5) does not appear here as the term  $d\ell/d\xi$ , like  $L(\alpha_o)$ , is in scaled units. Evaluating (11.11) we obtain

$$\mathcal{F}_1(\epsilon, \lambda, \phi) = 84.9 f_o \text{ photon cm}^{-2} \text{sec}^{-1} \text{keV}^{-1} \quad (11.12)$$

In analogy with (9.38) and (9.36), the polarisation is given by

$$p = (f_1^2 + f_2^2)^{1/2} / f_0 \quad (11.13)$$

and the orientation of the plane of polarisation by

$$\left\{ \begin{array}{l} \sin \\ \cos \end{array} \right\} 2\phi_0 = \left\{ \begin{array}{l} f_2 \\ f_1 \end{array} \right\} / (f_1^2 + f_2^2)^{1/2} \quad (11.14)$$

where  $\phi_0$  is the angle between the polarisation vector and the East-West direction, measured anti-clockwise from the West point.

We now consider in more detail the electron distribution functions discussed in §1. The first distribution, which is singular in both energy and pitch angle, can be represented by

$$g_{39}(E, \alpha_0) = N_{39} \delta(E - E_0) \delta(\alpha_0 - \alpha_{00}) \quad (11.15)$$

where  $N_{39}$  is the total number (in units of  $10^{39}$ ) of injected non-thermal electrons,  $E_0$  and  $\alpha_{00}$  are the energy and pitch angle common to all electrons, and  $\delta(x)$  is the Dirac delta function. Substituting (11.15) in (11.1) and (11.2) and carrying out the integrations we obtain

$$\left. \begin{array}{l} I_0 \\ P_0 \end{array} \right\} (\epsilon, \theta, \xi) = \frac{N_{39} n_8(\xi) \beta(E_0)}{L(\alpha_{00}) \cos \alpha(\xi, \alpha_{00})} \left\{ \begin{array}{l} Q_{ST} \\ Q_{SP} \end{array} \right\} (\epsilon, E_0, \theta, \alpha) \quad \begin{array}{l} (11.16) \\ (11.17) \end{array}$$

These equations hold if  $\epsilon < E_0$  and  $\alpha_{\min} < \alpha_{00} < \alpha_{\max}(\xi)$ , otherwise the integrals are zero. We note that due to the presence of  $\cos \alpha$  in the denominator these functions are singular at the mirror point. Near the mirror point we can expand (11.4) in the form

$$\cos \alpha \approx \left[ \left( \frac{1}{B} \frac{dB}{d\ell} \right)_{\xi_m} \delta \ell \right]^{1/2} \quad (11.18)$$

where  $\delta l$  is distance along the field line from the mirror point. Thus the asymptotic forms of  $I_0$  and  $P_0$  are

$$\left. \begin{array}{l} I_0 \\ P_0 \end{array} \right\} = \frac{N_{39} n_8 (\xi_m) \beta(E_0)}{L(\alpha_{00}) \left( \frac{1}{B} \frac{dB}{d\ell} \right)^{\frac{1}{2}} \xi_m} \left\{ \begin{array}{l} Q_{ST} \\ Q_{SP} \end{array} \right\} (\epsilon, E_0, \theta, \alpha) \delta l^{-\frac{1}{2}} \quad \left\{ \begin{array}{l} (11.19) \\ (11.20) \end{array} \right.$$

Considering now the total emission from the trap, we evaluate  $f_0$ ,  $f_1$  and  $f_2$  by substituting (11.16) and (11.17) in (11.8), (11.9) and (11.10). As noted above,  $I_0$  and  $P_0$  are zero if  $\xi < \xi_m$  since there are no electrons beyond the mirror points, therefore the upper limit of integration in (11.8) - (11.10) can be taken to be  $\xi_m$ . A difficulty in the integration of these equations, along the trap, which also occurs in the integration of (7.15) to obtain  $L(\alpha_0)$ , is that  $\cos \alpha$  appears in the denominator of all these integrals. As shown by (11.18) this results in a singularity of the form  $\delta l^{-\frac{1}{2}}$ , or equivalently  $(\xi_m - \xi)^{-\frac{1}{2}}$ , at the mirror point. In order to perform these integrals numerically, we change the variable of integration to  $x$ , where

$$\cos x = \frac{\xi - \xi_0}{\xi_m - \xi_0} \quad (11.21)$$

Differentiating (11.21), we find that

$$\frac{d\xi}{dx} = - (\xi_m - \xi_0) \sin x \quad (11.22)$$

which can be written in the form

$$\frac{d\xi}{dx} = - [(\xi_m - 2\xi_0 + \xi)(\xi_m - \xi)]^{\frac{1}{2}} \quad (11.23)$$

from which it is clear that the factor  $(\xi_m - \xi)^{\frac{1}{2}}$  removes the singularity from the integrand.

We consider now the second electron distribution, which may be represented by

$$g_{39}(E, \alpha_0) = \frac{N_{39}(\delta-1)}{E_0} \left(\frac{E}{E_0}\right)^{-\delta} \delta(\alpha_0 - \alpha_{00}) \quad (11.24)$$

where  $N_{39}$  is the number of non-thermal electrons (in units of  $10^{39}$ ) with energy greater than  $E_0$ ,  $\delta$  is the spectral index of the power law energy distribution,  $\delta(x)$  is the Dirac delta function, and  $\alpha_{00}$  is the initial pitch angle which all the electrons have. In this case (11.1) and (11.2) can be written

$$\frac{I_{P_0}}{P_0}(\epsilon, \xi, \lambda, \phi) = \frac{N_{39}(\delta-1) n_B(\xi)}{E_0 L(\alpha_{00}) \cos \alpha(\xi, \alpha_{00})} \times \int_{\epsilon}^{\infty} \beta(E) \left(\frac{E}{E_0}\right)^{-\delta} \left\{ \begin{array}{l} Q_{ST} \\ Q_{SP} \end{array} \right\}(\epsilon, E, \theta, \alpha) dE \quad \begin{array}{l} (11.25) \\ (11.26) \end{array}$$

Since  $\beta(E)$  is of order unity and the cross-sections are slowly varying functions of electron energy except near the high energy cutoff (see Chapter II) the form of the integrand is determined mainly by the electron energy spectrum, which changes rapidly. In order to extract this rapid variation from the integral we change the variable of integration to

$$x = (E/\epsilon)^{-(\delta-1)} \quad (11.27)$$

which, on differentiation, yields

$$\frac{dE}{dx} = - \frac{\epsilon}{\delta-1} \left(\frac{E}{\epsilon}\right)^{\delta} \quad (11.28)$$

In order to integrate (11.25) and (11.26) numerically we must replace the upper limit of the integral by a finite value, which we denote by  $E_1$ . Using (11.27) and (11.28), (11.25) and (11.26) become

$$\left. \begin{matrix} I_o \\ P_o \end{matrix} \right\} (\epsilon, \xi, \lambda, \phi) = \frac{N_{39} n_8(\xi)}{L(\alpha_{oo}) \cos \alpha (\xi, \alpha_{oo})} \left( \frac{\epsilon}{E_o} \right)^{-(\delta-1)}$$

$$\int_{\left(\frac{\epsilon}{E_1}\right)^{\delta-1}}^1 \beta(E) \left\{ \begin{matrix} Q_{ST} \\ Q_{SP} \end{matrix} \right\} (\epsilon, E, \theta, \alpha) dx \quad (11.29)$$

where

$$E = \epsilon/x^{1/(\delta-1)} \quad (11.31)$$

Note that if a high value of  $E_1$  were used in a direct numerical integration of (11.25) and (11.26) a large number of subdivisions of the interval  $(\epsilon, E_1)$  would be required in order to achieve a sufficient density of points in the most important part of the energy distribution, that is, for  $\epsilon < E \lesssim 3\epsilon$ . In practice  $E_1$  would have to be treated as a function of  $\epsilon$ . But in the formulation (11.29-30) the density of points in E-space is higher at lower energies (for fixed increments in  $x$ ) and almost independent of  $E_1$ , so we may choose the lower limit of integration  $(\epsilon/E_1)^{\delta-1}$  to be as small as we like (but not zero) so that the magnitude of  $E_1$  is limited only by the capacity of the computer.

The functions  $f_o$ ,  $f_1$  and  $f_2$  describing the overall X-ray emission from the trap are evaluated in a similar fashion to those of the first electron distribution, again using the change of variable (10.24) and integrating only as far as the mirror point.

The third electron distribution function can be represented by

$$g_{39}(E, \alpha_o) = \frac{N_{39}(\delta-1)}{\frac{1}{2}B\left(\frac{1}{2}, \frac{n+1}{2}\right)E_o} \left( \frac{E}{E_o} \right)^{-\delta} \left\{ \begin{matrix} \sin \\ \cos \end{matrix} \right\}^n \alpha_o \quad (11.32)$$

where  $B(x,y)$  is the beta function and the other symbols are as defined in (11.23). Applying the transformation (11.27), (11.25) and (11.26) become

$$\begin{aligned}
 \left. \begin{array}{l} I_0 \\ P_0 \end{array} \right\} (\epsilon, \xi, \lambda, \phi) &= \frac{N_{39} n_8(\xi)}{\frac{1}{2} B\left(\frac{1}{2}, \frac{n+1}{2}\right)} \left(\frac{\epsilon}{E_0}\right)^{-(\delta-1)} \int_{\alpha_{\min}}^{\alpha_{\max}(\xi)} \frac{\{\sin\}^n \alpha_0}{L(\alpha_0) \cos \alpha(\xi, \alpha_0)} \times \\
 &\int_{\left(\frac{\epsilon}{E_1}\right)^{\delta-1}}^1 \beta(E) \left\{ \begin{array}{l} Q_{ST} \\ Q_{SP} \end{array} \right\} (\epsilon, E, \theta, \alpha) dx d\alpha_0 \quad \left. \begin{array}{l} (11.33) \\ (11.34) \end{array} \right\}
 \end{aligned}$$

The total X-ray emission from the trap is evaluated as before, in this case the upper limit of the integrals along the trap is set equal to the value of  $\xi$  corresponding to the mirror points of electrons of initial pitch angle  $\alpha_{\min}$ .

Finally, we consider electron distribution function (iv). We take the particular form of relationship appropriate to acceleration by an electric field discussed in §1, that is

$$\sin \alpha_0 = (E^*/E)^{\frac{1}{2}} \quad (11.35)$$

where  $E^*$  is a parameter, roughly identified with the thermal energy of an electron prior to acceleration. The distribution can then be written.

$$g_{39}(E_1, \alpha_0) = \frac{N_{39}(\delta-1)}{E_0} \left(\frac{E}{E_0}\right)^{-\delta} \delta(\alpha_0 - \sin^{-1}(E^*/E)^{\frac{1}{2}}) \quad (11.36)$$

The equations for  $I_0$  and  $P_0$  in this case are

$$\begin{aligned}
 \left. \begin{array}{l} I_0 \\ P_0 \end{array} \right\} (\epsilon, \xi, \lambda, \phi) &= N_{39} n_8(\xi) \left(\frac{\epsilon}{E_0}\right)^{-(\delta-1)} \times \\
 &\int_{x_0}^{x_1} \frac{\beta(E) \left\{ \begin{array}{l} Q_{ST} \\ Q_{SP} \end{array} \right\} (\epsilon, E, \theta, \alpha)}{L(\alpha_0) \cos \alpha(\xi, \alpha_0)} dx \quad \left. \begin{array}{l} (11.37) \\ (11.38) \end{array} \right\}
 \end{aligned}$$

where

$$E = \epsilon/x^{1/(\delta-1)} \quad (11.31)$$

and

$$\alpha_0 = \sin^{-1}(E^*/E)^{\frac{1}{2}} \quad (11.39)$$

Previously we had  $x_0 = (\epsilon/E_1)^{\delta-1}$  and  $x_1 = 1$ , but in this case we have the additional requirement

$$\alpha_{\min} < \alpha_0(E) < \alpha_{\max}(\xi) \quad (11.40)$$

that is

$$\sin^2 \alpha_{\min} < E^*/E < \sin^2 \alpha_{\max}(\xi) \quad (11.41)$$

or

$$\left( \frac{\epsilon}{E^*} \sin^2 \alpha_{\min} \right)^{\delta-1} < x < \left( \frac{\epsilon}{E^*} \sin^2 \alpha_{\max}(\xi) \right)^{\delta-1} \quad (11.42)$$

As the lower limit in (11.42) is greater than  $(\epsilon/E_1)^{\delta-1}$ , which can be as small as we like, we can take

$$x_0 = \left( \frac{\epsilon}{E^*} \sin^2 \alpha_{\min} \right)^{\delta-1} \quad (11.43)$$

For the upper limit, we must take

$$x_1 = \min \left( 1, \left( \frac{\epsilon}{E^*} \sin^2 \alpha_{\max}(\xi) \right)^{\delta-1} \right) \quad (11.44)$$

This states that the lower limit of integration is the photon energy or the energy of an electron mirroring at the point  $\xi$ , whichever is greater.

The results presented for behind-the-limb bursts are obtained simply by cutting off the integrals over trap length at the point  $\xi_{\min}$  corresponding to the minimum height  $z_{\min}$  visible at the trap position. This is given by

$$z_{\min} = R_{\odot} (\operatorname{cosec} \theta - 1) \quad (11.45)$$

where  $R_{\odot}$  is the radius of the sun and  $\theta$  is the heliocentric distance, given by

$$\cos \theta = \cos \lambda \cos \phi \quad (11.46)$$

We have ignored the fact that the visible portion of the limb of the trap nearer to the solar limb is greater than that of the more distant limb. Although this may lead to inaccurate polarisation values, the X-ray fluxes deduced should not be too dissimilar from those which would be obtained by taking this effect into account.

Finally we specify values for some of the parameters defined in this analysis. We have studied the hard X-ray emission from traps of height  $5 \times 10^4$  km and  $10^5$  km, taking  $N_{39}$ , the number of non-thermal electrons injected into the trap, to be unity. When the electron energy distribution is a power law  $N_{39}$  represents the number of electrons with energy greater than  $E_0$ , which we take to be 25 keV. These values are representative of a large flare. It is difficult to justify the choice of a specific value for the parameter  $\alpha_{\min}$ , which we have defined as the smallest initial pitch angle of any trapped electron. Electrons of smaller pitch angle are assumed to have penetrated down to the dense chromosphere where they were scattered out of the trap. Obviously the transition from trapping to precipitation occurs over a range of pitch angle and depends on the detailed structure of density and magnetic field in the chromosphere and lower corona. As the height of the transition region is small compared to the dimensions of the trap and, more importantly, the magnetic field close to the sunspot is not well represented by our model fields, we can only make inspired guesses at the value of  $\alpha_{\min}$ . We take  $\alpha_{\min}$  to correspond to a mirror height of  $5 \times 10^3$  km above the photosphere.

CHAPTER IVTHE ELECTRON TRAP MODEL - DIRECTIVITY  
AND POLARISATION OF X-RAY EMISSION1. INTRODUCTION

In this chapter results obtained from the analysis described in Chapter III are presented. We are concerned here with total hard X-ray emission from the trap; the spatial distribution of emission will be discussed in Chapter V.

In §2 we present results obtained for electron distribution (i) which is singular in electron energy and pitch angle. This enables some insight to be gained into the importance of trap geometry. That is, we investigate the sensitivity of the directivity and polarisation to the magnetic field model and to the density structure of the corona.

In §3 we study the characteristics of distribution (i) in more detail. As mentioned in Chapter III, the characteristics of X-ray emission from more complicated electron distribution functions can be expressed in terms of a linear combination of the parameters describing emission from simpler distributions. Therefore we can draw some conclusions from study of the results of this section as to the trends to be expected when X-ray emission from more complex electron distributions are considered.

Characteristics of the radiation produced by electrons with the energy and pitch angle distributions (ii), (iii), and (iv), as defined in §11 of Chapter III, are discussed in §4, 5 and 6 respectively. Finally, a summary and discussion of the results obtained is given in §7 and a brief comparison with observational data made in §8.

## 2. PRELIMINARY INVESTIGATIONS

First of all, we examine the dependence of the emission characteristics on magnetic field structure. Electron distribution (i) (equation III (11.15)), which is singular in energy and pitch angle, is used here. We take the electron energy to be 100 Kev and look at two initial pitch angles,  $30^\circ$  and  $60^\circ$ . The photon flux and polarisation are calculated at photon energies of 30 Kev and 80 Kev. Results obtained using each of the three field models discussed in Chapter III are compared.

In addition to studying different field configurations, we investigate the dependence of emission characteristics on trap height. Not only does the rate of field convergence in the limbs of the trap depend on trap height, but the ratio of vertical distance travelled by an electron of given pitch angle to the density scale height of the atmosphere is changed. Therefore the directivity and polarisation of emission has been calculated for a range of trap heights, from  $5 \times 10^4$  km to  $10^5$  km.

For the purpose of these investigations we take the trap to lie on the equator as the polarisation vector always lies in the North-South or East-West direction in this case, and so the predicted polarisations for each field model may be plotted together and compared easily.

Photon fluxes and polarisations as a function of solar longitude for a trap height of  $10^5$  km shown in Figures 2.1 - 2.4. Here we have used Reimers' (1971) model atmosphere, defined by equation III (10.1-3). In these figures the curves marked D, L and M illustrate the results obtained using the dipole, linecharges and monopoles fields respectively. Positive values of polarisation indicate that the plane of polarisation lies in the East-West direction, while negative values correspond to North-South polarisation.

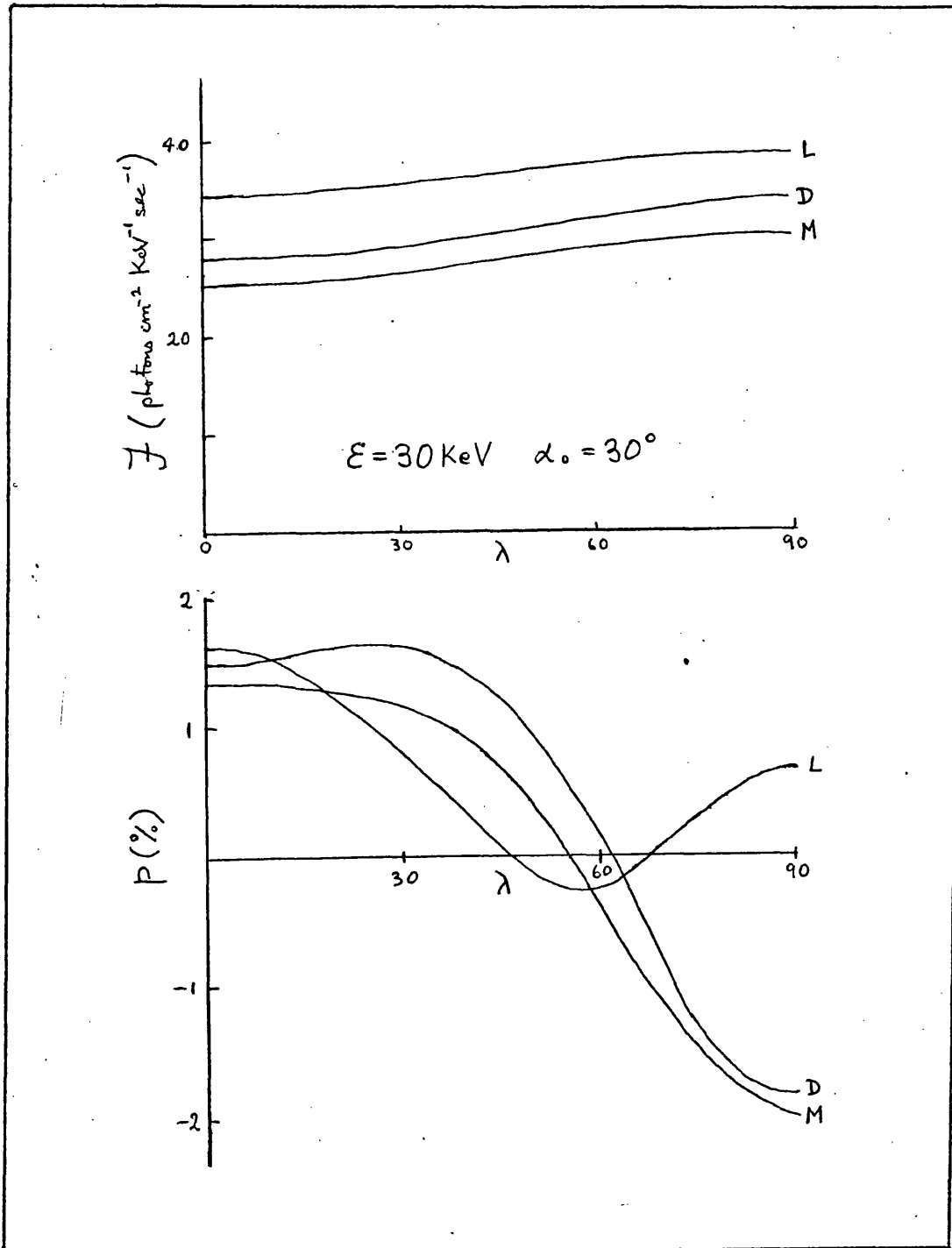


Figure 2.1 Directivity and polarisation of 30 KeV photons emitted by 100 KeV trapped electrons of  $30^\circ$  initial pitch angle, for dipole, linecharges and monopoles traps of height  $10^5 \text{ km}$  on the equator.

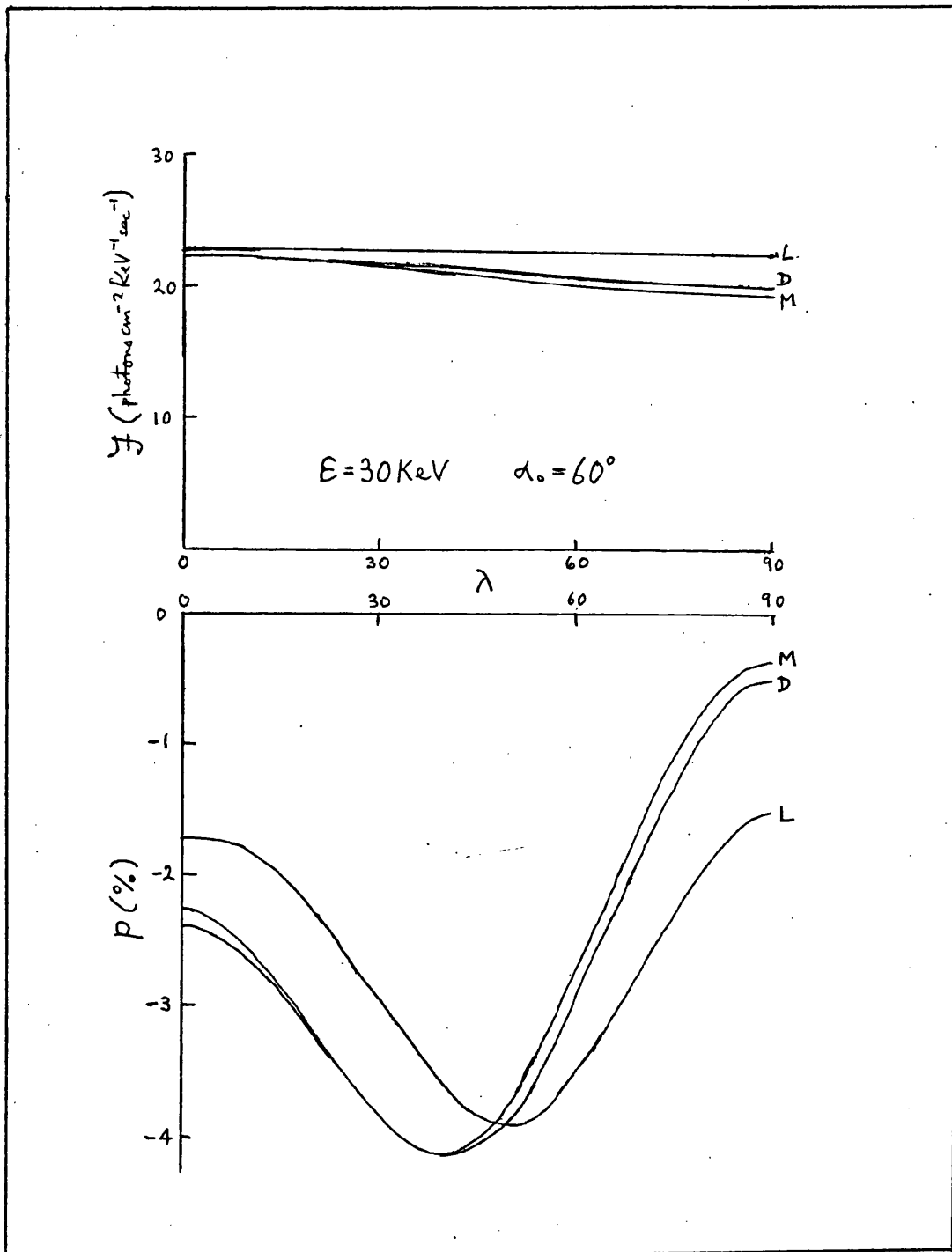


Figure 2.2 Directivity and polarisation of 30 KeV photons emitted by 100 KeV trapped electrons of  $60^\circ$  initial pitch angle, for dipole, linecharges and monopoles traps of height  $10^5$  km on the equator.

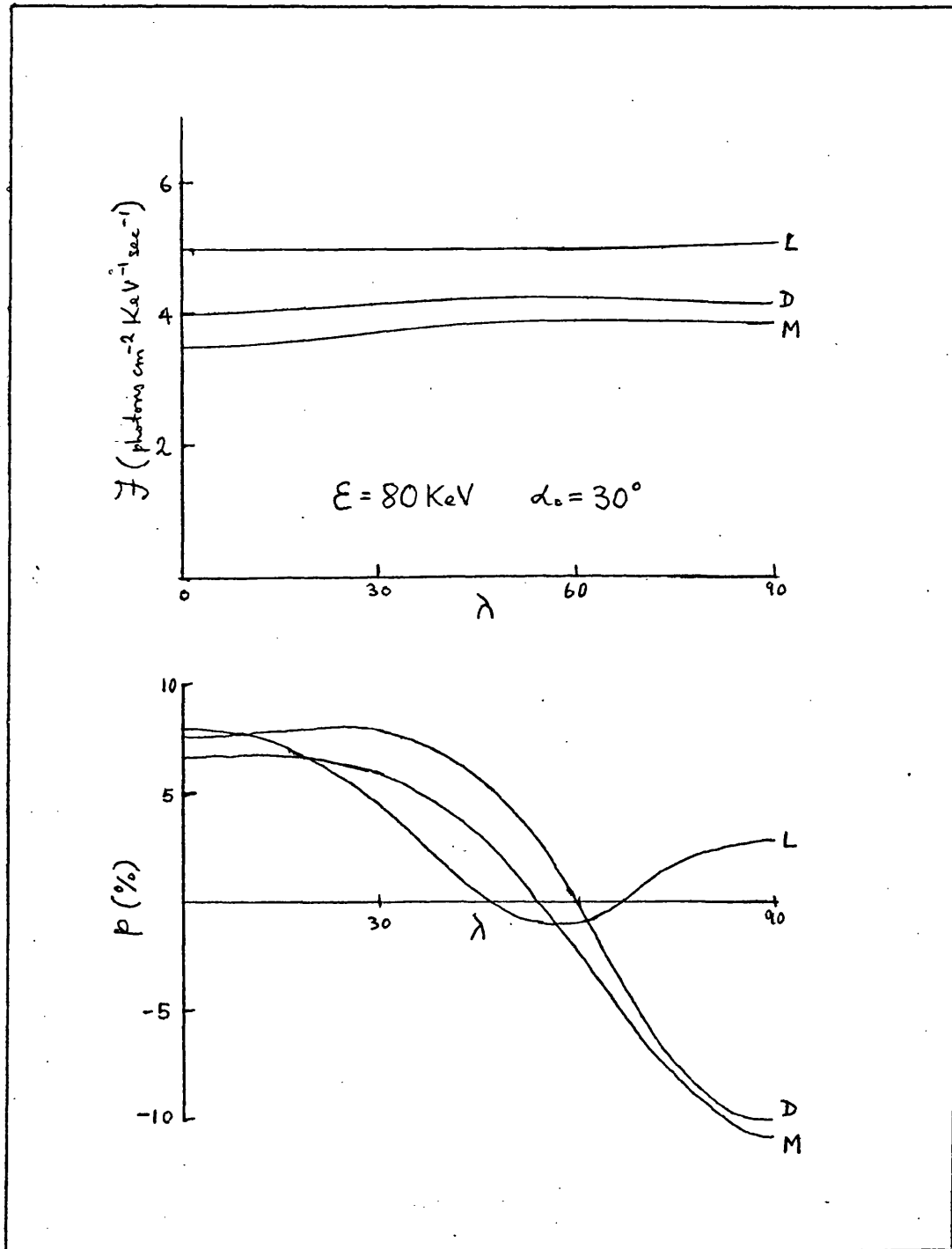


Figure 2.3 Directivity and polarisation of 80 KeV photons emitted by 100 KeV trapped electrons of  $30^\circ$  initial pitch angle, for dipole, linecharges and monopoles traps of height  $10^5$  km on the equator.

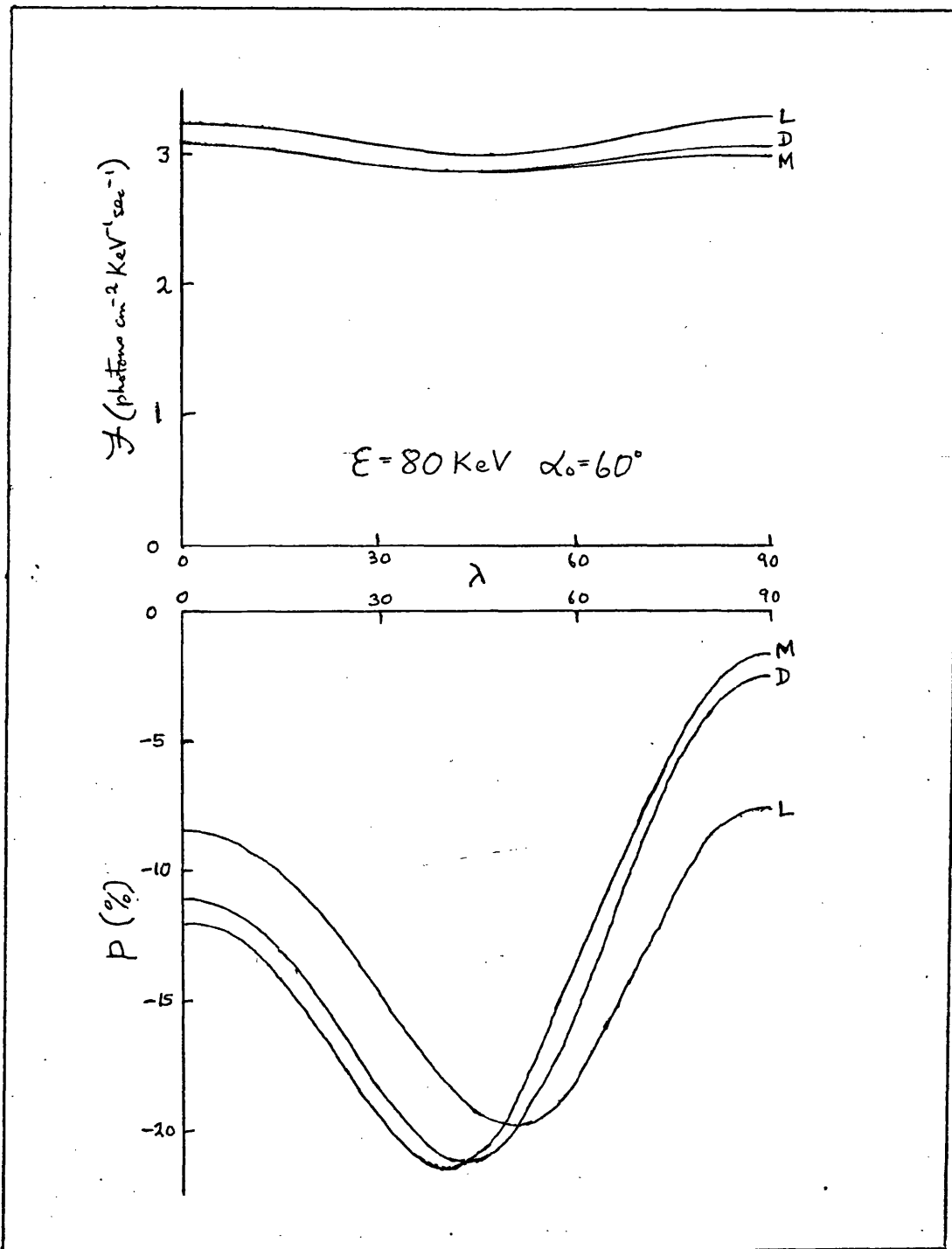


Figure 2.4. Directivity and polarisation of 80 KeV photons emitted by 100 KeV trapped electrons of  $60^\circ$  initial pitch angle, for dipole, linecharges and monopoles traps of height  $10^5$  km on the equator.

It is immediately clear that the general trends of solutions are similar for all field models. There is a difference in scaling of photon fluxes due to the variation of mirror point height between field models. Directivity and polarisation of emission from the dipole and monopoles traps are almost identical in all cases, but in some instances the predictions of the linecharges field model are somewhat different.

We may summarise the directivity results as follows.

- (i) For low photon energy and small initial pitch angles (Figure 2.1) there is  $\sim 20\%$  limb brightening.
- (ii) Low photon energy and large pitch angles (Figure 2.2) gives  $\sim 12\%$  limb darkening, except for the linecharges trap which predicts  $< 5\%$  variation in intensity.
- (iii) When the photon energy is near the short wavelength limit and the trapped electrons have small initial pitch angles (Figure 2.3), the intensity rises by  $\sim 10\%$  to peak at a longitude of  $\sim 50^\circ$ - $60^\circ$  and then falls slightly towards the limb. The linecharges trap again gives an exceptional result, the intensity being constant except for an increase of  $< 2\%$  at the limb.
- (iv) Finally, in Figure 2.4, the directivity of high energy radiation from electrons of large initial pitch angle is shown. In this case there is a minimum in photon flux at a longitude of  $\sim 50^\circ$  where the flux is  $10\%$  lower than at disc centre. The flux rises again towards the limb, increasing by  $\sim 5\%$ .

Considering now the polarisation, we notice immediately that the shape of the polarisation curves is independent of photon energy. It is also apparent that the linecharges field model gives results noticeably different from those of the dipole and monopoles fields. At a photon energy of 30 Kev we find that

- (i) for an initial pitch angle of  $30^\circ$  the polarisation is  $\sim 2\%$  at disc centre, the plane of polarisation lying in an East-West direction. The degree of polarisation falls with increasing longitude, passing through zero at  $\lambda \approx 60^\circ$  at which point the direction of polarisation becomes North-South. The degree of polarisation then increases to  $\sim 2\%$  at the limb.

(ii) For an initial pitch angle of  $60^\circ$  the polarisation is always in the North-South direction, rising from  $\sim 2\%$  at disc centre to a peak value of  $\sim 4\%$  at a longitude of  $\sim 45^\circ$ , after which the degree of polarisation falls to  $\sim 0.3\%$  at the limb.

The degree of polarisation at 80 Kev is about 5 times greater than that at 30 Kev. As discussed in Chapter II, polarisation increases at photon energy approaches the short wavelength limit.

In Figure 2.1 we see that at the limb the polarisation of X-rays from a linecharges trap containing electrons of  $30^\circ$  initial pitch angle is in the opposite direction to that predicted by the other models. For electrons of  $60^\circ$  initial pitch angle the polarisation of emission from the linecharges trap is again significantly different from that of the other models, being slightly smaller at disc centre and a factor of 4 greater at the limb.

This is possibly due to the fact that electrons of  $30^\circ$  initial pitch angle in a linecharges field mirror at approximately the same height as  $15^\circ$  pitch angle electrons in a monopoles field (see Figures 3.3 and 3.4 of Chapter III). We will see in §3 that the behaviour of the directivity and polarisation of emission from electrons of  $15^\circ$  initial pitch in a monopoles field is similar to that shown here by emission from  $30^\circ$  pitch angle electrons in a linecharges field.

Comparing our results with those obtained by Elwert & Haug (1970, 1971), discussed in §2 of Chapter III, we find that the directivity predicted at low photon energy agrees with the relativistic calculations of Elwert & Haug (1971), if these are taken to represent a "uniform horizontal field" approximation to the trap. If, on the other hand, the result obtained by Elwert and Haug for  $90^\circ$  pitch angle electrons is taken to represent emission from the vertical limbs of a trap, their prediction of 30% limb brightening does not agree with our results. This suggests that emission from the upper part of the trap is more important than emission from the limbs.

The polarisation curves, however, tell a different story. According to Elwert & Haug's (1970) non-relativistic calculations the "uniform horizontal field" approximation to the trap predicts an East-West polarisation of 50% at disc centre, falling to zero at the limb, for electrons of  $30^\circ$  pitch angle. In the case of  $60^\circ$  pitch angle electrons the polarisation should be North-South, rising from 15% at disc centre to a maximum of  $\sim 30\%$  at a longitude of  $\sim 45^\circ$ , then falling to zero at the limb. Taking Elwert & Haug's  $90^\circ$  pitch angle results as representative of a trap in which emission from the limbs dominates, the polarisation should rise from zero at disc centre to a maximum of  $\sim 70\%$  in the North-South direction at the limb.

It is appropriate at this point to remark that our results are not directly comparable with those of Elwert and Haug as they consider power law electron energy distributions. Hence the polarisations found by Elwert & Haug are larger than those obtained here. The mean energy of electrons which emit photons of a given energy, and hence the fraction of the photons emitted close to the short wavelength limit, is determined by the steepness of the electron spectrum, therefore the degree of polarisation depends on the electron spectrum. Since the bulk of emission at photon energy  $\epsilon$  comes from electrons with energy  $E$  in the range  $\epsilon < E < \alpha\epsilon$ , where  $\alpha \sim 2 - 3$  for typical power law electron spectra, the polarisation we have found for photons of 30 Kev emitted by 100 Kev electrons is much lower than that to be expected from a more realistic electron energy distribution.

Returning to a consideration of the longitude - dependence of polarisation, we look first at trapped electrons of  $30^\circ$  initial pitch angle. Since the degrees of polarisation at disc centre and at the limb are approximately equal we deduce that the contributions from the top of the trap and from the limbs are approximately the same. The argument is set out formally below.

Using subscripts T and L to denote association with the top and limbs of the trap respectively, and subscripts 0 and 90 to denote values at disc centre and at the limb, we have

$$P = \frac{I_{EW} - I_{NS}}{I_{EW} + I_{NS}} = \frac{(I_{EW} - I_{NS})_T + (I_{EW} - I_{NS})_L}{(I_{EW} + I_{NS})_T + (I_{EW} + I_{NS})_L} \quad (2.1)$$

where  $P$  is the polarisation and subscripts EW and NS denote radiation polarised in the East-West and North-South directions respectively. This equation can be written

$$P = \frac{I_T P_T + I_L P_L}{I_T + I_L} \quad (2.2)$$

which, evaluated at disc centre, is

$$P_o = \left( \frac{I_T}{I_T + I_L} \right)_o P_{T_o} \quad (2.3)$$

since  $P_{L_o} = 0$ . Similarly, at the solar limb,

$$P_{90} = \left( \frac{I_L}{I_T + I_L} \right)_{90} P_{L_{90}} \quad (2.4)$$

since  $P_{L_{90}} = 0$ . The directivity we define as

$$D = \frac{(I_T + I_L)_{90}}{(I_T + I_L)_o} \quad (2.5)$$

$D$  has a value of 1.2 since we have found 20% limb-brightening.

We have also, from our results, that

$$P_o/P_{90} = 1 \quad (2.6)$$

where, from (2.3) and (2.4)

$$\frac{P_o}{P_{90}} = \frac{(I_T + I_L)_{90}}{(I_T + I_L)_o} \frac{(I_T P_T)_o}{(I_L P_L)_{90}} = D \frac{(I_T P_T)_o}{(I_L P_L)_{90}} \quad (2.7)$$

According to Elwert & Haug (1971),

$$\frac{I_{T_{90}}}{I_{T_0}} \approx 1.2 \quad ; \quad \frac{I_{L_{90}}}{I_{L_0}} \approx 1.3 \quad ; \quad \frac{P_{T_0}}{P_{L_{90}}} \approx -\frac{0.5}{0.7} \quad (2.8)$$

Hence, using (2.5), (2.7) and (2.8)

$$\frac{I_{T_0}}{I_{L_{90}}} \approx \frac{1}{1.2} \times \frac{0.7}{0.5} \approx 1.15 \quad (2.9)$$

Which gives, using (2.8) again,

$$\frac{I_{T_0}}{I_{L_0}} \approx 1.55 \quad ; \quad \frac{I_{T_{90}}}{I_{L_{90}}} \approx 1.35 \quad (2.10)$$

In this crude analysis we have approximated the trap by two regions, a horizontal flux tube containing electrons with pitch angle equal to the initial pitch angle, and a vertical field in which the electrons have  $90^\circ$  pitch angles, representing emission from near the mirror points. We see that emission from both the top of the trap and the limbs is important.

We cannot perform such an idealised analysis for the  $60^\circ$  pitch angle results as emission from the mirror points does not take place in the vertical limbs of the trap. In this case our results agree with the "uniform horizontal field" interpretation of Elwert & Haug's (1970) results, except that the polarisation does not fall to zero at the limb. This shows that emission from the mirror points does make an appreciable contribution.

A final comment on these results. As the polarisation at disc centre in the case of  $60^\circ$  initial pitch angles is approximately

equal, but in the opposite direction to that from  $30^\circ$  initial pitch angle, we expect that if there is a distribution in pitch angle of the trapped electrons, the polarisation at disc centre may be small. This is contrary to the "uniform horizontal field" model, which predicts that the polarisation is maximal near disc centre and falls to zero at the limb.

We now consider briefly the influence of atmospheric density structure on the predicted directivity and polarisation. We have seen that, at least in the case of  $30^\circ$  initial electron pitch angles, radiation from the limbs of the trap and from the top of the trap are both significant. Therefore the form of variation of density with height may be expected to noticeably affect results. An examination of the magnetic field structures shown in Figures III 3.2 - 3.4 reveals that for the pitch angles considered so far the paths of electrons lie almost entirely in the region of large density scale height above  $5.8 \times 10^4$  km (see III (10.1 - (10.3))). The exception to this is the linecharges trap containing electrons of  $30^\circ$  initial pitch angle, which, as we have seen above, gives significantly different results from the other models.

The effect of varying the relationship of electron path to density structure is illustrated in Figure 2.5. Here photon flux and polarisation at 30 KeV is plotted against longitude for an initial pitch angle of  $30^\circ$ . The figure marked on each flux curve is trap height in units of  $10^5$  km. We see that the variation of flux with longitude is virtually independent of trap height. The only visible effect of changing the trap height is to scale the photon flux according to the mean density encountered by the electrons. The polarisation curves all lie within the hatched area in the lower figure. The maximum variation in mirror point density relative to that at the top of the trap in the results presented here is only 10%, but calculations in which other density distributions were used yielded similar results.

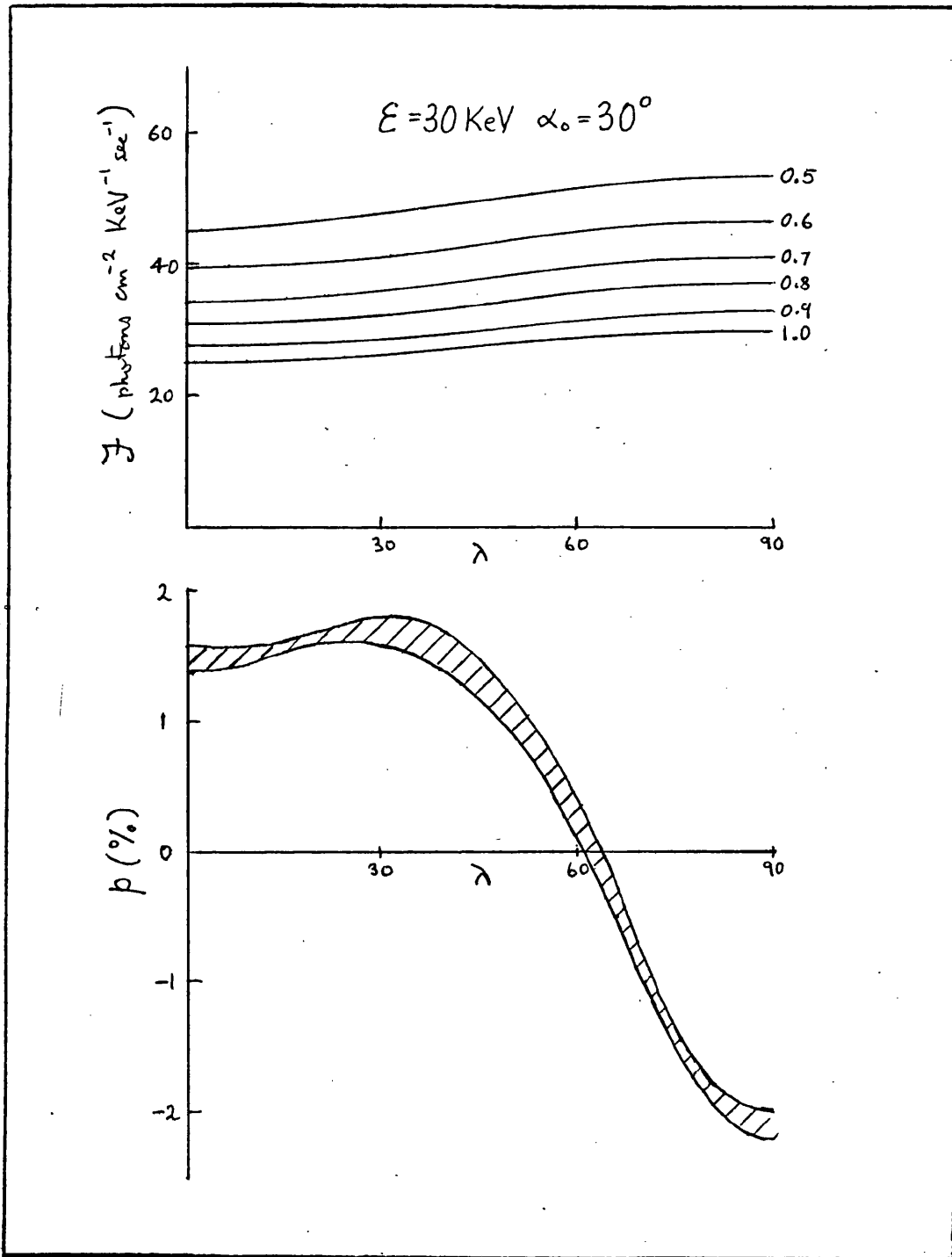


**Figure 2.5** Directivity and polarisation of 30 KeV photons emitted by 100 KeV electrons of  $30^\circ$  initial pitch angle in a monopoles trap on the equator. Figures against each curve in the upper figure are trap heights in units of  $10^5$  km. The polarisation curves lie within the hatched area for all trap heights.

In summary, we have found that small initial pitch angles tend to give limb-brightening and East-West polarisation, while large pitch angles give limb-darkening and North-South polarisation. Results are not too sensitive to the field model used, although results obtained using the linecharges field model are slightly different from those obtained from the dipole and monopole fields. Characteristic of the X-ray emission are insensitive to trap height and do not depend strongly on the density structure of the model atmosphere.

As a standard field model for the work described in the remainder of this chapter and in Chapter V we adopt the monopoles trap of height  $5 \times 10^4$  km.

### 3. ELECTRON DISTRIBUTION (i)

Having established a "standard" trapping field model, we now examine briefly the dependence of photon flux and polarisation on the orientation of the trap relative to the observer for electron distribution (i), which is singular in electron energy and pitch angle. As before, we take the electron energy to be 100 Kev. Results obtained for photons energies of 30 and 80 Kev and for pitch angles of  $15^\circ$ ,  $30^\circ$ ,  $45^\circ$ ,  $60^\circ$  and  $75^\circ$  are shown in Figures 3.2-3.11.

In these figures continuous lines are contours of constant photon flux, degree of polarisation is given by the broken contours and the direction of polarisation is indicated by heavy lines. The photon flux at any position is given by  $\mathcal{F} = \mathcal{F}_{\min} + \Delta\mathcal{F} \times (n-1)$ , where  $n$  is the number assigned to each contour.  $\mathcal{F}_{\min}$  is given in each figure caption.  $\Delta\mathcal{F}$  is 1.0 for  $\epsilon = 30$  Kev and 0.1 for  $\epsilon = 80$  Kev. The degree of polarisation is  $p = \Delta p \times (n-1)$  where  $n$  is the contour number.  $\Delta p$  is 0.5 for  $\epsilon = 30$  Kev and 2.0 for  $\epsilon = 80$  Kev.

As a reminder of the significance of latitude and longitude in defining the orientation of the trap, Figure 3.1 depicts schematically

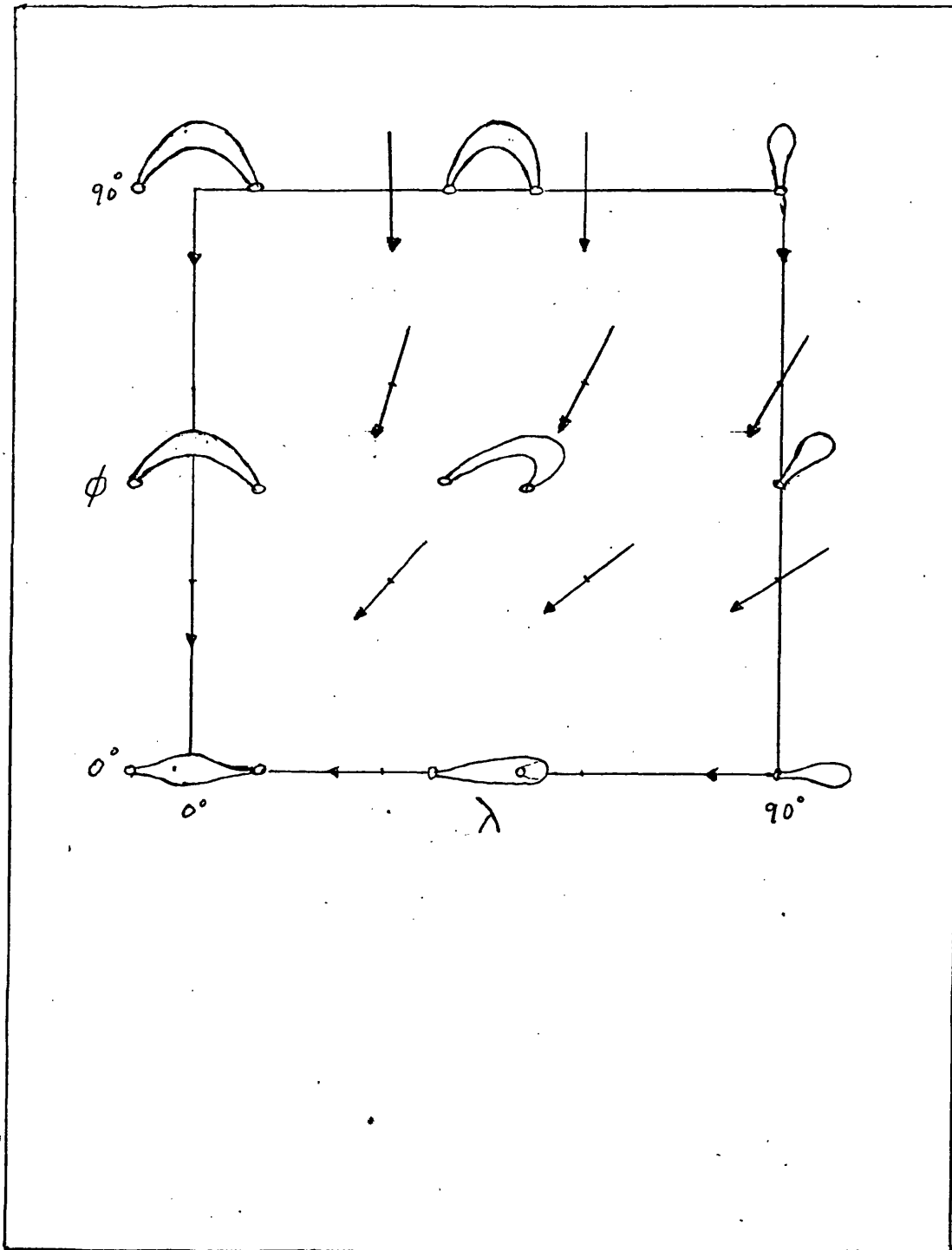


Figure 3.1 Schematic representation of the appearance of the trap at several latitudes and longitudes. Also shown is radial direction (direction towards disc centre) as a function of latitude and longitude.

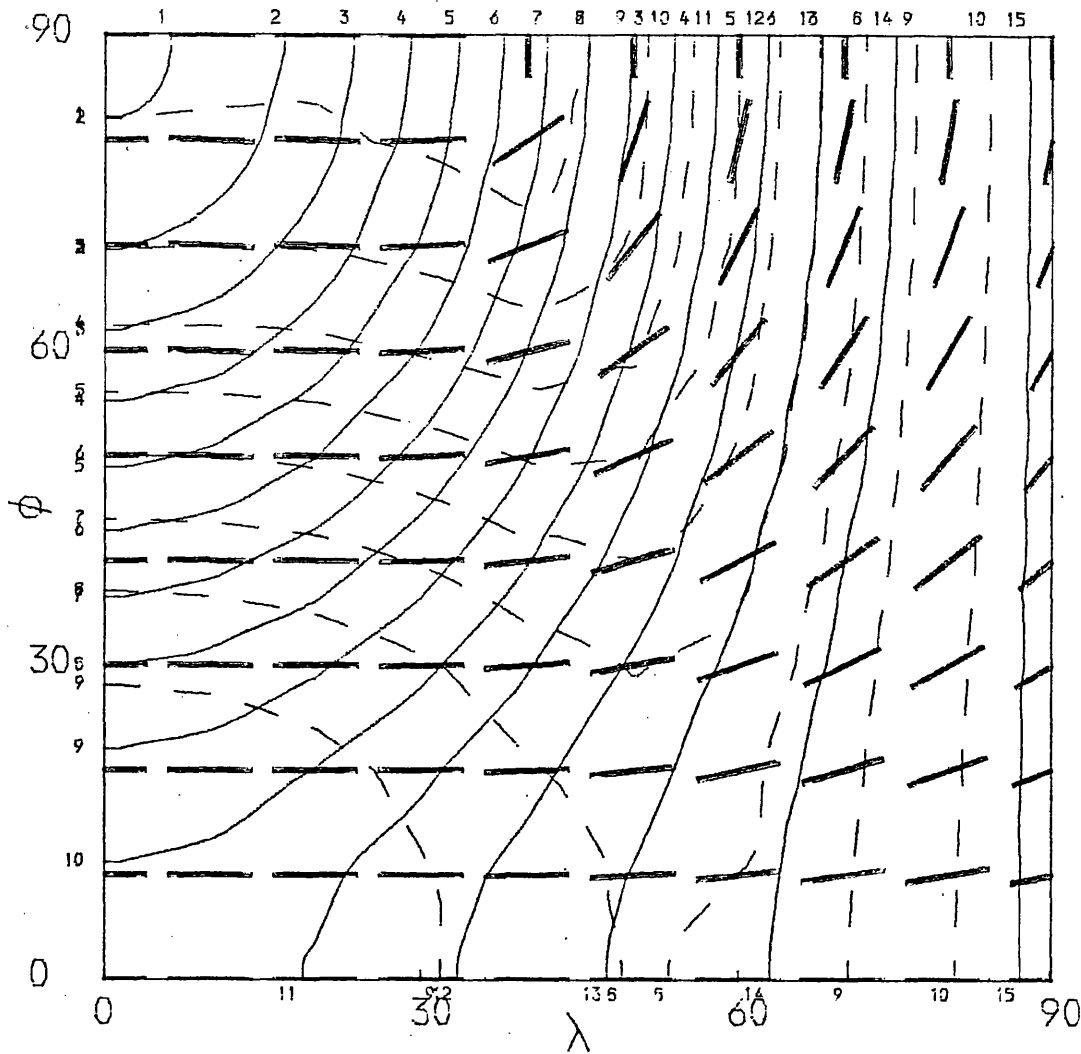


Figure 3.2 Electron distribution (i). Photon flux and polarisation at  $\epsilon = 30$  KeV from trapped electrons of energy  $E = 100$  KeV and initial pitch angle  $\alpha_0 = 15^\circ$ .  
 $\mathcal{F} = 48 + (n_F - 1) \text{ cm}^{-2} \text{ sec}^{-1} \text{ KeV}^{-1}$ ;  $p = (n_p - 1)/2 \%$

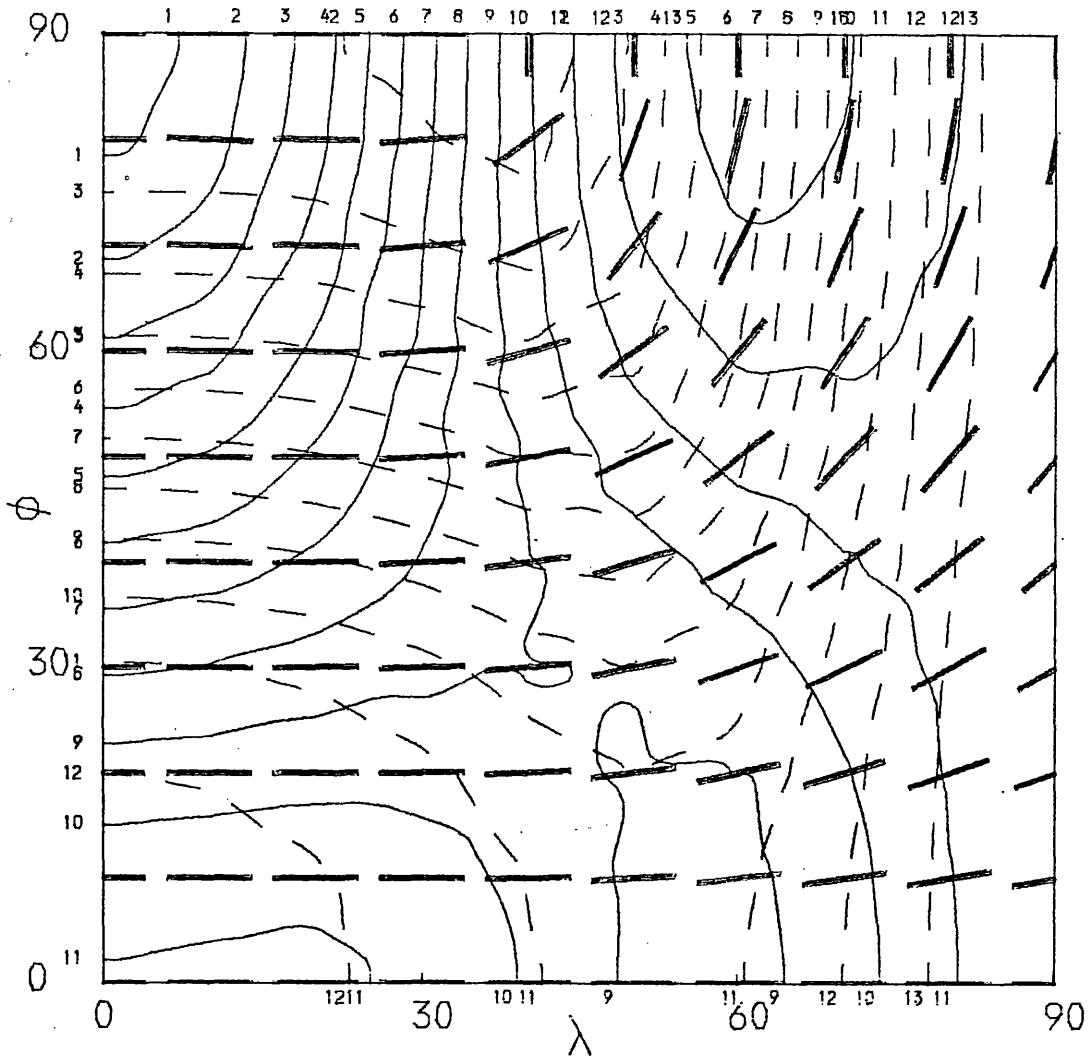
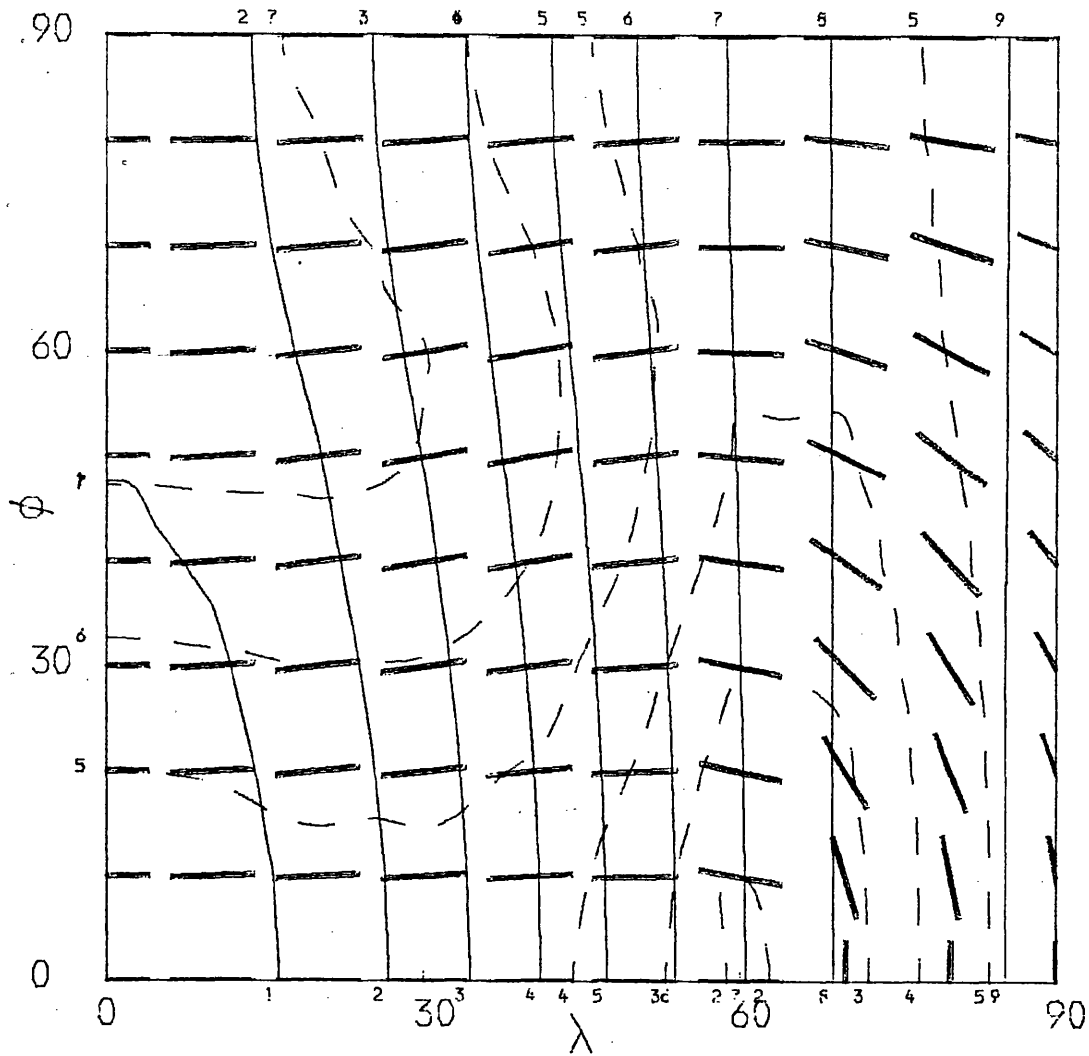


Figure 3.3 Electron distribution (i). As Figure 3.2 for  $\epsilon = 80$  keV.

$$\mathcal{F} = 6.9 + 0.1 (n_p - 1) \text{ cm}^{-2} \text{ sec}^{-1} \text{ KeV}^{-1}; \quad p = 2(n_p - 1)\%$$



**Figure 3.4** Electron distribution (i). Photon flux and polarisation at  $\epsilon = 30$  KeV from trapped electrons of energy  $E=100$  KeV and initial pitch angle  $\alpha_0 = 30^\circ$ .

$$\mathcal{F} = 46 + (n_F - 1) \text{ cm}^{-2} \text{ sec}^{-1} \text{ KeV}^{-1}; \quad p = (n_p - 1)/2 \%$$

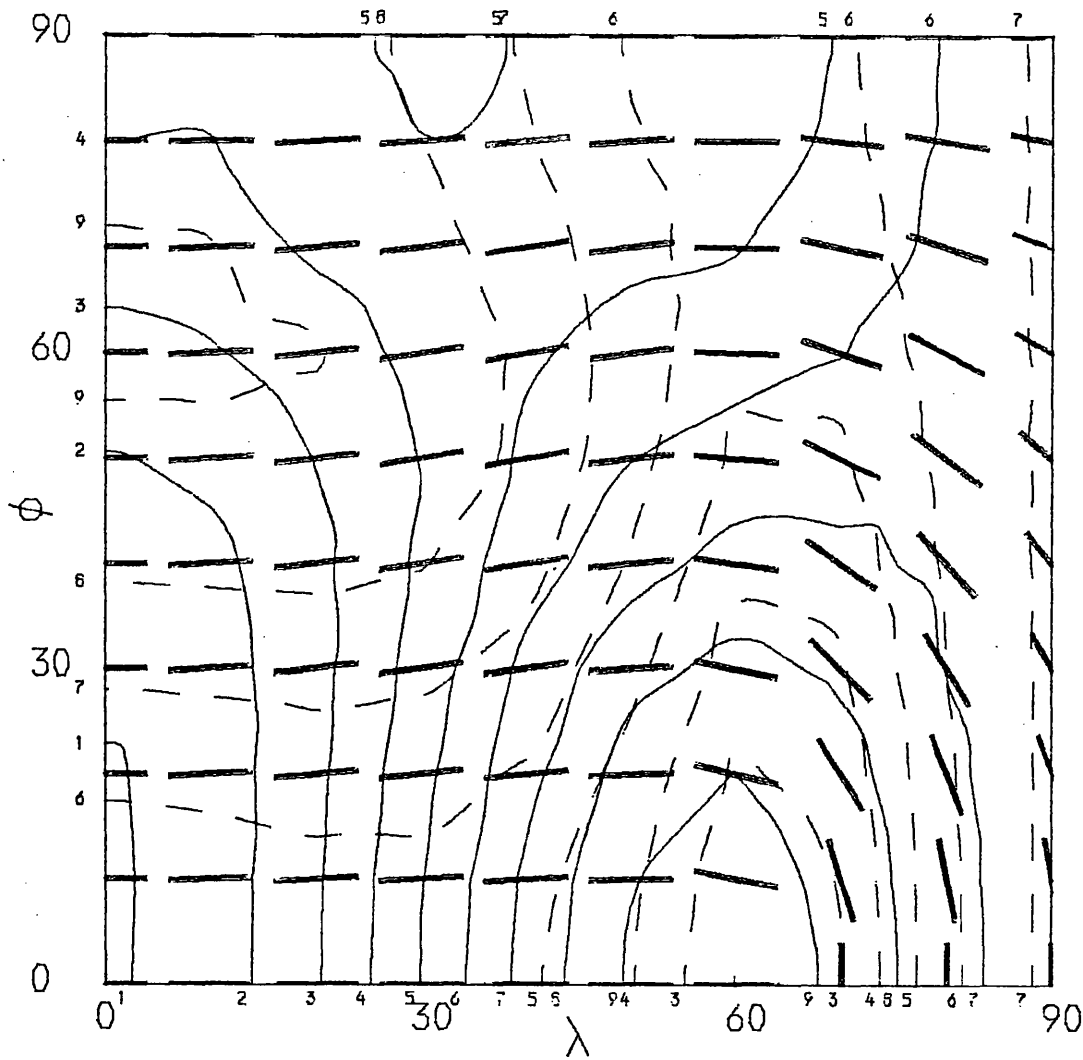
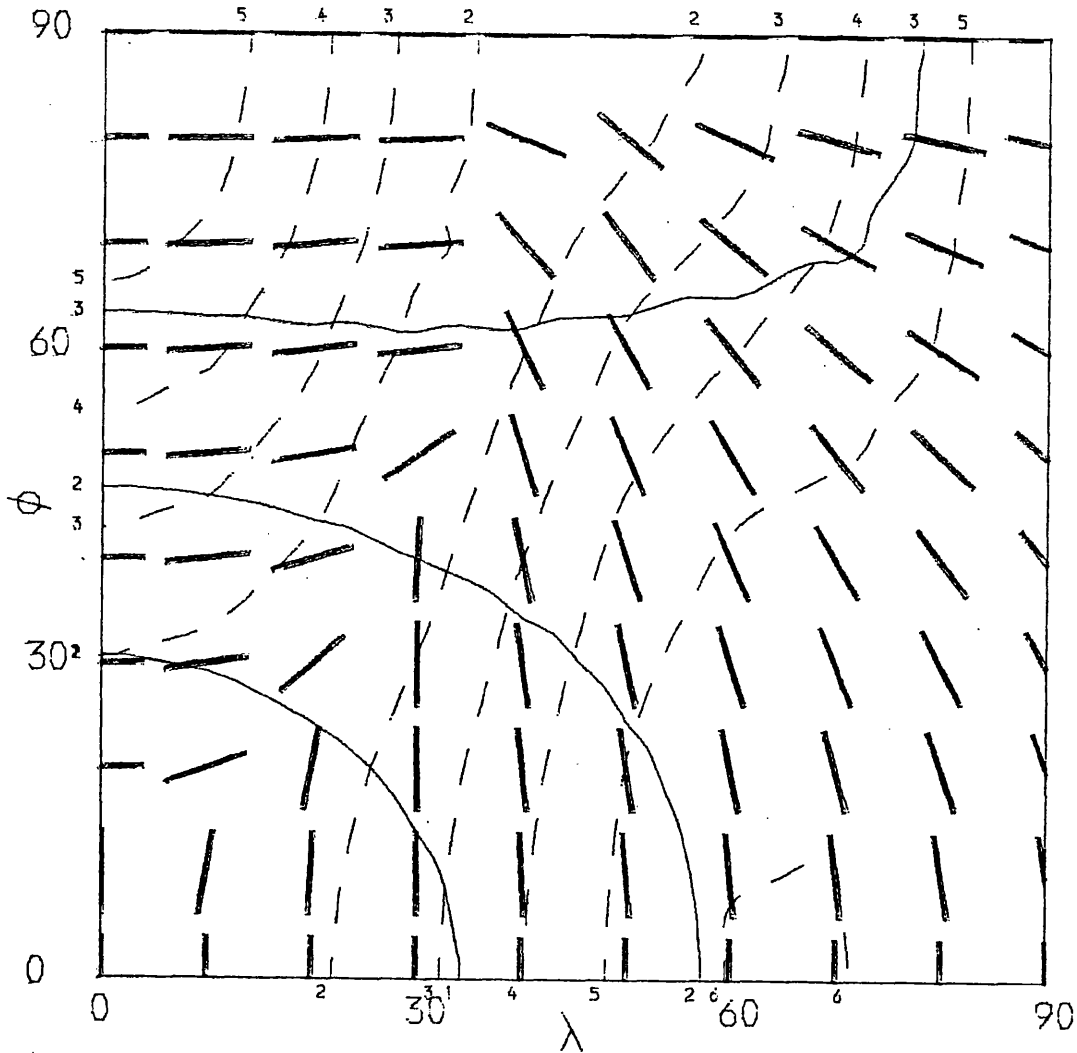


Figure 3.5 Electron distribution (i). As Figure 3.4 for  $\epsilon = 80$  keV.

$$\mathcal{N} = 6.3 + 0.1 (n_F - 1) \text{ cm}^{-2} \text{ sec}^{-1} \text{ keV}^{-1}; p = 2(n_p - 1)\%$$



**Figure 3.6** Electron distribution (i). Photon flux and polarisation at  $\epsilon = 30$  KeV from trapped electrons of energy  $E = 100$  KeV and initial pitch angle  $\alpha_0 = 45^\circ$

$$\mathcal{F} = 41.5 + (n_F - 1) \text{ cm}^2 \text{ sec}^{-1} \text{ KeV}^{-1}; \quad p = (n_p - 1) / 2 \%$$

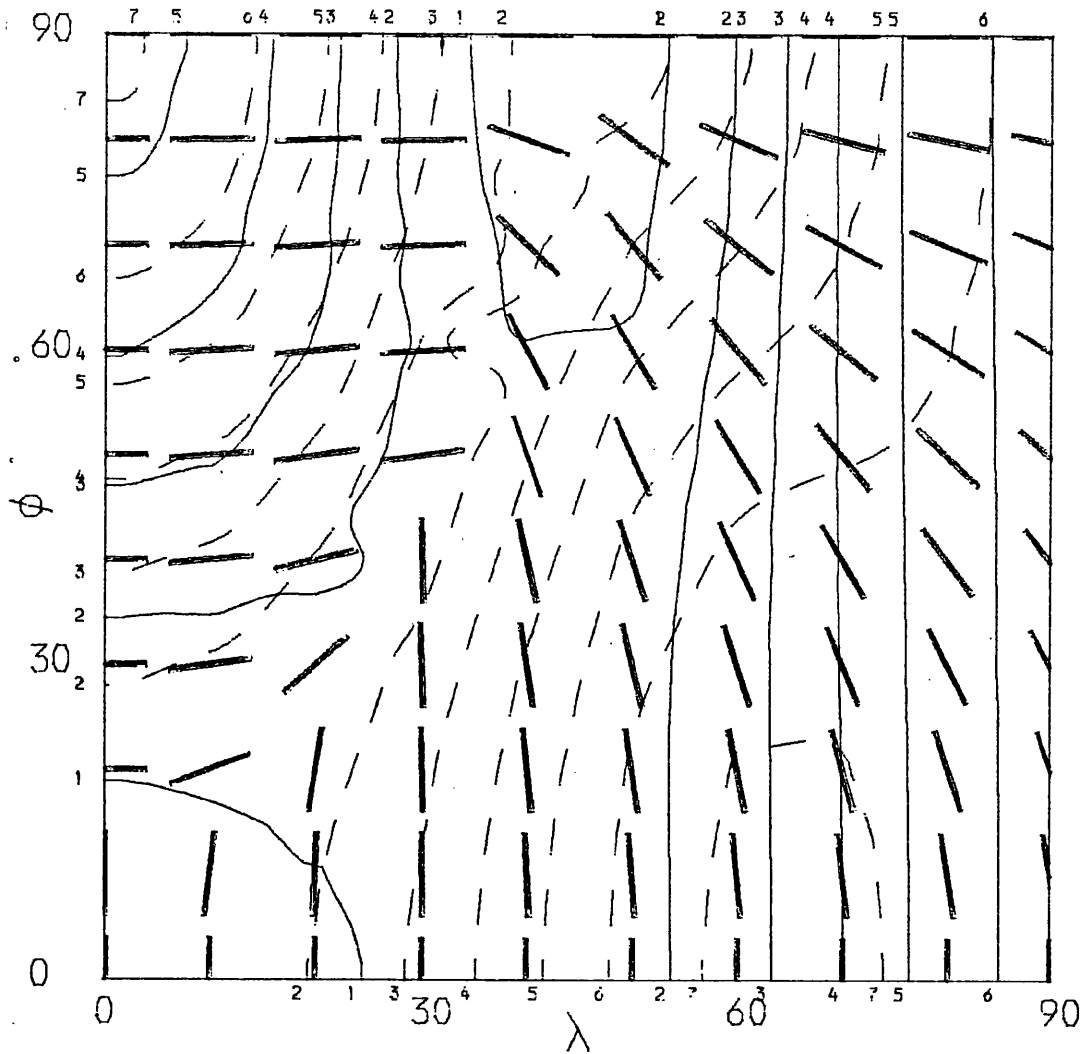


Figure 3.7 Electron distribution (i). As Figure 3.6 for  $\epsilon = 80$  keV.

$$\mathcal{Y} = 5.8 + 0.1(n_p - 1) \text{ cm}^{-2} \text{ sec}^{-1} \text{ KeV}^{-1}; p = 2(n_p - 1) \%$$

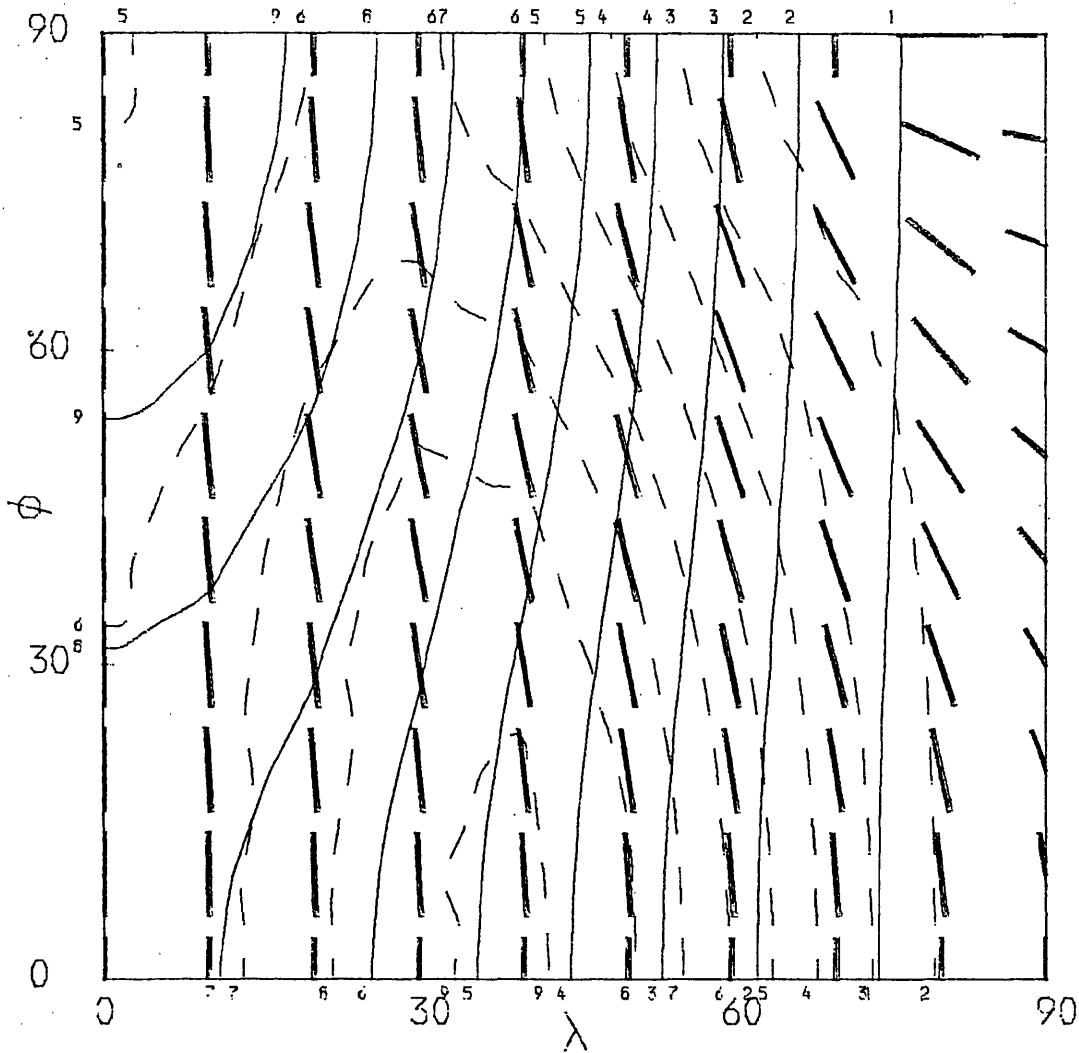


Figure 3.8 Electron distribution (i). Photon flux and polarisation at  $\epsilon = 30$  KeV from trapped electrons of energy  $E = 100$  KeV and initial pitch angle  $\alpha_0 = 60^\circ$ .

$$\mathcal{F} = 35 + (n_F - 1) \text{ cm}^{-2} \text{ sec}^{-1} \text{ KeV}^{-1}; \quad p = (n_p - 1) / 2 \%$$

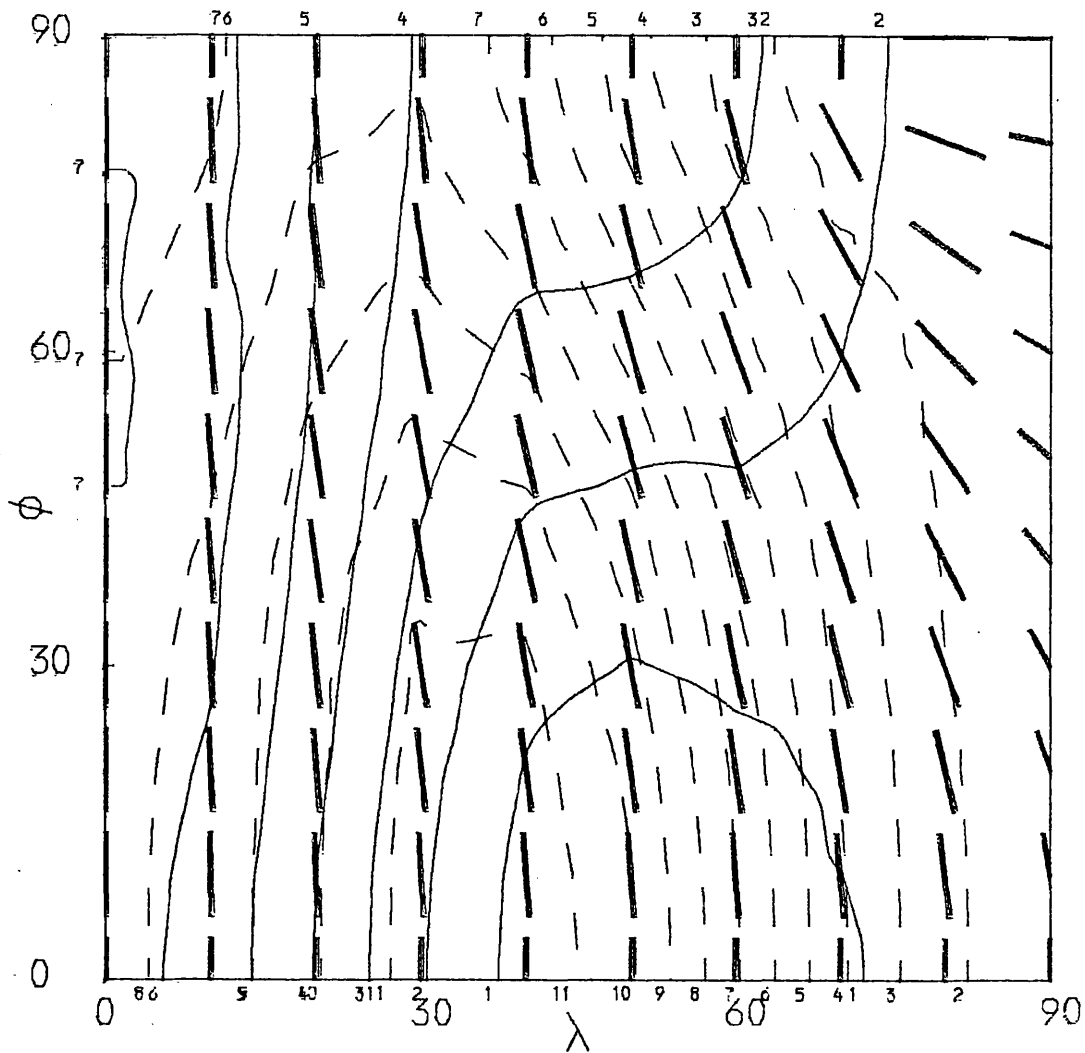
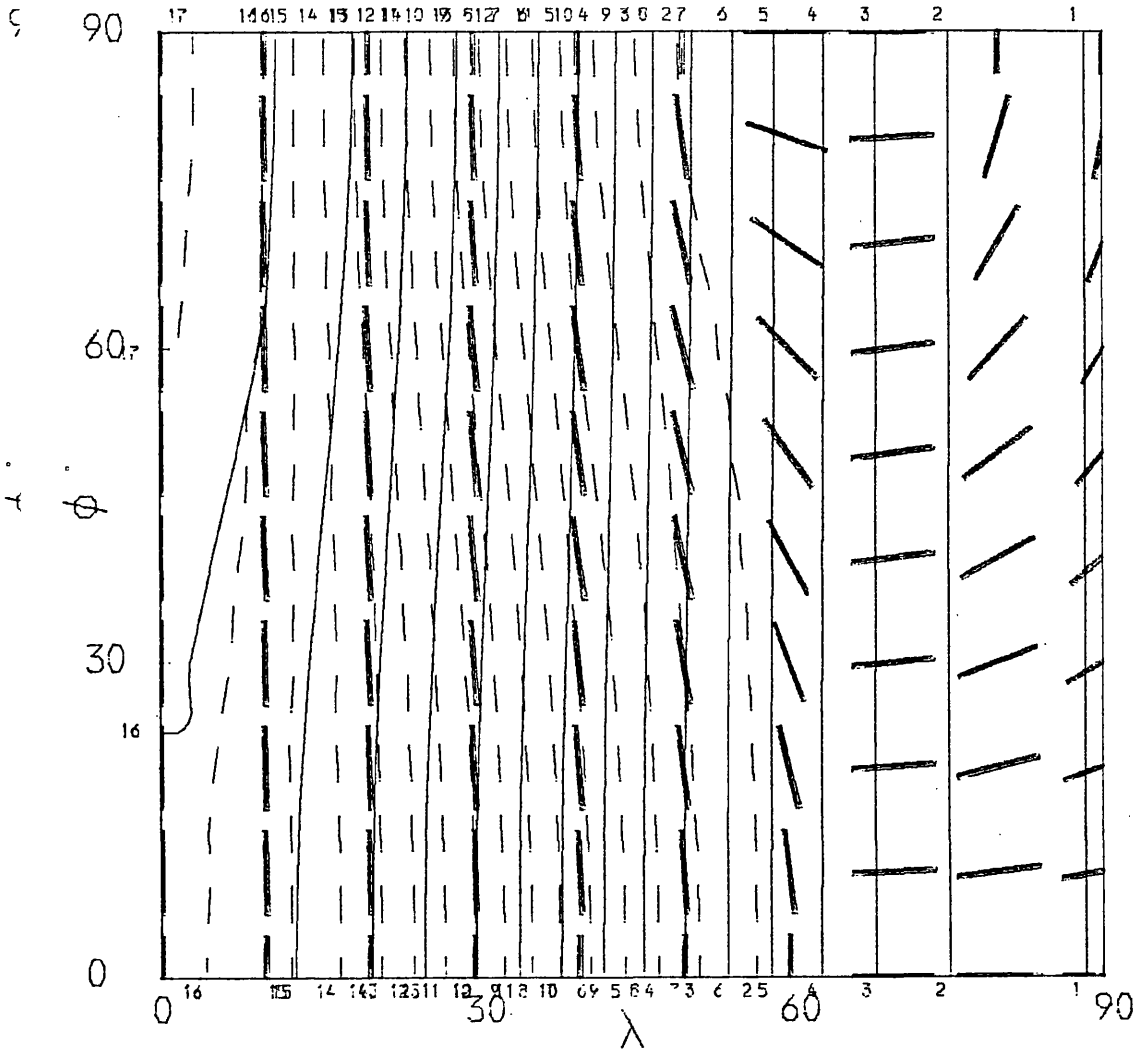


Figure 3.9 Electron distribution (i). As Figure 3.8 for  $\epsilon = 80$  keV.

$$\mathcal{J} = 5.2 + 0.1 (\bar{n}_F - 1) \text{ cm}^{-2} \text{ sec}^{-1} \text{ KeV}^{-1}; \quad p = 2(n_p - 1) \%$$



**Figure 3.10.** Electron distribution (i). Photon flux and polarisation at  $\epsilon = 30$  KeV from trapped electrons of energy  $E = 100$  KeV and initial pitch angle  $\alpha_0 = 75^\circ$ .

$$\mathcal{F} = 28 + (n_F - 1) \text{ cm}^{-2} \text{ sec}^{-1} \text{ KeV}^{-1}; \quad p = (n_p - 1) / 2 \%$$

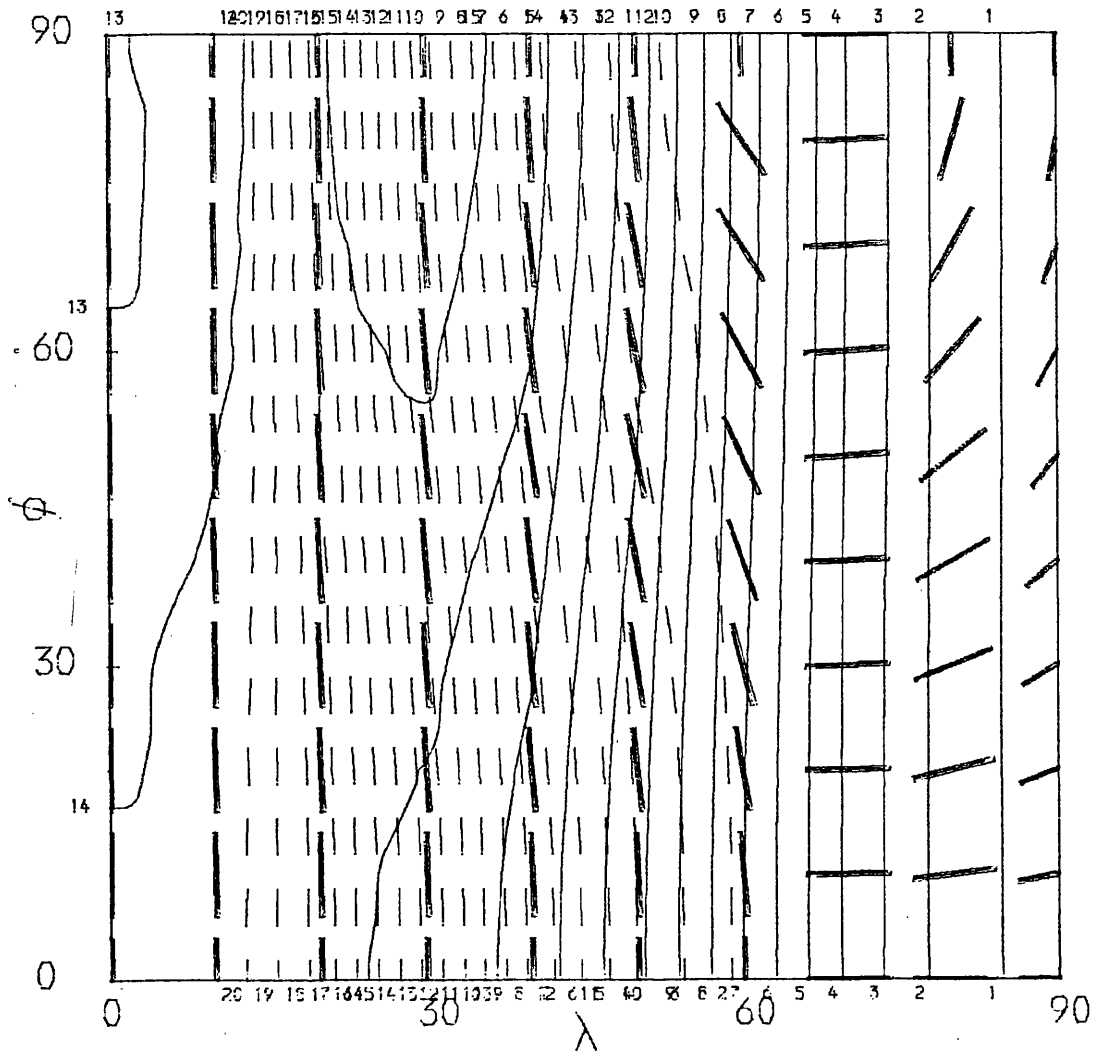


Figure 3.11 Electron distribution (i). As Figure 3.10 for  $\epsilon = 80$  keV.

$$\bar{\gamma} = 4.1 + 0.1(n_F - 1) \text{ cm}^{-2} \text{ sec}^{-1} \text{ KeV}^{-1}; p = 2(n_p - 1) \%$$

the projected appearance of the trap at several latitudes and longitudes. This figure also shows the radial direction at various latitudes and longitudes. If it is desired to compare the angle of polarisation with the radial direction in Figures 3.2 - 3.11, it must be remembered that the straight line towards the origin in these figures is not the radial direction. The direction of polarisation at the limb ( $\lambda = 90^\circ$ ) is either parallel to the limb or in the radial direction. In this section some numbers are quoted in the form  $x_1(x_2)$  where  $x_1$  refers to 30 KeV photon energy and  $x_2$  to 80 KeV. Note also that positions on the solar disc are given in the form  $(\phi, \lambda)$ .

From Figure 3.2 and 3.3 we see that for  $\alpha_0 = 15^\circ$  the intensity is lowest at  $(\phi, \lambda) = (90^\circ, 0^\circ)$  that is, when the trap is seen side-on. At a photon energy of 30 KeV the intensity increases monotonically towards the limb, increasing by  $\sim 30\%$ . Brightness at disc centre is  $\sim 20\%$  higher than at  $(90^\circ, 0^\circ)$ . For  $\epsilon = 80$  KeV the variation of intensity is more complicated. Again the lowest intensity occurs at  $(90^\circ, 0^\circ)$ , but in this case there are local maxima at disc centre  $(0^\circ, 0^\circ)$  and at the point  $(90^\circ, \sim 60^\circ)$ . At these points the increase in intensity is approximately 16% and 19% respectively.

The dependence of degree of polarisation on position is similar at both photon energies. Minimum polarisation ( $\sim 0\%$ ) occurs at the point  $(90^\circ, \sim 30^\circ)$  while maximum polarisation 5%(25%) is found at disc centre and at the limb. The direction of polarisation is East-West over most of the disc, swinging round to North-South for  $\lambda > 50^\circ$  at high latitudes.

Moving on to Figures 3.4 and 3.5, which show the behaviour of the X-ray emission for  $\alpha_0 = 30^\circ$ , we notice immediately that the direction of polarisation at the limb has reversed. The polarisation is still East-West over most of the disc, but it is now East-West at the limb at high latitudes and swings to North-South at the limb at low latitudes. The minimum in flux, which occurred at the pole for  $\alpha_0 = 15^\circ$  has moved down to disc centre. For  $\epsilon = 30$  KeV the flux increases by  $\sim 20\%$  from disc centre to limb but hardly changes between

the points (0,0) and (90,0). That is, no variation is observed if the trap is viewed side-on and rotated about its foot points. If the trap is observed at 80 Kev, however, the brightness increases by 6% in going from (0,0) to (90,0) but again little variation is seen when the trap is viewed side-on and rotated about its vertical axis. More variation occurs on the equator, where there is a maximum (14% up on disc centre) at  $\lambda \approx 60^\circ$ .

For  $45^\circ$  initial pitch angles the directivity is small at 30 Kev (Figure 3.6). We also see from this figure that the region in which the polarisation has swung round to North-South has extended inwards. Now East-West polarisation is only seen at high latitudes, that is, when the trap is viewed side-on. A line of minimum polarisation runs from the disc centre to the point (90,45). A maximum polarisation of  $\sim 3\%$  is found at the pole (90,0) and at the point (0,  $\sim 70$ ). The limb polarisation is almost as high.

At a photon energy of 80 Kev (Figure 3.7) the behaviour of the polarisation is similar, maximum polarisation in this case being  $\sim 15\%$ . However, directivity is higher. The intensity is lowest at disc centre and at the point (90,  $\sim 45$ ) and rises by  $\sim 10\%$  to maxima at the limb and at the pole.

From Figures 3.8 and 3.9 we see that when  $\alpha_0$  is increased to  $60^\circ$  the polarisation becomes North-South over almost all the disc. Also, limb-darkening occurs instead of limb-brightening. The intensity falls by  $\sim 25\%$  (15%) from a maximum near the pole. (For  $\epsilon = 80$  Kev the maximum and minimum actually occur at ( $\sim 70,0$ ) and (0,  $\sim 50$ ) respectively).

The degree of polarisation is also lower at the limb, rising from  $\sim 1\%$  (3%) there to 2.5% (15%) at the pole and 3% (15%) at disc centre and to a maximum of 5% (23%) at (0,  $\sim 40$ ).

Finally, looking at Figures 3.10 and 3.11, we notice that for  $\alpha_0 = 75^\circ$  the direction of polarisation at the limb has again reversed and is now back to what it was for  $\alpha_0 = 15^\circ$ . But here the polarisation is North-South for  $\lambda \lesssim 60^\circ$  whereas it was East-West for  $15^\circ$  pitch angles. The degree of polarisation is almost independent of latitude, rises from  $\sim 0.5\%$  (2%) at the limb to 9% (40%) at  $\lambda = 0^\circ$ . It could be anticipated in this case that results would not depend strongly on latitude as the electrons are trapped in the upper part of the flux tube. Therefore the "horizontal uniform field" approximation to the trap model is a good approximation. At a photon energy of 30 Kev the intensity increases by  $\sim 60\%$  on moving from the limb to the central meridian. The behaviour of the intensity at 80 Kev is similar, although the maximum (37% brightening) actually occurs at the point  $(90^\circ, 30^\circ)$ . On the central meridian the intensity is only slightly lower.

Finally, to draw together these results, we present Figure 3.12, which illustrates the variation of directivity and polarisation with longitude on the equator, for all values of pitch angles considered in this section. Here we see that at disc centre, the polarisation decreases monotonically with increasing pitch angle. It is positive (i.e. East-West) for small pitch angles, passes through zero for  $\alpha_0 = 45^\circ$  and when  $\alpha_0 = 75^\circ$  it is negative and  $\sim 75\%$  greater in magnitude than at  $\alpha_0 = 15^\circ$ .

At the limb, the behaviour of the polarisation is rather more complex. It is positive for  $\alpha_0 = 15^\circ$ , but decreases rapidly with increasing  $\alpha_0$  to reach a minimum at  $\alpha_0 \sim 30^\circ - 45^\circ$ . Here the degree of polarisation is  $\sim 2/3$  of that found for  $\alpha_0 = 15^\circ$ . On increasing the pitch angle further the polarisation becomes less negative. It is small and negative at  $\alpha_0 = 60^\circ$  and has passed through zero to become small and positive at  $\alpha_0 = 75^\circ$ .

This figure summarises many of the most important results found in this section. From Figures 3.2 - 3.11 we see that, with the possible exception of initial pitch angles of  $30^\circ - 45^\circ$ ,

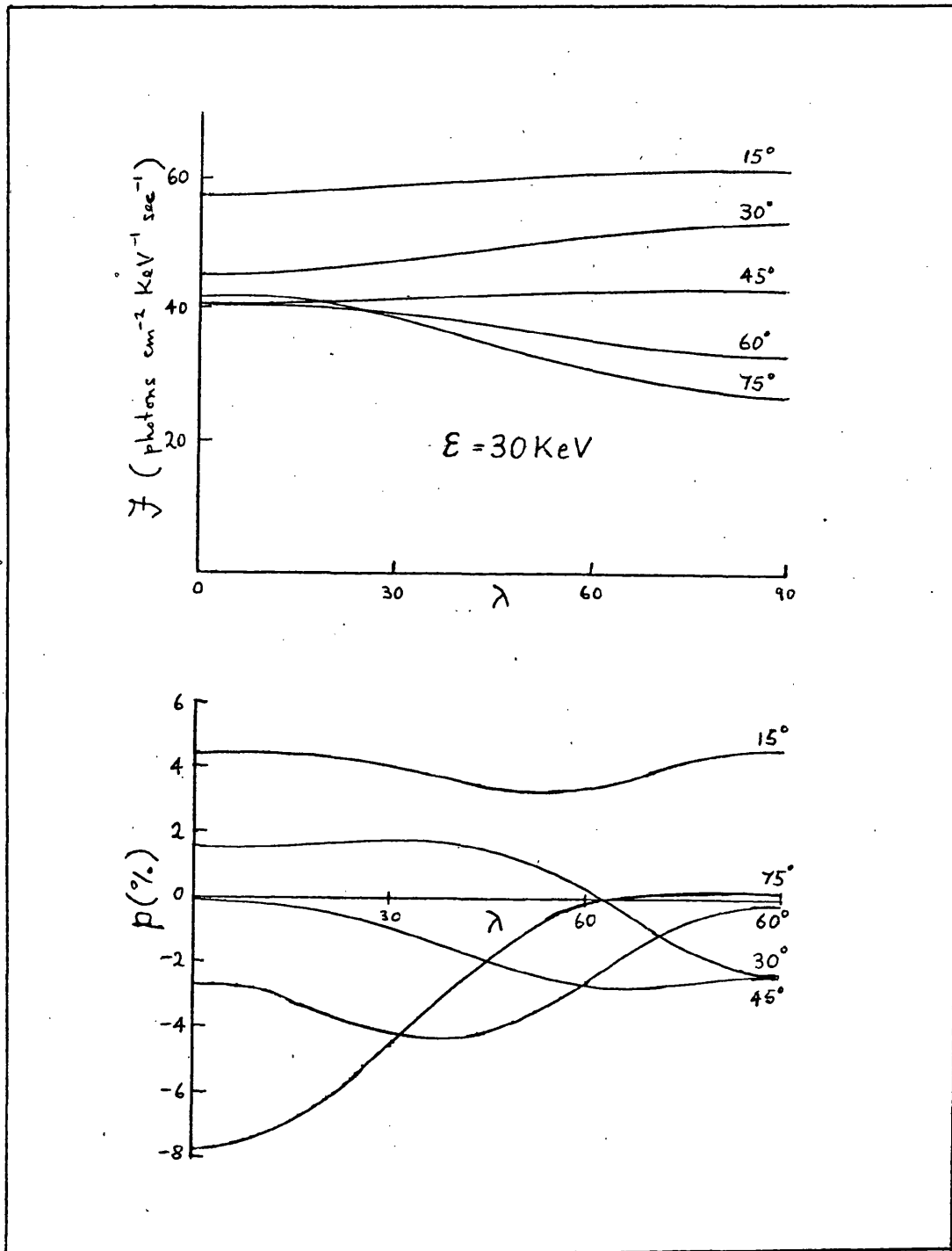


**Figure 3.12** Combined results, showing the variation of photon flux and polarisation at 30 KeV on the equator, as a function of longitude for pitch angles of  $15^\circ$ ,  $30^\circ$ ,  $45^\circ$ ,  $60^\circ$  and  $75^\circ$ . This figure summarises many important features of X-ray emission from the trap model.

characteristics of the X-ray emission are not strongly dependent on latitude for traps situated near the equator, say for  $\phi \lesssim 40^\circ$ . Since flares usually occur close to the solar equator Figure 3.12 is adequate in most cases to define the predicted behaviour of emission from a trap which lies parallel to the equator.

The results shown in Figure 3.12 are also sufficient to define approximately the characteristics of emission from traps situated near disc centre which are not orientated in the East-West direction. If such a trap lies within  $\sim 30^\circ - 40^\circ$  of disc centre then the "equator" which we have defined should be swung round until it lies parallel to the trapping field. Then the trap will be within  $40^\circ$  of this "equator" and, as mentioned above, characteristics of the emission from it will be determined principally by its "longitude", measured along the "equator". Positive and negative values of polarisation then correspond respectively to the polarisation vector being parallel or perpendicular to the trapping field.

For bursts nearer to the solar limb, the results presented as a function of both longitude and latitude (Figures 3.2 - 3.11) must be referred to, as the characteristics of the X-ray emission vary widely depending on whether the trap is seen end-on (trapping field East-West) or side-on (trapping field North-South).

The computation of X-ray flux and polarisation from electron distributions (ii), (iii) and (iv) involves the numerical evaluation of triple or quadruple integrals, and so requires a large amount of computer time. Therefore we try to gain some insight from the results of this section, into the behaviour of X-ray emission from the more realistic electron distributions to be examined in the following sections.

First of all, we note that the directivity is small. Maximal directional effects are found at small pitch angles (30% limb-brightening for  $\alpha_0 = 15^\circ$ ) and at large pitch angles (35% limb-darkening for  $\alpha_0 = 75^\circ$ ). Since these effects are much smaller than

would be expected on the basis of the behaviour of the bremsstrahlung cross-section alone (c.f. Chapter II), we conclude that the spiralling of the electrons and the effect of trap geometry dominate the behaviour of the X-ray flux. Therefore it is unlikely that the introduction of a power law energy spectrum or a distribution of pitch angles can increase the directivity.

We have already seen in Chapter II, where the results of this chapter were anticipated, that measurements of the directivity of hard X-ray bursts are unlikely to be helpful in discriminating between source models. (The significance of the directivity results obtained in this chapter will be discussed further in §7). Therefore the directivity of emission from electron distributions (ii), (iii) and (iv) will not be discussed in detail in the following sections.

We may draw some tentative conclusions concerning the polarisation too. We have found that the direction of polarisation and the form of its variation with position of the trap are independent of photon energy, for a fixed electron energy. Although this is true near the short wavelength limit, it is not clear what will happen when a power law energy distribution is introduced, since photons of different energies are then emitted by electrons of different energies. One effect which we do expect to find is an increase in the degree of polarisation with increasing deepness of the electron spectrum, since photons are then emitted closer to the short wavelength limit. We know (Chapter II) that the polarisation bremsstrahlung cross-section does not change its form drastically when the electron energy is varied. If the polarisation depends more strongly on pitch angle and trap geometry than on the bremsstrahlung cross-section, as suggested by the directivity results, a latitude and longitude dependence similar to that obtained in this section should be found for distribution (ii).

In the case of distribution (iii), in which the pitch angles are

distributed, it is likely that a  $\sin^n \alpha_0$  distribution, in which large pitch angles predominate, will have a polarisation pattern similar to that of Figure 3.11 ( $\alpha_0 = 75^\circ$ ) in which North-South polarisation predominates over most of the disc, while a  $\cos^n \alpha_0$  distribution will produce polarisation similar to that shown in Figure 3.3 ( $\alpha_0 = 15^\circ$ ), where East-West polarisation predominates. The degree of polarisation may be lower due to cancellation of the contributions from electrons of different pitch angles.

Since pitch angle is a function of electron energy in distribution (iv), we expect that in this case both magnitude and direction of the polarisation will depend on photon energy.

#### 4. ELECTRON DISTRIBUTION (ii)

In this section we study the directivity and polarisation of X-ray emission from trapped electrons with a power law distribution in energy. The initial pitch angles are discrete, as in distribution (i). We look at the same values of initial pitch angle used in the previous section, that is  $15^\circ$ ,  $30^\circ$ ,  $45^\circ$ ,  $60^\circ$  and  $75^\circ$ . As the results of this distribution are more expensive to obtain in terms of computer time, we have not made such an extensive survey as was done for distribution (i), but mainly attempted to determine in what respects the characteristics of the X-ray emission differ from those found in §3.

A new feature which we do examine more closely is the variation of spectral index from centre to limb. Attempts to measure this effect experimentally have been described in Chapter II. If the Bethe-Heitler approximation to the isotropic bremsstrahlung cross-section is used, the photon spectrum is predicted to be half a power steeper than the electron energy power law spectrum. We find that the photon spectral index can vary by almost one power for a given electron energy distribution, being a function of photon energy, initial pitch

angle and position of the trap.

First of all, we examine the dependence of polarisation on photon energy. Figure 4.1 illustrates the variation of polarisation with photon energy for initial pitch angles of  $30^\circ$  and  $60^\circ$  and electron spectral indices of 3 and 4.

In order to show how the energy-dependence of polarisation and spectral index varies with trap position, Figures 4.1 & 4.2 give results for positions  $(\phi, \lambda) = (0,0), (0,45), (0,90), (30,30)$  and  $(90,0)$ . At the point  $(30,30)$  the polarisation is not strictly North-South or East-West as it is for the other positions considered. However, the polarisation angle is close to  $0^\circ$  or  $90^\circ$  as in distribution (i) (Figures 3.4 and 3.8). Therefore Figure 4.1 shows the polarisation as positive ( $\phi_p \approx 0^\circ$ ) or negative ( $\phi_p \approx 90^\circ$ ).

The behaviour of the polarisation is very similar for both values of the spectral index, being slightly higher for  $\delta = 4$ , as anticipated in §3. The direction and relative magnitudes of the polarisation at different positions of the trap are similar to those found for distribution (i).

We examine the  $30^\circ$  pitch angle results first.

Referring to Figure 4.1 we see that at low photon energy a trap at position  $(\phi, \lambda) = (90,0)$  produces the most positive polarisation. The other trap positions may be ranked in the order  $(0,0), (30,30), (0,45)$  and  $(0,90)$ . (The polarisations at points  $(30,30)$  and  $(90,0)$  are almost equal). At high photon energy, the order is the same except that the points  $(0,0)$  and  $(0,45)$  cross over at  $\epsilon \approx 80$  Kev. Note that the polarisation of X-rays from a trap at  $(\phi, \lambda) = (30,30)$  or  $(0,45)$  falls less rapidly with photon energy than it does at the other positions considered. In Table 4.1 the results for  $\delta = 3$  are compared with those for distribution (i).

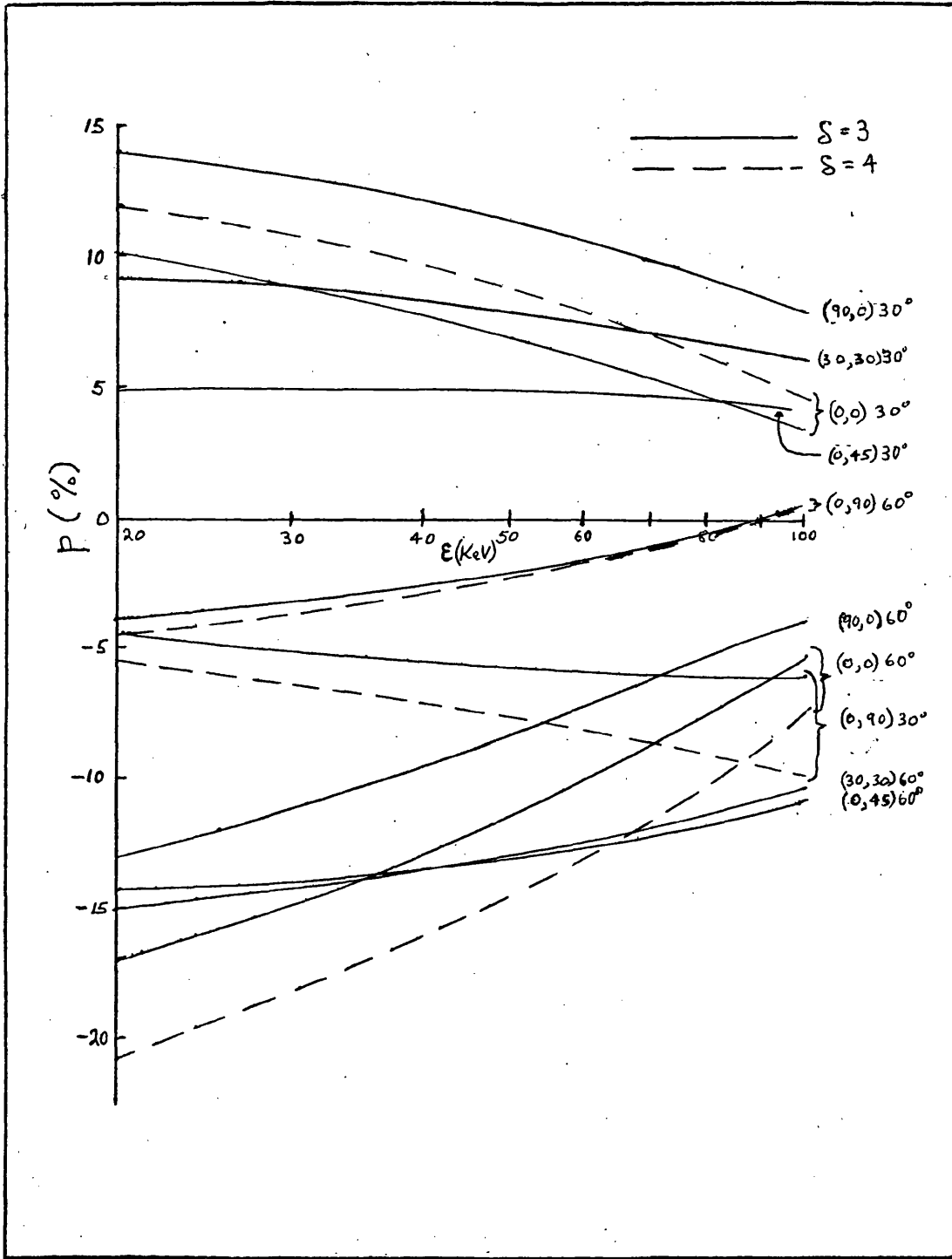


Figure 4.1 Electron distribution (ii). Polarisation as a function of photon energy at various trap positions for  $\alpha_0 = 30^\circ$  and  $60^\circ$ . Against each curve is marked  $(\phi, \lambda) \alpha_0$ .

TABLE 4.1 Polarisation for distributions (i) and (ii)

$$\alpha_0 = 30^\circ$$

		$\epsilon = 30 \text{ KeV}$			$\epsilon = 80 \text{ KeV}$		
$\phi$	$\lambda$	$P_{(i)}$	$P_{(ii)}$	$P_{(ii)}/P_{(i)}$	$P_{(i)}$	$P_{(ii)}$	$P_{(ii)}/P_{(i)}$
90	0	3.1	14	4.5	15.6	9.0	1.7
30	30	2.5	9.5	3.8	12.5	7.5	1.7
0	0	1.6	10	6.2	8.4	4.6	1.8
0	45	1.5	5	3.3	7.0	4.6	1.5
0	90	-2.2	-4.5	2.0	-12.1	-6.0	2.0

It is apparent that the dependence of polarisation on pitch angle and trap orientation is similar in both sets of results. The much smaller spread in the ratio  $P(i)/P(ii)$  at 80 KeV suggests that the typical energy of electrons in power law distribution (ii) emitting photons of 80 KeV is around 100 KeV. (The mono-energetic electrons in distribution (i) have energy 100 KeV). Since the short wavelength limit is undefined in a power law spectrum, polarisation does not necessarily increase with photon energy. In this case the electron-energy dependence of the bremsstrahlung cross-section determines the variation of polarisation with photon energy. From Figure 4.1 we see that except for  $(\phi, \lambda) = (0, 90)$  polarisation decreases slowly with increasing photon energy.

Most of the general comments above apply to the results for  $\alpha_0 = 60^\circ$ , also shown in Figure 4.1. Again the degree of polarisation tends to decrease with increasing photon energy, falling less rapidly in the case of  $(\phi, \lambda) = (0, 45)$  and  $(30, 30)$ . A point worthy of note is that the polarisation of X-rays from a trap at the limb  $(\phi, \lambda) = (0, 90)$  passes through zero at  $\epsilon \approx 90 \text{ KeV}$ , becoming positive at higher energies.

We now examine briefly the variation of the photon spectral index  $\gamma$  with energy. This, in effect, defines the extent of the deviation of the photon spectrum from a power law, given that the electron spectrum is a power law. Since we have no grounds for assuming that in reality the electron spectrum is exactly a power law, attempts to infer physical source characteristics (other than the electron spectrum) from the shape of the observed spectrum are unlikely to be meaningful.

However, later on in this section we look at the variation in spectral index as a function of position of the trap, a feature which represents a possible method of distinguishing between source models (see Chapter II). We define the spectral index of the photon spectrum by the fluxes at 25 KeV and 75 KeV, that is

$$\gamma = (\ln \mathcal{F}_{25} - \ln \mathcal{F}_{75}) / (\ln 75 - \ln 25), \quad (4.1)$$

and so do not take account of the detailed shape of the spectrum. Therefore it is useful at this point to get some idea of the magnitude of deviations of the photon spectrum from a power law.

The variation of spectral index with photon energy is shown in Figure 4.2. When the trap is viewed from above  $((\phi, \lambda) = (0, 0))$ , or nearly so  $(30, 30)$ , there is practically no deviation from a power law, but if it is viewed end-on  $(0, 90)$ , the spectral index varies appreciably with energy, decreasing with energy for small pitch angles and increasing for large pitch angles. For a trap at position  $(90, 0)$ , that is, side-on, the spectrum only deviates from a power law appreciably for large pitch angles, in which case it hardens at high energy.

We consider now the variation of photon flux, polarisation and spectral index with longitude, for a trap on the equator. The upper part of Figure 4.3 depicts the directivity at photon energies of 25 KeV and 75 KeV for electron spectral index  $\delta = 3$ . Results

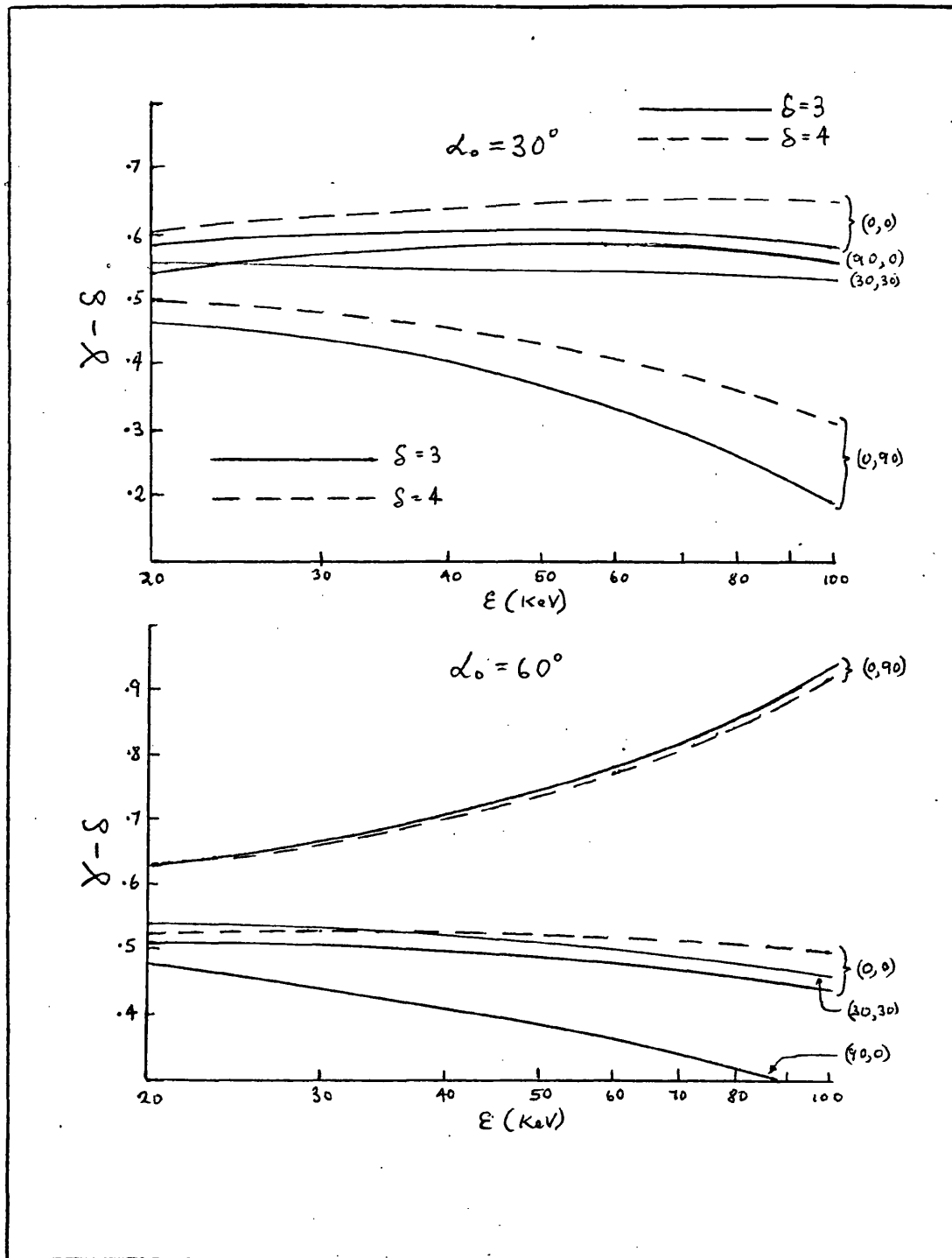


Figure 4.2 Electron distribution (ii). Variation of spectral index with photon energy at various trap positions for initial pitch angles of  $30^\circ$  and  $60^\circ$ . Position  $(\phi, \lambda)$  of the trap is shown against each curve.

are shown for initial pitch angles of  $15^\circ$ ,  $30^\circ$ ,  $60^\circ$  and  $75^\circ$ . Note that the apparent directivities are exaggerated as the  $\mathcal{J}$ -axis is expanded. It will also be noticed that the fluxes are much lower than those found in §3 for distribution (i). This is due to the fact that the bulk of electrons in the power law spectrum (85% for  $E_0 = 10$  KeV,  $\delta = 3$ , as assumed here) have energy less than 25 KeV and so do not contribute to the X-ray emission at this energy.

Several points are immediately clear from these results. The directivity is practically zero at 25 KeV, but at 75 KeV the maximum directional effect is a limb-darkening of  $\sim 40\%$  for  $\alpha_0 = 75^\circ$ . This is slightly greater than the largest variation found for distribution (i), which also occurred for  $\alpha_0 = 75^\circ$ , being a limb-darkening of  $\sim 35\%$ . The maximum degree of limb-brightening ( $\sim 30\%$  for  $\alpha_0 = 30^\circ$ ) is the same in both cases.

In the lower half of Figure 4.3 the variation of spectral index (defined by (4.1)) with longitude is illustrated. The largest effect is a softening of the spectrum, by  $\Delta\gamma \sim 0.5$ , at limb, for  $\alpha_0 = 75^\circ$ . As for the directivity, the amount of variation at small pitch angles is greater at  $\alpha_0 = 30^\circ$  than at  $\alpha_0 = 15^\circ$ . For  $\alpha_0 = 30^\circ$  the spectrum is  $\sim 0.2$  powers harder at the limb. Although the precise value of  $\gamma$  obtained depends on the photon energies chosen to define the effective spectral index, general trends in the variation of are clearly the same.

The variation of polarisation with longitude for a trap on the equator is shown in Figure 4.4. As we have already seen from Figure 4.1, polarisation is generally higher at 25 KeV than at 75 KeV. Figure 4.4 should be compared with Figure 3.12, which shows the polarisation as a function of longitude for distribution (i). It is clear that the longitude - dependence of polarisation is very similar in form for both electron distributions. The difference is chiefly one of degree. The maximum polarisation for each pitch angle in Figure 4.4 is approximately 5 times higher than those shown in Figure 3.12, where the photon energy  $\epsilon$  is 30 KeV, and is comparable

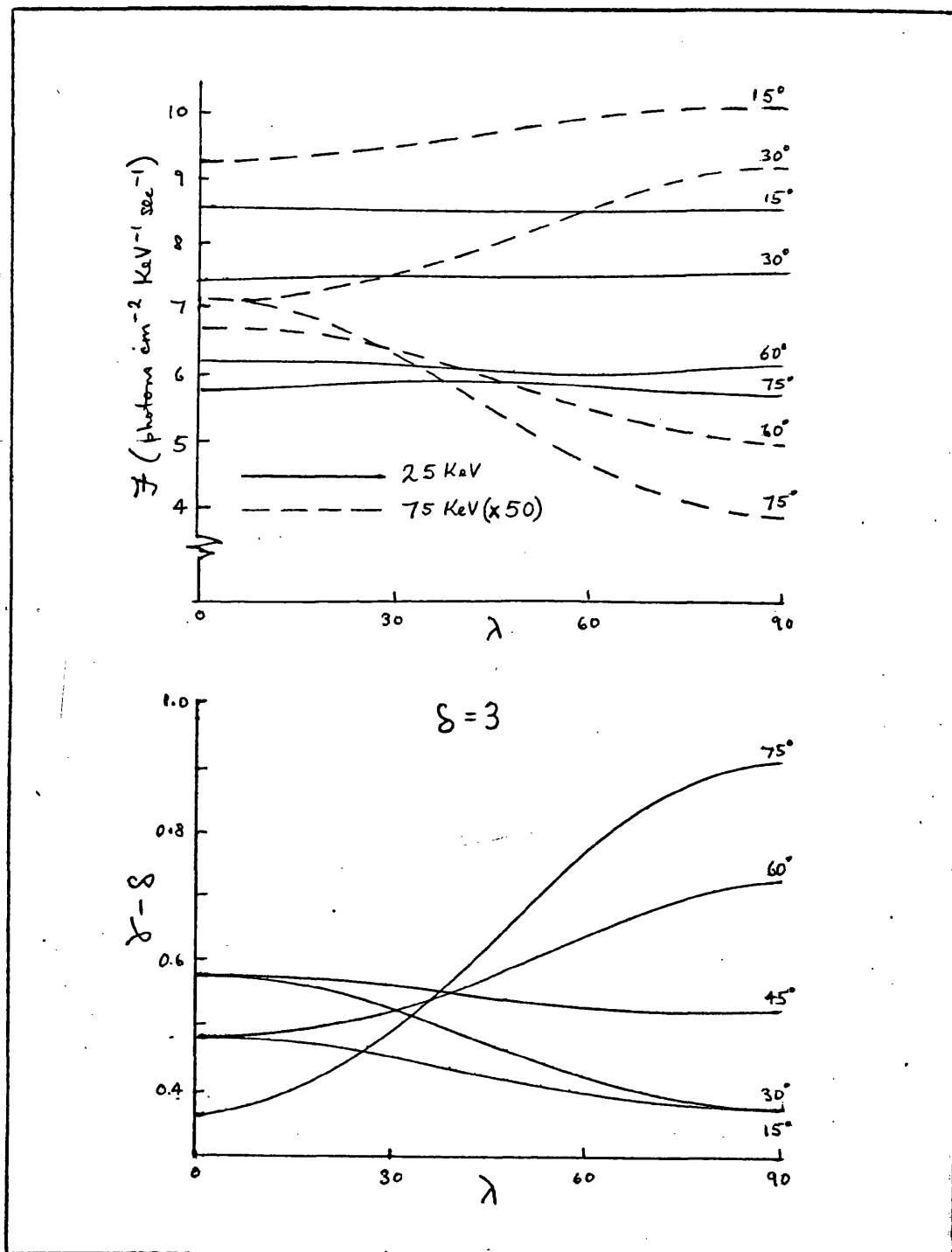


**Figure 4.3** Electron distribution (ii). Directivity (upper figure) and spectral index (lower figure) of X-ray emission from a trap on the equator for a range of initial pitch angles. Fluxes at 75 KeV (broken lines) are scaled up by x 50. The electron spectral index,  $\delta$ , is 3.

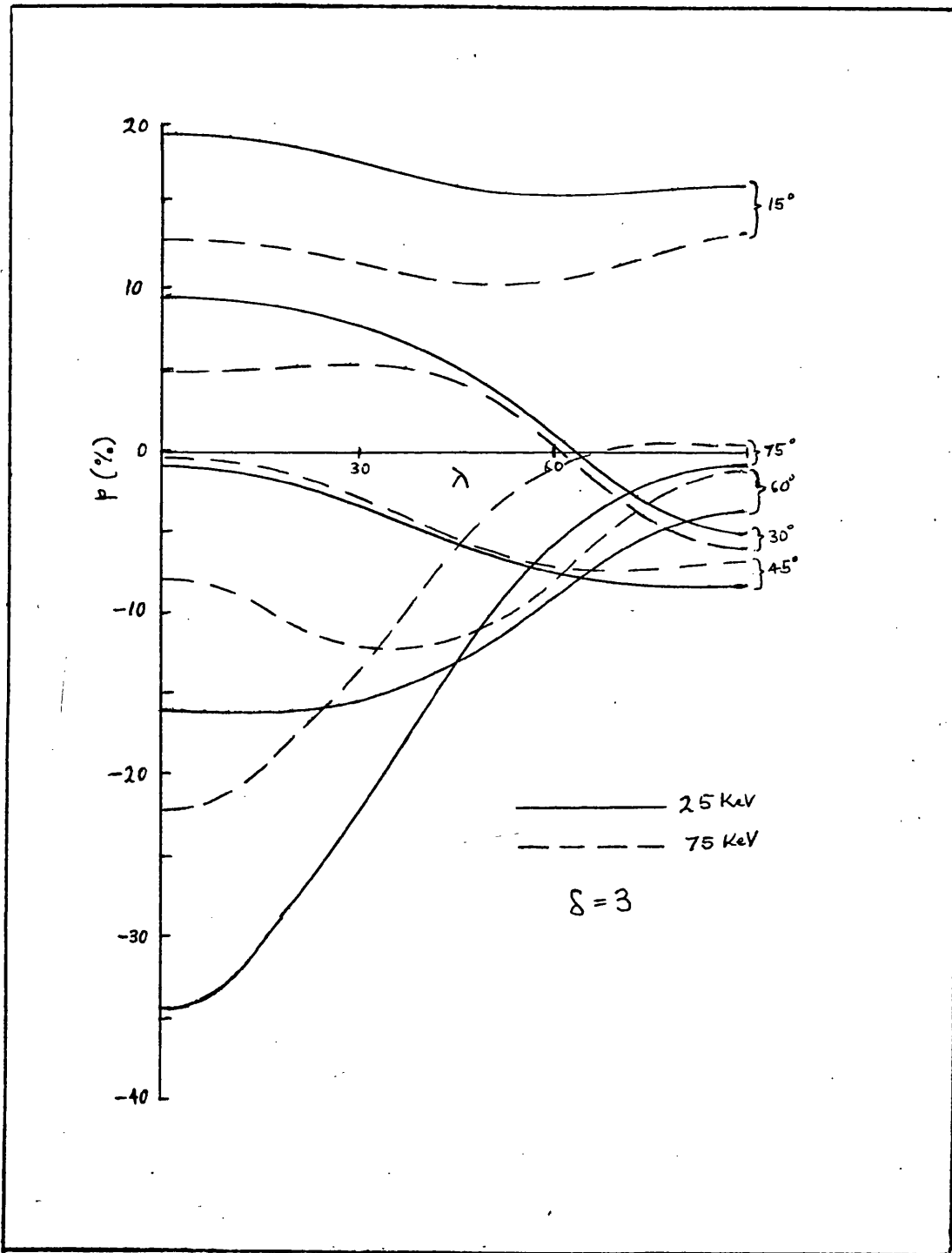


**Figure 4.4** Electron distribution (ii). Polarisation at 25 KeV and 75 KeV as a function of longitude for a trap on the equator, for a range of initial pitch angles. Compare this figure with the corresponding one (Figure 3.12) for distribution (i).

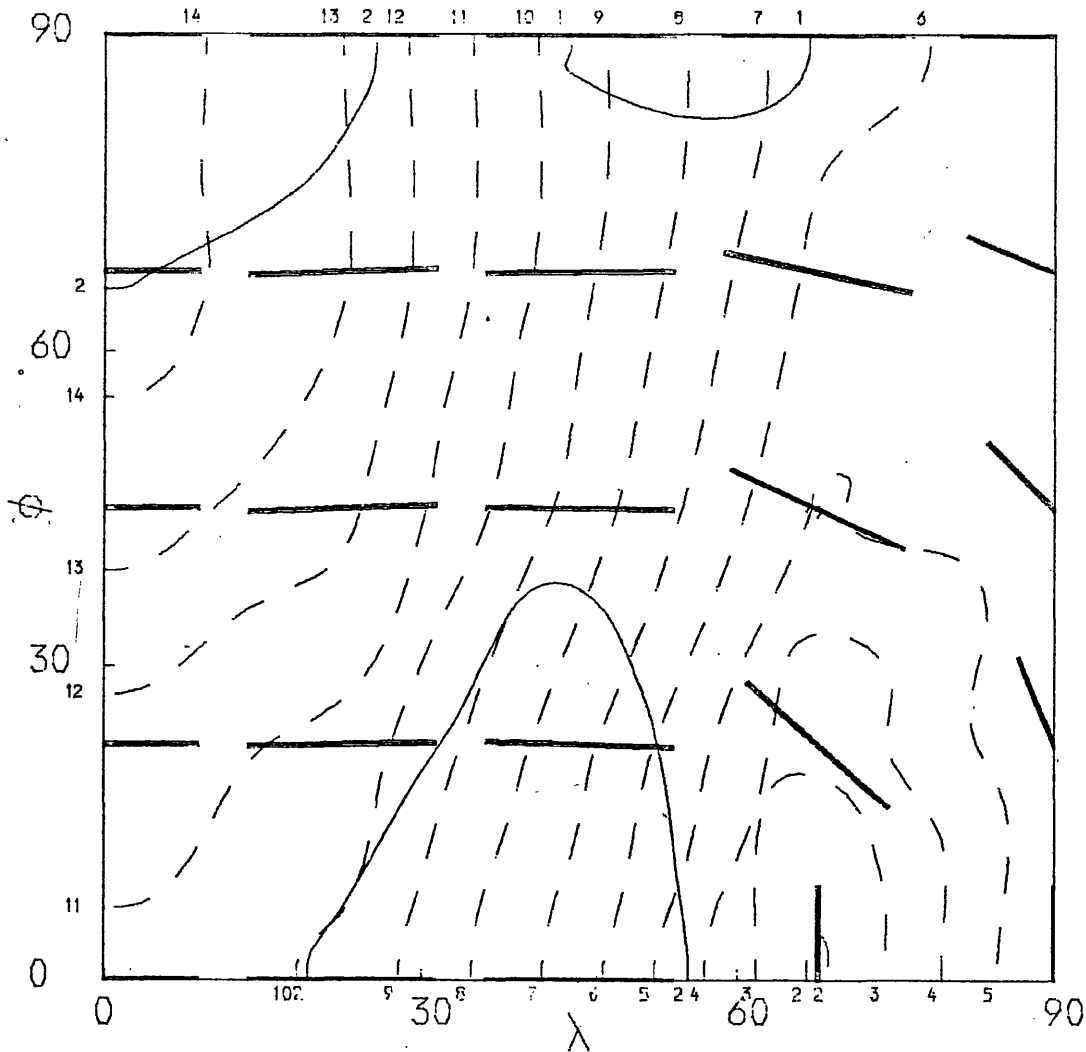
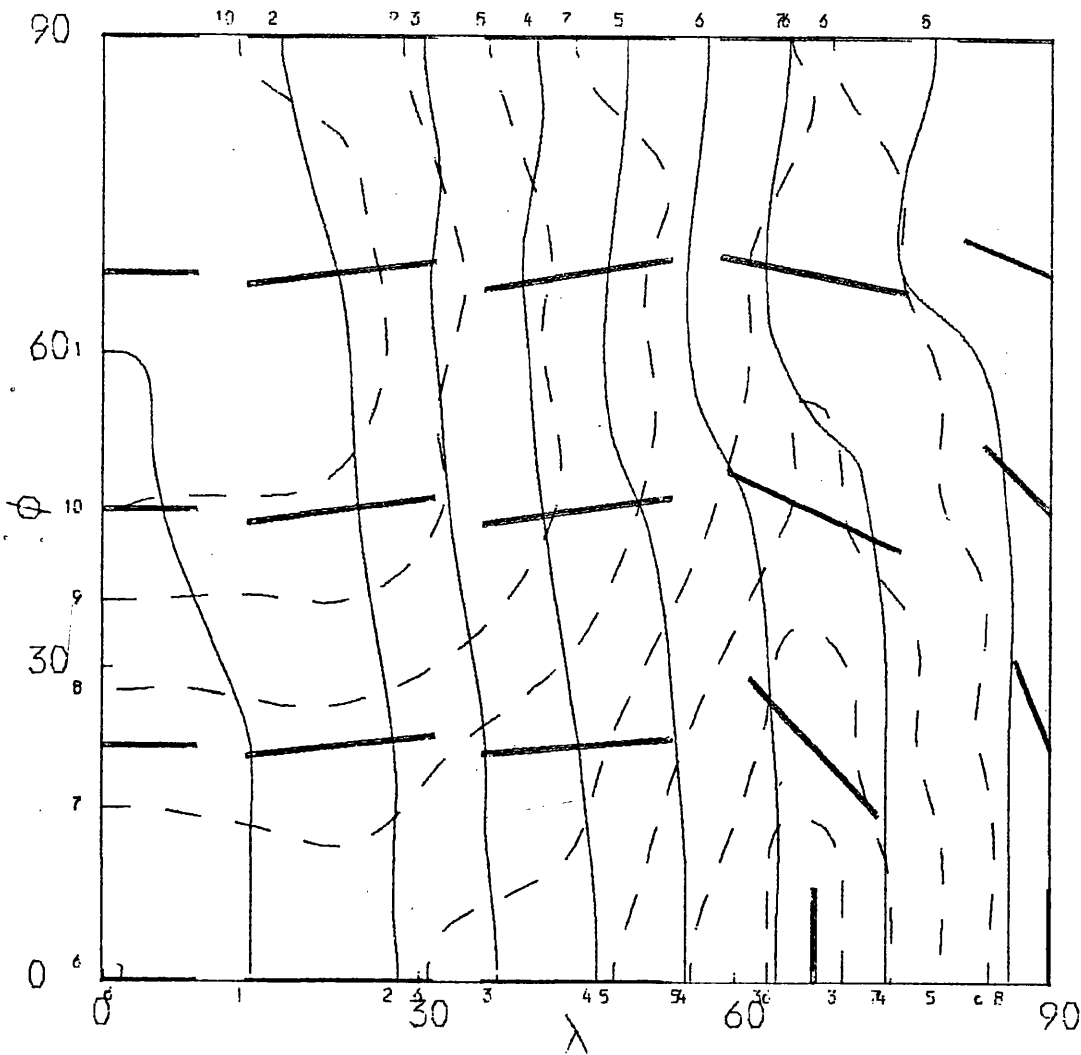


Figure 4.5 Electron distribution (ii). Photon flux and polarisation at  $\epsilon = 25$  KeV for initial pitch angle  $\alpha_0 = 30^\circ$  and electron spectral index  $\delta = 3$ .

$$\mathcal{F} = 7.4 + 0.1 (n_F - 1) \text{ cm}^{-2} \text{ sec}^{-1} \text{ KeV}^{-1}; \quad p = (n_p - 1) \%$$



**Figure 4.6** Electron distribution (ii). Photon flux and polarisation at  $\epsilon = 75$  KeV for initial pitch angle  $\alpha_0 = 30^\circ$  and electron spectral index  $\delta = 3$ .

$$\mathcal{J} = 0.145 + 0.005 (n_F - 1) \text{ cm}^{-2} \text{ sec}^{-1} \text{ KeV}^{-1}; \quad p = (n_p - 1) \%$$

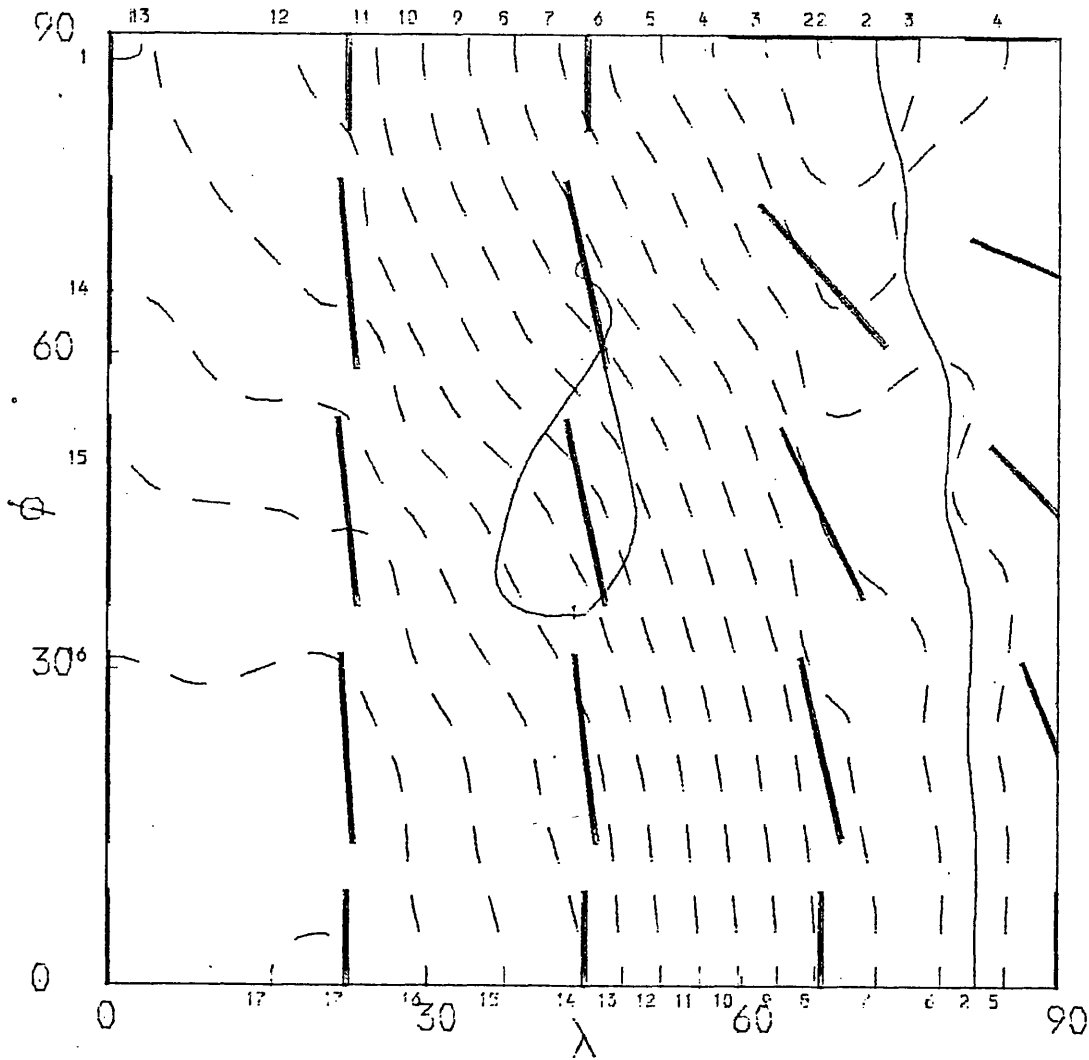
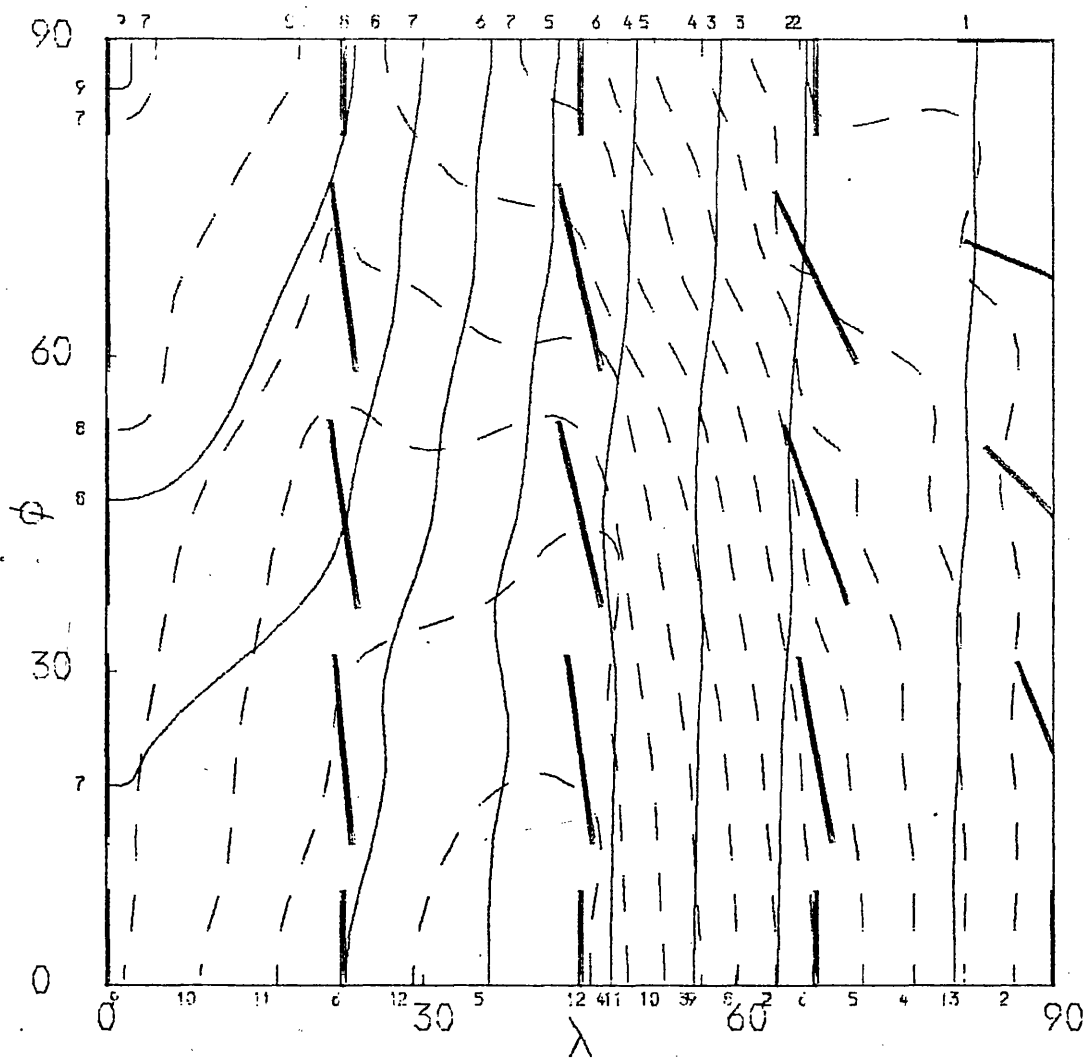


Figure 4.7 Electron distribution (ii). Photon flux and polarisation at  $\epsilon = 25$  KeV for initial pitch angle  $\alpha_0 = 60^\circ$  and electron spectral index  $\delta = 3$ .

$$\mathcal{F} = 6.1 + 0.1 (n_F - 1) \text{ cm}^{-2} \text{ sec}^{-1} \text{ KeV}^{-1}; \quad p = (n_p - 1) \%$$



**Figure 4.8** Electron distribution (ii). Photon flux and polarisation at  $\epsilon = 75$  KeV. for initial pitch angle  $\alpha_0 = 30^\circ$  and electron spectral angle  $\delta = 3$ .

$$\mathcal{F} = 0.105 + 0.005 (n_F - 1) \text{ cm}^{-2} \text{ sec}^{-1} \text{ KeV}^{-1}; \quad p = (n_p - 1) \%$$

with the maximum polarisation for distribution (i) at 80 KeV (see Figures 3.3, 3.5, 3.7, 3.9 and 3.11).

Finally, Figures 4.5 - 4.8 show the distribution of photon flux and polarisation as a function of trap position, for initial pitch angles of  $30^\circ$  and  $60^\circ$ , at photon energy 25 KeV and 75 KeV. Because of the wider grid spacing used in computing these results, the contours are not as well defined as those presented in 3. Superfluous wiggles should be ignored.

From Figures 4.5 and 4.7 we see that the directivity is low ( $\lesssim 3\%$ ) at 25 KeV, as we found from the fluxes calculated on the equator only. At 75 KeV the maximum directional effects amount to  $\sim 35\%$  variation. A comparison of these figures with Figures 3.4, 3.5, 3.8 and 3.9 shows that the dependence of the polarisation on latitude and longitude is very similar, as we suspected from a study of the longitude dependence only.

For distribution (i) the direction of polarisation is independent of photon energy. Here we see that it depends weakly on photon energy, the maximum difference between the polarisation angles at 25 and 75 KeV being  $\lesssim 10^\circ$ .

## 5. ELECTRON DISTRIBUTION (iii)

We now examine briefly the effect and polarisation of X-ray emission of the introduction of a distribution over pitch angle on the directivity. Since this electron distribution involves the evaluation of a quadruple integral and so is expensive in computer time, we calculate only the characteristics of X-ray emission from a trap on the equator, for  $\sin^2 \alpha_0$  and  $\cos^2 \alpha_0$  initial pitch angle distributions. The variation of photon flux and spectral index across the disc are shown in Figure 5.1, while Figure 5.2 illustrates the variation of polarisation.

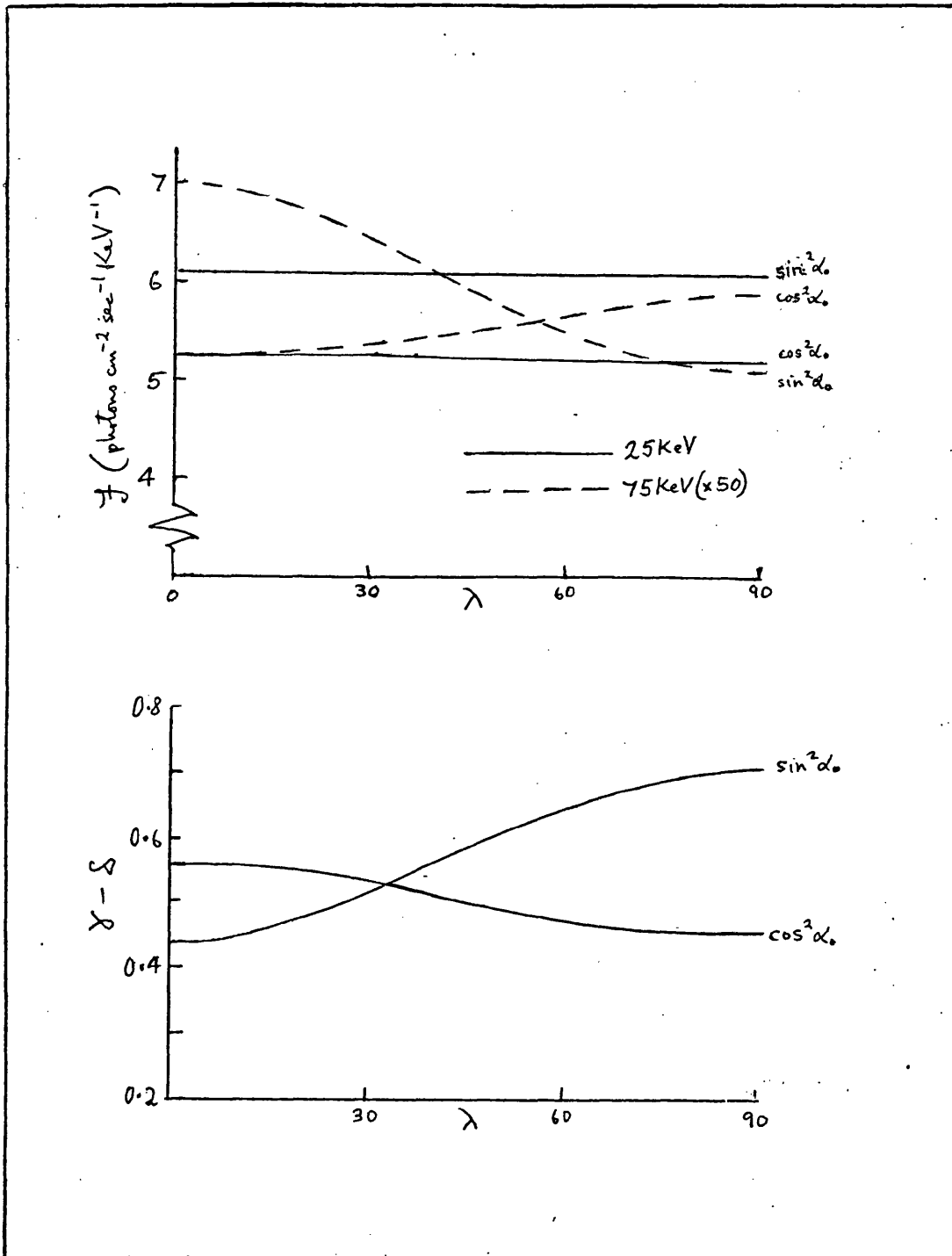


**Figure 5.1** Electron distribution (iii). Photon flux and spectral index as a function of longitude for a trap on the equator at photon energies of 25 and 75 KeV. Results are shown for pitch angle distributions of the form  $\sin^2 \alpha_0$  and  $\cos^2 \alpha_0$ . The electrons have an  $E^{-3}$  energy distribution.

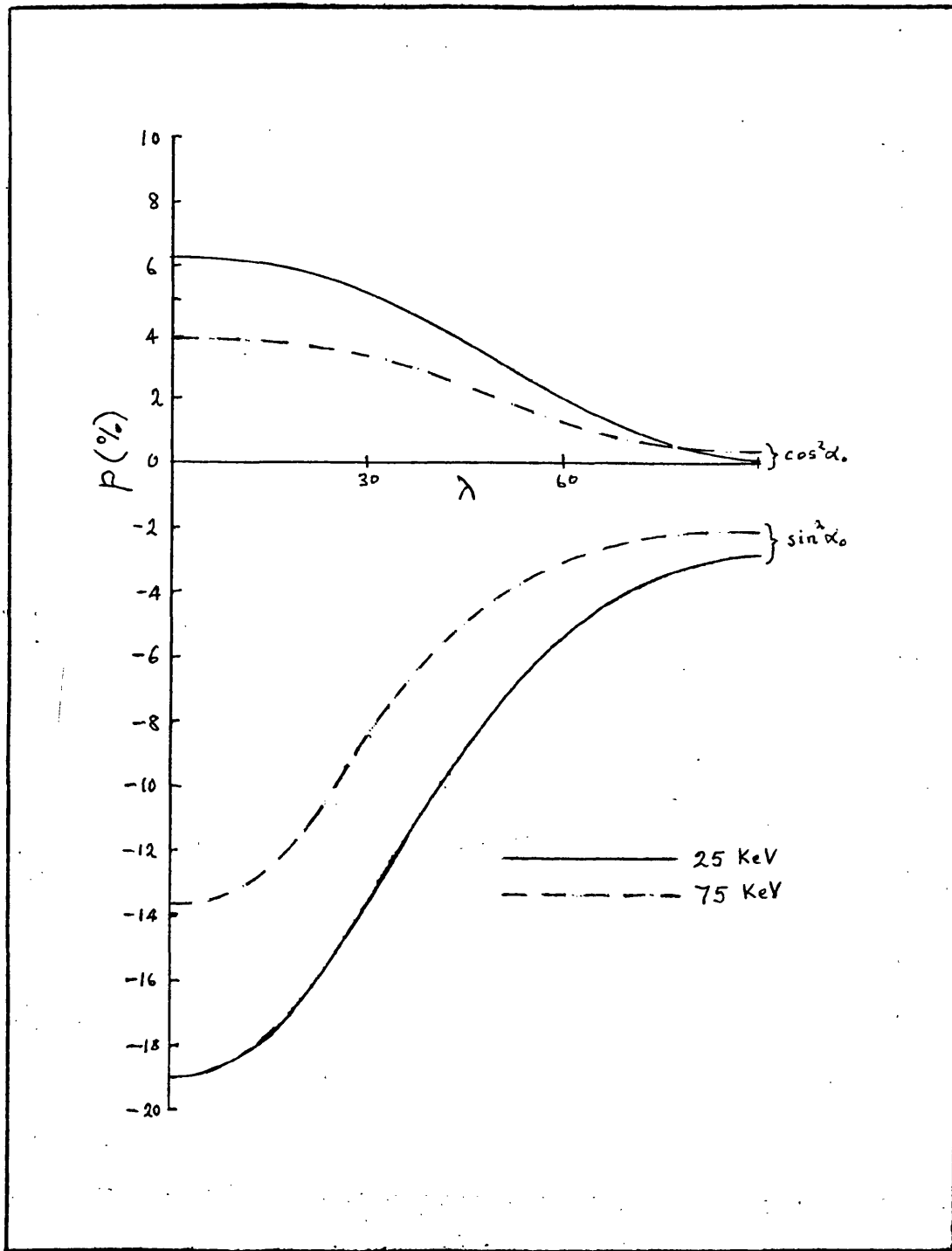


**Figure 5.2** Electron distribution (iii). Polarisation as a function of longitude for a trap on the equator, at photon energies of 25 and 75 KeV. Results are shown for pitch angle distributions of the form  $\sin^2 \alpha_0$  and  $\cos^2 \alpha_0$ . The electrons have an  $E^{-3}$  energy distribution.

As anticipated, results are similar to those obtained previously, but variations are of reduced magnitude due to partial cancellation of the contributions from electrons of different pitch angles. From the upper part of Figure 5.1, we see that at 75 KeV limb-brightening of  $\sim 12\%$  occurs for the  $\cos^2 \alpha_0$  distribution and limb-darkening of  $\sim 25\%$  for the  $\sin^2 \alpha_0$  distribution. These values may be compared with those found for distribution (ii), where an initial pitch angle of  $30^\circ$  gave 30% limb-brightening and an initial pitch angle of  $75^\circ$  gave 45% limb-darkening. Thus cancellation of the effects produced by different pitch angle electrons have reduced the directivity.

Electrons which penetrate to a depth of greater than  $5 \times 10^3$  km above the photosphere are assumed to be lost instantly through collisional degradation. This means that electrons of initial pitch angle less than  $13^\circ$  do not contribute to the emission and so the photon flux is lower when small pitch angles predominate.

The variation of spectral index across the disc, shown in the lower part of Figure 5.1, is similar to that found for large and small pitch angles in distribution (ii), but the extent of variation is reduced by  $\sim 50\%$ .

Turning now to the polarisation, shown in Figure 5.2, we look first at the results for a  $\sin^2 \alpha_0$  initial pitch angle distribution. The greatest number of electrons (per unit pitch angle range) have pitch angles of  $90^\circ$  and would alone give a maximum polarisation larger than that of the  $75^\circ$  pitch angle electrons in distribution (ii). However, the presence of electrons in the distribution which emit radiation polarised in the opposite direction reduces the maximum polarisation to only half of that seen in Figure 4.4. The longitude dependence of polarisation for a  $\cos^2 \alpha_0$  initial pitch angle electron distribution is similar to that shown in Figure 4.4 for  $\alpha_0 = 15^\circ$ . In this case the polarisation is reduced to  $\sim 1/3$  of the value found for distribution (ii).

## 6. ELECTRON DISTRIBUTION (iv)

In this distribution, initial pitch angle is related to electron energy by

$$\sin^2 \alpha_0 = E^*/E \quad (6.1)$$

where  $E^*$  is a constant.

Since the electron pitch angles are energy dependent, this distribution should provide more interesting results than the previous two distributions. These have in the main confirmed and quantified the tentative conclusions drawn from distribution (i).

Although the situation here is more complex than has been considered previously we can still anticipate some general trends from the results obtained in previous sections. We expect that the directivity will still be small. Polarisation at low photon energies should be similar to that found previously for large pitch angles, while at high photon energies it should follow the trends previously found for small pitch angles. We expect that, as in distribution (iii), the peak values of polarisation will be reduced somewhat from those found for distribution (ii) because of averaging over a range of pitch angles. This occurs since photons of energy  $\epsilon$  are emitted predominantly by electrons with energy  $\epsilon$  to  $\sim 2 - 3 \times \epsilon$ , over which range the electron pitch angle changes appreciably, particularly at low energy.

In previous distributions we have taken the power law electron energy spectrum to extend to infinity. In this case, however, the spectrum cuts off at the energy corresponding to an initial pitch angle of  $13^\circ$ . Since electrons of smaller pitch angle mirror below  $5 \times 10^3$  km and are assumed to be stopped instantly.

Figure 6.1 illustrates the relationship between initial pitch angle and electron energy for  $E^* = 5, 10$  and  $20$  KeV. For any given value of  $E^*$ , the electron spectrum extends over only a limited

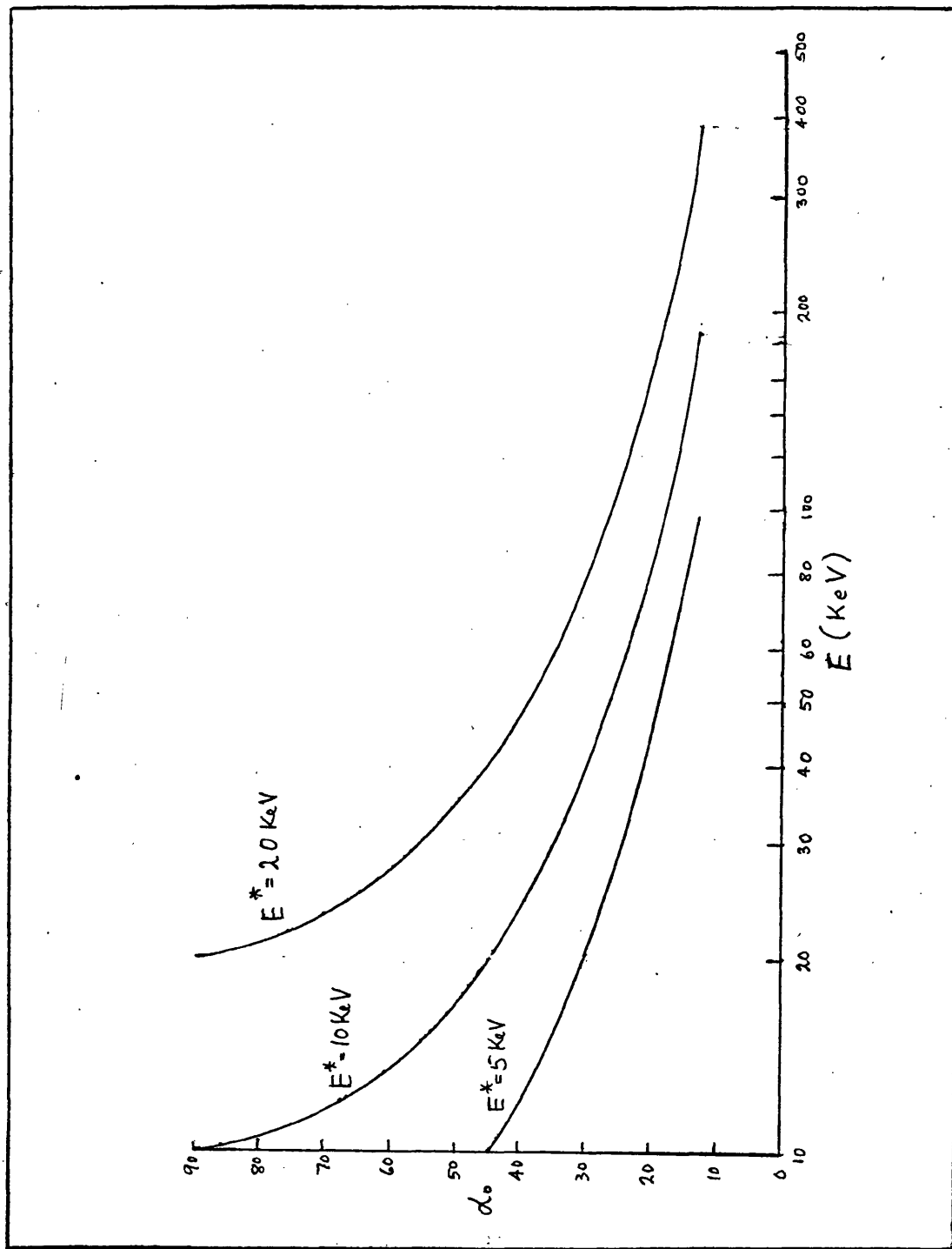


Figure 6.1 Electron distribution (iv). Initial pitch angle as a function of electron energy for  $E^* = 5, 10$  and  $20 \text{ KeV}$ .

range of energy. It is fairly certain from observation that the non-thermal X-ray spectrum extends down to 10 KeV, and Kahler and Kreplin (1971) claim that in some cases it extends down to less than 5 KeV. Since the spectrum we use here ceases to be non-thermal at  $E \approx E^*$ , the electron distribution with  $E^* = 5$  KeV would appear to be the most realistic of those shown in Figure 6.1.

On the other hand, X-ray spectra are frequently observed to extend to energies greater than 300 KeV (see, for example, Suri *et al.*, 1975). This suggests that the curve shown in Figure 6.1 for  $E^* = 20$  KeV is the most realistic.

But solar flares, and the hard X-ray bursts associated with them, are extremely diverse in nature. If we try to explain not those bursts whose spectrum extends to high energy, but those which exhibit a break in the photon spectrum, then this model is more successful. The break in the photon energy, at which the "power-law index" increases by  $\sim \frac{1}{2} - 2$  powers is usually found in the energy range 60-100 KeV, but sometimes at higher energy. Although the pitch angle/energy relationship used here implies a definite cutoff in the photon spectrum at 97, 195 or 390 KeV for  $E^* = 5, 10$  or 20 KeV, respectively, in reality a certain spread in pitch angle associated with a given electron energy is to be expected. Thus some electrons with energy higher than the cutoff energy will remain trapped. Note that the value of the cutoff energy depends critically on the assumed minimum pitch angle for trapping. In addition to the expected spread in the energy/pitch angle relationship, the finite diameter of a real coronal trap, as opposed to the single field line approximation considered here, will give rise to a dispersion in minimum pitch angle.

Whether the photon spectrum above the break predicted by this model, when the above considerations are taken into account, is close enough to a power law to satisfy the observational evidence, is an open question which will not be considered further here.

As in §4, we begin by examining the dependence of spectral index and polarisation on photon energy. Results are shown in Figures 6.2, 6.3 and 6.4, for  $E^* = 5, 10$  and  $20$  KeV respectively. The trap position  $(\phi, \lambda)$  is shown against each curve. It is immediately clear that the introduction of an energy dependent pitch angle distribution has complicated matters considerably. Even for  $E^* = 20$  KeV, where the cutoff energy is nearly  $300$  KeV, the photon spectrum below  $100$  KeV could hardly be described as a power law. Both spectral index and polarisation are stronger functions of photon energy and trap orientation than in the electron distributions considered previously.

We can, however, find some general trends in the behaviour of the polarisation. The results shown in Figures 6.2, 6.3 and 6.4 begin to make sense if we plot the polarisation as a function of  $\epsilon/E^*$  (Figure 6.5). Here the three left most curves, spanning  $1 < \epsilon/E^* < 5$ , are for  $E^* = 20$  KeV, the middle three for  $E^* = 10$  KeV, and the rightmost set for  $E^* = 5$  KeV. Note that, from (6.1), the ratio of cutoff energy  $E_c$  to  $E^*$  is constant. For the field model and mirror height cutoff used,  $E_c/E^* = 19.5$ , therefore the upper limit of  $\epsilon/E^*$  in Figure 6.5 represents the short wavelength limit.

The polarisation is negative when  $\epsilon = E^*$ , as might be expected since most of the electrons emitting photons of this energy have large pitch angles and are trapped near the top of the arch. If the trap is viewed from above  $((\phi, \lambda) = (0, 0))$  the polarisation becomes positive at  $\epsilon/E^* \approx 1.5$  and increase monotonically with photon energy. If trap is viewed side-on  $((\phi, \lambda) = (90, 0))$  the polarisation becomes positive and reaches a peak value of  $\sim 12\%$  at  $\epsilon/E^* \approx 2$ , thereafter decreasing with photon energy to become small near the short wavelength. Polarisation of emission from a trap seen end-on  $((\phi, \lambda) = (0, 90))$  becomes more negative initially, reaching a minimum of  $\sim -8\%$  at  $\epsilon/E^* \approx 2$ , after which it increases monotonically with photon energy passing through zero at  $\epsilon/E^* \approx 4$ , to attain a large positive value ( $\sim 45\%$ ) at the short wavelength limit.

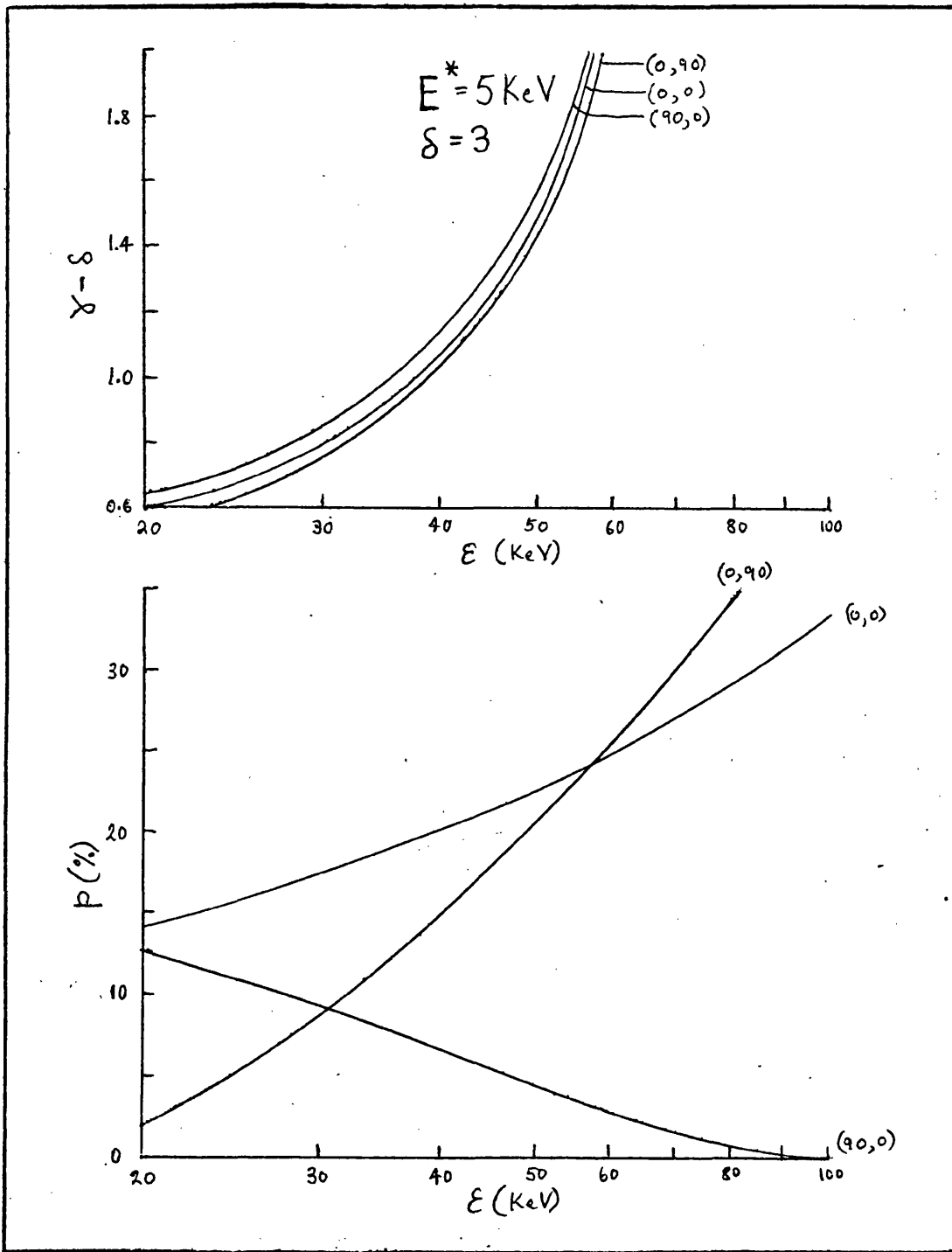
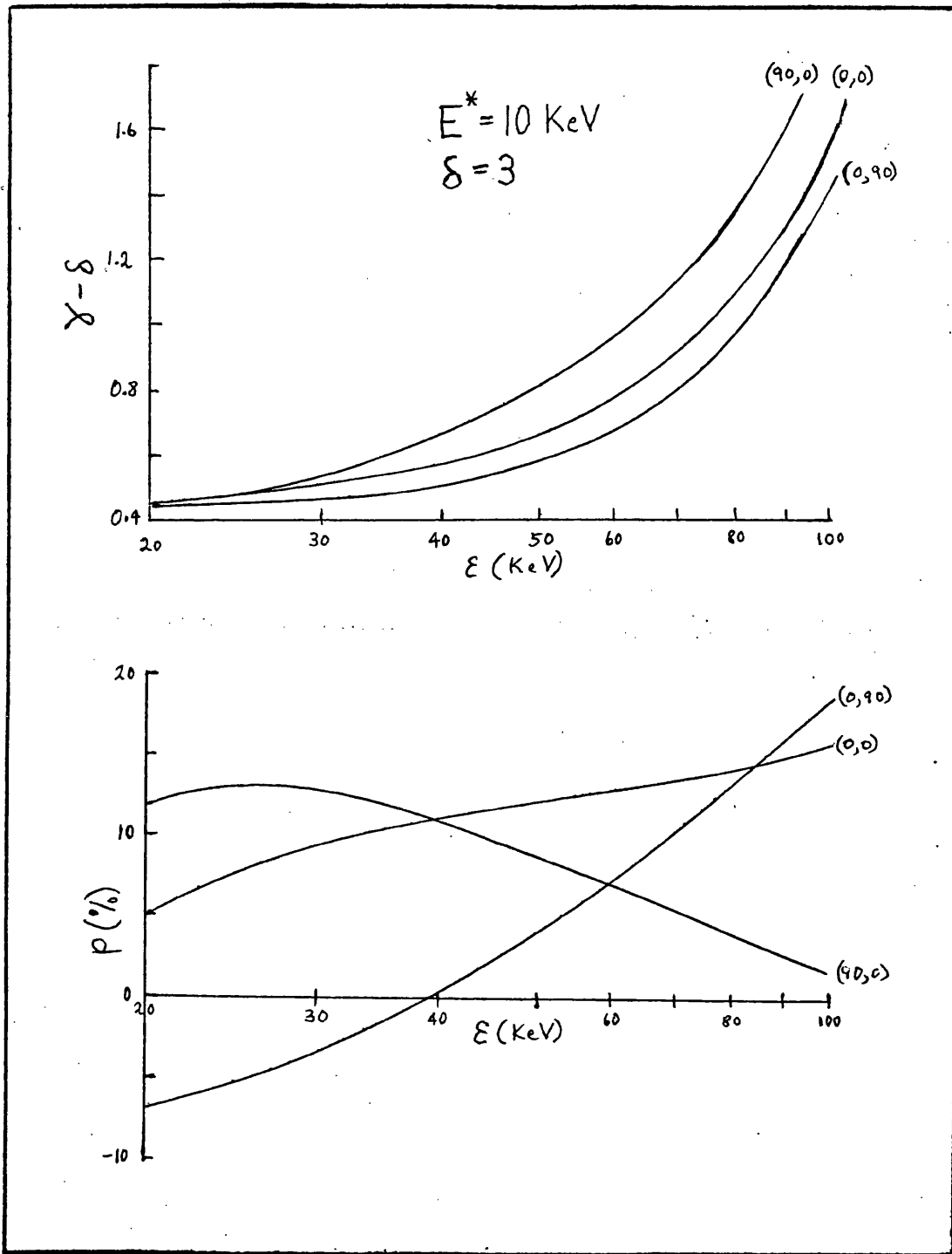


Figure 6.2 Electron distribution (iv). Spectral index and polarisation as a function of photon energy for  $E^* = 5 \text{ KeV}$  and  $\delta = 3$ . Results are shown for a trap at positions  $(\phi, \lambda) = (0, 0)$ ,  $(0, 90)$  and  $(90, 0)$  (top view, end-on and side-on).



**Figure 6.3** Electron distribution (iv). Spectral index and polarisation as a function of photon energy for  $E^* = 10 \text{ KeV}$  and  $\delta = 3$ . Results are shown for a trap at positions  $(\phi, \lambda) = (0, 0)$ ,  $(0, 90)$  and  $(90, 0)$  (top view, end-on and side-on).

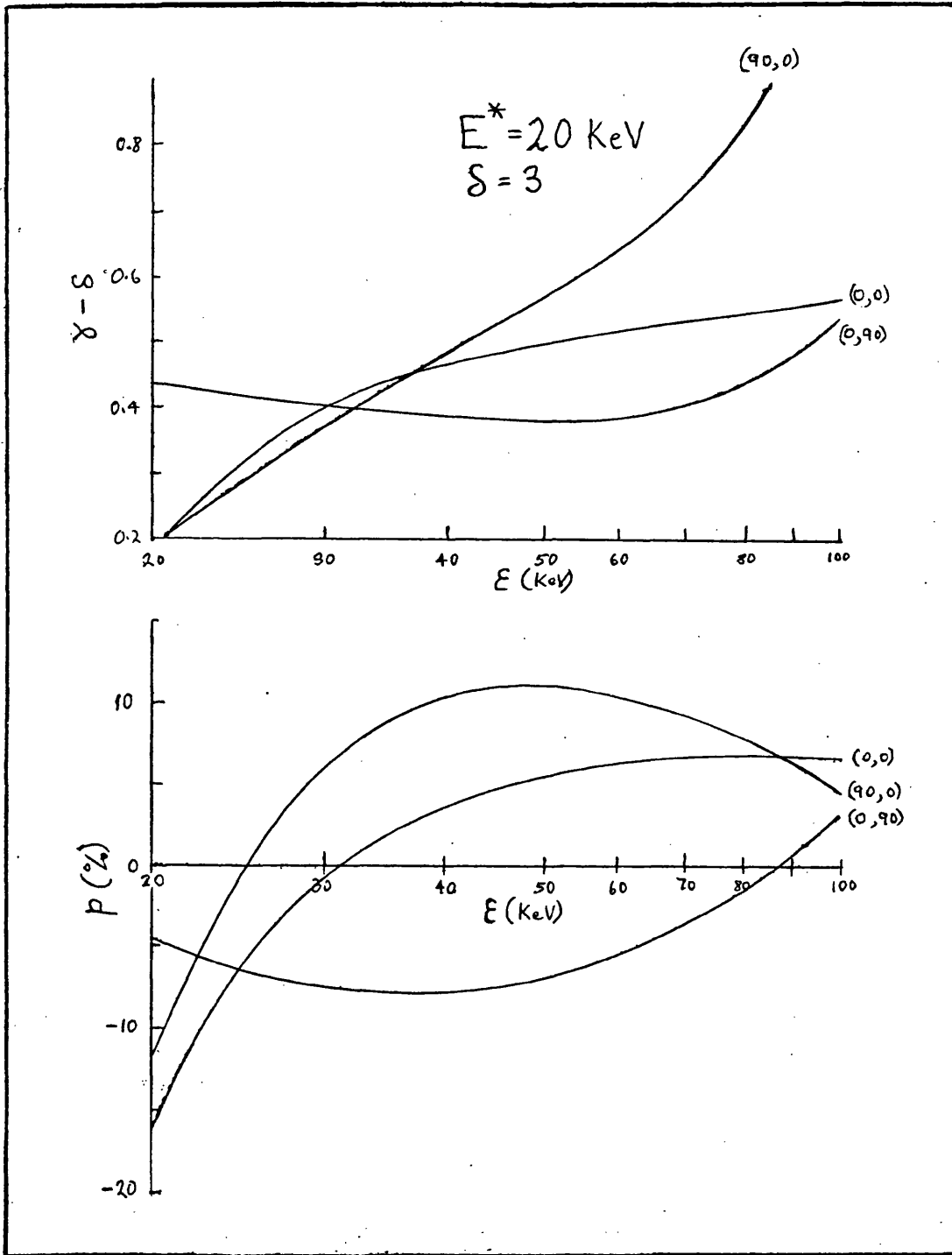


Figure 6.4 Electron distribution (iv). Spectral index and polarisation as a function of photon energy for  $E^* = 20$  keV and  $\delta = 3$ . Results are shown for a trap at positions  $(\phi, \lambda) = (0,0)$ ,  $(0,90)$  and  $(90,0)$  (top view, end-on and side-on).

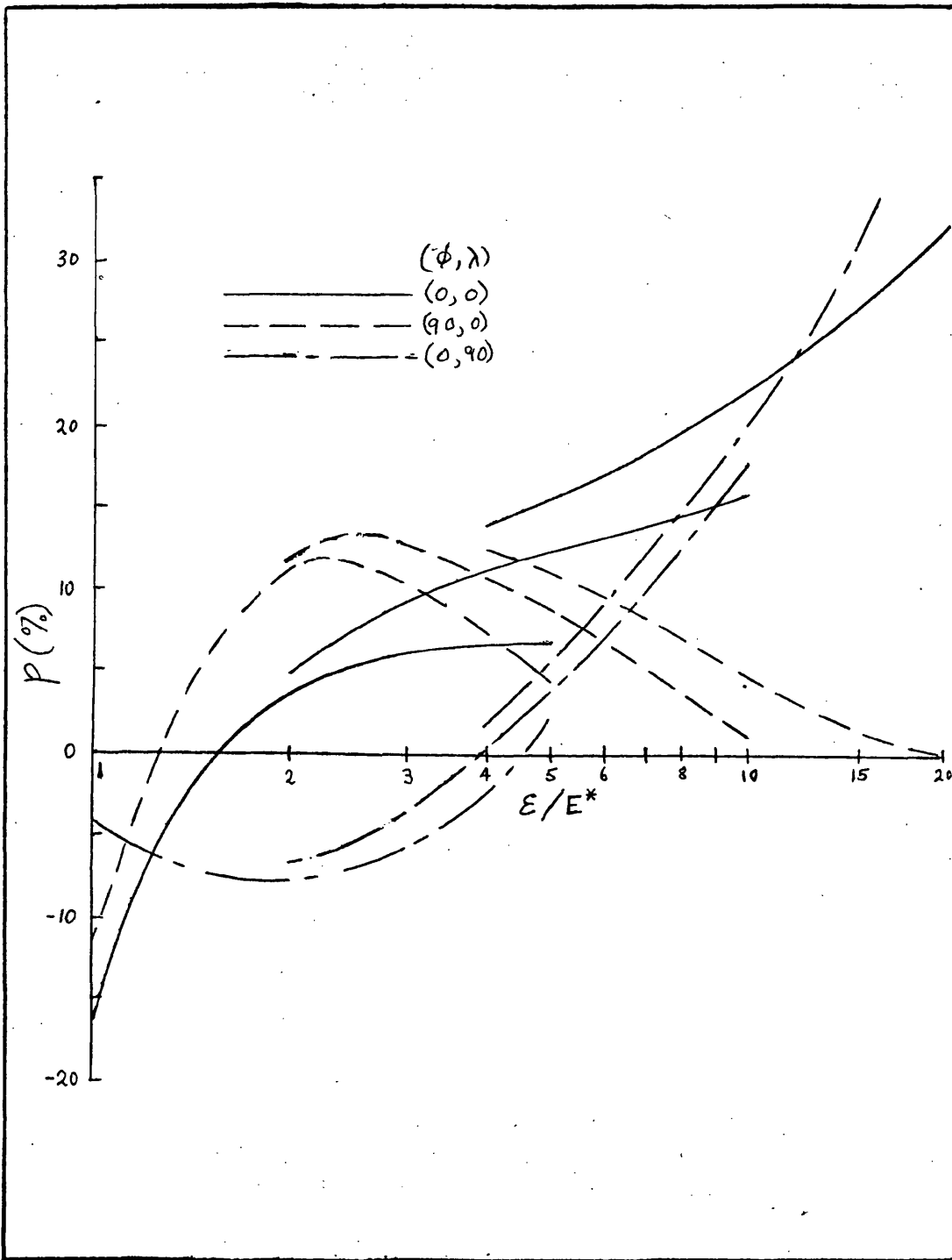


Figure 6.5 Combined results of Figures 6.2 - 6.4, showing polarisation as a function of  $\epsilon/E^*$ .

A mental concatenation of the spectral index curves in Figures 6.2, 6.3 and 6.4, in a manner similar to Figure 6.5, shows that the spectral index is also primarily a function of  $\epsilon/E^*$ . Therefore results showing the dependence of X-ray intensity and polarisation on trap orientation are presented for only one value of  $E^*$ , namely  $E^* = 10$  KeV. Figures 6.6 - 6.11 show the photon flux and polarisation at photon energies of 12, 16, 25, 40, 75 and 150 KeV respectively. In all cases the electron spectral index is 3. On the flux contour labelled  $n$ , the flux is  $2.5 \times n\%$  up on the minimum flux, while on polarisation contour (broken line)  $n$ , the degree of polarisation is  $2.5 \times n\%$ . Thus a comparison of these results illustrates the variation with photon energy of directivity and polarisation over the disk. Since the directivity at 16 KeV and 25 KeV is too small to show more than one contour, the positions of maximum and minimum intensity have been marked + and - respectively in Figures 6.7 and 6.8.

The only generalisation apparent from these results is that minimum brightness occurs near the pole  $(\phi, \lambda) = (90, 0)$  while maximum brightness occurs on the equator or limb.

From Figure 6.1 we see that the initial pitch angles corresponding to energies of 12, 16, 25, 40, 75 and 150 KeV are approximately  $80^\circ$ ,  $60^\circ$ ,  $45^\circ$ ,  $30^\circ$ ,  $30^\circ$  and  $15^\circ$  respectively. Since photons of energy  $\epsilon$  are emitted predominantly by electrons with rather higher energy ( $\epsilon < E \lesssim 2-3 \epsilon$ ) we expect that the characteristics of X-ray emission at the above energies might be similar to the results obtained previously for initial pitch angles of  $60^\circ$ ,  $45^\circ$ ,  $30^\circ$ ,  $15^\circ$ ,  $15^\circ$  and  $15^\circ$  respectively. In Table 6.1 the gross characteristics of the results displayed in Figures 6.6 - 6.11 are compared with the results obtained for electron distribution (i). (Figures 3.2 - 3.11).

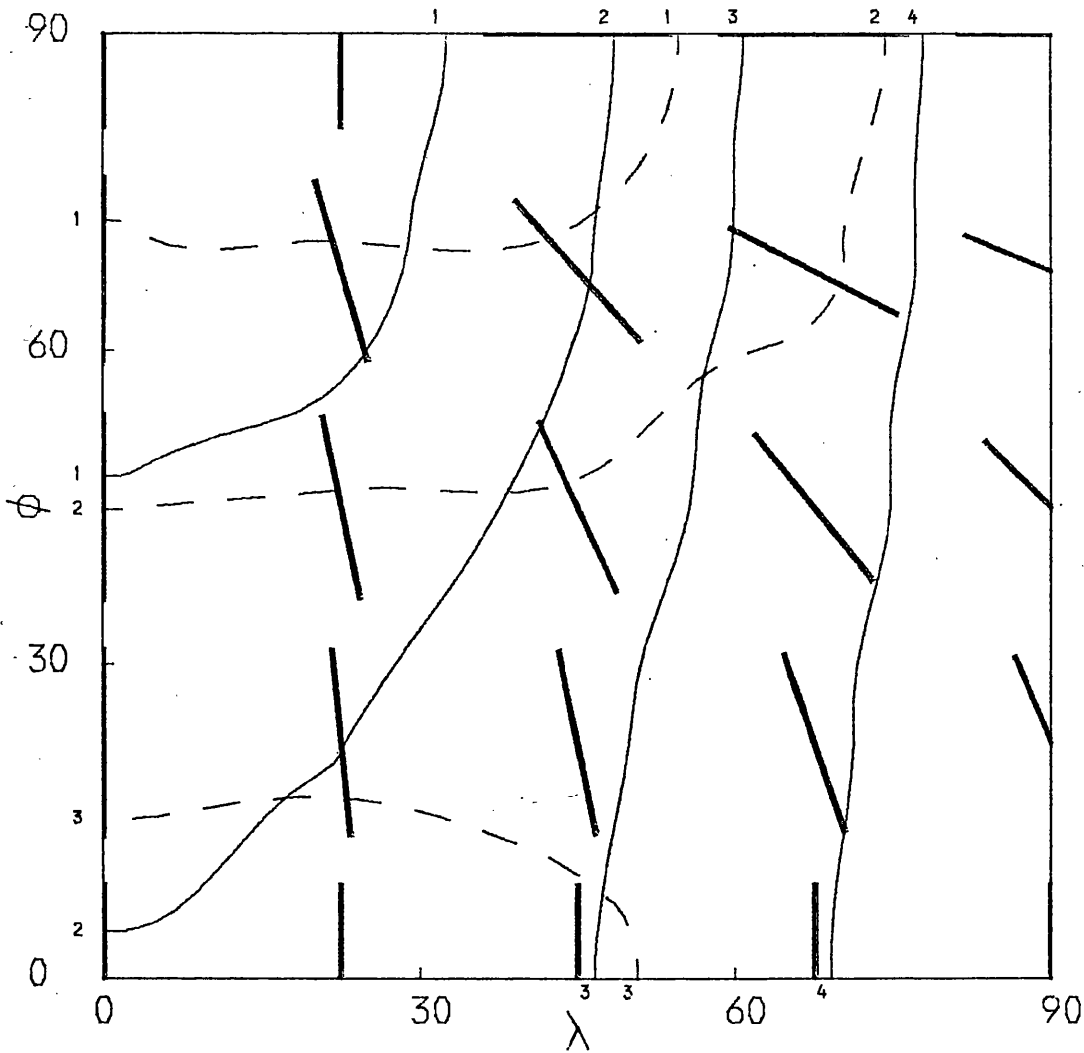


Figure 6.6 Electron distribution (iv). Photon flux (—) and polarisation (---) at  $\epsilon = 12$  KeV, for  $E^* = 10$  KeV and  $\delta = 3$ .  $\mathcal{Y} = \mathcal{Y}_{\min} (1 + n_F/40)$ ;  $p = n_p/40$ .  $\mathcal{Y}_{\min} = 85.9$   $\text{cm}^{-2} \text{sec}^{-1} \text{KeV}^{-1}$ .

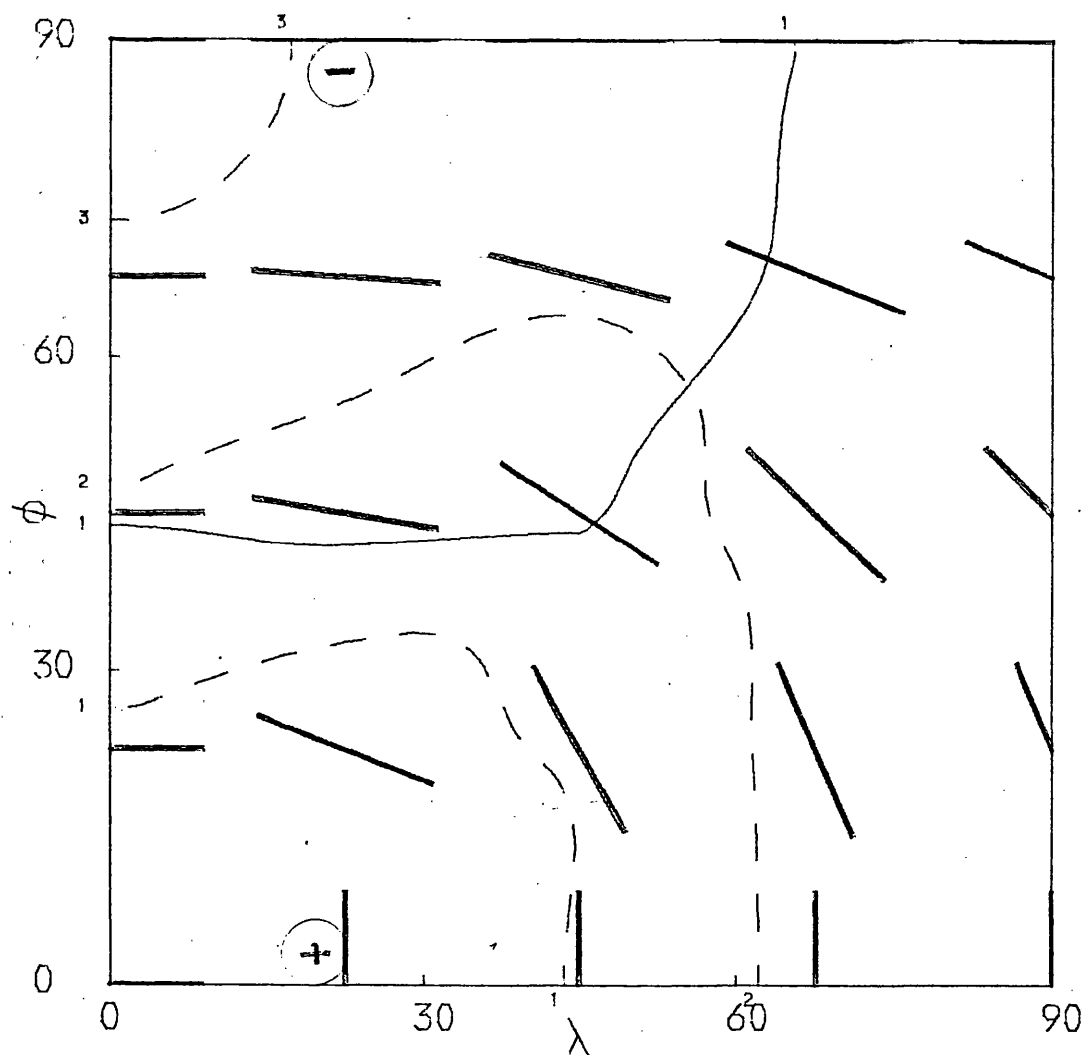


Figure 6.7 Electron distribution (iv). Photon flux (————) and polarisation (-----) at  $\epsilon = 16$  KeV, for  $E^* = 10$  KeV and  $\delta = 3$ .  $\mathcal{F} = \mathcal{F}_{\min} (1 + n_F/40)$ ;  $p = n_p/40$ .  $\mathcal{F}_{\min} = 33.1$   $\text{cm}^{-2} \text{sec}^{-1} \text{KeV}^{-1}$ .

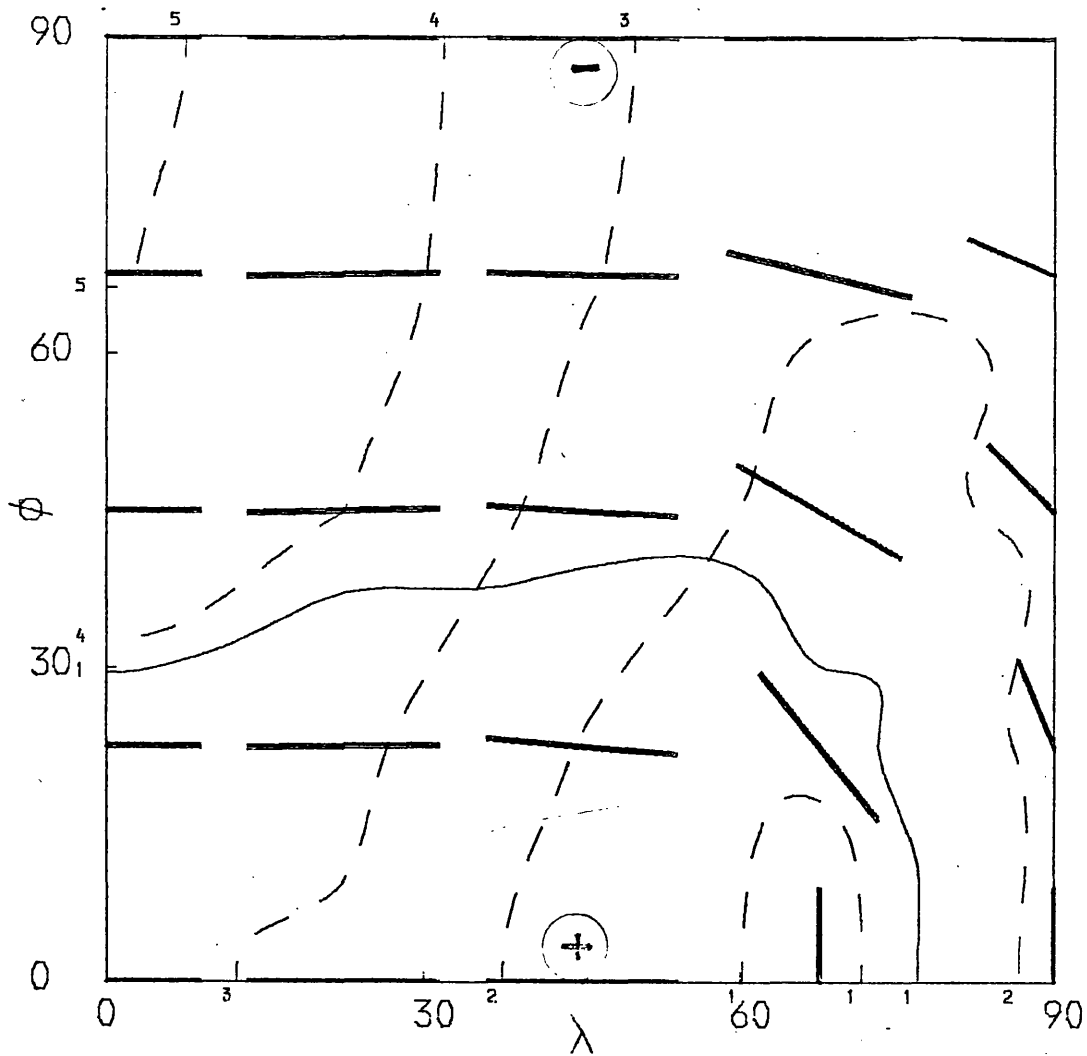


Figure 6.8 Electron distribution (iv). Photon flux (————) and polarisation (-----) at  $\epsilon = 25$  KeV, for  $E^* = 10$  KeV and  $\delta = 3$ .  $\mathcal{J} = \mathcal{J}_{\min} (1 + n_F/40)$ ;  $p = n_p/40$ .  $\mathcal{J}_{\min} = 7.20$   $\text{cm}^{-2} \text{sec}^{-1} \text{KeV}^{-1}$ .

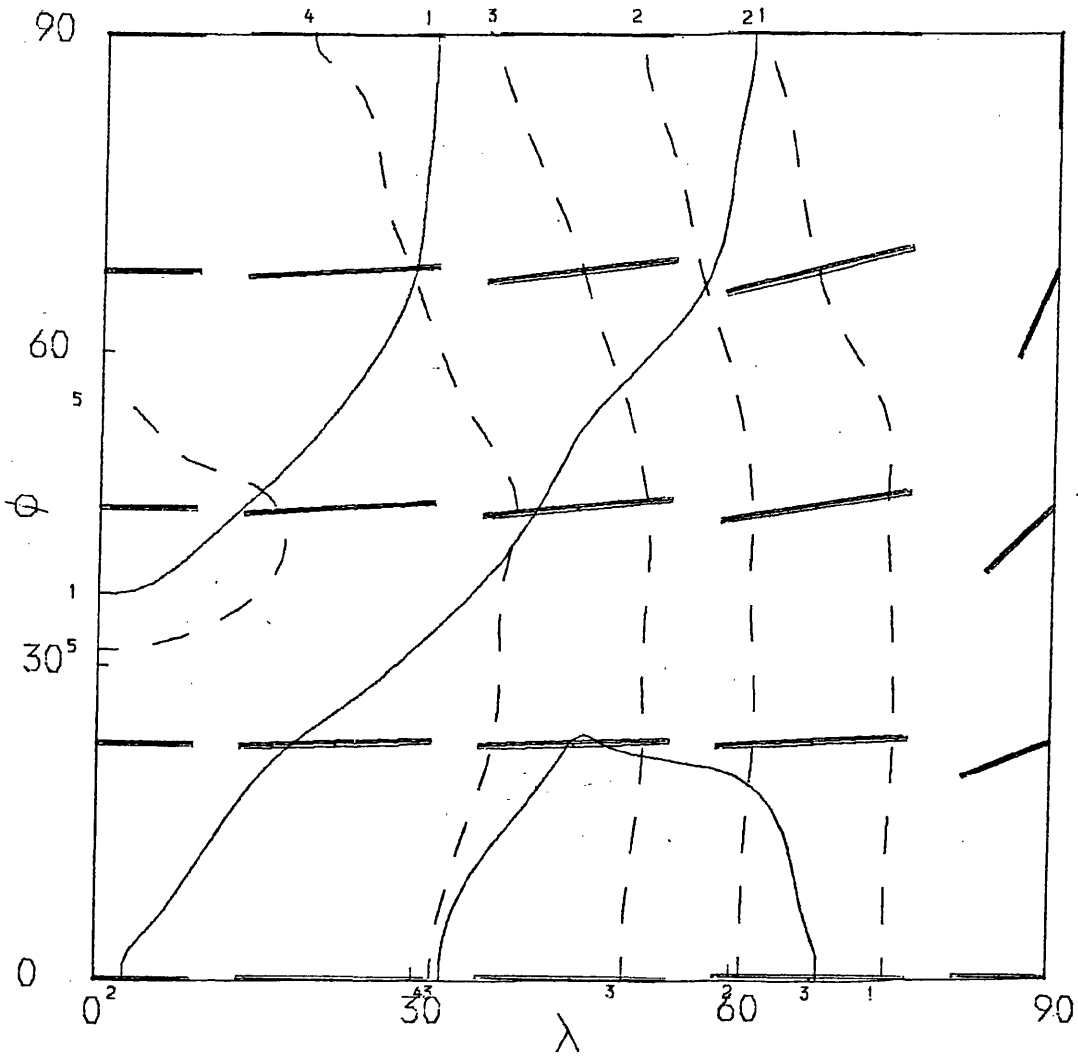


Figure 6.9 Electron distribution (iv). Photon flux (—) and polarisation (---) at  $\epsilon = 40$  KeV, for  $E^* = 10$  KeV and  $\delta = 3$ .  $\mathcal{F} = \mathcal{F}_{\min}(1 + n_F/40)$ ;  $p = n_p/40$ .  $\mathcal{F}_{\min} = 1.35$   $\text{cm}^{-2} \text{sec}^{-1} \text{KeV}^{-1}$ .

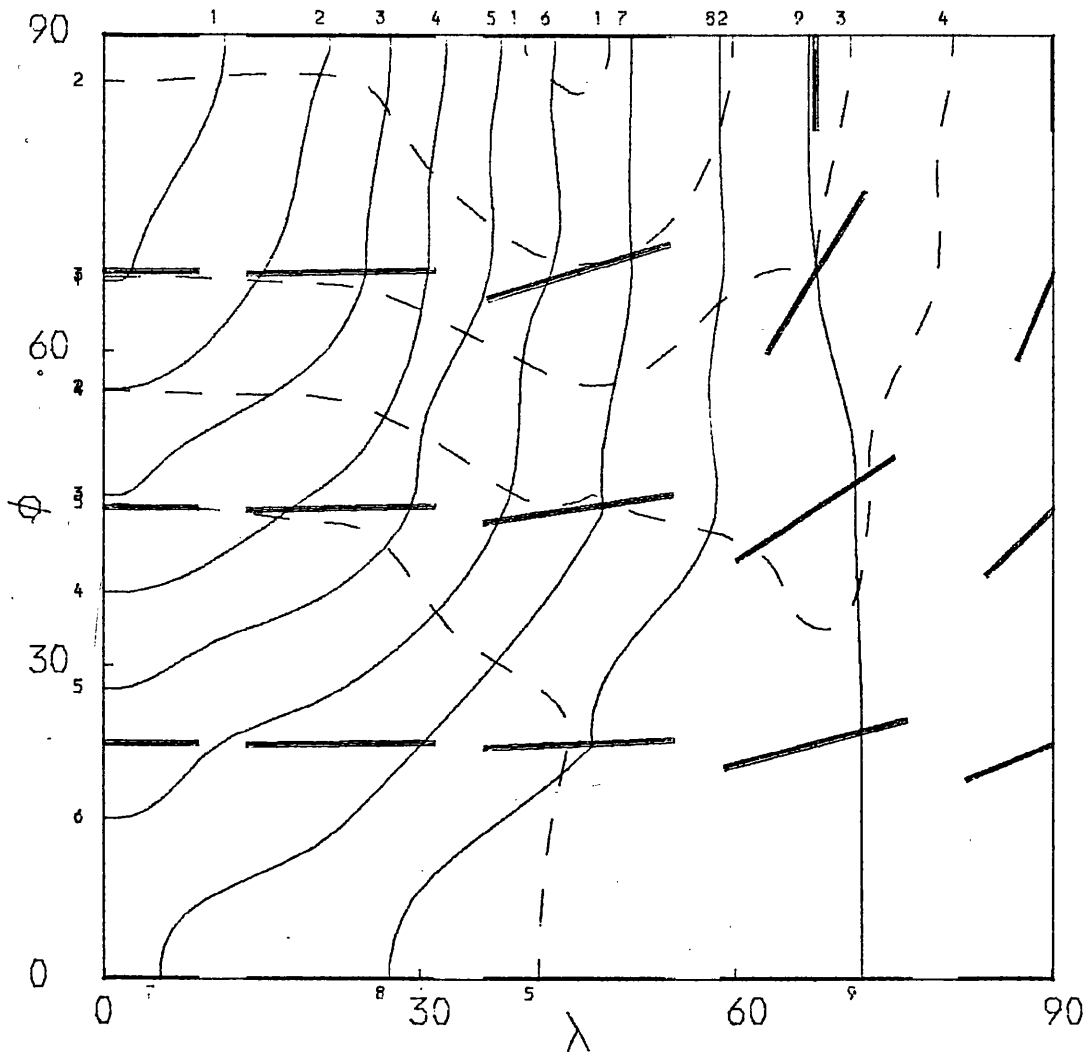


Figure 6.10 Electron distribution (iv). Photon flux (—) and polarisation (---) at  $\epsilon = 75$  KeV, for  $E^* = 10$  KeV and  $\delta = 3$ .  $\mathcal{F} = \mathcal{F}_{\min}(1 + n_F/40)$ ;  $p = n_p/40$ .  $\mathcal{F}_{\min} = 0.116$   $\text{cm}^2 \text{sec}^{-1} \text{KeV}^{-1}$ .

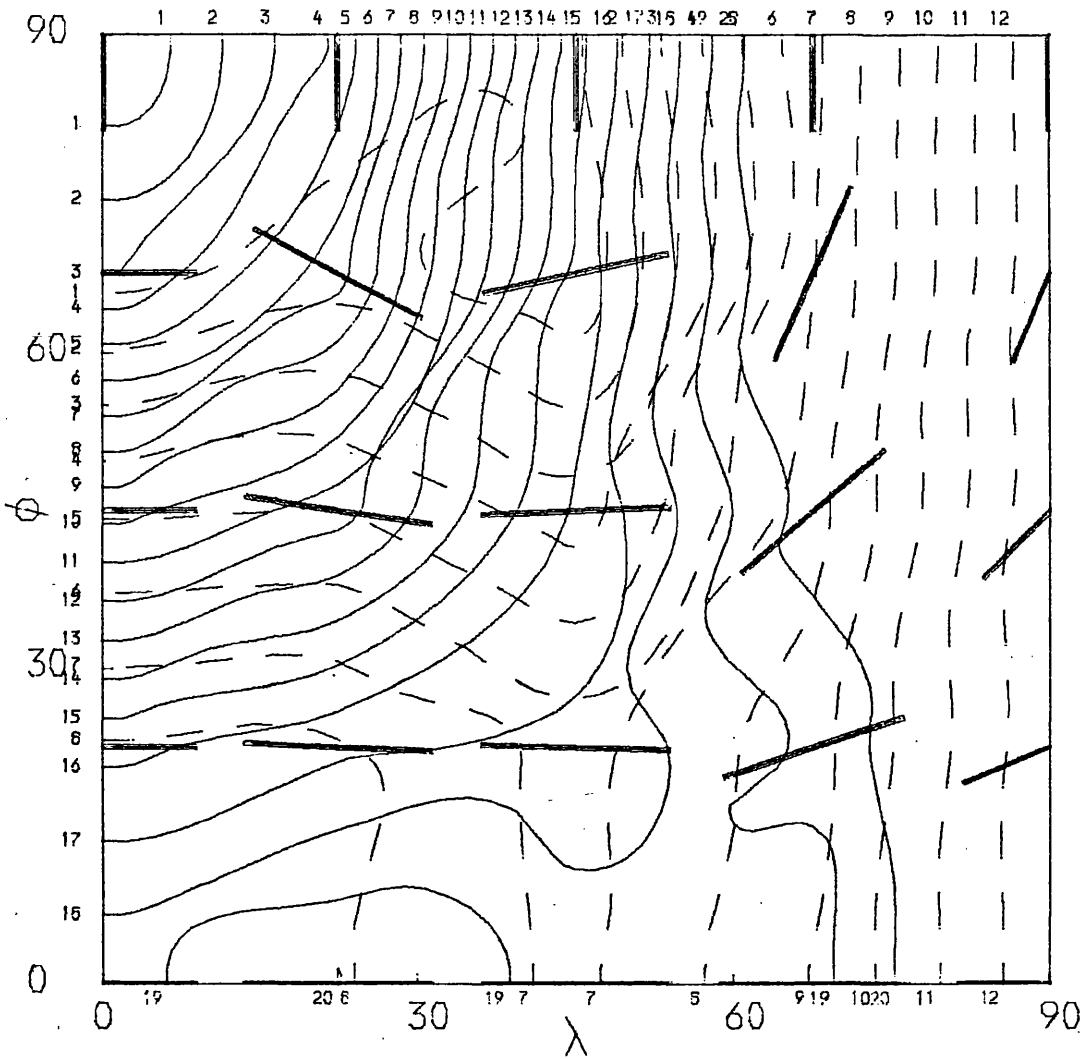


Figure 6.11 Electron distribution (iv). Photon flux (————) and polarisation (-----) at  $\epsilon = 150$  KeV, for  $E^* = 10$  KeV and  $\delta = 3$ .  $\mathcal{F} = \mathcal{F}_{\min} (1 + n_F/40)$ ;  $p = n_p/40$ .  $\mathcal{F}_{\min} = 2.80 \times 10^{-3} \text{ cm}^{-2} \text{ sec}^{-1} \text{ KeV}^{-1}$ .

Table 6.1 Comparison of the energy dependence of directivity and polarisation with results obtained for distribution (i)

		PHOTON ENERGY (KeV)									
		12	16		25	40	75	150			
Directivity	? 15 30	? 15 30	? 15 30	? 15 30	30 80	15 30	15 30	15 30	$\alpha_o$	$\epsilon$ (KeV)	
	10 30	3 30	3 30	3 30	8 14	24 30	50 20	$D_{iv}(\%)$	$D_i(\%)$		
Polarisation	60 30	30 30	30 30	30 30	15-30 80	15 80	15 80	$\alpha_o$	$\epsilon$ (KeV)		
	8 5	8 4	13 4	14 20	14 25	30 25	$P_{iv}(\%)$	$P_i(\%)$			

The top row of figures in each entry of Table 6.1 give the initial pitch angle and photon energy in distribution (i) which correspond most closely to the distribution (iv) result. The maximum directivity or polarisation for distributions (iv) and (i) respectively are given by the bottom row of figures.

Starting with the high energy results, we find that at 150 KeV the forms of the directivity and polarisation distributions are very similar to those found for distribution (i) with  $\alpha_0 = 15^\circ$  and  $\epsilon = 80$  KeV. This is to be expected since the cutoff in the electron spectrum at 200 KeV in distribution (iv) represents an approximation to the monoenergetic electrons of distribution (i). At lower photon energy the effective pitch angle in distribution (iv) increases, as anticipated.

Below 40 KeV, however, the behaviour of the directivity ceases to be like that of distribution (i). At 12, 16, and 25 KeV minimum brightness occurs near the pole and maximum brightness on the equator or limb. Figures 3.8-3.11 show that for pitch angles of  $60^\circ$  and  $75^\circ$ , which would be expected to correspond to the results discussed here, brightness is lowest on the equator or limb and highest near the pole. The only distribution (i) directivity which at all resembles the directivity patterns for  $\epsilon = 12, 16$  and  $25$  KeV occurs for  $\alpha_0 = 15^\circ$ .

The pattern of polarisation directions, on the other hand, shows a trend of increasing effective pitch angle right down to 12 KeV, where it is similar to the  $60^\circ$  pitch angle results of distribution (i). The position dependence of the degree of polarisation, however, is not quite the same as can be seen by comparing Figures 3.4, 3.5 and 6.7 and Figures 3.8, 3.9 and 6.6.

## 7. SUMMARY AND DISCUSSION

The major difficulty in presenting the predicted directivity and polarisation of hard X-ray emission is the large number of free parameters describing the trapping model - geometry of the trapping field, atmospheric density structure, the two variables required to specify the orientation of the trap relative to the observer, photon energy, the electron energy distribution and the electron pitch angle distribution.

In §2 we tried to show that the characteristics of the hard X-ray emission were not sensitive to the field model used. Results obtained for the dipole, linecharges and monopole field models Figures 2.1 - 2.4, were not wildly dissimilar, the greatest discrepancy arising for the linecharges model, where the directivity and polarisation for a given electron initial pitch angle were similar to those found for a rather smaller pitch angle in the other models. This effect is probably due to the form of the differential path length of the spiralling electron, which depends on the rate of change of magnetic field strength in the limbs of the trap. The monopoles field, which was thought to give the most realistic representation, was adopted as the standard field model.

Perhaps more convincing was the demonstration of the insensitivity of the directivity and polarisation to trap height and atmospheric density structure (Figure 2.5), although the density scale height, relative to the trap height, does not vary greatly in this case. A widely different density structure would probably produce an effective shift in the value of  $\alpha_0$ , as did the linecharges magnetic field.

Having chosen a trap height of  $5 \times 10^4$  km, we examined in detail the dependence of photon flux and polarisation on orientation of the trap and on initial pitch angle (Figures 3.2 - 3.11), for mono-energetic electrons with a singular pitch angle distribution (Distribution (i)). We found the following results:-

- (i) The detailed variation of intensity with trap orientation is complex, but for practical purposes may be described by (ii) and (iii) below.
- (ii) Directivity is higher at low photon energy, but small ( $\sim 35\%$ ) in all cases.
- (iii) Small pitch angles give limb-brightening; large pitch angles give limb-darkening. This assumes that the trap lies in the equatorial direction. A trap seen side-on at the limb is less bright for small pitch angles and is approximately the same brightness as at disc centre for large pitch angles.
- (iv) The direction of polarisation is independent of photon energy (for a fixed electron energy), being predominately East-West for small pitch angles and North-South for large pitch angles.
- (v) The degree of polarisation is larger ( $\sim 25\%$ ) at high photon energy (that is, nearer to the short wavelength limit).

In §4 we examined the effect of the introduction of a power law distribution in electron energy (Distribution (ii)) taking the spectral index  $\delta$ , to be 3. When studying the dependence of results on spectral index we also took  $\delta = 4$ . Results were as follows :-

- (i) Directivity is very small ( $\sim$  few percent) at low photon energy (25 KeV), but at 75 KeV it is very similar in both magnitude ( $\sim 35\%$ ) and position-dependence to the low photon energy (30 KeV for 100 KeV electrons) results of distribution (i). (Figures 4.3, 4.5, 4.6, 4.7 and 4.8).
- (ii) For small pitch angles the X-ray spectrum hardens by  $\sim \frac{1}{4}$  power in going from disc centre to limb, while for large pitch angles it softens by up to  $\frac{1}{2}$  a power. (Figure 4.3).
- (iii) In most cases the degree of polarisation decreases with increasing photon energy, being of about the same magnitude at 25 KeV as it was at 80 KeV in distribution (i). The degree of polarisation increases slightly if the electron energy spectral index is increased (Figure 4.1).
- (iv) The functional dependence of both magnitude and direction of polarisation on trap orientation is very similar to that found for distribution (i). The degree of polarisation at 25 KeV is  $\sim 20\%$ . (Figures 4.4, 4.5, 4.6 and 4.7).

(v) Whereas in distribution (i) we found the direction of polarisation to be independent of photon energy, it is now energy-dependent, but only very weakly.

In §5 we found that the introduction of a distribution over pitch angle (Distribution (iii)) washes out the directivity, variation in spectral index and polarisation to some extent. But results for  $\sin^2 \alpha_0$  and  $\cos^2 \alpha_0$  initial pitch angle distributions (Figures 5.1 and 5.2) were similar to those of distribution (ii) for large and small pitch angles respectively.

The functional dependence of directivity and polarisation of X-ray emission from electron distribution (iv) on trap orientation and photon energy is more complex than in the case of the electron distributions considered previously. Considering the energy dependence, we found that the characteristics of the emission are best described as functions of  $\epsilon/E^*$  (Figure 6.5). The variation of both the degree and direction of polarisation with trap orientation is similar to that found for distribution (i) near the short wavelength limit, if a pitch angle rather less than that deduced from Figure 6.1 with  $\epsilon = E$  is assumed.

## 8. COMPARISON OF RESULTS WITH OBSERVATIONS

In this section we compare the predictions of the trap model with observational evidence concerning the directivity, variation of spectral index and polarisation of hard X-ray emission. A more extensive account of the predictions of all current hard X-ray source models and their compatibility with observational evidence will be found in Chapter II, where the results obtained in this chapter are also discussed.

We have found that in all cases the directivity is less than 50%, in agreement with the results of Datlowe's (1975) statistical study of observational data. However, as demonstrated in Chapter II, directivity measurements are unlikely to be helpful in discriminating between source models. Only the thin target model can be tentatively excluded on these grounds.

Another possible method of distinguishing between hard X-ray source models lies in the variation of spectral index across the disc, which is in essence a measure of directivity, differential in photon energy. Kane (1974) found no variation in spectral index across the disc, while Datlowe et al (1974) found that bursts near the limb have a softer spectrum ( $\sim \frac{1}{2}$  power). This result disagrees with the prediction of the thick target model, but provides support for the thin target model. No variation of spectral index, except for that induced by the albedo contribution, would be expected for the thermal model. As discussed in Chapter II, the albedo contribution causes the spectrum to harden slightly at the limb in these cases. In the case of the trap model, if the axis of the trap is assumed to lie parallel to the equator, the spectrum hardens by  $\sim \frac{1}{4}$  power if small pitch angles predominate, and softens by  $\sim \frac{1}{2}$  power for large pitch angles. Thus a trap containing electrons of predominantly large pitch angles is in agreement with Datlowe's results.

We now consider polarisation as an observational test of X-ray source models. Unfortunately, only three observations are available. The results obtained by Tindo et al (1972) are shown in Figure 8.1. Tindo et al claim that the fact that the directions of polarisation all lie within  $10^\circ$  of the radial direction provides support for the thick target model. However these directions also lie within  $\sim 10^\circ$  of the East-West direction, which is likely polarisation direction for X-ray emission from a trap lying parallel to the equator. Nakada et al (1974), whose polarisation experiment was not entirely successful, suggest that the observed polarisation is not always radial.

The magnetic field direction in the limb flare of 24 October 1970, observed by Tindo et al, is not clear, but in H $\alpha$  there appears to be

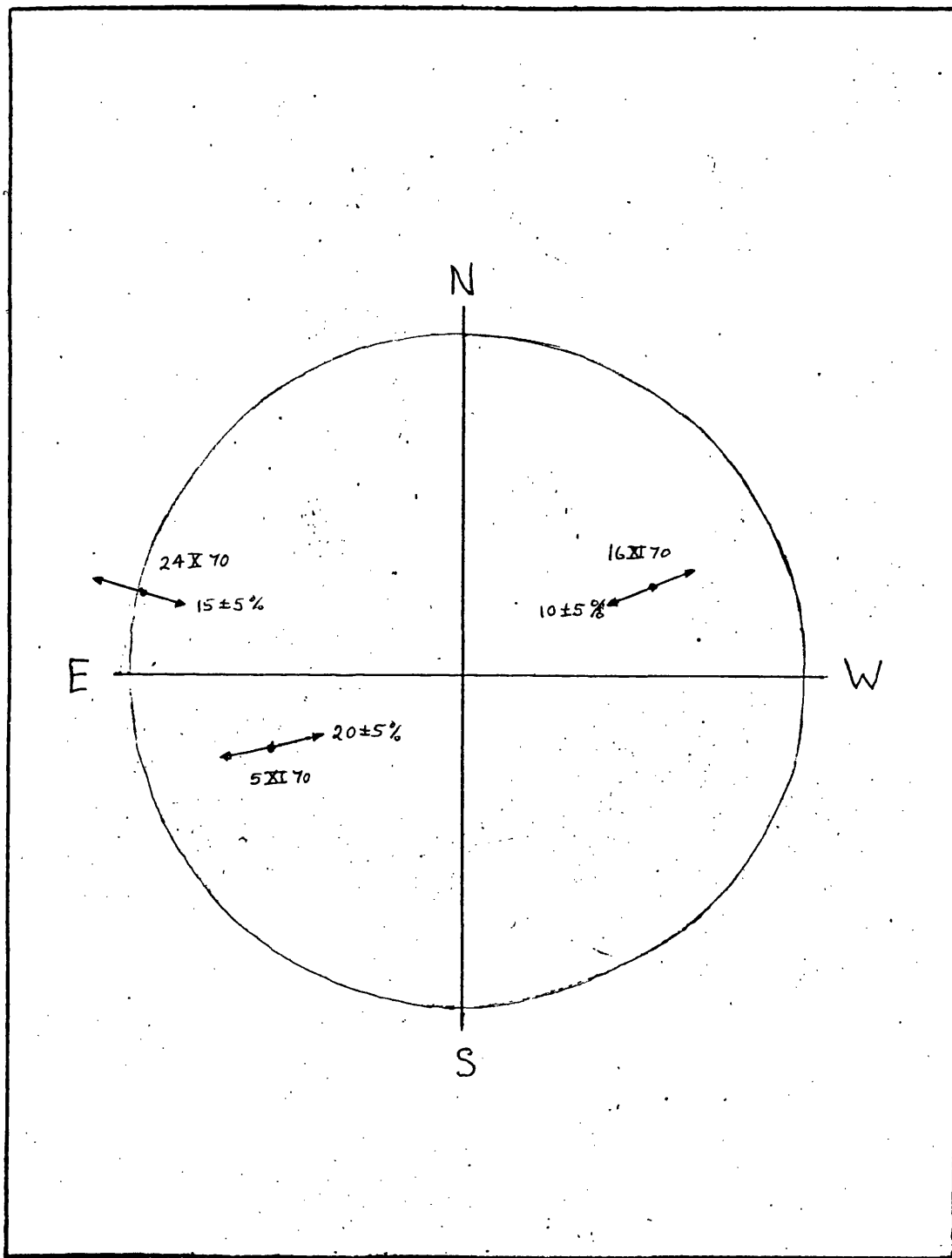


Figure 8.1 The hard X-ray polarisation measurements of Tindo et al (1972).

several magnetic arches seen more or less side-on. Emission from a trap on the limb can only be polarised in the radial or tangential direction, regardless of magnetic field direction. Assuming the trap to be end-on, then electron pitch angles of  $\sim 20^\circ$  give the requisite direction and magnitude of polarisation. If the trap is side-on, pitch angles of  $\sim 60^\circ$  give the observed polarisation. This is contrary to Tindo *et al* (1972) who state that the polarisation from a trap on the limb is zero. Tindo *et al* claim to know the magnetic field direction in the flare of 5 November 1970, but they do not state what it is. They do say, however, that the polarisation from a trap containing electrons of  $> 60^\circ$  initial pitch angles is in the wrong direction. Since their schematic diagram of the trap shows the polarisation to be parallel to the magnetic arch, whereas we know that for  $60^\circ$  pitch angles the polarisation is in fact perpendicular to the field direction, the polarisation may be in the correct direction. Certainly the degree of polarisation is correct ( $\sim 12\%$ ). The same degree of polarisation but in an approximately perpendicular direction would be obtained in electrons of  $\sim 15^\circ$ - $30^\circ$  initial pitch angles predominated in the trap. If the arch seen in  $H\alpha$  in this flare (see Tindo *et al.* (1972)) can be taken to represent the field direction, electrons of  $15^\circ$ - $30^\circ$  pitch angle would in fact produce emission polarised in the observed direction. The magnetic field direction in the flare of 16 November 1970 is unknown, but the degree of polarisation is certainly compatible with that predicted by the electron trap model.

Finally, the following observations are suggested as being of value in establishing the viability of the trap model.

- (i) Observation of a degree of polarisation  $> 30\%$  would eliminate the trap model (and all others except the thin target model).
- (ii) Consistent observation of a non-zero polarisation in flares at disc centre would eliminate all but the trap model.
- (iii) If the direction of polarisation is commonly found to be parallel/perpendicular to the magnetic field direction in a flare, this would suggest that the source is an electron trap containing electrons of small/large pitch angles.

- (iv) Simultaneous measurement of polarisation over a range of photon energies may be useful. The thick target model would be favoured if degree of polarisation is independent of photon energy, while a degree of polarisation increasing with photon energy would favour the thin target model. (See Chapter II). In the trap model, polarisation should decrease slowly with increasing photon energy for most trap orientations, while a more complex photon energy and position dependence of the polarisation, like those illustrated in Figure 6.5, could indicate a correlation between electron energy and pitch angle.
- (v) Spatially resolved hard X-ray measurements, when they become available, will hopefully (but probably not!) provide a definitive test of source models.

CHAPTER VTHE ELECTRON TRAP MODEL - SPATIAL DISTRIBUTION  
OF X-RAY FLUX AND POLARISATION1. INTRODUCTION

Although the equations describing the spatial distribution of hard X-ray emission from the trap have been set up for the general case in Chapter III, we consider here only one specific aspect of this study. We examine the changes in photon flux and polarisation when part of the trap is occulted, as in a behind-the-limb event. Knowledge of the exact form of spatial distribution may become important when the next generation of satellite-borne hard X-ray detectors materialise, since these will include a hard X-ray imaging detector able to resolve spatially a structure with dimensions typical of those of the trap. (See Brown *et al.*, 1975).

Since the photon flux from a partly occulted trap is merely the integral of the spatially distributed emission over the visible part, the results given here will indicate the gross features of the spatial distribution of emission. The spatially resolved appearance of the trap can only be determined in detail by calculating the intensity of emission from each point on each limb of the trap, for a variety of trap positions. The results presented here give the sum of the fluxes from both limbs of the trap at a given height, for a trap near the solar limb.

Although we found in Chapter IV that the directivity of total emission from the trap is small, it does not necessarily follow that directional effects are negligible when the spatially resolved emission is considered. But in practice the combination of a finite spread in electron pitch angles and other parameters describing the trap model, and the finite spatial resolution of instrumentation should render such effects of secondary importance. The results presented here do not give any direct indication of the spatially resolved polarisation, but then neither do current or projected hard X-ray polarimeters.

The one spatially resolved observation available at present (Takakura et al., 1971) indicates only that the hard X-ray source is probably smaller than  $10^5$  km in one of its dimension. Behind-the-limb observations by Roy & Datlowe (1975) and McKenzie (1975) give further information about the spatial structure of the hard X-ray source. The few results available indicate that hard X-ray emission extends to a height of at least  $3 \times 10^4$  km. It is not yet clear whether the X-ray flux is significantly reduced by occultation in a behind-the-limb burst. These observations are discussed in more detail and compared with the predictions of other X-ray source models in Chapter II.

In the following sections we study the photon flux and polarisation of X-ray emission as a function of angular distance of the trap behind the limb. Figure 1.1 illustrates the relationship between  $\theta$ , the angular distance of the trap from the limb and  $z_{\min}$ , the minimum height visible at the trap position. The three positions marked  $\theta_1$ ,  $\theta_2$  and  $\theta_3$  correspond respectively to the positions at which occultation of emission from the trap begins, for our assumed minimum electron mirror height of  $5 \times 10^3$  km; the position at which a trap of height  $5 \times 10^4$  km disappears from view; and the position at which a trap of height  $10^5$  km disappears from view.

We look at two particular trap orientations; end-on and side-on. Results presented for the "side-on" case represent accurately the predictions of the trap model. However, in the "end-on" case, we do not take account of the fact that the limb of the trap further from the solar limb is occulted more rapidly than the nearer, as illustrated in Figure 1.1. We treat the trap as though both limbs were occulted at height  $z_{\min}$  corresponding to the position of the centre of the trap. This approximation should not invalidate our conclusions concerning the variation of photon flux, although it does mean that, in the case of a singular pitch angle distribution, instead of two sudden decreases in flux, separated by  $\sim 8^\circ$ , corresponding to the occultations of the mirror point in each limb, we see only one. Since the singular pitch angle distribution is an idealisation, in reality a finite spread in initial pitch angle would be expected to produce a smooth variation

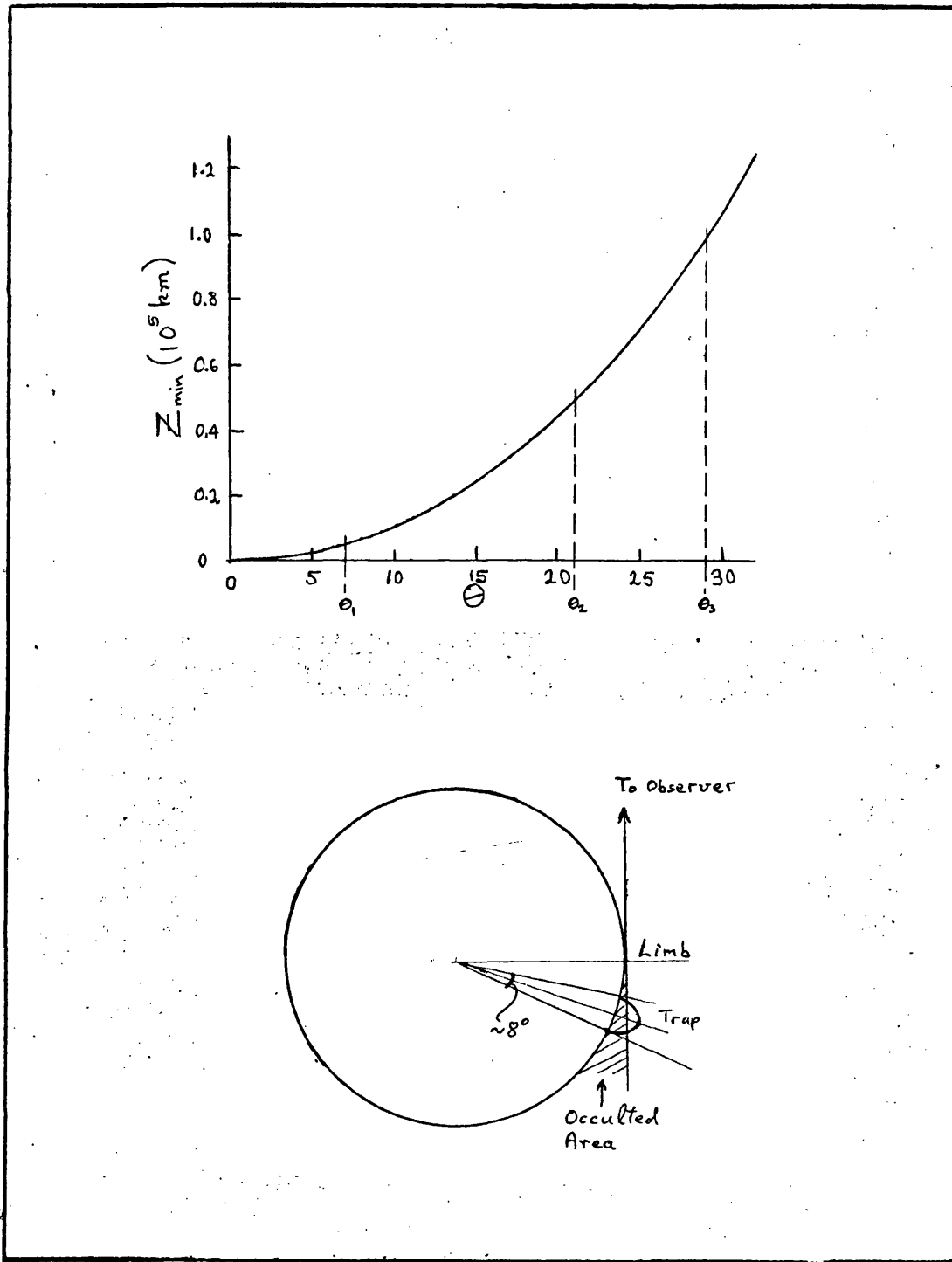


Figure 1.1

Upper figure:- Minimum visible height as a function of angular distance behind the limb.

Lower figure:- Schematic illustration of the occultation of an "end-on" trap.

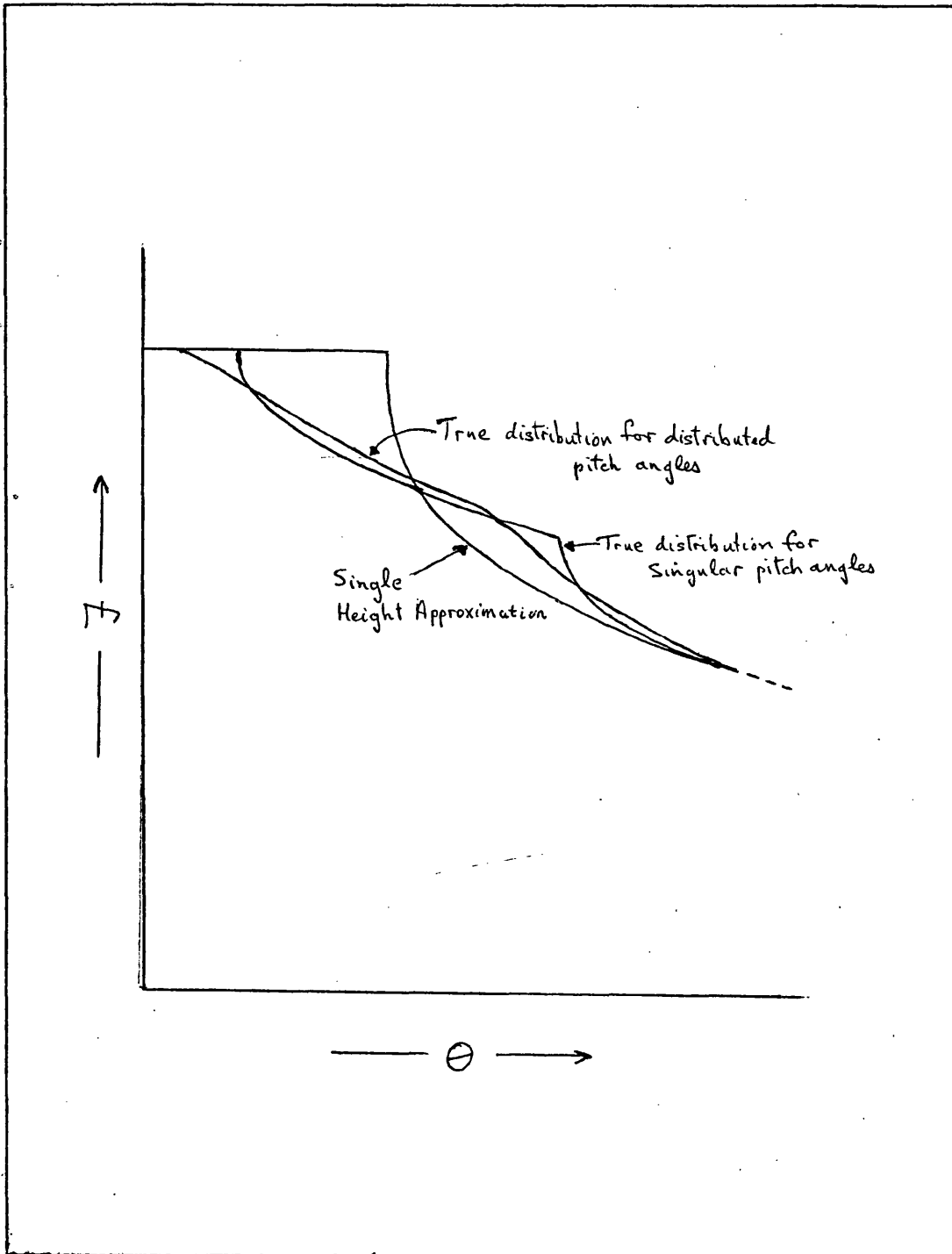


Figure 1.2

Comparison of "true" relationship between photon flux and distance of trap behind the limb, with predictions for a singular pitch angle distribution, where the difference in minimum height visible in each limb is allowed for in one case, but not the other.

in photon flux with distance behind the limb. These three functional forms are illustrated in Figure 1.2.

The effect of the above approximation on the polarisation is less certain, since the observed degree of polarisation depends critically on the cancellation of opposite polarisation from different parts of the trap. However, the results presented here should at least give some indication of the behaviour of the X-ray polarisation in a behind-the-limb event.

In Chapter IV the trap was only seen side-on at the pole  $((\phi, \lambda) = (90, 0))$ , where the direction of positive (East-West) polarisation was parallel to the trapping field. Here we continue to define East-West polarisation to be positive, but we take the trap to be on the equator, regardless of its orientation. Therefore positive polarisation means that radiation is polarised perpendicular to the "side-on" trap, and so is in the radial direction in both cases.

Throughout this chapter we take the spectral index of the electron energy spectrum to be 3.

## 2. ELECTRON DISTRIBUTION (ii)

Figure 2.1 illustrates the variation of photon flux with distance behind the limb for initial pitch angles of  $15^\circ$ ,  $30^\circ$  and  $60^\circ$ . In this case the trap is parallel to the equator. To better illustrate the energy dependence of directivity, the photon flux at 75 keV has been scaled up so that on the solar limb it is equal to the 25 keV flux. Photon flux drops sharply as the electron mirror points are occulted, due to the singularity in emission at the mirror points. The enhancement of 75 keV photon flux relative to the 25 keV flux when the lower part of the trap is occulted (hardening of the spectrum) is better illustrated by the variation of spectral index, also shown in Figure 2.1. The amount of hardening is small ( $\Delta\gamma \sim 0.1 - 0.4$ ).

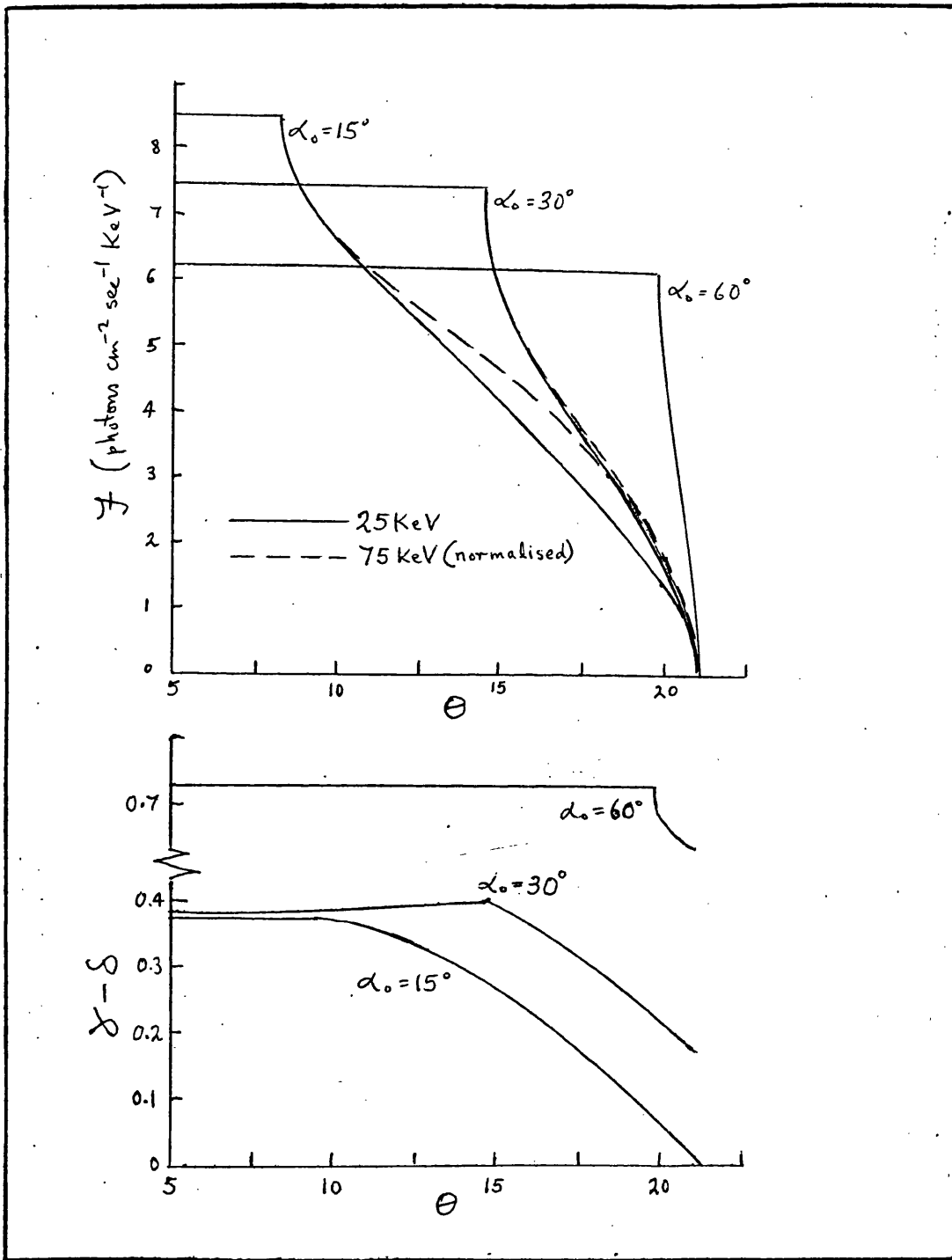


Figure 2.1

Electron distribution (ii). Photon flux at 25 keV and 75 keV (normalised) and spectral index as a function of distance behind the limb for a trap parallel to the equator (end-on).

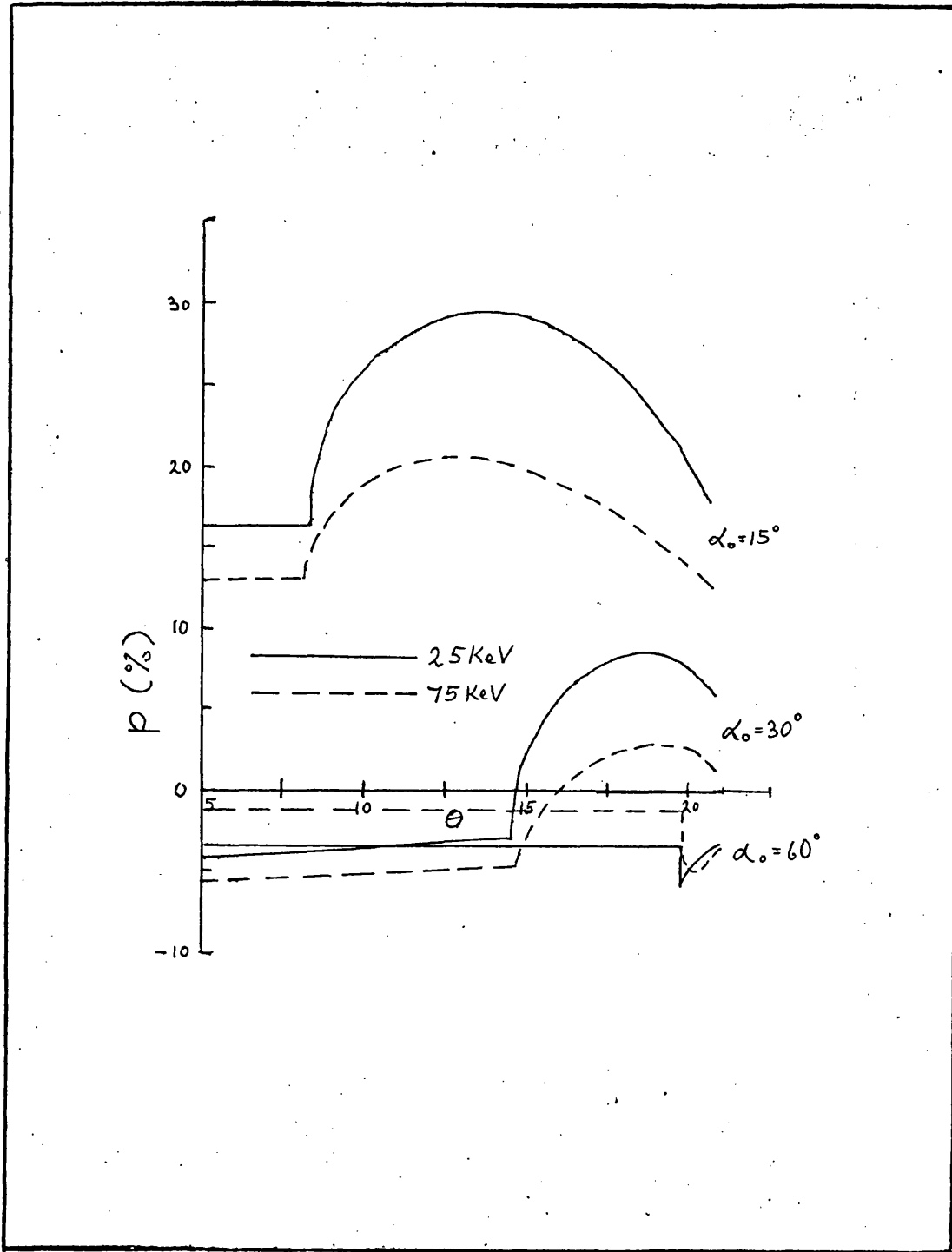


Figure 2.2 Electron distribution (ii). Polarisation at 25 keV as a function of distance behind the limb for a trap parallel to the equator (end-on).

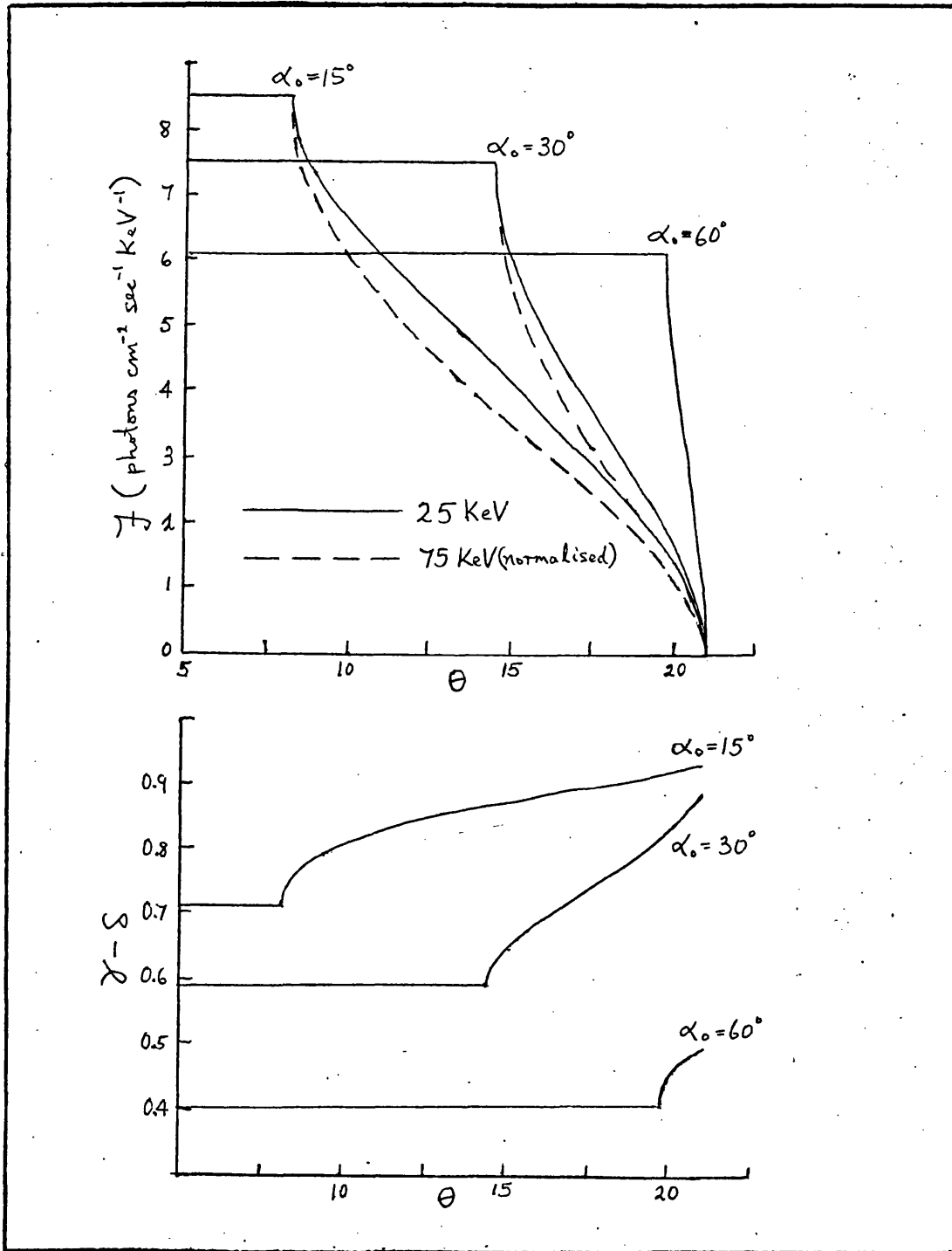


Figure 2.3

Electron distribution (ii). Photon flux at 25 keV and 75 keV (normalised) and spectral index as a function of distance behind the limb for a trap parallel to the solar limb (side-on).

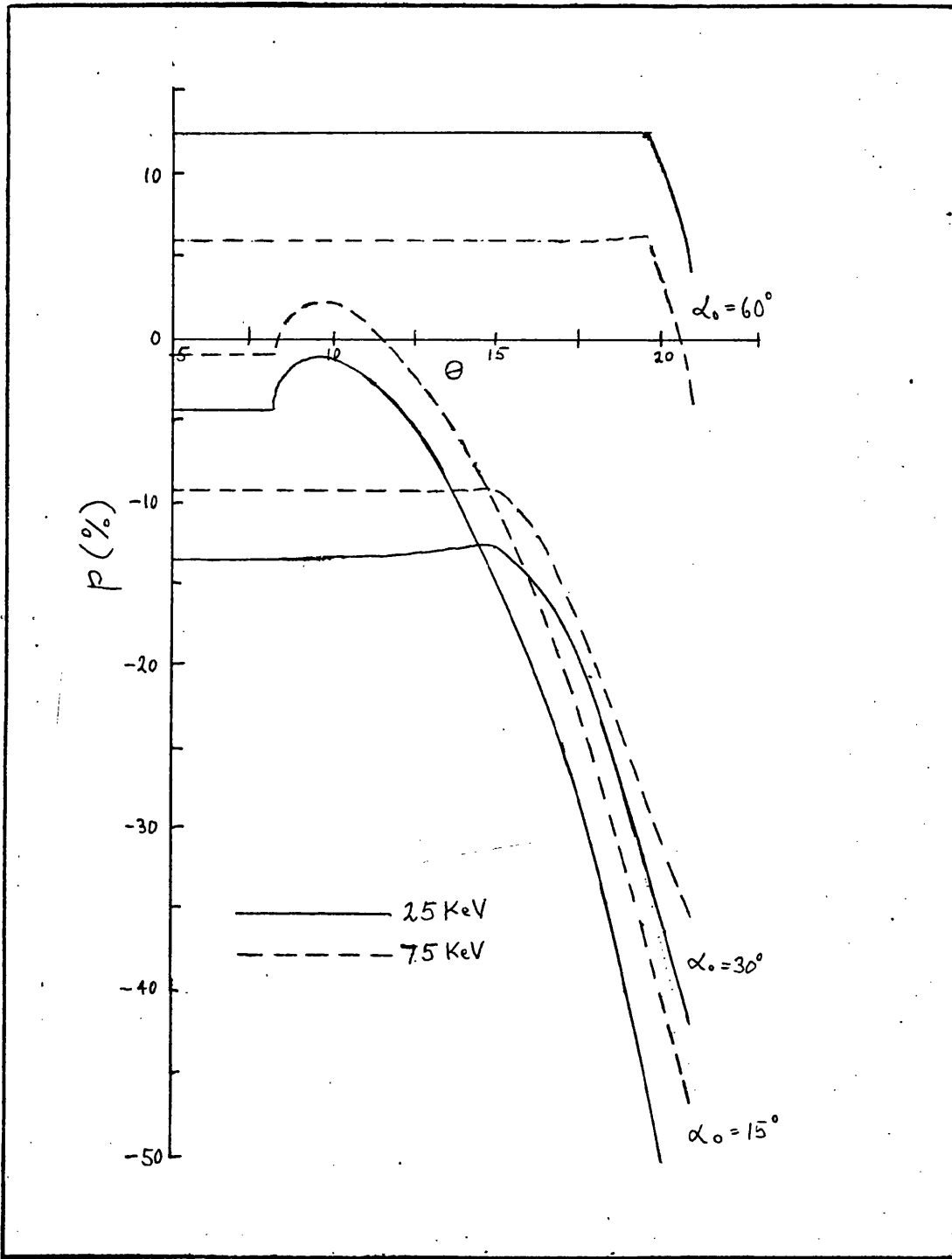


Figure 2.4

Electron distribution (ii). Polarisation at 25 keV and 75 keV as a function of distance behind the limb for a trap parallel to the solar limb (side-on).

Polarisation as a function of distance behind the limb, again for a trap seen end-on, is shown in Figure 2.2. In all cases the degree of polarisation reaches a maximum of approximately twice its value at the limb when the trap is partly occulted and decreases again as more of the trap is occulted. For an initial pitch angle of  $30^\circ$  the direction of polarisation changes from tangential at the limb to radial when the trap is partly occulted. If the initial pitch angle is  $15^\circ$  or  $60^\circ$  the polarisation remains radial or tangential, respectively.

Figure 2.3 shows the variation of photon flux and spectral index for a trap parallel to the limb, that is, seen side-on. In this case the spectrum softens as the trap is occulted, the change in spectral index again being small ( $\Delta\gamma \sim 0.1 - 0.3$ ). The dependence on distance behind the limb of the polarisation of X-ray emission from a trap seen side-on is illustrated in Figure 2.4. In all cases the polarisation tends to the tangential direction. When the limbs of the trap are occulted, results are in accordance with earlier predictions, for example Haug (1972), where the trap is approximated by a uniform horizontal magnetic field.

### 3. ELECTRON DISTRIBUTION (iii)

In this section we consider a trap containing electrons with a distribution of initial pitch angles. The two distributions examined in Chapter IV,  $\sin^2\alpha_0$  and  $\cos^2\alpha_0$ , are used again here. Results are presented only for the "end-on" case. The dependence of photon flux and spectral index on distance behind the limb is illustrated in Figure 3.1. The form of the variation of photon flux is almost independent of energy, as demonstrated by the constancy of the spectral index.

When small pitch angles predominate ( $\cos^2\alpha_0$  distribution), the spectrum hardens slightly when most of the trap is occulted. A slight softening of the spectrum is evident in the  $\sin^2\alpha_0$  case, contrary to the results obtained for distribution (ii). However, in that case

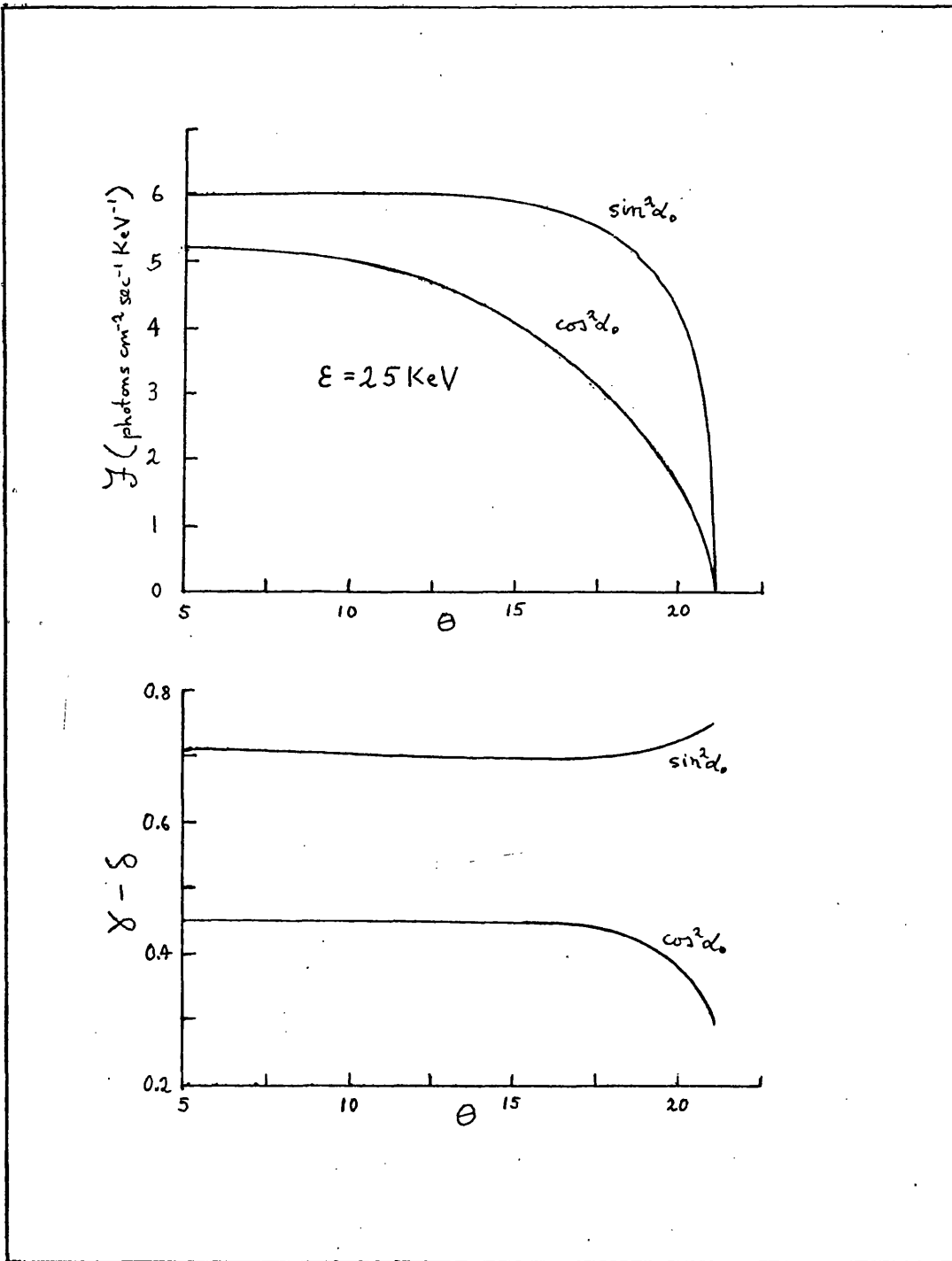


Figure 3.1

Electron distribution (iii). Photon flux and spectral index as a function of distance behind the limb. The trap is parallel to the equator (end-on).

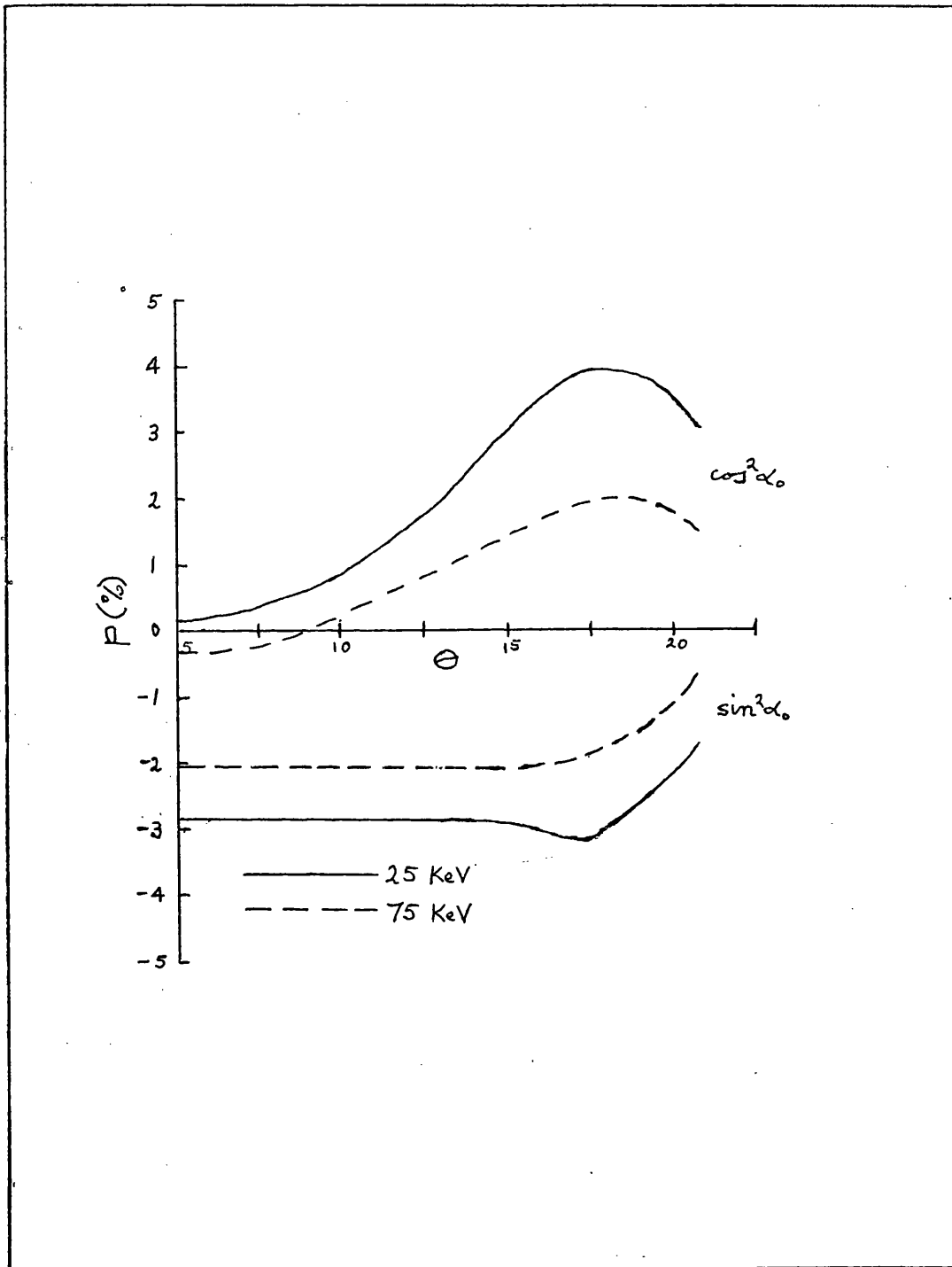


Figure 3.2

Electron distribution (iii). Polarisation as a function of distance behind the limb for a trap parallel to the equator (end-on).

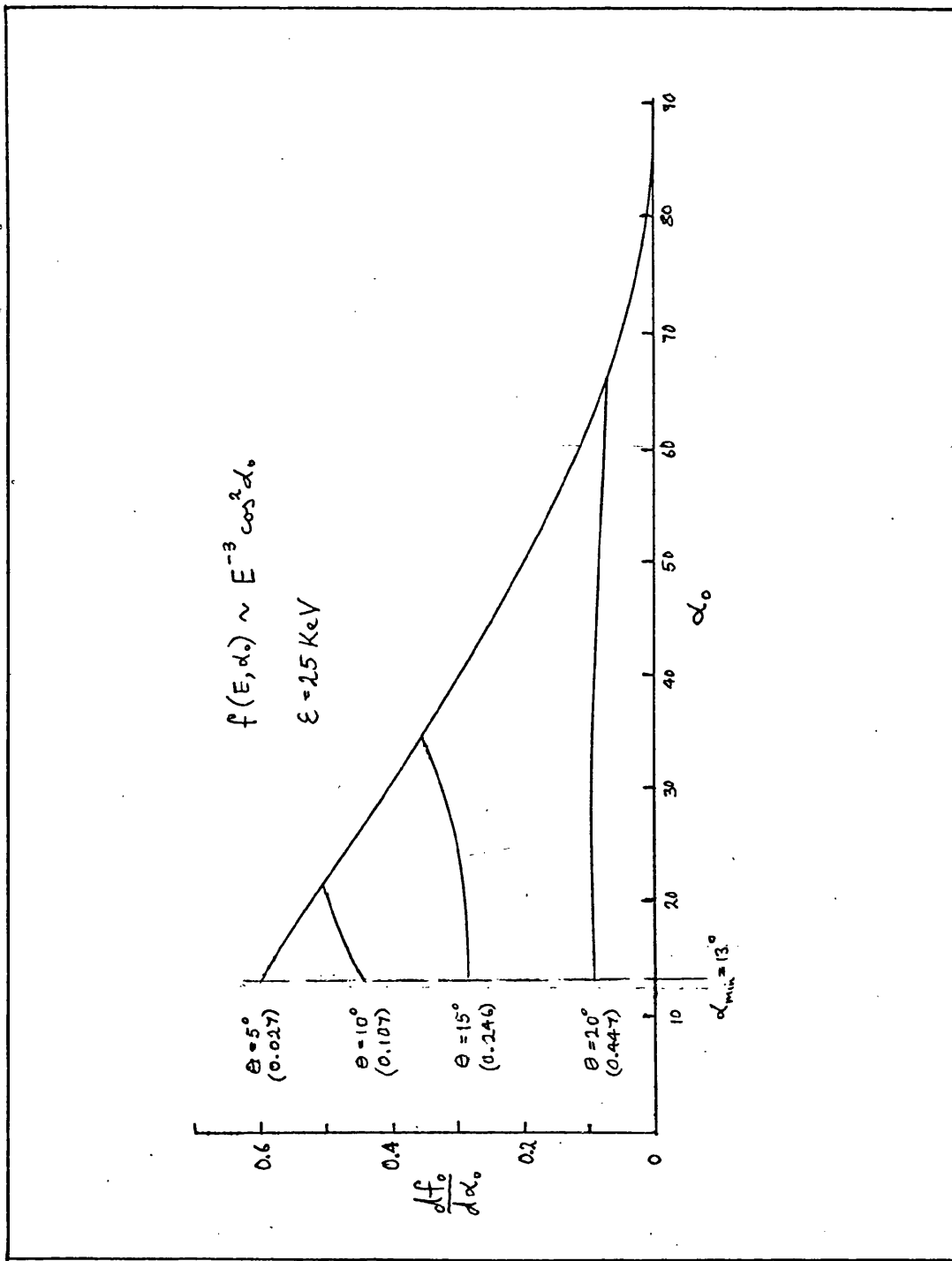


Figure 3.3

Electron distribution (iii). The integrand of the integral over  $\alpha_0$  for a  $\cos^2 \alpha_0$  initial pitch angle distribution. Each branch of the curve is labelled by  $\theta$ , the distance behind the limb, and the corresponding minimum visible height ( $z_{\min}$ ) in units of  $10^5 \text{ km}$ .

the largest initial pitch angle examined was only  $60^\circ$  because the cutoff in photon flux as the trap moves away from the limb is almost instantaneous at larger pitch angles.

The variation of polarisation with distance behind the limb is shown in Figure 3.2. Although the degree of polarisation is rather lower, its functional forms for the  $\cos^2 \alpha_0$  and  $\sin^2 \alpha_0$  pitch angle distributions are similar to the results shown in Figure 2.2 for initial pitch angles of  $30^\circ$  and  $60^\circ$  respectively.

Finally, some insight into the dependence of photon flux on distance of the trap behind the limb can be gained from Figure 3.3. This shows the contribution to  $f_0$ , which is proportional to the photon flux (see §11 of Chapter III), from electrons of each initial pitch angle in the  $\cos^2 \alpha_0$  distribution. Against each branch of the curve are shown  $\theta$ , the distance behind the limb, and  $z_{\min}$ , the minimum visible height, in units of  $10^5$  km.

For  $\theta = 5^\circ$ ,  $z_{\min}$  is less than  $z_c = 5 \times 10^3$  km, the cutoff height below which electrons are assumed to be lost instantaneously. Therefore the trap is unocculted and the largest contribution to the photon flux comes from electrons of small initial pitch angle, which predominate. As the trap moves further behind the limb, these electrons contribute less since the parts of their trajectories near the mirror points are obscured. For example, the contribution from electrons of minimum initial pitch angle ( $13^\circ$ ) is reduced to half its original value at  $\theta = 15^\circ$ , where  $z_{\min} = 0.246$ . Therefore we deduce that half of the X-ray emission from these electrons comes from the lower half of the trap, and half from the upper. The "break-point" in each curve occurs at the initial pitch angle whose mirror point height is equal to the minimum visible height.

#### 4. ELECTRON DISTRIBUTION (iv)

Photon flux, spectral index and polarisation of emission from

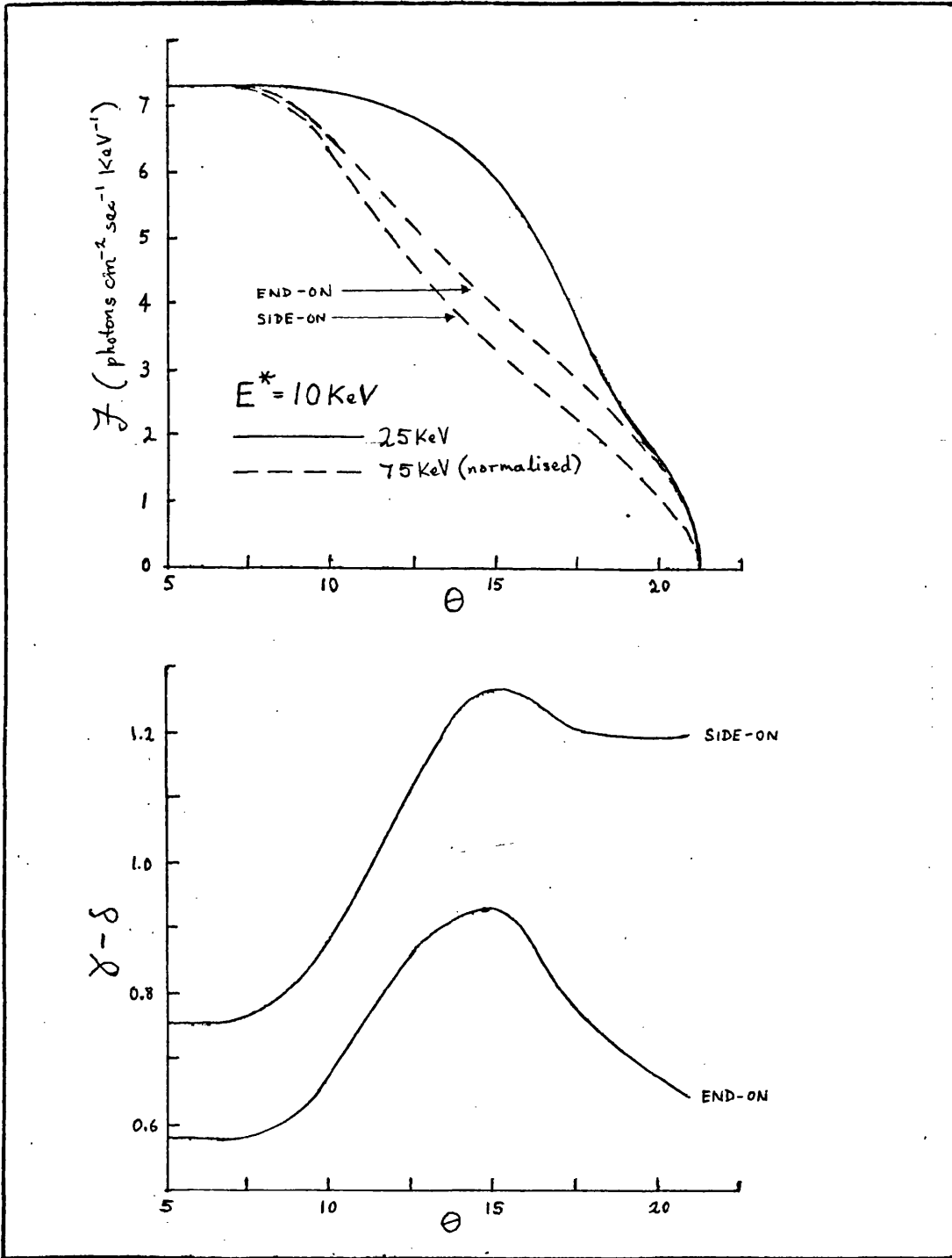


Figure 4.1 Electron distribution (iv). Photon flux and spectral index as a function of distance behind the limb.

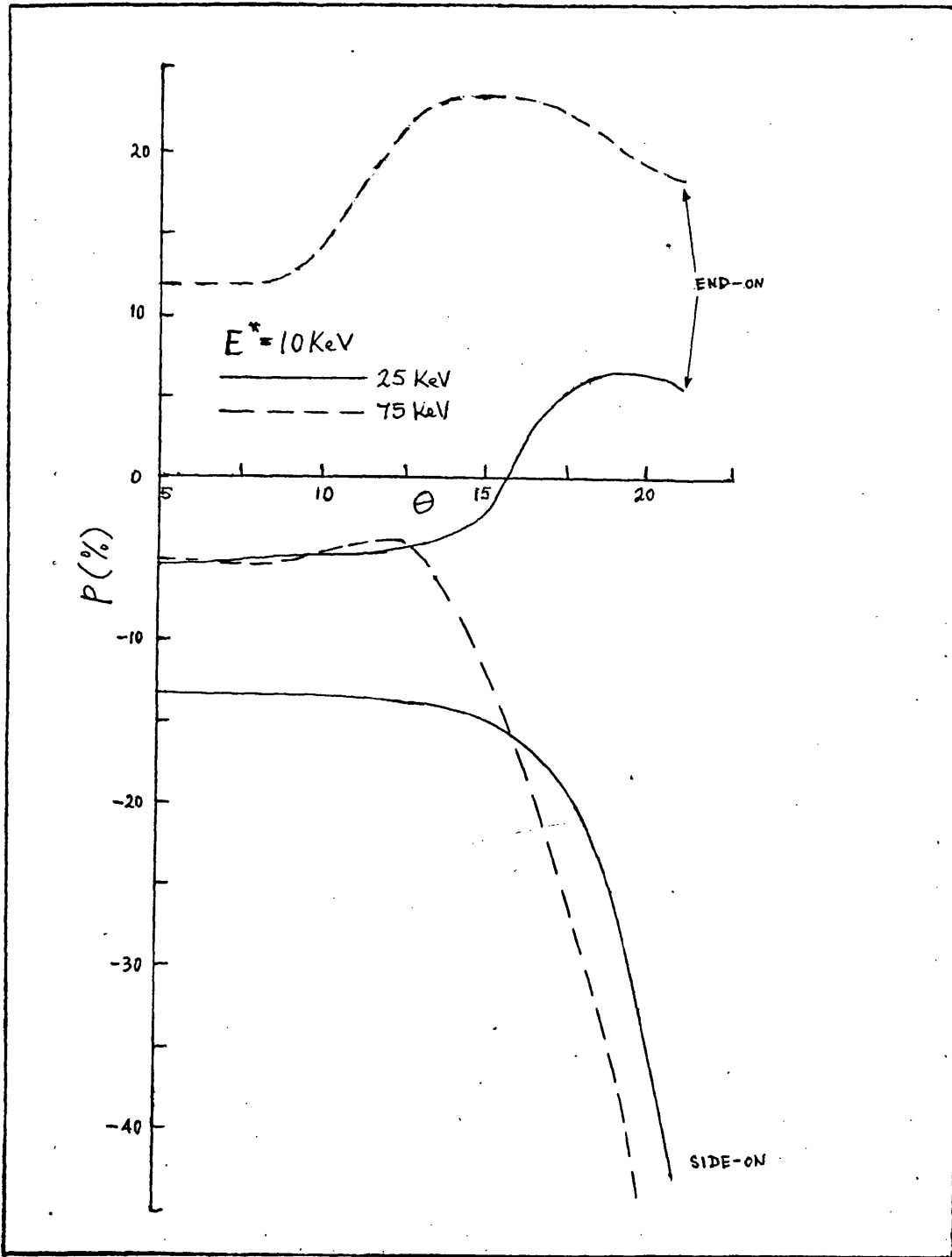


Figure 4.2

Electron distribution (iv). Polarisation as a function of distance behind the limb.

electron distribution (iv) as functions of distance behind the limb are shown in Figures 4.1 and 4.2, for  $E^* = 10$  keV. The flux at higher photon energy falls off more rapidly as the trap is occulted. This is to be expected, since higher energy electrons, having smaller pitch angles, penetrate further down the limbs of the trap. The spectrum therefore softens appreciably ( $\Delta\gamma \sim \frac{1}{2}$  in the side-on case) as the trap disappears behind the limb. For both end-on and side-on orientations of the trap, the spectral index reaches its maximum value when half the trap is occulted ( $\theta \sim 15^\circ$ ). In the end-on case it decreases almost to its original value as most of the trap is occulted.

The behaviour of the polarisation (Figure 4.2) is similar to the small pitch angle results ( $\alpha_0 = 15^\circ$  and  $30^\circ$ ) shown in Figures 2.2 (end-on) and 2.4 (side-on) for electron distribution (ii). The polarisation at 25 keV is similar to the  $30^\circ$  pitch angle results for distribution (ii) while that at 75 keV is closer to the results for  $15^\circ$  pitch angles. This is in accordance with the discussion in §6 of Chapter IV.

## 5. SUMMARY AND COMPARISON WITH OBSERVATION

The results obtained in this chapter show a variety of different trends from which it is difficult to draw any general conclusions. Probably the most significant results for photon flux are those of distribution (iii) (Figure 3.1) which do not exhibit the somewhat artificial "step" in intensity as the mirror points in distribution (ii) are occulted.

No large variations in spectral index have been found. In distribution (ii) the spectral index increases or decreases by up to  $\frac{1}{3}$ , according to whether the trap is seen side-on or end-on. Maximum change in spectral index was found for electron distribution (iv), where the spectrum softens by half a power.

The behaviour of the polarisation, illustrated in Figures 2.2, 2.4, 3.2 and 4.2, is varied. These results suggest that the degree of polarisation of emission from a partly occulted trap should be larger than that from a trap on the limb if small pitch angles predominate in the trap, and smaller if large pitch angles predominate.

Finally, in Figure 5.1, the predicted behaviour of the photon flux is compared with observation. The data are taken from Brown & McClymont (1975) (see also Roy & Datlowe, 1975) and from McKenzie (1975). Each data point represents peak photon flux  $J_{20}$  at 20 keV from an event which is believed to have occurred a distance  $\theta$  behind the limb. Since distance behind the limb is deduced from the calculated position of the (extended) active region in which the flare is thought to have occurred, there is an uncertainty of  $\sim 4^\circ$  in the position of the hard X-ray source. If the source is an electron trap, this uncertainty is unimportant since it is comparable with the dimensions of the trap.

More important is the fact that each observed flux  $J_{20}$  represents only a sample from a distribution which ranges over several orders of magnitude. Therefore the few data points shown in Figure 5.1 are not sufficient to define the dependence of mean photon flux on distance behind the limb.

The upper set of curves shown in Figure 5.1 are the predictions of the electron trap model for electron distribution (ii) with initial pitch angles of  $15^\circ$ ,  $30^\circ$  and  $60^\circ$ . Although the computations were performed at 25 keV photon energy, the absolute fluxes are approximately correct for comparison with the observations made at 20 keV if a cutoff of  $\sim 10$  keV is assumed in the non-thermal electron spectrum. The difference in photon energies compensates nicely for the fact that the spectral indices found observationally are on average around one power steeper than those calculated here. Therefore the upper set of curves are typical of a large event.

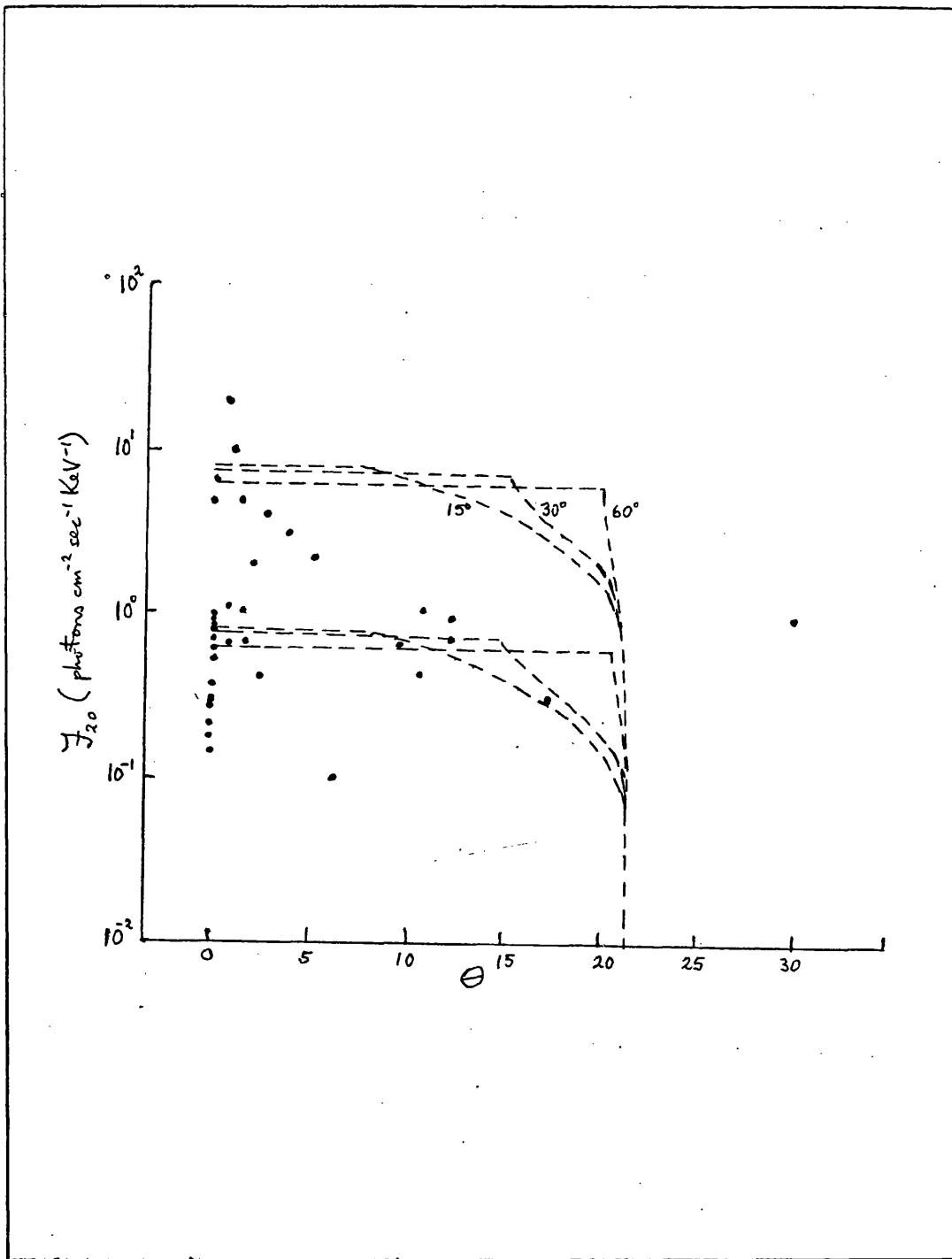


Figure 5.1 Behind-the-limb data from Brown & McClymont (1975) and McKenzie (1975). Superimposed curves are the predictions of the trap for electron pitch angles of  $15^\circ$ ,  $30^\circ$  and  $60^\circ$ . The upper set of curves represent the results obtained in this chapter, the lower are scaled down by a factor of 10.

The lower set of curves show the photon flux expected in a fairly small event, in which the non-thermal energy is down by a factor of 10. The median peak photon flux in the sample of behind-the-limb bursts shown in Figure 5.1 is the same as that found on the limb. Therefore, if the energy contents of the behind-the-limb events are typical of disc flares (that is, small events), the electron trap model provides an acceptable explanation of these.

However, Datlowe et al., (1974) claim that behind-the-limb events tend to last longer than the average disc flare, which suggests that behind-the-limb events are intrinsically larger. If events behind the limb are appreciably (e.g. an order of magnitude) larger, the data do not support the trap model, since little variation in intensity occurs until the trap is almost completely occulted. Of course, the trap height can be chosen for each event so that any desired ratio of disc to behind-the-limb flux is obtained. But statistically, the probability that each event represents an almost occulted trap must be very low.

Obviously the amount of behind-the-limb data available at present is very limited. Until sufficient data is gathered to allow a statistical study to be made, any conclusions drawn must be regarded as speculative.

CHAPTER VITHE ROLE OF MASS MOTION IN ENERGY TRANSFER IN A  
HEATED FILAMENT - ANALYSIS AND COMPUTATIONAL PROCEDURE1. INTRODUCTION

While many authors have discussed thermal conduction as a mechanism for the transfer of energy in a flaring region (for example, Culhane et al (1970), Brown (1974a), Craig (1975a) ), few have considered the role of mass motion. Except under extreme conditions of compression or rarefaction caused by a pressure wave, dynamical processes cannot directly play a major part in the heating and cooling of a plasma, being responsible for the transport of energy from one point in space to another rather than the transfer of energy from one fluid element to another.

However the influence of mass motion on a temperature/density structure can profoundly affect the process of thermal conduction, thus indirectly controlling the redistribution of thermal energy in the plasma. Two mechanisms by which control can be exerted are immediately apparent. The first arises because the efficiency of thermal conductivity is a strong function of temperature. Thus, if the kinetic energy of the plasma is comparable to its thermal energy, the reduction in temperature from the value anticipated when mass motion is neglected causes a significant decrease in thermal conduction. Secondly, macroscopic transport of the plasma affects the temperature gradient, again leading to a substantial change in the rate of energy transport due to thermal conduction.

Apart from its influence on energy transport, mass motion in flares is of interest in its own right, as is shown by the ejection of  $\sim 10^{16}$  gm of plasma in a large flare, and motion of material in filaments and prominences.

In this chapter the significance of dynamical effects in determining the structure of the heated region is investigated. In particular we examine the influence of mass motion on the

conductive flux, pressure distribution and soft X-ray emission measure.

## 2. DISCUSSION OF PREVIOUS WORK.

Shmeleva and Syrovatskii (1973) examined the distribution of temperature and emission measure in the solar atmosphere, obtaining a semi-analytic solution by equating the rate of energy transfer into an element of plasma by thermal conduction to its radiative energy loss. The solution is obtained for a point energy source in two limiting cases, both being in a steady state. One case, in which a constant density region is assumed, corresponds to the initial phase of fast heating where the time to reach a static temperature gradient is assumed short compared to the timescale for development of mass motion. The other limiting case is that of slow heating. Here it is assumed that both an equilibrium temperature structure and steady dynamical state have been attained, so that the temperature structure may be found under the assumption of constant pressure. Although these results are of interest because of their generality, their usefulness is restricted due to lack of knowledge as to where and when, if ever, conditions of constant density or pressure apply.

Heating of the chromospheric flare by a vertical beam of electrons has been considered by Brown (1973a), on the assumption that the atmosphere moves at constant pressure in response to the energy input. Brown's calculation is complementary to that of Shmeleva and Syrovatskii as he neglects thermal conduction and equates collisional heating of the plasma by the non-thermal electrons to the radiative losses. He shows that the deeper layers of the atmosphere can attain a state of energy balance with the electron beam, energy being dissipated by radiation and upward expansion at a velocity comparable with that observed in surge motions. However above the level at which the temperature exceeds  $\sim 3 \times 10^4$  K (at the peak of the radiative loss function) the material becomes radiatively unstable. The mass of material lying above this level is shown to be comparable with the observed

mass of plasma ejecta in large flares.

In contrast to the steady-state solutions discussed above, Strauss and Papagiannis (1971) solved the time-dependent equation of energy transport for a coronal filament heated by a stream of high energy particles descending from the top of the arch. They assumed a constant density plasma and took into account thermal conduction and radiative losses. Their purpose was to demonstrate that thermal bremsstrahlung from a multi-thermal plasma is compatible with the spectrum and time evolution of a hard X-ray burst. The special requirements of this model led them to adopt an extremely narrow high density filament into which a large amount of energy is injected. Strauss and Papagiannis assumed an electron density of  $2 \times 10^{11} \text{ cm}^{-3}$  and found a maximum temperature of  $60 \times 10^6 \text{ K}$  at the end of the heating phase which lasts for  $\sim 5$  minutes. Their results indicate that a pressure gradient of  $\sim 5 \times 10^{-7} \text{ dynes cm}^{-3}$  exists throughout the heating phase. The above values indicate (c.f. §3) that the timescale for development of important mass motion is  $\sim 100$  seconds. Thus the assumption of constant density made by Strauss and Papagiannis is inconsistent with the results they obtain. This is also true of the work of Landini et al. (1975).

The most thorough analysis of this type has been performed by Kostjuk & Pikel'ner (1974) who examined the heating of the chromospheric flare by a beam of non-thermal electrons with a power law energy distribution. Their calculations included the effects of mass motion, thermal conduction and radiation. Their results agree with and quantify those of Brown (1973a), showing that above a certain level, corresponding to the level of radiative instability found by Brown, the atmosphere expands upward at a velocity of  $\sim 10^8 \text{ cm s}^{-1}$ , reaching a temperature of  $\sim 5 \times 10^6 \text{ K}$ . The enhanced pressure in this region causes a pressure wave to propagate downward, heating and at first compressing the lower part of the atmosphere, which subsequently expands upward at a velocity  $\sim 2 \times 10^6 \text{ cm s}^{-1}$ .

Our analysis is similar to that of Kostjuk and Pikel'ner, but applied to a closed coronal filament instead of the freely

expanding chromosphere. We are primarily concerned with the influence of mass motion on the evolutionary time scale of the flare, and on the soft X-ray emission measure structure.

### 3. THE IMPORTANCE OF MASS MOTION

Insight into the possible importance of different energetic processes in determining the structure of the flare region can be gained from consideration of order of magnitude estimates.

It is known from soft X-ray observations that plasma at a temperature of  $\sim 20 \times 10^6$  K exists in flare regions having dimensions  $\leq 10^{10}$  cm. Therefore temperature gradients of  $\geq 2 \times 10^{-3}$  K cm $^{-1}$  must exist. If the temperature gradient is along the magnetic field lines, as in the case of the filamentary structure we assume here, then the equation of motion of an ionised hydrogen plasma (neglecting convective terms) is

$$\rho \frac{\partial v}{\partial t} = \nabla P = \nabla (2\rho RT) = \frac{2\rho RT}{L} \quad (3.1)$$

where  $T/L$  is the temperature gradient.

Inserting the above numerical values we obtain

$$\frac{\partial v}{\partial t} \approx 2 RT/L = 3 \times 10^5 \text{ cm sec}^{-2} \quad (3.2)$$

We take mass motion to be important when the kinetic energy density of the plasma is equal to the maximum thermal energy density (a rather severe requirement). Denoting the time scale for development of important mass motion by  $\tau_K$ , we have, approximately

$$\frac{1}{2} \left( \frac{\partial v}{\partial t} \tau_K \right)^2 = 3 RT \quad (3.3)$$

that is,

$$\tau_K = (6 RT)^{1/2} / \frac{\partial v}{\partial t} \quad (3.4)$$

Inserting numerical values, we find

$$\tau_K \approx 300 \text{ sec} \quad (3.5)$$

We compare  $\tau_K$  with the timescale for dissipation of the pressure gradient by thermal conduction. Omitting dynamical terms, the energy equation is

$$\frac{\partial}{\partial t} (3\rho RT) = \nabla \cdot (K \nabla T) \quad (3.6)$$

which can be crudely approximated by

$$\frac{3\rho RT}{\tau_c} = \frac{KT}{L^2} \quad (3.7)$$

where  $\tau_c$  is a conduction time scale. In the solar corona,  $K$ , the coefficient of thermal conduction, is given approximately by

$$K = 10^{-6} T^{5/2} \quad (3.8)$$

in c.g.s. units.

Thus from (3.7) and (3.8) we obtain

$$\tau_c \approx \frac{3\rho RL^2}{10^{-6} T^{5/2}} = \frac{3n_e kL^2}{10^{-6} T^{5/2}} \quad (3.9)$$

where  $n_e$  is electron density and  $k$  is Boltzmann's constant.

Observations suggest that the electron density in the soft X-ray flare region is  $\sim 10^{10} - 10^{11} \text{ cm}^{-3}$ . Inserting these values, and the numerical values used previously, in (3.9) we obtain

$$\tau_c \approx 250 - 2500 \text{ sec} \quad (3.10)$$

This rather crude analysis suggests that mass motion is likely to be at least as important as thermal conduction in determining the structure of a flaring region, particularly if the

density is high.

$$(\tau_c/\tau_K \sim 1 \text{ for } n_e = 10^{10} \text{ cm}^{-3}; \tau_c/\tau_K \sim 8 \text{ for } n_e = 10^{11} \text{ cm}^{-3}).$$

We can also estimate the likely importance of radiative energy loss as a dissipation mechanism. We note that a meaningful comparison between the rates of energy dissipation due to conduction and to radiation is difficult to make for two reasons. Firstly, conduction can only be considered to be a dissipative mechanism if heat is conducted out of the region under consideration, whereas radiation represents an absolute loss of energy. Secondly, the conduction time scale calculated above is the time for the region to come to equilibrium and so neutralise the pressure gradient, a feat which radiative dissipation is unable to accomplish due to the weak temperature dependence of the radiative loss function. However, the conduction time scale can be compared with the radiative time scale calculated below, as the value of  $\tau_c$  calculated in (3.10) can also be taken to be typical of the time required to bring the hot region into thermal equilibrium with its surrounding.

Considering only the radiative term, the energy equation takes the form

$$\frac{\partial}{\partial t} (3\rho RT) = - n_e^2 f(T) \quad (3.11)$$

where  $f(T)$  is the radiative loss function, which has been calculated for cosmic abundances (Cox and Tucker, 1969) and for solar abundances (Tucker and Koren, 1971). Therefore, to an order of magnitude

$$\frac{3\rho RT}{\tau_R} \approx \frac{3 n_e kT}{\tau_R} = n_e^2 f(T) \quad (3.12)$$

where  $\tau_R$  is the radiative cooling time scale.

Thus

$$\tau_R \approx \frac{3 kT}{n_e f(T)} \quad (3.13)$$

In the temperature region of interest  $f(T)$  is a weak function of  $T$ , and is given by

$$f(T) \approx 2 \times 10^{-23} \text{ erg cm}^3 \text{ sec}^{-1} (2 \times 10^6 \text{ K} < T < 10^8 \text{ K}) \quad (3.14)$$

Inserting this value and the values of temperature and density used previously ( $T = 20 \times 10^6 \text{ K}$ ,  $n_e = 10^{10} - 10^{11} \text{ cm}^{-3}$ ) in (3.13) we obtain

$$\tau_R \approx 4.2 \times 10^3 - 4.2 \times 10^4 \text{ sec} \quad (3.15)$$

Comparing this result with the conduction timescale given by (3.10) we see that at low density ( $n_e = 10^{10} \text{ cm}^{-3}$ ) radiation should be unimportant ( $\tau_R/\tau_C \approx 100$ ) but at the higher density of  $10^{11} \text{ cm}^{-3}$   $\tau_R \approx \tau_C$ , implying that radiative losses are as important as conduction of heat out of the source region.

However, there is a further point which must be noted. In its quiescent preflare state the filament must be maintained against radiative losses by a steady energy flux (for example, acoustic flux from the photosphere). The role of radiative cooling during the flare depends on the effect that the occurrence of the flare has on the ambient energy input. If this is unaffected, radiation does not influence the development of the flare unless there are large density fluctuations in the hot region, because radiation depends weakly on temperature although a strong function of density.

#### 4. DEFINITION OF THE PROBLEM

Although the order of magnitude estimates made in §3 can provide clues to the probable importance of different physical processes in a flare, it is obvious that useful discussion requires a more detailed analysis. We ask the following questions:-

- (1) How great is the influence of dynamical processes on energy redistribution in a heated plasma?
- (2) What form do the effects produced by mass motion take?
- (3) How sensitively do any such effects depend on physical conditions in the flare region?
- (4) Under what circumstances (if any) do the approximations of constant density or constant pressure hold?

In order to answer these questions we consider a definite structure, shown schematically in Figure 4.1. A coronal filament of length  $\sim 10^{10}$  cm and cross-sectional area  $\sim 10^{17}$  cm<sup>2</sup>, containing plasma of initial electron density  $\sim 10^{11}$  cm<sup>-3</sup> and temperature  $\sim 2 \times 10^6$  K has a pulse of energy injected into it at the top of the arch. Approximately  $10^{30}$  ergs are injected in a period of  $\sim 1$  minute. We follow the evolution of the filament into the decay phase.

Before pursuing this study further, we simplify the problem by making the following assumptions and postulates.

(1) We assume that the filamentary structure can be represented in one - dimensional geometry. This requires that the magnetic pressure is much greater than the gas pressure so that no motion takes place perpendicular to the axis of the flux tube. Thus we require

$$\frac{B^2}{8\pi} \gg 2 n_e kT \quad (4.1)$$

which, for an electron density of  $10^{10}$ - $10^{11}$  cm<sup>-3</sup> and a temperature of  $20 \times 10^6$  K becomes

$$B \gg 40 - 120 \text{ gauss.} \quad (4.2)$$

As this is typical of the field strength in a coronal filament, (4.2) is probably not invariably true and some lateral expansion of the flux tube in response to an energy input is to be expected. At present we assume a rigid flux tube of uniform cross-section.

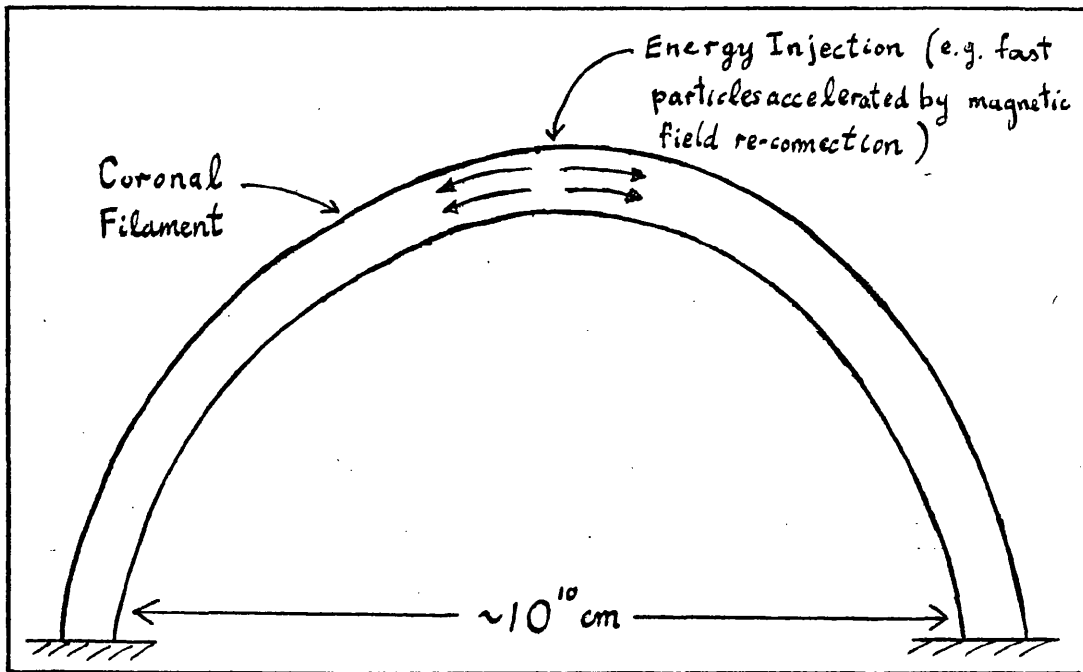


Figure 4.1 Schematic representation of a coronal filament heated by injection of flare energy at the top of the arch. Electron density is  $\sim 10^{10}$ - $10^{11}$   $\text{cm}^{-3}$ .

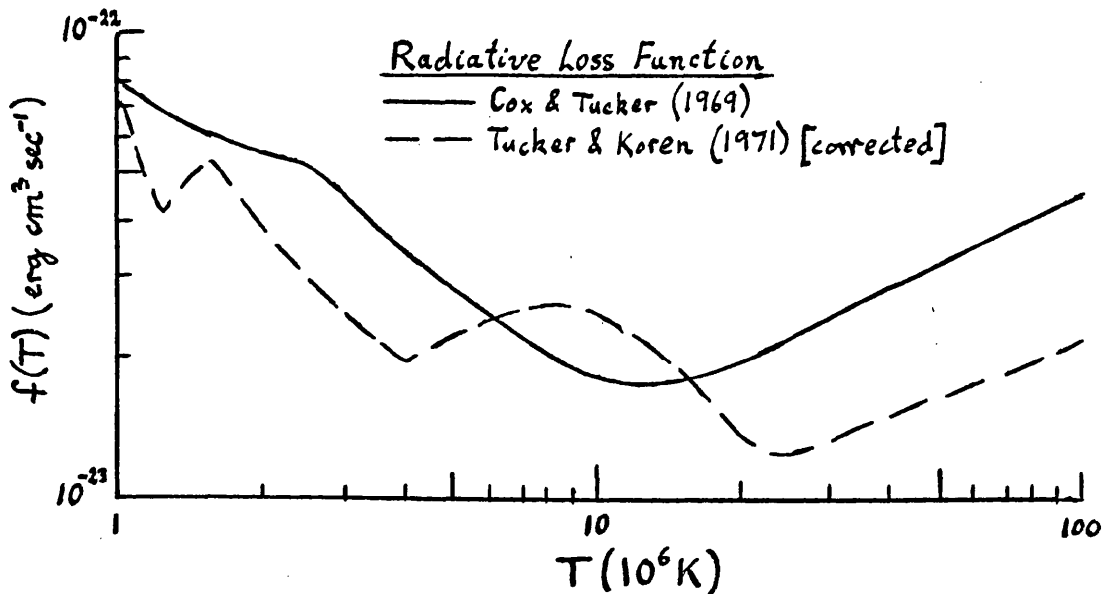


Figure 4.2 Temperature dependence of the radiative loss function for cosmic abundances (Cox & Tucker, 1969) and for solar abundances (Tucker & Koren, 1971).

In order that the problem be one-dimensional we also require that the rate of energy input be uniform across the flux tube. This is difficult to justify as nothing is known about the energy injection mechanism. However our one-dimensional treatment can be justified by noting that, due to the smallness of thermal conduction and viscous stress across the field lines the flux tube can be considered as a bundle of narrower flux tubes each independent of the others, and across each of which the energy injection rate is effectively constant. Thermal conductivity and viscous stress across the field lines are very small in a plasma of coronal density with a magnetic field greater than a fraction of a gauss as the ion cyclotron radius is much less than the mean free path (Spitzer, 1962).

It must be noted, however, that if energy input rate were a function of position across the flux tube our conclusions concerning the gross properties of the filament, in particular the soft X-ray differential emission measure, would be modified due to smearing of the structure over a range of physical conditions.

(2) We assume that the plasma consists of fully ionised hydrogen in which the electron and proton gases are in thermal equilibrium at any point. The main effect of the neglect of helium and heavy ions is that the density is underestimated by  $\sim 20\%$ , which leads to an overestimation of fluid velocity and kinetic energy. However this should not be severe enough to invalidate our conclusions. The contribution of heavy ions to the radiative loss function is of course included. The function used in our calculations is that computed for cosmic element abundances by Cox and Tucker (1969), shown in Figure 4.2.

In view of the fact that the solar abundance loss function (Tucker and Koren, (1971)) is very similar to this, and as was shown in the previous section, radiation is probably of minor importance in coronal flare energetics this discrepancy should not appreciably affect our conclusions. Since the material we are dealing with

is at coronal temperatures, the assumption of full ionisation is undoubtedly justified. In order to satisfy the assumption of a common electron and proton temperature, we are forced to hypothesise that the energy input mechanism heats the electrons and protons equally.

For typical densities and energy injection timescales, a difference of  $\sim 50\%$  between the electron and proton temperatures is to be expected if the injected energy is absorbed principally by the electrons and transferred to the protons through electron-proton collisions, as in the case of heating by a beam of high energy electrons. This could appreciably affect the efficiency of thermal conduction and the intensity of soft X-ray emission.

These three hypothesis - pure hydrogen plasma, fully ionised, with the electrons and protons in equilibrium, allow us to write for the pressure

$$P = 2 \rho RT \quad (4.3)$$

and for the thermal energy per unit volume

$$\epsilon = 3 \rho RT \quad (4.4)$$

where  $\rho$  is the density, given by

$$\rho = m_p n_e \quad (4.5)$$

and  $R, T$  are the gas constant and plasma temperature. (These relations were used in deriving equations (3.1 - (3.10)).

(3) We neglect the effect of gravity. The gravitational potential energy a fluid element at the top of the arch (of height  $h$ ) would lose in moving to the foot of the flux tube is

$$\epsilon_G = gh \quad (4.6)$$

where  $g$  is the acceleration due to gravity. For a maximum arch height of  $5 \times 10^9$  cm

$$\epsilon_G \approx 1.4 \times 10^{14} \text{ erg gm}^{-1} \quad (4.7)$$

As this is fairly small compared to a typical thermal energy density of  $\sim 5 \times 10^{15} \text{ erg gm}^{-1}$  the influence of gravity can be neglected to a first approximation, particularly in view of the fact that a fluid element is expected to move only a small distance compared to the length of the filament. This assumption allows us to consider a plasma of initially uniform density and temperature.

While this simplification may allow us better insight into the fundamental processes governing the flare heating, it introduces a problem in the decay phase. This is due to an unphysical aspect of the initial state of the plasma, that is, it is a state of unstable equilibrium. The radiative loss function decreases monotonically as the temperature rises from  $\sim 6 \times 10^5 \text{ K}$  to  $10^7 \text{ K}$ , so that if a perturbation on a plasma with an initially uniform temperature in that range causes the temperature to rise at one point, the temperature will continue to rise until a thermal gradient is established such that the thermal conductive flux out of the hotter regions balances the excess energy input due to the difference between the quiescent energy input and the smaller radiative losses at the new temperature. Therefore the filament does not return to its initial state in the decay phase, but tends towards a new equilibrium state.

Possibly the most significant effect of our assumption of an initially uniform structure lies in the observation that a shock is formed in the filament, as it is known that a compression wave running into a region of increasing density may be prevented

from forming a shock. Thus the inclusion of a realistic model atmosphere in our analysis may suppress formation of the shock. Even if this does happen, it is unlikely that our fundamental conclusion that mass motion is important will be altered.

(4) We assume that material in the filament is optically thin, so that there is no re-absorption of radiation emitted in accordance with the radiative loss function.

(5) We take account of viscosity. Although this effect is usually neglected, it can be important in regions of low density and high temperature. The fact that the presence of a viscous term in the momentum equation allows an unconditionally stable method of numerical solution (see §6) to be used provides further motivation for its inclusion.

The momentum equation with the effect of viscosity included is given by

$$\rho \frac{Dv}{Dt} = - \frac{\partial}{\partial z} \left( P - \frac{4}{3} \mu \frac{\partial v}{\partial z} \right) \quad (4.8)$$

$$\text{where } \mu = 2.21 \times 10^{-15} T^{5/2} / \ln \Lambda \quad (4.9)$$

is the viscous coefficient (Spitzer, 1962).

$\rho$ ,  $v$  and  $P$  are respectively density, fluid velocity and pressure and  $\ln \Lambda$  is the Coulomb logarithm.  $\ln \Lambda$  has a value of  $\sim 20$  in the solar corona. The Reynolds number of a flow (ratio of inertial to viscous forces) is given by

$$R_e = \frac{\rho v L}{\mu} \quad (4.10)$$

where  $\rho$  and  $v$  are characteristic values of density and velocity and  $L$  is a typical scale length for velocity variation. If we take

$$v = c = \sqrt{2RT} \quad (4.11)$$

where  $c$  is the sound speed, we obtain

$$R_e \sim n_{10} L_9 \left( \frac{40}{T_6} \right)^2 \quad (4.12)$$

where  $n_{10}$  is electron density in units of  $10^{10} \text{ cm}^{-3}$ ,  $L_9$  is the velocity scale length in units of  $10^9 \text{ cm}$  and  $T_6$  is temperature in units of  $10^6 \text{ K}$ .

Viscous effects become more important as  $R_e$  decreases, becoming dominant when  $R_e \sim 0(1)$ . In a three dimensional fluid, viscosity can dramatically alter the flow pattern by suppressing the onset of turbulence, even if the Reynolds number is much greater than unity. However in the filament which we consider turbulence is not possible as motion across the flux tube is suppressed by the strong magnetic field. Thus we expect that viscosity will only be important if  $R_e \sim 0(1)$ . For an electron density of  $10^{10} \text{ cm}^{-3}$  and a velocity scale length of  $10^9 \text{ cm}$ , viscosity becomes important when  $T \sim 40 \times 10^6 \text{ K}$ . For a higher density of  $n_e = 10^{11} \text{ cm}^{-3}$  the temperature must increase to  $120 \times 10^6 \text{ K}$  before viscous effects begin to dominate.

From these considerations we conclude that if the scale length for variation of velocity is not small compared to the overall length of the filament, viscosity is important only in regions of high temperature and low density. However we retain this term in the equations mainly because, as mentioned above, its presence enables a stable numerical method of solution to be used.

(6) For the energy injection mechanism we take the representation used by Strauss and Papagiannis (1971). The rate of heating varies along the filament according to a Gaussian profile so that

$$Q(z,t) = \frac{q(t)}{\sqrt{2\pi} \ell} e^{-\frac{z^2}{2\ell^2}} \text{ erg cm}^{-3} \text{ sec}^{-1} \quad (4.13)$$

where  $z$  is a spatial variable running along the filament with origin at the centre of the filament,  $\ell$  is a scale length of heating and  $q(t)$  is the total energy flux into the filament ( $\text{erg cm}^{-2} \text{ sec}^{-1}$ ).

This form is unrealistic in that the energy flux would be expected to be degraded as a function of column density of material passed through, rather than geometric distance, and furthermore, the rate of heating of a given volume element, which is equal to the rate of degradation of the energy flux in passing through that volume, should be proportional to the local density. Thus, for example, if material near the centre of the filament expands when heated, the lower density in this region will cause the rise in temperature to be abnormally high. These objections do not apply to the work of Strauss and Papagiannis as they assume a uniform plasma of constant density. As we start with such a plasma, so that column density is proportional to geometric distance initially, we assume that any unphysical aspects of (4.13) will not dramatically affect our conclusions. This view is supported by Strauss and Papagiannis, who claim that the exact spatial form of energy input is unimportant as thermal conduction controls the distribution of energy. In Chapter VII we consider briefly an electron-heated model in which a more realistic form of energy input is used. There we find that our conclusions are indeed unaltered, but that Strauss & Papagiannis are not strictly correct.

## 5. THE EQUATIONS

The following equations describing the dynamics of a one dimensional one-component fluid govern the evolution of the filament.

### Conservation of mass

$$\rho \frac{D\rho}{Dt} = -\rho \frac{\partial v}{\partial z} \quad (5.1)$$

### Momentum equation

$$\rho \frac{Dv}{Dt} = - \frac{\partial}{\partial z} \left( P - \frac{4}{3} \mu \frac{\partial v}{\partial z} \right) \quad (5.2)$$

### Energy equation

$$\rho \frac{De}{Dt} = Q + \frac{\partial}{\partial z} \left( K \frac{\partial T}{\partial z} \right) - \left( P - \frac{4}{3} \mu \frac{\partial v}{\partial z} \right) \frac{\partial v}{\partial z} - n_e^2 f(T) \quad (5.3)$$

The 5 terms in the energy equation represent respectively - energy injection due to a source; thermal conduction through the fluid element; work done by pressure; conversion of kinetic energy to thermal energy through viscosity; and loss of energy by radiation.

The symbols used are defined as follows :-

- $\rho$  = density ,
- $v$  = fluid velocity ,
- $P$  = gas pressure ,
- $\mu$  = coefficient of viscosity,
- $e$  = internal energy/unit mass,
- $Q$  = energy source
- $K$  = coefficient of thermal conduction,
- $T$  = temperature,
- $n_e$  = electron density ,
- $f(T)$  = radiative loss function,

$$\frac{D}{Dt} = \text{total time derivative} = \frac{\partial}{\partial t} + v \frac{\partial}{\partial z} ,$$

and  $z$  = spatial coordinate running along axis of flux tube with origin at the centre.

As established in (4.3-5) we have the following relations between these quantities:-

$$\rho = m_p n_e \quad (5.4)$$

$$e = 3 RT \quad (5.5)$$

$$P = 2\rho RT = 2 n_e kT \quad (5.6)$$

where  $k$  is Boltzmann's constant,  $R$  is the gas constant and  $m_p$  is the mass of the proton.

Both thermal conductivity and viscosity are strongly anisotropic in the presence of a magnetic field. As we consider only the effect of conduction and viscous stress parallel to the field, produced by gradients in the same direction, the general tensor form of these terms reduces to the simple form defined by (5.3) and (5.7), (5.12) below.

The coefficient of thermal conduction is given by (Spitzer, 1962)

$$K = K_0 T^{5/2} / \ln \Lambda \quad (5.7)$$

where  $K_0 = 1.844 \times 10^{-5}$  (c.g.s units) (5.8)

and  $\ln \Lambda$  is the Coulomb logarithm, having a value of  $\sim 20$  in the solar corona and being given more precisely by

$$\Lambda = \Lambda_0 T/n_e^{1/2} = \Lambda'_0 T/\rho^{1/2} \quad (5.9)$$

where

$$\Lambda_0 = 8.0324 \times 10^6 \quad \text{and} \quad \Lambda'_0 = 1.0389 \times 10^{-5}$$

(c.g.s units) (5.10)

Viscous stress is given by

$$\eta = \frac{4}{3} \mu \frac{\partial v}{\partial z} \quad (5.11)$$

where the coefficient of viscosity  $\mu$  has the same form as the coefficient of thermal conduction (5.7), being given by (Spitzer, 1962)

$$\mu = \mu_0 T^{5/2} / \ln \Lambda \quad (5.12)$$

where  $\mu_0$  has the value

$$\mu_0 = 2.21 \times 10^{-15} \quad (\text{c.g.s units}) \quad (5.13)$$

A coordinate system more suitable for solving problems of one dimensional fluid motion than the fixed Eulerian grid used in (5.1-3) is the Lagrangian coordinate system. Here a given spatial coordinate value is identified with a specific fluid element rather than a fixed point in space. Using the Lagrangian system, the development of shock fronts can be handled more easily than is possible in the case of Eulerian coordinates. A second advantage is that it enables the paths of fluid elements to be tracked, which can sometimes give better

insight into a problem that merely knowing the fluid density and velocity, which is all the information obtainable ( directly ) from the Eulerian formulation. As mentioned previously, we expect realistic energy input mechanisms to depend on column density rather than geometric depth. As the Lagrangian coordinate is identified with column density, such inputs are more easily handled in this system.

To transform (5.1-3) to a Lagrangian formulation we define a column density variable

$$\xi = \int_0^z \rho(z') dz' \quad (5.14)$$

from which it follows that

$$\frac{\partial}{\partial z} \rightarrow \rho \frac{\partial}{\partial \xi} \quad (5.15)$$

As the Lagrangian system moves with the fluid the total time derivative is identical to the partial time derivative in this representation. Therefore we have also the transformation

$$\frac{D}{Dt} = \frac{\partial}{\partial t} \Big|_z + v \frac{\partial}{\partial z} \Big|_t = \frac{\partial}{\partial t} \Big|_{\xi} \quad (5.16)$$

Defining the specific volume

$$v = 1/\rho \quad (5.17)$$

(5.1-3) can be written as (see, for example, Zel'dovich & Raizer, 1966)

$$\frac{\partial v}{\partial t} = \frac{\partial v}{\partial \xi} \quad (5.18)$$

$$\frac{\partial v}{\partial t} = -\frac{\partial P^*}{\partial \xi} \quad (5.19)$$

$$\frac{\partial (3RT)}{\partial t} = Q^* + \frac{\partial}{\partial \xi} \left( \frac{K}{V} \frac{\partial T}{\partial \xi} \right) - P^* \frac{\partial v}{\partial \xi} - \frac{1}{V} f_M(T) \quad (5.20)$$

where  $Q^*$  is the rate of energy input per unit mass, that is,

$$Q^* = Q/\rho = QV \text{ erg gm}^{-1}\text{sec}^{-1} \quad (5.21)$$

Here we have incorporated the viscous stress term and pressure in the term  $P^*$ , so that

$$P^* = P - \frac{4}{3} \mu \frac{\partial v}{\partial z} \quad (5.22)$$

or

$$P^* = \frac{1}{V} \left( 2RT - \frac{4}{3} \mu \frac{\partial v}{\partial \xi} \right) \quad (5.23)$$

$f_M(T)$  is the radiative loss function expressed in terms of mass density instead of number density, that is

$$\rho^2 f_M(T) = n_e^2 f(T) \quad (5.24)$$

so that 
$$f_M(T) = m_p^{-2} f(T) \text{ erg cm}^3 \text{ gm}^{-2} \text{ sec}^{-1} \quad (5.25)$$

As the coordinate system is moving with the fluid we have in addition the equation

$$\frac{\partial z}{\partial t} = v \quad (5.26)$$

which enables us to find the position of a fluid element in space.

If (5.18) is integrated directly numerical errors can result in non-conservation of mass (see Richtmyer & Morton, 1967). This can be avoided by integrating the set of equations (5.19), (5.20), (5.26) instead of (5.18), (5.19), (5.20).

In this case we obtain  $V$  from the equation

$$V = \frac{\partial z}{\partial \xi} \quad (5.27)$$

which is easily derived from (5.18) and (5.26).

This equation simply expresses conservation of mass, as can be clearly seen if we write it in the differential form

$$\Delta\xi = \frac{1}{V} \Delta z \quad (5.28)$$

and note that if  $\Delta\xi$  is a fixed increment in column density then we can write

$$\Delta\xi = \rho_0 \Delta x \quad (5.29)$$

where  $\Delta x$  is the corresponding initial space increment and  $\rho_0$  the initial density.

Then we have, from (5.17), (5.28) and (5.29)

$$\rho \Delta z = \rho_0 \Delta x \quad (5.30)$$

Thus the total mass in the space interval  $\Delta z$  is conserved as this interval expands or contracts.

Note that the energy source term ( $Q$  in (5.3),  $Q^*$  in (5.20)) must contain a contribution responsible for maintaining the filament against radiation in its quiescent state, as discussed in §4. This contribution is initially equal to

$$Q_0 = \rho_0^2 f_M(T_0) \quad (5.31)$$

If we assume that the quiescent input per unit volume remains constant during the flare, we have a source term

$$Q_{0V} = \rho_0^2 f_M(T_0) \text{ erg cm}^{-3} \text{ sec}^{-1} \quad (5.32)$$

in (5.3) and

$$Q_{0V}^* = \rho_0^2 f_M(T) / \rho \text{ erg gm}^{-1} \text{ sec}^{-1} \quad (5.33)$$

in (5.20), whereas if we take the quiescent input per unit mass to remain constant, the contributions to (5.3) and (5.20) are given by,

respectively,

$$Q_{OM} = (\rho/\rho_0) \rho_0^2 f_M(T_0) \text{ erg cm}^{-3} \text{ sec}^{-1} \quad (5.34)$$

and

$$Q_{OM}^* = \rho_0 f_M(T_0) \text{ erg gm}^{-1} \text{ sec}^{-1} \quad (5.35)$$

We will see in Chapter VII that, as might be expected physically, the choice of constant energy input per unit mass gives more physically satisfactory results.

As the filament is assumed to be symmetric about its centre, the equations are integrated in one half of the filament only, subject to the boundary conditions at the centre

$$\frac{\partial \rho}{\partial z} = 0 ; \quad \frac{\partial T}{\partial z} = 0 ; \quad v = 0 \quad (5.36)$$

and at the end of the flux tube ( $z = z_0$ )

$$\frac{\partial \rho}{\partial z} = 0 ; \quad T = T_0 ; \quad v = 0 \quad (5.37)$$

where  $T_0$  is the initial temperature. This condition, which corresponds to a fixed boundary held at constant temperature, is unimportant for the purposes of the present investigation, as we stop the computation as soon as any observable effects have propagated to the end of the filament. This is necessary as subsequent behaviour of the filament is determined by the exact nature of this boundary, and meaningful results can only be obtained by incorporating a realistic model of the structure of the lower solar atmosphere. As such a sophistication is unnecessary to our present purpose of illustrating the importance of mass motion to the evolution of a flare, we merely take the length of the flux tube to be sufficient to allow us to observe the initial development of the flare.

## 6. NUMERICAL METHOD FOR SOLUTION OF THE EQUATIONS

In this section we discuss the choice of a numerical method for the solution of equations (5.19), (5.20) and (5.26). Preliminary results of the integration of these equations showed that a shock front develops in the filament. It was initially hoped that the dissipation provided by the real viscosity (5.22) incorporated in equations (5.19) and (5.20) would be sufficiently large to control the shock. However this turned out not to be the case, and it was found necessary to add a pseudo-viscous term to the equations.

The necessity for this procedure stems from the fact that the passage of a shock front causes an increase in entropy of the fluid, that is, kinetic energy is converted into thermal energy. This transformation can only occur through the action of a dissipative mechanism such as viscosity. If such a term is not included in the equations representing the physical system the undissipated kinetic energy appears in the form of spurious oscillations behind the shock front. While the viscous term (5.22) helps to control these oscillations it is insufficient to damp them out completely.

It must be pointed out that the persistence of the oscillations when the physically correct viscous term is used does not mean that the oscillations are real. They arise because of the discretisation of the equations necessary in order to obtain a numerical solution. In a discretised representation of the physical system, all particles in an element of plasma are effectively replaced by a "super-particle", which interacts with neighbouring super-particles. Instead of having thermal energy in the form of random motion of individual particles, we attribute the macroscopic qualities of density and temperature to each super-particle. The passage of a shock front sets the super-particles in motion, in the same manner in which true particles in the gas would be thermally excited. (This was pointed out by R. Peierls (unpublished work) - see Richtmyer & Morton, 1967). However in our representation we do not recognise this motion as thermal energy, but regard it as macroscopic flow of the gas. The purpose of pseudo-viscosity is therefore to compensate for this

unphysical aspect of the discretised equations, by converting the energy of macroscopic oscillation to true internal energy.

The following analogy may clarify the above description. We compare a piston-driven shock in a fluid with a similar discrete system consisting of a line of billiard balls. Figure 6.1 shows the progression of the "shock front" along the line of balls. When the piston, travelling at velocity  $V$ , strikes the first ball this moves off with velocity  $2V$ , and comes to rest on striking the second ball, which moves off with velocity  $2V$ . It is apparent that the shock front moves forward (relative to the piston) at velocity  $V$ , and that each ball is alternatively at rest or moving at velocity  $2V$ . The balls marked with an 'X' in Figure 6.1 have just started moving. The temporal oscillation in velocity of a ball is illustrated at the foot of Figure 6.1; it is readily seen that a similar spatial oscillation exists as alternate balls are either moving or at rest.

These oscillations are analogous to the oscillations found behind a shock front in the absence of viscosity. If the billiard ball collisions are taken to be inelastic, so that the concepts of internal energy and dissipation enter the picture, half of the kinetic energy of the balls behind the shock would be converted to thermal energy (analogous to the temperature attribute of a super particle) and the balls would settle down to a steady movement to the right at velocity  $V$ .

In addition to its role as a convertor of kinetic energy to thermal energy, pseudo-viscosity has another function to perform, which again arises from the discretisation process necessary for a numerical solution of the equations. Because the finite difference numerical methods used to solve differential equations break down if variables change on a scale length comparable with the grid spacing, in a computer simulation we wish to spread the shock front over a few grid points even if the shock is strong enough that its physical thickness is less than this. Ordinary viscosity, which is a linear term of the form

$$\mu \frac{\partial v}{\partial z} \quad (6.1)$$

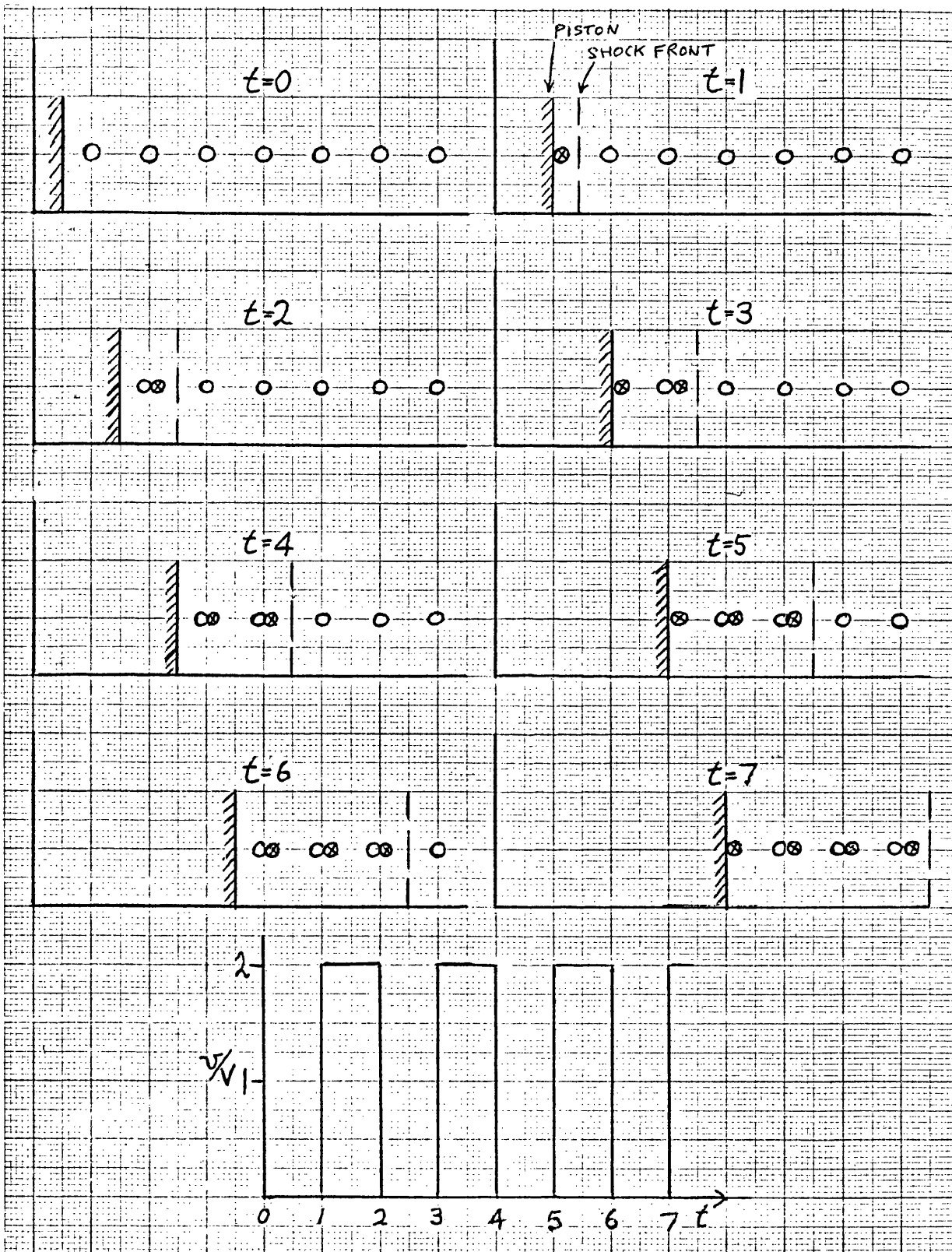


Figure 6.1 Illustration of the origin of oscillations behind a shock front in numerical simulation of fluid dynamic problems.

was shown by Becker (1922) to cause the thickness of the transition region (shock front) to vary with shock strength, approaching zero for a strong shock.

Von Neumann & Richtmyer (1950) found that a pseudo-viscous term which is quadratic in the velocity gradient has the desired effect, acting as a small viscosity for weak shocks and a large viscosity for strong shocks. Richtmyer & Morton (1967) give as a suitable form for this term in the Lagrangian formulation

$$q = \begin{cases} (\rho_0 \ell)^2 \left( \frac{\partial v}{\partial \xi} \right)^2 & \frac{\partial v}{\partial \xi} < 0 \\ 0 & \frac{\partial v}{\partial \xi} > 0 \end{cases} \quad (6.2)$$

(for a shock moving in the direction of increasing  $\xi$ ) where  $\rho_0$  and  $\ell$  are constants having dimensions of density and length respectively. They show, by means of analytic solution of a simple system, and by supporting numerical results, that where this form is used the Rankine-Hugoniot conditions across the shock are satisfied to a high degree of accuracy. This means that the smeared out shock travels with the same speed as a discontinuous physical one and produces the same entropy increase. They also show that the shock thickness is related to the parameter  $(\rho_0 \ell)$  in (6.2) by

$$t \sim 2 \sqrt{2/(\gamma + 1)} (\rho_0 \ell) / \rho \quad (6.3)$$

where  $\gamma$  is the ratio of specific heats of the fluid. Taking  $\gamma = 5/3$  and assuming that we require a shock thickness  $\rho t$  in  $\xi$ -space of  $\sim 4 \Delta \xi$ , where  $\Delta \xi$  is the grid spacing, we find

$$\rho_0 \ell = 1.7 \Delta \xi \quad (6.4)$$

Pseudo-viscosity is incorporated in our equations by redefining  $P^*$ , the pressure and viscous stress term in (5.19) and (5.20), to include the pseudo-viscous contribution given by (6.2). Thus, from (5.22) we now define

$$P^* = P - \frac{4}{3} \mu \frac{\partial v}{\partial z} + q \quad (6.5)$$

or

$$P^* = \frac{1}{V} \left[ 2 RT - \frac{4}{3} \mu \frac{\partial v}{\partial \xi} + (\rho_0 \ell)^2 \left( \frac{\partial v}{\partial \xi} \right)^2 \right] \quad (6.6)$$

In equations (6.5) and (6.6) we have not explicitly shown that the pseudo-viscous term, as defined in (6.2), is zero where  $\frac{\partial v}{\partial \xi} > 0$ . In order to avoid cumbersome notation, we will henceforth not note this fact explicitly.

In practice it makes very little difference whether the pseudo-viscous contribution is included outside the shock or not as this term is second order in the velocity gradient. In a shock front<sup>2</sup> the pseudo-viscous term is greater than the real viscosity by  $\sim 10^2$ , while outside the shock, in regions where the physical viscosity would normally be unimportant, both are small and of comparable size. As the pseudo-viscosity term is independent of temperature it does not contribute in high temperature regions where the real viscosity becomes important.

The next step in preparing the equations for numerical solution is to write them in dimensionless form by expressing the physical variables in terms of convenient scale values. As this procedure is only necessary in order to restrict the range of numbers to that which can be handled by the computer and is not essential to the method, it will be omitted here.

At this point we must decide on the formulation of the finite difference approximation to the equations. Firstly we have a choice of an explicit or an implicit method of solution. A simple example will serve to illustrate the difference in these techniques. To solve the equation

$$\frac{\partial y}{\partial t} = \frac{\partial y}{\partial x} \quad (6.7)$$

we write

$$y_i^{j+1} = y_i^j + \int_{t_j}^{t_{j+1}} \frac{\partial y}{\partial t} dt$$

that is,

$$y_i^{j+1} = y_i^j + \int_{t_j}^{t_{j+1}} \frac{\partial y}{\partial x} dt \quad (6.8)$$

where we have spatial grid points

$$x_i, i = 1, 2, \dots, N$$

separated by intervals of  $\Delta x$   
and temporal grid points

$$t_j, j = 1, 2, \dots$$

separated by intervals of  $\Delta t$   
and

$$y_i^j = y(x_i, t_j) \quad (6.9)$$

We now have a choice of approximations to (6.6). Two possibilities are

$$y_i^{j+1} = y_i^j + \left[ \left( \frac{\partial y}{\partial x} \right)_i^j + O(\Delta t) \right] \Delta t \quad (6.10)$$

or

$$y_i^{j+1} = y_i^j + \left[ \left( \frac{\partial y}{\partial x} \right)_i^{j+1} + O(\Delta t) \right] \Delta t \quad (6.11)$$

Introducing the finite difference approximation

$$\left( \frac{\partial y}{\partial x} \right)_i = \frac{y_{i+1} - y_{i-1}}{2 \Delta x} + O(\Delta x^2) \quad (6.12)$$

(6.10) and (6.11) become

$$y_i^{j+1} = y_i^j + \frac{1}{2 \Delta x} (y_{i+1}^j - y_{i-1}^j) + O(\Delta x^2 \Delta t) + O(\Delta t^2) \quad (6.13)$$

and

$$y_i^{j+1} = y_i^j + \frac{1}{2\Delta x} (y_{i+1}^{j+1} - y_{i-1}^{j+1}) + O(\Delta x^2 \Delta t) + O(\Delta t^2) \quad (6.14)$$

(6.11) is an explicit method of solution as all quantities on the RHS are known and the solution at time  $(j+1)$  at each  $i$  can be obtained immediately. (6.12) is implicit - quantities as yet unknown appear on the RHS, so that the system of equations ( $i = 1, 2, \dots, N$ ) must be solved simultaneously.

Although it may appear to be disadvantageous to use an implicit method, the question of stability must also be considered.

An explicit method becomes unstable, resulting in the development of oscillations in the solution, if the time step exceeds a certain value. In the case of a hyperbolic equation (wave equation) of the form

$$\frac{\partial^2 y}{\partial t^2} = c^2 \frac{\partial^2 y}{\partial x^2} \quad (6.15)$$

stability requires that

$$\Delta t < \Delta x/c \quad (6.16)$$

while for a parabolic equation (heat conduction equation) of the form

$$\frac{\partial y}{\partial t} = \sigma \frac{\partial^2 y}{\partial x^2} \quad (6.17)$$

we must have

$$\Delta t < \Delta x^2/2\sigma \quad (6.18)$$

(Richtmyer & Morton, 1967). No stability criterion applies to implicit methods, in which the timestep may be chosen freely having regard only for the accuracy of the solution. The stability condition (6.16) can be at least partially understood by

noting that disturbances occurring at distances greater than 1 space-step from grid point  $i$  require a time  $\geq \Delta x/c$  to produce an effect at point  $i$ , as the maximum speed of propagation of a disturbance is the sound speed  $c$ . When using a finite difference approximation to (6.15) the time derivative at point  $i$  depends only on the value of  $y$  at the grid points  $i-1$ ,  $i$  and  $i+1$  and so does not take account of effects occurring outside this region of space. Therefore the timestep is required to be small enough that such effects cannot propagate to point  $i$  during the timestep, that is,

$$\Delta t < \Delta x/c$$

Although exact stability criteria cannot be obtained for equations more complex than (6.15) and (6.17), the parabolic nature of our energy equation can be seen by dropping terms other than the heat conduction term from the RHS of (5.3), giving

$$\rho \frac{D(3RT)}{Dt} = \frac{\partial}{\partial z} \left( K \frac{\partial T}{\partial z} \right) \quad (6.19)$$

Neglecting the convective term and the spatial variation of  $K$ , we obtain

$$\frac{\partial T}{\partial t} = \frac{K}{3\rho R} \frac{\partial^2 T}{\partial z^2} \quad (6.20)$$

Comparing this equation with (6.15) we see that an explicit method of solution would result in the restriction

$$\Delta t < \frac{3\rho R}{2K} \Delta z^2 = \frac{3 n_e k \ln \Lambda}{2 K_0 T^{5/2}} \Delta z^2 = 2.3 \times 10^{-14} \frac{\Delta z^2}{T_6^{5/2}} \text{ sec} \quad (6.21)$$

where we have set  $n_e = 10^{11} \text{ cm}^{-3}$  and taken  $\ln \Lambda = 20$ .  $T_6$  is the temperature in units of  $10^6 \text{ K}$ . For a typical grid spacing of  $10^8 \text{ cm}$  this implies

$$\Delta t < \left( \frac{8.8}{T_6} \right)^{5/2} \text{ sec} \quad (6.22)$$

Thus the allowable timestep is a strong function of temperature,

having a value of 1 sec when the maximum temperature is  $8.8 \times 10^6 \text{K}$ , and falling to only 0.05 sec if  $T$  rises to  $30 \times 10^6 \text{K}$ . In a test run using an explicit method of integration it was found that the allowable timestep was even smaller than this in practice, falling to  $\sim 0.025$  sec when the temperature rose to  $\sim 20 \times 10^6 \text{K}$ . Clearly use of an explicit method would result in an enormous number of integration steps being required to simulate the evolution of a flare and a large amount of computer time would be required.

As the momentum equation is basically hyperbolic, the dynamical stability criterion is given by

$$\Delta t < \Delta z/c = \Delta z/\sqrt{2RT} \approx 1.7 \text{ sec} \quad (6.23)$$

for  $\Delta z = 10^8$  cm and  $T = 20 \times 10^6 \text{K}$ .

As this is an acceptable limitation on the timestep it would be feasible to integrate the momentum equation explicitly were it not for the parabolic component introduced into the equation by the viscosity terms. These are small outside the shock front and would give a timestep limitation greater than (6.23), however in the shock front the viscous terms dominate and could give rise to instability if a timestep of order 1 second were used. Therefore we use an implicit method for the solution of the momentum equation also.

## 7. FORMULATION OF THE FINITE DIFFERENCE EQUATIONS

Here we derive a 2nd order accurate finite difference approximation to equations (5.19), (5.20), (5.26) and (5.27). The order of accuracy of a finite difference scheme is defined to be the order of the error term before integration is carried out. As the integration process effectively multiplies the whole equation by the steplength, the error in the final value of the variable is one power higher. For example, given the equation

$$\frac{\partial y}{\partial t} = f(y,t) \quad (7:1)$$

then a possible finite difference approximation is

$$\frac{y_{j+1} - y_j}{\Delta t} = f(y_j, t_j) + O(\Delta t) \quad (7.2)$$

which has a first order error. Thus the final value of  $y$  is given by

$$y_{j+1} = y_j + \Delta t f(y_j, t) + O(\Delta t^2) \quad (7.3)$$

which has a first order accuracy.

The finite difference scheme we use is required to be accurate to 2nd order as we have physically real diffusion terms in our equations (thermal conduction and viscosity). Use of a 1st order accurate method introduces anomalous numerical diffusion, which can lead to unphysical results (Richtmyer & Morton, 1967). To achieve 2nd order accuracy we "centre" the  $(i,j)^{\text{th}}$  equation so that the finite difference approximations are symmetric. The connection between centring and order of accuracy can be illustrated by considering a simple example. A first order approximation to  $\frac{dy}{dx}$  at point  $x_i$  is given by

$$\left(\frac{dy}{dx}\right)_i = \frac{y_{i+1} - y_i}{\Delta x} + O(\Delta x) \quad (7.4)$$

while a centred second order approximation is

$$\left(\frac{dy}{dx}\right)_i = \frac{y_{i+1} - y_{i-1}}{2\Delta x} + O(\Delta x^2) \quad (7.5)$$

A common procedure is to centre the equations used to step from time  $t_j$  to time  $t_{j+1}$  about the point  $(i, j+\frac{1}{2})$ . As our equations are non-linear, use of this method would force us to solve the implicit finite difference equations by iteration. To avoid this we use the information obtained at time  $t_{j-1}$  and centre the equations at the point  $(i,j)$ . We are then able to evaluate non-linear terms,

such as the radiative loss function, at time  $t_j$  where the values of the physical variables are already known.

Writing out the momentum equation (5.19) in full, using the definition of  $P^*$  in (6.6), we have

$$\frac{\partial v}{\partial t} = - \frac{\partial}{\partial \xi} \left[ \frac{1}{V} \left\{ 2RT - \frac{4}{3} \mu \frac{\partial v}{\partial \xi} + (\rho_0 \ell)^2 \left( \frac{\partial v}{\partial \xi} \right)^2 \right\} \right] \quad (7.6)$$

which can be expressed as

$$\frac{\partial v}{\partial t} = - \frac{\partial}{\partial \xi} \left( \frac{2RT}{V} \right) + \frac{\partial}{\partial \xi} \left( \frac{4\mu}{3V} \right) \frac{\partial v}{\partial \xi} + \frac{1}{V} \left[ \frac{4}{3} \mu - 2(\rho_0 \ell)^2 \frac{\partial v}{\partial \xi} \right] \frac{\partial^2 v}{\partial \xi^2} \quad (7.7)$$

In finite difference form, this equation can be written

$$\begin{aligned} \frac{1}{2\Delta t} (v_i^{j+1} - v_i^{j-1}) &= \frac{-1}{2\Delta \xi} \left[ \left( \frac{2RT}{V} \right)_{i+1}^j - \left( \frac{2RT}{V} \right)_{i-1}^j \right] \\ &+ \frac{1}{(2\Delta \xi)^2} \left[ \left( \frac{4\mu}{3V} \right)_{i+1}^j - \left( \frac{4\mu}{3V} \right)_{i-1}^j \right] (v_{i+1}^j - v_{i-1}^j) \\ &+ \frac{1}{V_i^j} \left[ \frac{4}{3} \mu_i^j - 2(\rho_0 \ell)^2 \frac{1}{2\Delta \xi} (v_{i+1}^j - v_{i-1}^j) \right] \times \\ &\quad \frac{1}{\Delta \xi^2} (v_{i+1}^j - 2v_i^j + v_{i-1}^j) \end{aligned} \quad (7.8)$$

where

$$\left( \frac{2RT}{V} \right)_i^j = 2R \frac{T_i^j}{V_i^j}, \quad (7.9)$$

from (5.12)

$$\mu_i^j = \mu_0 \frac{(T_i^j)^{5/2}}{\ell n \Lambda (V_i^j, T_i^j)} \quad (7.10)$$

and

$$\left( \frac{4\mu}{3V} \right)_i^j = \frac{4}{3} \mu_0 \frac{(T_i^j)^{5/2}}{V_i^j \ell n \Lambda (V_i^j, T_i^j)} \quad (7.11)$$

In order to obtain an implicit formula, while retaining a linear form which can be solved without iteration, we approximate the second derivative of  $v$  with respect to  $\xi$  in (7.8), at time  $t_j$ , by the mean of its value at times  $t_{j-1}$  and  $t_{j+1}$ . That is, we write

$$\begin{aligned} (v_{i+1}^j - 2v_i^j + v_{i-1}^j) &= \frac{1}{2} \left[ (v_{i+1}^{j+1} - 2v_i^{j+1} + v_{i-1}^{j+1}) + \right. \\ &\quad \left. (v_{i+1}^{j-1} - 2v_i^{j-1} + v_{i-1}^{j-1}) \right] + O(\Delta t^2) \end{aligned} \quad (7.12)$$

We found (6.4) that the value of  $(\rho_0 \ell)$  required to spread the shock front over a few grid points was

$$\rho_0 \ell = \alpha \Delta \xi \quad (7.13)$$

where  $\alpha \approx 1.7$ .

Substituting from (7.12) and (7.13) into (7.8) and taking terms evaluated at time  $t_{j+1}$  to the LHS, we obtain

$$\begin{aligned} v_{i-1}^{j+1} - (2 + \beta_i^j) v_i^{j+1} + v_{i+1}^{j+1} &= \\ - (v_{i-1}^{j-1} - (2 - \beta_i^j) v_i^{j-1} + v_{i+1}^{j-1}) & \\ + \frac{\Delta t}{\Delta \xi} \beta_i^j \left\{ \left[ \left( \frac{2RT}{V} \right)_{i+1}^j - \left( \frac{2RT}{V} \right)_{i-1}^j \right] - \frac{1}{2\Delta \xi} \left[ \left( \frac{4\mu}{3V} \right)_{i+1}^j - \left( \frac{4\mu}{3V} \right)_{i-1}^j \right] \right\} & \\ (v_{i+1}^j - v_{i-1}^j) \} & \end{aligned} \quad (7.14)$$

where

$$\beta_i^j = \frac{\Delta \xi^2}{\Delta t} \left/ \left( \frac{1}{v_i^j} \left[ \frac{4}{3} \mu_i^j - \alpha^2 \Delta \xi (v_{i+1}^j - v_{i-1}^j) \right] \right) \right. \quad (7.15)$$

Following a similar procedure for the energy equation (5.20) we write

$$\frac{\partial T}{\partial t} = \frac{1}{3R} \left\{ Q^* + \frac{\partial}{\partial \xi} \left( \frac{K}{V} \right) \frac{\partial T}{\partial \xi} + \frac{K}{V} \frac{\partial^2 T}{\partial \xi^2} - P^* \frac{\partial v}{\partial \xi} - \frac{1}{V} f_M(T) \right\} \quad (7.16)$$

which in finite difference form becomes

$$\begin{aligned} \frac{1}{2\Delta t} (T_i^{j+1} - T_i^{j-1}) &= \frac{1}{3R} Q_i^{*j} + \frac{1}{(2\Delta \xi)^2} \left[ \left( \frac{K}{V} \right)_{i+1}^j - \left( \frac{K}{V} \right)_{i-1}^j \right] (T_{i+1}^j - T_{i-1}^j) \\ &+ \left( \frac{K}{V} \right)_i^j \frac{1}{\Delta \xi^2} (T_{i+1}^j - 2T_i^j + T_{i-1}^j) - P_i^{*j} \frac{1}{2\Delta \xi} (v_{i+1}^j - v_{i-1}^j) \\ &- \frac{1}{V_i^j} f_M(T_i^j) \end{aligned} \quad (7.17)$$

where from (5.7)

$$\left( \frac{K}{V} \right)_i^j = K_0 \frac{(T_i^j)^{5/2}}{V_i^j \ln \Lambda (V_i^j, T_i^j)} \quad (7.18)$$

and from (6.6) and (7.8)

$$P_i^{*j} = \frac{1}{V_i^j} \left\{ 2RT_i^j - \frac{4}{3} \mu_i^j \frac{1}{2\Delta \xi} (v_{i+1}^j - v_{i-1}^j) + \alpha^2 \frac{1}{4} (v_{i+1}^j - v_{i-1}^j)^2 \right\} \quad (7.19)$$

Replacing the 2nd derivative of  $T$  with respect to  $\xi$  at time  $t_j$  in (7.17) by the mean of its value at  $t_{j-1}$  and  $t_{j+1}$ , as we did in the case of the momentum equation in (7.12), and taking terms evaluated at  $t_{j+1}$  to the LHS, we obtain

$$\begin{aligned} T_{i-1}^{j+1} - (2 + \gamma_i^j) T_i^{j+1} + T_{i+1}^{j+1} &= \\ - (T_{i-1}^{j-1} - (2 - \gamma_i^j) T_i^{j-1} + T_{i+1}^{j-1}) & \\ - \frac{2\Delta t}{3R} \gamma_i^j \left\{ Q_i^{*j} + \frac{1}{(2\Delta \xi)^2} \left[ \left( \frac{K}{V} \right)_{i+1}^j - \left( \frac{K}{V} \right)_{i-1}^j \right] (T_{i+1}^j - T_{i-1}^j) \right. & \\ \left. - P_i^{*j} \frac{1}{2\Delta \xi} (v_{i+1}^j - v_{i-1}^j) - \frac{1}{V_i^j} f_M(T_i^j) \right\} & \end{aligned} \quad (7.20)$$

where

$$\gamma_i^j = \frac{\Delta \xi^2}{\Delta t} \left/ \left( \frac{1}{3R} \left( \frac{K}{V} \right)_i^j \right) \right. \quad (7.21)$$

In order to keep track of the fluid elements, and to evaluate the density, we must also integrate (5.26) which is

$$\frac{\partial z}{\partial t} = v \quad (7.22)$$

Assuming that we have already solved (7.14) to obtain a value for  $v$  at time  $t_{j+1}$ , we can integrate (7.22) by a straightforward application of Simpson's Rule, which gives

$$z_i^{j+1} - z_i^j = \frac{\Delta t}{3} (v_i^{j+1} + 4v_i^j + v_i^{j-1}) \quad (7.23)$$

As Simpson's Rule is 4th order accurate, this formula more than meets the requirement of 2nd order accuracy.

Finally we must obtain the density at time  $t_{j+1}$  from (5.27),

$$v = \frac{\partial z}{\partial \xi} \quad (7.24)$$

To maintain 2nd order accuracy, we must use a more exact finite difference formula than the normal centred approximation to a first derivative as no integration is performed on (7.24), the error in the finite difference formula being the actual error in  $v$ . Therefore we use the 3rd order accurate formula

$$v_i^{j+1} = \frac{-z_{i+2}^{j+1} + 8z_{i+1}^{j+1} - 8z_{i-1}^{j+1} + z_{i-2}^{j+1}}{12 \Delta \xi} \quad (7.25)$$

except for the 2 points nearest the end of the flux tube ( $i = N-1, i=N$ ) where we use the one-sided, 2nd order accurate formula

$$v_i^{j+1} = \frac{11 z_i^{j+1} - 18 z_{i-1}^{j+1} + 9 z_{i-2}^{j+1} - 2 z_{i-3}^{j+1}}{6 \Delta \xi} \quad (7.26)$$

## 8. SOLUTION OF THE FINITE DIFFERENCE EQUATIONS

The finite difference approximations to the momentum equation (7.14) and the energy equation (7.20) are seen to conform to the general equation

$$Y_{i-1} - a_i Y_i + Y_{i+1} = b_i \quad i = 0, 1, \dots, N \quad (8.1)$$

This system of equations can be written in the form of a tri-diagonal band matrix

$$\begin{bmatrix} \diagup & & & & \\ & \diagdown & & & \\ & & 1 & -a_{i-1} & 1 \\ & & & \diagdown & \\ & & & & 1 & -a_i & 1 \\ & & & & & \diagdown & \\ & & & & & & 1 & -a_{i+1} & -1 \\ & & & & & & & \diagdown & \\ & & & & & & & & \diagup & & \end{bmatrix} \begin{bmatrix} \cdot \\ \cdot \\ y_{i-1} \\ y_i \\ y_{i+1} \\ \cdot \\ \cdot \end{bmatrix} = \begin{bmatrix} \cdot \\ \cdot \\ b_{i-1} \\ b_i \\ b_{i+1} \\ \cdot \\ \cdot \end{bmatrix} \quad (8.2)$$

We solve the system of equation by reducing the matrix to bi-diagonal form (see Richtmyer & Morton, 1967). The bi-diagonal form we use is defined by the transformation of (8.1) to

$$Y_i - c_i Y_{i+1} = -d_i \quad (8.3)$$

Assume that the  $(i-1)^{\text{th}}$  row is in bi-diagonal form and we now require to reduce the  $i^{\text{th}}$  row to bi-diagonal form. Writing the matrices of coefficients as a single partitioned matrix, we have

$$\left[ \begin{array}{cccccc|c} \cdot & \cdot & 0 & 1 & -c_{i-1} & \cdot & \cdot & -d_{i-1} \\ \cdot & \cdot & \cdot & 1 & -a_i & 1 & \cdot & b_i \end{array} \right] \quad (8.4)$$

We perform the following row operations on row  $i$ .

Subtracting the  $(i-1)^{\text{th}}$  row, we have

$$\left[ \begin{array}{cccccc|c} \cdot & 0 & 1 & -c_{i-1} & \cdot & \cdot & -d_{i-1} \\ \cdot & \cdot & 0 & -a_i + c_{i-1} & 1 & \cdot & b_i + d_{i-1} \end{array} \right] \quad (8.5)$$

Dividing by  $-a_i + c_{i-1}$  gives

$$\left[ \begin{array}{cccccc|c} \cdot & 0 & 1 & -c_{i-1} & \cdot & \cdot & -d_{i-1} \\ \cdot & \cdot & 0 & 1 & \frac{1}{-a_i + c_{i-1}} & \cdot & \frac{b_i + d_{i-1}}{-a_i + c_{i-1}} \end{array} \right] \quad (8.6)$$

Therefore we define

$$c_i = 1/(a_i - c_{i-1}) \quad (8.7)$$

and

$$d_i = c_i(b_i + d_{i-1}) \quad (8.8)$$

so that the  $i^{\text{th}}$  equation is now in the form (8.3). When this procedure has been carried out for all the equations, each can be written in the form

$$y_i = c_i y_{i+1} - d_i \quad (8.9)$$

Thus given  $y_{i+1}$  we can find  $y_i$ , or vice versa.

In the above discussion we have treated the band matrix as though it was of infinite extent, neglecting to consider the effect of boundary conditions.

As the fluid velocity must be anti-symmetric about the origin (grid point 0), we require

$$v_0 = 0 ; v_{-1} = -v_1 \quad (8.10)$$

Thus the 0<sup>th</sup> equation is redundant, reducing to an identity, and the 1<sup>st</sup> equation becomes

$$-a_1 v_1 + v_2 = b_1 \quad (8.11)$$

If we set

$$a_0 = b_0 = 0 \quad (8.12)$$

then the application of (8.7) and (8.8) for  $i=1,2,\dots,N-1$  gives the correct transformation of (7.14) to bi-diagonal form. At the end of the flux tube we have a fixed boundary, which requires

$$v_N = 0 \quad (8.13)$$

so that the  $(N-1)$ <sup>th</sup> equation becomes

$$v_{N-2} - a_{N-1} v_{N-1} = b_{N-1} \quad (8.14)$$

The boundaries of the band matrix therefore take the form

$$\left[ \begin{array}{cccccc|c} -a_1 & 1 & \cdot & \cdot & \cdot & \cdot & b_1 \\ 1 & -a_2 & 1 & \cdot & \cdot & \cdot & b_2 \\ \cdot & & & & & \cdot & \cdot \\ \cdot & & & & & \cdot & \cdot \\ \cdot & \cdot & \cdot & 1 & -a_{N-2} & 1 & b_{N-2} \\ \cdot & \cdot & \cdot & \cdot & 1 & -a_{N-1} & b_{N-1} \end{array} \right] \quad (8.15)$$

which in bi-diagonal form is

$$\begin{bmatrix} 1 & -c_1 & \cdot & \cdot & \cdot & \cdot & \cdot \\ 0 & 1 & -c_2 & \cdot & \cdot & \cdot & \cdot \\ \cdot & \cdot & \cdot & \cdot & \cdot & \cdot & \cdot \\ \cdot & \cdot & \cdot & \cdot & \cdot & \cdot & \cdot \\ \cdot & \cdot & \cdot & 0 & 1 & -c_{N-2} & -d_{N-2} \\ \cdot & \cdot & \cdot & \cdot & 0 & 1 & -d_{N-1} \end{bmatrix} \quad (8.16)$$

Thus we have

$$v_{N-1} = -d_{N-1} \quad (8.17)$$

and by successive application of (8.9) for  $i=N-2, N-3, \dots, 1$  we find the velocities at all grid points.

The boundary conditions for the energy equation are slightly different. Symmetry about the origin requires that

$$\frac{\partial T}{\partial z} = 0 \quad (8.18)$$

which we represent in finite difference form as

$$T_{-1} = T_1 \quad (8.19)$$

Thus the equation for the central temperature  $T_0$  becomes

$$-a_0 T_0 + 2T_1 = b_0 \quad (8.20)$$

By setting

$$c_0 = 2/a_0 \quad (8.21)$$

and

$$d_0 = b_0/a_0 \quad (8.22)$$

and applying (8.7) and (8.8) for  $i=1,2,\dots,N-1$  we reduce the matrix to bi-diagonal form. At the end of the filament, we have

$$T_N = T^* \quad (8.23)$$

where  $T^*$  is the initial temperature. Thus the  $(N-1)^{\text{th}}$  equation becomes

$$T_{N-2} - a_{N-1} T_{N-1} = b_{N-1} - T^* \quad (8.24)$$

After reduction of (7.20) to bi-diagonal form, we therefore set

$$T_{N-1} = c_{N-1} T^* - d_{N-1} \quad (8.25)$$

before solving by back-substitution using (8.9).

CHAPTER VIITHE ROLE OF MASS MOTION IN ENERGY TRANSFER IN A  
HEATED FILAMENT - RESULTS AND CONCLUSIONS1. INTRODUCTION

In this chapter results computed from the analysis of the previous chapter are presented. The evolution of a heated filament under four different models of energy input is examined in an attempt to discriminate between general effects and model-dependent ones. The source electron density and temporal variation of energy input rate found by Strauss & Papagiannis (1971) to give agreement with hard X-ray data form the basis for Model I. The initial electron density is  $10^{11} \text{ cm}^{-3}$  and the energy input rate is constant, being equal to  $10^{11} \text{ erg cm}^{-2} \text{ sec}^{-1}$ . This model should give an indication of the time necessary for a pressure equilibrium to be set up in the presence of a constant energy input. Model II also has an initial density of  $10^{11} \text{ cm}^{-3}$ , but energy is injected in the form of a pulse, a total of  $5 \times 10^{12} \text{ ergs cm}^{-2}$  being injected over a period of one minute. This gives peak temperatures comparable with those inferred for the soft X-ray flare and allows the decay phase to be studied.

In order to examine the influence of density on the evolution of the filament we have studied two models with a lower initial density of  $10^{10} \text{ cm}^{-3}$ . Model III, like Model I, has an extended energy input while the energy input to Model IV takes the form of a pulse as in Model II. In Model III the energy input rate is  $10^{10} \text{ ergs cm}^{-2} \text{ sec}^{-1}$  while in Model IV a total of  $10^{12} \text{ ergs cm}^{-2}$  is injected in one minute. In all models the initial temperature is taken to be  $2 \times 10^6 \text{ K}$  and the scale length of heating ( $l$  in VI (4.13)) is set equal to  $2 \times 10^9 \text{ cm}$ , the value used by Strauss and Papagiannis, this length being of the order of the stopping distance of a deka-Kev electron and so is appropriate to particle heating.

## 2. PRELIMINARY INVESTIGATIONS

First of all, we illustrate the effect of the form of quiescent energy input and of pseudo-viscosity. The energy source term  $Q^*$  is given by

$$Q^*(\xi, t) = Q_0^* + V Q(z(\xi), t) \quad (2.1)$$

where  $V$  is the specific volume,  $Q(z, t)$  is given by VI (4.13) and  $Q_0^*$  is given by VI (5.33) or VI (5.35) depending on whether the quiescent input is assumed constant per unit volume or per unit mass.

As mentioned in Chapter VI, a shock front develops in the filament and it was found necessary to introduce a pseudo-viscous term into the equations to control this. Results of a test computation are shown in Figure 2.1. Figures (a)-(d) illustrate the form of the shock in Model I 165 seconds after the start of heating while Figure (e)-(h) show the shock profile after 230 seconds in Model II. Use of physical viscosity alone leads to the results depicted in figures (a), (c), (e) and (g) while the inclusion of the pseudo-viscous term VI (6.2) with  $\alpha = 1.7$  gives the results shown in figures (b), (d), (f) and (h). Figures (a), (b), (e) and (f) (labelled  $Q_{OV}$ ) were obtained on the assumption of a constant quiescent input per unit volume while the assumption of constant quiescent input per unit mass leads to the results shown in figures (c), (d), (g) and (h) (labelled  $Q_{CM}$ ).

It is apparent from these results that the real viscosity is insufficient to stabilise the behaviour of the fluid behind the shock, particularly when the quiescent input is constant per unit volume (figures (a) and (e)). In the case of constant quiescent input per unit mass (figures (c) and (g)) oscillations are present but the general form of the shock profile is similar to that obtained with pseudo-viscosity.

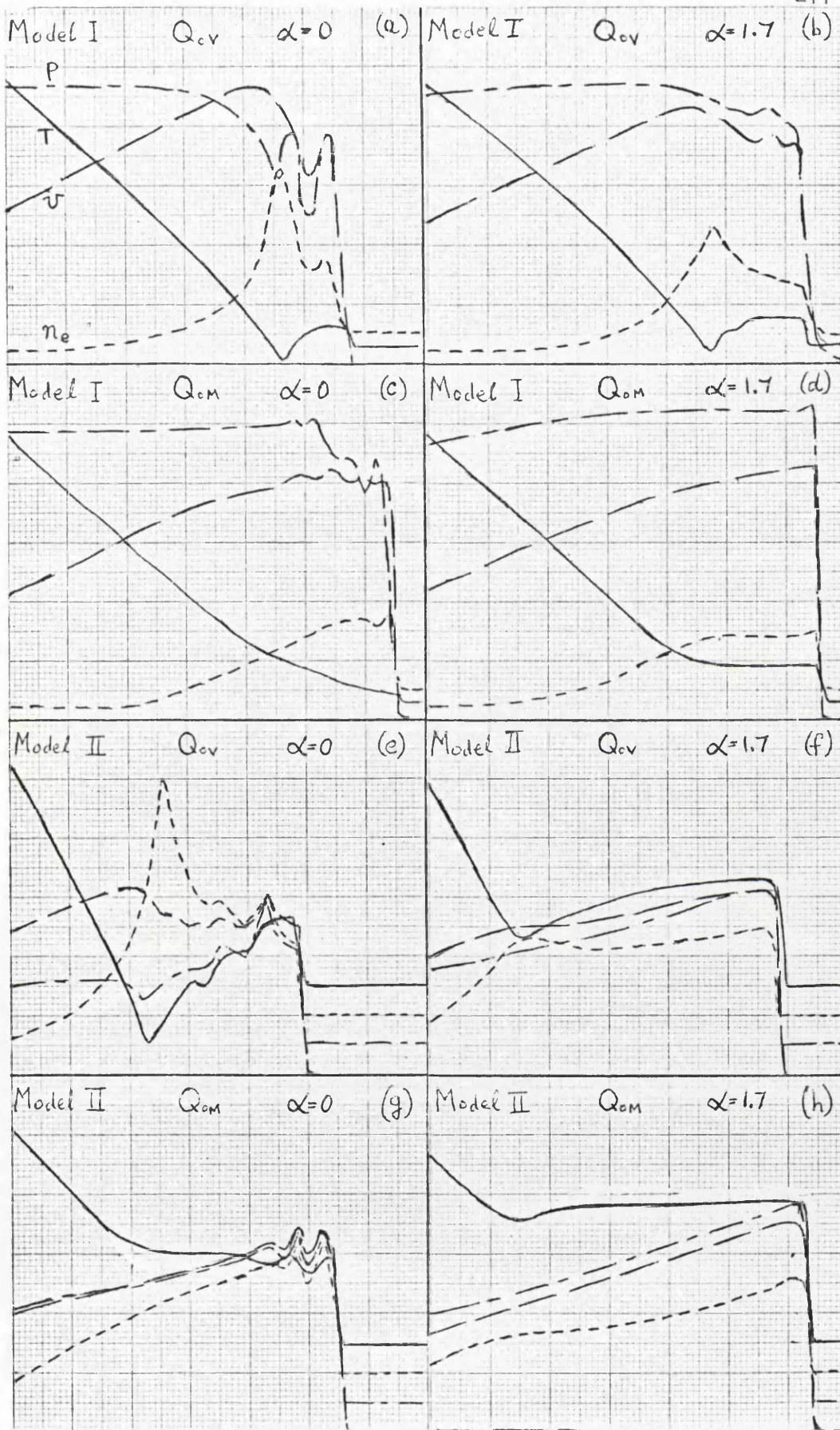


Figure 2.1 Stability of the shock front for quiescent input per unit volume/mass, with/without pseudo-viscosity.

We select figure (g) for further study as it appears to be the most "physical" of the results obtained without pseudo-viscosity. As it is not immediately obvious that the oscillations visible in (g) are non-physical or that the use of pseudo-viscosity in (h) has resulted in a "better" solution, we examine these results more closely by applying the Rankine-Hugoniot conditions across the shock front. In the absence of thermal conduction, which can be neglected here as the temperature gradient is small ahead of and behind the shock, these conditions may be written (Bray & Loughhead, 1974)

$$\frac{\rho_1}{\rho_2} = \frac{u_1}{u_2} \quad (2.2)$$

$$\frac{u_1}{u_2} = \frac{(\gamma+1) M^2}{(\gamma-1) M^2 + 2} \quad (2.3)$$

$$\frac{P_2}{P_1} = \frac{2\gamma M^2 - (\gamma-1)}{\gamma+1} \quad (2.4)$$

$$\frac{T_2}{T_1} = \frac{[2\gamma M^2 - (\gamma-1)] [(\gamma-1)M^2 + 2]}{(\gamma+1)^2 M^2} \quad (2.5)$$

Here subscripts 1 and 2 refer to the values of variables immediately in front of, and behind, the shock respectively,  $\rho$ ,  $P$ ,  $T$  and  $\gamma$  having their usual meanings.  $M$  is the Mach number of the shock front relative to the material ahead of it,

$$M = U/c_1 \quad (2.6)$$

where  $U$  is the shock speed and  $c_1$  is the sound speed in the medium in front of the shock, given by

$$c_1 = \sqrt{\gamma 2 R T_1} \quad (2.7)$$

$u_1$  and  $u_2$  refer to reduced velocities, that is the flow velocities relative to the shock. If the velocities of material ahead of

and behind the shock are  $v_1$  and  $v_2$  in the stationary frame of reference then we have

$$u_1 = v_1 - U \quad (2.8)$$

and

$$u_2 = v_2 - U \quad (2.9)$$

Table 2.1 displays the appropriate values of the above variables for the cases illustrated in Figure 2.1 (g) and (h)

TABLE 2.1

	(g) no pseudo-viscosity	(h) with pseudo-viscosity	Units
$n_{e1}$		1.0	$10^{11} \text{ cm}^{-3}$
$v_1$		0	$10^7 \text{ cm sec}^{-1}$
$T_1$		2.0	$10^6 \text{ K}$
$n_{e2}$	3.2	2.6	$10^{11} \text{ cm}^{-3}$
$v_2$	3.5	3.5	$10^7 \text{ cm sec}^{-1}$
$T_2$	4.0	5.1	$10^6 \text{ K}$

We now test the validity of solutions (g) and (h) by checking whether the values shown in Table 2.1 satisfy the Rankine-Hugoniot conditions. The results obtained by the following procedure are shown in Table 2.2. Substituting for  $\rho_2/\rho_1 = n_{e2}/n_{e1}$  in (2.2) we obtain a value for  $u_1/u_2$ , which together with  $v_1$  and  $v_2$  from Table 2.1 enables us to find  $U$  using (2.8) and (2.9). Taking  $\gamma = 5/3$  and using (2.6) and (2.7) we obtain a value for  $M$ , while from (2.3) we calculate an independent value of  $M$ , denoted  $M^*$  in Table 2.2. Finally we use the Mach numbers  $M$  and  $M^*$  to obtain  $T_2$  and  $T_2^*$  from (2.5)

TABLE 2.2

	(g) no pseudo-viscosity	(h) with pseudo-viscosity	Units
$U$	5.1	5.7	$10^7 \text{ cm sec}^{-1}$
$M$	2.2	2.4	$10^7 \text{ cm sec}^{-1}$
$M^*$	3.5	2.4	$10^7 \text{ cm sec}^{-1}$
$T_2$	4.6	5.2	$10^6 \text{ K}$
$T_2^*$	9.2	5.2	$10^6 \text{ K}$

Referring to Table 2.2 we see that when the pseudo-viscous term is included the two values of Mach number are in agreement and the temperature behind the shock required to satisfy the Rankine-Hugoniot conditions is close to the actual value obtained in Table 2.1. However when pseudo-viscosity is omitted the calculated values do not satisfy the Rankine-Hugoniot conditions. The discrepancy between the two Mach numbers derived from the Rankine-Hugoniot conditions indicates an inconsistency, and as a consequence the values of  $T_2$  and  $T_2^*$  required to satisfy the Rankine-Hugoniot conditions on the assumption of the correctness of  $M$  and  $M^*$  respectively are widely different from the values obtained computationally (Table 2.1). Therefore all subsequent computations include the pseudo-viscous term (with the parameter  $\alpha$  equal to 1.7).

Comparing Figure 2.1(b) with (d) we see that an unusual feature is introduced when the quiescent energy input is constant per unit volume. A region of high density and low temperature separates from the shock front and falls behind it. This phenomenon can be understood qualitatively by considering the energy balance behind the shock front, illustrated schematically in Figure 2.2. We assume that a shock wave similar to that occurring in Figure 2.1(d) has developed (Figure 2.2(i)) and evaluate the rate of heating per unit mass experienced by a fluid element in passing through the shock.

Initially the quiescent input balances the radiative losses ( $t < t_0$  in Figure 2.2(ii)). As the material passes into the high density region behind the shock radiative losses increase dramatically (as the square of the density) but as the material is being heated strongly by the shock there is a net increase in temperature. Once the material passes out of the region of shock heating radiative losses cause it to cool rapidly because of the high density. (See Figure 2.2(iii)). Thus a temperature minimum develops behind the shock giving rise to a pressure gradient which decelerates the cooler material (Figure 2.2(iv)), causing it to separate from the shock front. This material piles up, leading to the formation of a peak in the

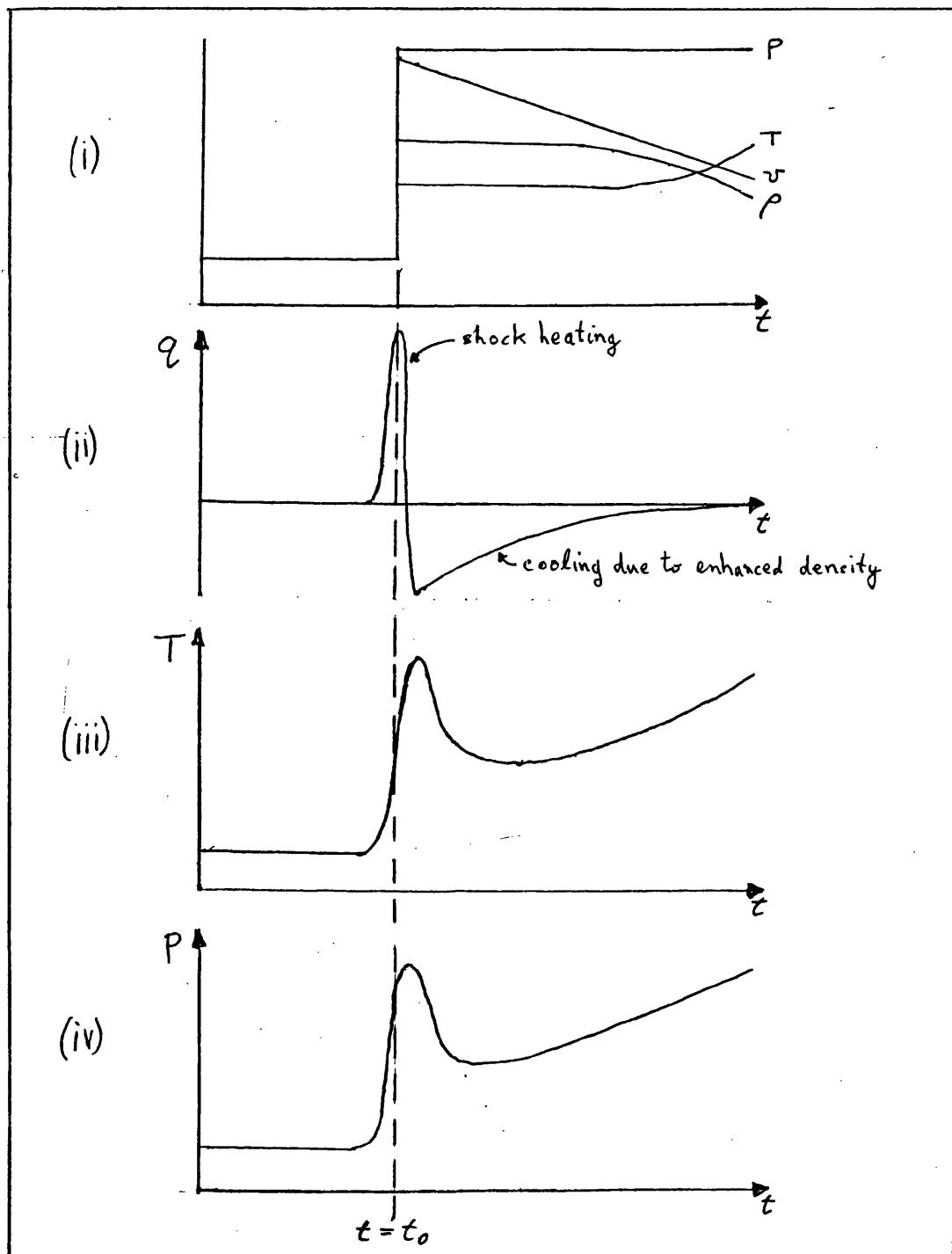


Figure 2.2 Schematic illustration of the energy balance behind a shock front.

density which enhances radiative losses (but with no enhancement of the input) thus causing a further drop in temperature. This effect can also be seen in Figure 2.1 (f), although not as markedly as in (b).

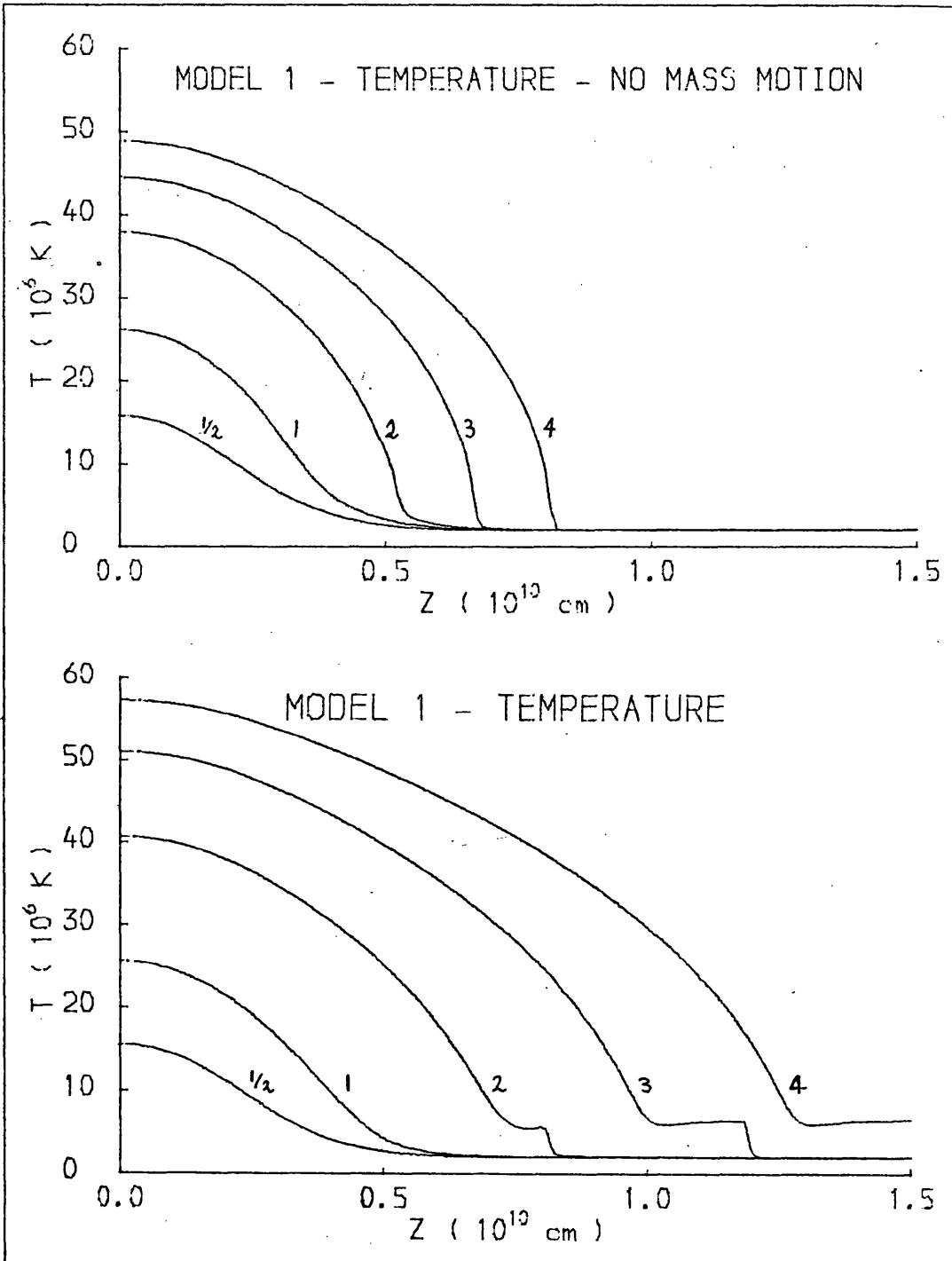
For the remainder of this chapter we assume that the quiescent input is constant per unit mass as this form of energy deposition seems more physically reasonable than one independent of density.

### 3. MODEL I ( CONTINUOUS ENERGY INJECTION , HIGH DENSITY )

In §3 - 6 we examine the evolution of the temperature, velocity, density and pressure distributions in each model. We also compare the temperature distribution in each case with that obtained when mass motion is inhibited. In presenting these results we take the length of the flux tube to be  $3 \times 10^{10}$  cm in order to follow the evolution of the models for a reasonable period of time without encountering the boundaries at the ends of the tube. As this distance is rather large for an active region structure some of the results discussed here may not be directly applicable to the heating of a coronal filament.

The evolutions of temperature structure, with and without mass motion, in Model I are shown in Figures 3.1 and 3.2. Strauss and Papagiannis (1971), who developed this model initially, took the length of the filament to be such that a noticeable temperature gradient did not develop at the end of the filament during the time interval of interest. They found that for the rather low initial temperature assumed ( $< 10^5$  K) effects propagated less than  $1.5 \times 10^{10}$  cm in a time of 30 minutes. For an initial temperature of  $2 \times 10^6$  K the effect of flare heating propagates to the end of the flux tube in only 12 minutes. (This curve is not shown in Figure 3.1).

When mass motion is allowed, an even more dramatic increase in the efficiency of transport of thermal energy is evident (Figure 3.2). Here the effect of flare heating is transported at the velocity of the shock front, reaching the end of the filament in less than 4 minutes.



Figures 3.1 & 3.2 Figures 3.1 (upper) and 3.2 (lower). Evolution of the temperature structure in Model I, with and without mass motion. Time in minutes from start of heating is shown against each curve.

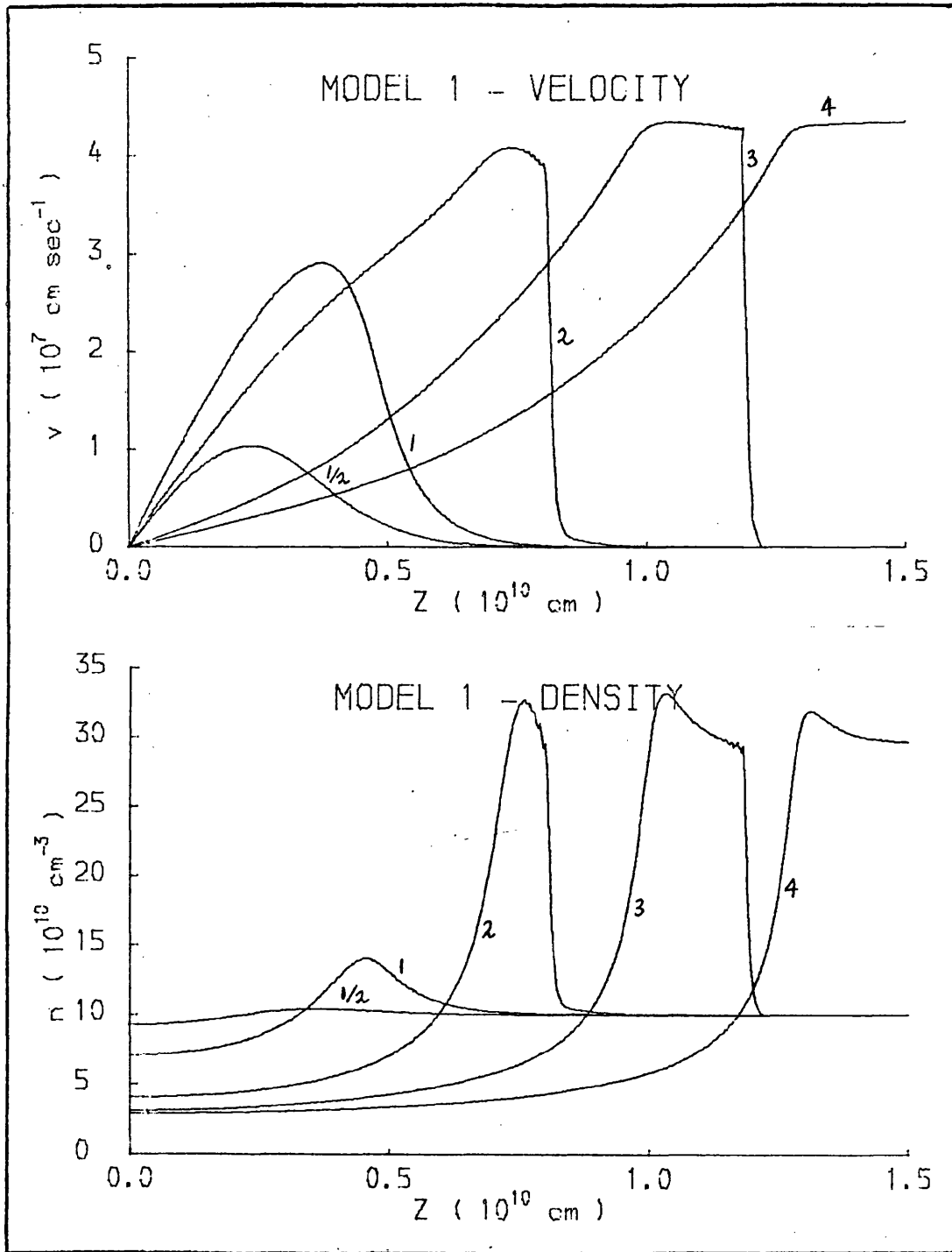
Convective energy transport becomes significant about 2 minutes after heating begins, (compare curves in Figures 3.1 and 3.2 for 1 minute and 2 minutes), coinciding with the formation of the shock front.

Another interesting feature is seen in Figure 3.2. A region of constant temperature ( $\sim 6 \times 10^6$  K) appears behind the shock front and grows in length as the shock moves down the flux tube. The origin of this feature will be clarified when we examine Figure 3.6. It will also be noticed that temperatures at the centre of the filament are similar in Figures 3.1 and 3.2, being slightly higher in Figure 3.2 once mass motion is fully developed. This difference is due to the decrease in density near the centre of the filament because of convection of material out of this region. As a result the rate of energy input per particle is increased.

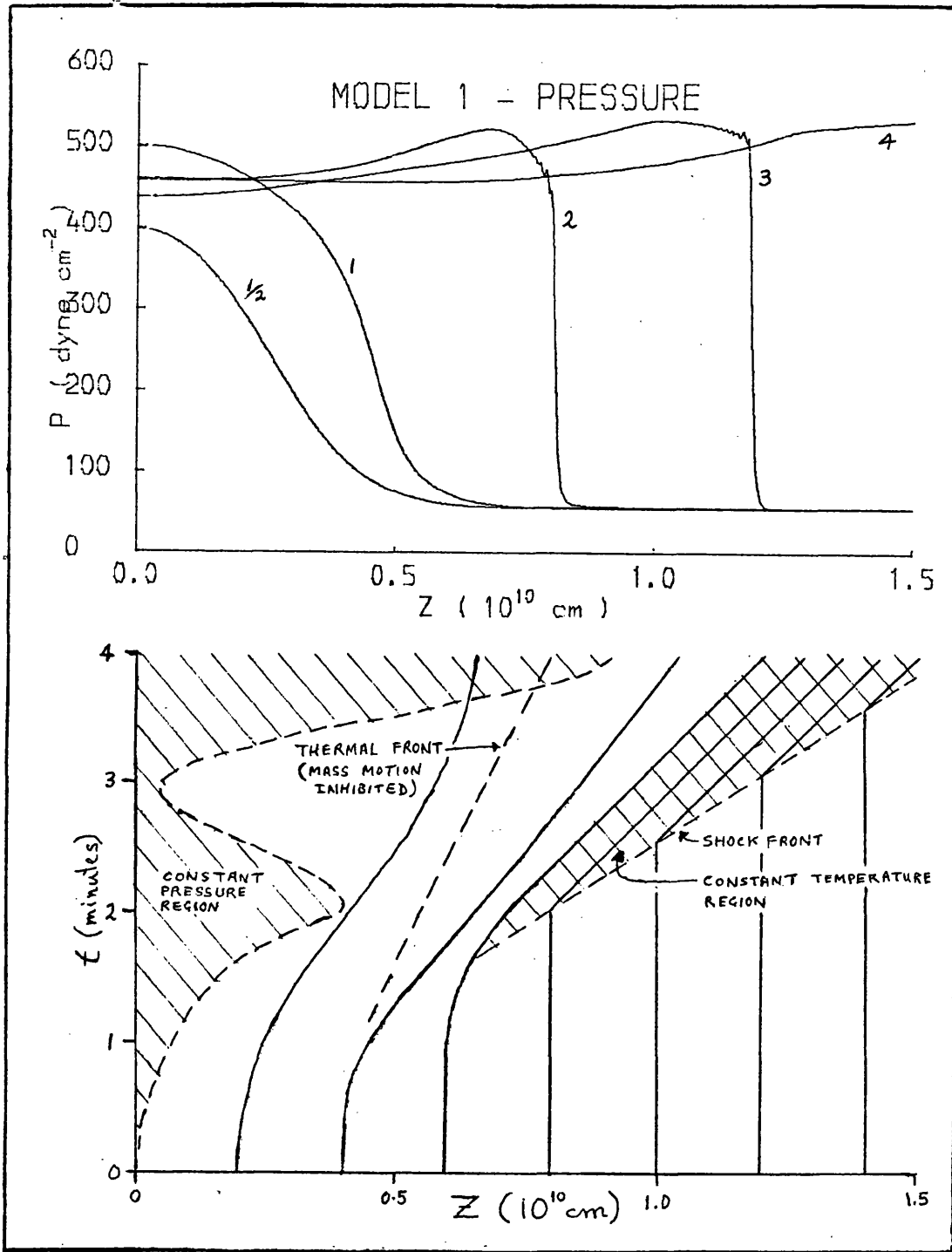
Evolution of the velocity and density distributions when mass motion is allowed is shown in Figures 3.3 and 3.4. The flow becomes supersonic ( $c = 2.35 \times 10^7$  cm sec<sup>-1</sup>) in less than 60 seconds and the compression wave steepens into a shock front  $\sim 100$  seconds after the start of heating. The density immediately behind the shock is  $\sim 3$  times greater than the initial density, while the density at the centre of the filament has dropped to  $\sim 0.3$  of its initial value after 4 minutes.

Figure 3.5 illustrates the development of the pressure distribution. When mass motion becomes fully developed  $\sim 100$  seconds after the start of heating, the pressure becomes uniform out to  $z \approx 5 \times 10^9$  cm after which the central pressure begins to drop due to convection of material away from the centre of the filament, reaching a minimum at  $\sim 170$  seconds. The central pressure then rises again, so that after 4 minutes the pressure distribution is uniform out to  $z \approx 10^{10}$  cm.

In Figure 3.6 world lines of the fluid elements are shown and regions of constant pressure and constant temperature delineated. For comparison the space-time path of the thermal front in Figure 3.1 (no mass motion) is also shown. This diagram immediately shows the



Figures 3.3 & 3.4 Figures 3.3 (upper) and 3.4 (lower). Evolution of velocity and density in Model I. Time in minutes from start of heating is shown against each curve.



Figures 3.5 & 3.6 Figure 3.5 (Upper). Evolution of the pressure distribution in Model I. Time in minutes from start of heating is shown against each curve.

Figure 3.6 (Lower): World lines of fluid particles in Model I. Also shown are the regions of constant temperature and pressure, and the space-time path of the thermal front when mass motion is inhibited.

significance of the constant temperature region of Figure 3.2. As this region extends from the world line of the fluid element where the shock formed to the shock front itself, it is clear that the constant temperature region consists of all material which has been shocked. Provided that the speed of the shock remains constant, the Rankine-Hugoniot jump conditions ensure that the temperature behind the shock does likewise. For the special case where the material ahead of the shock is at rest and  $\gamma = 5/3$ , we can use the Rankine-Hugoniot equations (2.3), (2.6), (2.8) and (2.9) to derive the following relation between the fluid velocity behind the shock and the shock speed

$$M = \frac{2}{3} v/c \left( 1 + \sqrt{1 + \left(\frac{2}{3} v/c\right)^{-2}} \right) \quad (3.1)$$

where  $M$  is the Mach number of the shock,  $v$  is the flow velocity behind the shock and  $c$  is the sound speed in the medium ahead of the shock. It is apparent from Figure 3.3 that the shock is in fact accelerating, as the peak velocity behind the shock is increasing ( $v = 4.5 \times 10^7$  cm sec<sup>-1</sup> at  $t = 4$  minutes). Applying (3.1) at  $t = 3$  minutes where  $v = 4.3 \times 10^7$  cm sec<sup>-1</sup> we find that

$$M = 2.80 \quad (3.2)$$

or 
$$U = 6.56 \times 10^7 \text{ cm sec}^{-1}$$

and from (1.5) we have

$$T_2 = 6.78 \times 10^6 \text{ K} \quad (3.3)$$

Evaluating (2.1) and (1.5) at  $t = 4$  minutes, we find

$$M = 2.90 \quad (3.4)$$

and 
$$T_2 = 6.96 \times 10^6 \text{ K} \quad (3.5)$$

Thus the changes in shock speed and temperature are only 3% over this 1 minute period and are too small to be apparent in Figure 3.2 or 3.6.

It now remains to show that the time-scale for variation of temperature in this region is sufficiently long that a significant drop in temperature does not occur during an interval of  $\sim 1$  minute. The energy equation in Lagrangian form VI (5.20) can be written

$$\frac{\partial T}{\partial t} = \frac{1}{3n_e R} \left\{ Q(z,t) + \frac{\partial}{\partial z} \left( K \frac{\partial T}{\partial z} \right) - P \frac{\partial T}{\partial z} - n_e^2 f(T) \right\} \quad (3.6)$$

As the energy input term is negligible compared with the quiescent input for  $z \geq 7 \times 10^9$  cm we may write (see VI (5.34))

$$Q(z,t) = Q_{0M} = \left( n_e / n_{e_0} \right) n_{e_0}^2 f(T_0). \quad (3.7)$$

where  $n_{e_0}$  and  $T_0$  are the initial electron density and temperature respectively. Also, as the region under consideration is nearly isothermal, thermal conduction is small (estimated maximum rate of energy deposition  $\sim 10^{-2}$  erg  $\text{cm}^{-3}$   $\text{sec}^{-1}$ ). Therefore (3.6) becomes

$$\frac{\partial T}{\partial t} = \frac{-1}{3n_e k} \left\{ n_e^2 f(T) - n_e n_{e_0} f(T_0) - P \frac{\partial v}{\partial z} \right\} \quad (3.8)$$

If we neglect the small variations ( $\leq 10\%$ ) in density, pressure and velocity over a period of  $\sim 1$  minute around  $t = 3$  minutes and ignore the weak temperature dependence of the radiative loss function, we can solve (3.8) to obtain

$$T = T_0 e^{-t/\tau} \quad (3.9)$$

where

$$\tau = \frac{3}{2} P / \left( n_e^2 f(T) - n_e n_{e_0} f(T_0) + P \frac{\partial v}{\partial z} \right) \quad (3.10)$$

From the results shown in Figures 3.2 - 3.5 we obtain

$$\begin{aligned}
 n_e &\approx 3.1 \times 10^{11} \text{ cm}^{-3} \\
 T &\approx 6 \times 10^6 \text{ K} \\
 P &\approx 500 \text{ dynes cm}^{-2} \\
 \frac{\partial v}{\partial z} &\approx 2 \times 10^{-4} \text{ sec}^{-1} \\
 n_{e_0} &= 10^{11} \text{ cm}^{-3} \\
 T_0 &= 2 \times 10^6 \text{ K}
 \end{aligned}
 \tag{3.11}$$

Evaluating the radiative losses from Figure VI 4.2 and inserting these values in (3.10) we obtain

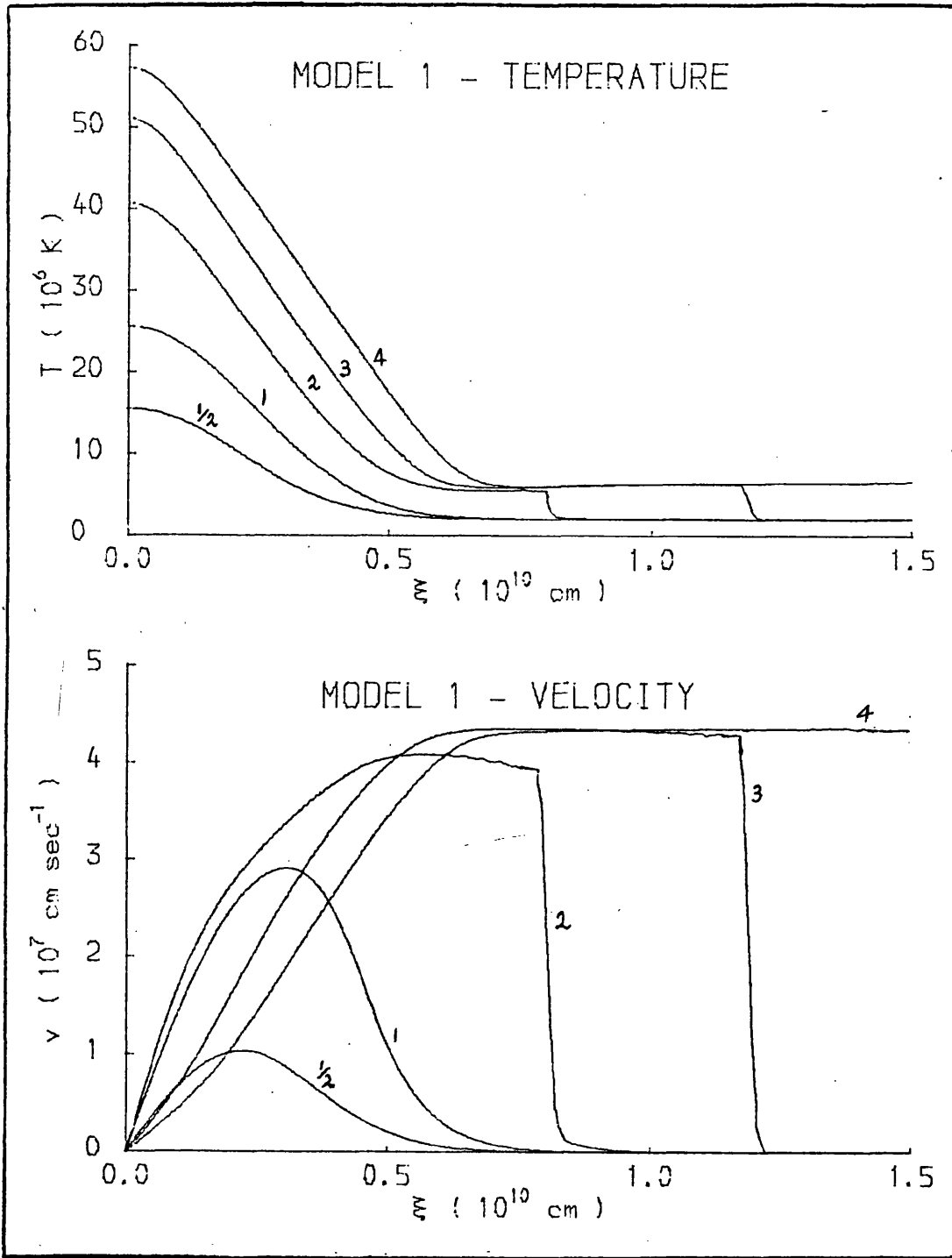
$$\tau \approx 750 / (2.2 - 1.7 + 0.1) \approx 1250 \text{ sec} = 20 \text{ min} \tag{3.12}$$

Inserting this value in (3.9) we find a rate of fall of temperature of  $\sim 3 \times 10^5$  K/minute. This result is in satisfactory agreement with Figure 3.2. Note that in this case the rate of energy loss through work done against pressure is small ( $\sim 20\%$ ) compared to the rate of radiative energy loss. This not always true, as we shall see when considering Model II.

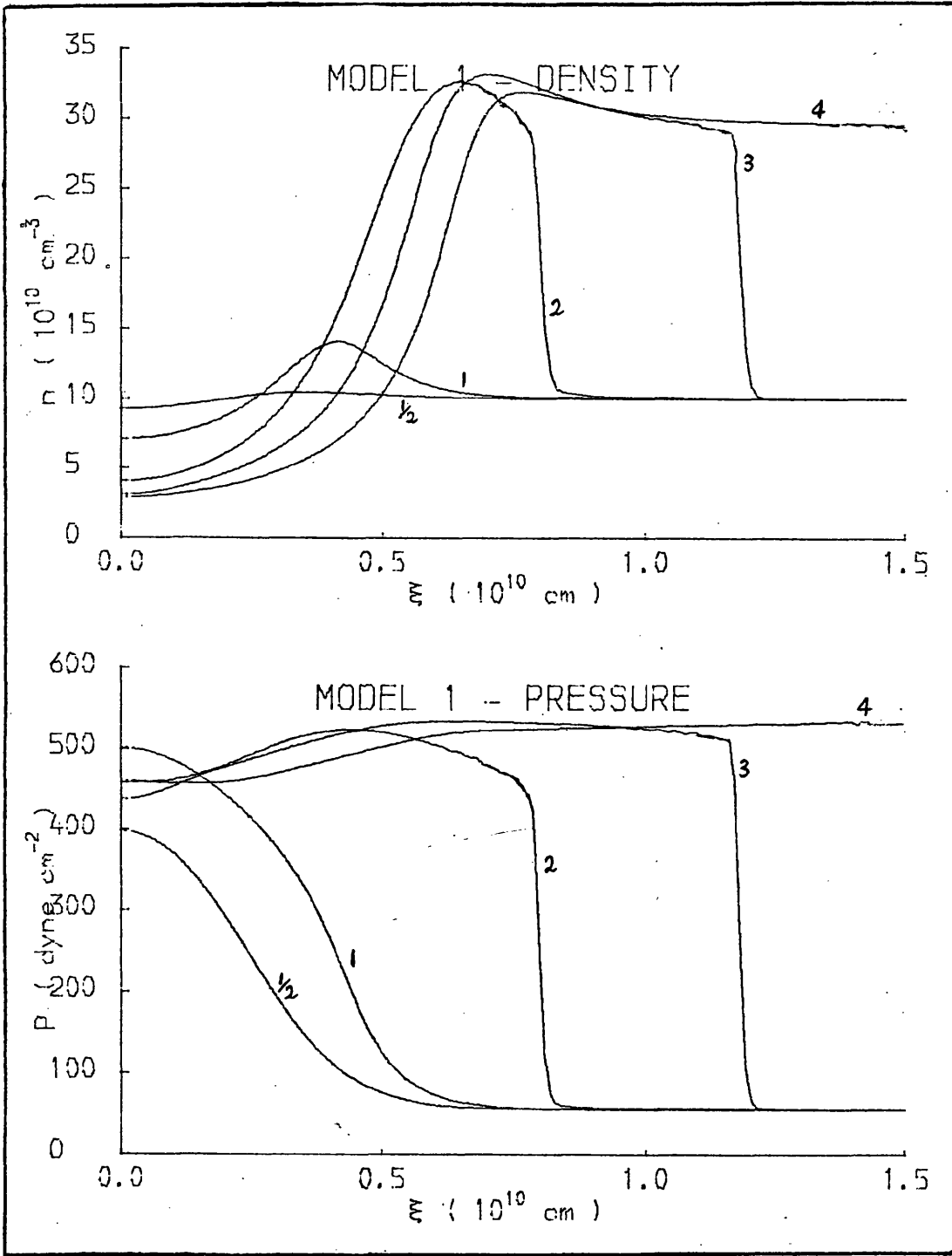
Finally in Figures 3.7 - 3.10 we plot the distribution of temperature, velocity, density and pressure against the Lagrangian coordinate  $\xi'$ , defined by

$$\xi' = \xi / \rho_0 = \frac{1}{\rho_0} \int_0^z \rho(z') dz' \tag{3.13}$$

$\xi'$  specifies the initial coordinate of a fluid element, so that Figures 3.7 - 3.10 enable the evolution of physical conditions in any given element of plasma to be followed. There are two features visible in these figures which were not readily apparent from Figures 3.2 - 3.6. In Figure 3.7 we see that even after 4 minutes the



Figures 3.7 & 3.8 Figures 3.7(upper) and 3.8(lower). Evolution of temperature and velocity in Model I, plotted against the Lagrangian coordinate  $\xi'$ . Time in minutes from start of heating is shown against each curve.



Figures 3.9 & 3.10 Figures 3.9(upper) and 3.10(lower). Evolution of density and pressure in Model I, plotted against the Lagrangian coordinate  $\xi'$ . Time in minutes from start of heating is shown against each curve.

central peak in temperature has not propagated beyond  $\xi' \approx 7 \times 10^9$  cm, close to the point where shock heating began. Comparing this figure with Figure 3.1, where the thermal front has reached  $z \approx 8 \times 10^9$  cm after 4 minutes, we see that the presence of mass motion has in fact inhibited thermal conduction. Examining Figure 3.8 we see that (on the time-scale presented here) the velocity of a fluid element which has passed through the shock does not change appreciably. This is to be expected because of the uniform pressure distribution behind the shock (Figure 3.10).

#### 4. MODEL II ( IMPULSIVE ENERGY INJECTION , HIGH DENSITY )

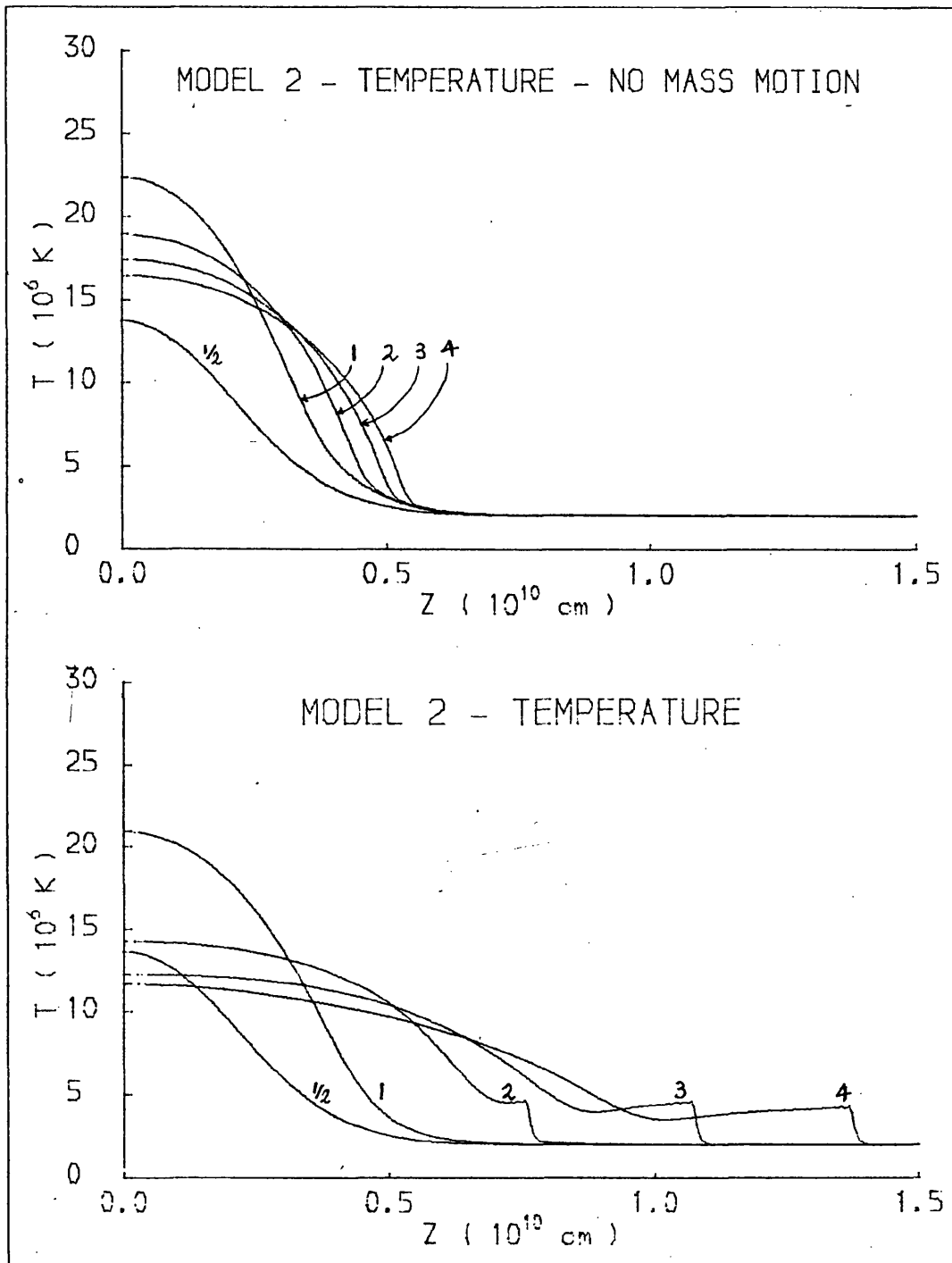
Corresponding results for Model II are shown in Figures 4.1 - 4.10. The evolution of temperature structure with and without mass motion is shown in Figures 4.1 and 4.2. These results differ fundamentally from those of Model I since the energy input cuts off after one minute in Model II, whereas it remains constant in Model I. Thus the results presented for Model II are concerned with the decay phase. From Figures 4.1 and 3.1 we see that when mass motion is inhibited the speed of propagation of the thermal front is much lower in Model II, mainly because of the lower central temperature. But when mass motion is allowed (Figures 4.2 and 3.2) the speed of propagation of thermal energy by the shock is almost as high as in Model I.

It is apparent from Figures 4.1 and 4.2 that the central temperature falls slowly around  $10 - 15 \times 10^6$  K. This is due to the decrease in radiative losses with temperature (as discussed in §4 of Chapter VI) and, when mass motion is allowed, to the decreased central density which causes radiative losses to fall off more rapidly than the ambient input. Despite this additional heating mechanism, the central temperature is lower when mass motion is allowed. The difference must be due to cooling of the plasma by expansion as material is convected out of the central region. The constant temperature plateau found in Model I is also seen in Figure 3.12 but in this case a large drop in temperature some distance behind the shock is apparent.

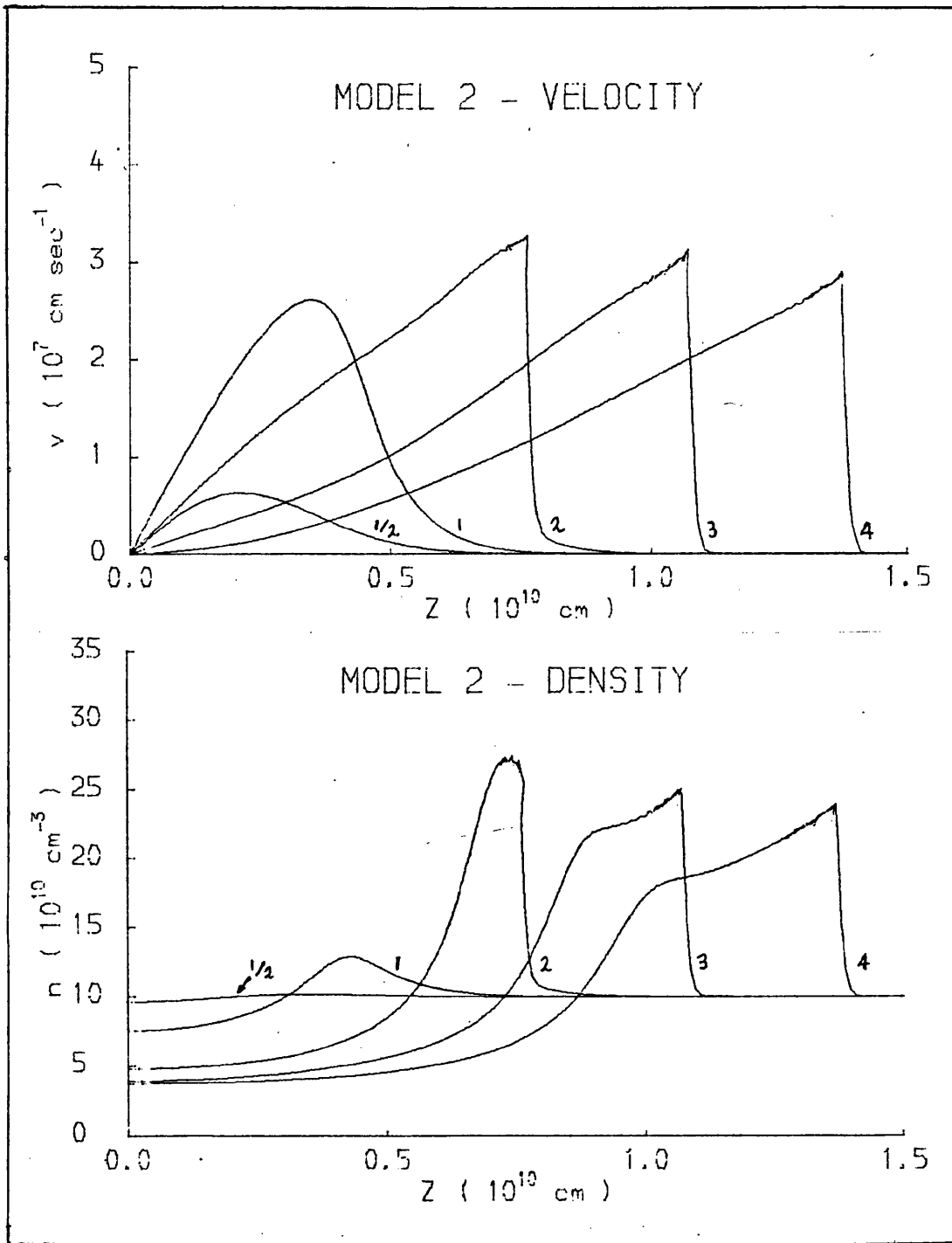
Evaluating the time scale for temperature variation from (3.10) at  $z = 10^{10}$  cm, we find that after 4 minutes  $\tau \approx 12$  minutes, which is compatible with a drop in temperature of  $\sim 5 \times 10^5$  K in a time of  $\sim 1$  minute, as observed in Figure 4.2. Whereas in Model I we found that radiative losses accounted for most of the temperature drop (Equation (3.12)) in this case work done against pressure is the dominant form of energy loss. Radiative losses are only slightly greater than the ambient input, so that the net radiative energy loss is less than 10% of the work done against pressure.

Figure 4.3 illustrates the development of the velocity profile. The peak velocity behind the shock and the speed of the shock itself are seen to decrease as the energy carried by the shock front is dissipated in heating material passing through it. The density distribution (Figure 4.4) develops similarly to that of Model I, but the pressure distribution (Figure 4.5) becomes uniform only in the central region, whereas in Model I it becomes almost uniform throughout the region behind the shock. World lines of the fluid elements and regions of constant temperature and pressure are shown in Figure 4.6. As in Model I, the constant temperature region consists of material which has passed through the shock front.

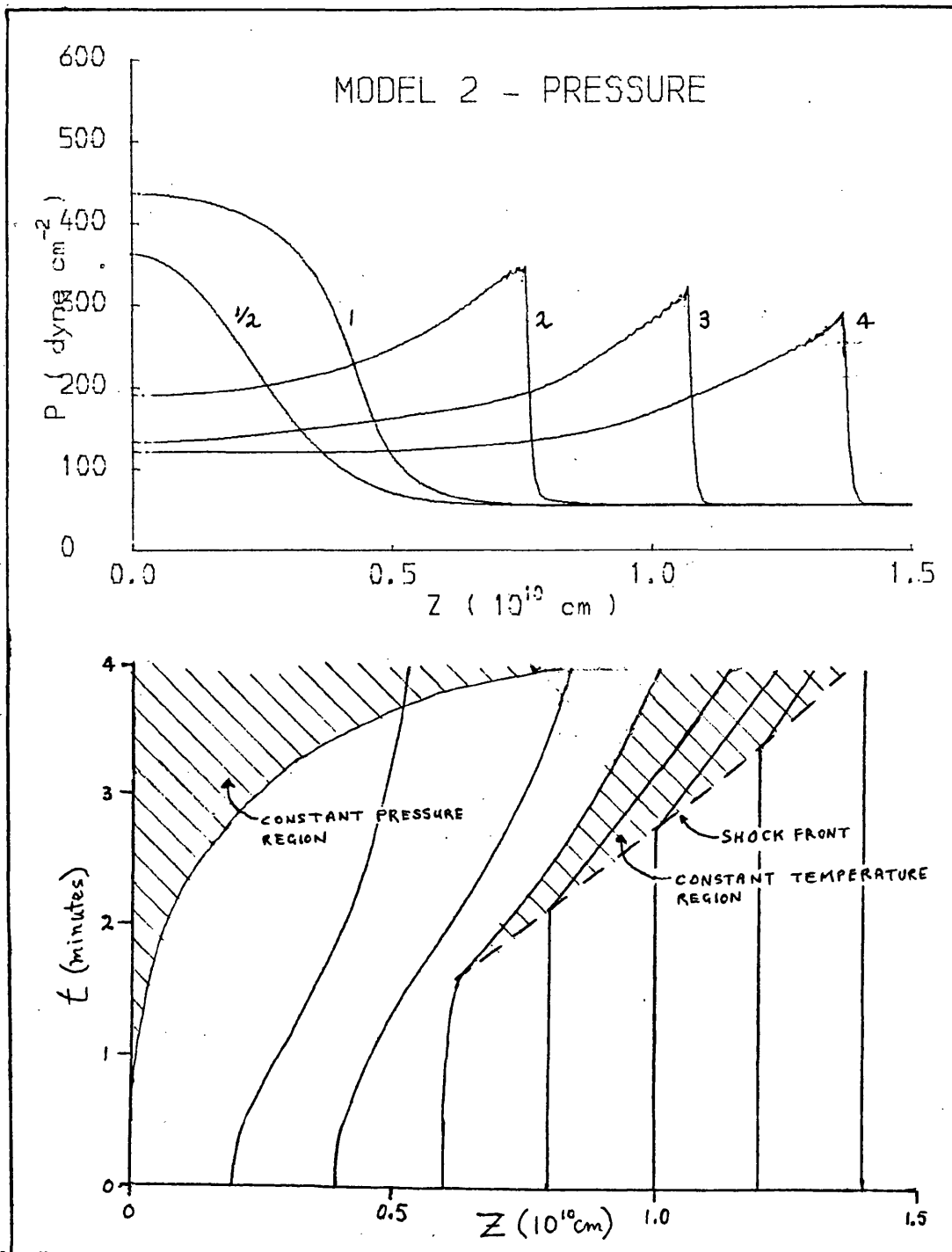
Finally the evolution of temperature, velocity, density and pressure are plotted against the Lagrangian coordinate in Figures 4.7 - 4.10. From Figure 4.7 we see that, as was found in Model I, the central rise in temperature does not propagate beyond the point where shock heating began at  $\xi' \approx 6 \times 10^9$  cm. The initial phase of development of the velocity distribution ( $t \lesssim 2$  minutes; Figure 4.8) is similar to that observed in Model I (Figure 3.8). However, after the energy input cuts off the distribution relaxes so that for  $t \gtrsim 4$  minutes the velocity is an almost linear function of  $\xi'$ , unlike the velocity distribution in Model I, where we noted that the velocity of a fluid element which has passed through the shock front falls very slowly.



Figures 4.1 & 4.2 Figures 4.1 (upper) & 4.2 (lower). Evolution of the temperature structure in Model II, with and without mass motion. Time in minutes from start of heating is shown against each curve.

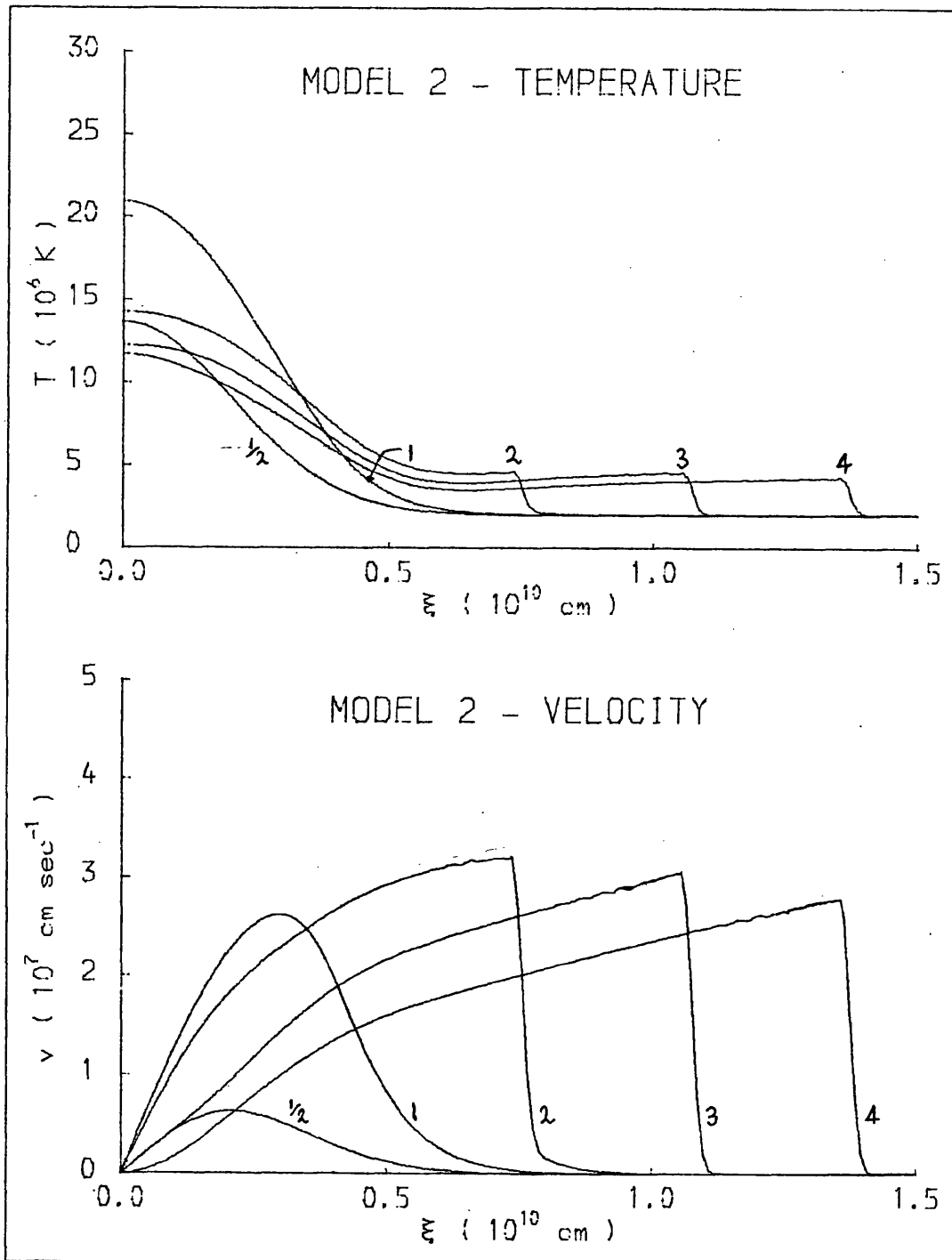


Figures 4.3 & 4.4. Figures 4.3 (upper) & 4.4 (lower). Evolution of velocity and density in Model II. Time in minutes from start of heating is shown against each curve.

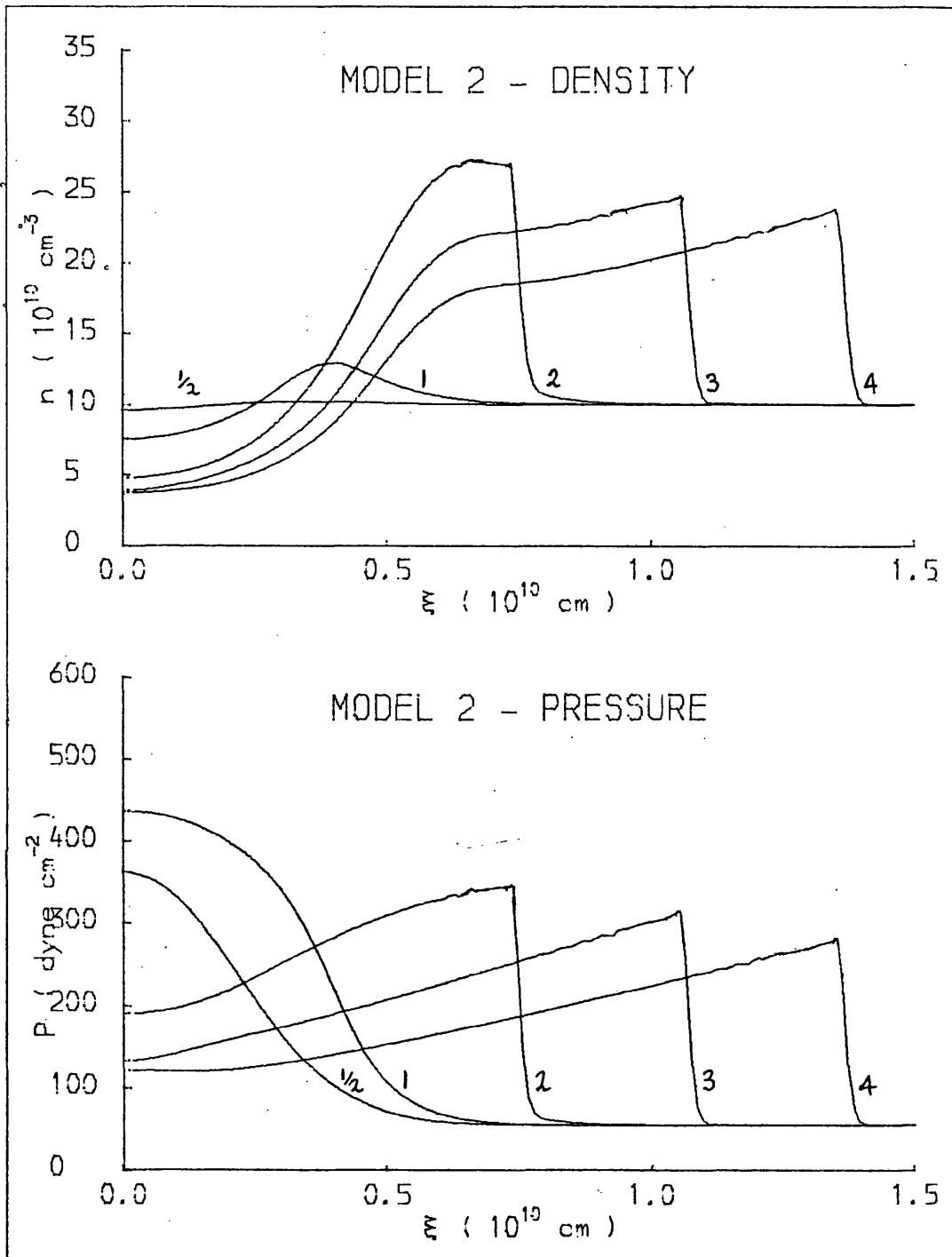


Figures 4.5 & 4.6 Figure 4.5 (Upper). Evolution of the pressure distribution in Model II. Time in minutes from start of heating is shown against each curve.

Figure 4.6 (Lower). World lines of fluid particles in Model II. Also shown are the regions of constant temperature and pressure, and the space-time path of the thermal front when mass motion is inhibited.



Figures 4.7 & 4.8. Figures 4.7 (upper) & 4.8 (lower). Evolution of temperature and velocity in Model II, plotted against the Lagrangian coordinate  $\xi'$ . Time in minutes from start of heating is shown against each curve.



Figures 4.9 & 4.10. Figures 4.9 (upper) & 4.10 (lower). Evolution of density and pressure in Model II, plotted against the Lagrangian coordinate  $\xi'$ . Time in minutes from start of heating is shown against each curve.

### 5. MODEL III ( CONTINUOUS ENERGY INJECTION , LOW DENSITY )

Having examined the evolution of a filament containing plasma of high ambient density under the influence of both steady and impulsive energy inputs, we now study the response of a low density filament to the same forms of heating. The rates of energy injection are reduced from those used in Models I and II in view of the lower density of Models III and IV.

In Figure 5.1 the evolution of temperature, so prominent a feature of Model I, only shows signs of developing after 3 minutes. The reason for this can be found in Figure 5.3, where the development of the temperature distributions, with and without mass motion, are compared. We see that the difference in velocity of propagation of the thermal front in these two cases is not so marked as in Model I. Only after 3 minutes does the shock wave begin to outrun thermal conduction.

Applying (3.10) to the region of constant temperature just behind the shock at  $t = 3$  minutes, we find that the timescale for temperature variation in this region is  $\tau \approx 15$  minutes, which is of the same order as the value found for Model I. However, this timescale is determined by work done against pressure, whereas radiative energy loss is the dominant mechanism in Model I. In Model III the radiative energy loss rate is  $\lesssim 5\%$  of the rate of dissipation of internal energy through expansion. Radiative losses are much smaller than in Model I because of the reduced density, while the rate of expansion is higher since the velocity profile behind the shock has not yet flattened out at  $t = 3$  minutes (c.f. Figure 3.3).

Evolution of the density and pressure distributions is illustrated in Figure 5.2. The difference between the velocity distributions in Models I and III is reflected in the density profiles. On the timescale presented here, the peak in density behind the shock front has not spread out as it did in Model I (c.f. Figure 3.4).

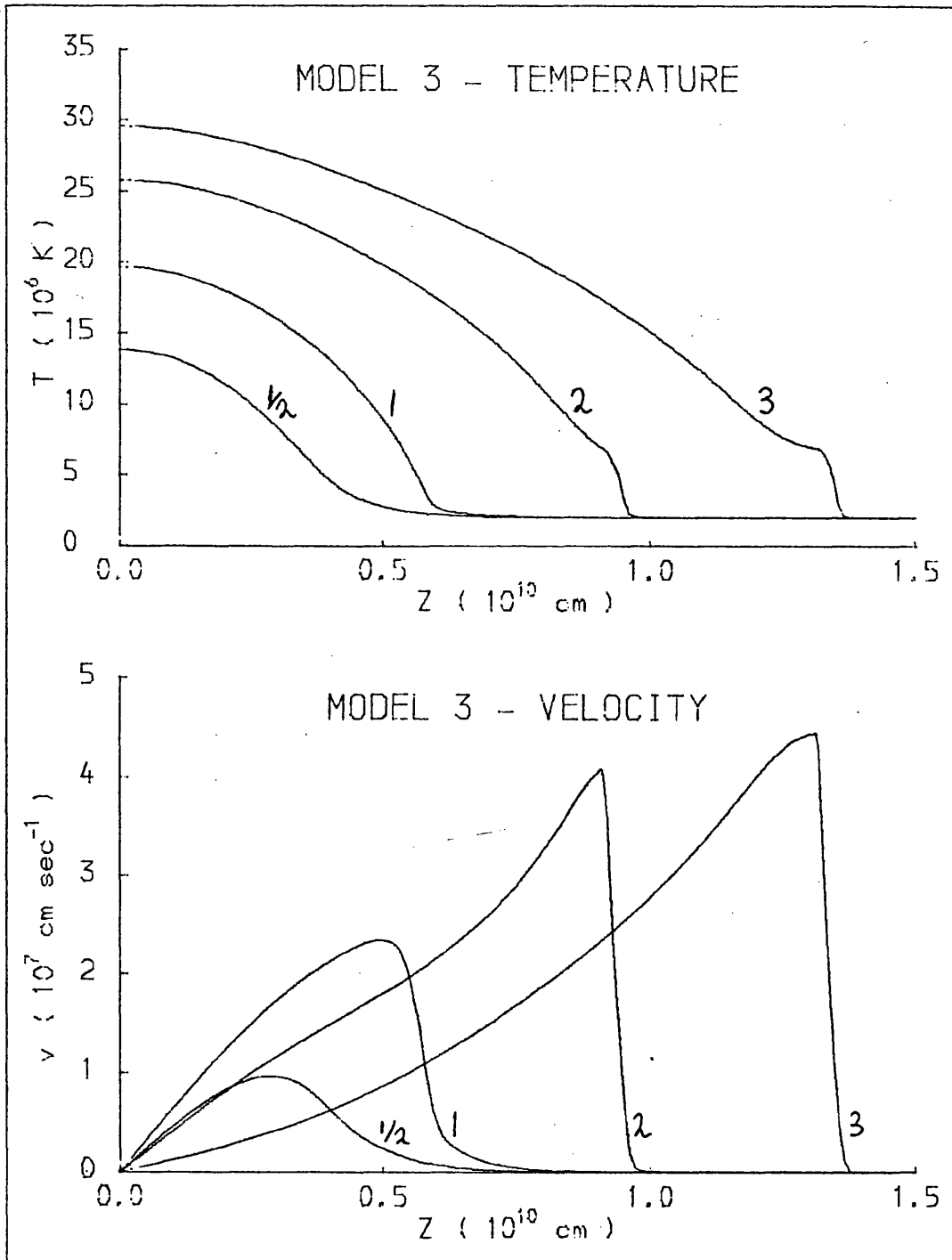
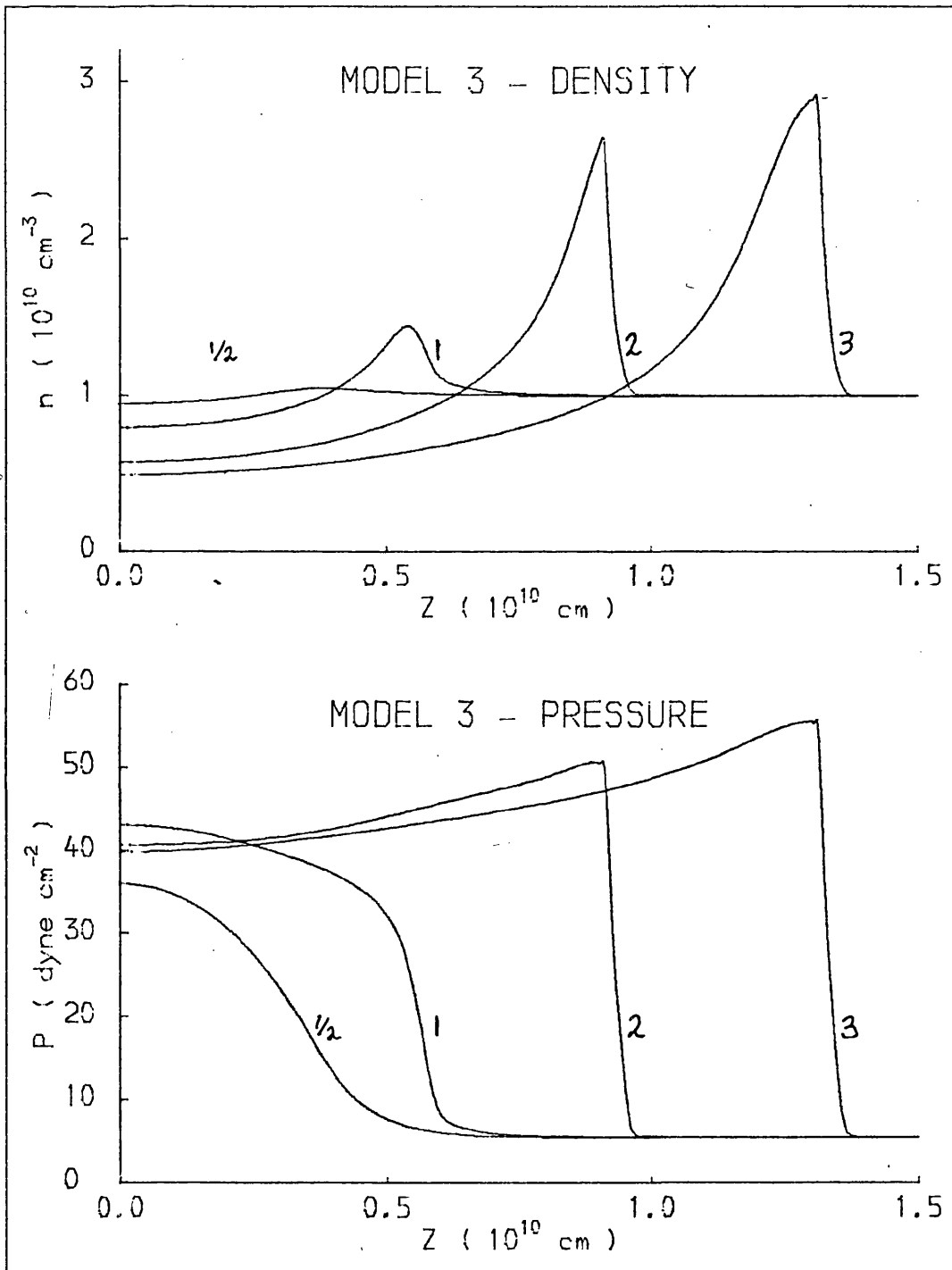


Figure 5.1 Evolution of the temperature and velocity distributions in Model III. Time in minutes from start of heating is shown against each curve.



**Figure 5.2** Evolution of density and pressure in Model III. Time in minutes from start of heating is shown against each curve.

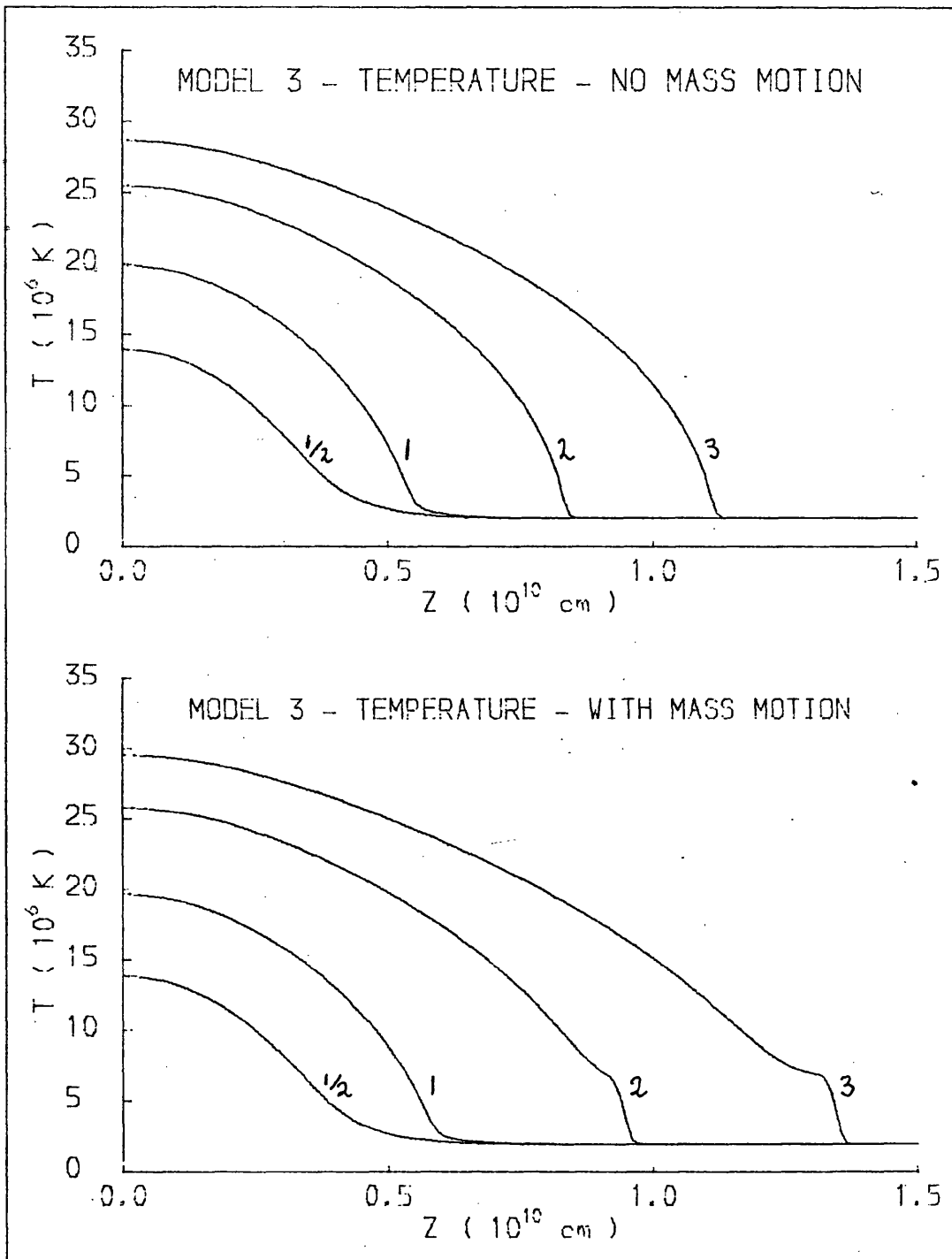


Figure 5.3 Evolution of the temperature distribution with/without mass motion in Model III. Time in minutes from start of heating is shown against each curve.

Finally, in Figure 5.3, we compare the development of the temperature distribution with that obtained when mass motion is inhibited. The similarity of the thermal front velocities has already been remarked on. Despite the fact that the central temperature is only half that of Model I, speed of propagation of the thermal front in the absence of mass motion ( $\approx$  Mach 2) is twice that of Model I.

This result appears to be at variance with the conclusion of Bessey & Kuperus (1970), who show that the speed of propagation of heat by thermal conduction must be much less than the speed of sound. We note, however, that the temperature structures presented in Figure 5.3 (and all other results obtained with mass motion inhibited) are unphysical. Redistribution of energy by thermal conduction at constant density cannot take place without the creation of pressure gradients, and hence mass motion. When mass motion is inhibited the continuity and momentum equations, which together define the sound speed, drop out. Only the equation of thermal conduction, a diffusion equation, is left. Mathematically then, the sound speed is not defined.

#### 6. MODEL IV ( IMPULSIVE ENERGY INJECTION , LOW DENSITY )

We now consider the effect of impulsive heating on a filament of low ambient density. Figure 6.1 illustrates the evolution of the temperature and velocity distributions. We see that although the shock speed is increasing in Model III (Figure 5.1) but decreasing in Model IV, the Model IV shock front is slightly in advance of the shock in Model III. This must be due to the higher rate of energy input over the first minute in Model IV.

Comparing the evolution of the temperature distribution in Model IV with that of Model II (Figure 4.2), we see that the rise and fall of central temperature are similar, but that the extended region of constant temperature found in Model II is hardly noticeable in Model IV. As we found when comparing the Model III results with those of Model I, the region of constant temperature only begins to appear after 3 minutes.

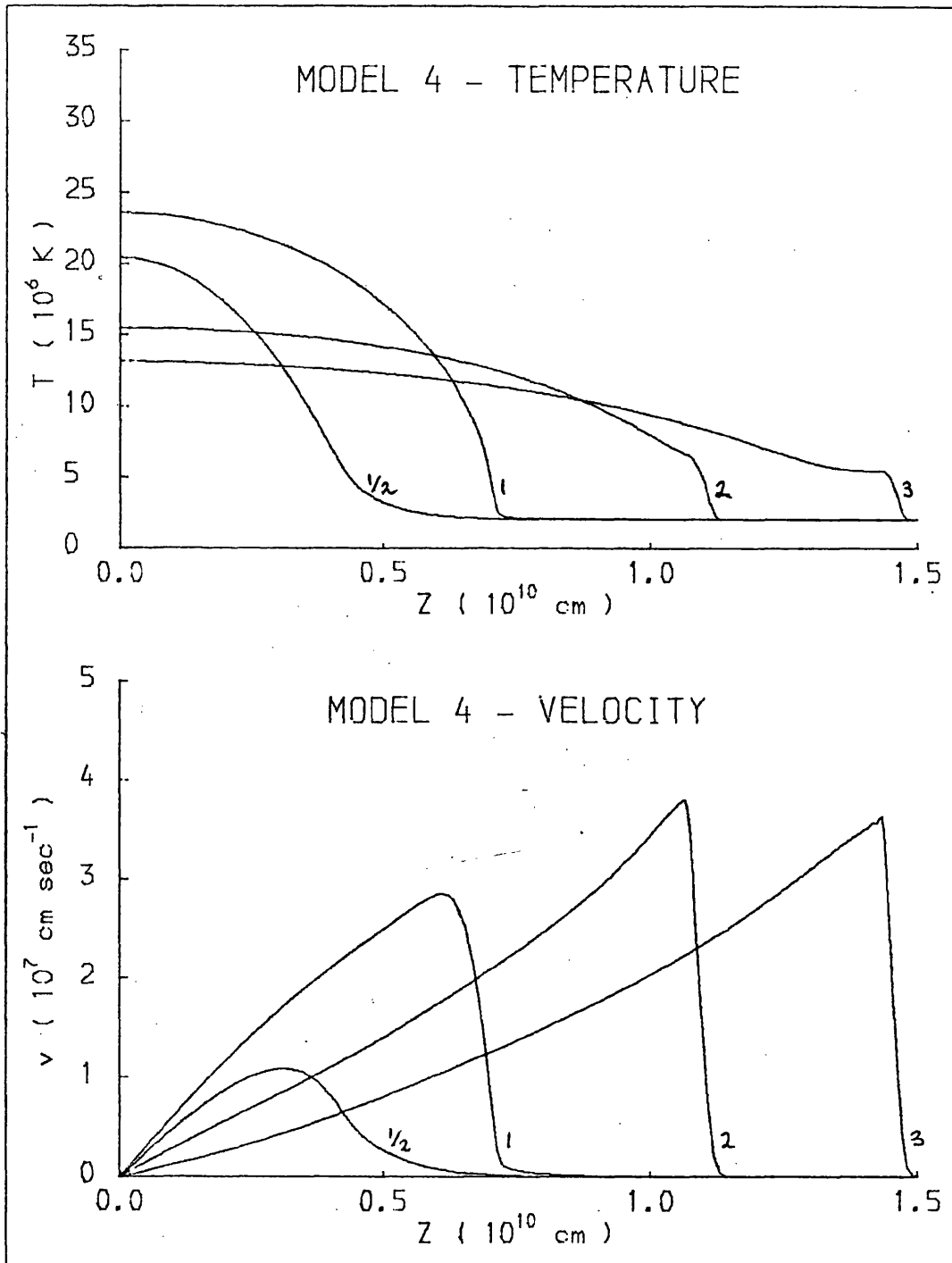


Figure 6.1 Evolution of the temperature and velocity distributions in Model IV. Time in minutes from start of heating is shown against each curve.

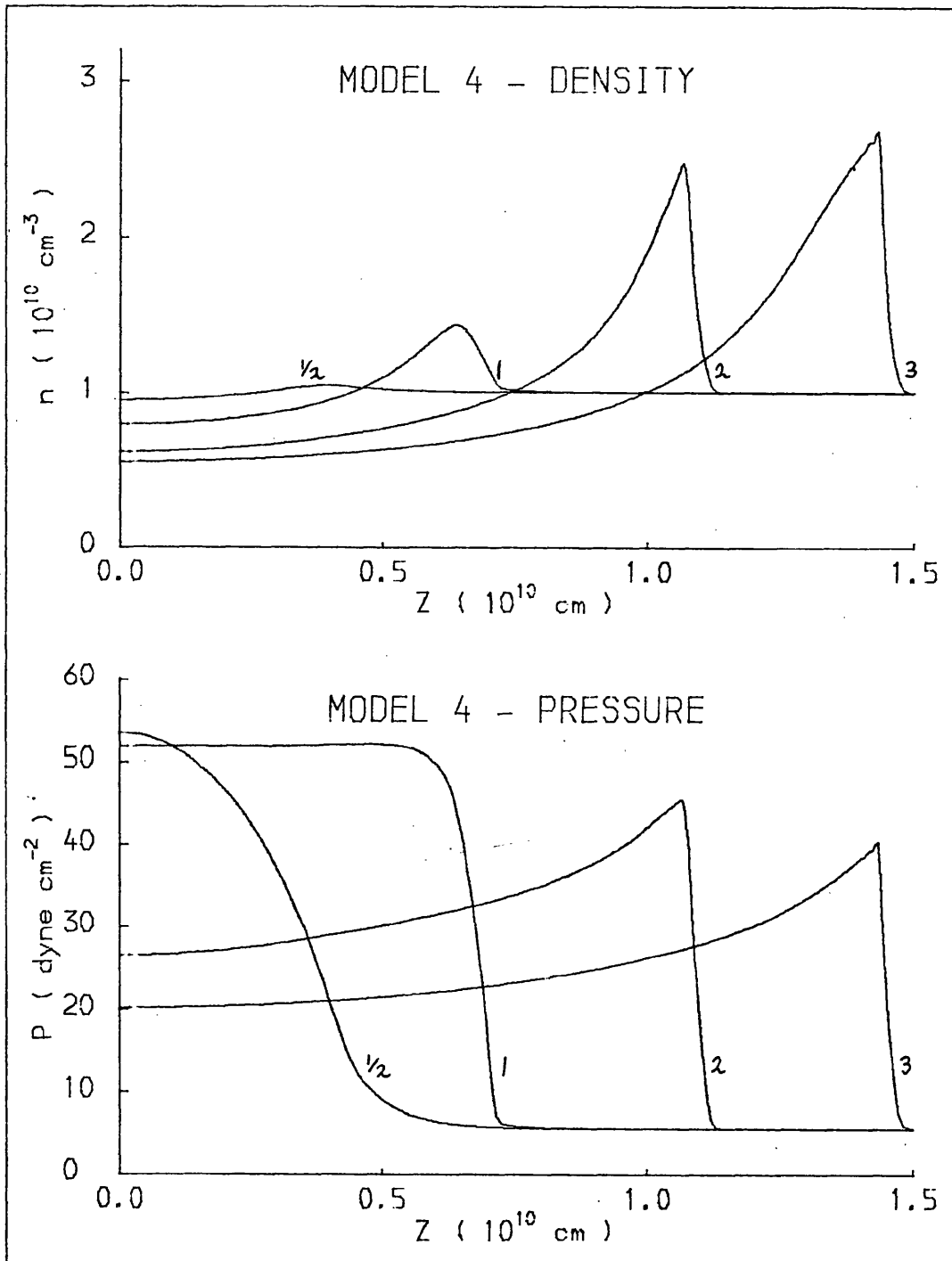


Figure 6.2 Evolution of density and pressure in Model IV.  
Time in minutes from start of heating is shown against each curve.

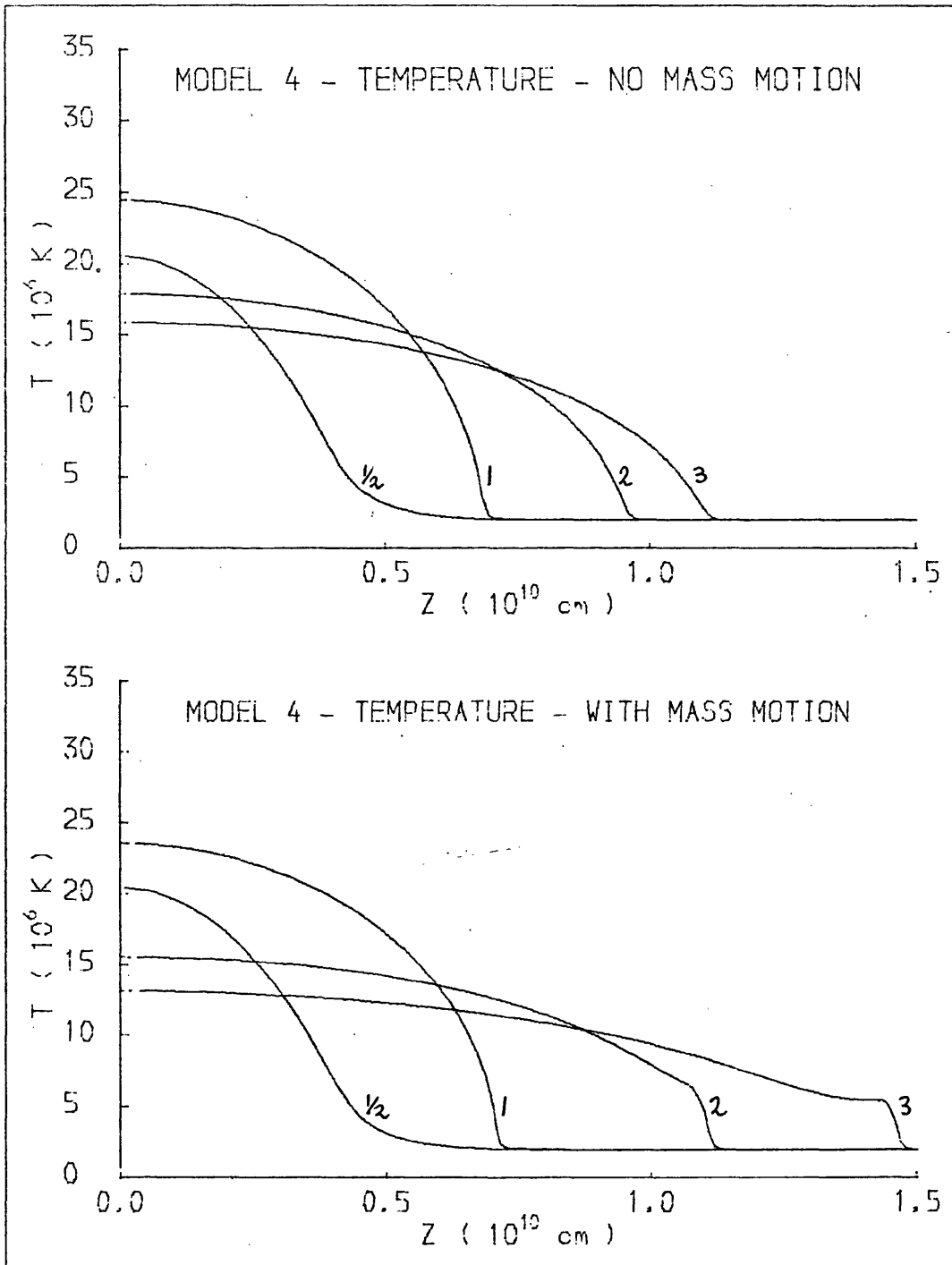


Figure 6.3 Evolution of the temperature distribution with/without mass motion in Model IV. Time in minutes from start of heating is shown against each curve.

The Model IV density distribution (Figure 6.2) evolves similarly to that of Model III (Figure 5.2). The spreading out of the peak behind the shock, found in Model II (Figure 4.4), associated with the growth of the constant temperature region, is not seen here. The pressure distribution (Figure 6.2) develops in a similar manner to that of Model II (Figure 4.5).

Finally, the development of the temperature distributions, with and without mass motion, are illustrated in Figure 6.3. It is clear that if mass motion is inhibited the thermal front decelerates much more rapidly when the energy source is removed. In fact,  $7\frac{1}{2}$  minutes elapse before the effect of heating becomes apparent at the end of the filament if mass motion is suppressed.

## 7. ENERGY TRANSPORT IN THE FILAMENT

Having watched the evolution of a flaring filament under a range of conditions, we now examine more closely the mechanisms responsible for the transport of energy through the filament. We wish to discover which of the processes of convection, conduction and work done against pressure dominate in which regions, and what effects these processes produce.

First of all, we study the energetics of shock heating.

A noticeable feature of the results presented in §3-6 is that the speed of the shock front is very similar in all models. This is due to the strong dependence of rate of deposition of energy by the shock on shock speed. The gain in thermal energy of the plasma in passing through the shock is

$$\frac{d\epsilon}{dV} = \frac{3}{2} (P_2 - P_1) \quad \text{erg cm}^{-3} \quad (7.1)$$

where  $P_1$  and  $P_2$  are the pressures just ahead of and behind the shock. Thus the rate of deposition of energy by the shock is

$$\frac{d\epsilon}{dt} = \frac{3}{2} (P_2 - P_1) Mc \quad \text{erg cm}^{-2} \text{sec}^{-1} \quad (7.2)$$

where  $M$  is the Mach number of the shock and  $c$  the velocity of sound in the medium ahead of the shock. Using the Rankine-Hugoniot equation (2.4) we can write (7.2) as

$$\begin{aligned} \frac{d\epsilon}{dt} &= \frac{3}{2} P_1 Mc \left( \frac{P_2}{P_1} - 1 \right) \\ &= \frac{3}{2} P_1 Mc \left( \frac{2\gamma M^2 - (\gamma - 1)}{\gamma + 1} - 1 \right) \end{aligned}$$

which reduces to

$$\frac{d\epsilon}{dt} = \frac{3\gamma}{\gamma + 1} P_1 c M(M^2 - 1) \quad (7.3)$$

Setting  $\gamma = 5/3$  and using VI (5.6) and (2.7) this becomes

$$\frac{d\epsilon}{dt} = 8.61 \times 10^7 n_{10} T_6^{3/2} M(M^2 - 1) \text{ erg cm}^{-2} \text{sec}^{-1} \quad (7.4)$$

where  $n_{10}$  is the electron density in units of  $10^{10} \text{ cm}^{-3}$  and  $T_6$  is the temperature in units of  $10^6 \text{ K}$ , these values both applying in the undisturbed material ahead of the shock. Thus

$$\frac{d\epsilon}{dt} \sim M^3 \quad \text{for } M \geq 3 \quad (7.5)$$

We can estimate crudely the expected shock speed by equating the rate of dissipation of energy by the shock to the rate of energy injection. Results, shown in Table 7.1, are in surprisingly good agreement with the observed shock speed.

TABLE 7.1

Model	$\bar{F}$ (erg cm <sup>-2</sup> sec <sup>-1</sup> )	M (calculated)	M (actual) <sup>+</sup>
I	10 <sup>11</sup>	3.5	2.8
II	2.1 x 10 <sup>10</sup> *	2.2	2.2
III	10 <sup>10</sup>	3.5	2.8
IV	4.2 x 10 <sup>9</sup> *	2.7	2.5

\* Averaged over 4 minutes

+ Calculated at 2<sup>m</sup> < t < 3<sup>m</sup>

We now consider briefly the evolution of total thermal and kinetic energy in the filament. Total thermal energy is given by

$$E_{TH} = 2 \int_0^{z_0} 3 n_e k T dz \quad (7.6)$$

or, in Lagrangian form

$$E_{TH} = 6 R \int_0^{\xi_0} T d\xi \quad (7.7)$$

and total kinetic energy

$$E_{KE} = 2 \int_0^{z_0} \frac{1}{2} \rho v^2 dz \quad (7.8)$$

or

$$E_{KE} = \int_0^{\xi_0} v^2 d\xi \quad (7.9)$$

Results are illustrated in Figure 7.1, where several interesting features are apparent. Firstly, we notice that less than 15% of the total energy injected appears as kinetic energy (c.f. Bessey & Kuperus, 1970). In Models I and III the growth rate of kinetic energy is greater than that of thermal energy at  $t = 4$  minutes, but this does not alter the conclusion that the total kinetic energy is small in a flaring filament, since the filament length assumed here ( $3 \times 10^{10}$  cm) can be regarded as an upper limit.

We notice also that in Models II and IV the total kinetic energy continues to grow up to  $t \approx 3$  minutes, whereas the total thermal energy begins to decay immediately the heating ends after 1 minute. Thus the pressure gradients in the filament, established during impulsive heating, drive mass motions which increase the kinetic energy. Radiative cooling is augmented by these mass motions, which cool the plasma by expansion.

Having established that mass motion is of minor importance energetically when the total energy content of the flaring filament is considered, we now examine the role of mass motion in the transport of energy through the filament. We note first that just behind the shock, where the fluid velocity is highest, the kinetic energy density is still smaller than the thermal energy density, but not negligible in comparison to it. At  $t = 3$  minutes the ratios of kinetic to thermal energy densities are: Model I, 0.6; Model II, 0.4; Model III, 0.55; Model IV, 0.5.

In order to delineate more precisely the role of mass motion, we consider both the transport of energy through space and the transfer of energy through the plasma. We examine each term in the energy equation separately and compare the contributions of thermal conduction, convection of thermal energy, convection of kinetic energy and work done by pressure. Convective terms drop out when the transfer of energy through the plasma is considered, since we follow the motion of each fluid element.

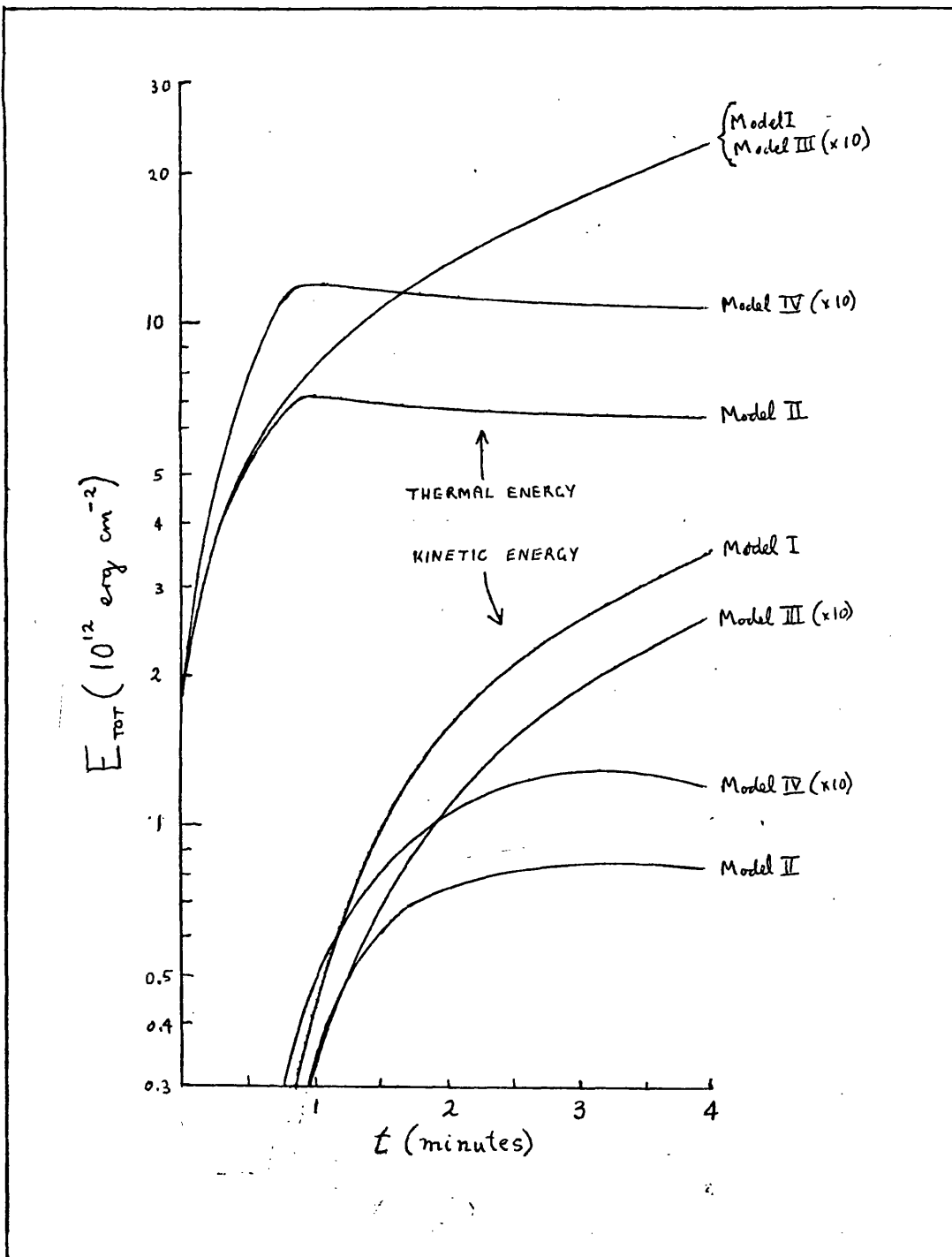


Figure 7.1 Total thermal and kinetic energy in the filament as a function of time.

Considering first the transport of energy through space, we obtain from the momentum equation VI (5.2) and the energy equation VI (5.3), the following expressions for the rates of thermal energy deposition due to conduction, convection and work done by pressure;

$$\left( \frac{\partial \epsilon}{\partial t} \right)_{\text{cond}} = \frac{\partial}{\partial z} \left( K \frac{\partial T}{\partial z} \right) \quad \text{erg cm}^{-3} \text{ sec}^{-1} \quad (7.10)$$

$$\left( \frac{\partial \epsilon}{\partial t} \right)_{\text{conv}} = - \frac{\partial}{\partial z} \left( v \frac{3}{2} n_e kT \right) \quad (7.11)$$

$$\left( \frac{\partial \epsilon}{\partial t} \right)_P = - P \frac{\partial v}{\partial z} \quad (7.12)$$

The rates of deposition of kinetic energy due to convection and work done by pressure are given by

$$\left( \frac{\partial}{\partial t} \frac{1}{2} \rho v^2 \right)_{\text{conv}} = \frac{\partial}{\partial z} \left( v \frac{1}{2} \rho v^2 \right) \quad (7.13)$$

$$\left( \frac{\partial}{\partial t} \frac{1}{2} \rho v^2 \right)_P = - v \frac{\partial P}{\partial z} \quad (7.14)$$

In Figure 7.2 the energy deposition rates defined above are shown at  $t = 30$  seconds in Models I and III. Results obtained for Models II and IV are similar to those of Models I and III respectively. Even at this early stage in the flare development, convection of thermal energy is the most important form of energy transport in Model I (Curve 2). Thermal conduction and work done by pressure (Curves 1 and 3) are of comparable importance. Although the energy deposition rates due to these processes are smaller than that due to convection, no one mechanism could be said to dominate. Curves 4 and 5

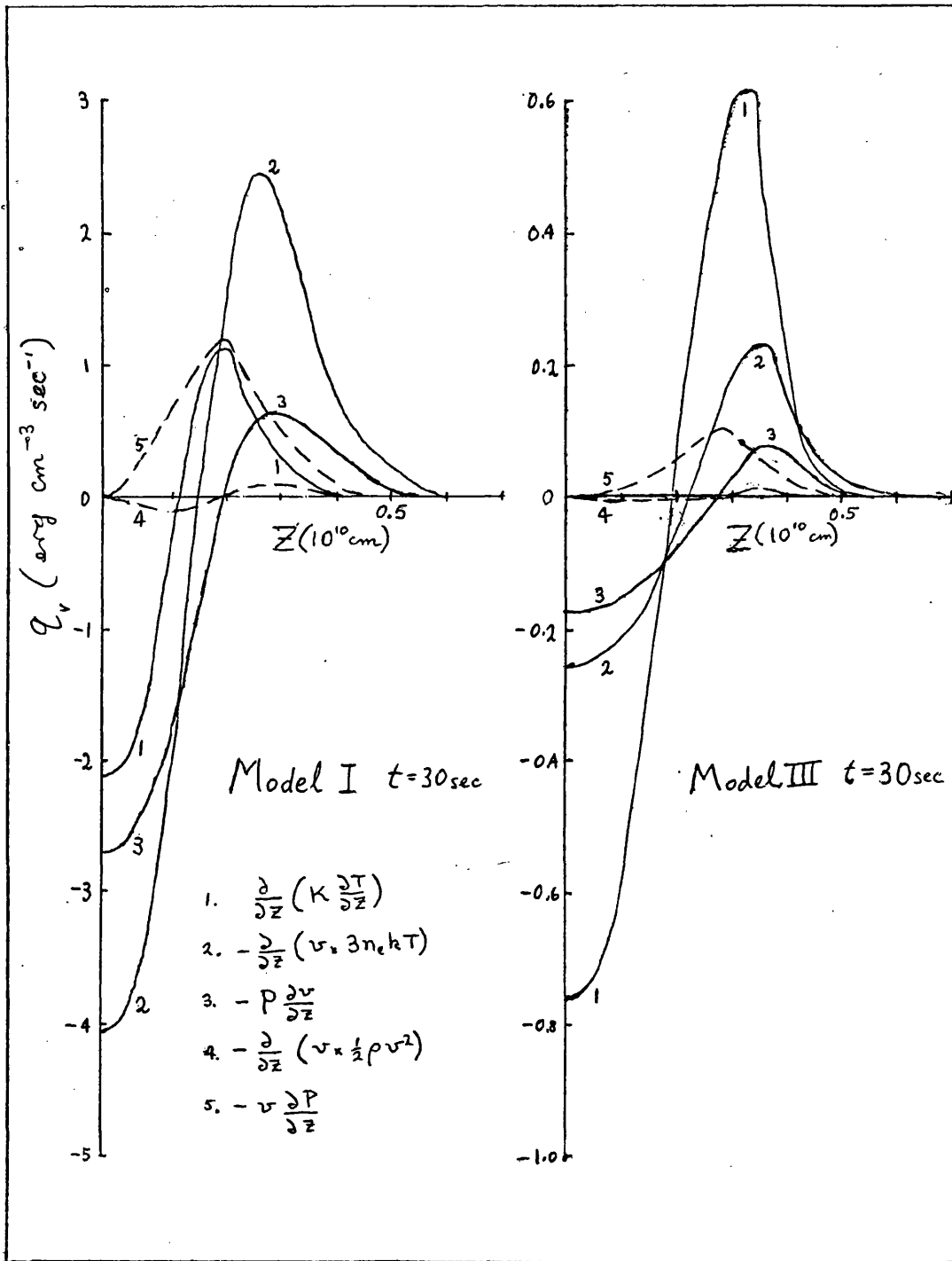


Figure 7.2 Energy transport in Models I and III, after 30 seconds.

illustrate the convection of kinetic energy and the creation of kinetic energy by acceleration of the plasma, respectively. In Model III, thermal conduction (Curve 1) is the most important process. Convection and work done by pressure (Curves 2 and 3) are less important, but not negligible.

Energy deposition rates at  $t = 3$  minutes in Models I and III are shown in Figures 7.3 and 7.4. Because of the finite grid spacing used in computing these results, maximum values in the narrow peaks at the shock front are somewhat uncertain. In both models, three regimes are apparent. In a narrow region close to the origin, thermal conduction (Curve 1) dominates. The energy extracted from this region by conduction is deposited over a wide domain which extends almost from the origin to just behind the shock front. The inward flux of energy here is partially (in Model III, almost completely) balanced by convection of energy out of the region (Curve 2) and by work done against pressure (that is, cooling of the plasma by expansion) (Curve 3). Finally, across the shock large fluctuations occur. Transport of hot, dense material into the undisturbed region ahead of the shock (Curve 2) is the dominant process, but the compression and heating of material as the shock passes through it (Curve 3) and thermal conduction across the shock front (Curve 1) are not negligible.

After the energy source in Models II and IV has been removed, energy fluxes in the shock region are similar to those of Models I and III respectively, but all energy transport mechanisms become less significant behind the shock. The energy deposition rates due to convection and work done by pressure fall substantially in Model II and slightly in Model IV. But in both cases the most drastic reduction is in thermal conduction, which becomes negligible soon after heating ends. Thus the evolution of the filament in the decay phase is controlled by mass motion.

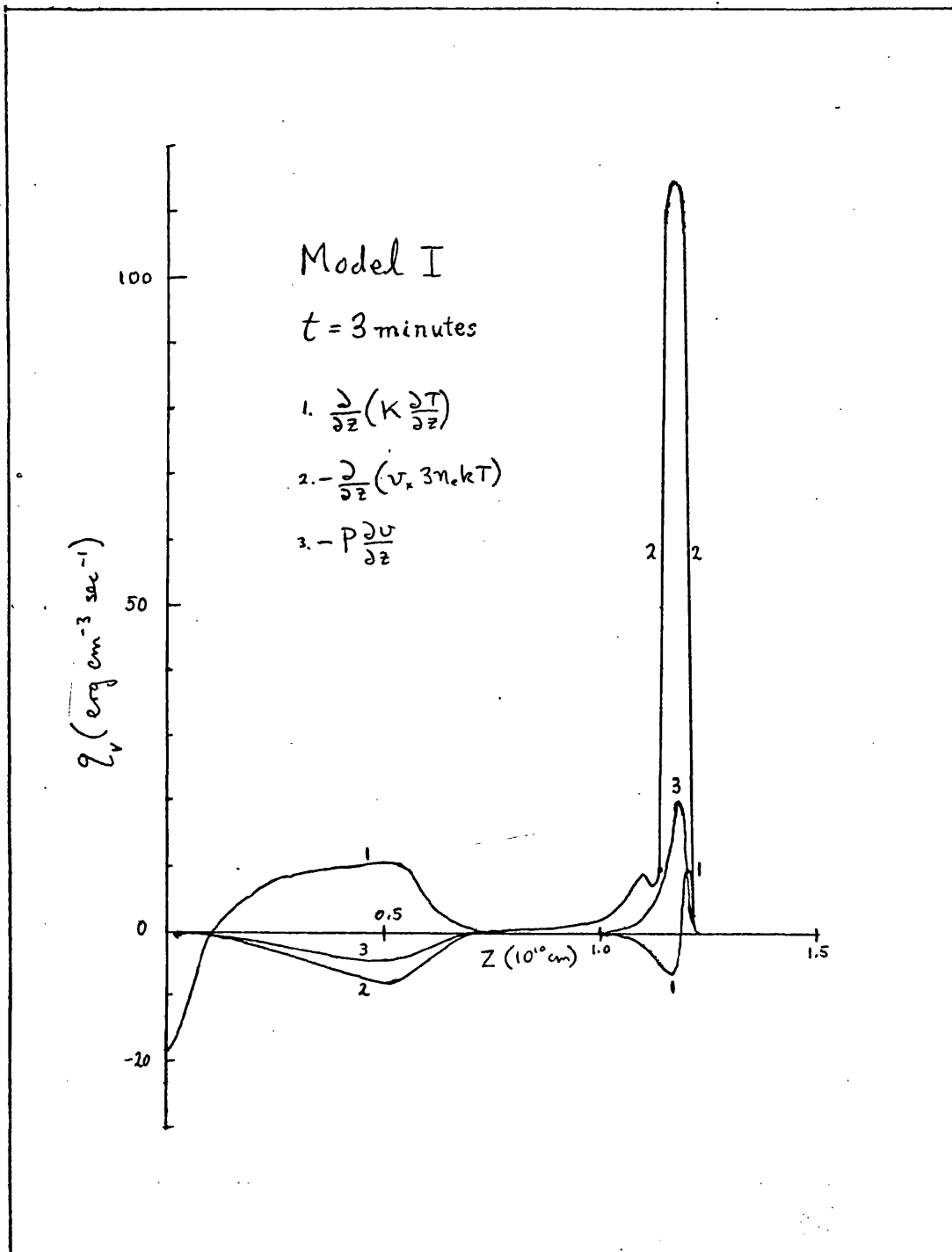


Figure 7.3 Energy transport in Model I after 3 minutes.

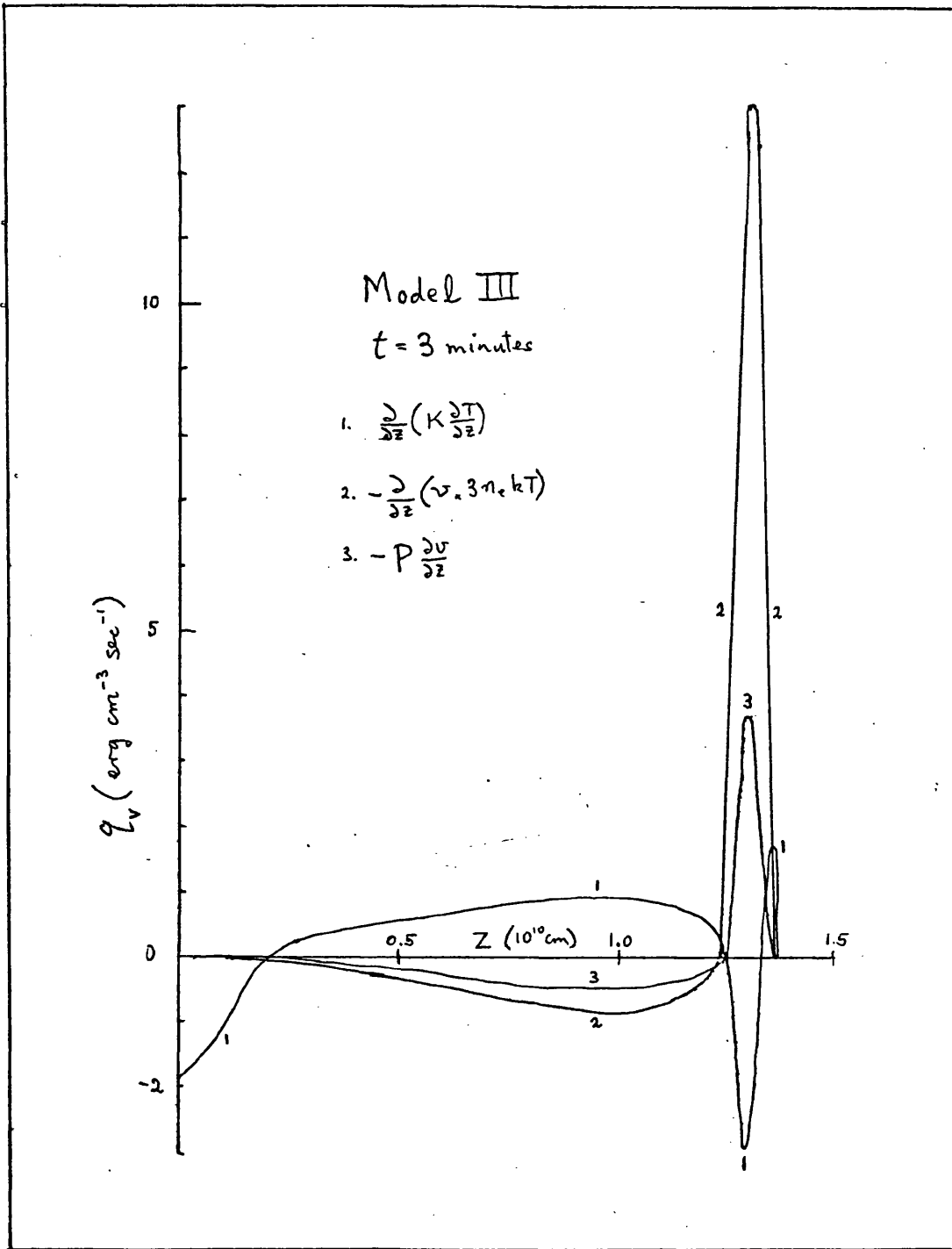


Figure 7.4 Energy transport in Model III after 3 minutes.

We now turn our attention to the transfer of energy through the plasma. Since we are interested in processes which affect conditions in a given fluid element we must evaluate the rates of energy deposition per unit mass while following the fluid element, that is, using a Lagrangian system. Since convective terms drop out, we are left with thermal conduction and work done by pressure. The relevant equations are

$$\left(\frac{\partial e}{\partial t}\right)_{\text{cond}} = \frac{\partial}{\partial \xi} (\rho K \frac{\partial T}{\partial \xi}) = \frac{1}{\rho} \frac{\partial}{\partial z} (K \frac{\partial T}{\partial z}) \quad (7.15)$$

$$\left(\frac{\partial e}{\partial t}\right)_P = -P \frac{\partial v}{\partial \xi} = -\frac{P}{\rho} \frac{\partial v}{\partial z} \quad (7.16)$$

$$\left(\frac{\partial \frac{1}{2} v^2}{\partial t}\right)_P = -v \frac{\partial P}{\partial \xi} = -\frac{v}{\rho} \frac{\partial P}{\partial z} \quad (7.17)$$

These equations are, except for the factor  $1/\rho$ , identical to the non-convective equations of energy transport through space, that is, (7.10), (7.12) and (7.14).

Since the plasma density has not become significantly non-uniform after 30 seconds of flare heating, results obtained from (7.15 - 7.17) are virtually identical to those shown in Figure 7.2. In interpreting this figure in the present context, the spatial coordinate  $z$  should be replaced by the Lagrangian coordinate  $\xi'$ , and  $1 \text{ erg cm}^{-3} \text{ sec}^{-1}$  equated to  $6 \times 10^{12}$  ( $6 \times 10^{13}$ )  $\text{erg gm}^{-1} \text{ sec}^{-1}$  in Model I (III). Curves 1, 3 and 5 are relevant and the comments made previously concerning these are applicable here. Thus at high density (Models I and II), heating and cooling of the plasma by compression and expansion due to mass motion is comparable with the conductive energy redistribution.

Energy deposition rates per unit mass in Models I and III at  $t = 3$  minutes are illustrated in Figure 7.5. The most striking feature of these results is the enhancement of thermal conduction (Curve 1) near the origin, compared to that seen in Figures 7.3 and 7.4. Note that a comparison of these figures may be misleading, since the largest contribution at the shock front in Figures 7.3 and 7.4 comes from convection, which does not appear in Figure 7.5. Curves 1, 3 and 5 in Figures 7.3 and 7.4 should be compared with curves 1, 2 and 3, respectively, in Figure 7.5. However, the ratio of deposition rates near the origin to those near the shock are significantly higher in Figure 7.5 than in Figures 7.3 and 7.4. This difference occurs because the density near the origin is low ( $\sim 0.4$  x ambient), while just behind the shock it is high ( $\sim 3$  x ambient). Therefore in comparison to energy deposition rates per unit volume, the rates per unit mass near the centre of the filament are enhanced by a factor of  $\sim 7$  relative to the rates behind the shock front.

In Figure 7.5 peak values at the shock are ill-defined, as in Figures 7.3 and 7.4, and represent only lower limits to the maximum energy deposition rates. Again the filament may be divided into 3 domains. Close to the centre of the filament, thermal conduction dominates (Curve 1). In the region which extends out to just behind the shock, energy conducted out of the central region is deposited. In Model III we found that in considering transport of energy through space, convection of energy out of this region, together with work done against pressure, tended to balance the conductive deposition of energy (Figures 7.3 and 7.4). But convection no longer plays a part. Although work done against pressure (Curve 2) is smaller than conductive deposition, so that there is a net energy input to the region, it is not negligible. In the third region near the shock, conduction across the shock front, heating of the plasma by compression and acceleration of the fluid (Curve 3) are all of comparable importance energetically.

In the decay phase of Models II and IV (at  $t = 3$  minutes) energy

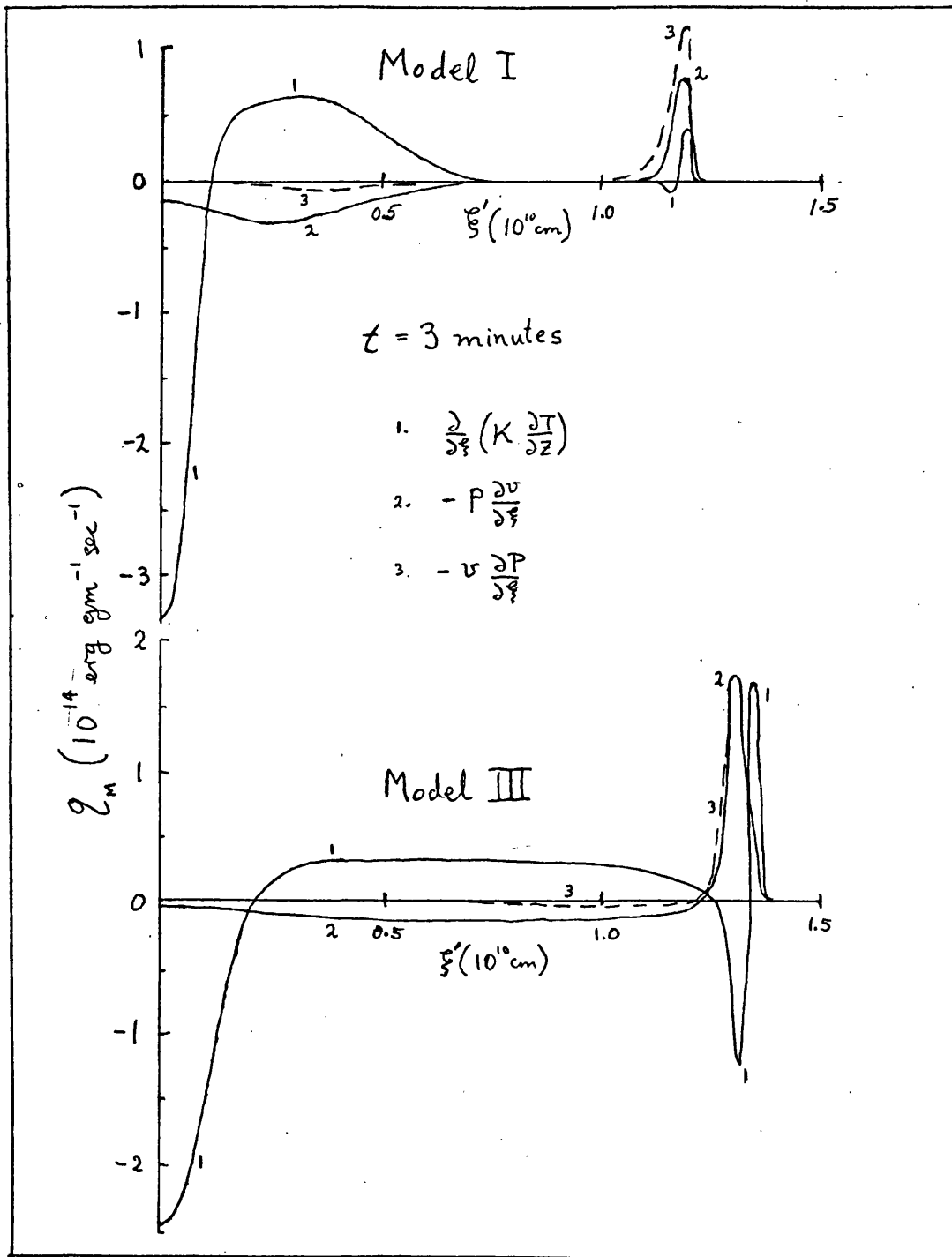


Figure 7.5 Energy transfer through the plasma in Models I and III after 3 minutes.

deposition rates at the shock are similar to those of Models I and III respectively. However, as is the case when energy transport through space is considered, the rates in regions 1 and 2 (from the centre of the filament out to the shock) are much lower. In Model II, thermal conduction falls to  $< 10^{12}$  erg gm<sup>-1</sup> sec<sup>-1</sup> (indistinguishable from zero in Figure 7.5) throughout region 2, and is  $\leq 4 \times 10^{12}$  erg gm<sup>-1</sup> sec<sup>-1</sup> in region 1. Work done against pressure retains the same form as in Model I, but decreases by a factor of  $\sim 5$ . Since this contribution is  $\sim 5 \times 10^{12}$  erg gm<sup>-1</sup> sec<sup>-1</sup>, work done against pressure dominates in region 2.

In region 2 of Model IV, thermal conduction decreases by a factor of  $\sim 10$  from the value found for Model III, while work done against pressure falls to  $\sim 5 \times 10^{12}$  erg gm<sup>-1</sup> sec<sup>-1</sup>, or  $\sim 2/5$  of its Model III value. Therefore, conduction is less important, but not negligible ( $\approx 1/2$  of the work done contribution). In region 1, both processes are equally important, each extracting energy at a rate of  $\sim 4 \times 10^{12}$  erg gm<sup>-1</sup> sec<sup>-1</sup>.

## 8. THE SOFT X-RAY DIFFERENTIAL EMISSION MEASURE

In the preceding sections, we have studied the evolution of the filament under various conditions, and examined the role of mass motion in energy transport through the filament. We now consider the question: can the presence of mass motions in a filament be inferred from observation?

Soft X-ray emission is the best indicator of the existence of a plasma in the temperature regime we consider. But without spatial resolution, the amount of information about the structure of the emitting region which can be deduced from soft X-ray measurements is very limited. The only function characteristic of the source which can be deduced directly from spectrally resolved observations is the differential emission measure, which we discuss in accordance with the

definition of Craig & Brown (1975).

The thermal X-ray spectrum of an optically thin source is given by

$$I(\epsilon) = \int_{\tau} F(\epsilon, T(\underline{r})) n_e^2(\underline{r}) d\tau \quad (8.1)$$

where  $I(\epsilon)$  is the differential photon energy flux,  $F(\epsilon, T)$  is the spectral distribution function,  $T$  and  $n_e$  are temperature and electron density in the source region and the integral extends over the source volume  $\tau$ .

We transform the volume integral in (8.1) to an integral over a temperature domain. Writing

$$d\tau = dS_T dT/|\nabla T| \quad (8.2)$$

where  $dS_T$  is an element of surface at constant temperature, we see that the differential volume occupied by material at temperature  $T$  to  $T + dT$  is

$$dV = \sum_i \left( \int_{S_{T_i}} \frac{dS}{|\nabla T|} \right) dT \quad (8.3)$$

where we have summed over all disjoint surfaces at temperature  $T$  in the source. A schematic representation of (8.2) and (8.3) is given in Figure 8.1.

Using (8.2) we can write (8.1) as

$$I(\epsilon) = \sum_i \int_T \int_{S_{T_i}} F(\epsilon, T) n_e^2(\underline{r}) \frac{dS dT}{|\nabla T|} \quad (8.4)$$

or

$$I(\epsilon) = \int_T F(\epsilon, T) \xi(T) dT \quad (8.5)$$

where

$$\xi(T) = \sum_i \int_{S_{T_i}} n_e^2(\underline{r}) \frac{dS}{|\nabla T|} \quad (8.6)$$

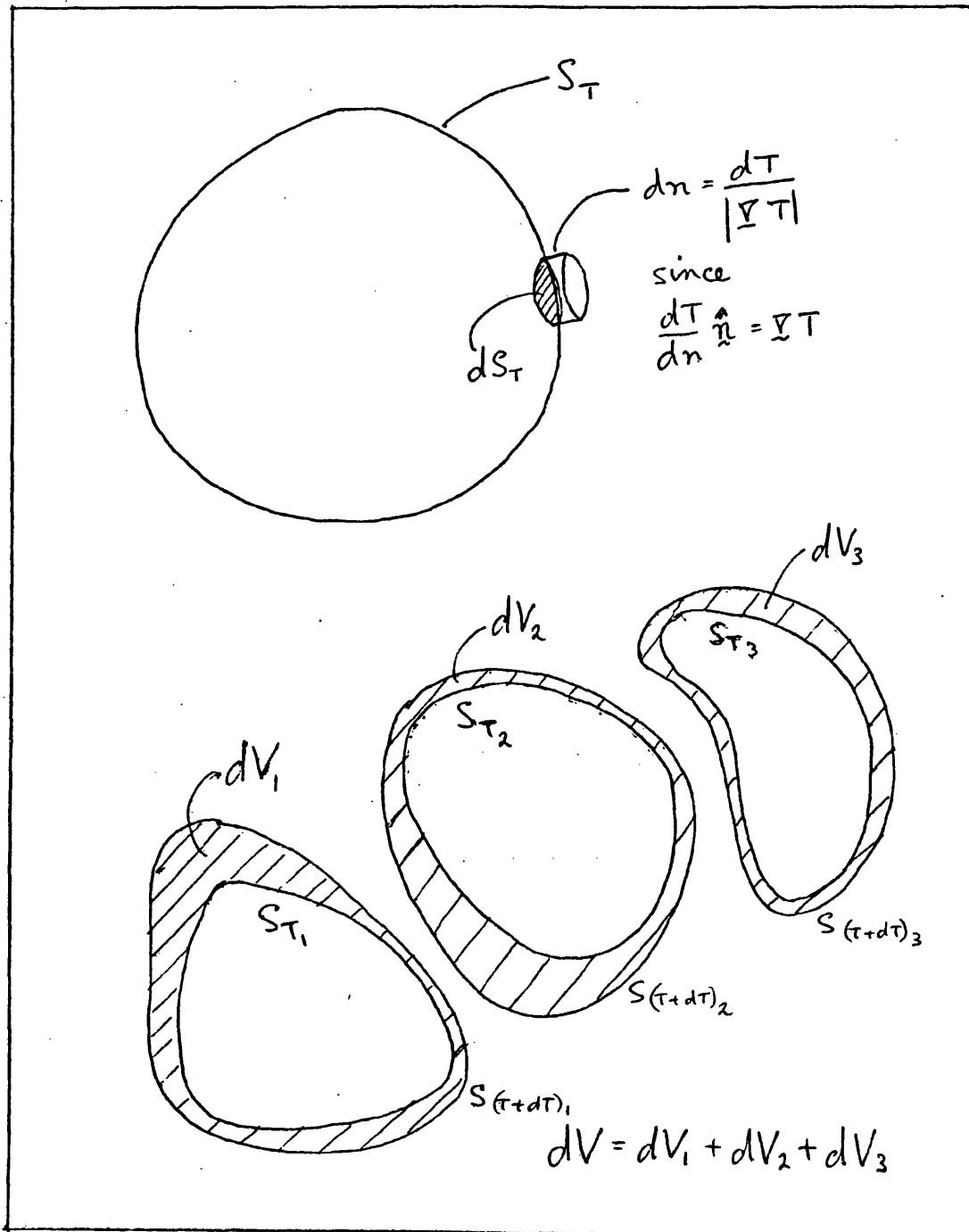


Figure 8.1 Definition of the volume increment associated with a temperature increment and illustration of summation over disjoint surfaces of constant temperature.

is the differential emission measure.

The interpretation of  $\xi(T)$  is most readily seen on dividing (8.6) by (8.3), defining

$$\overline{n_e^2}(T) = \frac{\sum_i \int_{S_{T_i}} n_e^2(\underline{r}) \frac{dS}{|\nabla T|}}{\sum_i \int_{S_{T_i}} \frac{dS}{|\nabla T|}} = \xi(T) / \frac{dV}{dT} \quad (8.7)$$

Thus  $\overline{n_e^2}(T)$  is a mean square electron density obtained by averaging over the surfaces at temperature  $T$  in the X-ray source region, weighted with respect to the magnitude of the inverse temperature gradient at each point on these surfaces.

Therefore (8.6) can be written

$$\xi(T) = \overline{n_e^2}(T) \frac{dV}{dT}(T) \quad (8.8)$$

Even if  $\xi(T)$  can be determined from measured soft X-ray fluxes by inversion of (8.5), a process fraught with difficulties (see Craig & Brown, 1975), it is clear that detailed information on the source structure cannot be obtained from this function alone. Equation (8.6) shows that contributions to  $\xi(T)$  come from an unknown number of surfaces at temperature  $T$ , over each of which the density and temperature gradient vary in an unknown manner. Obviously ad hoc assumptions about the structure of the emitting region have to be made before any results of physical interest may be deduced from the differential emission measure.

By way of illustration of the severity of the problem of deducing physical results from the emission measure, we attempt to find the temperature structure of a source region about which restrictive

assumptions have been made. An assumption commonly made in discussing soft X-ray source models is that the source structure is filamentary and can therefore be treated as one-dimensional (e.g. Culhane et al., 1970; Korchak, 1971). We assume also a value for the (constant) cross-sectional area,  $A$ , of the filament and for the electron density,  $n_e$ , in the filament, which we also take to be constant.

Then, (8.3) can be written

$$\frac{dV}{dT} = A \sum_i \left| \frac{dZ}{dT} \right|_i \quad (8.9)$$

where the coordinate  $Z$  specifies position in the one-dimensional source, and the summation is taken over all points  $Z_i$  which are at temperature  $T$ . From (8.8) and (8.9) we have

$$\sum_i \left| \frac{dZ}{dT} \right|_i = \frac{\xi(T)}{A n_e^2} \quad (8.10)$$

Since only the sum of the magnitudes of the temperature gradient is defined by this equation, we are forced to make another arbitrary assumption about the source structure. The simplest assumption is that the temperature structure is monotonic throughout the source. On this hypothesis, (8.10) can be integrated to give

$$Z = \frac{1}{A n_e^2} \int_{T_0}^T \xi(T') dT = Z(T) \quad (8.11)$$

where  $T_0$  is a conveniently chosen temperature, at which we take  $Z$  to be zero. This equation can now be inverted to give  $T(Z)$ .

Figure 8.2 illustrates the consequences of assuming a monotonic temperature structure when, in reality, this is untrue. Until spatially resolved spectroscopic observations of sufficient quality to enable  $\xi(T)$  to be determined as a function of position become available, it is clearly unsafe to attempt to infer physical quantities, such as

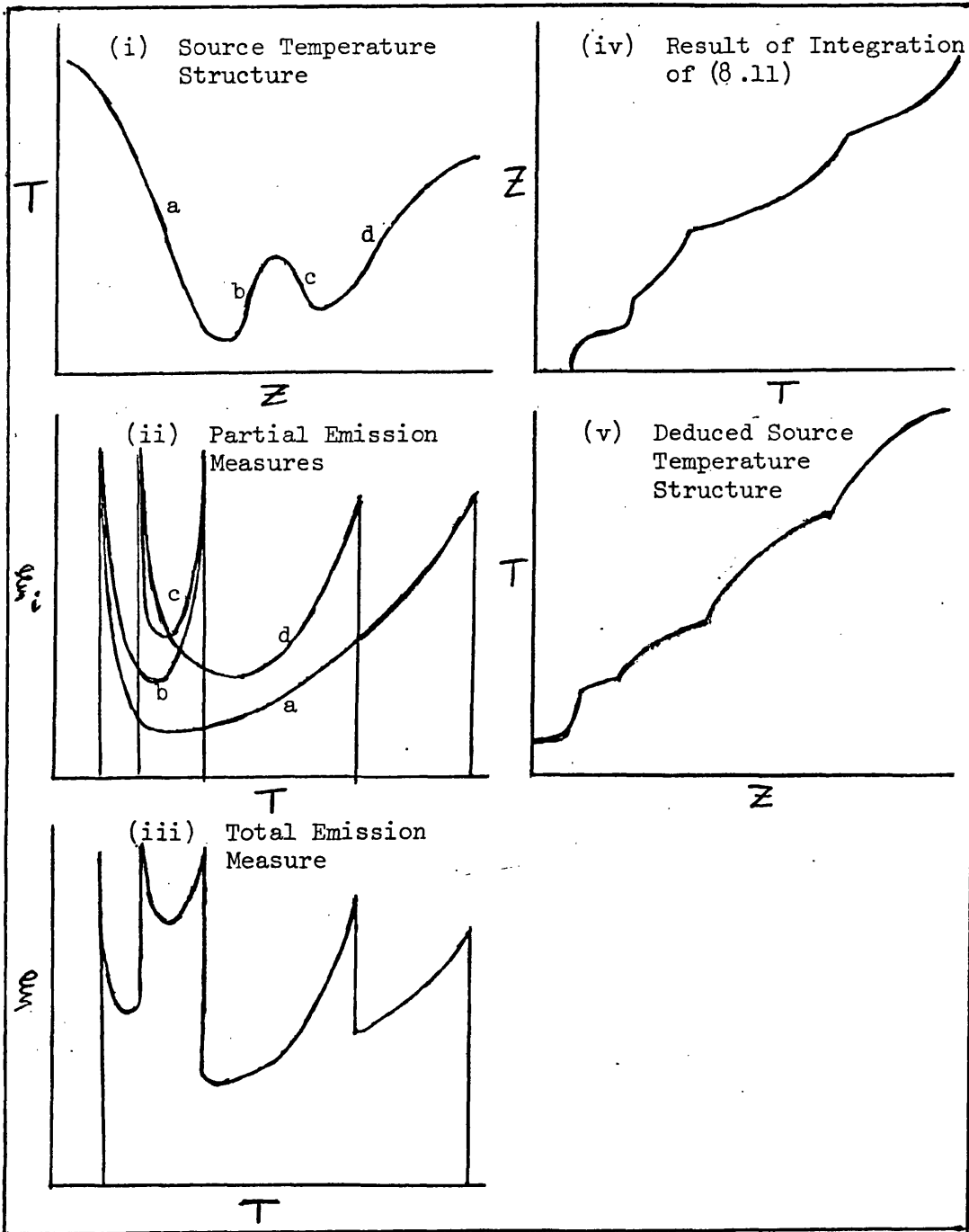


Figure 8.2

Illustration of the impossibility of deducing source temperature structure from the differential emission measure alone. For the purpose of calculating the emission measure the source is split into 4 regions a, b, c and d in each of which the temperature is monotonic.

conductive flux, from soft X-ray data. (Note that even spatially resolved observations give only a two-dimensional projection of the true source structure).

At present the only hope of deducing useful information from soft X-ray data appears to lie in the development of theoretical models whose predicted emission measures can be tested against observation. Even this technique is likely to meet with limited success, as Craig & Brown (1975) have shown that the X-ray spectrum is intrinsically insensitive to the emission measure because of the weak temperature dependence of the spectral distribution function  $F(\epsilon, T)$  in (8.5).

Leaving aside the question of interpretive difficulties, we now compute the differential emission measure predicted by the models considered in this chapter. A feature which will be prominent in the emission measure distributions of Models I and II and which will not appear when mass motion is inhibited, is apparent from the temperature and density distributions shown in Figures 3.1, 3.4, 4.1 and 4.4. The constant temperature plateau formed behind the shock front, over which the electron density is considerably enhanced, will give rise to a peak in the differential emission measure at a temperature of  $\sim 6 \times 10^6$  K.

Since the surfaces of constant temperature (cross-sections of the flux tube) are also surfaces of constant density, the general equation relating differential emission measure to the structure of the source region (8.6) reduces to

$$\xi(T) = 2A \sum_i n_e^2 \left| \frac{dZ}{dT} \right| \quad (8.12)$$

where  $A$  is the cross sectional area of the filament and the summation is taken over all points at temperature  $T$  in one half of the filament. The factor 2 takes account of the other half of the flux tube. It is apparent that the differential emission measure is singular for temperatures at which the temperature gradient in the source goes to zero. This occurs at the centre of the filament, in the constant

temperature plateau and in the undisturbed plasma ahead of the shock.

As we are interested in knowing how much material exists around a certain temperature, a quantity not readily apparent from a function singular near that temperature, we smooth the emission measure distribution by convoluting it with a Gaussian profile, whose half-width we take to be  $0.5 \times 10^6$  K. This value broadens the singular peaks sufficiently to allow a meaningful interpretation of the predicted emission measure structure, without smearing out significant detail. The smoothed differential emission measure is defined by

$$\hat{\xi}(T) = \int_{-\infty}^{\infty} \xi(T') G(T - T') dT' \quad (8.13)$$

where

$$G(x) = \frac{1}{\sqrt{2\pi} \sigma} e^{-x^2 / 2\sigma^2} \quad (8.14)$$

and  $\sigma = 0.5 \times 10^6$  K.

Substituting from (8.12) into (8.13) we obtain

$$\xi(T) = \int_{-\infty}^{\infty} 2A \sum_i \left[ n_e^2(T') \left| \frac{dZ}{dT'} \right| \right] G(T-T') dT'$$

which can be written

$$\hat{\xi}(T) = 2A \sum_k \int_{T_{\min_k}}^{T_{\max_k}} n_e^2(T') G(T-T') \left| \frac{dZ}{dT'} \right| dT' \quad (8.15)$$

where instead of summing over disjoint surfaces at the same temperature (denumerated by  $i$ ) we sum over regions in each of which the temperature is monotonic (denumerated by  $k$ ). Taking Figure 8.2(i) as an example, if the temperature  $T'$  lies in the range covered by region (c), then  $i$  picks out one point from each of the regions a, b, c and d, whereas summation over  $k$  represents the sum over the emission measures of the four regions a, b, c and d.

We now drop the cross sectional area  $A$  so that subsequent equations give the differential emission measure per unit cross section of the filament. We see that (8.15) can be written

$$\hat{\xi}(T) = 2 \sum_k \int_{z_{\min_k}}^{z_{\max_k}} n_e^2(Z) G(T-T'(Z)) dZ$$

that is

$$\hat{\xi}(T) = 2 \int_0^{z_0} n_e^2(Z) G(T-T'(Z)) dZ \quad (8.16)$$

Since density and temperature have been computed as functions of the Lagrangian coordinate  $y$  (used here instead of  $\xi$  to avoid confusion with emission measure)

$$y = \int_0^z \rho(z') dz' \quad (8.17)$$

we transform (8.16) to an integral over  $y$ ,

$$\hat{\xi}(T) = 2/m_p \int_0^{y_0} n_e^2(y) G(T-T'(y)) dy \quad (8.18)$$

where  $m_p$  is the proton rest mass.

The computed distribution of  $\hat{\xi}(T)$  for Models I and III, with and without mass motion, are shown in Figures 8.3 and 8.4. Results for Models II and IV are not presented, since the rise and subsequent fall in central temperature during the decay phase leads to a confusing display if all the results are plotted together. In Figure 8.3 (Model I) we see that, as anticipated, a prominent peak appears at  $T \approx 6 \times 10^6$  K for  $t \geq 2$  minutes, that is, after the shock has formed. There are two further significant differences between the results obtained with and without mass motion. Firstly,

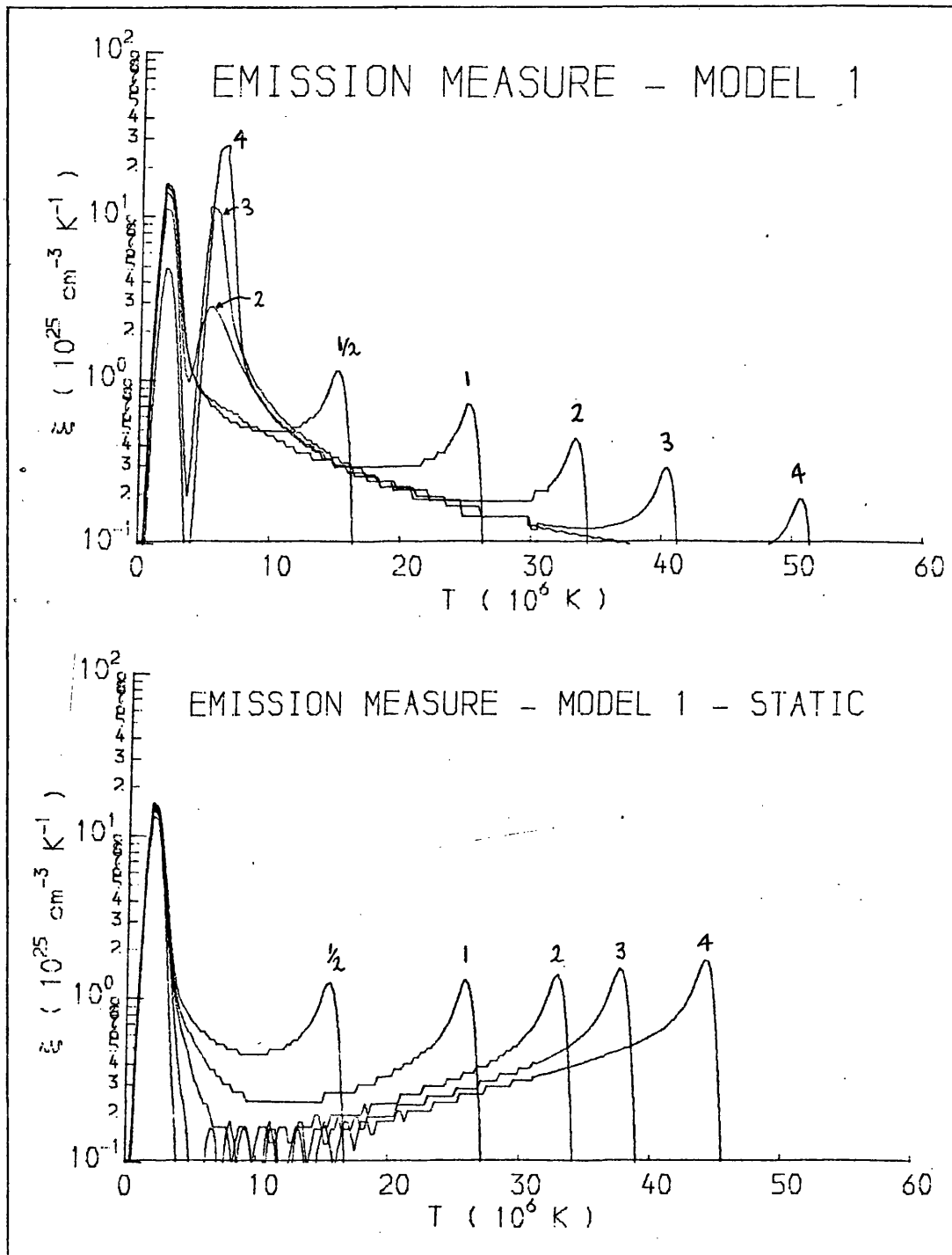


Figure 8.3 Differential soft X-ray emission measure: in Model I, with and without mass motion.

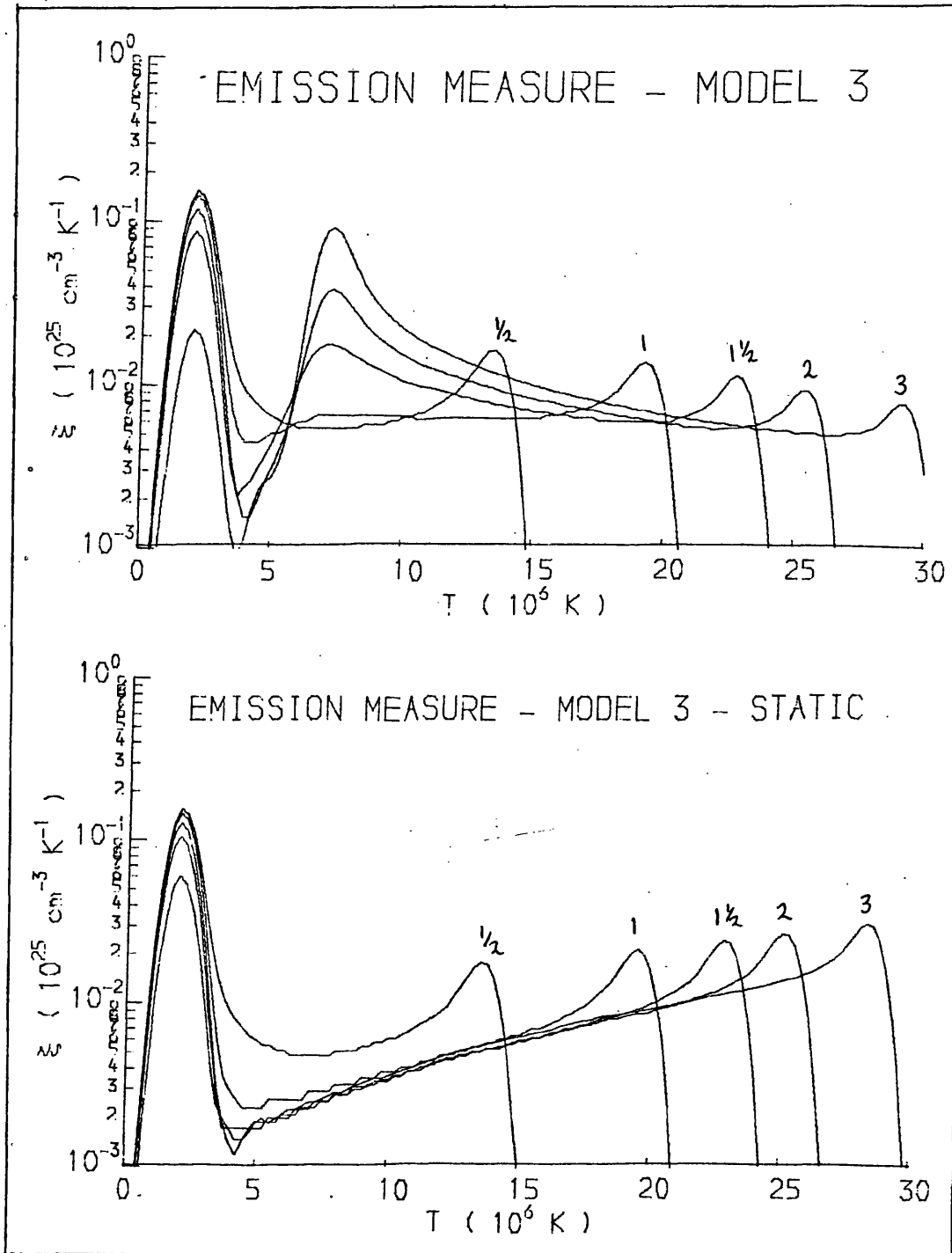


Figure 8.4 Differential soft X-ray emission measure of Model III, with and without mass motion.

when mass motion is inhibited, the peak in the differential emission measure at the central temperature has a constant value, whereas it decreases as material is convected away from the centre of the filament when mass motion is allowed. Secondly, in the range  $8 \times 10^6 \text{ K} \lesssim T \lesssim T_c$ , where  $T_c$  is the central temperature, the emission measure falls monotonically with increasing temperature when mass motion is allowed, but increases monotonically when mass motion is inhibited. (The "noise" at small values of emission measure is due to the fact that only a few grid points are contributing to the computational approximation to integral (8.19).)

The same trends are evident in the Model III results (Figure 8.4). Despite the insignificance of the constant temperature region in this model (see Figure 4.1), a strong peak in the emission measure at  $T \approx 7.5 \times 10^6 \text{ K}$  is evident. The width of the peak (c.f. Figure 8.3), which shows that material over a range of temperatures is contributing to the emission measure, demonstrates that the enhanced density behind the shock is sufficient to give rise to a peak in the emission measure, even if the temperature gradient is not very small. As in Model I, we find that the emission measure in the region  $8 \times 10^6 \text{ K} < T < T_c$  decreases with increasing temperature, but increases if mass motion is inhibited. Again the peak emission measure at  $T = T_c$  falls as the filament evolves, but less rapidly than in Model I. When mass motion is inhibited it rises slightly.

## 9. ELECTRON HEATING.

It was pointed out in §1 that the filament length assumed in this chapter,  $3 \times 10^{10} \text{ cm}$ , is rather large, so that some of the results obtained may not be directly applicable to the flare problem. In the models considered in §3-6, the shock always forms at a distance greater than  $5 \times 10^9 \text{ cm}$  from the origin. Therefore it may appear that in an actual filament of total length, say  $10^{10} \text{ cm}$ , shocks will not develop. In this section we will see that shocks can develop close to the centre of the filament if the bulk of the injected energy is

carried by non-thermal electrons having a power law distribution in energy with a low energy cutoff  $\lesssim 25$  keV.

The results presented in this section are of a preliminary nature. As we wish to establish only one result, a detailed derivation of the energy input term,  $Q^*$  in VI (5.20), will not be given. The non-thermal electrons, which are injected at the centre of the filament, are assumed to stream into both halves of the flux tube in equal numbers. A neutral sheet configuration of the type suggested by Sturrock (1972) is a feasible mechanism for the acceleration and injection of these electrons. In deriving the energy deposition rate, collective interactions are neglected, the electrons being assumed to decay collisionally according to the energy loss formula of Brown (1972)

$$E = E_0 (1 - 3 K_{\text{coll}} N(Z)/E_0^2)^{1/3} \quad (9.1)$$

In this equation, which takes account of scattering,  $E$  is the kinetic energy of an electron after passing through a column density  $N$  of ambient electrons,  $E_0$  is the initial energy of the electron and  $K_{\text{coll}}$  ( $= 3.64 \times 10^{-18}$  keV<sup>2</sup> cm<sup>2</sup>) is related to the collisional energy loss cross-section. We ignore the difference in electron and proton temperatures which is a consequence of electron heating. At the high density of  $10^{11}$  cm<sup>-3</sup> this effect should be of minor importance since the electron-proton equilibrium time is short.

The energy input of Model II, which injects  $5 \times 10^{12}$  erg cm<sup>-2</sup> over a period of 1 minute, is used here. A low energy cut-off in the power law ( $\delta = 4$ ) electron energy spectrum of 10 keV is assumed. This implies that the integral number flux of non-thermal electrons above 25 keV is  $3.5 \times 10^{17}$  cm<sup>-2</sup> at the peak energy injection rate, which occurs at  $t = 30$  seconds. For a reasonable value of the filament cross-sectional area of  $10^{17} - 3 \times 10^{18}$  cm<sup>2</sup>, the total number flux of electrons above 25 keV,  $F_{25}$ , is  $5 \times 10^{34} - 10^{36}$  sec<sup>-1</sup>.

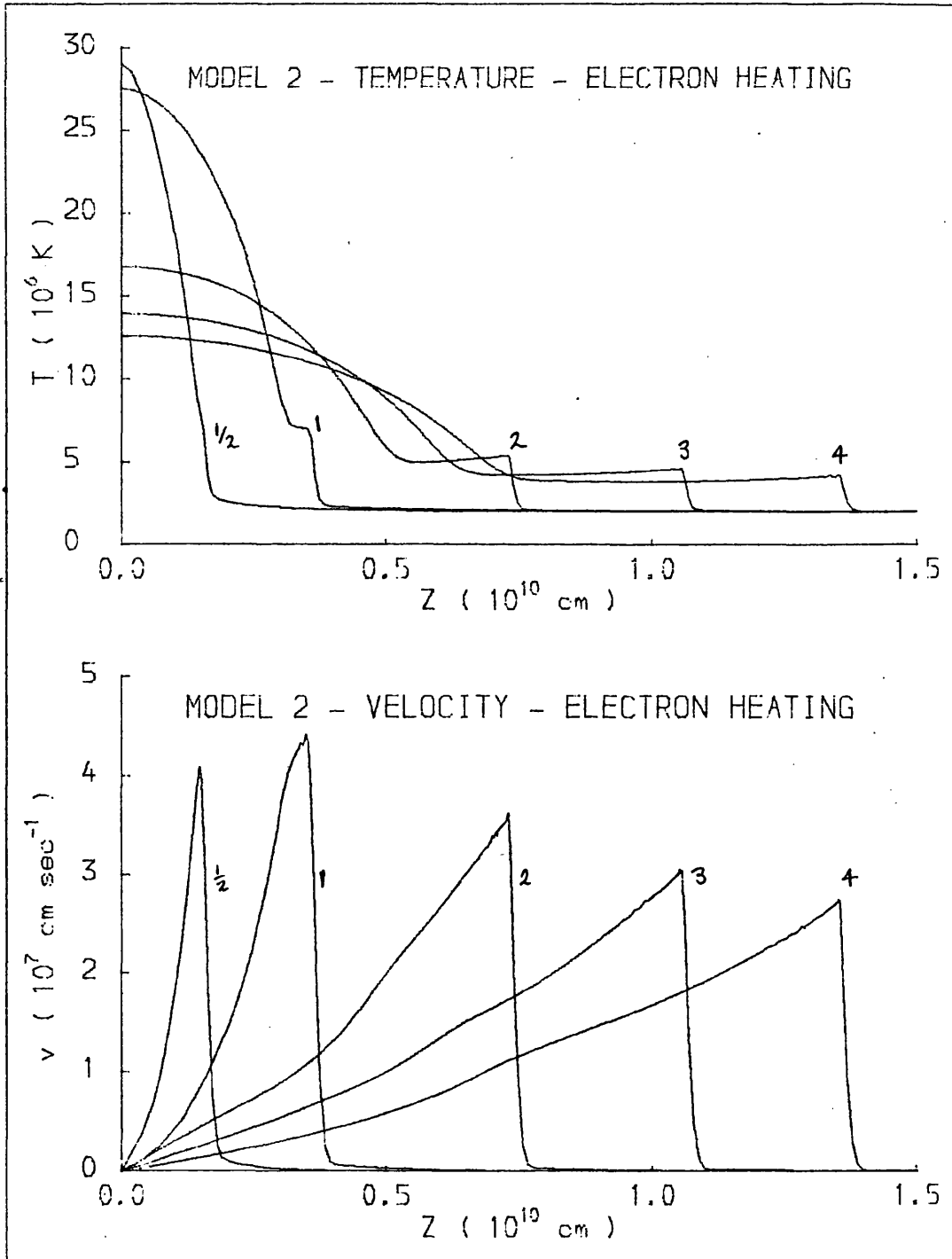


Figure 9.1 Evolution of temperature and velocity in Model II with electron heating. Time in minutes from the start of heating is shown against each curve.

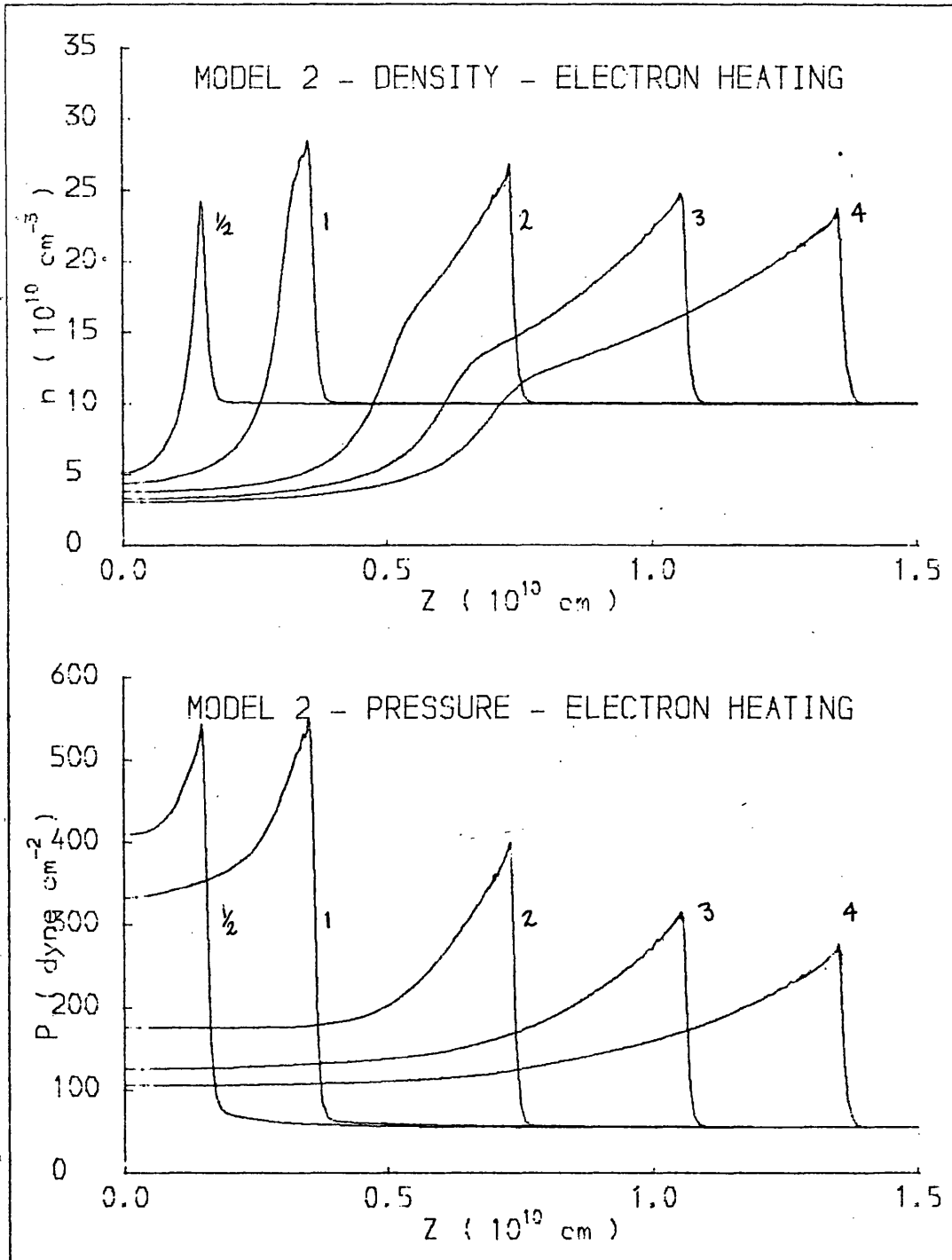


Figure 9.2 Evolution of density and pressure in Model II with electron heating. Time in minutes from the start of heating is shown against each curve.

This range of values is typical of electron numbers inferred from hard X-ray data for a small flare (see Hoyng et al., 1975).

Results are illustrated in Figures 9.1 and 9.2. It is clear that the shock has developed fully within 30 seconds of the start of heating, at a distance of less than  $2 \times 10^9$  cm from the centre of the filament. If these figures are compared with Figures 4.2 - 4.5, which show the evolution of Model II with the original form of heating, several other features worthy of note are apparent. Firstly, the region of constant temperature and enhanced density, which comprises the shocked material, is longer when electron heating is assumed since the shock develops closer to the origin. Therefore the peak in differential emission at  $T \approx 5 \times 10^6$  K will be even larger in this case. Secondly, there is a noticeable fall in the temperature just behind the shock throughout the decay phase. At  $t = 1$  minute the temperature is  $\sim 7 \times 10^6$  K, but at  $t = 4$  minutes it has fallen to  $4 \times 10^6$  K. Finally, the peak temperature at the centre of filament is higher during the impulsive phase under electron heating. This is due to the dumping of non-thermal energy in a narrow region close to the origin.

Clearly, energy injection in the form of fast electrons considerably shortens the timescale and length scale for the development of significant mass motions.

## 10. SUMMARY, DISCUSSION AND COMPARISON WITH OBSERVATION

We recall that the results presented in this chapter show only one half of the filament. By our assumption of symmetry, a pair of shock waves develop near the origin and propagate down to the footpoints of the filament. As mentioned in Chapter VI, the non-uniform density and non-uniform magnetic field in a real filament may upset our idealised calculations. But if the shocks do reach the chromosphere they could have a spectacular effect there. Nakagawa et al., (1973) have calculated the rate of decay of a shock propagating down through the chromosphere. Their analysis begins with the shock below the

transition region, whereas in our case the shock must propagate through the transition region. The effect of the sudden density increase on the shock front is not clear. However, we infer that the peak temperature reached in the chromosphere is probably  $\sim 1.5 \times 10^5$  K, the value found by Nakagawa et al., for an initial shock speed of  $4 \times 10^7$  cm sec<sup>-1</sup>. (Mach 30 in the chromosphere).

For a filament of length  $10^{10}$  cm, the effects of flare heating propagate to the ends of the filament in less than 100 seconds. Clearly then, the question of boundary conditions at the ends of the filament is a crucial one which must be answered before the decay phase of the flare can be studied properly.

Below are summarized the main conclusions drawn from §3-7.

- (i) Neglect of mass motion grossly falsifies the predicted evolution of a heated filament, particularly if the ambient plasma density is high.
- (ii) For reasonable values of the injected energy, shocks of Mach number 2.5 develop in a time of  $\lesssim 100$  seconds.
- (iii) In the decay phase, after the heating source is switched off, the rate of propagation of heat by thermal conduction falls rapidly, but the shocks created during energy injection go sailing on, decelerating very slowly.
- (iv) A region of almost constant temperature and enhanced density is formed behind the shock, giving rise to a large peak in the soft X-ray differential emission measure at  $\sim 5 \times 10^6$  K.
- (v) Despite its strong influence on the evolution of the filament, the kinetic energy involved in mass motion is  $\lesssim 15\%$  of the total thermal energy of the plasma.
- (vi) During the initial heating phase, transport of energy through space is mainly by convection if the density is high and by conduction if the density is low. But in both cases none of the processes of conduction, convection and work done by pressure can be regarded as negligible. Transport of energy through the plasma is mainly through work done by pressure if the density is high and by conduction

if the density is low. Again, neither process can be considered to dominate.

- (vii) If energy input to the filament continues once mass motion is under way, three domains of energy transport may be defined. Close to the origin thermal conduction dominates. In the region extending out to the shock, deposition of energy by conduction is partially balanced by cooling of the plasma due to work done against pressure. When energy transport through space is considered, convection of energy out of this region is also important. In the shock front itself, all forms of energy transfer are again significant.
- (viii) During the decay phase, after the heating source is removed, energy transport by all processes becomes small, except in the shock front. In particular, conduction drops dramatically. If the ambient plasma density is high, evolution of the filament is entirely controlled by mass motion. If the density is low, conduction is of comparable importance to work done by pressure.

In §8 we calculated the form of the soft X-ray differential emission measure. The following features, which do not appear if mass motion is inhibited, were found:-

- (i) A large peak in the emission measure at temperature  $T \approx 5 \times 10^6$  K. This is produced by the region of constant temperature and enhanced density behind the shock.
- (ii) The peak in the emission measure at the central temperature decreases as material is convected away from the centre of the filament. If mass motion is inhibited it remains the same size or increases.
- (iii) The emission measure in the region  $8 \times 10^6 \lesssim T < T_c$ , where  $T_c$  is the central temperature, decreases monotonically with increasing temperature. The opposite effect occurs if mass motion is inhibited.

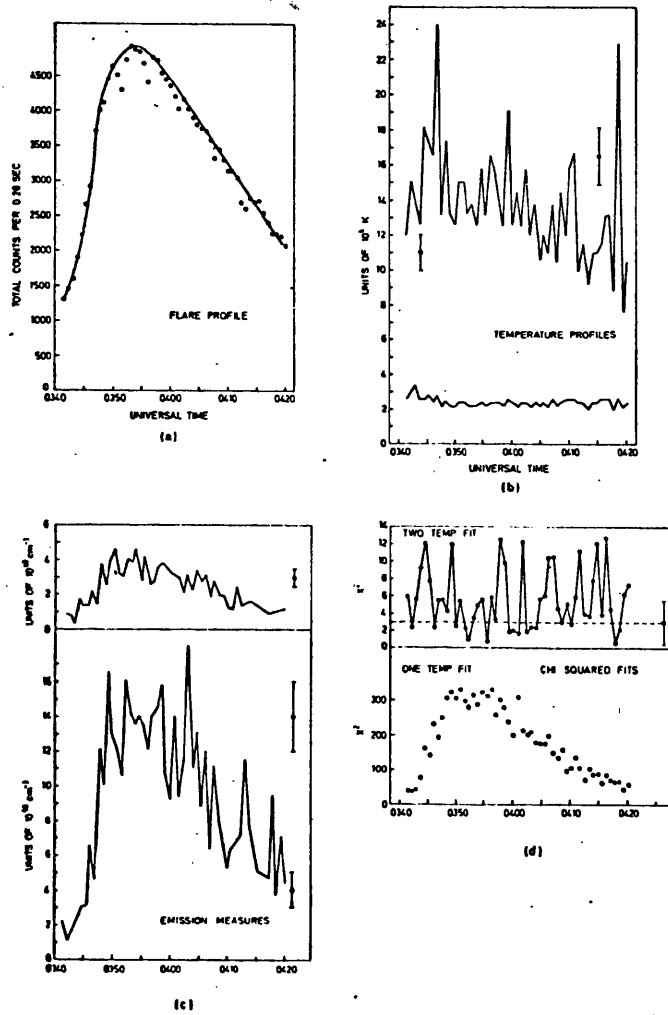
Finally, in §9, we found that if the energy source is taken to be an injected stream of non-thermal electrons, the shocks can develop close to the centre of the filament, in a distance short compared to

typical lengths of active region filaments.

The necessity for the development of self-consistent models of the soft X-ray flare, whose predicted emission measures can be compared with observation, was pointed out in §8. To start the ball rolling, we now compare, in a qualitative manner, the predictions of the models discussed in this chapter with emission measures deduced from soft X-ray observations.

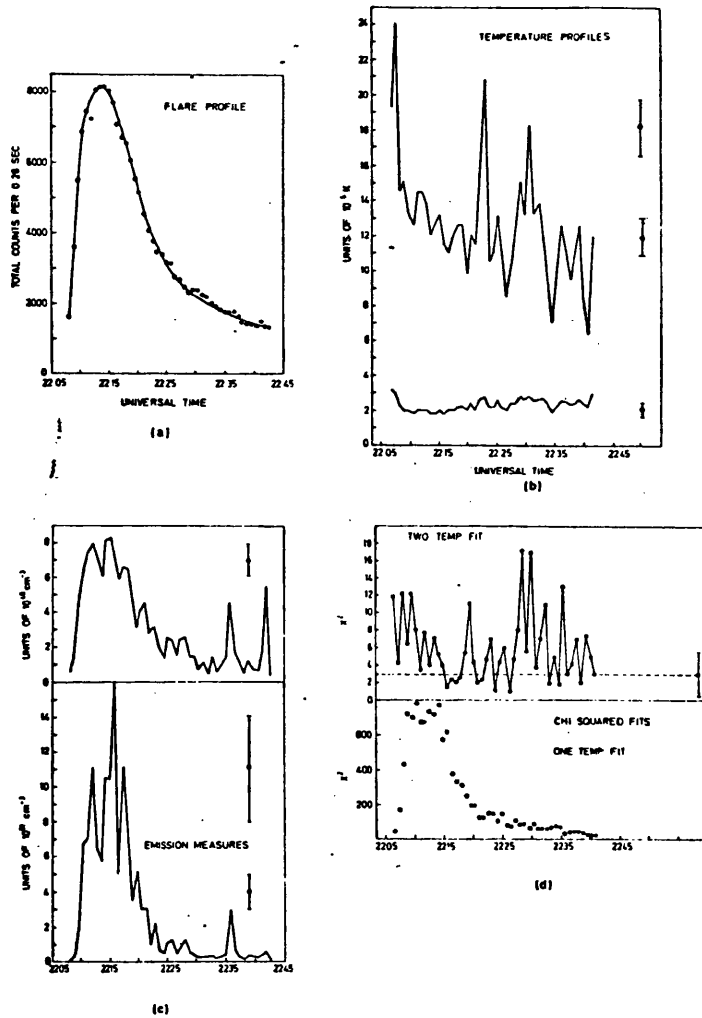
Two points are emphasised. Firstly, although the calculations presented in the preceding chapter and in this one include all effects which we believe to be of major importance, we do not regard these results as constituting a definitive model. Secondly, as pointed out in §8, the equation relating emission measure to soft X-ray flux is ill-conditioned (Craig & Brown, 1975). Therefore a large range of emission measure structures may satisfy the observations, even if these have good statistics. Herring & Craig (1973) have shown that single temperature analyses (that is, single delta-function emission measures) of soft X-ray data are unsatisfactory, but that two temperature analysis provide an acceptable fit to the data. Typical results, obtained from such analyses (Figures 10.1 and 10.2) indicate the existence of a low temperature plasma ( $T \lesssim 3 \times 10^6$  K) with an emission measure of  $\sim 10^{50} - 10^{51} \text{ cm}^{-3}$ , and a high temperature region ( $T \approx 15 \times 10^6$  K) which has an emission measure of  $\sim 5 \times 10^{48} \text{ cm}^{-3}$ . Note that the filament model is concerned with only the first few minutes of evolution of these flares.

It is appropriate to remark that Herring (1974) has developed a semi-empirical model which invokes shock heating to explain the two-temperature structure. Since the existence of a shock is postulated in Herring's analysis, his model is more restrictive than those we have developed here. Unlike the models considered here, it is the high temperature component which is heated by the shock in Herring's model. Herring interprets the two-temperature emission measure results as indicative of the existence of two distinct isothermal regions. In view of the ill-conditioning problem and



Details of the flare 15th September 1969. The total flux at any time considered was greater than 1000 counts. This selection criterion ensures reasonable statistics.

Figure 10.1 Two temperature emission measure analysis. From Herring & Craig (1973).



Details of the flare 5th September 1969. This shows a much faster rise and fall time than the previous flare profile. The same selection procedure was used.

Figure 10.2 Another two temperature emission measure analysis. From Herring & Craig (1973).

interpretive difficulties, it is more likely that the two-temperature analysis represents only a first approximation to a continuous distribution.

Craig (1975b) has confirmed this view by extending the two-temperature emission measure analysis to a two-Gaussian analysis. A low temperature and high temperature component were found as before, the emission measures associated with each being of the same order as in the two delta function analysis. But in this case the widths of the distributions were also determined. The low temperature component was found to be very narrow ( $\lesssim 0.1 \times 10^6$  K) while the high temperature component is broad and flat ( $\gtrsim 3 \times 10^6$  K). This emission measure structure is remarkably similar to those predicted here (Figures 8.3 and 8.4). Note that flare X-ray emission would not be expected to emanate from the undisturbed plasma at  $2 \times 10^6$  K ahead of the shock, since this is a quiescent plasma which existed before the flare began.

In order to compare our predictions more quantitatively with the data shown in Figures 10.1 and 10.2, we obtain an approximate total emission measure for each of the peaks in Figures 8.3 and 8.4 from

$$\Delta\xi \approx \xi(T_p) \Delta T_p A \quad \text{cm}^{-3} \quad (10.1)$$

where  $\xi(T_p)$  is the peak value of emission measure occurring at temperature  $T_p$ ,  $\Delta T_p$  is an estimated width of the peak and  $A$  is the cross-sectional area of the filament. Table 10.1 shows the results obtained when the cross-sectional area is assumed to lie in the range  $10^{17} \text{ cm}^2 < A < 3 \times 10^{18} \text{ cm}^2$ .

Table 10.1 Emission measures at  $t = 3$  minutes

Model	$T_p$ ( $10^6$ K)	$\Delta T_p$ ( $10^6$ K)	$\Delta \xi$ ( $\text{cm}^{-3}$ )
I	6	2	$2 \times 10^{49} - 5 \times 10^{50}$
	40	5	$2 \times 10^{48} - 5 \times 10^{49}$
III	7	$\sim 3$	$\sim 3 \times 10^{47} - 5 \times 10^{48}$
	30	$\sim 10 ?$	$2 \times 10^{47} - 5 \times 10^{48} ?$

We see that the emission measures predicted by Model I ( $n_{e_0} = 10^{11} \text{ cm}^{-3}$ ) agree with the values found by Herring & Craig, but the filament cross-section in Model III ( $n_e = 10^{10} \text{ cm}^{-3}$ ) would have to approach  $10^{20} \text{ cm}^2$  for the low temperature emission measures to be compatible. A structure of such dimensions could hardly be called a filament. It is possible, however, that simultaneous X-ray emission from several flaring filaments is observed. But if each filament had a cross sectional area of  $10^{17} \text{ cm}^2$   $\sim 500$  simultaneously erupting filaments would be required! Culhane *et al.*, (1970) also concluded that densities of  $10^9 - 10^{10} \text{ cm}^{-3}$  imply impossibly large structures. Model III also falls down because it predicts that the emission measures at high and low temperatures are of the same order, whereas by observation the emission measure at low temperatures is  $\sim 10^2 - 10^3$  greater than at high temperature.

The difference between the observed and predicted higher temperature of the two-temperature distribution is not a problem, since the predicted temperature depends on the energy injected. If we had calculated the emission measure from Model II instead of Model I, the central temperature would have achieved a maximum value of only  $20 \times 10^6 \text{ K}$  (at the end of heating,  $t = 1$  minute). Note also that the distribution of emission measure over temperature is fairly flat, particularly in Model III. The best fit delta function approximation will therefore occur at a temperature lower than the central temperature.

In Model II the central temperature falls to  $12-15 \times 10^6$  K after a few minutes. Figures 10.1 and 10.2 show that this behaviour is close to that actually observed. We reiterate that the results presented here are concerned only with the first few minutes of these observations.

There are several possible explanations of the discrepancy between the positions of the low temperature peaks. Temperatures derived from a two-temperature analysis represent some weighted average over the emission measure distribution and do not necessarily coincide with peaks in the distribution, although they should give an indication of the temperature domains from which significant contribution to the X-ray flux originate. Craig (1975b) in a one-temperature analysis of the flare shown in Figure 10.1, found that the best fitting temperature was around  $5 \times 10^6$  K. The poor fit to the data obtained by this method (see Figure 10.1) does not necessarily mean that the derived temperature represents only an average over an emission measure distribution in which little material actually exists around  $5 \times 10^6$  K. Rather, it indicates that appreciable emission in a different energy range has been detected, but not allowed for in the analysis.

In order to complete this observational test of the model, we must discuss the time variation of the emission measure. In both Figures 10.1 and 10.2 we see that the low temperature emission measure behaves as expected, increasing continuously throughout the first 5 minutes of the flare. The high temperature emission measure however, does not since it increases, rather than falls, during the rising phase of the flare. However, there are two features of the models which may possibly account for this behaviour. Firstly, although it was stated that the high temperature emission measure falls as material is convected away from the centre of the filament, in the decay phase this effect is compensated by the flattening of the temperature profile near the origin as the temperature falls. Results obtained for Model II (not shown) indicate that in this model the emission measure remains constant during the decay phase. Secondly, if electron heating is invoked, the temperature gradient near the origin is initially very

steep (Figure 9.1). Since this implies that there is little material at temperatures close to the central temperature, the emission measure may rise initially.

In most respects, the model appears to be compatible with observation. A high density in the filament is required to give a sufficiently high emission measure. It will be of interest to attempt to use the form of emission measure predicted here as a fitting function in the reduction of soft X-ray data. This will give a more quantitative evaluation of the plausibility of the model, than the qualitative comparisons made here.

In conclusion, most of the questions set out in Chapter VI have been answered satisfactorily. We have shown that the influence of mass motion is of vital importance in a heated filament. In particular, we have demonstrated that the assumption of one dominant process of energy transfer is wrong. Analyses such as those performed by Strauss & Papaggianis (1971), Zaumen & Acton (1974), Landini *et al.* (1975) and Moore & Datlowe (1975) lack self-consistency and their results, being physically impossible, cannot be taken as a guide to the behaviour of a real flare.

The question which we have not answered - when do the approximations of constant density or constant pressure apply - has been rendered of secondary importance by the discovery of the shock. In reality, the situation is obviously of much greater complexity than could be described by an analysis in either approximation. Although the region behind the shock is at near constant pressure for  $t > 2$  minutes, this is a transient phenomena. Cooling of the central region of the filament or reflection of the shocks at the chromosphere will cause mass flows back to the central region during the decay phase of the flare.

We have accomplished our primary purpose of demonstrating the importance of mass motion, but many more questions have sprung up. For example, does a non-uniform initial density distribution

significantly affect the results obtained here? Does lateral expansion of the flux tube subject to the pressure of the heated plasma affect the formation of shocks? What happens when the shocks propagate down to the chromosphere? How does this affect the subsequent evaluation of the filament? Can limits be set on the form of the emission measure, under more general conditions than those considered here?

REFERENCES

- Becker, R. 1922: Z. Physik 8,321.
- Beigman, I.L. 1974: preprint.
- Benz, A.O. & Gold, T. 1971: Solar Phys. 21,157.
- Bessey, R.J. & Kuperus, M. 1970: Solar Phys. 12,216.
- Boardman, W.J. & Billings, D.E. 1969: Astrophys. J. 156,731.
- Bray, R.J. & Loughhead, R.E. 1974: The Solar Chromosphere, Wiley.
- Brown, J.C. 1972a: Solar Phys. 25,158.
- 1972b: *ibid.* 26,441.
- 1973a *ibid.* 31,143.
- 1973b *ibid.* 32,227.
- 1974a *ibid.* 36,371.
- 1974b: in Newkirk (ed) Coronal Disturbances, IAU Symp.57,p395.
- 1975: in Kane (ed) Solar Gamma-, X- and EUV Radiation,  
IAU Symp.68,p245.
- Brown, J.C., McClymont, A.N. & McLean, I.S. 1974: Nature 247,448.
- Brown, J.C. & Hoyng, P. 1975: Astrophys. J. 200,734.
- Brown, J.C. & McClymont, A.N. 1975: Solar Phys. 41,135.
- Brown, J.C. & Melrose, D.B. 1975: to be submitted to Solar Phys.
- Brown, J.C. & McClymont, A.N. 1976: in preparation.
- Brown, J.C., van Beek, H.F. & McClymont, A.N. 1975:  
Astron. Astrophys. 41,395.
- Chiu, Y.T. 1970: Solar Phys. 13,426.
- Christiansen, W.N., Matthewson, D.S., Pawsey, J.L., Smerd, S.F.,  
Boischet, A., Denisse, J.F., Simon, P., Kakinuma, T.,  
Dodson-Prince, H. & Firor, J. 1960: Ann.Astrophys.23,75.
- Chubb, T.A., Kreplin, R.W. & Friedman, H. 1966: J. Geophys. Res. 71,3611.
- Cox, D.P. & Tucker, W.H. 1969: Astrophys. J. 157,1157.
- Craig, I.J.D. 1975a: in Kane (ed) Solar Gamma-, X- and EUV Radiation,  
IAU Symp.68,p187.
- 1975b: Ph.D. thesis, University College London.
- Craig, I.J.D. & Brown, J.C. 1975: to appear in Astron. Astrophys.
- Culhane, J.L., Veseccky, J.F. & Phillips, K.J.H. 1970: Solar Phys. 15,394.
- Datlowe, D.W. 1975: in Kane (ed) Solar Gamma-, X and EUV Radiation,  
IAU Symp.68,p191.

- Datlowe, D.W. & Lin, R.P. 1973: Solar Phys. 32,459.
- Datlowe, D.W., Elcan, M.J. & Hudson, H.S. 1974: Solar Phys. 39,155.
- Donnelly, R.F. 1969: Astrophys.J. 158,L165.
- Elwert, G. 1939: Ann. Physik 34,178.
- 1968: in Kiepenheuer (ed) IAU Symp.35,p439.
- Elwert, G. & Haug, E. 1970: Solar Phys. 15,234.
- 1971: *ibid.* 20,413.
- Falciani, R., Landini, M., Righini, A. & Rigutti, M. 1968:  
in Kiepenheuer (ed) IAU Symp.35,p451.
- Frost, K.J. & Dennis B.R. 1971: Astrophys. J. 165,655.
- Gluckstern, R.L. & Hull, M.H. 1953: Phys. Rev. 90,1030.
- Gluckstern, R.L., Hull, M.H. & Breit, G. 1951: Science 114,480.
- Haug, E. 1972: Solar Phys. 25,425.
- Henoux, J. 1975: Solar Phys. 42,219.
- Herring, J.R.H. 1974: Solar Phys. 39,175.
- Herring, J.R.H. & Craig, I.J.D. 1973: Solar Phys. 28,169.
- Hoyng, P. 1975: Ph.D. thesis, Utrecht University.
- Hoyng, P., Brown, J.C. & van Beek, H.F. 1975: to appear in Solar Phys.
- Hudson, H.S. 1972: Solar Phys. 24,414.
- 1973: in Ramaty & Stone (eds) High Energy Phenomena on the Sun,  
NASA SP-342,p162.
- Kahler, S.W. 1971: Astrophys. J. 164,365.
- 1975: in Kane (ed) Solar Gamma-, X- and EUV Radiation,  
IAU Symp.68,p211.
- Kahler, S.W. & Kreplin, R.W. 1971: Astrophys. J. 158,531.
- Kane, S.R. 1974: in Newkirk (ed) Coronal Disturbances, IAU Symp.57,p105.
- Kane, S.R. & Anderson, K.A. 1970: Astrophys. J. 162,1003.
- Kane, S.R. & Donnelly, R.F. 1971: Astrophys. J. 164,151.
- Korchak, A.A. 1967: Soviet Astron. AJ 11,258.
- 1971: Solar Phys. 18,284.
- Kostjuk, N.D. & Pikel'ner, S.B. 1974: Astron. Zh. 51,1002.
- Kundu, M.R. 1961: J. Geophys. Res. 66,4308.
- Landini, M., Fossi, B.C. & Pallavicini, R. 1975: Solar Phys. 44,101.
- Lin, R.P. 1970: Solar Phys. 12,266.
- 1971: *ibid.* 15,453.
- 1974: in Newkirk (ed) Coronal Disturbances, IAU Symp.57,p201.
- Lin, R.P. & Anderson, K.A. 1967: Solar Phys. 1,446.

- Lin, R.P. & Hudson, H.S. 1971: Solar Phys. 17,412.
- Lorrain, P. & Corson, D. 1970: Electromagnetic Fields and Waves, Freeman.
- McKenzie, D.L. 1975: Solar Phys. 40,183.
- Melrose, D.B. & Brown, J.C. 1975: to appear in MNRAS.
- Moore, R.L. & Datlowe, D.W. 1975: Solar Phys. 43,189.
- Nakada, M.P., Neupert, W.M. & Thomas, R.J. 1974: Solar Phys. 37,429.
- Nakagawa, Y., Wu, S.T. & Han, S.M. 1973: Solar Phys. 30,111.
- von Neumann, J. & Richtmyer, R.D. 1950: J. Appl. Phys. 21,232.
- Peterson, L.E. & Winckler, J.R. 1959: J. Geophys. Res. 64,697.
- Petrosian, V. 1973: Astrophys. J. 186, 291.
- Pinter, S. 1969: Solar Phys. 8,142.
- Pneuman, G.W. 1972: Astrophys. J. 177,293.
- Priest, E.R. & Raadu, M.A. 1975: Solar Phys. 43,177.
- Reimers, D. 1971: Astron. Astrophys. 14,198.
- Richtmyer, R.D. & Morton, K.W. 1967: Difference Methods for Initial-Value Problems, Interscience.
- Roy, J.-R. & Datlowe, D.W. 1975: Solar Phys. 40,165.
- Santangelo, N., Horstman, H., & Horstman-Moretti, E. 1973: Solar Phys. 29, 143.
- Sauter, F. 1934: Ann. Physik 20,404.
- Smith, D.F. 1974: in Newkirk (ed) Coronal Disturbances, IAU Symp.57,p253.
- Sommerfeld, A. 1951: Atombau und Spektrallinien, Vol.2, p374; Friedr. Vieweg und Sohn.
- Spitzer, L. 1962: Physics of Fully Ionised Gases, Interscience.
- Stewart, R.T. 1973: in Newkirk (ed) Coronal Disturbances, IAU Symp.57,pl61.
- Strauss, F.M. & Papaggianis, M.D. 1971: Astrophys. J. 164,369.
- Sturrock, P.A. 1972: in McIntosh & Dryer (eds) Solar Activity Observation and Prediction, pl63.
- Suri, A.N., Chupp, E.L., Forrest, D.J. & Reppin, C. 1975: Solar Phys. 43, 415.
- Švestka, Z. 1969: in de Jager & Švestka (eds) Solar Flares and Space Research, pl6.
- Sweet, P.A. 1969: Ann. Rev. Astron. Astrophys. 7,149.
- Takakura, T. 1967: Solar Phys. 1,304.
- Takakura, T. & Kai, K. 1966: Publ. Astron. Soc. Japan 18,57.
- Takakura, T. & Scalise, E. 1970: Solar Phys. 11,434.

- Takakura, T., Ohki, K., Shibuya, N., Fujii, M., Matsuoka, M.,  
Miyamoto, S., Nishimura, J., Oda, M., Ogawara, Y.  
& Ota, S. 1971: Solar Phys. 16, 454.
- Tindo, I.P., Ivanov, V.D., Mandel'shtam, S.L., & Shuryghin, A.I. 1972:  
Solar Phys. 24, 429.
- Tomblin, F.F. 1972: Astrophys. J. 171, 377.
- Tucker, W.H. & Koren, M. 1971: Astrophys. J. 168, 283.
- Zaumen, W.T. & Acton, L.W. 1974: Solar Phys. 36, 139.
- Zel'dovich, Y.B. & Raiser, Y.P. 1966: Physics of Shock Waves and  
High-Temperature Hydrodynamic Phenomena,  
Vol.1 & 2, Academic Press.
- Zirin, H. & Tanaka, K. 1973: Solar Phys. 32, 173.

UNIVERSITY OF GLASGOW

In respect of my thesis [title to be inserted]

- 1. I understand that no access to it will be allowed without my prior permission until one year has elapsed from the date of its deposit in the University Library.
- 2. Thereafter:-
  - \* a. I give permission for it to be made available to readers in the University Library or within another library.
  - \* b. I do not wish it to be made available to readers for a further two years without my written consent ~~or (failing a reply from me within 3 months to a request from the University Library) the consent of the Library Committee in consultation with the Higher Degrees Committee of the Faculty.~~
- 3. Once any restrictions on access have expired:-
  - a. I give permission for a photocopy to be made by the British Library for lending to other libraries.
  - b. I \* give/do not give permission for the University Library to ~~make photocopies for other libraries or individuals without my specific authorisation.~~ Note : Any prohibition on photocopying ~~will lapse~~ after five years from the date of deposit.

Signed Alexander N. McClymont  
 Date ..... 3 Feb 1976 .....

\* Strike out the sentence or phrase which does not apply.

# Determination of the Height of Hard X-ray Sources in the Solar Atmosphere by Measurement of Photospheric Albedo Photons\*

J. C. Brown, H. F. van Beek and A. N. McClymont\*\*

Space Research Laboratory of the Astronomical Institute, Utrecht

Received November 8, 1974

**Summary.** The importance and difficulties of determining the altitude of hard X-ray sources in the solar atmosphere are discussed. It is argued that the only unambiguous means of making this measurement is by utilising the photospherically scattered component of the radiation. Specifically, it is proposed that this can be done by measurement of the angular distribution of the large patch of photospheric albedo X-rays which is shown to accompany bright point primary X-ray sources.

Quantitative predictions are made of the brightness distribution of this albedo “image” and the practical feasibility of observing it is demonstrated in terms of the hard X-ray imaging spectrometer currently under development at the Space Research Laboratory in Utrecht.

**Key words:** Sun — X-rays — source heights

## 1. Introduction

Over the last decade, solar hard X-ray burst studies (at  $\geq 10$  keV) have made great progress in terms of all observables—intensity, time variations, spectra and polarisation (cf. reviews by Kane, 1974; Brown, 1974a)—with the exception of spatial resolution. Despite these advances, however, considerable controversy still surrounds the question of interpretive models of the hard X-ray flare (cf. Brown, 1974a). In particular, it remains unknown whether the bremsstrahlung X-rays are generated by electrons which:

- a) bombard the low chromosphere from above (the “thick-target” model—Brown, 1971, 1972a; Hudson, 1972 and others) as suggested by the synchronous chromospheric EUV bursts (Kane and Donnelly, 1971); or
- b) pass through the corona from below (the “thin-target” model—Datlowe and Lin, 1973) as suggested by interplanetary electron spectra; or
- c) are trapped in an oscillating coronal magnetic trap (the “electron-trap” model—Takakura and Kai, 1966; Brown, 1972b, 1973a) and so can readily explain the occurrence of “behind-the-limb” hard X-ray emission (Datlowe *et al.*, 1974), or

d) emit in the same region as they are produced—either as the continuously maintained high energy tail of a turbulent plasma region (cf. Hoyng *et al.*, 1974; Brown, 1974a) or as the Maxwellian electrons of a very hot, distributed temperature, plasma (Brown, 1974b).

The importance of distinguishing between these alternatives lies in the different interpretation they place on the process of fast electron generation in flares and on the total energy content of these electrons (and hence their role in overall flare energetics—cf. Brown, 1973b, 1973c). It currently seems likely that such a distinction must await the next generation of spaceborne hard X-ray detectors which will include spatial resolution—e.g. the instruments proposed for NASA’s Solar Maximum Mission—though, even then, imaging of a hard X-ray burst *on the disk* may not provide an unambiguous model assessment since the expected horizontal distribution of X-rays is dependent on the complex and unknown flare magnetic field geometry. Since, however, the above models predict source heights ranging from  $10^3$  km to  $10^5$  km above the photosphere (Brown and McClymont, 1975; McClymont, 1975), the ability to measure source height as well as horizontal location (or preferably both simultaneously) would be of great value in unravelling this problem. Direct resolution of the height of a source *at the solar limb* is, however, impossible with any projected instrumental resolution ( $\geq 5''$ ) for sources at the low end of the predicted height

\* Paper presented in summary at IAU/COSPAR Symposium 68 on “Solar  $\gamma$ -, X- and EUV-Radiation”, held in Buenos Aires, Argentina, June 11–14, 1974.

\*\* Currently on leave at Astronomy Center, University of Sussex, England.

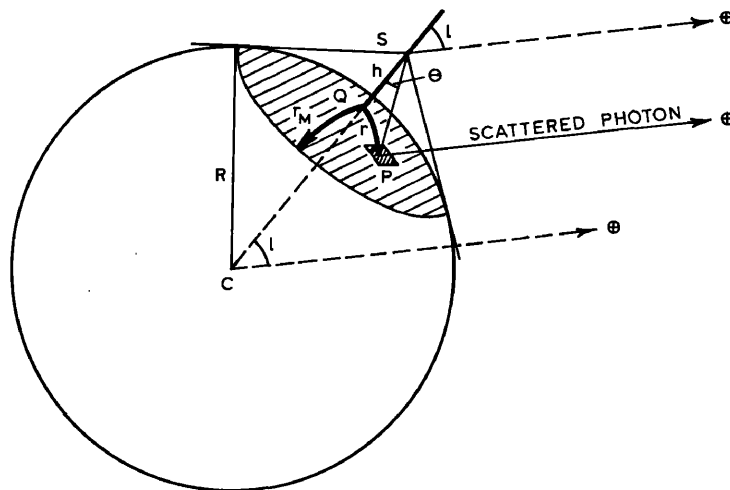


Fig. 1. Geometry of photospheric scattering of hard X-ray photons originating from a source  $S$ , at height  $h$ , showing a typical photon scattered to the earth ( $\oplus$ ) from point  $P$  at distance  $r$  from subsolar point  $Q$

range ( $10^3$  km  $\cong 1''.4$  at the earth) while, even for sources in the  $10^4$ – $10^5$  km range ( $14''$ – $2''.3$ ), this method cannot distinguish low sources located exactly at the limb from high sources near the limb since only a two-dimensional projection is actually observed.

To overcome this difficulty it is necessary to obtain some form of stereo observation of the source, such as from two satellites widely separated in space. Fortunately, however, the sun itself provides us with a ready means of achieving this with a single satellite. Tomblin (1972) and Santangelo *et al.* (1973) have shown that the dense photosphere Compton backscatters a large fraction of the photons from a hard X-ray source in the solar atmosphere. Though this is a scattering rather than a reflection process, it effectively provides a "mirror" behind the source of primary X-rays which can be considered as providing a parallactic "height-finder" in several ways. In this paper we propose one such method, based on direct angular resolution of the patch of albedo X-rays which accompanies any primary source, and demonstrate that the necessary measurements are in fact practicable by reference to the characteristics of the hard X-ray heliograph currently under development in the Space Research Laboratory, Utrecht, and proposed for the NASA Solar Maximum Mission.

Other methods have been suggested for source height determination which utilise the albedo component. In particular in a preprint of Santangelo *et al.* (1973) it was proposed that a sharp feature on the time profile of a solar X-ray burst would be "echoed" from the photosphere at time  $\Delta t = 2h/c$  later where  $h$  is the source height. Even for sources at  $h \approx 10^5$  km, however,  $\Delta t \approx 1$  s which is barely observable and, furthermore, the echoed feature would be greatly spread in time by scattering occurring over a wide area of the photosphere (cf. Section 2). Secondly, Brown *et al.* (1974) have suggested that the X-ray polarisation introduced by the

scattered component late in the flare (when the primary source may be unpolarised) is dependent on the scattering geometry and so might permit inference of the source height. Detailed calculations (McClymont, 1975) show, however, that the effect is probably too small to be used reliably. And, finally, Acton (private communication) has pointed out that if spatially resolved X-ray polarimetry were feasible, the distribution of polarisation across the albedo patch might indicate the source height. McClymont's (1975) calculations show that this is indeed the case but that high polarimetric accuracy would have to be combined with a few arc seconds resolution to succeed in the measurement. Since such measurements are beyond available instrumentation, we are of the opinion that the technique proposed here is the only one feasible at present.

## 2. Spatial Distribution of the Albedo Photons

Tomblin (1972) and Santangelo *et al.* (1973) have investigated the effect of the photospheric backscattering on the spectrum and intensity of total X-rays received at the earth from a burst, but have not explicitly considered the spatial distribution of the scattered radiation. It is found that the peak reflectance occurs in a broad energy range from about 15 to 50 keV, and ranges from 80% down to 30% (= ratio of total scattered flux to primary flux) for bursts near disk centre to bursts near the limb (Fig. 1 of Santangelo *et al.*, 1973). (These reflectances only vary slightly with the primary source height—McClymont, 1975.) The optimum energy range for albedo observations is, therefore, about 15 keV and above since at lower energies the reflectance falls due to photoelectric absorption in the photosphere while at higher energies the flux (both primary and scattered) falls due to the steep photon spectra involved. The optimum thus corresponds well

with the highest channel (15–20 keV) of the Utrecht heliograph (Section 3).

Figure 1 shows the geometry of photospheric scattering for a primary source  $S$  at height  $h$  (km), angular distance  $l$  from the disk centre as seen from the earth ( $\oplus$ ). An immediately obvious feature is that the patch of albedo radiation extends only as far as the solar horizon seen from  $S$ —i.e. over a disk of radius  $r_m \simeq (2hR)^{1/2}$  (for  $h \ll R$ ). Defining  $\varrho_m$  and  $\zeta$  as the angles subtended at the earth by distances  $r_m$  and  $h$  at the sun respectively, we find

$$r_m(\text{km}) \simeq 1.2 \times 10^3 \sqrt{h(\text{km})}$$

and

$$\varrho_m'' \simeq 1.57 \sqrt{h(\text{km})} \simeq 43.8 \sqrt{\zeta''}.$$

Thus for source heights  $h = 10^3$ ,  $10^4$  and  $5 \times 10^4$  km the angles  $\zeta$  (height of primary source seen at limb) are only about  $1''.3$ ,  $13''$  and  $65''$  respectively while the albedo extends over radii  $\varrho_m$  of  $49''.6$ ,  $157''$  and  $351''$  on the sun respectively. Hence observation of this patch requires much less spatial resolution than needed to resolve the source height itself—the essential advantage of the method. Furthermore, the available evidence both direct (Takakura *et al.*, 1971) and indirect (Zirin and Tanaka, 1973) indicates that the primary hard X-ray source itself is of small horizontal extent so that the method is unlikely to be vitiated by obscuration of the albedo distribution by the primary emission. In principle, therefore, we need only measure the size of the whole albedo area (circular at disk center, elliptical otherwise) in order to obtain  $\varrho_m$  and hence  $h$ . In practice, the albedo brightness falls off rapidly with distance from its center and the area over which albedo measurements can be made depends on the detailed distribution of brightness within the albedo boundaries in relation to the sensitivity and contrast limitations of the heliograph employed.

From the whole albedo area the X-ray flux at the earth is  $I_1 = fI_0$  where  $f$  is the reflectance and depends on the solar central distance  $l$  (Santangelo *et al.*, 1973), and  $I_0$  is the primary source flux, assumed for the moment to be isotropic (cf. Section 4). The distribution within this area is affected by three factors. Firstly the primary radiation incident per unit scattering area at  $P$  (Fig. 1) drops off like  $x^{-2} \simeq (h^2 + r^2)^{-1}$  due to the inverse square law and secondly like  $\cos\theta \simeq h/(h^2 + r^2)^{1/2}$  due to the angle of incidence increasing. (Curvature of the solar surface is neglected here since it affects only the edges of the distribution which are too faint to be observed.) Thirdly, the distribution is affected by the directivity of the scattering process itself. In a single Compton scattering, however, the anisotropy is fairly weak (Tomblin, 1972) while multiple scattering, as involved here (Santangelo *et al.*, 1973), reduces it still further. Neglecting this latter effect (cf. Appendix) therefore, and noting that the scattering area subtends  $2\pi$

steradians at the source  $S$  (since  $h \ll R$ ), we readily find that the brightness of the albedo area at angular distance  $\varrho$  from  $Q$  is

$$dI_1(\text{counts cm}^{-2} \text{ arcsec}^{-2}) \simeq \frac{fI_0}{2\pi} \frac{\zeta}{(\varrho^2 + \zeta^2)^{3/2}} \quad (2)$$

for a source at the disc center, with circular iso-brightness contours. Here we will only consider the disk center case, which has the simplest geometry, in order to establish the feasibility of the measurements. (In the appendix we present typical results of detailed calculations for a general case.) Though the reflectance  $f$  is maximal at the disk center ( $\simeq 0.6$  at 15–20 keV), it will not in fact be over-optimistic to consider this case since, near the limb (e.g.  $l = 70$ – $80^\circ$ ), the reduced reflectance ( $f \simeq 0.3$ ) will be partly compensated by the enhancement of surface brightness seen in projection (increased by a factor  $\sec l$ —i.e. about 4 times). Thus with  $f = 0.6$  we have

$$\frac{dI_1}{I_0}(\text{arcsec}^{-2}) \simeq 0.095 \frac{\zeta}{(\varrho^2 + \zeta^2)^{3/2}} \quad (3)$$

with  $\zeta$  and  $\varrho$  in arcsec.

Two instrumental factors will limit the area over which the albedo patch accompanying a primary source point will be visible, namely the instrumental response profile to the primary source (i.e. the “crosstalk” between the picture element containing the primary source and surrounding elements), and the background level above which the albedo counts have to be detected. In the following section we describe the main features of the Utrecht heliograph and establish the necessary characteristics.

### 3. Instrumentation

In June 1974, the Space Research Laboratory at Utrecht, the Netherlands, proposed a Hard X-ray Imaging Spectrometer for the NASA Solar Maximum Mission (SMM). The main characteristics of the instrument are:

- spatial resolution:  $8 \times 8$  arcsec square (FWHM) per image element
- field of view:  $4.3 \times 4.3$  arcmin square ( $32 \times 32$  image elements)
- energy range: 3.5–20 keV
- energy bands: 3.5–5.5, 5.5–8, 8–11, 11–15, 15–20 keV
- energy resolution: 18% at 6 keV
- detector efficiency: 3.5 keV: 50%; 8 keV: 90%; 20 keV: 50%
- effective collimator area:  $4.0 \text{ mm}^2$  per image element
- temporal resolution: varying from 2 to 80 seconds depending on the mode of operation.

The great advantage of the instrument is that it produces two-dimensional pictures in a photon energy range where grazing incidence techniques cannot be



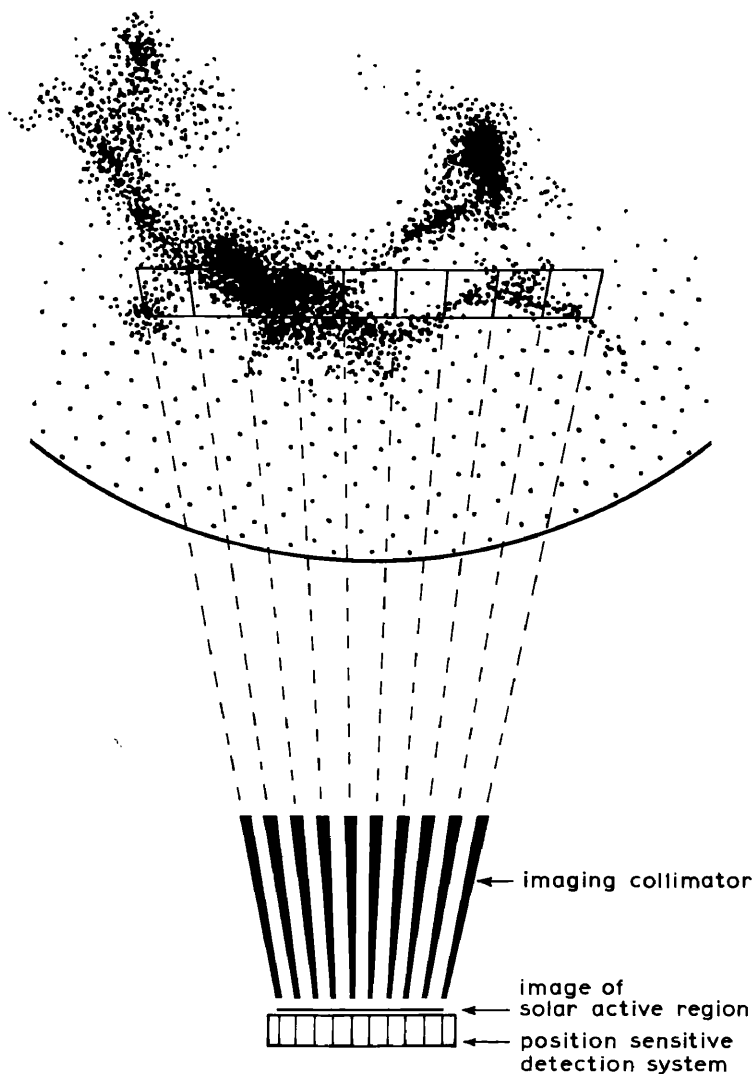


Fig. 2. Schematic impression of operation of the proposed instrument forming an image of the hard X-ray sun. The many X-ray bright points and extended sources would be expected (from grazing incidence results) to be typical of lower energies. As discussed in the text, the 15–20 keV band is expected to involve much smaller, isolated, sources, as required by the height determination technique proposed here. Note that only one row of 9 subcollimators is shown. The entire collimator consists of  $32 \times 32$  subcollimators

applied, but without the need for rotating or scanning movements of heavy parts of the instrument.

The operation of the instrument is shown schematically in Fig. 2.

Its basic elements are an imaging collimator, a position sensitive detector system, and the accompanying electronics. The imaging collimator produces an image of the solar active region on the entrance window of the detector, the latter having the capability to locate the position of the entering photons. This image consists of 1024 elements, grouped in a two-dimensional pattern of 32 rows and 32 columns. In fact, the entire imaging collimator is built up out of an array of 1024 subcollimators, compactly packed together and each having a field of view of  $8 \times 8$  arcsec square (FWHM). The subcollimator axes are offset so as to make angles of 8 arcsec between neighbouring pairs in two mutually perpendicular directions, resulting in a total field of view for the instrument of  $4.3 \times 4.3$  arcmin square.

In practice the 1024 subcollimators do not exist as separately demountable units, but are created by a suitable arrangement of patterns of holes in 10 collimator plates, kept in position by a stiff mechanical structure. Tungsten has been chosen as the plate material since its radiation absorption characteristics are well suited to the required energy range and for its good mechanical properties.

The detector system used is not a conventional position sensitive proportional counter devices. Instead, it consists of an array of 1024 separate detectors, each corresponding to one particular subcollimator. These small detectors, which have been named mini-proportional (mp) counters, represent a new development which started in the middle of 1973 at the Space Research Laboratory at Utrecht. Here, only a short explanation of the counters will be presented, an extensive description being given elsewhere (Van Beek, to be published).

The entire detector system consists of an entrance window, which covers all 1024 mp counters, and a grid behind which lies an array of spherical anodes, one situated below each grid hole. Photons are absorbed in the space between the entrance window and the grid to form primary electrons which drift towards the avalanche rooms in between the grid and the balls. Gas amplification starts in the neighbourhood of the balls to which the high voltage is applied. Dimensions of one counter are: height = 6 cm (distance between entrance window and the grid); sensitive area =  $0.625 \times 0.625 \text{ cm}^2$ . The Xe-filling will be at a pressure of 1.2 atm. The mp counters are connected to pre-amplifiers one per row and one per column in order to determine which one of the mp counters has detected a photon, a photon event being recorded when only one row and one column yield pulses. Thus the mp counters operate in an anti-coincidence mode relative to each other per row and per column. Pulse height analysis of the counter outputs is carried out with discriminators to define the energy channels (cf. list of instrument characteristics). For the albedo measurements the energy range 11 to 20 or 15 to 20 keV will be used.

In principle the instrument makes pictures of an active or flaring region for each of the five energy bands at the same time. The temporal resolution of the instrument depends only on the counting statistics, i.e. the minimum number of counts required for accepting the information as reliable. It is estimated that even for modest flares a temporal resolution capability of 2 s can be claimed for the production of pictures. For measuring the albedo radiation profile with sufficient accuracy, however, integration over periods up to 30 s may be necessary for moderate events. During the data reduction phase these integration periods can be chosen optimally by looking at the pictures produced every 2 s. So, spurious interpretation of albedo measurements due to local shifts or dimensional changes of the flaring region can be corrected or rejected.

Two characteristics of the instrument are of special importance in connection with the measurement of albedo radiation. These characteristics are: the contrast of the pictures produced by the instrument and the background count rate of the detector system.

#### Contrast of the Pictures

The contrast of the pictures obtained is found to depend mainly on the characteristics of the imaging collimator. Considering the case of a point source on the Sun, ideally only one subcollimator looking at that source should be open for radiation. In practice some "leakage" radiation will penetrate through the collimator plates at places where other subcollimators are located. The relative intensity of this radiation is given by the dashed curve in Fig. 3 as a function of the viewing angle  $\varrho$  of a subcollimator relative to that of the subcollimator open for radiation. It will be obvious

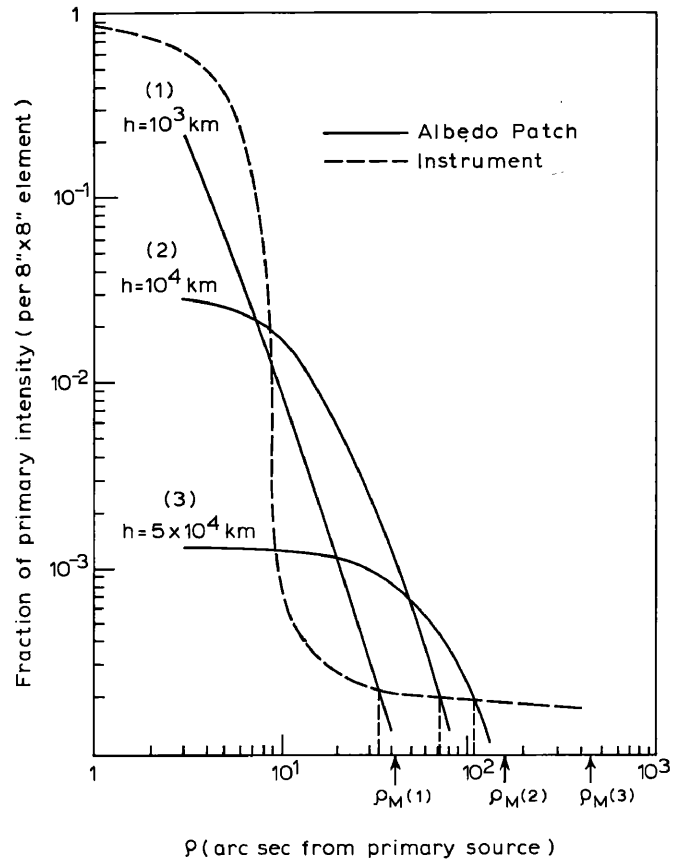


Fig. 3. Instrumental response profile (dashed curve) to a point source in terms of the intensity per image element ( $8'' \times 8''$ ) at angular distance  $\varrho''$  from the primary point relative to that of the primary image element. Superposed (solid curves) are predicted intensity distributions for the photospheric albedo radiation originating from three point X-ray sources at different heights  $h$  above the photosphere. Arrows on the  $\varrho$  axis indicate the theoretical albedo limit  $\varrho_m$  (solar horizon) for each height which may be compared with the instrumental detection limits  $\varrho_0$  (dashed vertical lines)—cf. Table 1

that albedo radiation can only be observed when it is more intense than the leakage radiation.

Secondly the high contrast required for the flare pictures puts stringent requirements on the detector system regarding the reliability of position determination of the detected photons. Even at high count rates the relative number of incorrect position determinations must be small to preserve good contrast. In this respect the mp counter array is superior to a conventional position sensitive detector system because the photon location is here a question of which detector has been triggered and not where an interaction has taken place in one detector. The method applied to assign the activated mp counter can then be completely digital and also fast. Analog electronics used in a number of conventional position sensitive detector systems on the other hand can be confused if two photons are detected at, or about, the same moment resulting in an irrelevant position determination unless special precautions have been taken. In the case of a mp counter set-up, "double" events are easily recognized and rejected.

Table 1

Source height		Albedo visible over instrument profile within radius $\varrho_0$ (arcsec)	No. of image elements within $\varrho_0$	Nos. of counts in 30 s			Variance in $n_{AL}$ $\sigma = ((n_{AL} + n_{BG} + n_{CT})/n_{AL})^{1/2}$
$h$ (km)	$\varrho$ (arcsec)			Albedo counts $n_{AL}$	Background counts $n_{BG}$	Cell leakage plus crosstalk counts $n_{CT}$	
$10^3$	1"37	34"	53	82	8	18	14%
$10^4$	13"7	71"	244	472	37	71	6%
$5 \times 10^4$	68"7	110"	590	332	89	166	9%

A further characteristic of a mp counter array is that it cannot be confused by a single photon event when, after a first interaction of the photon in the system, the *K* or *L* photon formed is absorbed elsewhere in that system. The mp counter array will interpret such events as two-photon events and will reject them as such.

#### Background Count Rate

The maximum background count rate per mp counter acceptable during the albedo radiation measurements depends on:

- the intensity of the albedo radiation over the area where the albedo radiation exceeds the collimator leakage radiation.
- the integration time allowed for performing one measurement.

Estimating that, for adequate statistics, some hundreds of albedo counts should be collected within 30 s over an area of 600 image elements at maximum, the background count rate should be less than  $5 \times 10^{-3}$  ct/s per mp counter.

Preliminary calculations show that this low background count rate can be achieved because the mp counters are operating in an anti-coincidence mode relative to each other. All cosmic particles which pass through more than one mp counter will therefore be ignored, while particles travelling parallel to the axis of a mp counter will generate a pulse exceeding the 20 keV level. Fast electrons ejected from the walls by gamma radiation or those resulting from gamma ray interactions in the gas will be subjected to the same anti-coincidence procedure. The residual background count rate will result mainly from low energy Compton electrons produced in the counter gas by gamma radiation and, to a much lesser extent, from Compton electrons ejected out of the grid material or the entrance window. The resulting background count rate proves to be very low since these electrons rarely have an energy falling within the instrument's energy range.

#### 4. Discussion and Conclusions

Superposed on the instrumental response profile to a point source at the disk centre in Fig. 3 are the results of Eq. (3) for the albedo brightness distribution relative

to the primary source brightness, for source heights  $h$  of  $10^3$ ,  $10^4$  and  $5 \times 10^4$  km. Results are in terms of fractional intensity per  $8'' \times 8''$  picture element as a function of the distance  $\varrho''$  from that element to the primary flare point.

Evidently the albedo is observable over a large number of picture elements though not over the entire area of photospheric scattering i.e. out to the solar horizon at  $\varrho_m$  (see Fig. 3). Table 1 lists the actual radii  $\varrho_0$  and the corresponding number of image elements, over which the albedo is visible above the instrumental profile, for each height.

Considering next the question of statistics, we take  $1300 \text{ photons cm}^{-2} \text{ s}^{-1}$  in 15–20 keV as typical of a moderate sized flare. Then with the instrumental background of  $5 \times 10^{-3} \text{ cts. s}^{-1}$  per mp counter quoted in Section 3, we find the % variances in the albedo count as shown in Table 1 after an integration time of 30 s. This is shorter than the average duration of such a typical burst and than the time scale on which the source height itself is expected to change. Since the instrumental time resolution is much less than this integration time, and since the satellite pointing will be continuously known to an accuracy of several arc seconds, no difficulty arises in integration of counts over this period. In larger flares, proportionately shorter times are sufficient for adequate albedo measurement. For very small flares, the burst duration may not be adequate to obtain sufficient accuracy.

Examination of Fig. 3 shows the limitations on the source height range detectable by means of the Utrecht instrument. Clearly for X-ray flares at heights  $\ll 10^3$  km, the albedo area is too small to be resolved while for flares at  $\geq 5 \times 10^4$  km the albedo is distributed over too large an area for its surface brightness to be accurately measurable. In this latter case, however, there may be a further possibility to utilise the albedo by determining only the centroid position of the albedo counts. Since this lies at the subsource point *Q* in Fig. 1, the measured angular distance between *Q* and the primary source *S* will yield the quantity  $h \cos l$  and hence  $h$  for flares not too near disk center (see Fig. 5, as discussed below).

We conclude that for the expected range of heights of hard X-ray flares, the albedo method we propose is capable of accurately inferring the height of a small

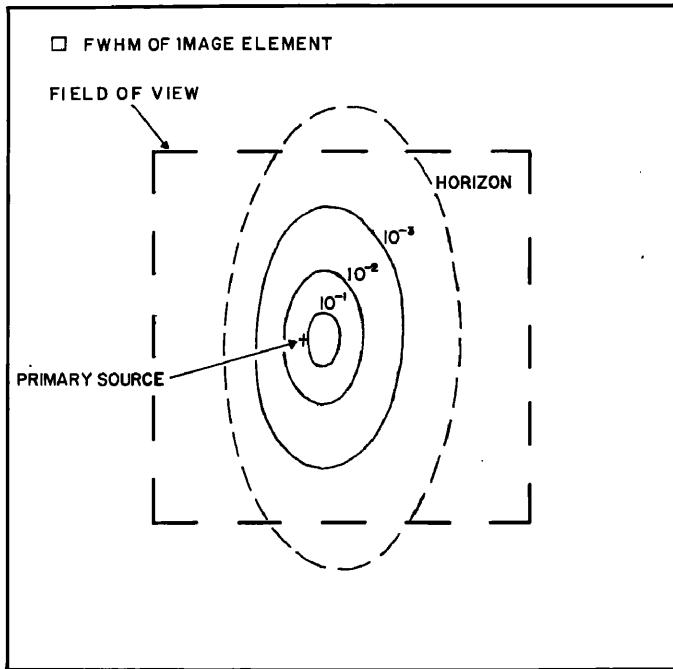


Fig. 4. Albedo count distribution computed for a primary source at height  $h=10^4$  km and  $60^\circ$  from disk center, using the anisotropic Compton cross-section. The results are in the form of isobrightness contours, brightness as a fraction of the primary source flux per image element ( $8'' \times 8''$ ). The size of one image element and of the total field of view of the Utrecht heliograph are indicated

source and so leading to considerable progress in the related flare problems discussed in Section 1.

Finally there are a number of idealisations in the preceding discussion which must be taken into account in any actual implementation of the proposed technique and which warrant at least brief discussion here.

Firstly our assumption of an isotropic primary source is not necessarily valid (cf. Elwert and Haug, 1971, 1972; Brown, 1972a). However, by comparison of the total intensity of all the albedo photons with the primary source intensity, the extent of downward (or upward) beaming of primary photons can be inferred and the effect of the primary source anisotropy on the albedo distribution corrected (cf. McClymont, 1975).

Secondly, we have considered only the case of a source at disk centre and treated Compton scattering as isotropic. Actual data analysis will have to be carried out by comparing results with theoretical albedo distributions for off-centre sources and for the true Compton cross-section. Typical computational results for such theoretical distributions (from McClymont, 1975) are shown as isobrightness contours in Figs. 5 and 6 for  $h=10^4$  km and  $h=5 \times 10^4$  km respectively, at  $60^\circ$  from the disk centre. The details of data reduction procedure, based on optimising the fit between data and computational models, are still to be worked out. This may be generalised to cover the case of more than one primary source being present at the time of observation, though at the relatively high photon energy chosen

this should be less of a problem than at more thermal energies.

Lastly perhaps the most important factor is our supposition of a point primary source. Though such observations as are available, both of hard X-rays directly (Takakura *et al.*, 1971) and of synchronous impulsive emissions such as microwaves (Vorpahl, 1973; Enome and Tanaka, 1973) and UV (Neupert *et al.*, 1974), are strongly indicative of a small source size, the possibility of significant source extension cannot be altogether excluded at present. (We would reiterate that by "significant" here we mean of a size which is a substantial fraction of the figures for  $\varrho_0$  shown in Table 1.) Two cases of importance arise which could lead to complication of an extended image supposedly of albedo origin (a) extension of the source in height; (b) horizontal source extension. We briefly assess the effect of these here.

#### a) Primary Source Extended in Height

Consider, for example the case of a "line" source uniform in brightness between heights  $h_1$  and  $h_2$  (corresponding to  $\zeta_1, \zeta_2$ ). Then Eq. (3) has to be replaced by one integrated between these limits and is found to give

$$\frac{dI_1}{I_0} = \frac{0.095}{\zeta_1 - \zeta_2} [(q^2 - \zeta_1^2)^{-1/2} - (q^2 - \zeta_2^2)^{-1/2}]$$

$$\simeq \frac{0.095}{\zeta_1 \zeta_2} \quad \text{for } q \ll \zeta \quad (4)$$

and

$$\simeq 0.095 \times \frac{1}{2} \frac{\zeta_1 + \zeta_2}{q^3} \quad \text{for } q \gg \zeta. \quad (5)$$

That is, the albedo photons are distributed *near* the primary source like the case of a point primary source at the *geometric mean* height  $\sqrt{h_1 h_2}$  of the extended source [Eq. (4)] while *distant* from the primary source the distribution is like that from a point source at the *arithmetic mean* height  $(h_1 + h_2)/2$  of the extended source [Eq. (5)]. Thus, since the method is based in practice principally on measurements at  $q \gg \zeta$ , the arithmetic mean height would be inferred.

#### b) Primary Source Horizontally Extended

Here we take the example of a primary source of zero vertical extent but *uniformly* distributed horizontally over a circular area, angular radius  $\varrho_s$ . Then integration of (3) over this finite primary source leads to a total albedo distribution

$$\frac{dI_1}{I_0} \simeq \left( \frac{dI_1}{I_0} \right)_{\text{point source}} \times \left( 1 + \frac{15}{8} \left( \frac{\varrho_s}{q} \right)^2 \right) \quad (6)$$

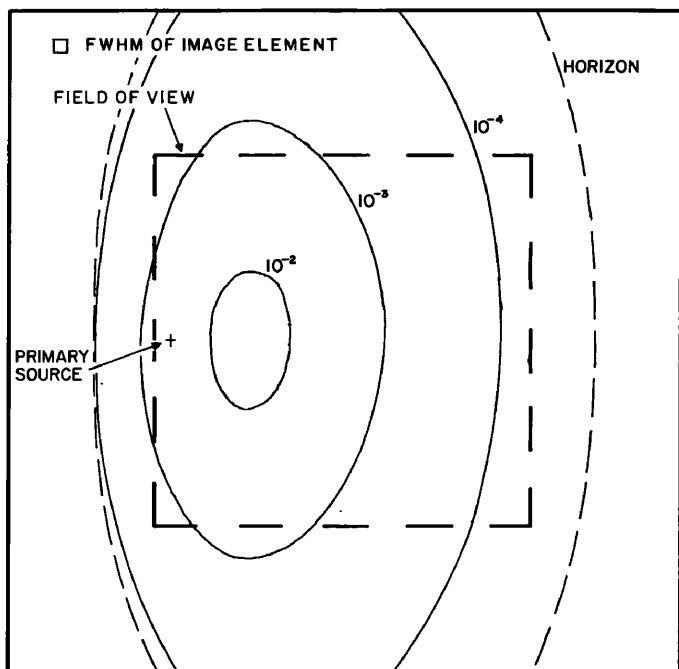


Fig. 5. As Fig. 4 but for  $h = 5 \times 10^4$  km

provided again that  $\varrho \gg \zeta$  and that  $\varrho_s$  is smaller than  $\varrho$ . This means that for a source at  $h = 10^4$  km, the error in direct application of (3) to the albedo distribution would have an error less than 20% provided the horizontal extent  $\varrho_s$  of the primary source did not exceed about  $20''$  while for  $h = 5 \times 10^4$  km, we must have  $\varrho_s \leq 35''$ , neither of which requirements seems over-severe.

In conclusion it should be added that here we have only considered the order of magnitude of the effects of finite primary sources. In the real case we can gain considerable advantage from our knowledge of the theoretical *shape* [Eq. (3) and Figs. 4 and 5] of the albedo from a point source and utilise this to reduce ambiguities due to deviation from this idealised case by optimal fitting.

*Acknowledgements.* We would like to acknowledge the support of ESRO and of the Dutch National Committee for Geophysics and Space Research (J.C.B.) and of a British S.R.C. Studentship (A. N. McC.) during this work.

## References

- Brown, J.C. 1971, *Solar Phys.* **18**, 489  
 Brown, J.C. 1972a, *Solar Phys.* **26**, 441  
 Brown, J.C. 1972b, *Solar Phys.* **25**, 158  
 Brown, J.C. 1973a, *Solar Phys.* **32**, 227  
 Brown, J.C. 1973b, *Solar Phys.* **31**, 143  
 Brown, J.C. 1973c, Proc. Leningrad Symp. Solar Cosmic Rays, June 1973  
 Brown, J.C. 1974a, in S. R. Kane (ed.), Solar  $\gamma$ -, X- and EUV-Radiation, Proc. IAU Symp. 68 (Buenos Aires, June 1974)  
 Brown, J.C. 1974b, in G. A. Newkirk (ed.) *Coronal Disturbances*, Proc. IAU Symp. 57 (Surfer's Paradise, Sept. 1973)  
 Brown, J.C., McClymont, A.N., McLean, I.S. 1974, *Nature* **247**, 448  
 Brown, J.C., McClymont, A.N. 1975, *Solar Phys.* **41**, 135  
 Datlowe, D.W., Lin, R.P. 1973, *Solar Phys.* **32**, 459  
 Datlowe, D.W., Elcan, M.J., Hudson, H.S. 1974, *Solar Phys.* **39**, 155  
 Elwert, G., Haug, E. 1971, *Solar Phys.* **15**, 234  
 Elwert, G., Haug, E. 1972, *Solar Phys.* **20**, 413  
 Enomé, S., Tanaka, H. 1973, in Ramaty and Stone (eds.) *High Energy Phenomena on the Sun*, GSFC, X-693-73-193  
 Hoyng, P., Brown, J.C., Stevens, G.A., van Beek, H.F. 1974, in S. R. Kane (ed.), Solar  $\gamma$ -, X- and EUV-Radiation, Proc. IAU Symp. 68 (Buenos Aires, June 1974)  
 Hudson, H.S. 1972, *Solar Phys.* **24**, 414  
 Kane, S.R., Donnelly, R.F. 1971, *Astrophys. J.* **164**, 151  
 Kane, S.R. 1974, in G. A. Newkirk (ed.) *Coronal Disturbances* Proc. IAU Symp. 57 (Surfer's Paradise, Sept. 1973)  
 McClymont, A.N. 1975, Ph. D. thesis, University of Glasgow  
 Neupert, W.M., Thomas, R.J., Chapman, R.D. 1974, *Solar Phys.* **34**, 349  
 Santangelo, N., Horstman, H., Horstman-Moretti, E. 1973, *Solar Phys.* **29**, 143  
 Takakura, T., Kai, K. 1966, *Publ. Astron. Soc. Japan* **18**, 57  
 Takakura, T., Okki, K., Shibuya, N., Fujii, M., Matsuoka, M., Miyamoto, S., Nishimura, J., Oda, M., Ogawara, Y., Ota, S. 1971, *Solar Phys.* **16**, 454  
 Tomblin, F.F. 1972, *Astrophys. J.* **171**, 377  
 Vorpahl, J.A. 1973, in Ramaty and Stone (eds.) *High Energy Phenomena on the Sun*, GSFC X-693-73-193  
 Zirin, H., Tanaka, T. 1973, *Solar Phys.* **32**, 173

J. C. Brown  
 A. N. McClymont  
 Department of Astronomy  
 University of Glasgow  
 Glasgow G12 8QQ, Scotland, UK

H. F. van Beek  
 Space Research Laboratory of the Astronomical Institute  
 Beneluxlaan 21  
 Utrecht, The Netherlands

HARD X-RAY EMISSION  
AND  
MASS MOTION  
IN SOLAR FLARES

by

Alexander N. McClymont

Thesis  
submitted to the  
University of Glasgow  
for the Degree of  
Ph.D.

Department of Astronomy  
University of Glasgow  
Glasgow, G12 8QW

• January 1976

## SUMMARY

Solar flares are perhaps the most remarkable transient events within the solar system. A century of observation has done little to elucidate their true nature. Their secrets are hidden even from the sophisticated satellite experiments which have kept up an intensive surveillance for the last decade. These experiments have, however, produced an indigestible mass of data. From these we must try to synthesis an overall picture of the flare and identify the physical processes responsible.

In this thesis two aspects of the flare problem are considered. The first concerns hard X-ray emission during the impulsive phase of the flare. The electron trap model of the hard X-ray source is analysed in detail and the predicted directivity and polarisation of its emission found to be compatible with hard X-ray observational data. Secondly, a self-consistent model of the soft X-ray flare is developed. Mass motion, which has previously been ignored in such models, is shown to be of vital importance.

In Chapter I, the observational evidence concerning all types of flare emission is summarised. The coherency of a picture of the flare in which energetic electrons play a central part is pointed out and the significance of hard X-ray emission as an indicator of the properties of these electrons noted. Current hard X-ray source models are described in Chapter II and their predictions for the flare X-radiation outlined. Other topics of importance to the hard X-ray problem - bremsstrahlung radiation, the albedo effect and modulation of the X-ray flux - are also discussed here. Finally, the predictions of the source models are compared with observation and important areas of experimental and theoretical research suggested.

The electron trap hard X-ray source model is analysed in Chapter III. This model, whose properties have only been guessed at until now, postulates that high energy electrons are trapped in a coronal magnetic arch where they emit bremsstrahlung radiation while decaying

collisionally on the time scale of the hard X-ray burst decay. Directivity and polarisation of the emission are predicted for a variety of trapped electron distributions over energy and pitch angle. Predicted properties of the hard X-ray emission are presented in Chapters IV and V. Chapter IV is concerned with the total X-ray flux from the trap while Chapter V deals with some aspects of the spatially resolved emission, in particular the predicted "behind-the-limb" X-ray flux. In both chapters, results are compared with the observational data available and observations which could help to discriminate between this and other source models suggested.

In Chapter VI a model of the soft X-ray flare is developed. The model consists of a high density coronal filament into the centre of which energy is injected during the impulsive phase of the flare. First, the potential importance of mass motion in this situation is demonstrated by dimensional analysis. Then a numerical treatment of the fluid dynamic equations is developed. Computational results describing the evolution of the filament, under a variety of conditions, are presented in Chapter VII. Conclusions drawn from the dimensional analysis are vindicated and deeper insight into the energy transport processes operating in the filament obtained. The soft X-ray differential emission measure is examined and it is suggested that the form is compatible with that inferred from observation.